

Contrails

AFML-TR-65-331

Cleared: December 7th, 1972

Clearing Authority: Air Force Materials Laboratory

FINAL REPORT ON
SHIELDED CERAMIC COMPOSITE STRUCTURE

Donald L. Kummer, Jerome J. Rosenthal,
David W. Lum, et al

TECHNICAL REPORT AFML-TR-65-331

OCTOBER 1965

1. Summary of Report

*** Export controls have been removed ***

11-22-72

ADVANCED FABRICATION TECHNIQUES BRANCH
AIR FORCE MATERIALS LABORATORY
RESEARCH AND TECHNOLOGY DIVISION
AIR FORCE SYSTEMS COMMAND.
UNITED STATES AIR FORCE
WRIGHT-PATTERSON AIR FORCE BASE, OHIO

This document is subject to special export controls and each transmittal to foreign governments or foreign nationals may be made only with prior approval of the Manufacturing Technology Division.

FOREWORD

This Final Technical Documentary Report covers all work performed under Contract AF33(657)-10996 from 1 June 1963 through 18 June 1965. The manuscript was released by the authors on 31 October 1965 for publication as an RTD Technical Documentary Report.

This project was performed by the Material and Process Development Department, General Engineering Division, McDonnell Aircraft Corporation (MAC), under Manufacturing Methods Project No. 7-997, "Shielded Ceramic Composite Structure." It was accomplished under the technical direction of Mr. Carl A. Tobin of the Advanced Fabrication Techniques Branch (MATF-2) Manufacturing Technology Division, Air Force Materials Laboratory, Wright-Patterson Air Force Base, Ohio.


Mr. Donald L. Kummer, Chief Ceramic Engineer, Material and Process Development Department, was the MAC Project Leader. Co-operating in the research and preparation of the report were: B. Fitzgerald, D. Lum, and J. Rosenthal (Material and Process Development); E. Stifel, A. Lopatin, and D. Hartbauer (Design); J. Hrinsin and R. Garrett (Strength); P. Beardsley and D. Schofield (Thermodynamics); and T. Coyle, J. Holliday, E. Kuhl, R. Merkel, and E. Malakelis (Structures Laboratory). All ceramic machining was accomplished by the Electromechanical Department, and the refractory metals fabrication and coating work was performed by the Manufacturing Division. This report has been given the MAC internal number A131.

Project 7-997 was accomplished as part of the Air Force Manufacturing Methods Program. The primary objective of the Manufacturing Methods Program is to develop, on a timely basis, manufacturing processes, techniques, and equipment for use in economical production of USAF materials and components. The project encompasses the following technical areas:

Ceramics, Refractory Materials, Thermal Insulation, Thermal Protection, Low Density Ceramics, Chemically Bonded Ceramics, Refractory Composite Structures, Thermal Shock Tests, Glide Re-entry Trajectory Analyses, Heat Transfer Analyses, Structural Analyses, Non-Metallic Materials, Metallic Materials, and Component Fabrication.

Your comments are solicited on the potential utilization of the information contained herein as applied to your present or future production programs. Suggestions concerning additional Manufacturing Methods development required on this or other subjects will be appreciated.

This report has been reviewed and is approved.


C.H. NELSON
Asst. Chief
Manufacturing Technology Division
AF Materials Laboratory

ABSTRACT

SHIELDED CERAMIC COMPOSITE STRUCTURE

Donald L. Kummer, Jerome J. Rosenthal,
David W. Lum, et al

Alumina, zirconia, and thoria were selected for use in composite ceramic heat shields for the leading surfaces of lifting orbital re-entry vehicles. Coated columbium and molybdenum were selected for substructure materials. Commercially available low density ($< 40\%$ of theoretical) and high density ($> 60\%$ of theoretical) alumina, zirconia, and thoria ceramics were evaluated for thermal shock resistance; and many high density, but no low density ceramics were found to be satisfactory. A sintered low density (95 lb/ft^3) thermal shock resistant zirconia was developed, but it was difficult to reproducibly manufacture. A sintered low density (125 lb/ft^3) thoria was developed that had low thermal shock resistance but could be reproducibly manufactured. Chemically bonded low and high density thermal shock resistant varieties of alumina, zirconia, and thoria were developed. Thermophysical properties were determined to temperatures as high as 4500°F for the ceramics utilized in this project. Analytical techniques were derived for predicting the thermal stress behavior of ceramics. Twenty-two subscale heat shield modules and three full size components were designed, fabricated, and environmentally tested. The full size components were a 3.0 inch radius, 3400°F leading edge; a 1.5 inch radius, 4000°F leading edge; and a 6.0 inch radius, 5000°F nose cap. The ceramic phase densities for these components were 57 lb/ft^3 , 97 lb/ft^3 , and 166 lb/ft^3 respectively. Satisfactory techniques were developed for processing, fabricating, and assembling ceramic heat shields. Typical launch vibration and acoustical environmental conditions were not found to be critical, but re-entry thermal environment was found to be very critical. A MAPP-OX thermal test facility was developed for full scale testing. The 1.5 inch radius leading edge survived thermal testing although testing was prematurely terminated due to a test fixture failure. During thermal testing, the 3.0 inch radius leading edge cracked but remained intact and did not spall; and the 6.0 inch radius nose cap underwent severe surface erosion. These two failures were attributed to a combination of design and material shortcomings and the severity of the MAPP-OX thermal test environment.

Note: Page iv is a blank page.

TABLE OF CONTENTS

<u>Section</u>	<u>Page</u>
I INTRODUCTION.	1
II SUMMARY	3
III CONCEPTUAL VEHICLE AND TRAJECTORY SELECTION	9
3.1 Re-Entry Equilibrium Temperatures.	9
3.2 Typical Re-Entry Trajectories.	15
3.3 Selection of Design Trajectories	15
IV MATERIALS	19
4.1 Material Property Survey	19
4.2 Ceramic Screening Tests.	24
4.3 Low Density Sintered Refractory Oxide Development.	51
4.4 Chemically Bonded Refractory Oxide Development	79
4.5 Determination of Material Properties	109
4.6 Materials Selections and Control for Full Scale Components	125
V DESIGN, FABRICATION, AND TESTING.	127
5.1 Stage 1 - Basic Design Concepts and Preliminary Layouts	127
5.2 Stage 2 - Subscale Design, Fabrication, and Testing	138
5.3 Stage 3a - Design and Fabrication of Full Scale Components.	195
5.4 Stage 3b - Full Scale Component Tests	228
VI THERMAL ANALYSES.	251
6.1 Methods of Analysis.	251
6.2 Thermal Models for Full Scale Components	254
6.3 Results of Temperature Analyses.	259
6.4 Thermal Analytical Model	273
6.5 Instrumentation of Full Scale Components	273
VII STRUCTURAL ANALYSES	277
VIII CONCLUSIONS	283
IX RECOMMENDATIONS	287
APPENDIX I - Environmental Test Procedures and Equipment	289
APPENDIX II - Thermophysical Property Measurement Methods and Apparatus	307
APPENDIX III - Analytical Thermal Model.	351
APPENDIX IV - Stresses Within a Ceramic Body During Rapid Heating	363
REFERENCES.	395
DISTRIBUTION LIST	397

LIST OF ILLUSTRATIONS

		Page
1.	Aerodynamic Characteristics of Modified Delta Wing Configuration . . .	10
2.	Leading Edge Stagnation Point Equilibrium Temperatures - 1959 ARDC Atmosphere, Sweep = 70° (Radius = 1.5 Inch)	12
3.	Leading Edge Stagnation Point Equilibrium Temperatures - 1959 ARDC Atmosphere, Sweep = 70° (Radius = 1.5 Inch)	12
4.	Leading Edge Stagnation Point Equilibrium Temperatures - 1959 ARDC Atmosphere, Sweep = 70° (Radius = 2.0 Inch)	12
5.	Leading Edge Stagnation Point Equilibrium Temperatures - 1959 ARDC Atmosphere, Sweep = 70° (Radius = 2.0 Inch)	12
6.	Leading Edge Stagnation Point Equilibrium Temperatures - 1959 ARDC Atmosphere, Sweep = 70° (Radius = 3.0 Inch)	13
7.	Leading Edge Stagnation Point Equilibrium Temperatures - 1959 ARDC Atmosphere, Sweep = 70° (Radius = 3.0 Inch)	13
8.	Leading Edge Stagnation Point Equilibrium Temperatures - 1959 ARDC Atmosphere, Sweep = 70° (Radius = 3.0 Inch)	13
9.	Leading Edge Stagnation Point Equilibrium Temperatures - 1959 ARDC Atmosphere, Sweep = 70° (Radius = 3.0 Inch)	13
10.	Nose Stagnation Point Equilibrium Temperatures (Radius = 6.0 In.) . . .	14
11.	Nose Stagnation Point Equilibrium Temperatures (Radius = 6.0 In.) . . .	14
12.	Nose Stagnation Point Equilibrium Temperatures (Radius = 4.0 In.) . . .	14
13.	Nose Stagnation Point Equilibrium Temperatures (Radius = 4.0 In.) . . .	14
14.	Typical Re-entry Trajectories	16
15.	Re-Entry Trajectory No. 1	17
16.	Re-Entry Trajectory No. 2	17
17.	Re-entry Trajectory No. 3	18
18.	Trajectory No. 1 For 4000°F Leading Edge	18
19.	Trajectory No. 2 For 3400°F Leading Edge	18
20.	Trajectory No. 3 For 5000°F Nose Cap	18
21.	Oxyacetylene Torch Facility For Thermal Shock Testing	32
22.	Commercial Low Density Foam Zirconias	37
23.	Commercial Low Density Burn-Out Zirconias	38
24.	Commercial Low Density Aluminas	39
25.	Commercial Low Density Foam Zirconia $\rho = 72 \text{ lb/ft}^3$	40
26.	Commercial Low Density Foam Zirconia $\rho = 40 \text{ lb/ft}^3$	41
27.	Commercial Low Density Foam Zirconia $\rho = 21 \text{ lb/ft}^3$	42
28.	Commercial Low Density Burn-Out Zirconia $\rho = 57 \text{ lb/ft}^3$	43
29.	Commercial Low Density Burn-Out Zirconia $\rho = 125 \text{ lb/ft}^3$	44
30.	Commercial Low Density Burn-Out Zirconia $\rho = 143 \text{ lb/ft}^3$	44
31.	Commercial Low Density Foam Zirconia $\rho = 75 \text{ lb/ft}^3$	45
32.	Commercial Low Density Foam Zirconia $\rho = 21 \text{ lb/ft}^3$	45
33.	Commercial Low Density Burn-Out Zirconia $\rho = 140 \text{ lb/ft}^3$	46
34.	Dense Thermal Shock Resistant Zirconia $\rho = 270 \text{ lb/ft}^3 \sim 25\% \text{ Porosity}$.	47
35.	Dense Thoria $\rho = 440 \text{ lb/ft}^3 \sim 30\% \text{ Porosity}$	48
36.	Dense Thoria $\rho = 440 \text{ lb/ft}^3 \sim 30\% \text{ Porosity}$	48
37.	Dense Aluminas	49
38.	Norton Company Low Density Zirconia $\rho = 39 \text{ lb/ft}^3$	55
39.	Norton Company Low Density Zirconia $\rho = 64 \text{ lb/ft}^3$	55
40.	Norton Company Low Density Zirconia $\rho = 82 \text{ lb/ft}^3$	55

		Page
41.	Norton Company Low Density Zirconia (Pore Size-0.050 Inch Diameter)	55
42.	Norton Company Low Density Zirconia (Pore Size-0.149 Inch Diameter)	55
43.	Norton Company Oxyacetylene Torch Facility For Thermal Shock Testing.	57
44.	Norton Company Oxyacetylene Torch Facility For Thermal Shock Testing	57
45.	Zirconia Body MZ8, Thermal Shock Tested - Rating 1	60
46.	Zirconia Body MZ14, Thermal Shock Tested - Rating 3	60
47.	Zirconia Body MZ33, Thermal Shock Tested - Rating 5	60
48.	Norton Company Low Density Zirconia With Flamesprayed Zirconia Coating	62
49.	Low Density Zirconia Bodies Fired in Hydrogen	64
50.	Norton Company Low Density Zirconia - After Thermal Shock Test	66
51.	Norton Company Low Density Foam Filled Zirconia With Flamesprayed Zirconia Coating - After Thermal Shock Test	67
52.	Norton Company Low Density Zirconia With Flamesprayed Chromia Coating - After Thermal Shock Test	68
53.	Pore Structure and ThO ₂ "Fibers" In Body T-51	78
54.	Norton, Phase II, Low Density ThO ₂ $\rho \sim 125$ lb/ft ³ (Body T-68)	78
55.	Chemically Bonded Dense ($\sim 25\%$ Porosity) Zirconia Samples $\rho = 270$ lb/ft ³	84
56.	Chemically Bonded ($\sim 25\%$ Porosity) Zirconia Samples - $\rho = 270$ lb/ft ³	84
57.	Low Density Sintered ZrO ₂ With Chemically Bonded, Dense ZrO ₂ Surface, After Thermal Shock Test	93
58.	Chemically Bonded, Bubble ZrO ₂ ($\rho \sim 150$ lb/ft ³) After Thermal Shock Test	96
59.	Chemically Bonded Bubble ZrO ₂ ($\rho \sim 130$ lb/ft ³) After Thermal Shock Test	97
60.	Chemically Bonded, Low Density, Burn-Out ZrO ₂ ($\rho \sim 80$ lb/ft ³) After Thermal Shock Test	99
61.	Chemically Bonded, Low Density, Burn-Out ZrO ₂ ($\rho \sim 100$ lb/ft ³), After Thermal Shock Test	100
62.	Chemically Bonded Burn-Out Type Low Density Zirconia After Thermal Shock Test $\rho \sim 100$ lb/ft ³ (Mag:3x).	102
63.	Chemically Bonded Bubble Burn-Out Type Low Density Zirconia After Thermal Shock Test $\rho \sim 125$ lb/ft ³ (Mag:3x)	102
64.	Reinforced Castable Al ₂ O ₃ Subscale, After Thermal Test	106
65.	Wooden Molds For Material Properties Determination Samples	108
66.	Heat Capacity of Zirconia and Thoria	110
67.	Total Normal Emittance of Alumina (Cr ₂ O ₃ -Coated) In Air	111
68.	Total Normal Emittance of Zirconia in Air	111
69.	Total Normal Emittance of Thoria in Air	112
70.	Thermal Expansion of Alumina Bodies	112
71.	Thermal Expansion of Zirconia Bodies	114
72.	Thermal Expansion of Thoria Bodies	115
73.	Thermal Conductivity of Alumina Bodies	116
74.	Thermal Conductivity of Zirconia Bodies	117
75.	Thermal Conductivity of Thoria Bodies	118
76.	Conductivity of MAC LA-2 Al ₂ O ₃ at Reduced Pressures	118
77.	Conductivity of Norton RA 5058 Al ₂ O ₃ at Reduced Pressures	119
78.	Conductivity of Ipsen ICB-3400 Al ₂ O ₃ at Reduced Pressures	119
79.	Conductivity of Zircoa Y-714 ZrO ₂ at Reduced Pressures	120
80.	Conductivity of Norton LZ 5991 ZrO ₂ at Reduced Pressures	120

81.	Conductivity of MAC LZ-1 ZrO ₂ At Reduced Pressures	121
82.	Conductivity of Zircoa Y-1193C ThO ₂ At Reduced Pressures	121
83.	Conductivity of Norton LT-5006 ThO ₂ At Reduced Pressures	122
84.	Conductivity of MAC LT-1 ThO ₂ At Reduced Pressures	122
85.	Composite Plot of Ultimate Flexural Strength Versus Temperature . . .	123
86.	Composite Plot of Initial Flexural Modulus Versus Temperature . . .	124
87.	Design Concept of Dense Ceramic Tile Covering On A Variable Density Ceramic	128
88.	Design Concept of Skinned Low Density Ceramic	129
89.	Design Concept of Small Modules (Rods, Tubes)	130
90.	3.0 Inch Radius Leading Edge - Sintered Ceramic Tile	131
91.	3.0 Inch Radius Leading Edge - Reinforced Chemically Bonded Ceramic	132
92.	Leading Edge Temperatures - Trajectory No. 2	133
93.	1.5 Inch Radius Leading Edge-Sintered Ceramic Tile	134
94.	1.5 Inch Radius Leading Edge-Reinforced Chemically Bonded Ceramic .	134
95.	1.5 Inch Radius Leading Edge-Ceramic Layer	135
96.	Leading Edge Temperatures-Trajectory No. 1	136
97.	6.0 Inch Radius Nose Cap-Small Modules-Two Designs	136
98.	6.0 Inch Radius Nose Cap-Large Module, Variable Density	137
99.	Nose Cap Temperatures-Trajectory No. 3	138
100.	Vibration Input Levels RMS Acceleration vs Time	139
101.	Stagnation Point Temperature Histories	140
102.	Subscale Thermal Test Facility	141
103.	3400°F Test Specimen-3.0 Inch Radius Leading Edge- Variable Density Tile Design	142
104.	3400°F Test Specimen-3.0 Inch Radius Leading Edge Variable Density Tile Design, Revision A	142
105.	3400°F Test Specimen-3.0 Inch Radius Leading Edge-Variable Density Tile Design Revision A (Thermal Test)	144
106.	3400°F Test Specimen-3.0 Inch Radius Leading Edge-Reinforced Castable Alumina Design	145
107.	Metal Subassembly-3400°F Test Specimen Reinforced Castable Alumina Design	145
108.	3400°F Test Specimen-3.0 Inch Radius Leading Edge-Reinforced Castable Alumina Design (Thermal Test)	146
109.	3400°F Test Specimen-3.0 Inch Radius Leading Edge Tile Design . . .	147
110.	Metal Subassembly-3400°F Test Specimen-Tile Design	148
111.	3400°F Test Specimen-3.0 Inch Radius Leading Edge Tile Design Revision A	148
112.	3400°F Test Specimen-3.0 Inch Radius Leading Edge-Tile Design Revision A (Thermal Test)	150
113.	3400°F Test Specimen-3.0 Inch Radius Leading Edge-Tile Design Revision B	151
114.	3400°F Test Specimen-3.0 Inch Radius Leading Edge-Tile Design Revision B (Thermal Test)	152
115.	3400°F Test Specimen-3.0 Inch Radius Leading Edge-Pin Tile Design .	153
116.	Metal Subassembly-3400°F Test Specimen-Pin Tile Design	153
117.	3400°F Test Specimen-3.0 Inch Radius Leading Edge-Pin Tile Design (Test Results)	154
118.	3400°F Test Specimen 3.0 Radius Leading Edge Pin Tile Design Revision A	154
119.	3400°F Test Specimen 3.0 Inch Radius Leading Edge-Pin Tile Design Revision A (Thermal Test)	155

120. 4000°F Test Specimen-1.5 Inch Radius Leading Edge Key Block Design 156

121. High Density Metal Subassembly -4000°F Test Specimen - Key Block Design 157

122. 4000°F Test Specimen-1.5 Inch Radius Leading Edge-High Density Key Block Design (Thermal Test) 158

123. 4000°F Test Specimen-1.5 Inch Radius Leading Edge Key Block Design-Revision A 159

124. 4000°F Test Specimen-1.5 Inch Radius Leading Edge-High Density Key Block Design-Revision A (Thermal Test) 160

125. 4000°F Test Specimen-1.5 Inch Radius Leading Edge-Low Density Key Block Design-Revision B 161

126. 4000°F Test Specimen-1.5 Inch Radius Leading Edge-Low Density Key Block Design-Revision B (Thermal Test) 162

127. 4000°F Test Specimen-1.5 Inch Radius Leading Edge Block Design . . . 163

128. 4000°F Test Specimen-1.5 Inch Radius Leading Edge Block Design (Thermal Test) 164

129. 4000°F Test Specimen-1.5 Inch Radius Leading Edge Block Design Revision A 165

130. 4000°F Test Specimen-1.5 Inch Radius Leading Edge Block Design Revision A (Thermal Test) 166

131. 4000°F Test Specimen-1.5 Inch Radius Leading Edge Reinforced Chemically Bonded Design 167

132. Metal Subassembly-4000°F Test Specimen-Reinforced Chemically Bonded Design 167

133. 4000°F Test Specimen-1.5 Inch Radius Leading Edge-Reinforced Chemically Bonded Design (Thermal Test). 168

134. 4000°F Test Specimen-1.5 Inch Radius Leading Edge-Pin Tile Design . 169

135. 4000°F Test Specimen-1.5 Inch Radius Leading Edge (Thermal Test) . . 170

136. 4000°F Test Specimen-1.5 Inch Radius Leading Edge Tile Design Revision A 171

137. 4000°F Test Specimen-1.5 Inch Radius Leading Edge-Pin Tile Design Revision A (Thermal Test). 172

138. 4000°F Test Specimen 1.5 Inch Radius Leading Edge-Pin Tile Design Revision B (Thermal Test) 173

139. 5000°F Test Specimen-Nose Cap-Tile Design 174

140. 5000°F Test Specimen-Nose Cap-Tile Design (Vibration Test) 175

141. 5000°F Test Specimen-Nose Cap-Tile Design 176

142. 5000°F Test Specimen-Nose Cap Tile Design-Revision A 177

143. 5000°F Test Specimen-Nose Cap-Tile Design-Revision A (Thermal Test) 178

144. 5000°F Test Specimen-Nose Cap-Tube Reinforced Castable Design . . . 179

145. Metal Subassembly-5000°F Test Specimen-Tube Reinforced Castable Design 179

146. 5000°F Test Specimen-Nose Cap-Tube Reinforced Castable Design (Thermal Test) 180

147. 5000°F Test Specimen-Nose Cap-Tube Reinforced Castable Design Revision A 181

148. 5000°F Test Specimen-Nose Cap-Tube Reinforced Castable Design, Revision A (Thermal Test) 182

149. 5000°F Test Specimen-Nose Cap-Variable Density Block Design 183

150. 5000°F Test Specimen-Nose Cap-Variable Density Block Design (Thermal Test) 184

151. 5000°F Test Specimen-Nose Cap Pre-Loaded Tile Design 185

152.	5000°F Test Specimen-Nose Cap-Pre-Loaded Tile Design (Thermal Test)	186
153.	Diamond Tools Used For Fabrication Of Ceramic Components	188
154.	Surface Grinding Of Low Density ZrO ₂ Block	188
155.	Ceramic Parts After Machining	189
156.	Grinding of Contour on Low Density ZrO ₂ Block	191
157.	5000°F Test Specimen-Nose Cap Spring Coupled, Tube Reinforced Castable Design	194
158.	3400°F Full Scale Test Specimen 3.0 Inch Radius Leading Edge	196
159.	3.0 Inch Radius Leading Edge Metal Structure	198
160.	Metal Assembly For 3.0 Inch Radius Leading Edge In Projected Views	160
161.	3.0 Inch Radius Leading Edge Temperatures Radiating Substructure	200
162.	Cutting Low Density Al ₂ O ₃ With Diamond Band-Saw Blade	203
163.	Drilling Low Density Al ₂ O ₃ With A Diamond Core Drill	203
164.	Grinding Cylindrical Surface For 3.0 Inch Radius Leading Edge Al ₂ O ₃ Tile	205
165.	Low Density Al ₂ O ₃ Tiles For 3.0 Inch Radius Leading Edge	206
166.	3.0 Inch Radius Leading Edge Partial Assembly, Displaying Insulation	206
167.	3.0 Inch Radius Leading Edge Final Assembly	207
168.	4000°F Full Scale Test Specimen-1.5 Inch Radius Leading Edge	208
169.	1.5 Inch Radius Leading Edge Metal Structure	209
170.	Assembled 1.5 Inch Radius Leading Edge	210
171.	Metal Assembly For 1.5 Inch Radius Leading Edge In Projected Views	211
172.	1.5 Inch Radius Leading Edge Temperatures Radiating Substructure	212
173.	1.5 Inch Radius Leading Edge Final Assembly	216
174.	5000°F Full Scale Test Specimen-6.0 Inch Spherical Radius Nose Cap	217
175.	6.0 Inch Radius Shield Nose Cap Temperatures	219
176.	6.0 Inch Radius Nose Cap Support Structure and Substructure	221
177.	Grinding Interior of Sintered Zirconia Ring For 6.0 Inch Radius Nose Cap	223
178.	Conical Face On Sintered Zirconia Ring For 6.0 Inch Radius Nose Cap After Grinding	223
179.	Grinding Exterior of Sintered Zirconia Ring For 6.0 Inch Radius Nose Cap	224
180.	Components For the 6.0 Inch Radius Nose Cap	225
181.	6.0 Inch Radius Nose Cap Ceramic Assembly	226
182.	Finish Grinding on 6.0 Inch Radius Nose Cap	227
183.	Finished 6.0 Inch Radius Nose Cap	227
184.	Failure As A Result of Vibration of the 1.5 Inch Leading Edge	229
185.	Failure As A Result of Vibration of the 6.0 Inch Radius Nose Cap	231
186.	Exploratory Study of Nose Cap Vibration Failure	232
187.	Thermal Test Condition for Full Scale 3.0 Inch Radius Leading Edge	234
188.	Thermal Test Conditions for Full Scale 1.5 Inch Radius Leading Edge	234
189.	Thermal Test Conditions for Full Scale 6.0 Inch Radius Nose Cap	235
190.	MAPP-OX Thermal Testing of 3.0 Inch Radius Leading Edge	236
191.	3.0 Inch Radius Leading Edge After Thermal Test	238
192.	3.0 Inch Radius Leading Edge After Thermal Test	239
193.	MAPP-OX Thermal Testing of 1.5 Inch Radius Leading Edge	241
194.	MAPP-OX Thermal Testing of 1.5 Inch Radius Leading Edge	242
195.	1.5 Inch Radius Leading Edge After Thermal Test	244
196.	MAPP-OX Thermal Testing of 6.0 Inch Radius Nose Cap	246
197.	MAPP-OX Thermal Testing of 6.0 Inch Radius Nose Cap	247
198.	MAPP-OX Thermal Testing of 6.0 Inch Radius Nose Cap	248

	Page
199. 6.0 Inch Radius Nose Cap After Thermal Test	249
200. Leading Edge Heating Rate Distribution	252
201. Nose Surface Heating Rate Distribution	253
202. Leading Edge Thermal Model	255
203. 3.0 Inch Radius - 3400°F Leading Edge Thermal Model	256
204. 1.5 Inch Radius Leading Edge Thermal Model	257
205. 1.5 Inch Radius - 4000°F Leading Edge Thermal Model	258
206. Nose Cap Thermal Model - 6.0 Inch Radius	260
207. Thermal Analysis Model for Reinforced Castable Tube Design for 6.0 Inch Radius Nose Cap	261
208. Leading Edge Temperatures - Trajectory No. 2	261
209. Leading Edge Temperatures - Trajectory No. 2	262
210. 3.0 Inch Radius Leading Edge Temperatures - Insulated Substructure	263
211. 3.0 Inch Radius Leading Edge Temperatures - Radiating Substructure	264
212. 3.0 Inch Radius Leading Edge Temperatures - Cooled Substructure	265
213. 3.0 Inch Radius Leading Edge Temperatures - Radiating Substructure	266
214. Thermal Analysis of a 1.5 Inch Radius Leading Edge Configuration	267
215. Thermal Analysis of a 1.5 Inch Radius Leading Edge Configuration ("K" Factor = 4.0)	268
216. 1.5 Inch Radius Leading Edge Temperatures - Radiating Substructure	269
217. 1.5 Inch Radius Leading Edge Temperatures - Radiating Substructure	269
218. 1.5 Inch Radius Leading Edge Temperatures - Radiating Substructure	270
219. Nose Cap Temperatures - Trajectory No. 3	271
220. Nose Cap Temperatures - Trajectory No. 3	272
221. 6.0 Inch Radius Shield Nose Cap Temperatures	274
222. Thermal Analysis of a 6.0 Inch Radius Nose Cap Configuration, 55° Off Stagnation Point	275
223. Thermocouple Comparison	276
224. Shear Test Fixture	279
225. Diagonal Tension Failure	280
226. Typical Vibration Test Setup	289
227. Vibrational Test Setups for the 1.5 Inch Leading Edge	289
228. Vibration Input Levels RMS Acceleration vs Time	290
229. Vibration Input PSD Curves	291
230. Typical Acoustic Test Setup, Mounting Under Horn	292
231. Acoustic Test Setups for the 3.0 Inch Radius Leading Edge in the Three Orientations	292
232. Typical Thermal Test Setup	293
233. Test Specimen With Backside Water-Cooled In Thermal Test Fixture	293
234. Subscale Thermal Test Facility	294
235. Stagnation Point Temperature Histories	294
236. Test Firing of 2-1/4 Inch Diameter MAPP-OX Burner	296
237. Test Firing of Nine Banked 5/8 Inch Diameter MAPP-OX Burners	297
238. Thermal Test Conditions for Full Scale 3.0 Inch Radius Leading Edge	298

	Page
239. Thermal Test Conditions for Full Scale 1.5 Inch Radius Leading Edge	299
240. MAPP-OX Thermal Testing of Dummy Leading Edges	300
241. MAPP-OX Thermal Testing of 3.0 Inch Radius Leading Edge	302
242. MAPP-OX Thermal Testing of 1.5 Inch Radius Leading Edge	303
243. Thermal Test Conditions for Full Scale 6.0 Inch Radius Nose Cap	304
244. Low Density Chemically Bonded THO ₂ (MAC LT-1) After Thermal Test at 4700°F	305
245. 6.0 Inch Radius Nose Cap Ready for Thermal Test	306
246. MAPP-OX Thermal Testing of 6.0 Inch Radius Nose Cap	306
247. Ice Calorimeter, Drop-Type- Specimens to 5000°F	308
248. Heat Capacity Equipment With Drop Shield Tube in Place	309
249. Ice Mantle in Heat Capacity Ice Calorimeter	310
250. Apparatus for Measuring Total Normal Emittance	311
251. Cross Section of Emittance Apparatus With Flat Coil Furnace	312
252. Schematic of 160-Junction Thermopile in Emittance Equipment	314
253. Cross Section of Emittance Apparatus With Blackbody Furnace	315
254. Radiometer Output Versus Temperature for Blackbody Radiation	317
255. Calibration Standards for Total Normal Emittance	318
256. Correction for Mirror and Sapphire Window Emittance Apparatus	320
257. Correction for Brightness Temperature to True Temperature	321
258. Graphite Dilatometer Tubes for Measuring Thermal Expansion to 5000°F	324
259. Radial Inflow Thermal Conductivity Apparatus	325
260. Radial Inflow Thermal Conductivity Apparatus	326
261. Cross Section of Water Calorimeter	327
262. Cross Section of Vacuum Furnace for Determination of Thermal Conductivity	328
263. Thermal Conductivity Specimen for Radial Inflow Apparatus	329
264. Specimen Used for Determination of Thermal Conductivity in the Radial Inflow Apparatus	330
265. Comparative Rod Thermal Conductivity Apparatus	337
266. Schematic of Comparative Rod Thermal Conductivity Apparatus	338
267. Specimen Configuration for Comparative Rod Thermal Conductivity Apparatus	339
268. Typical Temperature Profile in Test Section	340
269. Thermal Conductivity of Type 316 Stainless Steel	341
270. Thermal Conductivity of Armco Iron	342
271. Thermal Conductivity of ATJ Graphite, With Grain	343
272. Thermal Conductivity of Thermocouple Grade Constantan Rod	344
273. Cross Sectional Schematic of the High Temperature Flexural Apparatus	348
274. Schematic Cross Section of the Deflection Measurement System	349
275. Comparison of Conductivity Due to Radiation for Cubical and Spherical Shaped Pores	355
276. Energy Paths Between Upper and Lower Surfaces of a Sphere	356
277. Shape Factors (Including Transmissivity) for Curved Surfaces	357
278. Transmitted and Absorbed Energy Within a Series of Planes Between Pores	360
279. Heat Absorbed at any Plane Due to Transmission	361
280. Typical Thermal History Component of Re-Entry Vehicle	367
281. Body Geometry	369

		Page
282.	Body Environment	369
283.	Solution of the One-Dimensional Heat Flow System	372
284.	Dimensionless Thermal Stress at Points Remote from Free Edges	373
285.	Dimensionless Thermal Stress at Points Remote from Free Edges	374
286.	Dimensionless Stress Distribution Two-Dimensional Body	375
287.	General Body Geometry (Top View).	391
288.	Subscale Thermal Test Facility	392

LIST OF TABLES

I	Ceramic Oxides - Thermal Properties	20
II	Ceramic Oxides - Mechanical and General Properties	22
III	Structural Materials - Thermophysical Properties	25
IV	Structural Materials - Mechanical Properties	28
V	Non-Structural Thermal Insulations	30
VI	Evaluation of Commercial Low Density Ceramics	35
VII	Evaluation of Commercial High Density Ceramics	50
VIII	Ranges of Intrinsic Variables in Low Density Zirconia Body Development	54
IX	Results of Investigation of Intrinsic Variables in Low Density Zirconia Bodies	59
X	Test Results - Intrinsic Variables in Low Density Zirconia Body Development	63
XI	Results of Thermal Shock Test on Superior Bodies	65
XII	Effect of Production Variables on Stabilization of Low Density Zirconia Bodies	70
XIII	Properties of Low Density Zirconia Body LZ5991 Produced in Pilot Plant Operation	70
XIV	Characteristics of Low Density Zirconia Bodies Produced During R & D Study in Phases II and III	72
XV	Ranges of Intrinsic Variables in Low Density Thoria Body Development	75
XVI	Results of Mineralizer and Reinforcement Additions to Low Density Thoria Bodies	77
XVII	Properties of Phases II-III Thoria Bodies	79
XVIII	Chemical Bonding Agents for Zirconia	80
XIX	Materials Utilized in Chemical Bonding Study	85
XX	High Density Surface Coatings	92
XXI	Bulk Density vs Mesh Size for Bubble Zirconia	95
XXII	Chemically Bonded Ceramics	107
XXIII	Thermophysical Properties Measured	109
XXIV	Environmental Conditions	128
XXV	Subscale Test Results	192
XXVI	Maximum Temperatures of 3.0 Inch Radius Leading Edge	263
XXVII	Maximum Temperatures of 1.5 Inch Radius Leading Edge	268
XXVIII	Maximum Temperatures of 6.0 Inch Radius Nose Cap	271
XXIX	Maximum Temperatures of 6.0 Inch Radius Nose Cap	274
XXX	Mechanical Properties	281
XXXI	The Probable Error That Can Be Anticipated in the Thermal Conductivity Data Obtained in the Radial Inflow Apparatus	335

	Page
XXXII	Values of Correction Factor, C_t 350
XXXIII	Stress Expressions for Areas Adjacent to Free Edges Remote from Corners 376
XXXIV	State of Stress Adjacent to the Free Edges Remote from Corner 377
XXXV	State of Stress Adjacent to the Free Edges Remote from Corner 378
XXXVI	State of Stress Adjacent to the Free Edges Remote from Corner 379
XXXVII	State of Stress Adjacent to the Free Edges Remote from Corner 380
XXXVIII	State of Stress Adjacent to the Free Edges Remote from Corner 381
XXXIX	State of Stress Adjacent to the Free Edges Remote from Corner 382
XL	State of Stress Adjacent to the Free Edges Remote from Corner 383
XLI	State of Stress Adjacent to the Free Edges Remote from Corner 384
XLII	State of Stress Adjacent to the Free Edges Remote from Corner 385
XLIII	State of Stress Adjacent to the Free Edges Remote from Corner 386
XLIV	State of Stress Adjacent to the Free Edges Remote from Corner 387
XLV	State of Stress Adjacent to the Free Edges Remote from Corner 388

SECTION I

INTRODUCTION

Radiation cooling of re-entry vehicles is very desirable because it is comparatively efficient, reliable, and simple, and does not result in dimensional change of aerodynamic surfaces due to mass loss as with ablation. Dissipation of re-entry heating by radiation is especially desirable for high L/D lifting re-entry vehicles. However, current metallic materials cannot be utilized at temperatures above approximately 3000°F because of their limited refractoriness and/or the temperature limit of associated oxidation protective coatings. Restricting a radiation cooled leading surface component for a glide re-entry vehicle to a maximum temperature of 3000°F imposes many penalties on re-entry velocity-altitude corridor, leading surface radius, and general vehicle performance. Therefore, for surface temperatures above approximately 3000°F, the refractory ceramics must be considered, with the oxide ceramics being much more useful because of their oxidation resistance.

Considerable effort has been directed toward ceramic nose caps for glide re-entry vehicles such as ASSET and Dyna-Soar, and under general research and development programs. In the majority of these programs, a relatively dense (approximately 270 lb/ft³) thermal shock resistant form of zirconia has been the primary ceramic material, and apparently successful composite nose caps have been designed, fabricated, and tested for operation to approximately 4000°F. However, the dense forms of the refractory oxides such as zirconia and especially thoria have high specific gravities and when used as the complete ceramic phase cause a high weight composite component.

Low density ceramic "foams" were evaluated by the Martin Company for 4000°F nose caps (Reference 1). Emphasis was placed on alumina and zirconia foams of approximately 30 and 45 lb/ft³ density, respectively, but neither could withstand the high heating rates simulating re-entry conditions. Therefore, the foams were impregnated with an ablator. This approach to the thermal shock problem may be successful, but restricts the component to one thermal cycle. For a future maneuvering vehicle which may make aerodynamic turns and then return to orbit to re-enter later, more than one thermal cycle is involved.

In the present project, the fabrication of composite ceramic heat shield structures utilizing unimpregnated, low density ceramics was of prime interest. The objectives of this project were to develop design concepts, materials, processes, and manufacturing methods; perform testing; and accomplish structural and thermal analyses for reinforced low density ceramic heat shields. Three leading surface components, temperature ranges, and ceramic phase densities were involved:

<u>Component</u>	<u>Surface Temperature Range</u>	<u>Maximum Composite Density of Ceramic Phase</u>
Leading Edge	3000 - 3400°F	50 lb/ft ³
Leading Edge	3400 - 4000°F	120 lb/ft ³
Nose Cap	4000 - 5000°F	Minimum possible

The project was divided into three phases:

Phase Ia - Trajectory and conceptual vehicle establishment; material, process, and fabrication development and evaluation; material property survey; preliminary design; and thermal and structural analyses.

Phase Ib - Design, analysis, fabrication, and testing of subscale modules; material property measurement.

Phase II - Design, analysis, fabrication, and testing of full size components.

The three phases were accomplished in chronological order with the information obtained in one phase applied to the succeeding phase. Naturally, some overlap of effort occurred between phases. For clarity of preparation, this report has been sectionalized into the areas of effort expended on:

- (a) Conceptual vehicle and trajectory selection
- (b) Materials
- (c) Design, fabrication, and testing
- (d) Thermal analyses
- (e) Structural analyses

SECTION II

SUMMARY

A hypothetical, conceptual vehicle was established which was representative of manned, orbital, high L/D, lifting re-entry vehicles. The investigations of this project were oriented to meet the heat shield requirements of this representative vehicle; therefore, the results of this work should be applicable to a variety of similar vehicles.

Based on the conceptual vehicle, glide re-entry trajectories for three leading surface components and their associated temperature ranges were established and component configurations selected. The components selected were a 1.5 inch radius leading edge for 3400-4000°F use, a 3.0 inch radius leading edge for 3000-3400°F use, and a 6.0 inch radius nose cap for 4000-5000°F use. Considerable trajectory analyses were accomplished to assure that the selected re-entry conditions and component radii were applicable to various future glide re-entry vehicles. The physical re-entry environment was also studied and pertinent conditions of noise level, load factor, vibration spectrum, etc., were established. Preliminary re-entry surface temperature-time profiles were derived, the boost environment was studied, and thermal and physical ascent conditions selected. The maximum surface temperatures were as stated above and the re-entry time was approximately one hour.

A material properties survey was conducted and the pertinent properties for applicable oxide ceramics, high temperature resistant metals, and thermal insulations were tabulated. These properties were utilized for preliminary design and thermal and structural analyses. This survey led to the selection of zirconia, alumina, and thoria as the ceramic materials for the 1.5 inch radius leading edge, 3.0 inch radius leading edge, and the 6.0 inch radius nose cap, respectively. Coated columbium (D-14) and coated molybdenum (TZM) were selected for substructure materials.

In conjunction with the material properties survey, screening and evaluation tests were performed on available sintered, low density ($\leq 40\%$ of theoretical) zirconia, alumina, and thoria ceramics and also on sintered, high density ($\geq 60\%$ of theoretical) forms of the same materials. Based on preliminary analyses of the flight environment, it was expected that the most difficult condition for the ceramics to meet would be the rapid surface heating rate of as high as 50°F/sec to 3400°F for alumina and 4000°F for zirconia and thoria. Many high density materials, but none of the low density materials, were capable of withstanding this thermal shock condition.

As low density ceramics were of primary interest in this project, it was necessary to institute a two-phase concurrent development program to obtain materials with the desired properties. One phase consisted of the improvement and refinement of existing sintered low density zirconia and thoria. For this phase the Refractories Division of the Norton Company, Worcester, Mass., was selected as the subcontractor. The other phase consisted of the development of chemically bonded low and high density alumina, zirconia, and thoria materials. This work was performed at McDonnell.

The Norton Company developed a sintered, partially stabilized (~50% cubic), low density (95 lb/ft³ or 26% of theoretical) zirconia body with a 0.05 inch diameter pore size and a crushing strength of 590 psi that was capable of withstanding surface heating rates to 50°F/sec to a peak temperature of 4000°F. However, considerable difficulty was experienced in reproducibly manufacturing this body. The low density zirconia was utilized in fabricating subscale and full scale heat shield components. Norton also developed a sintered, low density (125 lb/ft³ or 20% of theoretical) thoria body with a 0.05 inch diameter pore size and a crushing strength of 550 psi. This body could be readily reproduced in manufacturing, but was incapable of withstanding surface heating rates of 25°F/sec to a peak temperature of 4000°F. This material was not utilized in subscale or full scale heat shield components.

Chemically bonded low and high density varieties of alumina, zirconia, and thoria were developed by McDonnell which were capable of withstanding surface heating rates of 50°F/sec to peak temperature of 3400°F for alumina, 4000°F for zirconia, 4500°F for low density thoria, and 4900°F for high density thoria, with less than 3% shrinkage under these conditions. Sodium silicate was selected as the bonding agent for these materials and ground naphthalene powder was used as a burn-out agent to obtain low density. A phosphoric acid bonded chromia composition was developed for use as a surface coating on alumina to increase emittance at elevated temperatures.

Densities and crushing strengths of the six materials developed were as shown below.

<u>Material</u>	<u>Density</u> (lb/ft ³)	<u>Crushing Strength</u> (psi)
Low density alumina	65	475
High density alumina	150	8950
Low density zirconia	125	600
High density zirconia	230	8140
Low density thoria	200	300
High density thoria	390	6575

The design and fabrication of a 1.5 inch radius leading edge, a 3.0 inch radius leading edge, and a 6.0 inch radius nose cap were carried out in three stages -

- Stage 1 - Basic design concepts and preliminary layouts.
- Stage 2 - Subscale design, fabrication, and testing.
- Stage 3A - Design and fabrication of full scale components
- Stage 3B - Full scale component tests

The basic design concept utilized was a thermal insulating layer of ceramic material over a supporting metal substructure. The ceramic was of sufficient thickness to prevent the metal substructure from exceeding its temperature limit. Coated columbium and molybdenum alloys were used as the substructure at maximum temperatures of 2800 and 3000°F, respectively. Hot support structure enabled the use of the minimum thickness of insulating ceramic and provided

the lowest weight composite for the long time (~one hour) high temperature re-entry conditions. A water cooled substructure was investigated for the 3.0 inch radius leading edge as well as a hot support structure. The ceramic elements were mechanically attached to the supporting substructure except in the case of the water cooled substructure where bonding was considered. Mechanical joints were thought to be necessary to allow for differential movement between the ceramic and the metal support structure. This differential movement was appreciable because of the large difference in expansion coefficient between the ceramics and metals, the high temperature at the ceramic-metal interface, and the large thermal gradient through the ceramic. It was also thought that the ceramic material should be used as relatively small modular elements to minimize thermal stresses.

With these concepts in mind, three basic designs were employed for preliminary layouts, and all subsequent designs were variations of these three basic approaches -

- (a) Dense ceramic tile over low density ceramic.
- (b) Dense ceramic skin over low density ceramic.
- (c) Small dense ceramic modules in a low density ceramic matrix.

The preliminary layouts in conjunction with structural and thermal analyses and materials survey, screening, and development studies led to selection of materials, material configurations and thicknesses, and ceramic-to-metal attachment techniques for the subscale stage of design development. The subscale stage was conducted to facilitate the design, fabrication, and environmental testing of as many designs and design improvements as possible in an expeditious and economical manner.

Twenty-two subscale modules were designed and assembled. Seven represented the 3.0 inch radius leading edge, nine the 1.5 inch radius leading edge, and six the 6.0 inch radius nose cap. Twelve modules represented first generation designs, eight represented second generation designs, and two represented third generation designs. No major difficulties were encountered in their fabrication and assembly. Satisfactory techniques were developed for processing, fabricating, shaping, and assembling ceramics for utilization in the subscale modules. Subsequently, these techniques were used in the fabrication of full scale components.

Of 11 modules subjected to environmental vibration and/or acoustical testing, only one was affected, indicating this environment to be noncritical and readily accounted for by proper design. All 22 modules were thermally tested at representative re-entry heating conditions. Test duration was approximately one hour. The desired temperature-time profile was obtained by controlling the distance between an oxyacetylene torch and the module being tested, in response to the time-temperature readout of a monitoring pyrometer. Thirteen modules (six 1.5 inch radius, five 3.0 inch radius, and two 6.0 inch radius) were considered to have sufficiently withstood the testing to have been capable of surviving one complete flight. Three modules (one 3.0 inch radius and two 6.0 inch radius) were questionable as to flight survival. Six modules (three 1.5 inch radius, one 3.0 inch radius, and two 6.0 inch radius) definitely would not have survived.

As most failures occurred during thermal testing, this environment was the most critical. The subscale thermal testing program indicated that to overcome thermal stresses generated by the rapid heating, thermal shock resistant ceramic materials and designs which imposed no mechanical restraint on ceramic parts (so these parts could freely expand or change shape) were required.

A thorough analysis of the subscale testing in conjunction with consideration of fabrication, processing, and assembling requirements led to the selection of the three subscale designs listed below as the most promising designs for full scale components:

(a) 3.0 Inch Radius Leading Edge For 3400°F Use - tile design revision B; sintered, low density alumina tile outer surface attached to coated columbium substructure with coated molybdenum bolts and coated columbium leaf springs, with fibrous insulation between tile and substructure. The ceramic phase density was 48 lb/ft³ compared to an objective density of 50 lb/ft³.

(b) 1.5 Inch Radius Leading Edge For 4000°F Use - key block design revision B; sintered, low density zirconia blocks attached to coated molybdenum substructure with coated molybdenum bolts and coated columbium leaf springs. The ceramic phase density was 95 lb/ft³ compared to an objective density of 120 lb/ft³.

(c) 6.0 Inch Radius Nose Cap For 4500°F Use - tube reinforced castable design; dense thoria tubes attached to dense zirconia tubes with zirconia pins; tube assembly attached to coated molybdenum substructure with coated molybdenum pins; tube assembly filled with chemically bonded low density zirconia and thoria. The ceramic phase density was 175 lb/ft³ and the objective density was as low as possible.

The 4500°F maximum use temperature was specified for the nose cap because subsequent thermal testing with MAPP-OX (methyl-acetylene-propylene-propadiene gas and oxygen) burners developed for full scale thermal testing indicated that the low density chemically bonded thoria was incapable of withstanding temperatures above 4500°F under the high noise, pressure, and velocity conditions of these burners.

One full scale component of each of the above subscale designs was designed. Ceramic materials utilized included McDonnell developed chemically bonded low and high density ceramics, Norton developed sintered low density zirconia, commercially available low density alumina, and commercially available high density zirconia and thoria. To insure that the best available materials were utilized in the full scale components, all incoming materials were checked for density, cracks, and thermal shock resistance.

Thermal conductivity, thermal expansion, heat capacity, total normal emittance, modulus of rupture, Young's modulus, shearing strength, and modulus of rigidity were determined to temperatures as high as 4500°F for the ceramic materials utilized in the full scale components. Most of these properties were measured in a subcontract by Southern Research Institute, Birmingham, Alabama. These data were utilized in thermal and structural analyses of the full scale components.

The thermal analyses established minimum ceramic material thicknesses required to insulate the refractory metal substructures and to maintain desired ceramic-metal and ceramic-ceramic interface temperatures. Thermal analysis of the 3.0 inch radius leading edge considered four cases:

- (a) With no radiation heat exchange between leading edge substructure and wing panels (insulated substructure).
- (b) With radiation heat exchange between leading edge substructure and wing panels.
- (c) With radiation heat exchange between the substructure and a wing closure plate maintained at 200°F by water cooling.
- (d) With the substructure directly water cooled.

With water cooling of the substructure as indicated in (d), approximately 17 pounds of water per hour per running foot of leading edge would have been required, which led to the elimination of this approach. Case (b), which was the design utilized, resulted in lower substructure temperatures than case (a).

The structural analyses showed that the ceramics and the metal substructures in the full scale components would withstand the mechanical loads of boost and re-entry. Utilizing standard thermal stress analysis techniques and new techniques developed in this project, it was indicated that the ceramics would not withstand the thermal stresses imposed by re-entry heating. However, thermal stress analyses did not influence full scale design because the analyses were completed after the fact, the similar subscales did not fail, and the short time elevated temperature properties were considered more favorable than the properties measured after a long soak at temperature, which were the properties used in the analyses.

One full scale component of each of the three leading surfaces was fabricated and assembled without major difficulties. The ceramic phase densities were 57 lb/ft³ for the 3.0 inch radius leading edge, 96 lb/ft³ for the 1.5 inch radius leading edge, and 179 lb/ft³ for the 6.0 inch radius nose cap. Scale-up factors caused the density changes compared to the subscale modules.

The full scale components were subjected to simulated environmental vibration, acoustical, and thermal testing. No failure of the 3.0 inch radius leading edge occurred during vibration and acoustical testing. No failure of the 1.5 inch radius leading edge occurred during acoustical testing, but the chemically bonded low density zirconia potting in one bolt hole counterbore loosened during vibration testing. This testing exceeded specified g loads by a factor of approximately 1-1/2. This defect would be easily correctable by redesign of the counterbore to provide more positive entrapment of the potting material. The 6.0 inch radius nose cap survived acoustical testing, but partial failure occurred during vibration testing. This failure consisted of slight loosening of outer thoria segments caused by excessive tolerances at the pin joints where the thoria-zirconia tube assemblies attached to the molybdenum dome substructure. Obviously, decreasing these tolerances would correct this problem.

For the thermal test, each full scale component was installed on a fixture which established the proper orientation of the given leading edge with respect to a mobile burner head that consisted of MAPP-OX burners set up in an arrangement dictated by the component being tested. The desired surface temperature-time profile was attained by varying the specimen-to-burner head distance in response to the temperature-time readout of a monitoring pyrometer sighted on the stagnation point (line) and a thermocouple bonded on the surface at the stagnation point (line). It was found necessary to protect the Hastelloy X support structure for each component with watercooled shields during thermal testing, which created greater thermal gradients through the ceramics and consequent slightly greater thermal stresses than originally anticipated. During thermal tests, the open ends of the leading edges were closed with fixture brick of similar shape and ceramic material as used on the leading edge itself.

The 3.0 inch radius leading edge failed (cracked but remained intact with no spalling) during the one hour thermal test from a combination of overheating, excessive restraint of the alumina tiles by metal attachment members, vertical expansion gaps of excessive width which permitted flame penetration and melting in the gaps, and the severity of the MAPP-OX test environment. During thermal testing of the 1.5 inch radius leading edge, failure of the end fixture brick occurred, allowing flame penetration to the substructure which resulted in melting of the Hastelloy X support structure and oxidation of the coated molybdenum substructure. However, the condition of the component indicated that, had the end brick not failed and had a complete thermal test been carried out, the component would have successfully survived the thermal testing. The test lasted 240 seconds, during which time the component had been exposed to the peak surface temperature of 4000°F and had cooled to about 3600°F. Therefore, it had survived the most severe thermal shock condition of flight (the rapid heat-up to 4000°F). The premature cessation of the test resulted in a rapid cool-down condition which was not anticipated. One-third of the component was failed as a result of the loss of the metallic substructure, but the remaining two-thirds was intact and the zirconia contained only a few minor hairline cracks.

Total failure (erosion of the majority of the surface) of the 6.0 inch radius nose occurred during thermal testing. The chemically bonded low density thoria was unable to resist the dynamic conditions of the MAPP-OX burners (more severe than actual flight conditions) at a peak test temperature of 4600°F in a design which resulted in poorly supported, exposed edges of this material.

The velocity, noise, and pressure levels of the MAPP-OX, full scale test facility apparently created an environment more severe than flight conditions and influenced test results. Oxyacetylene torch thermal testing of 3.0 inch radius leading edge and 6.0 inch radius nose cap subscale modules made from the same materials (as the full scale components) had not resulted in failure of these modules.

SECTION III

CONCEPTUAL VEHICLE AND TRAJECTORY SELECTION

For realistic evaluation of materials and the development of representative designs and fabrication techniques, selection of a typical trajectory and vehicle was required. This selection was necessary because such factors as vehicle configuration, weight, maneuver capabilities, lift coefficient; whether the vehicle is manned or unmanned; and the particular mission objectives to be accomplished will determine the actual flight path and consequently the magnitude of the aerodynamic heating, surface heating rate, and duration of heating. Since the purpose of this program was to evaluate and develop heat shields applicable to future aerospace vehicles, emphasis was placed on lifting type, manned, orbital re-entry vehicles. The conceptual vehicle design would then include highly swept leading edges, a high temperature nose cap, and various aerodynamic control surfaces. The aerodynamic characteristics shown in Figure 1 were selected for use in the development of the desired flight environments, and are considered to be representative of a typical hypersonic delta wing configuration.

In order to determine suitable re-entry trajectories, assumptions of certain design parameters were necessary. For manned re-entry at orbital speeds, the acquisition of an equilibrium glide trajectory with W/SC_L (Weight over Surface area times Lift Coefficient) ranging from 100-500 psf after the initial dive into the atmosphere, is quite typical for lifting vehicles. The effects of small changes in the many flight variables on the vehicle performance and the methods employed to acquire an equilibrium glide are dependent on the overall design and capabilities of a particular spacecraft, and it was not the purpose of this program to examine them in detail. An initial value of W/SC_L equal to 300 psf was selected for design purposes, corresponding to maximum L/D (Lift over Drag) conditions from Figure 1. In addition, the following parameters were established:

<u>Component</u>	<u>Maximum Surface Temperature (OF)</u>	<u>Emittance at Maximum Temperature</u>
Nose Cap	5000	0.4
Leading Edge	4000	0.7
Leading Edge	3400	0.7

3.1 RE-ENTRY EQUILIBRIUM TEMPERATURES

The selection of a trajectory and component radius which would provide the desired temperatures was initiated by developing equilibrium temperature plots as a function of velocity and altitude for various nose and leading edge radii and surface emittances. By superimposing the velocity-altitude profile of any given trajectory on these altitude-velocity plots of constant equilibrium temperatures, the resulting equilibrium temperatures may be established for various sets of vehicle parameters and trajectories, providing that the vehicle attitude, nose or leading edge radius, and surface emittance are within the limits presented in the following section. (Equilibrium temperature calculations for both the leading edge and nose were based on the 1959 ARDC atmosphere.)

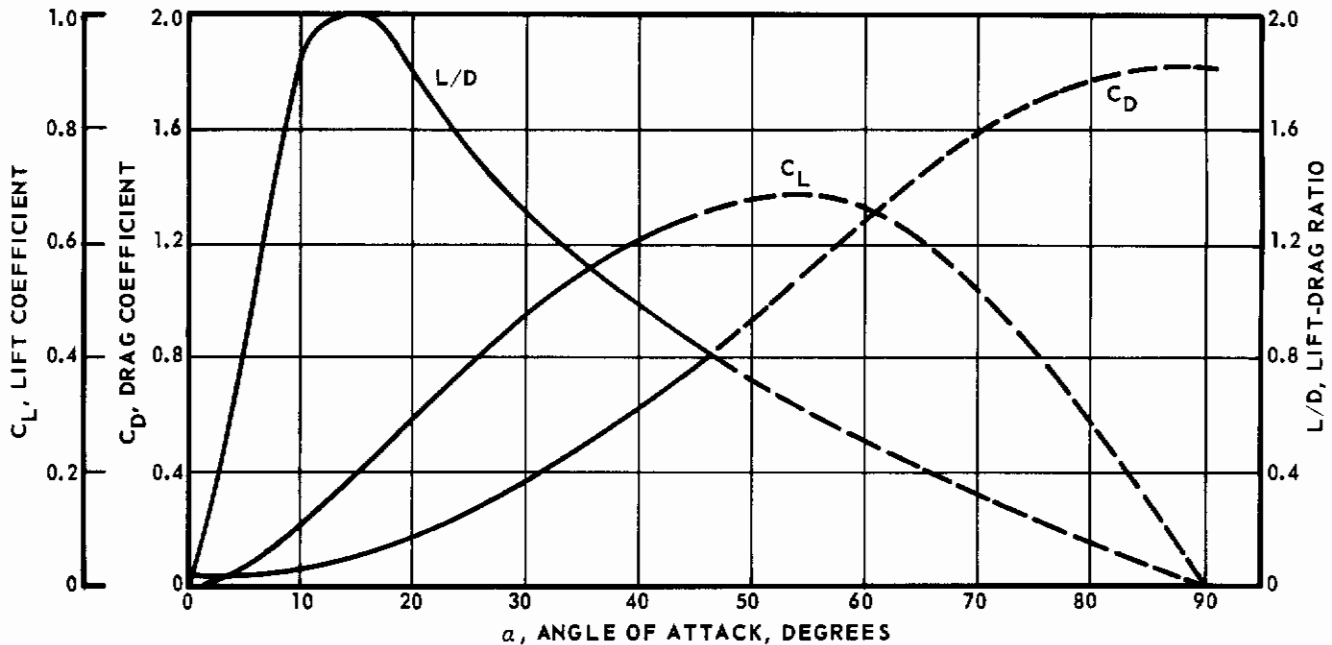


FIGURE 1 - AERODYNAMIC CHARACTERISTICS OF MODIFIED DELTA WING CONFIGURATION

Lees' approximate equation for laminar stagnation point convective heating (Reference 2) was used in the development of the re-entry equilibrium temperatures. This equation is as follows:

$$q_s = \frac{15.5}{\sqrt{R_0}} (2^{0.5n}) (\rho_\infty)^{0.5} \left(\frac{V_\infty}{1000}\right)^3 \left(1 - \frac{h_w}{h_s}\right) (K_{Ac}) \quad (1)$$

- where
- n = 0 for a planar body (leading edge)
 - = 1 for a body of revolution (nose cap)
 - R₀ = leading surface radius (ft)
 - ρ_∞ = free stream density (lb sec² ft⁻⁴)
 - V_∞ = free stream velocity (ft/sec)
 - h_w = wall enthalpy (Btu/lb)
 - h_s = stagnation enthalpy (Btu/lb)
 - K_{Ac} = sweep correction factor (for leading edges)
 - q_s = convective heating rate (Btu/ft²-sec)

The basic parameters affecting the stagnation temperatures of the nose cap and leading edges are listed below:

- (a) Increase the nose or leading edge radius - decrease in temperature.
- (b) Increase in emittance - decrease in temperature.
- (c) Increase in sweep angle of leading edge - decrease in temperature.
- (d) Increase in effective sweep angle of leading edge by decreasing angle of attack - decrease in temperature.

Hot gas radiation from the shock wave becomes very significant for high speed, deep penetration type re-entries. For most manned re-entry vehicles, however, the maximum deceleration limits permissible (~ 10 g) do not result in trajectories where radiation heating is important. For the purposes of this program, hot gas radiation was neglected.

3.1.1 Leading Edge Equilibrium Temperatures

Lees' approximate equation for laminar stagnation line convective heat flux, modified according to recent heat transfer tests conducted on a typical lifting type hypersonic glide vehicle, was employed to calculate the leading edge stagnation line heat flux. These tests showed that the correction factor is a function of vehicle angle of attack and distance from the nose tip. For the equilibrium temperature calculations made in this program, the stagnation line heat flux was taken as 91% of Lees' approximate equation for both 0° and 20° angles of attack.

Figures 2 through 9 show equilibrium temperature curves for a leading edge with a 70° sweep angle for the following range of parameters:

- (a) Free stream velocities from 8,000 to 28,000 feet per second;
- (b) Altitudes from 20,000 to 320,000 feet;
- (c) Angles of attack of 0 and 20° ;
- (d) Leading edge radii of 1.5, 2.0, and 3.0 inches;
- (e) Emittance of 0.7 except for the 3.0 inch radius leading edge, which is presented for both 0.7 and 0.4 emittances;
- (f) Constant temperature lines of 2000, 2500, 3000, 3500, 4000, 4500, and 5000°F .

From this study a 3.0 inch radius was selected for the 3400°F leading edge and a 1.5 inch radius for the 4000°F leading edge.

3.1.2 Nose Cap Equilibrium Temperatures

Nose stagnation point equilibrium temperature curves based on 82% of Lees' equation are presented in Figures 10 through 13 for the following range of parameters:

- (a) Free stream velocities from 8,000 to 28,000 feet per second;
- (b) Altitudes from 20,000 to 340,000 feet;
- (c) Nose radii of 4.0 and 6.0 inches;
- (d) Emittances of 0.4 and 0.6;
- (e) Constant temperature lines of 2000, 2500, 3000, 3500, 4000, 4500, and 5000°F .

From this study, a 6.0 inch radius was selected for the 5000°F nose cap.

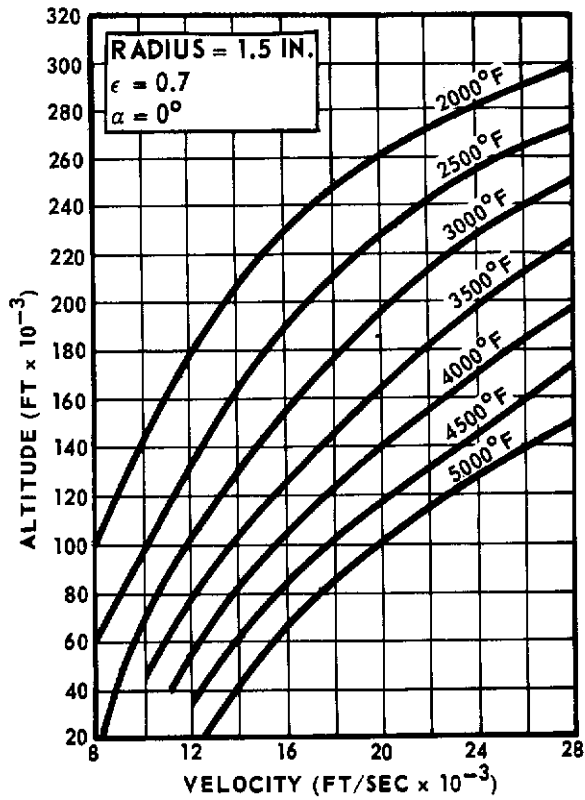


FIGURE 2

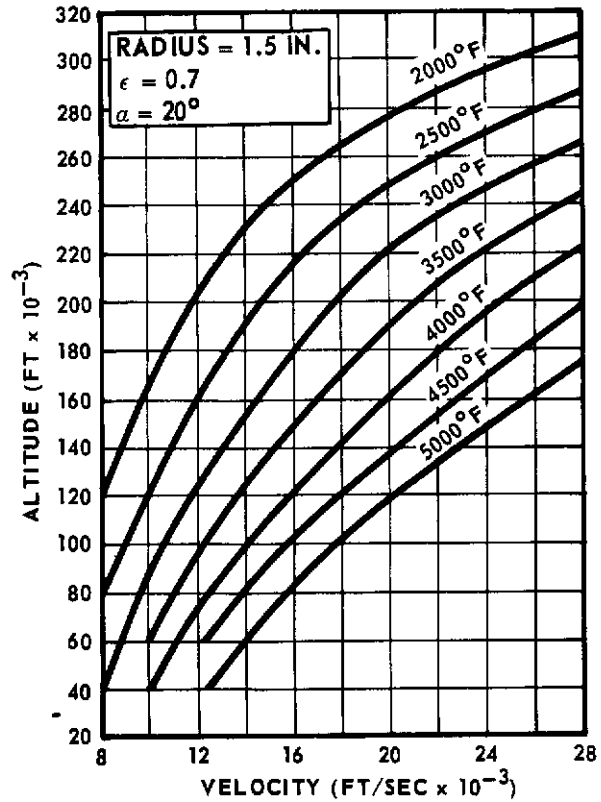


FIGURE 3

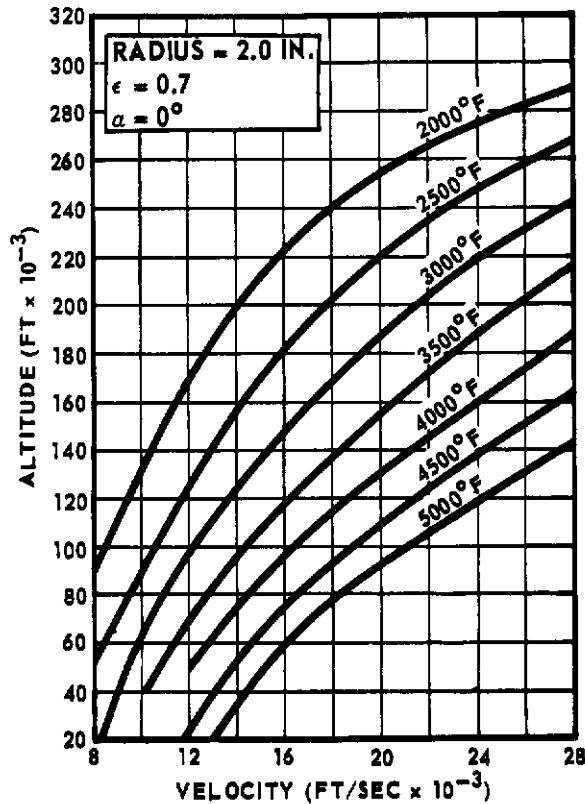


FIGURE 4

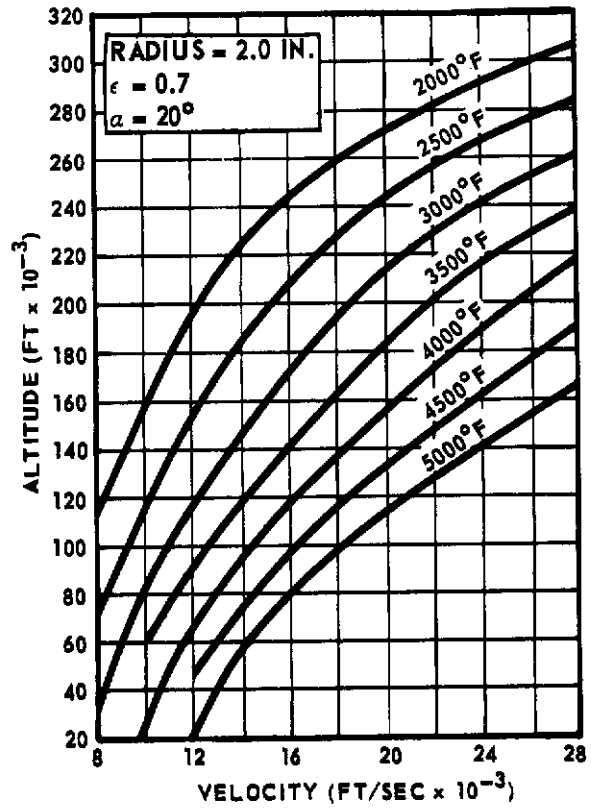


FIGURE 5

**LEADING EDGE STAGNATION POINT EQUILIBRIUM TEMPERATURES
1959 ARDC ATMOSPHERE, SWEEP = 70°**

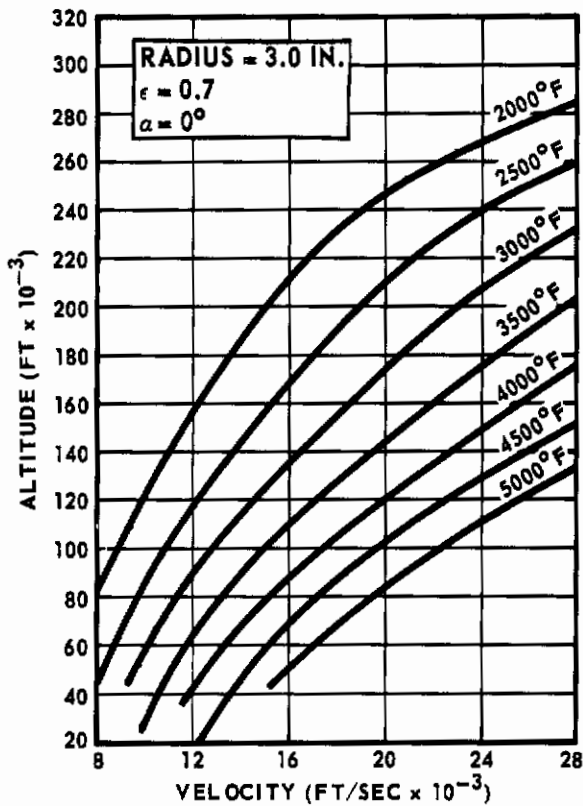


FIGURE 6

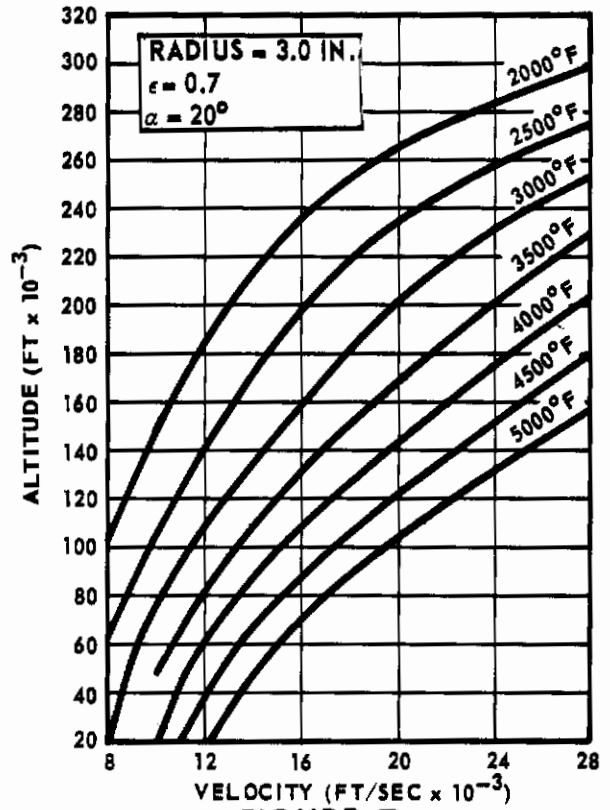


FIGURE 7

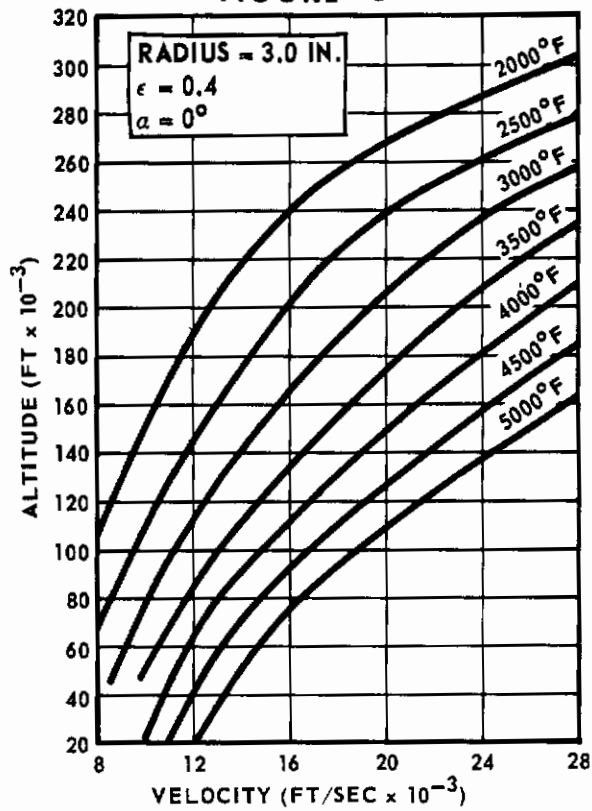


FIGURE 8

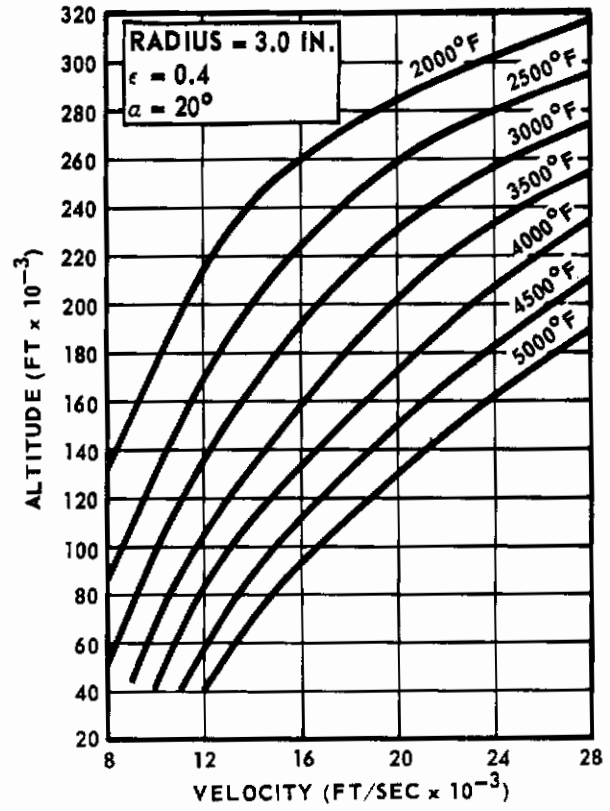


FIGURE 9

LEADING EDGE STAGNATION POINT EQUILIBRIUM TEMPERATURES
1959 ARDC ATMOSPHERE, SWEEP = 70°

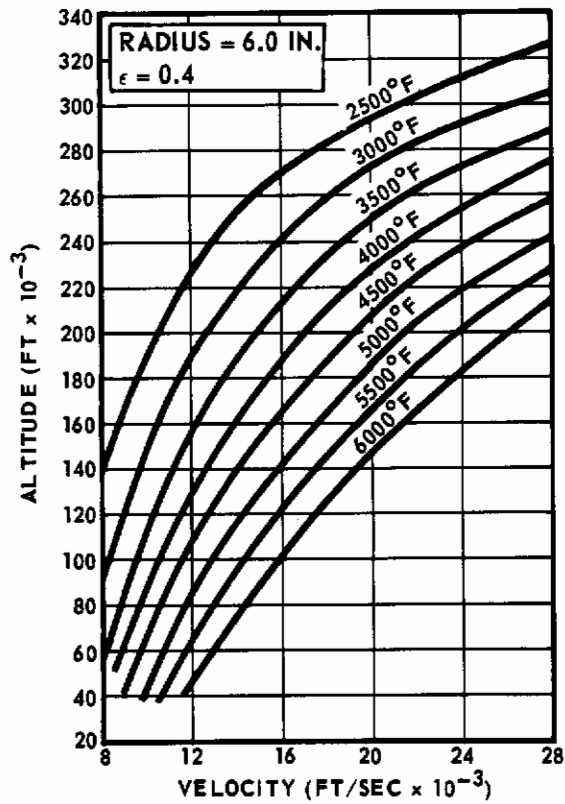


FIGURE 10

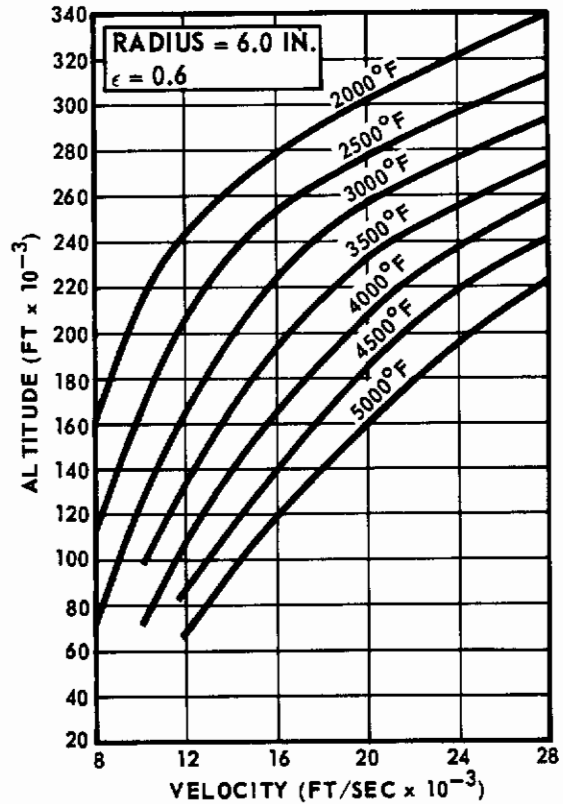


FIGURE 11

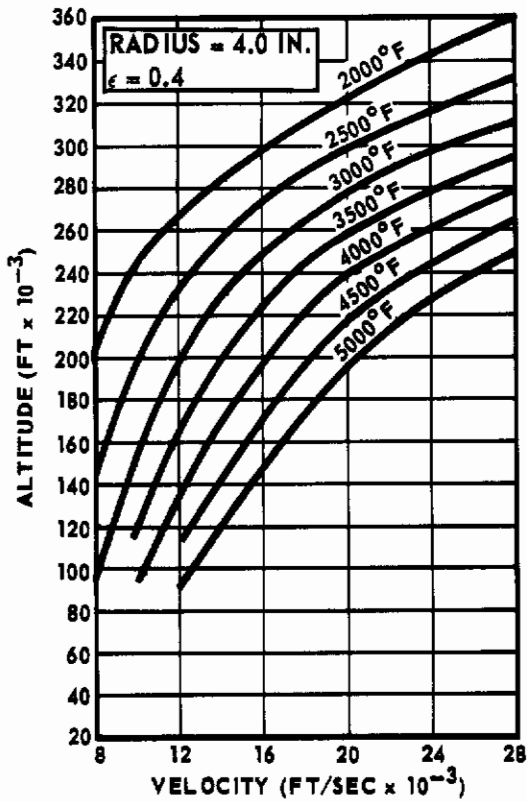


FIGURE 12

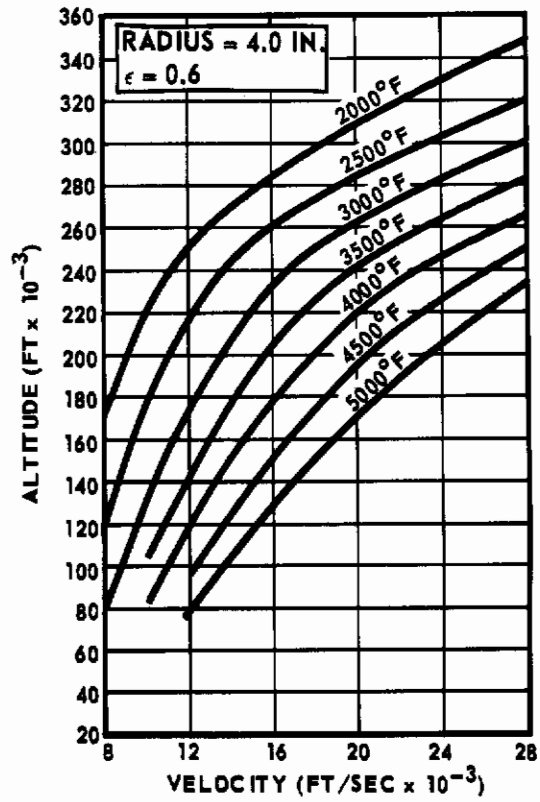


FIGURE 13

**NOSE STAGNATION POINT EQUILIBRIUM TEMPERATURES
1959 ARDC ATMOSPHERE**

3.2 TYPICAL RE-ENTRY TRAJECTORIES

Figure 14 shows some orbital and super-orbital re-entry trajectories for various types of vehicles (some identified by letter only for security reasons). Also shown are the 5000°F nose cap equilibrium temperature (Radius = 6.0 inches) and the 4000°F leading edge equilibrium temperature (Radius = 1.5 inches) for surface emittances of 0.4 and 0.7. It can be seen from this figure that, in general, the super-orbital re-entries would be too severe for the components using only radiation cooling techniques, developed under the present program. Re-entries from orbital speeds may or may not produce excessive temperatures, depending on depth of penetration into the atmosphere, emittance, and nose or leading edge radius.

3.3 SELECTION OF DESIGN TRAJECTORIES

Since the requirements of this program were to develop leading surfaces capable of withstanding a defined maximum temperature level, the selection of a re-entry trajectory was fairly arbitrary, as long as it was representative of advanced aerospace re-entry environments. A simplified approach was followed in order to arrive at a design trajectory suitable for each heat shield.

Defining re-entry as beginning at an altitude of 400,000 feet and a speed of 24,200 fps, various re-entry flight path angles were examined to determine the peak equilibrium temperature reached during the initial dip into the atmosphere for a vehicle with $W/SC_L = 300$ psf. Re-entry angles of -3.0° , -2.5° , and -2.0° resulted in the desired maximum equilibrium temperature levels for the 4000°F leading edge, the 3400°F leading edge, and the 5000°F nose cap, respectively, with re-entry flight at L/D maximum conditions. Since a sharp spike in the equilibrium temperature-time history was produced, it was decided to change the vehicle attitude at the proper time after the initial perigee in order to fly ballistically until equilibrium glide for a $W/SC_L = 300$ psf was obtained. This increased the time spent in the highest temperature environment. Vehicle temperatures during the equilibrium glide phase remain at high levels since the lines of constant equilibrium temperature closely parallel the equilibrium glide trajectories.

Figures 15 through 17 show velocity and altitude versus time for each of the three trajectories obtained from the above investigation. Figures 18 through 20 show each trajectory on a velocity-altitude plot with some lines of constant equilibrium temperature included. It should be noted that each trajectory was developed entirely independent of the others; i.e., the nose cap temperature based on the 4000°F leading edge trajectory would exceed 5000°F. In addition, for each trajectory the angle of attack was held constant at 15° throughout the entire flight. However, since the desired temperature level for each component was obtained by using these trajectories, no additional detail trajectory analyses were undertaken.

Obviously, many other trajectories exist which would also satisfy the program requirements utilizing different criteria than chosen here. However, the component radii selected and the temperature-time histories established are very representative for advanced lifting re-entry vehicles. In general, it is felt that these trajectories are quite severe with respect to maximum temperature and time-at-temperature for a lifting, manned, orbital re-entry vehicle. Therefore, the leading surface component radii are near maximum for the maximum surface temperatures used in this program.

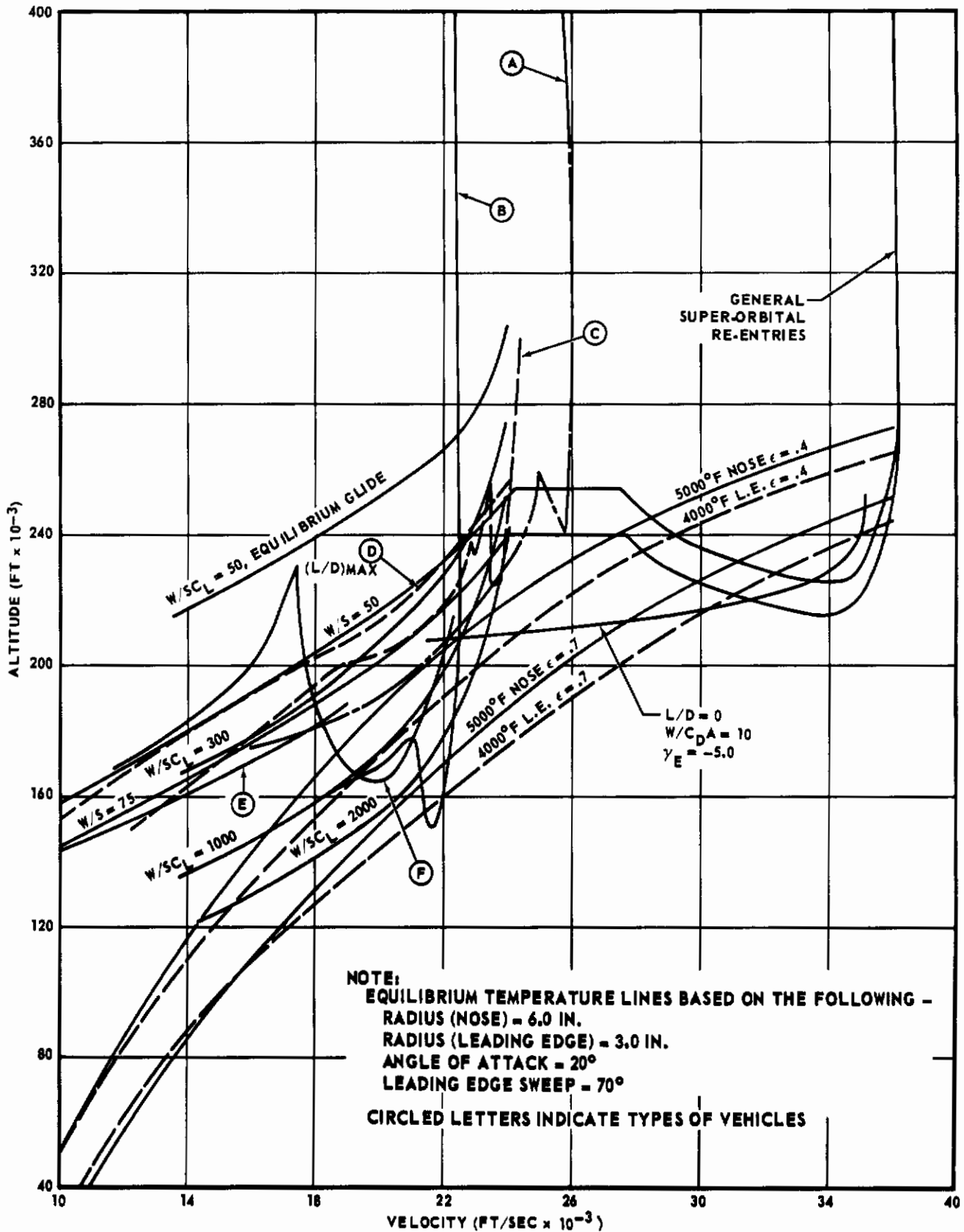


FIGURE 14 - TYPICAL RE-ENTRY TRAJECTORIES

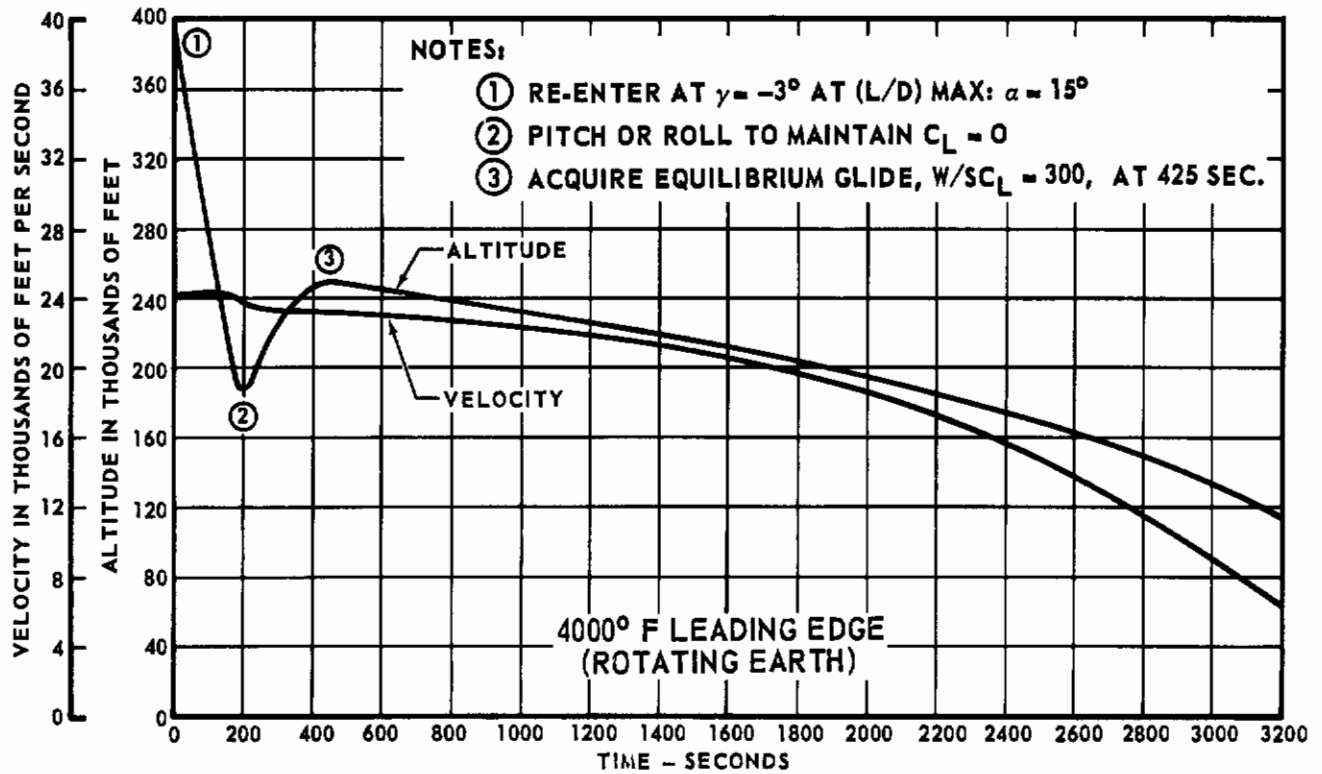


FIGURE 15 - RE-ENTRY TRAJECTORY NO. 1

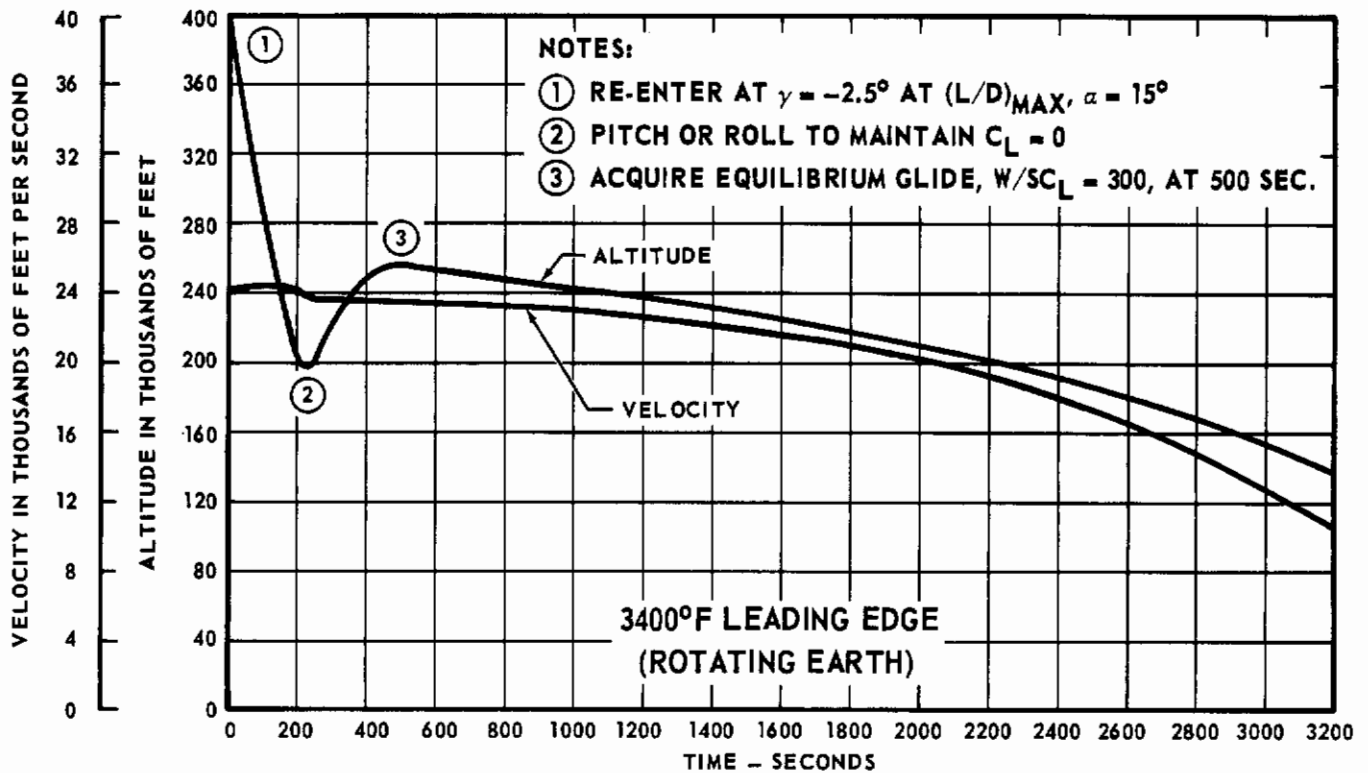


FIGURE 16 - RE-ENTRY TRAJECTORY NO. 2

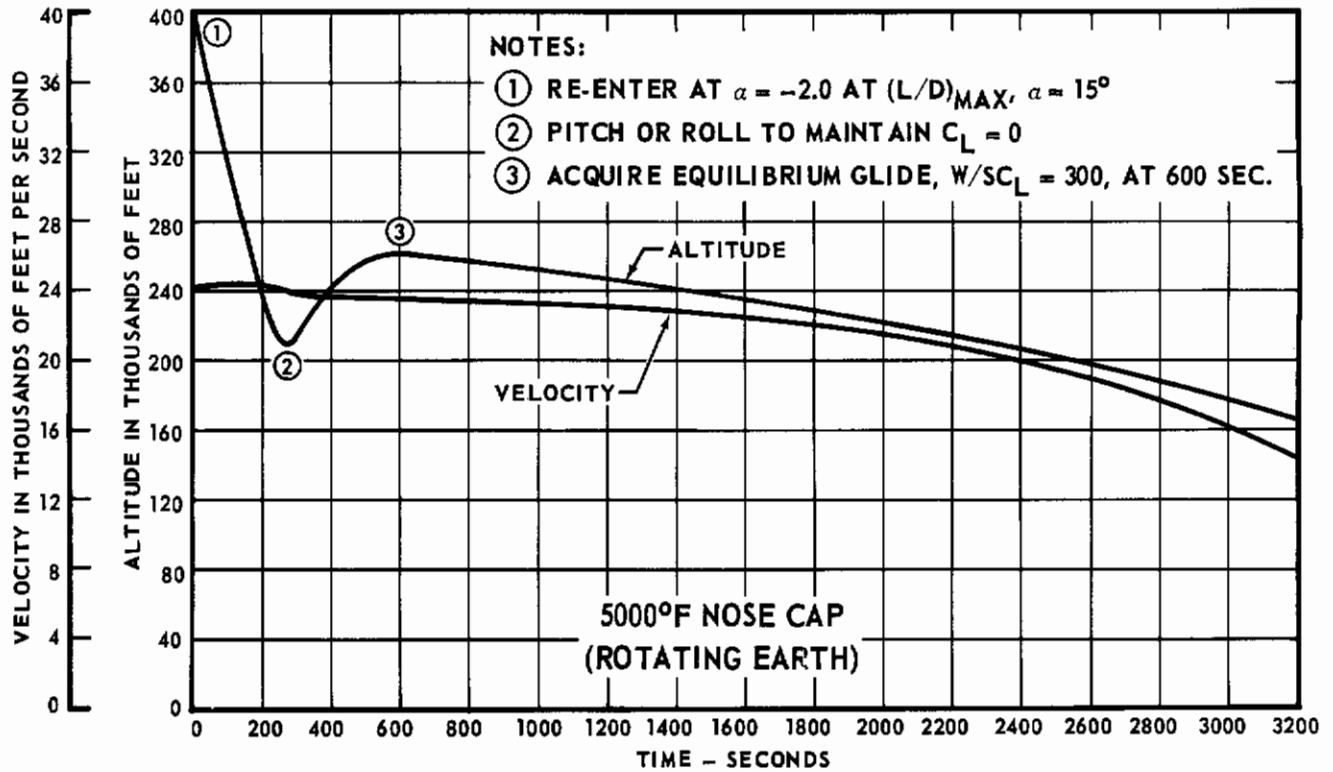


FIGURE 17 - RE-ENTRY TRAJECTORY NO. 3

RE-ENTRY TRAJECTORIES

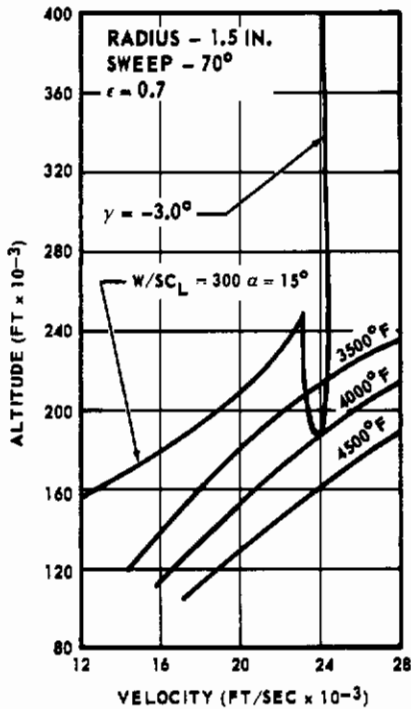


FIGURE 18 - TRAJECTORY NO. 1 FOR 4000° F LEADING EDGE

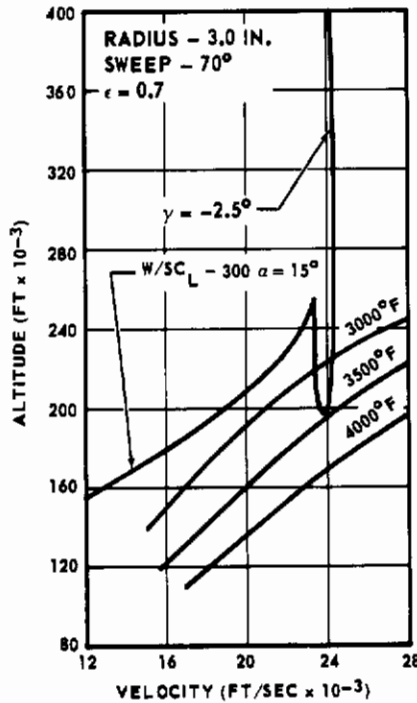


FIGURE 19 - TRAJECTORY NO. 2 FOR 3400° F LEADING EDGE

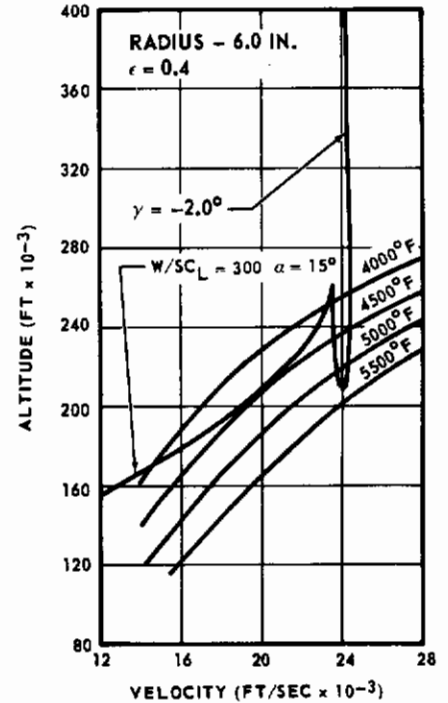


FIGURE 20 - TRAJECTORY NO. 3 FOR 5000° F NOSE CAP

SECTION IV

MATERIALS

Extensive materials and processing work was required for this project. A survey was necessary to determine availability of materials and material properties and thereby enable initial materials selection, preliminary design, and structural and thermal analyses. In conjunction with this survey, evaluation and screening tests were performed on state of the art low and high density ceramic materials. Since satisfactory sintered low density ceramics and chemically bonded ceramics were not available, materials improvement and development work was performed. Final selection of ceramic materials for full scale heat shield components was made and steps were taken to insure that quality materials were used. The thermophysical properties of the selected materials were measured as necessary.

4.1 MATERIAL PROPERTY SURVEY

A survey was conducted to obtain properties of applicable ceramic and metallic materials considered as being at least semi-commercially available for use in this project. Thermal, mechanical, and physical properties; fabrication requirements; availability; supplier; cost; etc. were tabulated. The majority of the data compiled came from vendors, the literature, cognizant organizations, and experimental investigations. Some of the data were "estimated" because certain specific properties required for preliminary design and analyses were not available at time of need. Estimations were primarily based upon data available for similar materials. The "most probable data" were derived using the best available data originating from several sources. The data compiled for ceramic materials were utilized for preliminary design and thermal and structural analyses. Design properties for the selected ceramics were measured later in the program (see Section 4.5). The properties compiled for the metals and thermal insulation were utilized throughout the program.

Tables I and II show the pertinent properties of each basic oxide ceramic material. The material form, including macro and microstructure, is important because it influences physical, thermal, and mechanical properties. Selection of materials for inclusion in these tables were based on availability and qualitative comparisons. Emphasis was placed on those ceramics having good thermal shock resistance, high melting point, and low thermal diffusivity.

This preliminary survey resulted in the selection of thoria (for 4000-5000°F), zirconia (for 3400-4000°F), and alumina (for 3000-3400°F) as the oxide ceramics for further consideration and utilization. These three materials met the preliminary requirements of refractoriness, cost, and availability. Hafnia was eliminated because of high cost, poor availability, questionable usefulness at 5000°F, too high a density for the 4000°F application, and a low experience factor. Magnesia would have been marginal for use at 5000°F but perhaps suitable for 4000°F. It was eliminated because of its high vapor pressure at high temperatures, reputation for poor thermal shock resistance, and poor availability in a low density form. Beryllia was eliminated because of its toxicity and accompanying handling

**TABLE I - CERAMIC OXIDES
THERMAL PROPERTIES**

METRIAL DESCRIPTION	THERMAL PROPERTIES		THERMAL EXPANSION COEFFICIENT ($\mu\text{m}/\text{m}/^\circ\text{C}$)	TOTAL NORMAL ENTRITANCE	SHOCK RESISTANCE
	HEAT DUCTILITY ($\text{J}/\text{m}^2/\text{cm}^2$)	HEATING POWER ($^\circ\text{C}$)			
1. Thoria Body (=85% Porosity)	510*	5970*	500 ^g	500 ^g	0.66**
			1000	1000	0.55
			1500	2000	0.39
			2000	3000	0.47
			2500	4000	0.53
			3000	5000	0.40
2. Thoria Insulating Body (=80% Porosity)	195*	5970*	SAME AS ABOVE	SAME AS ABOVE	---
			SAME AS ABOVE	SAME AS ABOVE	---
			SAME AS ABOVE	SAME AS ABOVE	---
			SAME AS ABOVE	SAME AS ABOVE	---
			SAME AS ABOVE	SAME AS ABOVE	---
			SAME AS ABOVE	SAME AS ABOVE	---
3. Boride Body (=75% Porosity)	560	5970*	500 ^g	1500 ^g	0.65
			1000	2000	0.95
			1500	2500	0.84
			2000	3000	0.81
			2500	3500	0.90
			3000	4000	0.97
4. Magnesia Body (=25% Porosity)	172	5070*	500 ^g	100 ^g	0.73
			1000	200	0.65
			1500	300	0.52
			2000	400	0.39
			2500	500	0.34
			3000	600	0.315
5. Strontia Insulating Body (=85% Porosity)	38	4600*	500 ^g	1000 ^g	0.71**
			1000	2000	0.53
			1500	3000	0.39
			2000	4000	0.46
			2500	5000	0.67
			3000	6000	0.67
6. Strontia Insulating Body (=85% Porosity)	153	4600*	SAME AS ABOVE	SAME AS ABOVE	---
			SAME AS ABOVE	SAME AS ABOVE	---
			SAME AS ABOVE	SAME AS ABOVE	---
			SAME AS ABOVE	SAME AS ABOVE	---
			SAME AS ABOVE	SAME AS ABOVE	---
			SAME AS ABOVE	SAME AS ABOVE	---

*Estimate
--- Not Probable

**TABLE I - CERAMIC OXIDES —
THERMAL PROPERTIES (CONTINUED)**

MATERIAL DESCRIPTION	PHYSICAL PROPERTIES		THERMAL CONDUCTIVITY		SPECIFIC HEAT		THERMAL EXPANSION		THERMAL STABILITY		SPARK RESISTANCE
	WALL THICKNESS (Inch/CM)	HEATING POWER (W/Inch ² /CM ²)	(W/Inch ² /Inch ² /°F)	(W/Inch ² /Inch ² /°C)	(W/Inch ² /Inch ² /°F)	(W/Inch ² /Inch ² /°C)	(Inch/Inch/°F)	(Inch/Inch/°C)	TEMPERATURE RANGE (°F)	TEMPERATURE RANGE (°C)	
7. Zirconia (≈21% Porosity)	269	4800*	500°F 6.1 1000 6.1 2000 6.1 3000 10.5 4000 13.4	6.1 6.1 6.1 10.5 13.4	500°F 0.137* 1000 0.146 2000 0.156 3000 0.166 4000 0.175	1000°F 4.2x10 ⁻⁶ 2000 4.46 3000 5.27 4000 5.87	500°F 0.71 1000 0.53 2000 0.39 3000 0.53 4000 0.70	500°F 1.940 2040 2540 3040 3540	0.71 0.53 0.39 0.46 0.49 0.51 (a)	Excellent (Survived very high heating rates 50-800°F/sec)	
8. Zirconia Bubble Coated	120*	4600*	500°F 2.0* 1000 2.3 2000 2.9 3000 3.6 4000 6.4	2.0* 2.3 2.9 3.6 6.4	SAME AS ABOVE	SAME AS ABOVE	SAME AS ABOVE	SAME AS ABOVE	SAME AS ABOVE	Excellent (MAC experience, survived heating rate of 50°F/sec)	
9. Beryllia Body (≈5% Porosity)	180	4450*	R.T. 1500 600 768 1900 312	6.5 6.0 7.1 9.7 10.9	500°F 0.25 1000 0.455 2000 0.54 3000 0.775	500°F 4.2x10 ⁻⁶ 1040 4.51 2040 5.13 3040 5.68 4040 6.13	1940 2040 2540 3040 3540	0.25 0.455 0.54 0.775 0.75 0.72 0.70 0.305 0.295	Poor (From MAC experience specimens spalled and cracked upon heating)		
10. Aluminum Insulating Body (≈80% Porosity)	29.5	3720*	500°F 1.87 1000 5.99 2000 5.07 3000 5.68 3300 5.94 (a)	6.5 6.0 7.1 9.7 10.9	500°F 0.185 1000 0.253 2000 0.260 3000 0.305 3400 0.318	500°F 4.2x10 ⁻⁶ 1040 4.41 2040 4.96 3040 5.64	SAME AS ABOVE	SAME AS ABOVE	SAME AS ABOVE		
11. Aluminum Bubble-Type Insulating Body	84	3720*	500°F 1.87 1000 5.99 2000 5.07 3000 5.68 3300 5.94 (a)	6.5 6.0 7.1 9.7 10.9	SAME AS ABOVE	SAME AS ABOVE	SAME AS ABOVE	SAME AS ABOVE	SAME AS ABOVE	---	
12. Alumina Body (≈21% Porosity)	194	3720*	944°F 1970 22.5 17.1 2900 17.2 3300 18.4	22.5 17.1 17.2 18.4	SAME AS ABOVE	SAME AS ABOVE	SAME AS ABOVE	SAME AS ABOVE	SAME AS ABOVE	Excellent (From MAC experience, survived Laboratory Thermal Shock Test)	
13. Alumina Bubble Coated	50*	3720*	500°F 1.87 1000 5.99 2000 5.07 3000 5.68 3300 5.90	6.5* 6.0 7.1 9.7 10.9	SAME AS ABOVE*	SAME AS ABOVE*	SAME AS ABOVE*	SAME AS ABOVE*	SAME AS ABOVE*	---	
14. Magnesia Alumina Spinel Body (≈30% Porosity)	137	3070*	212°F 137 754 1472 2192	71.0 51.0 27.3 22.0	R.T. 0.194	212°F 2.1x10 ⁻⁶ (177° - 2460°)	---	---	---	---	

***Post Probable
**Estimates

- REFERENCES**
- (A) - Static
 - (B) - Dynamic
 - (1) "Beryllium in Aerospace Structures", The Brush Beryllium Company
 - (2) "Alloy CB 752 for MAC Evaluation", Union Carbide
 - (3) "Fabricable Columbium Alloy", Data Sheet (1-1-63) DuPont
 - (4) Progress Report, SGB 291, 1/63, Stauffer Metals Division
 - (5) "Magnesia Alumina Spinel Body", Technical Data 283C
 - (6) "Magnesia Alumina Spinel Body", Technical Data 283C
 - (7) "Magnesia Alumina Spinel Body", Technical Data 283C
 - (8) "Magnesia Alumina Spinel Body", Technical Data 283C
 - (9) "Magnesia Alumina Spinel Body", Technical Data 283C
 - (10) "Magnesia Alumina Spinel Body", Technical Data 283C
 - (11) "Magnesia Alumina Spinel Body", Technical Data 283C
 - (12) "Magnesia Alumina Spinel Body", Technical Data 283C
 - (13) "Magnesia Alumina Spinel Body", Technical Data 283C
 - (14) "Magnesia Alumina Spinel Body", Technical Data 283C
 - (15) "Magnesia Alumina Spinel Body", Technical Data 283C
 - (16) "Magnesia Alumina Spinel Body", Technical Data 283C
 - (17) "Magnesia Alumina Spinel Body", Technical Data 283C
 - (18) "Magnesia Alumina Spinel Body", Technical Data 283C
 - (19) "Magnesia Alumina Spinel Body", Technical Data 283C
 - (20) "Magnesia Alumina Spinel Body", Technical Data 283C
 - (21) "Magnesia Alumina Spinel Body", Technical Data 283C
 - (22) "Magnesia Alumina Spinel Body", Technical Data 283C
 - (23) "Magnesia Alumina Spinel Body", Technical Data 283C
 - (24) "Magnesia Alumina Spinel Body", Technical Data 283C
 - (25) "Magnesia Alumina Spinel Body", Technical Data 283C
 - (26) "Magnesia Alumina Spinel Body", Technical Data 283C
 - (27) "Magnesia Alumina Spinel Body", Technical Data 283C
 - (28) "Magnesia Alumina Spinel Body", Technical Data 283C
 - (29) "Magnesia Alumina Spinel Body", Technical Data 283C
 - (30) "Magnesia Alumina Spinel Body", Technical Data 283C
 - (31) "Magnesia Alumina Spinel Body", Technical Data 283C
 - (32) "Magnesia Alumina Spinel Body", Technical Data 283C
 - (33) "Magnesia Alumina Spinel Body", Technical Data 283C
 - (34) "Magnesia Alumina Spinel Body", Technical Data 283C
 - (35) "Magnesia Alumina Spinel Body", Technical Data 283C
 - (36) "Magnesia Alumina Spinel Body", Technical Data 283C
 - (37) "Magnesia Alumina Spinel Body", Technical Data 283C
 - (38) "Magnesia Alumina Spinel Body", Technical Data 283C
 - (39) "Magnesia Alumina Spinel Body", Technical Data 283C
 - (40) "Magnesia Alumina Spinel Body", Technical Data 283C
 - (41) "Magnesia Alumina Spinel Body", Technical Data 283C
 - (42) "Magnesia Alumina Spinel Body", Technical Data 283C
 - (43) "Magnesia Alumina Spinel Body", Technical Data 283C
 - (44) "Magnesia Alumina Spinel Body", Technical Data 283C
 - (45) "Magnesia Alumina Spinel Body", Technical Data 283C
 - (46) "Magnesia Alumina Spinel Body", Technical Data 283C
 - (47) "Magnesia Alumina Spinel Body", Technical Data 283C
 - (48) "Magnesia Alumina Spinel Body", Technical Data 283C
 - (49) "Magnesia Alumina Spinel Body", Technical Data 283C
 - (50) "Magnesia Alumina Spinel Body", Technical Data 283C
 - (51) "Magnesia Alumina Spinel Body", Technical Data 283C
 - (52) "Magnesia Alumina Spinel Body", Technical Data 283C
 - (53) "Magnesia Alumina Spinel Body", Technical Data 283C
 - (54) "Magnesia Alumina Spinel Body", Technical Data 283C
 - (55) "Magnesia Alumina Spinel Body", Technical Data 283C
 - (56) "Magnesia Alumina Spinel Body", Technical Data 283C
 - (57) "Magnesia Alumina Spinel Body", Technical Data 283C
 - (58) "Magnesia Alumina Spinel Body", Technical Data 283C
 - (59) "Magnesia Alumina Spinel Body", Technical Data 283C
 - (60) "Magnesia Alumina Spinel Body", Technical Data 283C
 - (61) "Magnesia Alumina Spinel Body", Technical Data 283C
 - (62) "Magnesia Alumina Spinel Body", Technical Data 283C
 - (63) "Magnesia Alumina Spinel Body", Technical Data 283C
 - (64) "Magnesia Alumina Spinel Body", Technical Data 283C
 - (65) "Magnesia Alumina Spinel Body", Technical Data 283C
 - (66) "Magnesia Alumina Spinel Body", Technical Data 283C
 - (67) "Magnesia Alumina Spinel Body", Technical Data 283C
 - (68) "Magnesia Alumina Spinel Body", Technical Data 283C
 - (69) "Magnesia Alumina Spinel Body", Technical Data 283C
 - (70) "Magnesia Alumina Spinel Body", Technical Data 283C
 - (71) "Magnesia Alumina Spinel Body", Technical Data 283C
 - (72) "Magnesia Alumina Spinel Body", Technical Data 283C
 - (73) "Magnesia Alumina Spinel Body", Technical Data 283C
 - (74) "Magnesia Alumina Spinel Body", Technical Data 283C
 - (75) "Magnesia Alumina Spinel Body", Technical Data 283C
 - (76) "Magnesia Alumina Spinel Body", Technical Data 283C
 - (77) "Magnesia Alumina Spinel Body", Technical Data 283C
 - (78) "Magnesia Alumina Spinel Body", Technical Data 283C
 - (79) "Magnesia Alumina Spinel Body", Technical Data 283C
 - (80) "Magnesia Alumina Spinel Body", Technical Data 283C
 - (81) "Magnesia Alumina Spinel Body", Technical Data 283C
 - (82) "Magnesia Alumina Spinel Body", Technical Data 283C
 - (83) "Magnesia Alumina Spinel Body", Technical Data 283C
 - (84) "Magnesia Alumina Spinel Body", Technical Data 283C
 - (85) "Magnesia Alumina Spinel Body", Technical Data 283C
 - (86) "Magnesia Alumina Spinel Body", Technical Data 283C
 - (87) "Magnesia Alumina Spinel Body", Technical Data 283C
 - (88) "Magnesia Alumina Spinel Body", Technical Data 283C
 - (89) "Magnesia Alumina Spinel Body", Technical Data 283C
 - (90) "Magnesia Alumina Spinel Body", Technical Data 283C
 - (91) "Magnesia Alumina Spinel Body", Technical Data 283C
 - (92) "Magnesia Alumina Spinel Body", Technical Data 283C
 - (93) "Magnesia Alumina Spinel Body", Technical Data 283C
 - (94) "Magnesia Alumina Spinel Body", Technical Data 283C
 - (95) "Magnesia Alumina Spinel Body", Technical Data 283C
 - (96) "Magnesia Alumina Spinel Body", Technical Data 283C
 - (97) "Magnesia Alumina Spinel Body", Technical Data 283C
 - (98) "Magnesia Alumina Spinel Body", Technical Data 283C
 - (99) "Magnesia Alumina Spinel Body", Technical Data 283C
 - (100) "Magnesia Alumina Spinel Body", Technical Data 283C

(CONCLUDED)

TABLE II - CERAMIC OXIDES
MECHANICAL AND GENERAL PROPERTIES

MATERIAL DESCRIPTION PRODUCER AND/or SUPPLIER	MECHANICAL PROPERTIES			CHEMICAL AND/OR PHYSICAL STABILITY	FABRICATION (FORMING, FIRING & MACHINING)	AVAILABILITY AND/OR COST
	MODULUS OF RUPTURE (psi)	COMPRESSIVE STRENGTH (psi)	MODULUS OF ELASTICITY (psi)			
1. Thoria Body (~20% Porosity) Zirconium Corporation of America Solon, Ohio	R.T. 1500 *	---	---	Slightly Reduced by Carbon @ 2600°F, Rapidly Reduced @ 3000°F. Some Degree of Reaction with the Metals Co, Ti, Zr, Ba, & Sn @ 3200°F (Inert Atm.)	Selected Grades Mixed, Cold Pressed, Dried and Fired (Self-Bonded) Note: Toxicity when machining	Special Shapes (Machined) \$400/lb. Simple Shapes (Unmachined) \$60 - 90/lb. Delivery: 1-3 mos.
2. Thoria Insulating Body (~80% Porosity) NOT AVAILABLE AT PRESENT	---	---	Same as Above	(a)	Selected Grades Mixed with Burnout Met'l, Cold-Pressed and Fired or Selected Grades Mixed with Fuming Agents or Action, Cast in Place, Cured and Fired	---
3. Bafria Body (~1% Porosity) Zirconium Corporation of America Solon, Ohio	---	---	---	---	Selected Grades Mixed, Cold-Pressed, Dried and Fired (Self-Bonded)	Special Shapes (Machined) \$650/lb. Delivery: 3 mos.
4. Magnesia Body (~21.5% Porosity) Horton Co. Worcester, Mass.	600* 930 1830 2190 2550	70*	760* 392 728 1118 20.0 1812 2182 2372	Reduced in Carbonaceous Atm. @ Elevated Temp Some Degree of Reaction with the Metals Co, Ti, Zr, Ba, & Sn @ 3200°F (Inert Atm.)	Same as Above	Bricks, Blocks and Misc. Shapes \$300/lb. Delivery: 7 mos.
5. Zirconia Insulating Body (~9% Porosity) Jenax Insulation Rockford, Illinois	R.T. 370	R.T. 651 (Creeping Strength)	---	Unstable in Halogen, Sulphurous or Carbonaceous Atm. @ High Temp. Some Degree of Reaction with the Metals Co, Ti, Zr, Ba & Sn @ 3200°F (Inert Atm.)	Selected Grades Mixed, Mixture Expanded by Whipping, Poured Into Molds, Dried and Fired. Recently Cut, Sawn or Ground	Std. Brick Size 2 1/2 x 4 1/2 x 9 \$40/lb3 Produced on Laboratory Basis
6. Zirconia bubble-type Insulating Body Horton Co. Worcester, Mass.	R.T. 300	(b)	---	Same as Above	Zirconia bubbles Mixed With Magnesia, Cold-Pressed, Dried or Pressed, Dried and Fired (Self-Bonded)	Bricks, Blocks & Misc. Shapes \$475 - 1,000/lb. Delivery: 2 1/2 - 7 1/2 mos. Extra-Mold Cost if Not In Stock
7. Zirconia Body (~22.5% Porosity) Horton Co. Worcester, Mass. Zirconium Corporation of America Solon, Ohio	R.T. 1900	(a)	4,310,000* 3,477 1,970 1,968 2,031 2,040 2,485	Same as Above	Selected Grades Mixed, Pressed, Dried and Fired (Self-Bonded)	Bricks, Blocks & Misc. Shapes Delivery: 2 1/2 - 7 1/2 mos. Extra - Mold Cost if Not In Stock

*Estimate

TABLE II - CERAMIC OXIDES - MECHANICAL AND GENERAL PROPERTIES (CONTINUED)

MATERIAL DESCRIPTION PRODUCERS AND/OR SUPPLIERS	MODULUS OF RUPTURE (PSI)	MECHANICAL PROPERTIES COMPRESSIVE STRENGTH (PSI)	MODULUS OF ELASTICITY (PSI)	CHEMICAL AND/OR PHYSICAL STABILITY	FABRICATION FORMING, FIRING & MACHINING	AVAILABILITY AND/OR COST
8. Zirconia Bubbles Densated MAC Formulation	---	---	---	Instable in Halogens, Sulphurous or carbonaceous Atm. @ High Temp. Some Degree of Reaction with the Metals Cu, Ni, Zr, Be and Si @ 3000°F (Inert Atm.) (g)	Selected Grades, Bubbles & Binder Mixed, Tamped in Press, Cured (Chemically Bonded)	Simple Shapes Produced on Laboratory Basis
9. Beryllia Body (~5% Porosity) The Beryllium Corp. Reading, Pa.	R.T. 25,000	R.T. 190,000 2000°F 80,000	43,000 x 10 ⁶	Rapidly Volatilizes in Presence of Water Vapor @ Elevated Temp. Unstable in Halogen or Sulphurous Atm. Some Degree of Reaction with the Metals Cu, Ti, Zr, Be, & Si @ 3000°F (Inert Atm.) (g)	Selected Grades Mixed, Cold-Pressed & Fired or Hot-Pressed (Self-Bonded) Note Toxicity When Machining.	Misc. Shapes
10. Alumina Insulating Body (~80% Porosity) Insum Lubricates Rockford, Illinois	R.T. 4.98	R.T. 1179 (Crushing Strength)	---	Water Vapor & Reducing Atm. React with Alumina @ High Temp. Some Degree of Reaction with the Metals Ti, Zr, Be & Si @ 3000°F (Inert Atm.) (g)	Selected Grades Mixed, Mixture Expanded by Whipping, Paused into Molds, Dried & Fired. Readily Cut, Sawn or Ground	Std. Brick Size 9 x 4 1/2 x 2 1/4 \$.04 - .10/lb Produced on Laboratory Basis
11. Alumina Bubble-type Insulating Body Norton Co. Worcester, Mass.	R.T. 500 2300°F <3>	---	---	Same as Above	Alumina Bubbles Mixed with Fine Alumina Powder - Tamped or Pressed, Dried & Fired (Self-Bonded)	Bricks, Blocks, Plates and Misc. Shapes \$.65/lb Delivery: 2 1/2 - 7 1/2 Weeks Mold Cost Extra if not in Stock
12. Alumina Body (~21% Porosity) Norton Co. Worcester, Mass.	R.T. 2750 1830°F 1960	---	---	Same as Above	Selected Four-Grains Mixed, Cold-Pressed, Dried and Fired (Self-Bonded)	Bricks, Blocks, Plates and Misc. Shapes \$.15/lb Delivery: 2 1/2 - 7 1/2 wks.
13. Alumina Bubbles Cemented %C Formulation	---	---	---	Same as Above	Selected Grain, Bubbles & Binder Mixed, Tamped in Place & Cured (Chemically Bonded)	Simple Shapes Produced on Laboratory Basis
14. Magnesia Alumina Spinel Body (~30% Porosity) Laboratory Equipment Corp. St. Joseph, Mich.	---	---	---	---	Selected Grains Mixed, Cold-Pressed, Dried and Fired (Self-Bonded)	---

(a) Vendor Data
 (b) Goldsmith, et al., "Thermophysical Properties of Solid Materials," USAF AFML-TR-58-475 (III), November 1960
 (c) Anon, "The Thermal Properties of Twenty-Six Solid Materials to 5000°F or Their Destruction Temperatures," ASD-TDR-62-767, August 1962
 (d) E. Rynkiewicz, "Oxide Ceramics," Academic Press, New York, 1960
 (e) R. M. Davis and C. M. Lewicki, "High Temperature Composite Structure," USAF AFML-TR-62-418, June 1962

(f) W. D. Bailey, et al., "Mechanical Property Survey of Refractory Nonmetallic Crystalline Materials and Intermetallic Compounds," USAF AFML-TR-59-448, January 1960
 (g) W. D. Kilgery, "Oxides for High Temperature Applications," International Symposium High Temperature Technology, October 1959
 (h) D. J. Powers, "Thermal and Mechanical Testing of Foam Alumina and Foam Zirconia," Bell Aerospace Company, SR 63-15(M), 25 September 1961

(CONCLUDED)

difficulty, high thermal conductivity, questionable vapor pressure at high temperatures, and poor availability in a low density form. Spinel was eliminated because of questionable vapor pressure at high temperature, poor availability, and a low experience factor. Zircon was not considered because it dissociates at $\sim 3000^{\circ}\text{F}$. These were the only commonly available high melting point oxide ceramic materials given serious consideration.

Tables III and IV list property data for applicable alloys, refractory metals, high temperature service titanium alloys, and beryllium. These nineteen alloys are commercially available and have relatively high strength-to-weight ratios and elevated temperature stability. All of the alloys tabulated are wrought alloys available in sheet form. Table V lists property data for the currently available conventional insulation materials. Preliminary designs indicated application of this type of material as thermal insulation between the metallic substructure and outer ceramic surface. Alloy and thermal insulation selection was straight-forward and was accomplished during design. Material improvement and property measurement were not required.

4.2 CERAMIC SCREENING TESTS

The re-entry times (~ 1 hour) together with the temperatures and the requirement for dimensional stability dictated the use of oxide ceramics as the external insulating material. Further, the density restrictions necessitated the use of relatively low density ($\sim 25\%$ of theoretical density) oxide ceramics.

Brittle materials such as ceramics are noted for their relatively poor thermal shock resistance, i.e., inability to withstand stresses induced by the imposition of non-linear thermal gradients. Past experience and preliminary stress calculations indicated that the most difficult requirement for the ceramics to fulfill in this program was the ability to survive the expected high surface heating rates. If the ceramics could withstand this condition, it was felt they would survive the other environmental conditions.

Because of the thermal shock limitation (particularly for the low density materials), it was decided to subject samples of candidate ceramics to a thermal shock test as a means of screening out and selecting the more promising materials. Vendors submitted samples 1 inch x 1 inch x 1/4 inch to 1 inch thick and 2 inches x 2 inches x 1/4 inch to 1 inch thick of standard production and laboratory stage materials. The test consisted of subjecting the samples to surface heating rates of $25\text{-}50^{\circ}\text{F}/\text{sec}$ (expected rates determined in preliminary trajectory analyses) to a maximum temperature of 3400°F for alumina and spinel ($\text{MgO}\cdot\text{Al}_2\text{O}_3$) and 4000°F for zirconia and thoria; holding ten minutes at temperature; removing the heat source; and allowing the sample to cool naturally in static air. The testing was performed using the oxyacetylene torch facility shown in Figure 21. The sample was placed on the movable platform, exposed edges guarded with dense zirconia blocks, and elevated upward into the flame at a rate to yield the desired surface heating rate. All temperatures were monitored with an optical pyrometer, using emittance values given in Table I, for true temperature correction purposes.

Text continued on page 33

**TABLE - III - STRUCTURAL MATERIALS -
THERMOPHYSICAL PROPERTIES**

NO.	ALLOY	DENSITY LB/IN ³	MODULUS E PSI x 10 ⁶	SPECIFIC HEAT		THERMAL CONDUCTIVITY		COEFFICIENT OF THERMAL EXPANSION TEMP. IN/IN/°F/ IN x 10 ⁻⁶	DILATERY (MARKS)	COSES (PER POUND)	SUPPLIERS
				TEMP. IN/IN/°F	TEMP. IN/IN/°F	TEMP. IN/IN/°F	TEMP. IN/IN/°F				
1	Beryllium	0.0665	TEMP. PSI x 10 ⁶ 500 43.0 600 42.0 800 41.5 1000 39.0 1200 36.0 1400 20.0 (a)	TEMP. IN/IN/°F 0 0.40 400 0.27 800 0.24 1200 0.70 1600 0.76 2000 0.81 (a)	TEMP. IN/IN/°F 0 1206 400 1020 800 884 1200 698 1600 516 2000 398 (a)	TEMP. IN/IN/°F 600 6.83 1000 7.19 1400 7.77 1800 8.26 2200 8.61 2600 9.06 3000 9.41 3400 9.84 (a)	3-4	804. \$300-\$500 814. \$70-\$90	The Beryl Beryllium Co. The Beryllium Corp.		
2	L 605	0.330	TEMP. PSI x 10 ⁶ 77 32.64 212 32.15 392 30.29 572 28.64 752 27.20 932 25.30 1112 26.35 1292 25.19 1472 23.71 1652 22.44 1832 21.18 (a)	TEMP. IN/IN/°F 80-212 0.092 (a)	TEMP. IN/IN/°F 70 64.8 100 67.2 300 81.6 500 117.2 700 171.2 900 217.2 1100 261.6 1300 297.2 1500 327.2 1700 351.6 1900 369.6 (a)	70-200 6.83 400 7.19 600 7.57 800 8.06 1000 8.54 1200 8.92 1400 9.30 1600 9.66 1800 9.94 2000 10.22 (a)	9-13	\$5 to 7.50	Rayson Steellite Co., Universal-Cyclops Steel Corp.		
3	0b 752	0.326	TEMP. PSI x 10 ⁶ 16	TEMP. IN/IN/°F 32 0.059 200 0.061 600 0.065 1000 0.066 1400 0.067 1800 0.067 2200 0.067 (a)	TEMP. IN/IN/°F 500 264.0 700 285.6 900 302.4 1000 309.6 1200 311.2 1400 313.6 1600 315.6 1800 317.4 2000 318.4 (a)	68-200 3.8 400 3.9 600 4.0 800 4.1 1000 4.1 1200 4.2 1400 4.2 1600 4.3 1800 4.3 2000 4.4 2200 4.5 (a)	8	\$197	Rayson-Steellite Co.		
4	X 110 (D43)	0.326	TEMP. PSI x 10 ⁶ 75 16.2 100 16.4 1500 16.4 2000 16.6 2500 12.9 3000 6.4 (a)	TEMP. IN/IN/°F --- (a)	TEMP. IN/IN/°F --- (a)	--- (a)	8	\$200	Dupont		
5	SCB 291	0.347	--- (a)	TEMP. IN/IN/°F --- (a)	TEMP. IN/IN/°F --- (a)	--- (a)	6	\$100	Stamffer		
6	FS 85	0.390	TEMP. PSI x 10 ⁶ R.T. 20 3000 12 (f)	TEMP. IN/IN/°F --- (f)	TEMP. IN/IN/°F 300 261.0 400 263.0 500 269.1 600 276.1 (f)	TEMP. IN/IN/°F 0-300 4.00 0-1500 4.50 0-2000 4.75 0-2700 5.17 (f)	8	\$175	Phansteel		

**TABLE III - STRUCTURAL MATERIALS --
THERMOPHYSICAL PROPERTIES (CONTINUED)**

NO.	ALLOY	DENSITY lb/in ³	MECHANICAL		SPECIFIC HEAT TEMP. °F BTU/lb-°F	THERMAL CONDUCTIVITY TEMP. °F BTU-in/ft ² -hr-°F	COEFFICIENT OF THERMAL EXPANSION		DELIVERY (WEEKS)	COSTS (PER POUND)	SUPPLIERS
			YIELD TEMP. °F	TENSILE STRENGTH TEMP. °F			TEMP. °F	IN/IN/°F			
7	IN4	0.310	212 172 1472	13.7 13.0 12.2	0.065	32 212 1112	343.0 377.5 431.1 431.0	0-800 3.75 0-800 3.62 0-1500 4.20	8	\$85	DuPont
8	B 66	0.305	15-31			175 410 780 1020 1310	276.0 298.8 300.0 347.2 381.6	80-500 4.02 80-1500 4.27 80-2500 4.73 80-3500 4.96	8	\$140	Westinghouse
9	7MM	0.369	R.T. 45		0.066*	800 1000 2000	960.0* 790.0 540.0-743.0	68-212 3.06* 752 3.18 1532 3.28 68-1852 3.41	8	\$80	Universal-Cyclops Fansteel, O.R. Sylvania, Westinghouse Climax, WAI Chang
10	Mo-5FI	0.369	R.T. 500 1600 2500	44 31 13	0.066	800 1000 2000	960.0 790.0 540.0-743.0	68-212 3.06 752 3.18 1532 3.28 68-1852 3.41	8	\$70	Same as TZM
11	Reame 41	0.298	80 500 1000 1500 1700	31.6 29.6 24.7 21.8	70 0.108	300 400 600 800 1000 1100 1200 1400	80.3 87.5 102.0 107.0 117.5 131.0 139.0 145.0 161.0	70-1000 7.5 1200 7.8 1500 8.4 1600 8.7 1600 8.70 1700 9.05 70-1800 9.35	9	\$9-418	Haynes-Stellite Universal-Cyclops Steel Kelsey-Hayes Co. Cannon-Managon Corp. G.R.
12	Inconel X	0.300	80 1200 1350 1500 1600 1800	31.0 29.1 25.6 24.4 23.2 22.1 20.0	70-812 0.10 70-1680 0.13	192 572 932 1292 1472 1632	102.0 140.8 174.0 211.0 236.0 296.0	80-800 6.70 600 7.60 1000 7.85 1200 8.10 1600 9.00	8-12	\$9, 3.50, 2.50	International Nickel Co.
15	T. D. Nickel	0.322	76 900 1500 2000	19.24 16.54 13.98 12.06	70-812 0.107	70 500 1100 1700	600.0 381.0 300.0 319.0 341.0	70- 1000*	4-6	\$15 - \$65	DuPont

TABLE III - STRUCTURAL MATERIALS -
THERMOPHYSICAL PROPERTIES (CONTINUED)

NO.	ALLOY	DENSITY LB/IN ³	MODULUS E		SPECIFIC HEAT TEMP. BTU/#/°F OF	THERMAL CONDUCTIVITY		COEFFICIENT OF THERMAL EXPANSION		DELIVERY (WEEKS)	COSTS (PER POUND)	SUPPLIERS
			TEMP. OF	PSI x 10 ⁶		TEMP. OF	BU-IN- IN-FT-°F	TEMP. OF	IN/IN/°F/ x 10 ⁻⁶			
14	Ti-10W	0.608	600	21.5	.0356	2600	353.0	1812	2.26	---	---	Pentecel; Kings Haynes, G.E.
			1400	12.0		3140	330.0					
			1200	9.0		2840	290.0					
			1000	9.5		4190	269.0					
			800	5.5		4590	290.0					
			1600	1.0		4910	222.0					
15	Ti-111	0.604	77	26.0	---	3260	210.0 (ab)	90-500	3.1	---	---	Westinghouse
			2550	21.1		3100	210.0					
16	Ti-300b-7.5V	---	2910	21.1	---	---	---	2500	4.0	---	---	---
			3270	20.2		3000	4.2					
17	Ti-5Al-1Mo-IV	0.156	715	18.5	R.T. 0.12 to 0.15	75	41.3	32-212	4.7	6-8	10.50 Base + 2.50 Up to \$2.50 Quan. .010 x 49 + \$65.00 4In. .125 - +1.50	Timet; Crucible; Bridgeport; Republic
			16.5	16.5		400	47.0					
18	Al10MT	0.161	R.T.	16.0	R.T. .125 to .152	600	67.2	1000	5.6	6-8	Base \$10.50 + Up to \$2.50 Quan. .010 x 49 + \$65.00 4In. .125 - +1.50	Timet; Republic Crucible Bridgeport
			715	16.5		800	86.4					
19	Tungsten	0.697	R.T.	16.0	0.032	54.0	54.0	32-212	5.2	6-8	---	Pensteel; G. E. Sylvania; Climax; Westinghouse; Reactive Metal
			1600	43		1420	810.0					
		(ad)	3200	20 (ad)	(ae)	3140	709.0	3652	3.68	(ae)	\$ 55-\$70	

* A - Static
B - Dynamic

REFERENCES

(a) Beryllium in Aerospace Structures, The Brush Beryllium Company
(b) AMS 5537
(c) Completion of Physical and Mechanical Property Data on Haynes Alloy Cb 752 for MAC Evaluation, Union Carbide.
(d) Fabricable Columbium Alloy, Data Sheet (1-1-65), DuPont
(e) Progress Report, SOB 291, 1/63, Stauffer Metals Division
(f) Progress Report, SOB 291, 1/63, Stauffer Metals Division
(g) AMS-182 McDonnell Material Specification
(h) Westinghouse Special Technical Data 52-364
(i) AMS-184 McDonnell Material Specification
(j) AMS-180 McDonnell Material Specification
(k) AMS 5545
(l) AMS 5546
(m) AMS-189 McDonnell Material Specification
(n) National Research Corporation, Letter 8 May 1961
(o) Westinghouse Special Technical Data 52-365
(p) Technical Service Department Titanium Metals Corporation of America

(a) Timet Buyers Guide (Data Section)
(b) Becktolz, J. G. & Sherman, P. E. Trans AMS 46, 397 (1954)
(c) Haynes Stainless Company Bulletin F-30, 041C, June 1962
(d) DuPont Data Sheet A 23414
(e) Westinghouse Letter, 11 July 1963 to McDonnell Aircraft Corporation
(f) McDonnell Design & Production Bureau Bulletin, Series #4, Bulletin #2
(g) International Nickel Company, Technical Bulletin T-58
(h) DuPont Data Sheet A-30682
(i) University of Dayton (Memo No. 281-S-161C-42)
(j) Component Metals Division NRC Quarterly Report Covering January through April 1960 and Quarterly Report No. 55-45
(k) Westinghouse Letter, 11 July 1963 to McDonnell Aircraft Corporation
(l) Design Data Manual on Tungsten, Hughes Tool Company, Report ATC 60-68
(m) Demarguery, J. Compt. Rend. 220 (1854)

(CONCLUDED)

**TABLE IV - STRUCTURAL MATERIALS --
 MECHANICAL PROPERTIES**

NO.	ALLOY	GUARANTEED MECHANICAL PROPERTIES			QUANTIFIED STRENGTH/DEN. RATIO			SHEET & FOIL AVAILABLE SIZES	TOLERANCES	WELD-** ABILITY	FORM-** ABILITY	ALLOY* DEVELOPMENT STATUS		
		TEMP. OF	FTU KSI	FTY KSI	% ELON.	STRAIN RATE	TEMP. °F						FTU DEN.	FTY DEN.
1	Beryllium 4% BeO (See Reference (a), Table III)	R.T.	70	55	3-5	---	R.T.	1050	827	0.005" to 0.250"	± 0.003 on + 0.005 on 0.250 - 0.010	D	C	X
2	L-605 5000-200r- 10M1-15W (See Reference (b), Table III)	R.T.	130	55	30	---	R.T.	394	167	.005" to .187"	ANS 2262	A	A	X
3	Cb 752 Cb-10W-2.5Zr (See Reference (c), Table III)	R.T. 2200	70 30	55 20	12 20	0.005 to yield 0.05 to fracture	R.T. 2200	215 92	169 81	.002 - .187	± 10%	A	A	Y
4	D-43 (X-110) Cb-12r-10M-.1C (See Reference (d), Table III)	R.T. 2200	73 34	62 23	10 10	0.005 to yield strength 0.05 to fracture	R.T. 2200	225 105	191 71	.002 - .187	+ .002 on .010 to .020 + .0025 on .021 to .030 + .003 on .031 - .060	C	B	Y
5	SCB 291 Cb-10W-10Zr (See Reference (e), Table III)	R.T. 800 2000 2500 3000	68 63 30 17 9	55 22 12 7	12 12 12 12	0.005 to yield strength 0.05 to fracture	R.T. 800 2000 2500 3000	186 182 86 49 26	158 144 63 35 20	.002 - .187	ANS 2242	A	A	Y
6	PS 85 Cb-20r-11W-12r (See Reference (f), Table III)	R.T. 2400 2600 2800 3000	70 20 14 12 9	50 -- -- --	20 -- -- --	0.005 to yield strength 0.05 to fracture	R.T. 2400 2600 2800 3000	179 51 36 31 23	128 --- --- ---	.002 - .187	± .001 on .030	A	A	Y
7	D-14 Cb-5Zr (See Reference (g), Table III)	R.T. 800 1600 1900 2200	64.1 48.5 34.5 16.9	51.1 34 29 27.5 11.7	15 7 6 10 10	0.005 to yield strength 0.05 to fracture	R.T. 800 1600 1900 2200	206 156 147 111 94	165 110 84 89 38	Same as X110		A	A	Y
8	B 66 Cb-3Mg-5V-12r (See Reference (h), Table III)	R.T. 800 1600 2200 2600	98 70 70 35 18	74 50 50 23 11.5	15 15 15 30 30	0.005 to yield strength 0.05 to fracture	R.T. 800 1600 2200 2600	321 230 230 115 59	243 164 164 75 38	.002 - .200	---	C	B	Y
9	ZM- Mo-5W1-.07Zr (See Reference (i), Table III)	R.T. 2000 2400	110 20 15	65 19 7	7 10 12	---	R.T. 2000 2400	299 140 40.	231 20. 20.	.010 - .187	---	C	B	X
10	Mo-5W1 (See Reference (j), Table III)	R.T. 500 1500 2500	76 47 32 15	61 39 12 11	21 26 25 12	---	R.T. 500 1500 2500	206 127 87 41	165 106 32 30	.010 - .187	---	C	B	X

TABLE IV - STRUCTURAL MATERIALS -
MECHANICAL PROPERTIES (CONTINUED)

NO.	ALLOY	GUARANTEED MECHANICAL PROPERTIES					QUARANTEED STRENGTH/ENR. RATIO				SHEET & FOIL AVAILABLE SIZES	TOLERANCES	WELDING ABILITY	FORMING ABILITY	ALLOY DEVELOPMENT STATUS
		TEMP OF	FTU ESI	FTY ESI	% ELON.	STRAIN RATE	TEMP. OF	FU ENR.	FY ENR.						
11	Temp. h1 5341-19C- 1046-1100- 3T1-1.7A1 (See Reference (k), Table III)	Sol. Heat'd R.T. H.T.A. R.T. H.T.A. 1400	170 100 170 130 140	100 100 130 110	30 10 3	---	Sol. Heat'd R.T. H.T.A. R.T. H.T.A. 1400	570 336 570 470	336 436 370	.010 to .187	---	B	A	X	
12	Inconel X 73M1-150r- 10B-2.4T1 (See Reference (l), Table III)	R.T.	130	65	40	---	R.T.	433	216	.002 - .187	---	B	A	X	
13	T.D. Nickel M1-21Mg (See Reference (m), Table III)	R.T. 1800	62 15	46 --	5 2	---	R.T. 1800	193 47	143	.010 to .187	AMS-2262 Table I	D	A	Y	
14	Ta-10W (See Reference (n), Table III)	RX R.T. As Rolled R.T. S.R. R.T. As Rolled 3000	75 120 100 8	60 115 105 6	15 -- 5 10	.01 1N/IN/MIN ---	RX R.T. As Rolled R.T. S.R. R.T.	123 197 164	99 189 173	.005 - .020	---	B	A	Y	
15	T-111 Ta-5W-2W (See Reference (o), Table III)	75* 800. 2400 3000 3500 * Typical Properties	90.4 57.2 37.3 14.8 13.0	43.0 23.5 11.9 12.6	29 15 36 48 34	---	75 800 2400 3000 3500	150 95 62 25 22	150 37 20 21	.010 to .200	---	B	A	Z	
16	Ta-30Cb-7.5V (See Reference (p), Table III)	---	---	---	---	---	---	---	---	---	---	B	A	Z	
17	Ti-6Al-1Mo-1V (See Reference (q), Table III)	R.T.	130	120	10	---	R.T.	834	770	.010 - .187	---	A	B	Y	
18	Al 10A4 Ti-5Al-2.5Sn (See Reference (r), Table III)	R.T.	120	115	10	---	R.T.	746	715	.010 - .187	+ 10% at base price	A	B	X	
19	Tungsten (See Reference (s), Table III)	800 1600	55 44	12 8	41 40	---	800 1600	78.7 63.0	17.2 11.5	.005 to .050	---	D	C	X	

* RATING CODE
X - Large Volume Commercial
Y - Commercial
Z - Experimental

** RATING CODE
A - Readily
B - With Difficulty
C - With Great Difficulty
D - Not Fractional

(CONCLUDED)

TABLE V - NON-STRUCTURAL THERMAL INSULATIONS

MATERIAL DESCRIPTION	PRODUCER, GEN/OR SYNTHESIS	COST (PER POUND)	DENSITY LB/FT ³	TEMPERATURE (°F)	SPECIFIC HEAT (BTU/LB/°F)	TERMINAL CONDUCTIVITY (100-150/IN. ² -FT. ² -°F)	COMMENTS
1. Dym-Q Quartz (99% Silicon)	Johns-Manville New York, N.Y.	\$35.00	4-10	+ 2750 (Continuous) + 3000 (Short Time)	200°F 0.20 500 0.24 1000 0.27 1500 0.29 2000 0.30 2500 0.30	900°F .64 1200 .61 1500 .59 1800 1.12 2100 1.10 2300 1.05	1) Stiff, rigid board 2) Free-Surface Micro-Quartz 3) Samples must be heated to Centour 4) Shrinkage occurs above 2750°F 5) To have been used on Dyna-Sear
2. Micro-Quartz (99% Silicon)	Johns-Manville New York, N.Y.	\$25.00	3-6	+ 1800 (Continuous) + 2400 (Short Time)	SAME AS ABOVE	400°F .44 800 .60 1200 1.04 1600 1.29	1) Fibrous Matt-Soft Flexible 2) Facing Need to Contain Insulation 3) Shrinkage Occurs Above 1800°F 4) Can be Free-Surface (Dym-Quartz)
3. Refrasil A-100 (99% Silicon)	H. I. Thompson Gardens, Calif.	\$25.00	3-10	+ 1800 (Continuous) + 2000 (Short Time)	SAME AS ABOVE *	400°F .36 800 .50 1200 .63 1600 .74 2000 .87 2400 .97	1) Fibrous Matt - Soft, Flexible 2) Facing Need to Contain Insulation 3) Shrinkage Occurs Above 1800°F 4) Can be Free-Surface 5) Presently Being Used on ASSET 6) K values presented were obtained using small Δ T (See note at end of table)
4. Irish Refrasil (Modified Refrasil) A-100	H. I. Thompson Gardens, Calif.	\$30.00 *	3-10	+ 2750 (Continuous)	SAME AS ABOVE *	600°F .45 1000 .55 1500 .70 1800 1.20 2200 1.40	1) Same as Refrasil Generally, though the temperature range is higher 2) Shrinkage occurs above 2750°F
5. Excelsior Q (Silicon Sparum)	Excelsior Coating, Inc. Quincy, Mass.	\$10.00	12	+ 1000 (Continuous) + 2500 (Short Time)	100°F 0.18 * 500 0.24 1000 0.27 1500 0.29 2000 0.30	R.F. 0.3 ρ = 12 ρ = 60 mm Hg	1) Molten Blocks 2) Difficult to Machine
6. Thermotex (Alumino-Silicate)	Johns-Manville New York, N.Y.	\$5.00	3-12	+ 2000 (Continuous) + 3000 (Short Time)	400°F 0.35 500 0.36 1000 0.42 1500 0.48 2000 0.47	ρ = 4 ρ = 10 mm Hg	1) Contains Small Amounts of Fibrous Matt-Soft, Flexible 2) Facing Need to Contain Insulation 3) Shrinkage occurs above 2000°F 4) K values presented were obtained using small Δ T (See note at end of table)

* REFRACTIVE
** - Density of specimen (lbs/cu. ft.)
*** - Pressure value at which conductivity was measured.

TABLE V - NON-STRUCTURAL THERMAL INSULATIONS (CONTINUED)

MATERIAL DESCRIPTION	PRODUCER AND/OR SKETCHERS	COST (PER POUND)	DENSITY LB/FT ³	TEMPERATURE RANGE (°F)	WEIGHT SAVING (%)	SPECIFIC HEAT (BTU/LB/°F)	THERMAL CONDUCTIVITY (BTU-IN/HR-FT ² -°F)	COMMENTS
7. Fibertex (Alumino-silicate)	Carborundum Co. Highland Falls, N.Y.	\$5.00	3 & 6	+2000 (Continuous) +3000 (Short Time) (c)	0.22	600°F ρ = .50 1000 ρ = .86 1400 ρ = 1.28 1800 ρ = 1.70 2000 ρ = 2.06	1) Fibrous mat-form, flexible 2) Shrinkage occurs above 2000°F 3) Packings needed to contain insulation 4) Used on A-8	
8. Fibergul (Polysium Fiberglass)	E. I. duPont Wilmington, Delaware	\$7.00	3-70	+2000 (Continuous)	N.F.	500°F ρ = .48 1000 ρ = .78 1500 ρ = .93 2000 ρ = 1.15	1) Max. thermal temp. @ 10 ⁻⁵ mm Hg is 1800°F 2) Don't heat 3) Container should be held in place insulation in place	
9. Min-I 2000 (Proprietary Formulation)	Johns-Manville New York, N.Y.	\$180.00	20	+1800 (Continuous) +2100 (Short Time)	0.201* 0.228 0.256 0.27 0.273 0.280	500°F ρ = .35 1000 ρ = .56 1500 ρ = .66 2000 ρ = .80	1) Molten Block 2) Very difficult to machine 3) Vibration will cause this material to crumble 4) Reorientation begins at 2000°F	
10. Fibrogul 700 Stabilized (Zirconia)	E. I. duPont Wilmington, Del.	\$60.00	3-30	+2400 (Continuous) +3300 (Short Time)	0.098* 0.120 0.140 0.160 0.177	1000°F ρ = 0.51 2000 ρ = 0.86 3000 ρ = 1.32 4000 ρ = 1.68 5000 ρ = 2.17 6000 ρ = 2.66 7000 ρ = 3.17 8000 ρ = 3.70	1) Positive shrinkage above 1800°F 2) Mechanically very poor 3) K values presented were obtained using small Δ T (see note at end of table)	
11. A8-17 (Proprietary)	Arthur D. Little, Inc. Cambridge, Mass.	\$3.00	6-20	+2800 (In absence of Oxygen)	0.271* 0.298 0.325 0.352 0.375	800 ρ = .099 600 ρ = .80 1000 ρ = .115 1500 ρ = 0.5 mm Hg 2000 ρ = .132	1) Powder insulation must be contained 2) Must be contained for optimum properties 3) Contains 20% Glass Fibers	
12. Super Insulation (Layers of Shields & Insulating Soya)	Landi Corp. North Providence, R.I. Johns-Manville New York, N.Y.	---	17	+2600 (Short Time) Actually dependent on Super Insulation	Dependent on Material and Construction	300 ρ = .018 750 ρ = .085 1150 ρ = .098	1) Requires Protection from Oxidation 2) Requires .01 mm Hg for optimal properties 3) Probably most difficult to install 4) Requires Licensing from Landi Corp.	

NOTE: Some of the K values presented were determined on an apparatus yielding small Δ T's. These figures cannot be used to compare materials with K values obtained with large Δ T's.

* REFERENCE

REFERENCES

- (a) Vendor Data
- (b) Boeing Design Manual 542.3, 3 November 1961
- (c) J. D. Fluhett, J. D. Klein, Thermal Conductivity of Five Different High Temperature Insulations, "Spacecraft Report No. 469, 30 June 1965

(CONCLUDED)

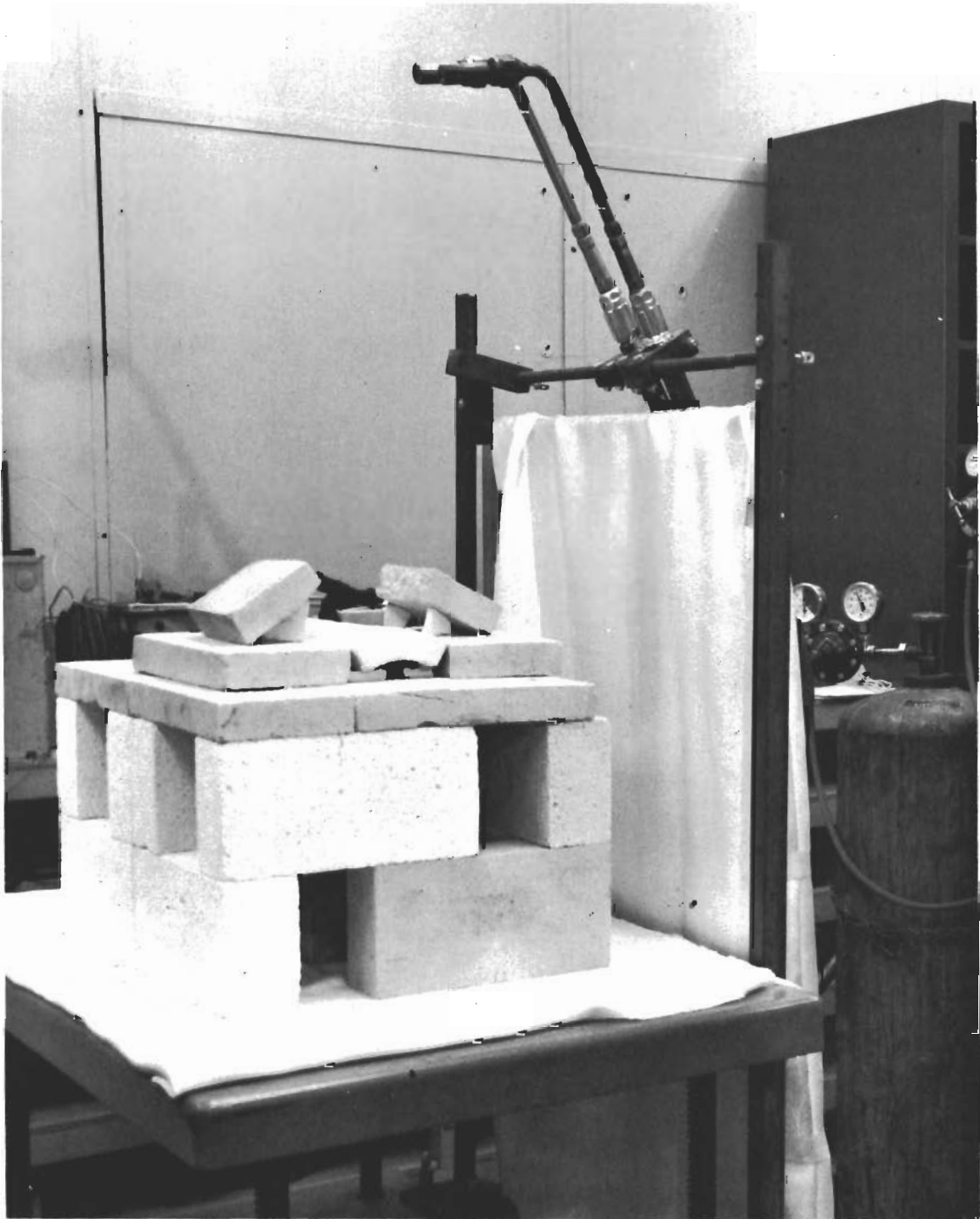


FIGURE 21 - OXYACETYLENE TORCH FACILITY FOR THERMAL SHOCK TESTING

Samples which remained integral after testing were visually examined (with the unaided eye and at 5-20X) for cracks and qualitatively checked for strength change by determining the ease or difficulty in breaking the sample in the hands. In the intended application, it was felt that some micro-cracking could be tolerated in ceramics so long as the materials remained integral and did not suffer considerable strength loss.

4.2.1 Low Density Ceramics

Due to program requirements, low density (~40% or less of theoretical density) ceramics were of primary interest, and the results of the thermal shock testing for this class of ceramics are presented in Table VI. Materials commercially available at the beginning and throughout the duration of this program are listed. Ideally, a density of 25% of theoretical or less was sought. In Table VI, the samples have been segregated into three classes based on means of achieving low density. (In some cases, this processing information was surmised and was not necessarily supplied by the manufacturer.)

The Foam classification indicates that the low density was attained by introducing a foaming or blowing agent into the ceramic mix during processing. The Burn-out classification indicates that the low density was attained by introducing into the ceramic mix a material which was subsequently decomposed, burned out, or leached out during processing. The Low Density Aggregate classification indicates that part of the composition consisted of a low bulk density material such as bubble zirconia.

Figure 22 is an illustration of some foamed zirconias; Figure 23 shows some burn-out zirconias; and Figure 24 shows some low density aluminas. Figures 25, 26, and 27 are close-ups of some of the foamed zirconias and Figures 28, 29, and 30 are close-ups of some of the burn-out zirconias. These pictures give an idea of the porosity and ceramic structure variations between burn-outs and foams and between classes of materials from various manufacturers. Figures 31 through 33 are 20X magnifications of some low density compositions. The two foam zirconias in Figures 31 and 32 had a very fine-grained, uniform ceramic structure. The burn-out zirconia in Figure 33 had a coarse, less uniform ceramic structure.

As indicated in Table VI, none of the low density materials, especially at 25% or less of theoretical density, proved satisfactory after thermal shock testing. The coarse-grained denser ceramics, such as the burn-out and low-density aggregate materials, were weakened less by the thermal shock and did not spall or crack into smaller pieces.

Although thermal shock resistance was considered the single most important material characteristic (without this characteristic the ceramic would be unusable), another very important characteristic was the thermal conductivity. Since the ceramics were to be utilized as thermal insulating overlays to protect a metallic substructure, low thermal conductivity was desirable. In addition to being dependent on the intrinsic properties of the basic material, the thermal conductivity of a ceramic body is dependent on the porosity content, size, shape, and distribution. Pore size becomes very important at elevated temperatures, where radiation is the dominant mode of heat transfer (especially at reduced pressures); and a low density

body with large sized porosity can have a thermal conductivity at elevated temperature which exceeds that of an equal or higher density body which has much smaller sized porosity. For instance, a body with an open structure and large porosity (as shown in Figure 27) which has a very low density presents little barrier to thermal radiation and is a poor thermal insulator at elevated temperatures.

Another material characteristic given consideration was the relative strength of the ceramic. Several ceramics in Table VI are listed as having low strength in the as-received condition. These materials could be readily chipped, broken, or even crushed by hand, making them subject to damage during the expected handling, machining, and installation operations. Many of the very low density ($<15\%$ of theoretical density) ceramics were so low in strength as to make them impractical for use. As expected, strength was closely related to density.

The availability of a ceramic was also taken into account, as indicated in Table VI. Some of the laboratory stage ceramics were not expected to progress beyond that stage in time to be utilized in this project. Not all the production ceramics listed in Table VI were available or evaluated early enough in the project to permit utilization.

Based on the samples evaluated, some observations were made concerning the processes utilized for achieving low density. The Foam process appeared most compatible with fine grained ceramic structures. This process seemed capable of yielding very low density materials with a variety of pore sizes and good porosity uniformity. As this process was dependent on the rheological and particle suspension properties of a slip or slurry, it was probably not readily adaptable to a wide variety of ceramic structures, especially coarse grained structures.

The Burn-out process appeared compatible with a variety of ceramic structures from coarse to fine, but did not appear to have the potential for making as low a density material as the foam process. The uniformity, size, and amount of the porosity was dependent respectively on the uniformity of dispersion, the size, and the quantity of the burn-out material.

The Low Density Aggregate process relied on the bulk density of the aggregate material to attain low density, which presented considerable limitations on attaining very low densities and a variety of porosities.

Of these three methods of attaining low density, it appeared that within the state-of-the-art at the time of the evaluation, the Burn-out process had the most versatility and was readily adaptable to a variety of ceramic structures, including a coarse grained structure and; therefore, had the greatest potential for achieving adequate thermal shock resistance. McDonnell's past experience (including evaluation of ceramic materials for the Air Force ASSET program) and a generally accepted condition in the Refractories industry was that in ceramic bodies with a porosity of 15-30% and a gradation of grain sizes, bodies with a coarse grained structure are more thermal shock resistant than comparable bodies with a fine grained structure. It was not known whether this same condition was true in bodies of 60-90% porosity, but it was reasoned that a correlation did exist.

Text continued on page 46

**TABLE VI - EVALUATION OF COMMERCIAL LOW DENSITY CERAMICS
FOAMS**

Description	Manufacturer	Density		Comments, As Received				Thermal Shock Testing		
		Lb / Ft ³	% Theoretical	Strength	Porosity Size	Uni- formity	Availability Status	Sample Size (Inches) *	Surface Heating Rate (°F/Sec)	Results
Al ₂ O ₃ ICB 3400	Ipsen	34	13.6	Low	Medium	Fair	Production	1 x 1 x 1/2	50	Weakened severely
Al ₂ O ₃ ICB 3400	Ipsen	34	13.6	Low	Medium	Fair	Production	1 x 1 x 1	50	Cracked, weakened
Al ₂ O ₃ ICB 3400	Ipsen	34	13.6	Low	Medium	Fair	Production	1 x 1 x 1	25	Weakened slightly
Al ₂ O ₃ - X 3343	LECO	60	24.0	Good	Medium	Fair	Laboratory	1 x 1 x 1/2	50	Little strength change, some micro cracks
Al ₂ O ₃ Alsimag 761	American Lava	21	18.4	Very low	Medium	Good	Production	1 x 1 x 1	50	Weakened slightly
Al ₂ O ₃ Alsimag 761	American Lava	17	6.8	Very low	Large	Good	Production	1 x 1 x 1	50	Weakened slightly
Al ₂ O ₃ Foam	Astro-Met Associates	19	7.6	Very low	Large	Good	Production	1 x 1 x 1/2	50	Weakened slightly
Al ₂ O ₃ Foam	United Technology Center	36	14.4	Fair	Medium	Good	Laboratory	1 1/4 x 1 x 3/4	50	Cracked & shrunk severely Slight melting.
Al ₂ O ₃ Foam	Melpar	35	14.0	Fair	Very small	Fair	Production	1 x 1 x 1/2	50	Weakened severely, melted
ZrO ₂ ICB 4200	Ipsen	40	11.2	Low	Medium	Fair	Production	1 x 1 x 1/2	50	Spalled & weakened severely
ZrO ₂ ICB 4200	Ipsen	40	11.2	Low	Medium	Fair	Production	1 x 1 x 1	50	Spalled & weakened severely
ZrO ₂ low density	Ipsen	60	16.8	Fair	Medium	Fair	Laboratory	1 x 1 x 1	50	Weakened
ZrO ₂ 4300D	Ipsen	63	17.6	Fair	Medium	Fair	Laboratory	1 x 1 x 1	50	Cracked, weakened
ZrO ₂ Z-48-180	Ipsen	85	23.8	Good	Medium	Fair	Laboratory	1 x 1 x 1	50	Weakened slightly
ZrO ₂ Foam	United Technology Center	40	11.2	Fair	Medium	Fair	Laboratory	1 x 1 x 1	50	Cracked & shrunk severely, slight melting
ZrO ₂ Foam	United Technology Center	40	11.2	Fair	Small	Fair	Laboratory	1 x 1 x 1	50	Cracked & shrunk severely, slight melting
ZrO ₂ Foam	Simoniz	35	9.8	Low	Medium	Good	Laboratory	1 x 1 x 1	50	Weakened
ZrO ₂ Foam un- stabilized low-fired	Simoniz	87	24.4	Very low	Large	Good	Laboratory	1 x 1 x 1	50	Spalled, cracked weakened severely
ZrO ₂ Foam un- stabilized high-fired	Simoniz	162	45.4	Good	Large	Good	Laboratory	1 x 1 x 1	50	Spalled, cracked weakened severely
ZrO ₂ Part. stabilized High fired	Simoniz	165	46.2	Good	Large	Good	Laboratory	1 x 1 x 1	50	Weakened, cracked slightly
ZrO ₂ - 356CY	Astro-Met Associates	21	5.9	Very low	Large	Good	Production	1 x 1 x 1	50	Spalled, cracked severely
ZrO ₂ - 359B0	Astro-Met Associates	39	10.9	Fair	Small	Good	Production	1 x 1 x 1	50	Weakened, cracked
ZrO ₂ - 217BY	Astro-Met Associates	28	7.8	Low	Medium	Good	Production	1 x 1 x 1	50	Weakened severely
ZrO ₂ - 278C10	Astro-Met Associates	34	9.5	Low	Small	Good	Production	1 x 1 x 1	50	Weakened
ZrO ₂ - 220AY	Astro-Met Associates	33	9.2	Low	Large	Good	Production	1 x 1 x 1	50	Weakened
ZrO ₂ - 244CO	Astro-Met Associates	40	11.2	Fair	Large	Good	Production	1 x 1 x 1	50	Weakened severely
ZrO ₂ - X3342	LECO	80	22.4	Good	Medium	Fair	Laboratory	1 x 1 x 1	50	Weakened & cracked slightly
ZrO ₂ Foam	Melpar	50	14.0	Low	Very small	Fair	Laboratory	1 x 1 x 1	50	Cracked & weakened severely
ZrO ₂ Foam high-fired	Melpar	72	20.2	Fair	Very small	Fair	Laboratory	1 x 1 x 1	50	Spalled & weakened severely
ZrO ₂ Foam low-fired	Melpar	55	15.4	Low	Very small	Fair	Laboratory	1 x 1 x 1	50	Spalled & cracked severely
ZrO ₂ Foam Low-fired	Melpar	75	21.0	Fair	Very small	Fair	Laboratory	1 x 1 x 1	50	Spalled & cracked severely

**TABLE VI - EVALUATION OF COMMERCIAL LOW DENSITY CERAMICS
(CONTINUED)**

FOAMS

Description	Manufacturer	Density		Comments, As Received				Thermal Shock Testing		
		Lb Fr ³	% Theo- retical	Strength	Porosity Size	Uni- formity	Availabil- ity Status	Sample Size (Inches) [*]	Surface Heating Rate °F/Sec	Results
ZrO ₂ Foam 3400 5-5	Melpar	70	19.6	Good	Very small	Fair	Laboratory	1 x 1 x ½	50	Spalled & cracked severely
ZrO ₂ Foam 3600 5-5	Melpar	70	19.6	Good	Very small	Fair	Laboratory	1 x 1 x ½	50	Spalled & cracked severely
ZrO ₂ Foam 3400 6-6	Melpar	75	21.0	Good	Very small	Fair	Laboratory	1 x 1 x ½	50	Spalled & cracked severely
ZrO ₂ Foam 3600 6-6	Melpar	87	24.4	Good	Very small	Fair	Laboratory	1 x 1 x ½	50	Spalled & cracked severely
ZrO ₂ Foam	T.A.M.	100	28.0	Fair	Very small	Fair	Laboratory	1 x 1 x ½	50	Weakened
ThO ₂ X3344	LECO	125	20.1	Low	Medium	Poor	Laboratory	1 x 1 x ½	50	Cracked, weakened severely
ThO ₂ Foam	Melpar	100	16.0	Fair	Very small	Fair	Laboratory	1 x 1 x 1	50	Cracked severely, weakened slightly
ThO ₂ Foam low-fired	Simoniz	105	16.8	Very low	Large	Good	Laboratory	1 x 1 x 1	50	Melted

BURN-OUTS

Al ₂ O ₃ TA4062	Norton	30	12.0	Low	Large	Fair	Production	1 x 1 x 1	50	Cracked, weakened severely
Al ₂ O ₃ TA5062	Norton	65	26.0	Good	Large	Fair	Production	1 x 1 x 1	50	Cracked & weakened
Al ₂ O ₃ TA5050	Norton	45	18.0	Fair	Medium	Fair	Laboratory	1 x 1 x 1	25	Cracked & weakened
ZrO ₂ - Low density	Norton	57	15.9	Low	Large	Fair	Laboratory	1 x 1 x 1	50	Weakened severely
ZrO ₂ - Y1085	Zircon	157	44.0	Good	Large	Fair	Laboratory	1 x 1 x 1	50	Weakened severely
ZrO ₂ - Y978	Zircon	143	40.2	Fair	Large	Fair	Laboratory	1 x 1 x 1	50	Weakened
ZrO ₂ - W1590	Zircon	129	36.2	Fair	Medium	Fair	Laboratory	1 x 1 x 1	50	Cracked, weakened
ZrO ₂ - W1616	Zircon	113	31.7	Fair	Medium	Fair	Laboratory	1 x 1 x 1	50	Cracked, weakened
ZrO ₂ - W1613	Zircon	149	41.7	Fair	Medium	Poor	Laboratory	1 x 1 x 1	50	Cracked, slightly weakened

LOW-DENSITY AGGREGATE

Al ₂ O ₃ RA4058	Norton	80	32.0	Good	Large	Fair	Production	2 x 2 x 1	50	Weakened very slightly
Al ₂ O ₃ RA5058	Norton	85	34.0	Good	Large	Fair	Production	2 x 2 x 1	50	Weakened slightly
Al ₂ O ₃ RA5058	Norton	85	34.0	Good	Large	Fair	Production	1 x 1 x 1	50	Weakened & cracked slightly
Al ₂ O ₃ RA5058	Norton	85	34.0	Good	Large	Fair	Production	1 x 1 x 1	25	Little strength change
Al ₂ O ₃ LA5969	Norton	80	32.0	Good	Large	Poor	Production	1 x 1 x 1	25	Weakened slightly
Al ₂ O ₃ LA5969	Norton	80	32.0	Good	Large	Poor	Production	1 x 1 x 1	50	Weakened, cracked
Al ₂ O ₃ - 269D	A.P. Green	80	32.0	Fair	Medium	Fair	Production	1 x 1 x ½	50	Weakened slightly
ZrO ₂ - RZ5603	Norton	150	42.1	Good	Large	Fair	Production	1 x 1 x ½	50	Weakened slightly
ZrO ₂ - Castable	Zircon	190	53.2	Good	Large	Fair	Laboratory	1 x 1 x 1	50	Weakened slightly
ZrO ₂ - Tamped	Zircon	160	44.8	Good	Large	Fair	Laboratory	1 x 1 x 1	50	Weakened slightly

* Last dimension is specimen thickness

(CONCLUDED)

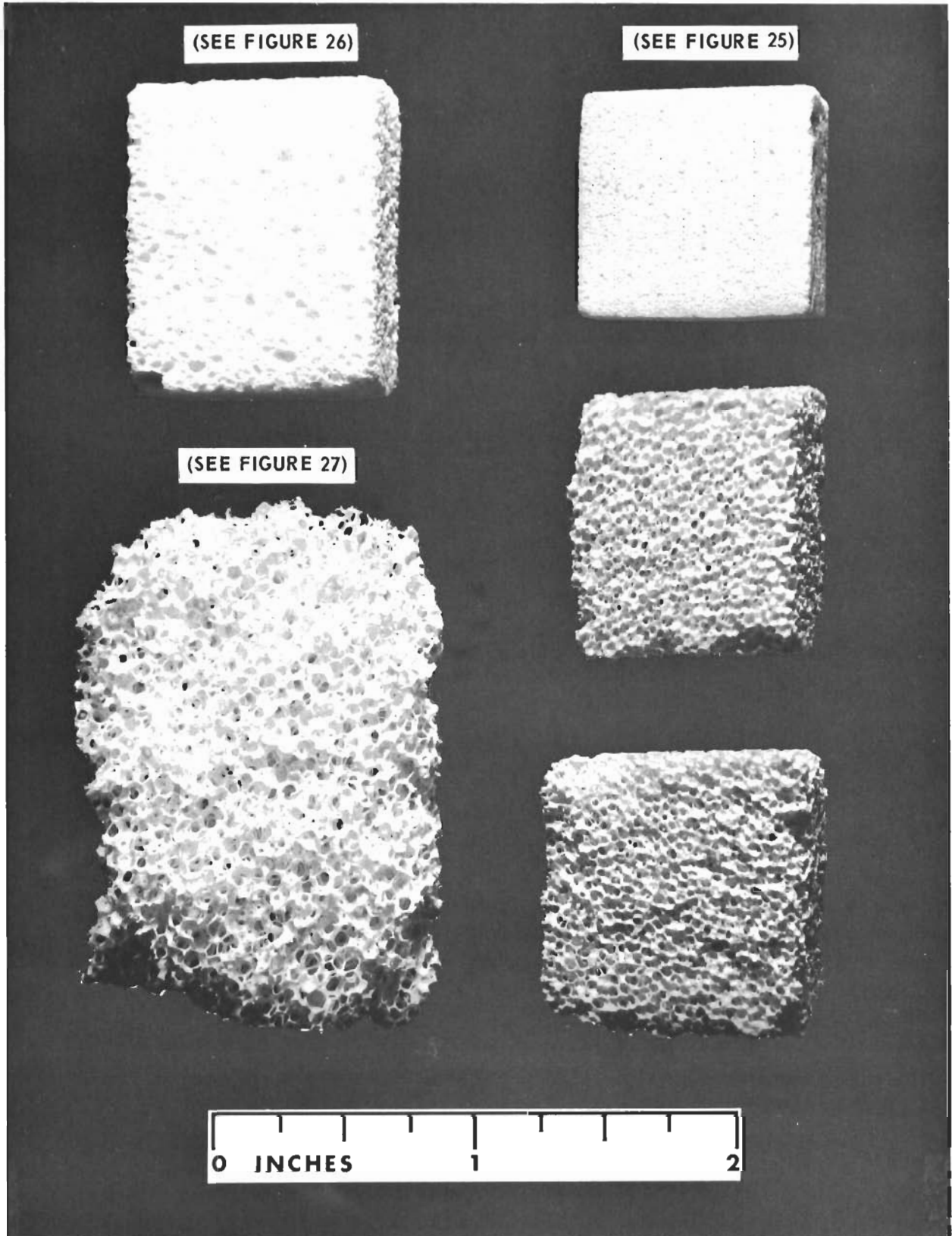


FIGURE 22 - COMMERCIAL LOW DENSITY FOAM ZIRCONIAS

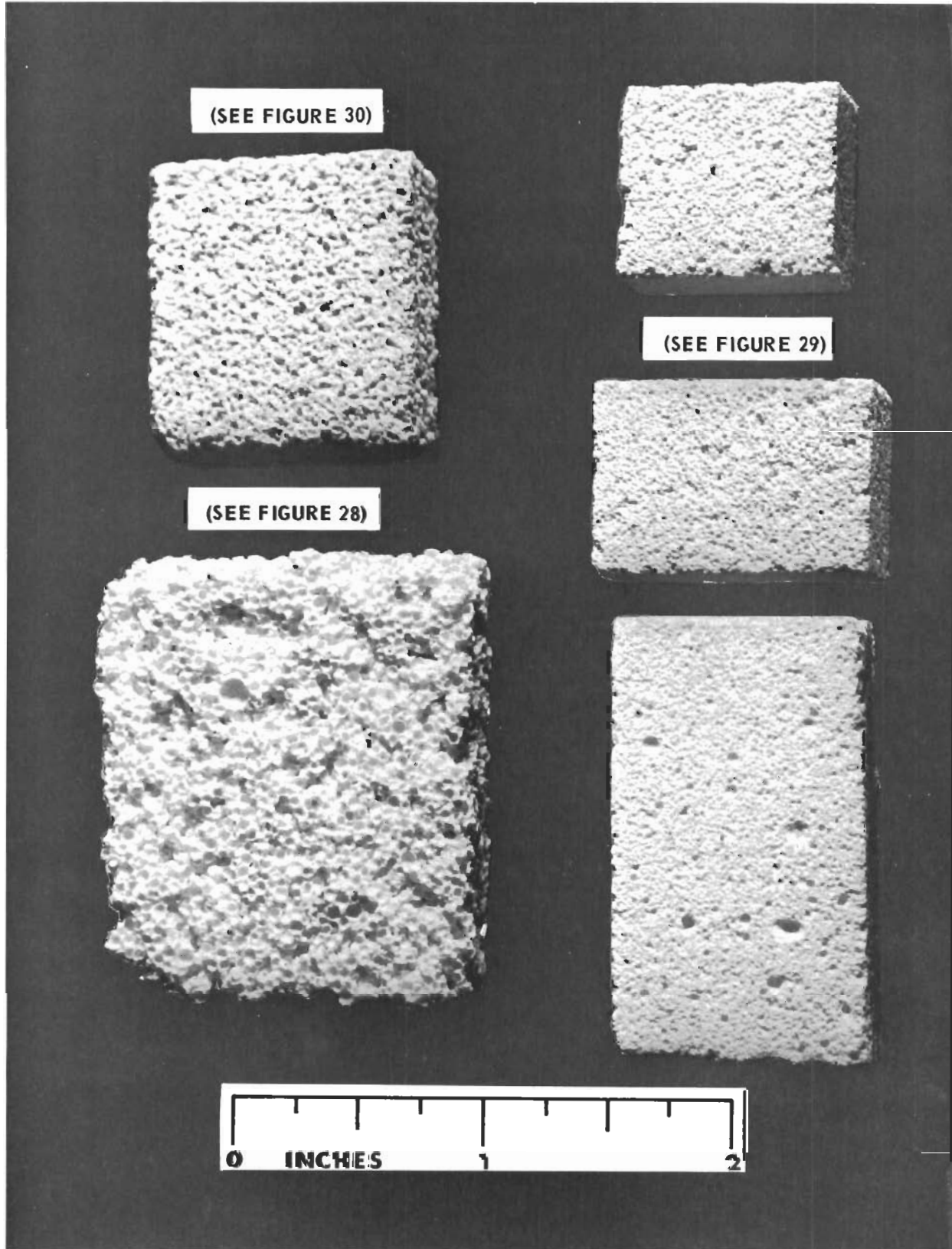


FIGURE 23 - COMMERCIAL LOW DENSITY BURN-OUT ZIRCONIAS

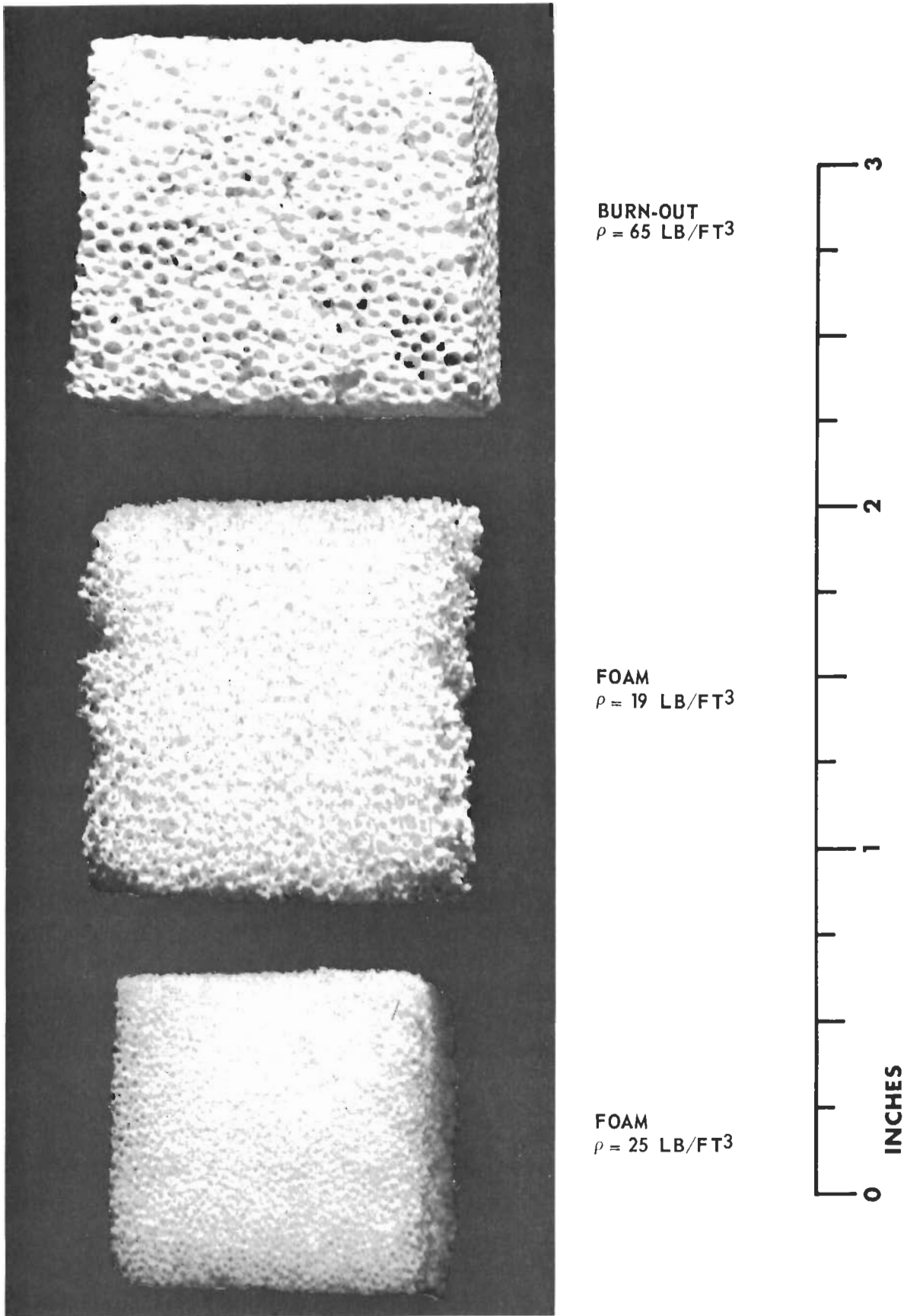


FIGURE 24 - COMMERCIAL LOW DENSITY ALUMINAS

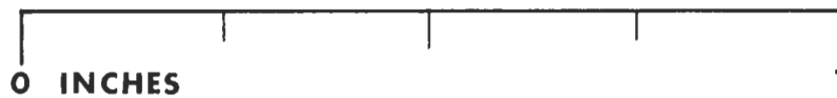
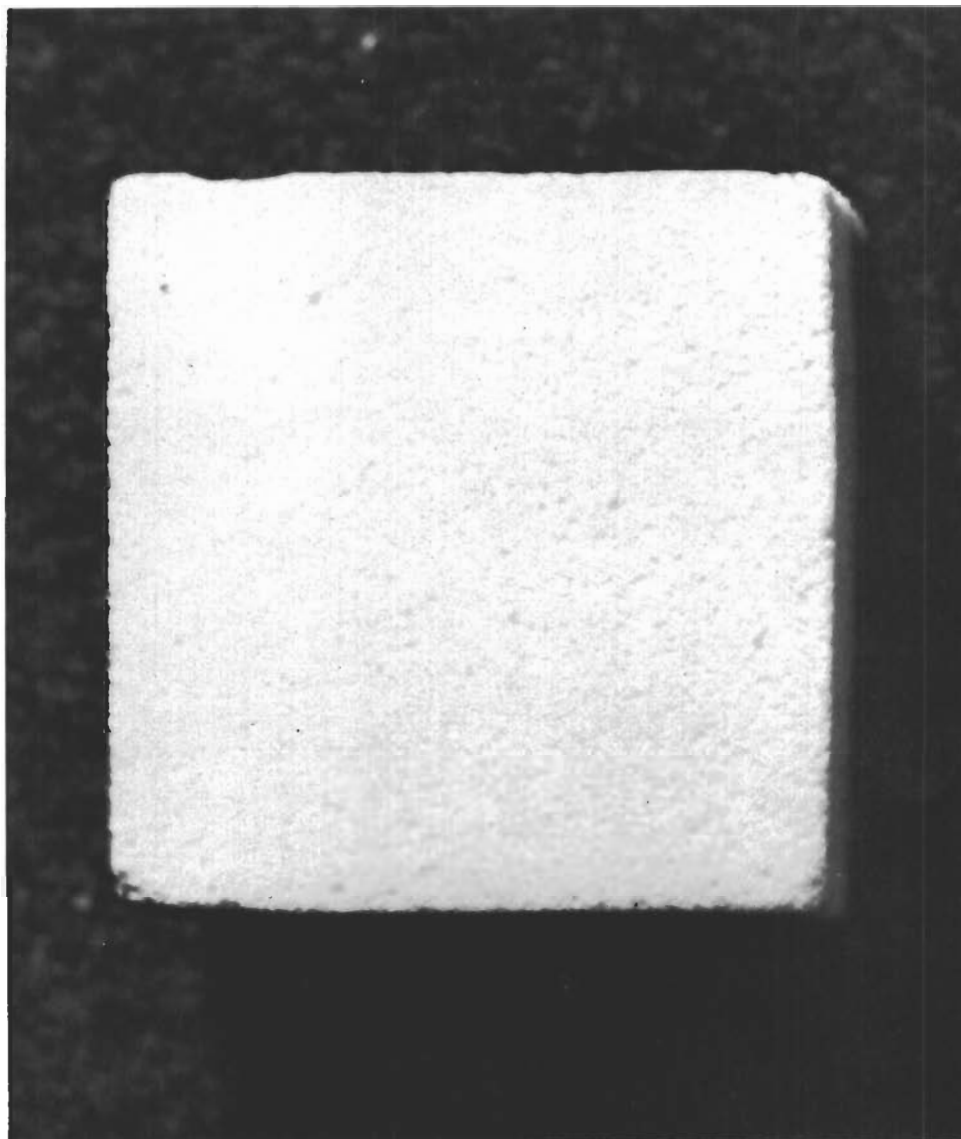


FIGURE 25 - COMMERCIAL LOW DENSITY FOAM ZIRCONIA
 $\rho = 72 \text{ LB/FT}^3$

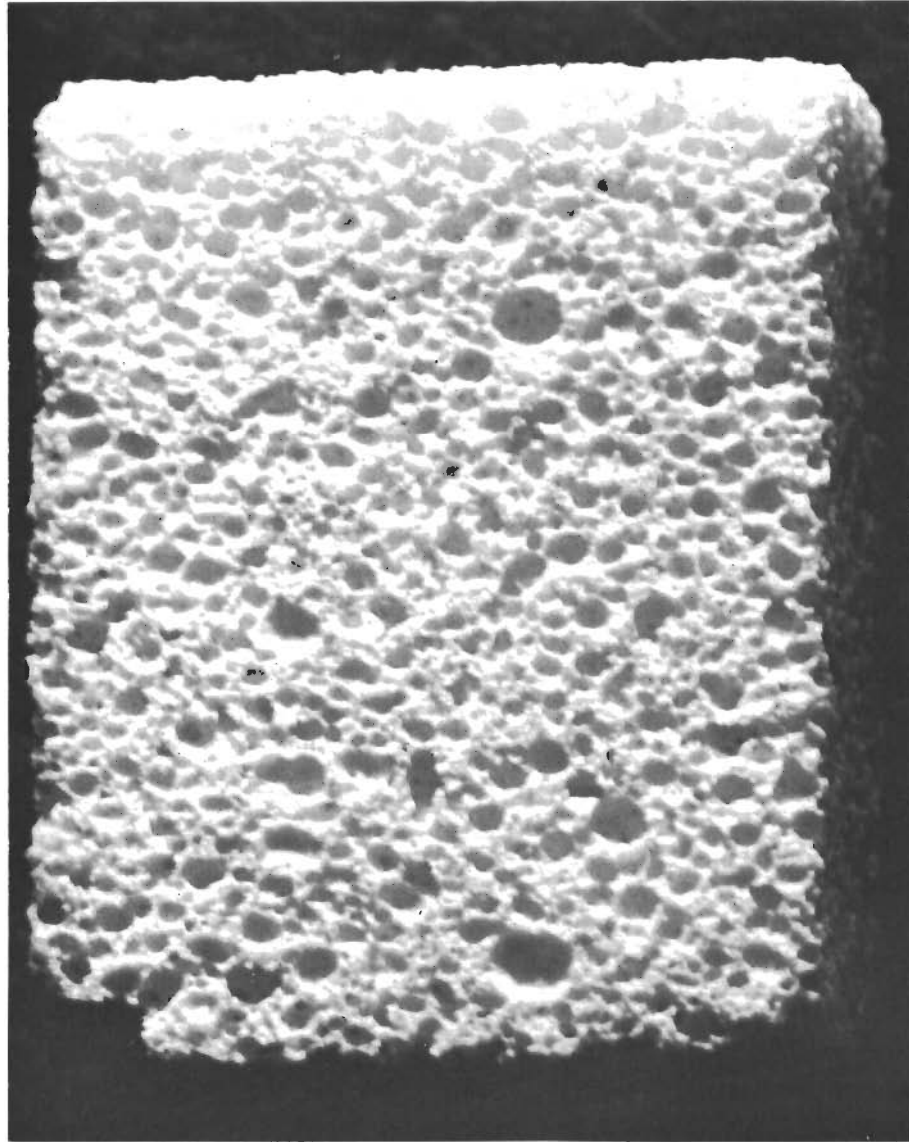


FIGURE 26 - COMMERCIAL LOW DENSITY FOAM ZIRCONIA
 $\rho = 40 \text{ LB/FT}^3$

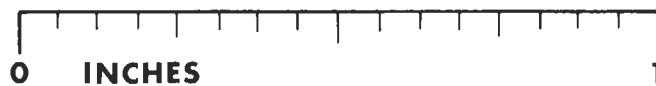
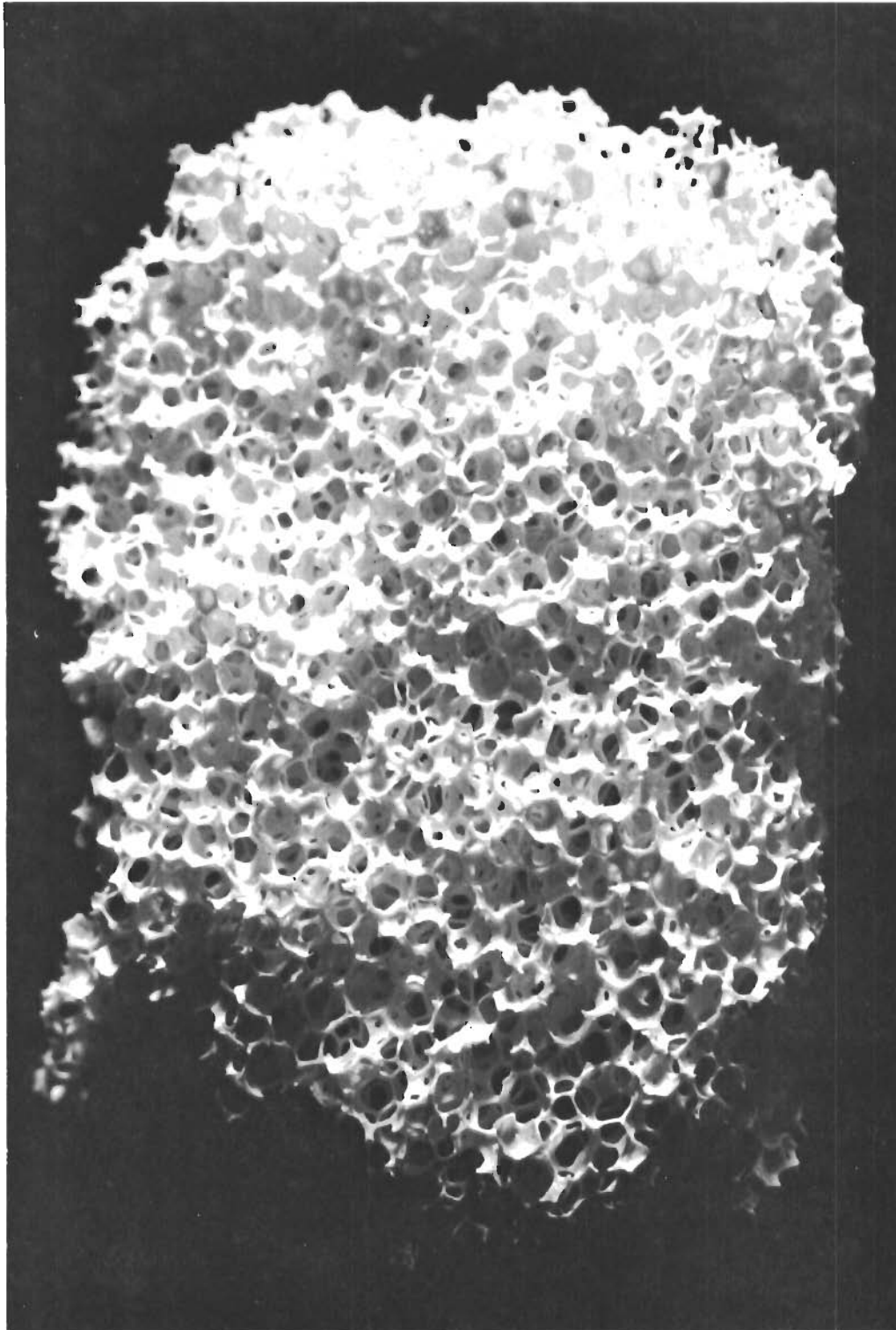


FIGURE 27 - COMMERCIAL LOW DENSITY FOAM ZIRCONIA
 ρ 21 LB/FT³

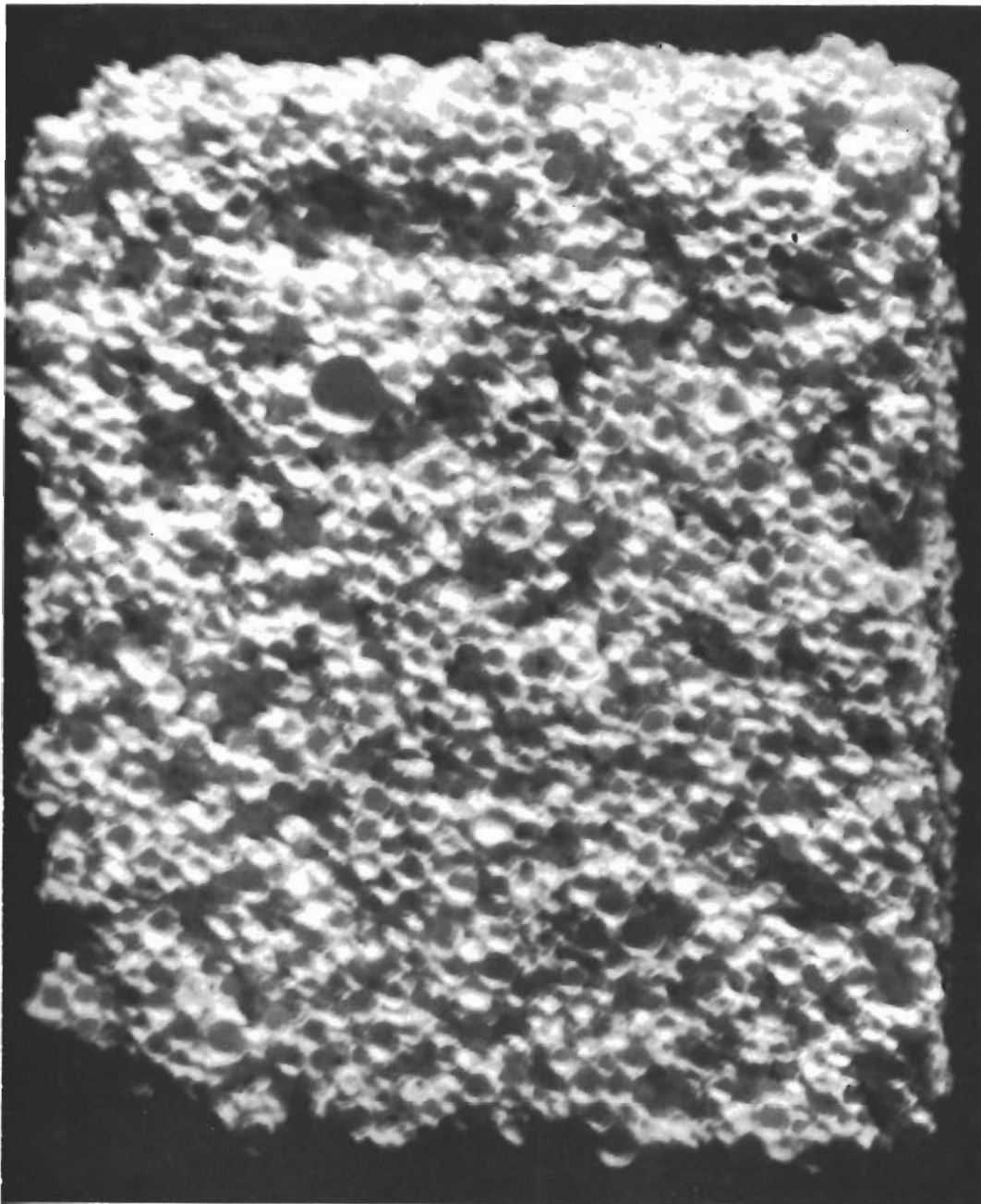


FIGURE 28 - COMMERCIAL LOW DENSITY BURN-OUT ZIRCONIA
 $\rho = 57 \text{ LB/FT}^3$

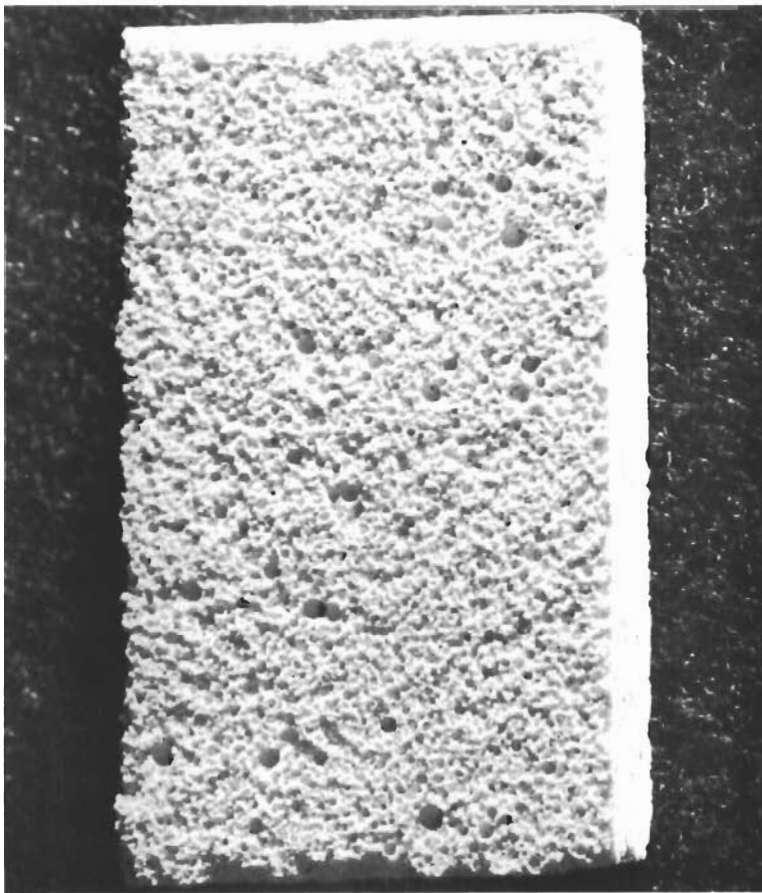


FIGURE 29 - COMMERCIAL LOW DENSITY BURN-OUT ZIRCONIA - $\rho=125 \text{ LB/FT}^3$

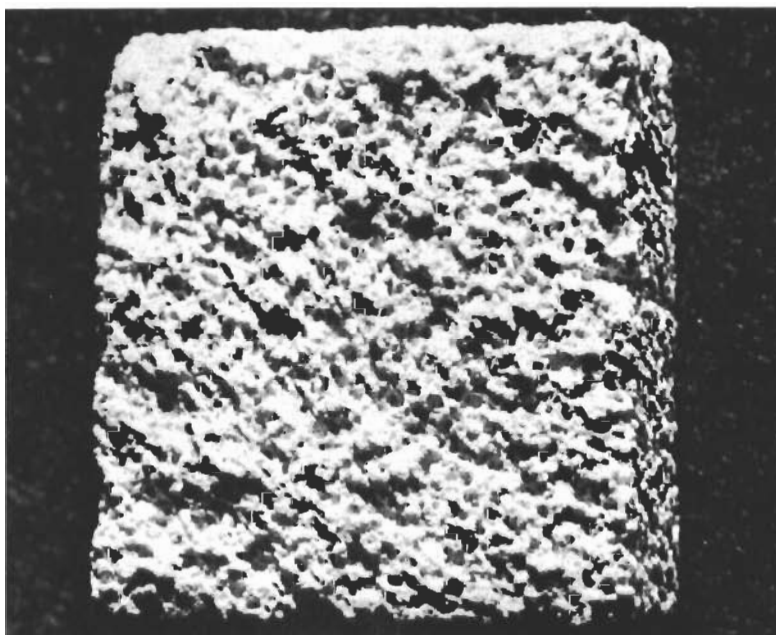
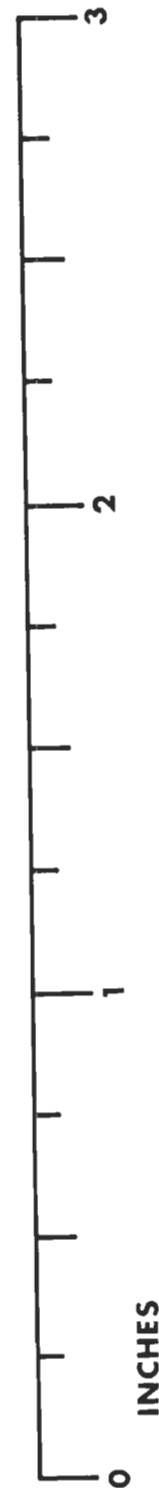
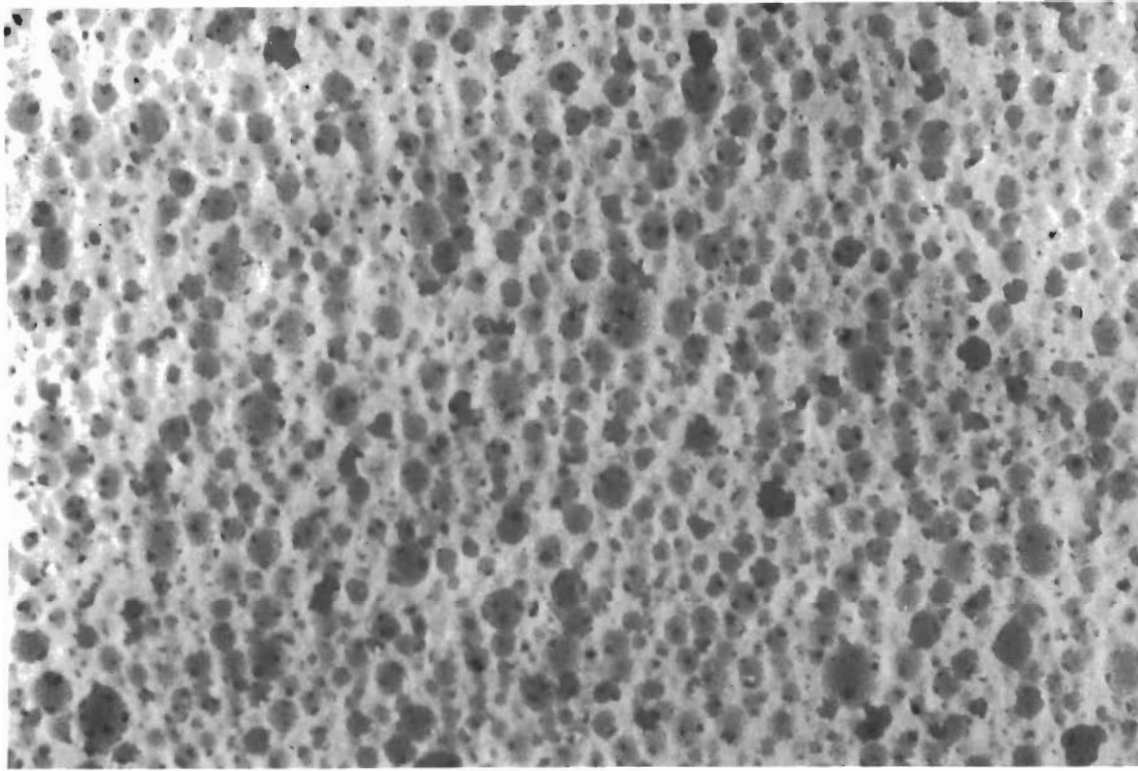


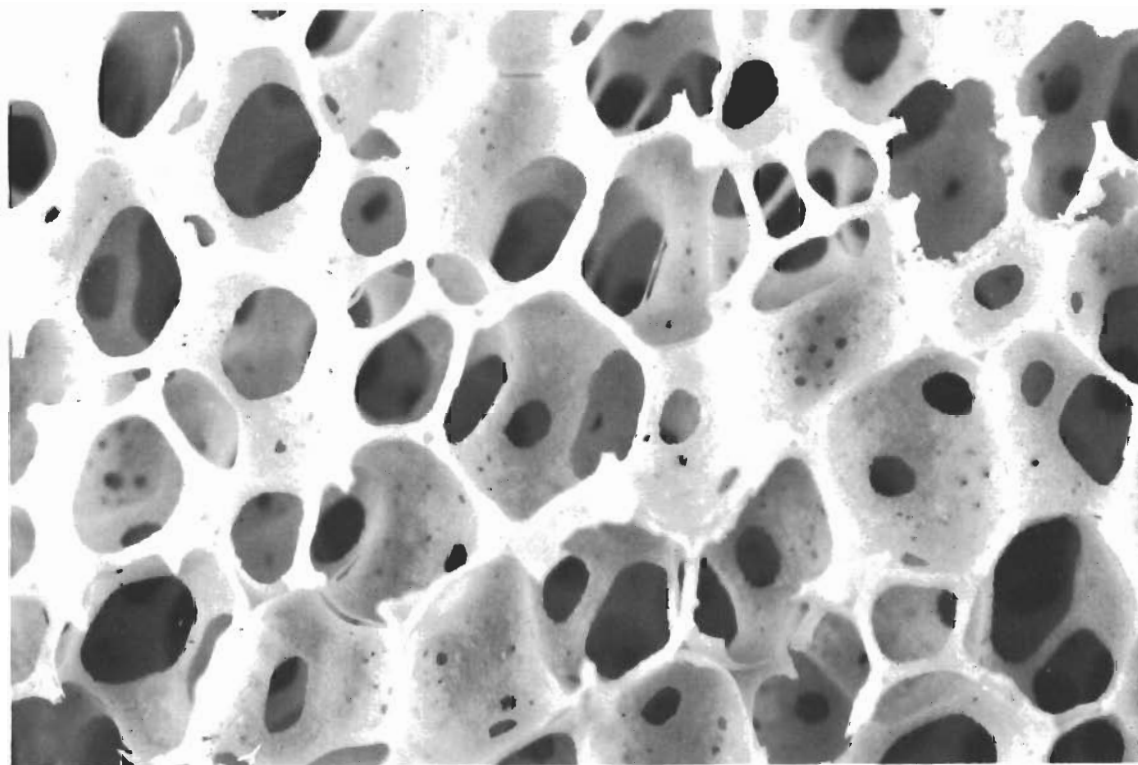
FIGURE 30 - COMMERCIAL LOW DENSITY BURN-OUT ZIRCONIA - $\rho=143 \text{ LB/FT}^3$





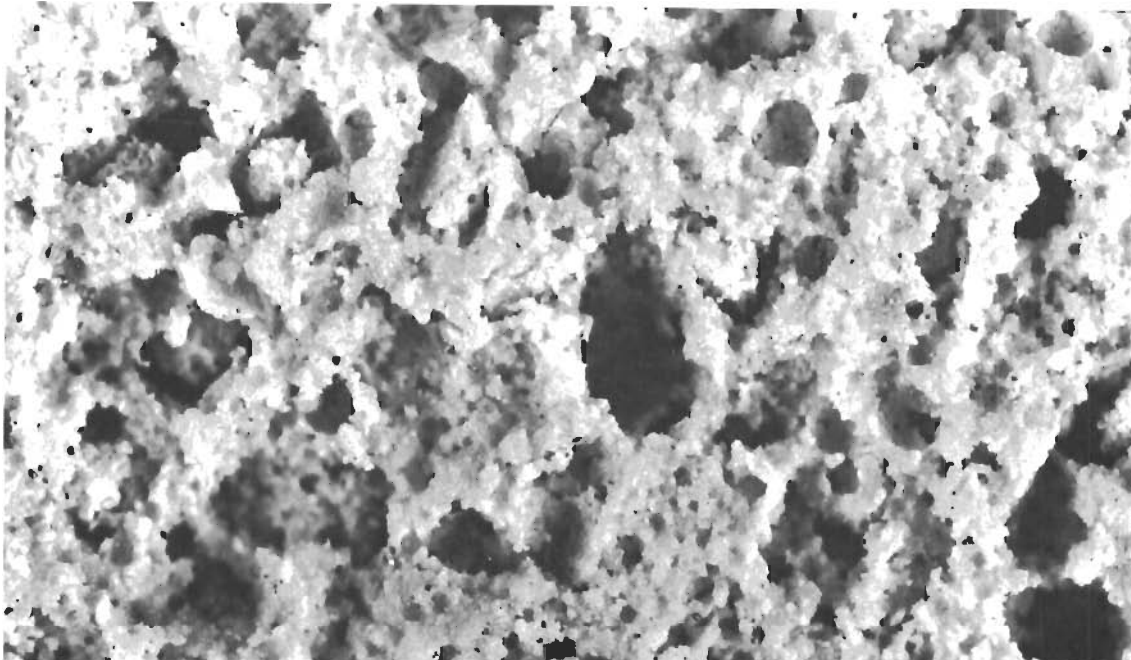
MAG = 20X

FIGURE 31 - COMMERCIAL LOW DENSITY FOAM ZIRCONIA - $\rho = 75 \text{ LB/FT}^3$



MAG = 20X

FIGURE 32 - COMMERCIAL LOW DENSITY FOAM ZIRCONIA - $\rho = 21 \text{ LB/FT}^3$



MAG = 20X

FIGURE 33 - COMMERCIAL LOW DENSITY BURN-OUT ZIRCONIA - $\rho = 140 \text{ LB/FT}^3$

The overall evaluation and screening led to the selection of the candidate low density materials listed below. Reasons for selection are included.

4.2.1.1 Alumina (Al_2O_3) - Three commercially available materials were selected.

(a) Ipsen ICB-3400 - Low density ($\sim 34 \text{ lb/ft}^3$). Strength low but adequate for handling. Pore size and body structure compatible to yield low thermal conductivity. Readily available commercially. Thermal shock resistance fair and perhaps adequate to permit use of material where heated surface would be covered with a more dense material.

(b) Norton RA5058 - Relatively high density ($\sim 85 \text{ lb/ft}^3$) but low enough to be utilized in a composite structure. Strength good. Pore size large but body structure tight enough to yield relatively low thermal conductivity. Readily available commercially. Thermal shock resistance good.

(c) Norton LA5969 - Similar to Norton RA5058, but slightly lower in density ($\sim 80 \text{ lb/ft}^3$), strength, and thermal shock resistance. Higher chemical purity than RA5058.

4.2.1.2 Zirconia and Thoria (ZrO_2 and ThO_2) - None of these commercially available low density materials were considered to have a satisfactory combination of properties to make them suitable for use. Although low density ceramics made by the burn-out process appeared to have the most potential for yielding a material of the desired properties, considerable improvement was required.

4.2.2 High Density Ceramics

Preliminary designs indicated possible need for thermal shock resistant, high density (~60% or greater of theoretical density) ceramics. Samples of these materials were obtained and subjected to evaluation and screening tests similar to those utilized for the low density ceramics. The results of the evaluation are presented in Table VII. Although some spinel materials were evaluated, their use was not anticipated because of limited availability and questionable material behavior at high temperatures and reduced pressures.

Figures 34 through 37 show some of the samples after thermal shock testing. Figure 34 is of a coarse grained zirconia sample that performed quite well. Figure 35 shows two different coarse grained thoria bodies from the same manufacturer; the body on the left cracked slightly (while remaining intact), and the body on the right withstood the rapid heating. Figure 36 shows a very coarse grained thoria ball which withstood the thermal shock test very well. This body had such coarse grains and low bond strength that the large grains could be picked out by fingernail before thermal shock testing. Figure 37 shows three alumina bodies, the one in the lower left corner being a very fine grained, high density, high strength, high purity, impervious material. This body cracked so severely during heating that it appeared to explode. The two coarse grained alumina compositions of somewhat lower density were visually unaffected by the thermal shock test even after two cycles.

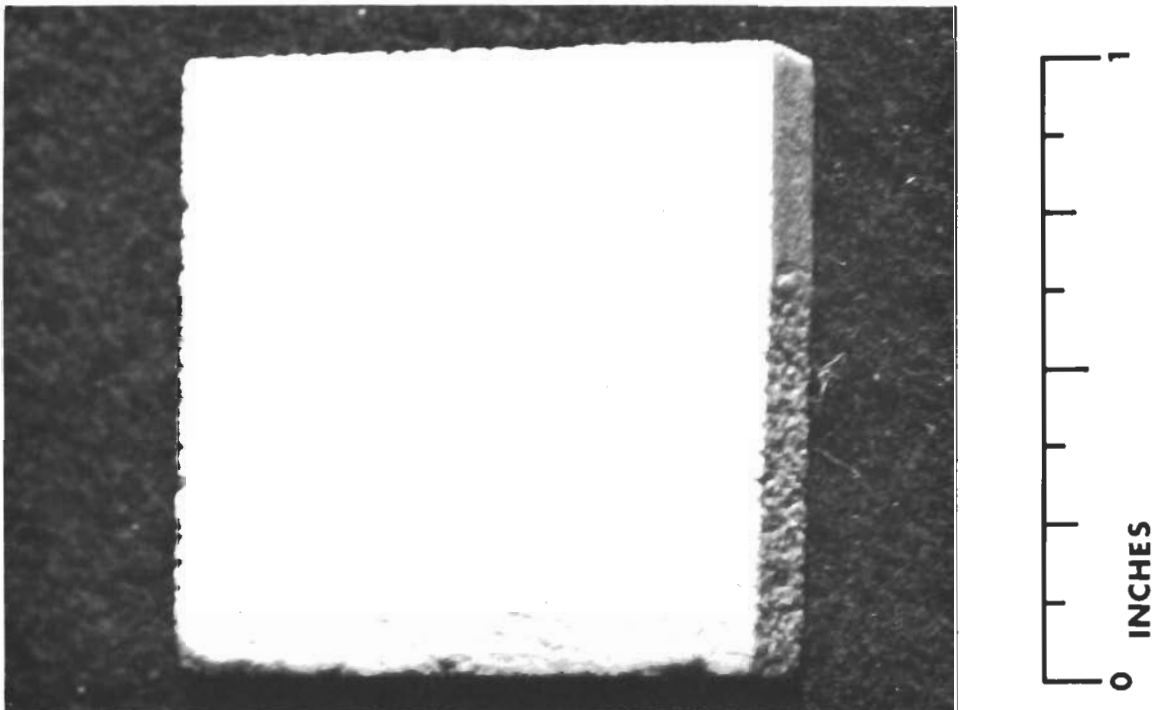


FIGURE 34 - DENSE THERMAL SHOCK RESISTANT ZIRCONIA -
 $\rho = 270 \text{ LB/FT}^3 \sim 25\% \text{ POROSITY}$

Text continued on page 51

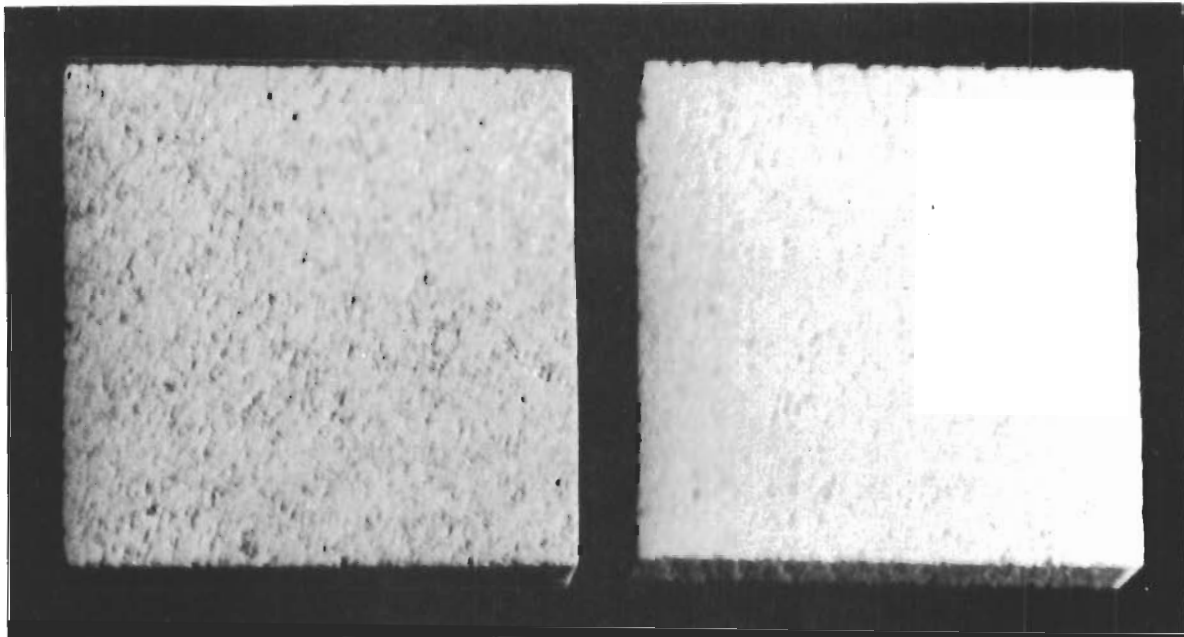


FIGURE 35 - DENSE THORIA - $\rho = 440 \text{ LB/FT}^3$ - $\sim 30\%$ POROSITY

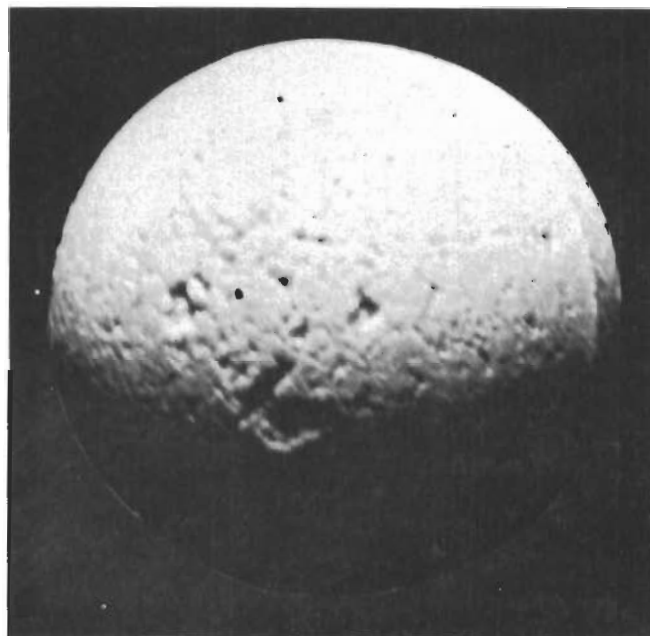
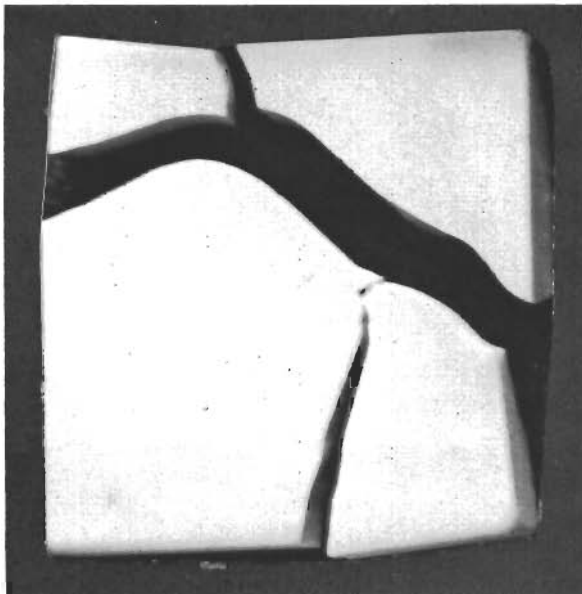


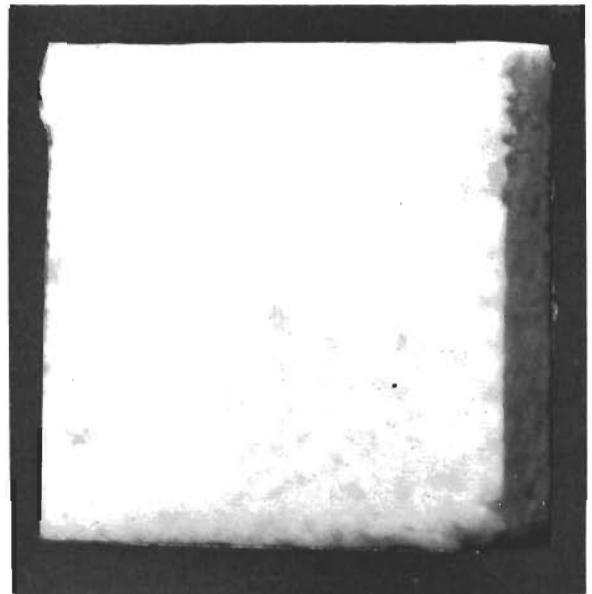
FIGURE 36 - DENSE THORIA - $\rho = 440 \text{ LB/FT}^3$ - $\sim 30\%$ POROSITY



(a) $\rho = 190 \text{ LB/FT}^3$



(b) $\rho = 240 \text{ LB/FT}^3$



(c) $\rho = 190 \text{ LB/FT}^3$



FIGURE 37 - DENSE ALUMINAS

TABLE VII - EVALUATION OF COMMERCIAL HIGH DENSITY CERAMICS

Description	Manufacturer	Density		Comments, as Received		Thermal Shock Testing		
		Lb./Ft. ³	% Theoretical	Grain Structure	Availability Status	Sample Size (Inches)*	Surface Heating Rate (°F/Sec)	Results
Al ₂ O ₃ - RA5190	Norton	190	76.0	Very coarse	Production	1 x 1 x 1/2	50	No change detected
Al ₂ O ₃ - RA5213	Norton	205	81.5	Coarse	Production	1 x 1 x 1/2	50	No change detected
Al ₂ O ₃ - RA5139	Norton	183	72.7	Fine	Production	1 x 1 x 1/2	50	Cracked & weakened slightly
Al ₂ O ₃ - X3305	LECO	221	88.0	Fine	Production	1D x 1/4	50	Cracked severely
Al ₂ O ₃ - X3306	LECO	228	90.6	Fine	Production	1D x 1/4	50	No change detected
Al ₂ O ₃ - X10919	Chas. Taylor	189	75.2	Coarse	Pilot	1 x 1 x 1/4	50	Melted slightly
Al ₂ O ₃ - X10842B	Chas. Taylor	195	77.5	Very coarse	Pilot	1 x 1 x 1/4	50	Melted slightly
Al ₂ O ₃ - X10659D	Chas. Taylor	152	60.4	Coarse	Pilot	1 x 1 x 1/4	50	Cracked, weakened
Al ₂ O ₃ - 99AD	A.P. Green	184	73.2	Coarse	Production	1 x 1 x 1/2	50	No change detected
Al ₂ O ₃ - 90B	A.P. Green	169	67.2	Coarse	Production	1 x 1 x 1/2	50	No change detected
Al ₂ O ₃ - 90B-38	A.P. Green	173	68.7	Coarse	Production	1 x 1 x 1/2	50	No change detected
Al ₂ O ₃ - 334D	A.P. Green	162	64.2	Coarse	Production	1 x 1 x 1/2	50	No change detected
Al ₂ O ₃ - 327D	A.P. Green	165	65.3	Coarse	Production	1 x 1 x 1/2	50	No change detected
Al ₂ O ₃ - 3221W	A.P. Green	167	66.2	Coarse	Production	1 x 1 x 1/2	50	No change detected
Al ₂ O ₃ - AD995	Coors	240	96.0	Very fine	Production	1 x 1 x 1/4	50	Cracked severely
Spinel - X11110D	Chas. Taylor	175	79.2	Coarse	Pilot	1 x 1 x 3/8	50	No change detected
Spinel - X11145	Chas. Taylor	155	70.3	Coarse	Pilot	1 x 1 x 3/8	50	No change detected
Spinel - X11147	Chas. Taylor	140	63.3	Coarse	Pilot	1 x 1 x 3/8	50	Warped & cracked severely
Spinel - X11104M	Chas. Taylor	160	72.4	Coarse	Pilot	1 x 1 x 3/8	50	Cracked slightly
Spinel - X 1105	Chas. Taylor	170	76.9	Coarse	Pilot	1 x 1 x 3/8	50	No change detected
Spinel - TMA5650	Norton	185	83.7	Coarse	Laboratory	1 x 1 x 1/2	50	No change detected
ZrO ₂ - RZ5601	Norton	265	74.2	Very coarse	Production	1 x 1 x 1/2	50	No change detected
ZrO ₂ - RZ5602	Norton	245	68.5	Medium	Production	1 x 1 x 1/2	50	No change detected
ZrO ₂ - RZ5602	Norton	245	68.5	Medium	Production	2 x 2 x 1/2	50	No change detected
ZrO ₂ - RZ5602	Norton	245	68.5	Medium	Production	2 1/2 x 2 1/2 x 1/8	50	No change detected
ZrO ₂ - RZ5605	Norton	215	60.2	Medium	Production	2 1/2 x 2 1/2 x 1/8	50	Cracked severely
ZrO ₂ - RZ5723	Norton	230	644	Medium	Production	1/2 D x 1	50	Cracked severely
ZrO ₂ - RZ5723	Norton	230	644	Medium	Production	5/8 OD x 3/8 ID x 1	50	No change detected
ZrO ₂ - Y-713	Zirconia	245	68.5	Medium	Production	1 x 1 x 1/4	50	No change detected
ZrO ₂ - Y-714	Zirconia	284	79.5	Medium	Production	2 x 2 x 1/4	50	Cracked, weakened
ZrO ₂ - Y-714	Zirconia	275	77.0	Medium	Production	1 x 1 x 1/4	50	No change detected
ZrO ₂ - Y-714	Zirconia	275	77.0	Medium	Production	1 x 1 x 1	50	Cracked, weakened
ZrO ₂ - Y-714	Zirconia	275	77.0	Medium	Production	1 x 1 x 1	25	Cracked, weakened
ZrO ₂ - W-1491	Zirconia	264	73.9	Coarse	Production	2 x 2 x 1/4	50	Cracked, weakened
ZrO ₂ - Y-1491	Zirconia	272	76.1	Coarse	Production	1 x 1 x 1/4	50	Cracked, weakened
ZrO ₂ - Y-601	Zirconia	255	71.4	Medium	Production	5/8 OD x 3/8 ID x 1	50	No change detected
ZrO ₂ - X10731	Chas. Taylor	271	75.7	Medium	Pilot	1 x 1 x 1/4	50	No Change detected
ZrO ₂ - X 11168	Chas. Taylor	215	60.2	Medium	Pilot	1 x 1 x 1/4	50	Weakened
ZrO ₂ - X3307	LECO	284	79.5	Medium	Production	1D x 1/4	50	No change detected
ZrO ₂ - X3308	LECO	265	74.2	Medium	Production	1D x 1/4	50	No change detected
ZrO ₂ - X3309	LECO	274	76.7	Medium	Production	1D x 1/4	50	Cracked, weakened slightly
ThO ₂ - T707	Norton	420	67.3	Coarse	Laboratory	1 x 1 x 1/4	50	Weakened
ThO ₂ - Y1193	Zirconia	440	70.5	Coarse	Production	1 x 1 x 1/4	50	Weakened, cracked
ThO ₂ - Y1193C	Zirconia	440	70.5	Coarse	Production	1 x 1 x 1/4	50	Weakened,
ThO ₂ - Y1193C	Zirconia	440	70.5	Coarse	Production	1OD x 1/4 ID x 1	50	Weakened,
ThO ₂ - Y1193	Zirconia	440	70.5	Coarse	Production	1/2 D x 1	50	Weakened, cracked
ThO ₂ - Y1193	Zirconia	440	70.5	Coarse	Production	1OD x 1/4 ID x 1	50	Weakened, cracked
ThO ₂ - Y1030	Zirconia	420	67.3	Coarse	Production	1 x 1 x 1/4	50	Weakened
ThO ₂ - Y1194	Zirconia	440	70.5	Medium	Production	3/8 D x 1	50	Weakened
ThO ₂ - X3303	LECO	595	95.4	Fine	Production	1D x 1/4	50	Weakened, cracked
ThO ₂ - X3304	LECO	530	84.9	Fine	Production	1D x 1/4	50	Weakened, cracked
ThO ₂ - 80% Density	LECO	490	78.6	Fine	Production	1/2 D x 1/2	50	Weakened, cracked

*Last dimension is specimen thickness

Of the samples evaluated, the materials at 60-80% theoretical density with a microstructure consisting of a gradation of grain sizes with a pre-dominating grain size of medium (~150 microns) to coarse (~2380 microns) had greater thermal shock resistance than the very fine grained, impervious ceramics. The LECO X3306 alumina was an exception to this statement. Some materials, such as the Zircoa Y-714 zirconia would withstand the 50°F/sec surface heating rate if a 1/4 inch thick sample were tested but thicker samples cracked during testing. Preliminary designs indicated possible use of the high density ceramics in thicknesses of 1/4 inch or less.

Since many of the high density ceramics appeared capable of withstanding the thermal shock conditions, material selection was based on the availability of desired ceramic shapes and on past experience in dealing with a particular vendor, his delivery capability, and his reputation and experience in making particular types and shapes of ceramics. None of the thoria materials tested was completely satisfactory, so selection was based on the best of the materials tested. The candidate materials selected for utilization are listed below:

- (a) Alumina - LECO X3306 - available in plates, rods.
Norton RA5213 - available in plates, blocks.
- (b) Zirconia - Zircoa Y-714 - available in plates, blocks.
Zircoa Y-601 - available in rods, tubes.
- (c) Thoria - Zircoa Y-1194 - available in rods, tubes.
Zircoa Y-1193C - available in rods, tubes, plates, blocks.

4.3 LOW DENSITY SINTERED REFRACTORY OXIDE DEVELOPMENT

The screening and evaluation tests revealed that at the beginning of this project there were no commercially available low density sintered zirconia or thoria ceramics which possessed the necessary combination of material properties (density, refractoriness, and thermal shock resistance) to meet the requirements of this program. The available low density alumina ceramics which were evaluated were less than satisfactory but it was felt the material shortcomings could be overcome by design and that better low density alumina would possibly be available later in the project.

In order to obtain the desired low density sintered zirconia and thoria ceramics, it was decided to issue a subcontract to a manufacturer to improve existing products to a level where the material requirements of this project would be satisfied. (It was not within the scope of the project, nor would scheduling requirements permit time, to develop radically new processes and materials.) A Work Statement was prepared to define materials requirements as outlined below, and submitted for quotation to various manufacturers working in the field of low density sintered refractory ceramic oxides.

(a) Temperature - Temperature resistances of 4000°F and 5000°F were required depending on varying conditions. Zirconia was to be used to meet the 4000°F requirement and thoria the 5000°F requirement.

(b) Heating Rate - The maximum temperature was to be achieved at a minimum surface heating rate of 50°F per second. The heating rate and

maximum temperature were to be achieved by use of a convective gas type heat source. The specimen was to be set on one-inch zirconia splits, with all voids between the specimen and zirconia split filled with zirconia grain. The specimen edges were to be guarded with a like material.

(c) Time at Maximum Temperature - The maximum temperature was to be held for a minimum of 10 minutes.

(d) Cooling Rate - After achieving and holding peak temperature for a minimum of 10 minutes, the material was to be cooled at a rate of 2 to 7^oF per second to 2000^oF and then at a more rapid cooling rate of 7 to 20^oF per second from 2000^oF to room temperature.

(e) Atmosphere - The ambient atmosphere during thermal cycling was to be oxidizing and at pressures from 760 mm Hg to 1×10^{-3} mm Hg. No thermal testing at less than one atmosphere pressure was required, but it was to be certified that no appreciable volatilization of material would occur.

(f) Strength - The ceramics were not to be highly loaded structural components so strength requirements except as related to thermal stress resistance and normal handling were to be low.

(g) Density - The material to be developed was to be a sintered ceramic with a maximum density of 20% of theoretical.

(h) Cycling Requirement - The material was to be capable of withstanding a minimum of one service cycle. One service cycle consisted of heating from ambient temperature to the maximum temperature (4000^oF for zirconia, 5000^oF for thoria) at the minimum heating rate of 50^oF/sec, holding the temperature for the specified minimum time, and cooling at the specified rate to room temperature.

(i) Acceptance Criteria for Thermal Shock Test - Visual inspection was to reveal no cracks or surface faults. Small cracks which did not affect mechanical integrity of the specimen would be acceptable.

(j) Surface Condition - The surface was to be capable of being prepared to a state suitable for aerodynamic application.

(k) Noise and Vibration - The material was to withstand sound pressure levels of approximately 145 to 155 db over the frequency range of 37.5 to 9600 cps. Random vibration levels were to be approximately 0.04g²/cps over the approximate frequency range of 300 to 1200 cps with a 12 db/octave roll-off above 1200 cps and a 6 db/octave roll-off below 300 cps.

Six manufacturers quoted on this Work Statement and submitted samples of their applicable products. These samples were representative of their current products and were not necessarily expected to meet the materials requirements. These samples are among those evaluated and listed in Table VI. Based on the evaluation and considerations discussed in Section 4.2.1, it was decided to select a subcontractor whose process employed the Burn-out technique for attaining low density and who had considerable past experience in producing thermal shock resistant ceramics.

The Refractories Division of the Norton Company, Worcester, Massachusetts, was selected for the subcontract for these reasons and because of their proposed engineering approach to attaining the Work Statement objectives and their competitive cost bid.

The originally planned work effort and evaluation tests are briefly presented here because some deviation was required during the development. The Work Statement called for the subcontract program to cover a seven month time span, divided into three phases - Materials Improvement; Reproducibility; and Producibility. The seven month time span was a requirement in order that the improved materials could be obtained in time for utilization in fabrication of subscale design modules for test.

In the first phase, Norton was to improve and refine their existing processes to yield zirconia and thoria materials which met the material requirements. As part of the product improvement phase and to demonstrate that the improved materials would meet the requirements set forth, Norton performed the following minimum evaluation tests:

- (a) Thermal Shock - The size of all specimens used in the thermal shock tests was a section (approximately 1/6) of a right circular cylinder approximately 5 inches inside diameter x 7 inches outside diameter x 3 inches long. The outside diameter was the heated surface.
- (b) Density determination
- (c) Uniformity determination by radiographic techniques
- (d) Microstructure study
- (e) Crushing strength

In the second phase, Norton was to establish the capability to consistently reproduce these materials within established limits to meet material specifications. To satisfactorily demonstrate the reproducibility capability, Norton produced three separate lots of parts, each lot consisting of at least nine units of each material. The final process specifications and quality control procedures evolved from Phase I were utilized to demonstrate reproducibility. McDonnell performed acceptance testing, including thermal shock, on these materials.

In the third phase, Norton was required to demonstrate their ability to produce quantities of uniform and consistent materials. The equivalent of 15 bricks (4-1/2 inches x 4-1/2 inches x 2-1/2 inches) of each type of the improved materials were to be delivered. In addition to the 15 zirconia and 15 thoria bricks, Norton was to furnish 20 zirconia and 20 thoria test specimens. The size of the specimens was to be the equivalent of a sector (approximately 1/6) of a right circular cylinder 5 inches inside diameter x 7 inches outside diameter x 3 inches long. As in Phase II, McDonnell performed acceptance testing on these materials.

In the course of the program during Phases II and III, it was decided that a specimen size of 4-1/2 inches x 2-1/2 inches x 2-1/2 inches was satisfactory for program needs, and the requirements for other sizes were deleted. It was also decided to eliminate microscopic and radiographic examinations.

4.3.1 Zirconia Development Program

4.3.1.1 Phase I - Materials Improvement - Materials improvement was divided into three steps. The first was the evaluation of intrinsic variables. The best bodies of the first step were used in the second step for evaluation of extrinsic variables. Experience from these two steps was used in a third step, the evaluation of a series of optimized bodies. All the samples produced in Phase I were the curved shape consisting of approximately 1/6 of a right circular cylinder 5 inches inside diameter x 7 inches outside diameter x 3 inches long. Sample fabrication and firing procedures developed in past work at Norton were utilized in preparing these samples.

(a) Step 1 (Evaluation of Intrinsic Variables) - The intrinsic variables of stabilization, density, pore size, and grain size were evaluated in terms of effect on crushing strength and thermal shock resistance for the various bodies. Thermal shock resistance was considered the most important single material characteristic for use in the intended heat shield application. Table VIII indicates the three ranges of each variable selected for trial.

TABLE VIII - RANGES OF INTRINSIC VARIABLES IN LOW DENSITY ZIRCONIA BODY DEVELOPMENT

Variables								
	Stabilization		Density (a)		Pore Size		Grain Size	
	Type	% Cubic (b) ZrO ₂	Type	% Theo- retical	Type	Diameter (inches)	Type	Ratio of 5 μ grains to 20 μ grains
Ranges	High	85	High	20	Large	0.140	Coarse (c)	6:4
	Medium	65	Medium	15	Medium	0.064	Medium	8:2
	Low	50	Low	10	Small	0.05	Fine	10:0

(a) Theoretical density ~ 360 lb/ft³.

(b) Balance is monoclinic at room temperature and tetragonal above the inversion temperature.

(c) In end of project study, a fine-to-coarse ratio of 2.5 to 7.5 was found feasible.

(1) Stabilization - Stabilization is the amount of cubic zirconia present in the fired structure. For this program, cubic zirconia was formed by the addition of calcia (CaO) to the zirconia. The greater the CaO content, the higher the stabilization, if all other things are equal. In this work, the stabilization was controlled by using mixes of fused zirconias (manufactured by Norton) containing different amounts of CaO. The range of stabilizations studies are shown in Table VIII.

Text continued on page 56

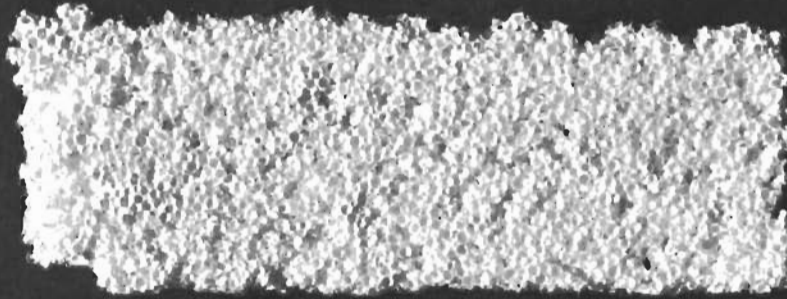


FIGURE 38 $\rho = 39 \text{ LB/FT}^3$

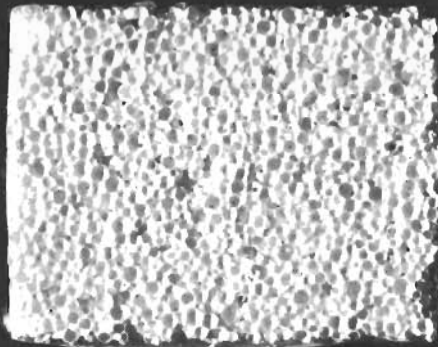


FIGURE 39 $\rho = 64 \text{ LB/FT}^3$,
PORE SIZE - 0.064 IN. DIAMETER

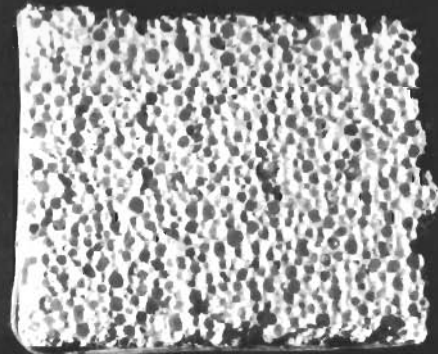


FIGURE 40 $\rho = 82 \text{ LB/FT}^3$

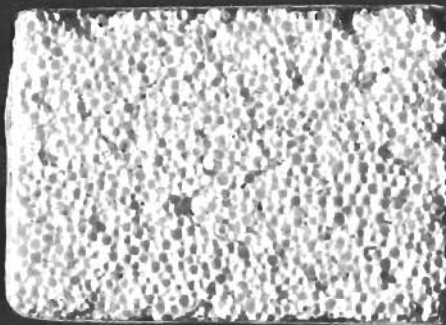


FIGURE 41 PORE SIZE - 0.050
IN. DIAMETER

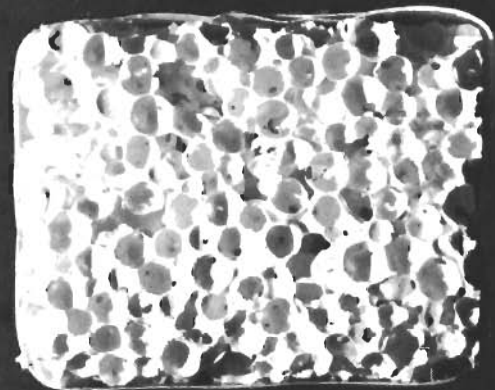


FIGURE 42 PORE SIZE - 0.140
IN. DIAMETER



SCALE - INCHES

NORTON COMPANY LOW DENSITY ZIRCONIA

High stabilized bodies were made of 100% high stabilized grain. This was zirconia grain with a stabilization of about 85% and a CaO content of about 4-1/2 w/o (weight percent). Medium stabilized bodies were made of 75 w/o of the high stabilized grain and 25 w/o of unstabilized grain containing no CaO, giving a body with about 65% cubic zirconia when matured. Low stabilized bodies were made of 28 w/o of the high stabilized grain previously described, 10 w/o of the unstabilized grain, and 62 w/o of a low stabilized grain of about 3 w/o CaO content. The low stabilized grain had a stabilization of about 40%. The low stabilized body made with this mixture of grains had a stabilization of about 50%.

In Phases II and III, when all the properly sized low stabilized (3 w/o CaO) grain was consumed, bodies of the low stabilization type were made by blending the other two zirconia grains, the high stabilized (4-1/2 w/o CaO) grain and unstabilized (0 w/o CaO) grain, in the correct proportions to yield a similar body with the desired 50% stabilization.

(2) Density - Density was varied simply by altering the ratio of zirconia to high purity burn-out material. Figure 38 shows a low density body of about 11% theoretical density. Figure 39 shows a medium density body of about 18% density. Figure 40 shows a dense body of 23% density.

(3) Grain Size - Variation in grain size of the fired bodies was achieved by varying the ratio of the amounts of fine fused zirconia grain to coarse fused zirconia grain. These grains were crushed to an average particle size of 5 microns for the fine grain and 20 microns for the coarse grain. The ratio was varied from 100 w/o of the fine grain for the fine grain body to 60 w/o fine, 40 w/o coarse grain for the coarse grain body. These are shown in Table VIII. Additional variations were tried near the end of the contract period to make a body considerably coarser by using a ratio of 25 w/o fine to 75 w/o coarse grain.

Both sizes of crushed fused grain (5 microns and 20 microns) were available in the high stabilized (4-1/2 w/o CaO) and unstabilized zirconias. Only the 5 micron size was available in the low stabilized (3 w/o CaO) grain.

(4) Pore Size - Pore size was controlled by the size of the burn-out particles. Pores ranged from 0.050 inch diameter (Figure 41) for the small size to 0.140 inch diameter for the large size (Figure 42). Figure 39 shows a body incorporating medium size pores 0.064 inch in diameter.

The four intrinsic variables above were evaluated by subjecting specimens to thermal shock testing. For these tests, various oxy-acetylene torches were evaluated and a 2-1/2 inch flame hardening tip was found to be satisfactory. The test fixture fabricated for utilization of this torch is shown in Figures 43 and 44. The outside diameter of the curved specimen was subjected to the heating. Fixturing or support brick were alumina or zirconia.

Text continued on page 58

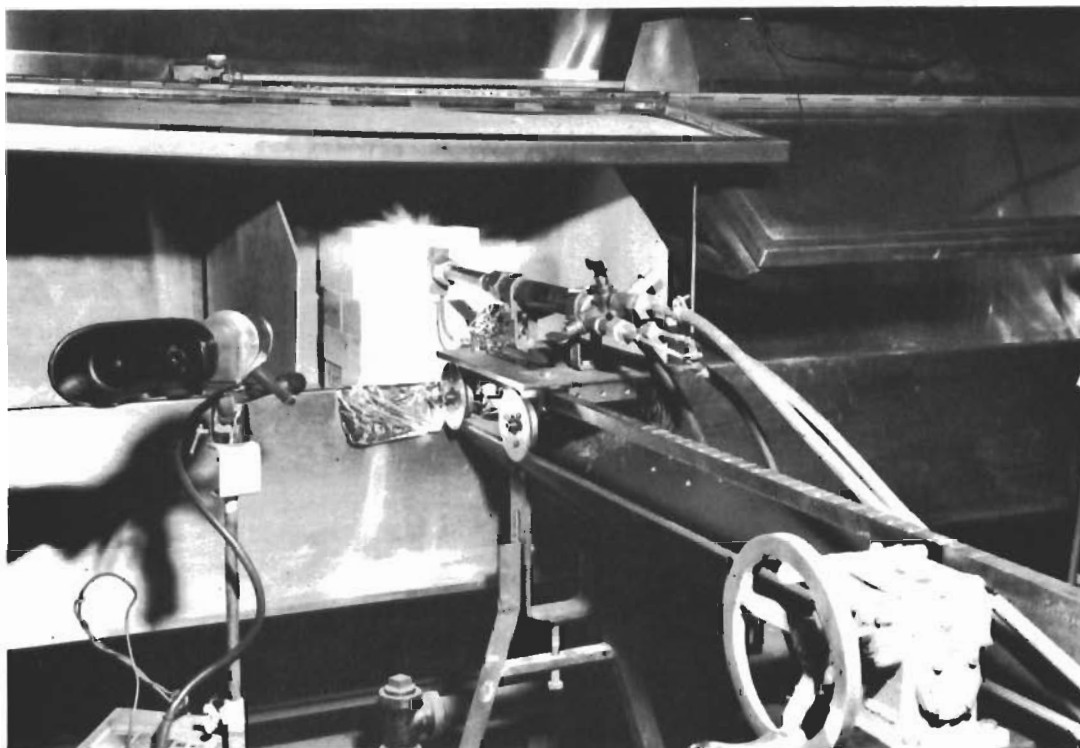


FIGURE 43 - NORTON COMPANY OXYACETYLENE FACILITY FOR THERMAL SHOCK TESTING

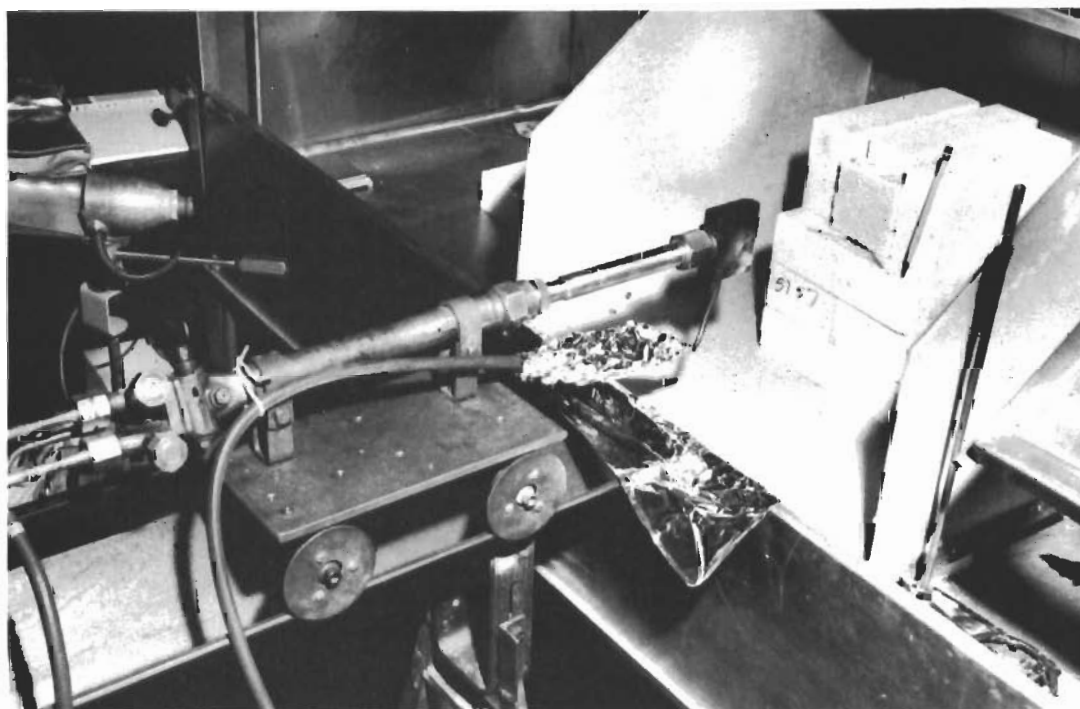


FIGURE 44 - NORTON COMPANY OXYACETYLENE TORCH FACILITY FOR THERMAL SHOCK TESTING

The test cycle used for zirconia was to heat from ambient to a surface temperature of 4000°F at 50°F/sec (total time to 4000°F was 80 seconds; soak at 4000°F for 10 minutes; cool from 4000°F to 2000°F at 200°F/minute; then cool in still air down to room temperature with no more heat applied. The desired cycle was achieved by manually cranking the torch carriage in or out while monitoring the surface temperature with a manually operated optical pyrometer and checking the time versus temperature with a stopwatch. To obtain the thermal drop across the specimen and; therefore, determine some rough relationship between the thermal conductivity of the various bodies, the back face temperature of the specimen was measured with a platinum/platinum-10% rhodium thermocouple with the output fed into a recording time-temperature indicator.

The specimens were examined after they had cooled to ambient temperature. The results of the investigation of all intrinsic variables are presented in Table IX. Specimen conditions can be identified using the numerical relative scale shown under Note D in the table.

Examples of tested zirconia specimens and their condition ratings are shown in Figures 45 through 47. Figure 45 shows body MZ8, which had a test rating of 1; the cracked parts were offset after test to give better contrast in the photograph. Figure 46 shows body MZ14, which had a rating of 3, indicating medium erosion. Figure 47 shows body MZ33, which had a rating of 5 although the slight cracking does not show in the photograph.

A summary of the results of the investigation of the intrinsic variables is presented below.

(1) Stabilization - The most highly stabilized bodies appeared the worst of the three ranges evaluated, both in manufacture and thermal test. The medium stabilization group appeared promising. The low stabilization bodies were slightly better in thermal shock resistance than those in the medium range, although this difference was not as great as that between the high and medium stabilization bodies. Low stabilization is accompanied by lower thermal expansion, which tends to improve thermal shock resistance.

(2) Density - In bodies containing many cell walls (small pore size), the low density bodies were not as thermal shock resistant as the denser ones because the small amount of material spread among the many walls made the individual walls weaker. Examples of this were the low density coarse grain bodies with small pores (bodies designated MZ1, 4, 7, and 8). When the low density body material was spread over fewer webs (MZ9), the body appeared much more promising. Also the medium grain size with medium pores (MZ5) and large pores (MZ6) appeared promising. The medium density group was the most promising as a whole. For a given density, the specimen performance improved as the grain sizing became coarser.

At higher densities, cracking failures during test became more of a problem. This tendency was reduced with coarser grain sizing and lower stabilization.

(3) Grain Size - The medium grain size performed best overall. The fine size tended to crack and erode. The coarse size was good at medium and high density, but in low density bodies it resulted in low strength.

**TABLE IX - RESULTS OF INVESTIGATION OF INTRINSIC VARIABLES
IN LOW DENSITY ZIRCONIA BODIES**

			GRAIN SIZE			CRYSTAL STABILIZATION		
			COARSE			} HIGH		
			MEDIUM					
			FINE					
			COARSE			} MEDIUM		
			MEDIUM					
			FINE					
			COARSE			} LOW		
			MEDIUM					
			FINE					

LOW	MEDIUM	HIGH	DENSITY																																																																																																						
<table border="1" style="width: 100%; border-collapse: collapse;"> <tr><td></td><td></td><td>(41)</td></tr> <tr><td>(35)</td><td></td><td></td></tr> <tr><td>0</td><td></td><td></td></tr> <tr><td>(34)</td><td></td><td></td></tr> <tr><td>0</td><td></td><td></td></tr> </table>			(41)	(35)			0			(34)			0			<table border="1" style="width: 100%; border-collapse: collapse;"> <tr><td></td><td></td><td></td></tr> <tr><td>(37)</td><td>18</td><td></td></tr> <tr><td>138</td><td>1</td><td></td></tr> <tr><td>(36)</td><td>18</td><td></td></tr> <tr><td>267</td><td>1</td><td></td></tr> </table>				(37)	18		138	1		(36)	18		267	1		<table border="1" style="width: 100%; border-collapse: collapse;"> <tr><td></td><td></td><td></td></tr> <tr><td>(39)</td><td>23</td><td></td></tr> <tr><td>579</td><td>2</td><td></td></tr> <tr><td>(38)</td><td></td><td></td></tr> <tr><td>NOT MADE</td><td></td><td></td></tr> </table>				(39)	23		579	2		(38)			NOT MADE																																																												
		(41)																																																																																																							
(35)																																																																																																									
0																																																																																																									
(34)																																																																																																									
0																																																																																																									
(37)	18																																																																																																								
138	1																																																																																																								
(36)	18																																																																																																								
267	1																																																																																																								
(39)	23																																																																																																								
579	2																																																																																																								
(38)																																																																																																									
NOT MADE																																																																																																									
<table border="1" style="width: 100%; border-collapse: collapse;"> <tr><td>(7)</td><td>12</td><td>(8)</td><td>11</td><td>(9)</td><td>9</td></tr> <tr><td><7</td><td>1</td><td>14</td><td>1</td><td>13</td><td>5</td></tr> <tr><td>(4)</td><td>10</td><td>(5)</td><td>11</td><td>(6)</td><td>10</td></tr> <tr><td>7</td><td>3.5</td><td>22</td><td>4</td><td>22</td><td>4</td></tr> <tr><td>(1)</td><td>12</td><td>(2)</td><td>11</td><td>(3)</td><td>11</td></tr> <tr><td>24</td><td>3</td><td>20</td><td>3</td><td>27</td><td>1</td></tr> </table>	(7)	12	(8)	11	(9)	9	<7	1	14	1	13	5	(4)	10	(5)	11	(6)	10	7	3.5	22	4	22	4	(1)	12	(2)	11	(3)	11	24	3	20	3	27	1	<table border="1" style="width: 100%; border-collapse: collapse;"> <tr><td>(16)</td><td>(17)</td><td>16</td><td>(18)</td><td>16</td></tr> <tr><td>NOT MADE</td><td>218</td><td>5</td><td>243</td><td>5</td></tr> <tr><td>(13)</td><td>19</td><td>(14)</td><td>18</td><td>(15)</td><td>15</td></tr> <tr><td>335</td><td>3</td><td>343</td><td>3</td><td>122</td><td>4.5</td></tr> <tr><td>(10)</td><td>19</td><td>(11)</td><td>17</td><td>(12)</td><td>17</td></tr> <tr><td>412</td><td>1</td><td>463</td><td>3</td><td>325</td><td>4.5</td></tr> </table>	(16)	(17)	16	(18)	16	NOT MADE	218	5	243	5	(13)	19	(14)	18	(15)	15	335	3	343	3	122	4.5	(10)	19	(11)	17	(12)	17	412	1	463	3	325	4.5	<table border="1" style="width: 100%; border-collapse: collapse;"> <tr><td>(25)</td><td>(26)</td><td>19</td><td>(27)</td><td>20</td></tr> <tr><td>NOT MADE</td><td>557</td><td>1</td><td>430</td><td>4.5</td></tr> <tr><td>(22)</td><td>(23)</td><td>23</td><td>(24)</td><td>21</td></tr> <tr><td>NOT MADE</td><td>572</td><td>3</td><td>436</td><td>1</td></tr> <tr><td>(19)</td><td>25</td><td>(20)</td><td>24</td><td>(21)</td><td>18</td></tr> <tr><td>707</td><td>1</td><td>559</td><td>3</td><td>239</td><td>1</td></tr> </table>	(25)	(26)	19	(27)	20	NOT MADE	557	1	430	4.5	(22)	(23)	23	(24)	21	NOT MADE	572	3	436	1	(19)	25	(20)	24	(21)	18	707	1	559	3	239	1	
(7)	12	(8)	11	(9)	9																																																																																																				
<7	1	14	1	13	5																																																																																																				
(4)	10	(5)	11	(6)	10																																																																																																				
7	3.5	22	4	22	4																																																																																																				
(1)	12	(2)	11	(3)	11																																																																																																				
24	3	20	3	27	1																																																																																																				
(16)	(17)	16	(18)	16																																																																																																					
NOT MADE	218	5	243	5																																																																																																					
(13)	19	(14)	18	(15)	15																																																																																																				
335	3	343	3	122	4.5																																																																																																				
(10)	19	(11)	17	(12)	17																																																																																																				
412	1	463	3	325	4.5																																																																																																				
(25)	(26)	19	(27)	20																																																																																																					
NOT MADE	557	1	430	4.5																																																																																																					
(22)	(23)	23	(24)	21																																																																																																					
NOT MADE	572	3	436	1																																																																																																					
(19)	25	(20)	24	(21)	18																																																																																																				
707	1	559	3	239	1																																																																																																				
<table border="1" style="width: 100%; border-collapse: collapse;"> <tr><td></td><td></td><td>(41)</td></tr> <tr><td>(29)</td><td>13</td><td>(40)</td></tr> <tr><td>37</td><td>3</td><td></td></tr> <tr><td>(28)</td><td>15</td><td></td></tr> <tr><td>37</td><td>1</td><td></td></tr> </table>			(41)	(29)	13	(40)	37	3		(28)	15		37	1		<table border="1" style="width: 100%; border-collapse: collapse;"> <tr><td>(49)</td><td>20</td><td>(42)</td><td>(43)</td><td>17</td></tr> <tr><td>5.5</td><td></td><td></td><td></td><td>5.5</td></tr> <tr><td></td><td>(31)</td><td>18</td><td></td><td></td></tr> <tr><td></td><td>317</td><td>5</td><td></td><td></td></tr> <tr><td></td><td>(30)</td><td>20</td><td></td><td></td></tr> <tr><td></td><td>296</td><td>1</td><td></td><td></td></tr> </table>	(49)	20	(42)	(43)	17	5.5				5.5		(31)	18				317	5				(30)	20				296	1			<table border="1" style="width: 100%; border-collapse: collapse;"> <tr><td>(44)</td><td>26</td><td>(45)</td><td>(46)</td><td>24</td></tr> <tr><td>590</td><td>6</td><td></td><td></td><td>4</td></tr> <tr><td></td><td>(33)</td><td>26</td><td>(47)</td><td></td></tr> <tr><td></td><td>509</td><td>5</td><td></td><td></td></tr> <tr><td></td><td>(32)</td><td>27</td><td>(48)</td><td></td></tr> <tr><td></td><td>699</td><td>4.5</td><td></td><td></td></tr> </table>	(44)	26	(45)	(46)	24	590	6			4		(33)	26	(47)			509	5				(32)	27	(48)			699	4.5																														
		(41)																																																																																																							
(29)	13	(40)																																																																																																							
37	3																																																																																																								
(28)	15																																																																																																								
37	1																																																																																																								
(49)	20	(42)	(43)	17																																																																																																					
5.5				5.5																																																																																																					
	(31)	18																																																																																																							
	317	5																																																																																																							
	(30)	20																																																																																																							
	296	1																																																																																																							
(44)	26	(45)	(46)	24																																																																																																					
590	6			4																																																																																																					
	(33)	26	(47)																																																																																																						
	509	5																																																																																																							
	(32)	27	(48)																																																																																																						
	699	4.5																																																																																																							

- | | | |
|-----|---|---|
| (A) | B | (A) BODY NUMBER (PREFIX WITH MZ) |
| C | D | B PERCENT THEO. DENSITY (THEO. DENSITY ~ 360 LB/FT ³) |
| | | C CRUSHING STRENGTH (PSI) |
| | | D THERMAL TEST RATING: 0 = BROKE IN MANUFACTURE |
| | | 1 = CRACKED APART IN 4000°F TEST |
| | | 2 = BADLY ERODED IN TEST |
| | | 3 = PIECES LOOSE AFTER TEST OR PUNKY, MEDIUM EROSION |
| | | 4 = CRACKS THROUGH BODY OR MILD EROSION |
| | | 5 = SURFACE CRACKS ONLY OR VERY SLIGHT EROSION |
| | | 6 = UNAFFECTED |



FIGURE 45 - ZIRCONIA BODY MZ8, THERMAL SHOCK TESTED - RATING 1.

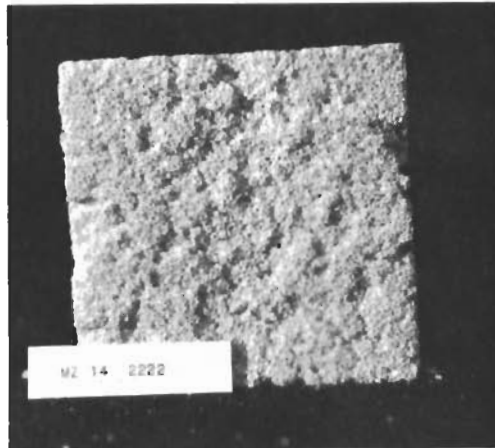


FIGURE 46 - ZIRCONIA BODY MZ14, THERMAL SHOCK TESTED - RATING 3.



FIGURE 47 - ZIRCONIA BODY MZ33, THERMAL SHOCK TESTED - RATING 5.

(4) Pore Size - Large and medium pore structures appeared promising. The small pore structures appeared promising only in the medium and high density bodies. In these cases there was sufficient material present to form the larger number of pore walls necessary per unit volume of the body with the smaller and more numerous pores.

(b) Step 2 (Evaluation of Extrinsic Variables) - Several modifications were added to or applied on the low density bodies. These modifications, described as extrinsic variables, were ROKIDE coating (flame sprayed coating), slurry coating, impregnation with a low density ceramic powder, and hydrogen firing to change the emittance by darkening the bodies. Six bodies were used in this evaluation and the resultant specimens tested in the 4000°F thermal shock test.

The ROKIDE Z (zirconia) coating was flame sprayed in three different thicknesses on the fired specimens. Figure 48 shows some coated samples. Slurry coating involved applying a dense layer of the same composition to the low density body. This was done in the green state, and subsequent differential firing shrinkage resulted in considerable warpage of the specimens.

Impregnation with a low density ceramic powder was an attempt to subdivide the pores into smaller ones which would provide better insulation at higher temperatures. At high temperatures, radiation across pores is a primary mode of heat transfer through a porous body. In this work, the fired low density zirconia structure was filled with a slip of the very low density body. This was subsequently low fired to remove the organic binders.

Hydrogen firing was tried in an attempt to render the zirconia darker and increase emittance. To accomplish this, the regular bodies were fired to maturity in a hydrogen atmosphere.

These extrinsic variables were evaluated by subjecting specimens to the 4000°F thermal shock test, with results as shown in Table X. (The slurry coated bodies are not included in the table because they had warped and deformed in firing during manufacture and were not tested.) Impregnation of the porous bodies had little effect on their behavior in the thermal shock test, although performance was improved in one case. Hydrogen firing changed the color of the zirconia only slightly, as indicated by Figure 49 which shows the bodies upon removal from the kiln. There was a definite darkening at the surface, but this disappeared a short distance inward. No improvement in thermal shock resistance or thermal insulation was noted over specimens fired in air. Also, since the hydrogen reduced zirconia will oxidize to its normal color when heated in air, such an alteration is not practical.

(c) Step 3 (Optimization of Superior Bodies) - From the experience gained in the first two steps, four zirconia bodies were picked for final development. The selected bodies were coarse grained, low stabilization, small and large pore size, and medium and high density. They were designated MZ49, 43, 44, and 46 (see Table IX).

Text continued on page 64

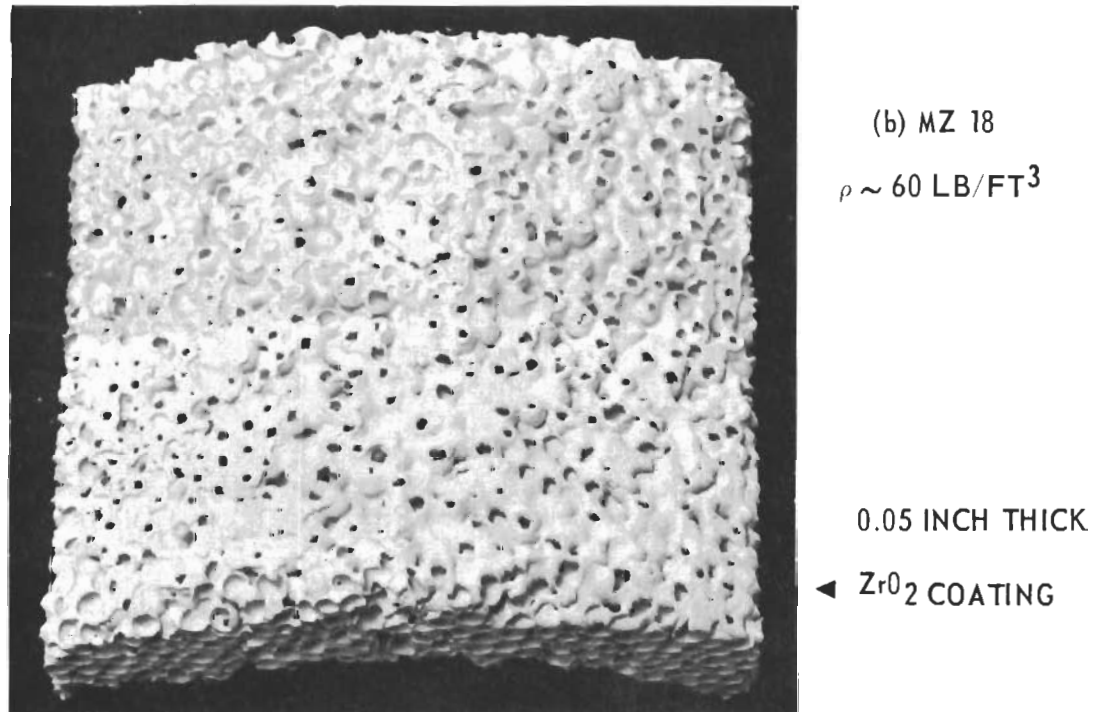
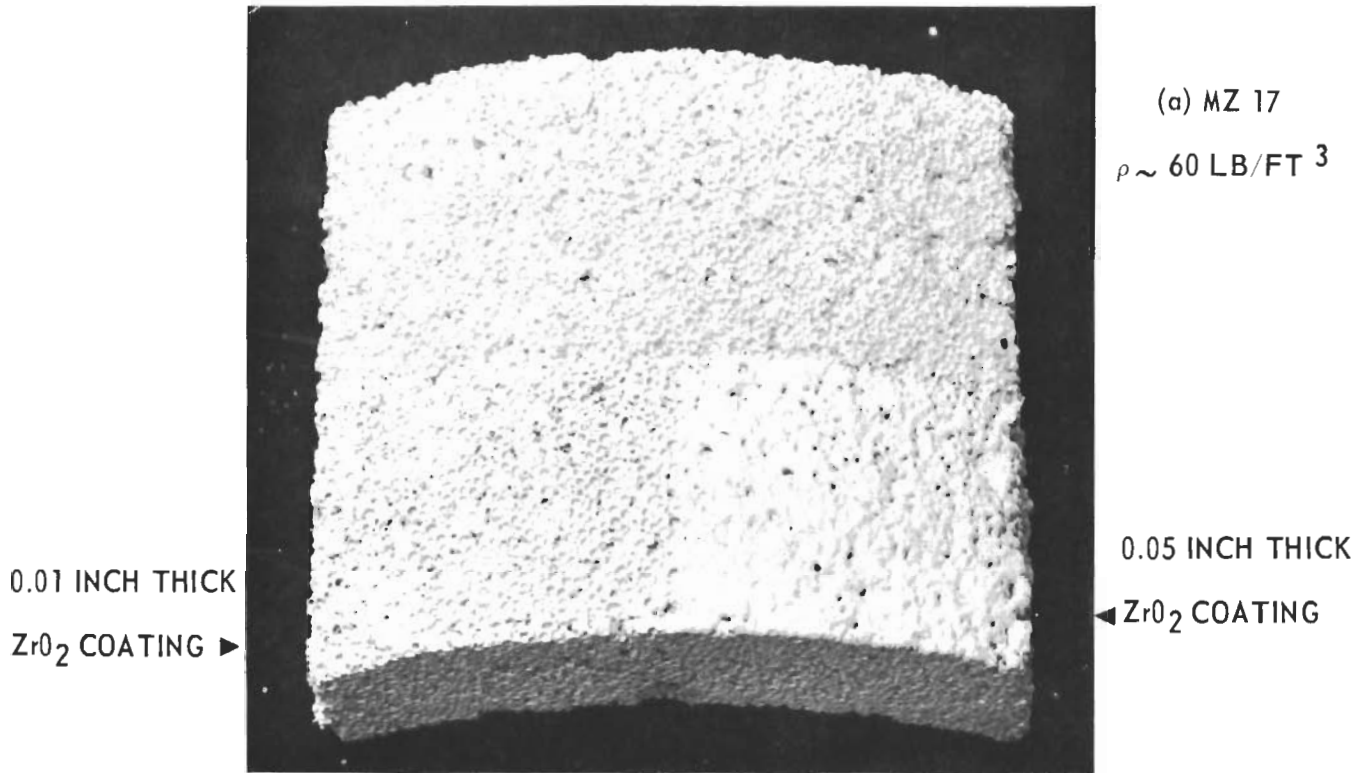


FIGURE 48 - NORTON COMPANY LOW DENSITY ZIRCONIA WITH FLAMESPRAYED ZIRCONIA COATING

**TABLE X - TEST RESULTS, EXTRINSIC VARIABLES
IN LOW DENSITY ZIRCONIA BODY DEVELOPMENT**

Body	Variable		4000°F Thermal Shock Test Results			
			Thermal Drop (°F/in.)		Test Rating	
	Type	Amount	1st Test	Retest	1st Test	Retest
MZ5	None	---	2040	---	5.5	---
	Rokide Z	0.01**	1975	---	3.5	---
		0.05	1900	---	4.0	---
		0.10	---	---	0	---
		Impregnation	---	2100	---	3.5
H ₂ fired	---	NR*	---	---	---	
MZ6	None	---	1975	1850	5.5	5.0
	Rokide Z	0.01	2000	---	3.0	---
		0.05	1800	1910	5.5	5.0
		0.10	1790	---	3.0	---
	Impregnation	---	1960	---	6.0	---
H ₂ fired	---	NR*	---	---	---	
MZ9	None	---	1950	---	6.0	---
	Rokide Z	0.01	2130	---	5.5	---
		0.05	1960	---	3.5	---
		0.10	1810	---	1.0	---
	Impregnation	---	1850	---	6.0	---
H ₂ fired	---	1880	---	4.5	---	
MZ14	None	---	2000	---	1.0	---
	Rokide Z	0.01	1970	---	4.0	---
		0.05	2100	---	4.0	---
	Impregnation	---	1850	---	5.0	---
H ₂ fired	---	NR*	---	---	---	
MZ17	None	---	2080	1920	5.0	5.0
	Rokide Z	0.01	2130	1900	5.5	3.0
		0.05	1720	---	3.0	---
	Impregnation	---	1980	---	5.0	---
	H ₂ fired	---	1890	---	5.0	---
MZ26	None	---	1910	1910	5.0	4.0
	Rokide Z	0.01	1940	1840	5.0	5.0
		0.05	1810	1810	3.5	1.5
	Impregnation	---	1870	---	4.5	---
H ₂ fired	---	2170	2180	4.5	4.0	

*Not run because other hydrogen fired specimens showed no change from air fired specimens.



FIGURE 49 - LOW DENSITY ZIRCONIA BODIES FIRED IN HYDROGEN

To each of these bodies, two extrinsic variables were applied - impregnation plus a 0.01 inch thick ROKIDE Z coating on the hot face; and a ROKIDE C (chromium oxide) coating 0.005 inch thick. The ROKIDE C was a very thin coating intended to increase emittance.

Results of the 4000°F thermal shock testing of these structures are presented in Table XI. (The results of the thermal shock test on the four basic bodies only are noted in Table IX.) Figure 50 shows the basic bodies in this series after test. Figure 51 shows the impregnated and ROKIDE Z coated bodies and Figure 52 shows these bodies with the ROKIDE C coating.

Some increase in thermal shock resistance occurred in bodies with the thin ROKIDE C coating. Three of the four bodies showed no damage as a result of the thermal shock test. However, as seen in Figure 52, the chromia coating was not stable at 4000°F and was partially lost in the area of torch impingement.

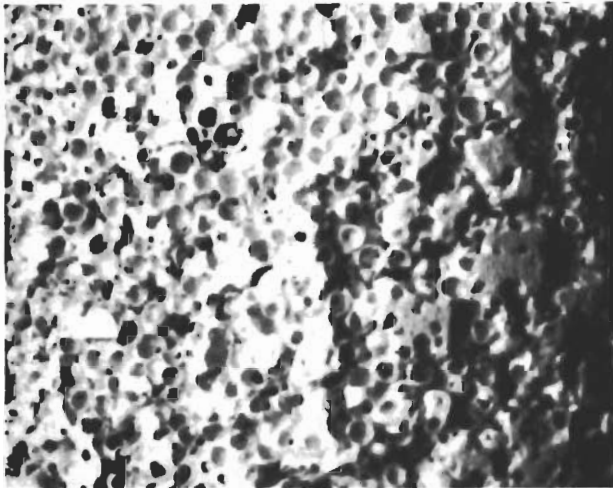
4.3.1.2 Phases II and III - Reproducibility and Producibility - As a result of the body development work in Phase I, MZ44, the low stabilization, high density, small pore, coarse grained zirconia body was selected for Phase II. This body was assigned the number LZ5991 and its properties are noted in Table IX. Although the density of this body (26% theoretical, or 95 lb/ft³), was higher than the original goal of 20%, the superior thermal shock resistance and high crushing strength justified the selection.

This basic body was to be used as made and fired without the application of any of the extrinsic variables since these proved to be of questionable merit. Also, this would permit machining the specimens to any configuration without necessitating further treatment after machining.

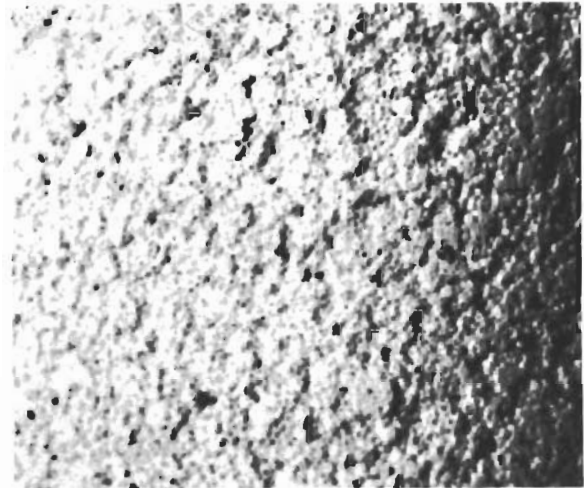
Text continued on page 69

TABLE XI - RESULTS OF THERMAL SHOCK TEST ON SUPERIOR BODIES

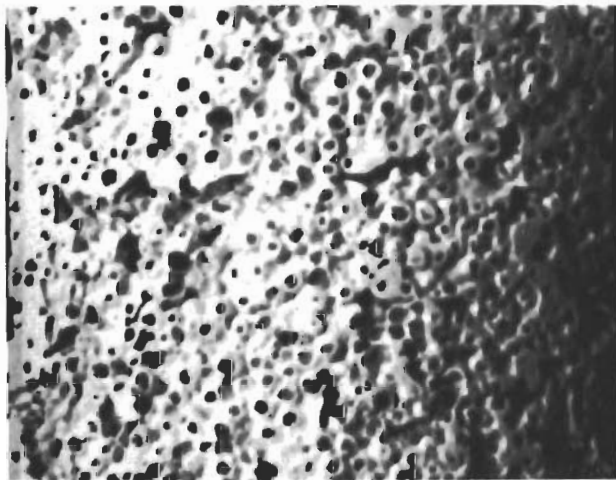
Body	Bulk Density (% Theoretical)	Extrinsic Variable	4000°F Thermal Shock Test Results	
			Thermal Drop (°F/in.)	Test Rating
MZ49	20 (~72 lb/ft ³)	None	2000	5.5
		ROKIDE C- 0.005"	1850	6
		Impregnation + ROKIDE Z 0.01"	1850	5
MZ43	17 (~60 lb/ft ³)	None	1670	5.5
		ROKIDE C 0.005"	1570	6
		Impregnation + ROKIDE Z 0.01"	1800	3.5
MZ44	26 (~95 lb/ft ³)	None	1900	6
		ROKIDE C 0.005"	1990	6
		Impregnation + ROKIDE Z 0.01"	1970	5
MZ46	24 (~86 lb/ft ³)	None	1650	4
		ROKIDE C 0.005"	1760	5
		Impregnation + ROKIDE Z 0.01"	1630	4



(a) MZ 43, $\rho \sim 60 \text{ LB/FT}^3$



(b) MZ 44, $\rho \sim 95 \text{ LB/FT}^3$

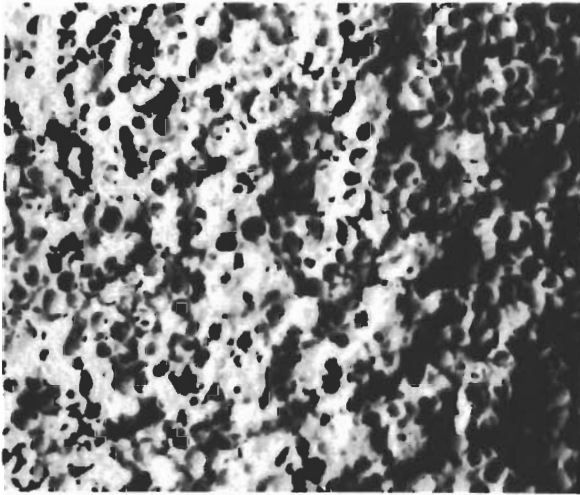


(c) MZ 46, $\rho \sim 86 \text{ LB/FT}^3$

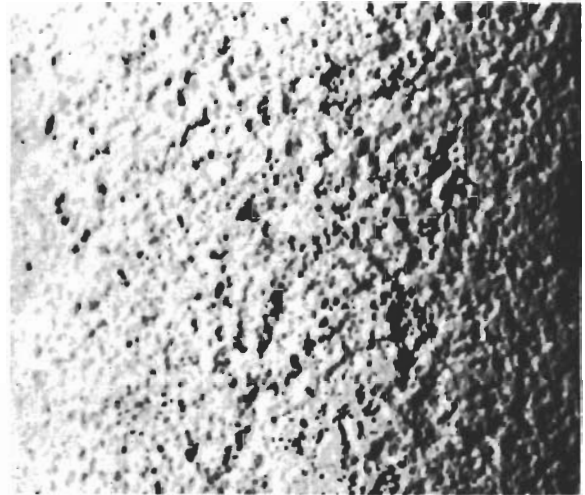


(d) MZ 49, $\rho \sim 72 \text{ LB/FT}^3$

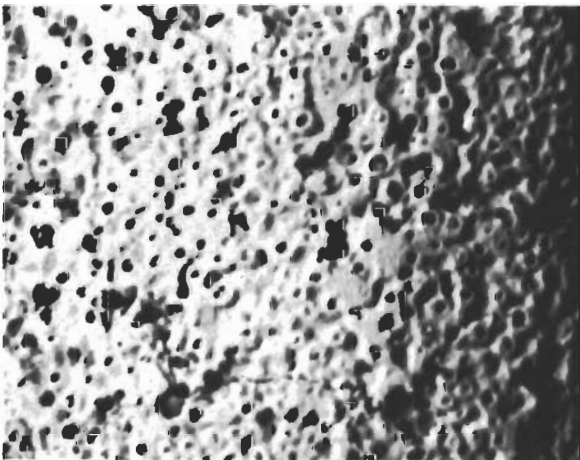
**FIGURE 50 - NORTON COMPANY LOW DENSITY ZIRCONIA
- AFTER THERMAL SHOCK TEST**



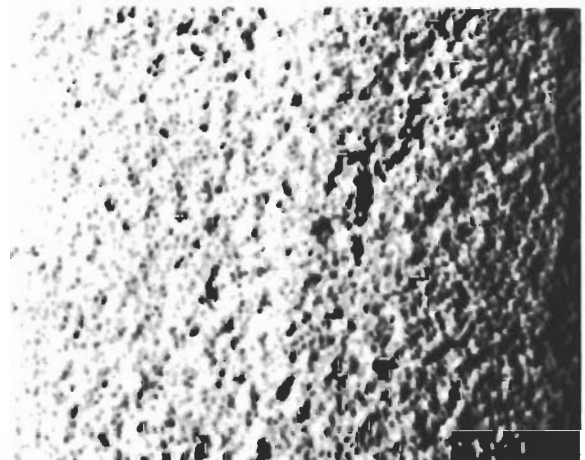
(a) MZ 43FZ, $\rho \sim 72 \text{ LB/FT}^3$



(b) MZ 44FZ, $\rho \sim 110 \text{ LB/FT}^3$

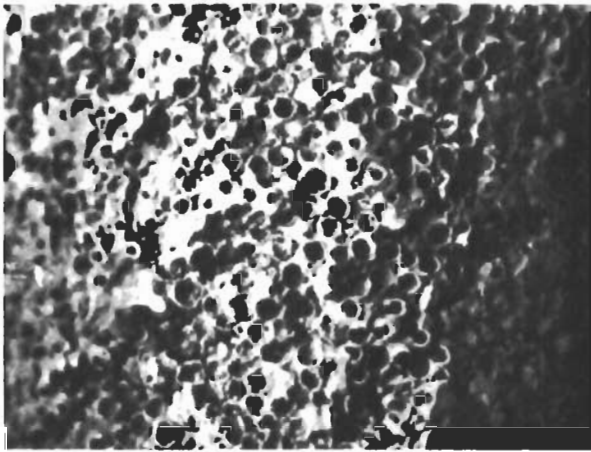


(c) MZ 46FZ, $\rho \sim 100 \text{ LB/FT}^3$

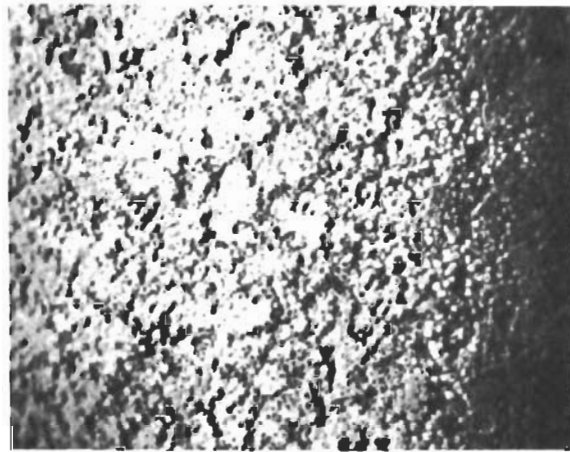


(d) MZ 49FZ, $\rho \sim 85 \text{ LB/FT}^3$

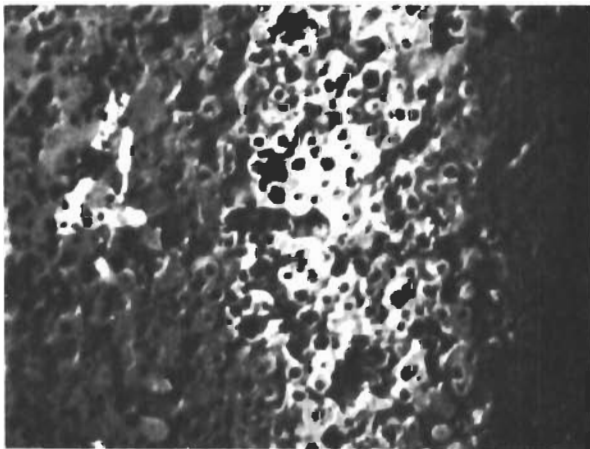
**FIGURE 51 - NORTON COMPANY LOW DENSITY FOAM FILLED
ZIRCONIA WITH FLAMESPRAYED ZIRCONIA COATING
- AFTER THERMAL SHOCK TEST**



(a) MZ 43C, $\rho \sim 60 \text{ LB/FT}^3$



(b) MZ 44C, $\rho \sim 95 \text{ LB/FT}^3$



(c) MZ 46C, $\rho \sim 86 \text{ LB/FT}^3$



(d) MZ 49C, $\rho \sim 72 \text{ LB/FT}^3$

FIGURE 52 - NORTON COMPANY LOW DENSITY ZIRCONIA WITH FLAMESPRAYED CHROMIA COATING - AFTER THERMAL SHOCK TEST

(a) Manufacturing Engineering Experience - The process of making the bodies was scaled up to a production size batch of 50 pounds. Each such batch would make 12 specimens 4-1/2 inches x 4-1/2 inches x 2-1/2 inches (manufacture of curved specimens was dropped at this time). However, transfer of the zirconia work from laboratory to manufacturing immediately produced several problems.

The first problem encountered was the presence of folds and voids in the parts; i.e., inhomogeneous structure. This was overcome by careful control of fabrication techniques. However, since the Phase I work had been completed approximately six weeks behind schedule with a resulting delay in the Phase II work, many of the subscale modules (see Section 5.2) were fabricated from a preliminary group of Phase II samples. Thermal shock testing at McDonnell on one-inch cubes cut from samples of the preliminary material had indicated that the thermal shock resistance was satisfactory.

The second problem to develop was the presence, in the central section of the parts, of small beads of zirconia which had pulled away from the pore walls, resulting in thinner pore walls in those areas. Careful control of moisture content during fabrication, and control of drying and firing procedures eliminated this problem.

The third problem, which was never completely overcome, was the cracking, especially on the surface, of parts during firing. The cracking appeared to be related to the firing cycle, especially the heating and cooling rates in the 1500-2000°F region. In this temperature region, unstabilized zirconia goes through a crystallographic inversion from monoclinic to cubic or tetragonal crystal habit or vice-versa. This inversion is accompanied by considerable volume change which can crack a part if sufficient thermal gradient exists through the cross-section of the part so that one area is undergoing the volume change while another is not.

A variety of firing procedures was tried in an attempt to correct the cracking problem. Samples were fired in a tunnel kiln versus periodic kiln; two step, low-fire in one kiln followed by a high-fire in a second kiln was tried; a variety of kiln settings were evaluated; firing cycles as long as two weeks were tried, with none of these procedures eliminating the cracking. The sample size was also changed to 4-1/2 inches x 2-1/2 inches x 2-1/2 inches from 4-1/2 inches x 4-1/2 inches x 2-1/2 inches in hopes the smaller size would be easier to produce crack-free.

Table XII gives the finally selected kiln cycle which minimized the cracking and which was used for most of the lots of parts shipped to McDonnell to meet the Phases II and III requirements. Table XIII lists properties of various zirconia batches. Crack-free specimens were cut out of 4-1/2 inch x 2-1/2 inch x 2-1/2 inch parts to determine these properties. It will be noticed in Table XIII that of four batches checked, only one had the high thermal shock resistance of the original MZ44, Phase I body.

**TABLE XII - EFFECT OF PRODUCTION VARIABLES
ON STABILIZATION OF LOW DENSITY ZIRCONIA BODIES**

Specimen from Production Batch No.	Stabilization* (% Cubic ZrO ₂)	Production Variables		
		ZrO ₂ Grain Types Used in Batch	CaO Content	Other
3	51	3	Normal	None
5	56	3	Normal	None
6	53	3	Normal	None
8	27	3	Low	None
9	42	2	Normal	None
11	44	2	Normal	None
14	25	2	Low	None
26	46	2	Normal	None
27	58	2	Normal	None
28	58	2	Normal	Periodic kiln fired - open setting
28	56	2	Normal	Periodic kiln fired - staggered setting
28	54	2	Normal	Tunnel kiln fired
23	47	2	Normal	None
23	41	2	Normal	None

*Accuracy of ±5%

Kiln cycle

Room temperature-1475°F at 140°F/hr or less

1475°F-3200°F at 105°F/hr or less

3 hr hold at 3200°F

3200°F to 1835°F at 125°F/hr or less

1835°F to 1475°F at 70°F/hr or less

1475°F to room temperature at 215°F/hr or less

**TABLE XIII - PROPERTIES OF LOW DENSITY ZIRCONIA BODY
LZ5991 PRODUCED IN PILOT PLANT OPERATION**

Specimen from Production Batch Number	Crushing Strength (psi)	Thermal Shock Test Rating
7	740	---
8	500	---
9	710	---
10	480	---
111	530	---
Average	590	---
4	---	6
14	---	4.5
15	---	4.5
16	---	4.5

As previously described, the original MZ44 body was made of a mixture of three fused zirconias, each with different amounts of CaO, to obtain the correct amount and distribution of cubic zirconia in the fired body. During pilot plant work, because of the large size of the batches, the supply of properly sized low stabilized grain became depleted. To alleviate this situation immediately, a number of pilot plant batches were made with a mixture of two fused zirconia grains with differing CaO content. The ratio of these two grains was selected to give the same total CaO content as previously obtained with the three zirconia grains. The original MZ44 low stabilized body was made of 28% high stabilized grain (4-1/2 w/o CaO), 62% low stabilized grain (3 w/o CaO), and 10% unstabilized grain (0 w/o CaO). To make similar bodies from two zirconia grains containing 4-1/2 w/o CaO and 0 w/o CaO, the quantities of the two were adjusted to give the same total CaO content (3.12 w/o).

A study was made of the effect of the change to the two-zirconia grain type body to see if similar stabilization was achieved with the similar CaO content. The results of stabilization measurements, presented in Table XII, show stabilization was similar in bodies that contained similar amounts of CaO whether this was added as three grains or two. Lower CaO contents resulted in lower stabilization. The three specimens in Table XIII that displayed poor thermal shock resistance were of the two-zirconia grain type body, while the composition of the specimen displaying good thermal shock resistance is not know.

The original Phase I body utilized a firing cycle with a 10-hour soak at 3200°F rather than the three hour soak used in Phases II and III.

Apparently some combination of fabrication technique, composition, and firing procedure yielded a crack-free body of good thermal shock resistance in Phase I and this combination was not reproduced in Phase II. Crystal stabilization did not appear to be the significant difference between MZ44 and the LZ5991. Electron microprobe analyses were made on two LZ5991 samples, which displayed an inhomogeneous distribution of calcia. There was no MZ44 on hand to analyze for comparison, as the preliminary lot received in Phase II had been consumed in subscale fabrication.

Samples of LZ5991 were sent to Southern Research Institute for determination of thermophysical properties. Thermal expansion measurements produced erratic results. This might have indicated sample-to-sample compositional and/or crystal stabilization variations, i.e., poor sample reproducibility and homogeneity.

Due to the continued problem of cracking during firing, the Phase II-III work was removed from the manufacturing area and returned to the laboratory. However, it was not possible to reproduce a material like the original MZ44 in the laboratory either, nor was the cracking problem overcome.

(b) Research and Development Experience - Table XIV presents a summary of the Norton Laboratory work which was performed as described below.

**TABLE XIV - CHARACTERISTICS OF LOW DENSITY ZIRCONIA BODIES
PRODUCED DURING R&D STUDY IN PHASES II - III**

Specimen Type	Structure Uniformity	Bulk Density (lb/ft ³)	Crushing Strength @ RT (psi)	4000°F Thermal Shock Test Results	
				Thermal Drop (°F/in.)	Test Rating
Step 1 35 Standard Shapes of LZ5991	Fair	104	---	2100	5.5
	Poor (Open areas)	98	---	2130	5.0
Step 2 Variation Study Standard LZ5991	Poor	88	500	1900	4.5
	Best liquid addition (+10%)	88	350	1950	4.5
	Best Coarse addition (2.5:7.5)	82	360	1820	4.75
Step 3 20 Standard shapes of each of best of variation study					
	MZ-44 body with additional liquid	Fair	75*	500	---
LZ5941 body with additional coarse	Fair	78*	450	---	5

*Mix formulation error produced too much pore induction, resulting in uniformly low density in all specimens.

(1) Shape Study - As a first step, a small number of specimens were made to the Phase II shape (2-1/2 inches x 2-1/2 inches x 4-1/2 inches), and to the Phase I curved shape (3 inches x 4 inches x 1-1/4 inches). This permitted a comparison of the effect of changing the shape of the specimen.

All 3 inch x 4 inch x 1-1/4 inch specimens had structures similar to those developed in similar shapes in the Phase I work. The structure of the 2-1/2 inch x 2-1/2 inch x 4-1/2 inch specimens was similar to the Phase I structure except there was a tendency toward a more open structure toward the bottom (a 2-1/2 inch x 4-1/2 inch face) of the shapes. Cracking during firing was not found to be shape-dependent.

Thirty-five 2-1/2 inch x 2-1/2 inch x 4-1/2 inch shapes were made. The structure variation became more evident when examining this large a number of specimens. Specimens were grouped into fair and poor classes and thermal shock tested, with results as shown in Table XIV, Step 1. Fair thermal shock resistance was indicated for samples with more uniform structures.

(2) Structure Study - Increased liquid contents were used to make the LZ5991 body more flowable and eliminate the structure variation found. Parts 2-1/2 inches x 2-1/2 inches x 4-1/2 inches were made with the standard 14% liquid content as well as with 14-1/2% and 15%, which represented increases of roughly 5% and 10% in the amount of water used in the batch. These mixes incorporated the blend of the two zirconia grains containing 4-1/2 w/o CaO and 0 w/o CaO previously described. The fine-to-coarse grain ratio (amount of 5 micron grain to 20 micron grain) was held constant at 6:4, which was standard for LZ5991 (Table VIII).

It was felt that the coarse fraction of zirconia grain could be increased and that this might result in a body with less tendency to crack on firing. Consequently, another series of bodies was made as 2-1/2 inch x 2-1/2 inch x 4-1/2 inch shapes with fine-to-coarse grain ratios of 6:4 (standard), 5:5, 4:6, 2.5:7.5 and 1.25:8.75. These mixes incorporated the blend of two zirconia grains previously described.

Thermal shock tests and crushing strength determinations were conducted on specimens containing each of these variations and the standard body. Tests results for the better formulations are shown in Step 2 of Table XIV. The tests indicated that an increase of 10% in the water content improved the moldability and uniformity of the mix. A fine-to-coarse ratio of 2.5:7.5 gave a body with adequate strength and fair thermal shock resistance.

From this work, two groups of 20 specimens, (2-1/2 inches x 2-1/2 inches x 4-1/2 inches) were made. The first incorporated the 2.5:7.5 fine-to-coarse fused zirconia grain, 10% additional water, and was a blend of the two kinds of zirconia containing 4-1/2 w/o CaO and 0 w/o CaO. The second group incorporated the standard 6:4 fine-to-coarse zirconia grain, 10% additional water, and was a blend of the three kinds of zirconia as originally developed in Phase I work (MZ44).

Examination of the fired specimens indicated that the random cracking problem still existed. Thermal shock tests and crushing strength determinations were made on specimens in both of these two groups. Results are shown in Step 3 of Table XIV.

Assuming the MZ44 body was reproduced compositionally, it did not have the thermal shock resistance of the Phase I samples. Other differences were a reduction in density, presence of cracks in fired parts, and a very non-uniform structure.

Approximately 80 parts (4-1/2 inches x 2-1/2 inches x 2-1/2 inches) representing eight lots, were received at McDonnell to satisfy the Phase II-III delivery requirements. Twenty-seven parts came from the laboratory effort. Well over half of these 80 parts were cracked as received, as determined by 2 to 20X visual examination. Density varied from 75 to 105 lb/ft³ as opposed to the Phase I density of 95 lb/ft³.

Thermal shock tests were performed on samples from each lot. In these tests, one inch cube samples were subjected to surface heating rates of 25°F/sec and 50°F/sec to a peak temperature of 4000°F and soaked 10 minutes at temperature. Samples 3.6 inches x 2.25 inches x 1.2 inches thick (some surfaced with chemically bonded zirconia to simulate the end use condition)

were subjected to the thermal environment of the 1.5 inch radius leading edge. From these thermal shock tests, it appeared that Lots 2, 2A, and 2AA (densities 85 to 95 lb/ft³) had the best, and Lot 3 the second best, thermal shock resistance. The parts for the full size 1.5 inch radius leading edge and 6.0 inch radius nose cap were made from these materials since scheduling requirements did not permit waiting any longer for better material, which as it turned out never evolved.

The thermal shock testing of the large samples resulted in fine cracking in all samples, but in all cases the samples were integral after testing and no surface erosion occurred. (One sample, supposedly of the original Phase I composition, was received and tested, and although it too had cracks after testing, these cracks were much finer than in any of the other lots tested.) None of the eight lots of zirconia received was as thermal shock resistant as the original Phase I MZ44 material.

Although considerable difficulties were experienced in reliably reproducing the low density zirconia body, the positive accomplishments of this development work should not be underestimated. In the Phase I studies, a very promising low density zirconia body at a density of 95 lb/ft³ was developed which had good strength (crushing strength ~ 590 psi) and good thermal shock resistance (capable of withstanding surface heating rates up to 50°F/sec). Even though the Phases II and III material was of poorer quality, it was possible to make use of this zirconia in fabrication of composite ceramic structures, both subscale and full scale. Prior to this program, there was no commercially available zirconia at a comparable density level which could have even been given serious consideration for utilization in this type of application.

4.3.2 Thoria Body Development Program

4.3.2.1 Phase I - Materials Improvement - The previous low density zirconia development was used as background technology for the thoria work. Except for stabilization, the same intrinsic variables of density, grain size, and pore size were considered. Only rectangular shaped specimens were made (3 inches x 3 inches x 1 inch or 4-1/2 inches x 2-1/2 inches x 2-1/2 inches). The ranges of the variables studied in this work are shown in Table XV.

Density ranged from 80 lb/ft³ (13% theoretical) to 125 lb/ft³ (20% theoretical). Also, a series was made with densities up to 190 lb/ft³ to investigate the effects of higher strength through greater density.

Two types of thoria grain were used, fused and calcined. Both were of 99.5% purity and of Norton manufacture. The calcined grain was of 5 micron size and the fused grain of 5 microns, 20, and 125 microns. After some preliminary mixes, fused thoria was restricted to the two coarser particle size fractions and calcined thoria was used for the fine particle size fraction. Proportions of the various particle sizes used are shown in Table XV.

Firing of specimens was accomplished in the same periodic kiln facilities as the zirconia specimens and with a similar firing schedule (Table XII).

TABLE XV - RANGES OF INTRINSIC VARIABLES IN LOW DENSITY THORIA BODY DEVELOPMENT

Variables										
	Density ^(a)		Pore Size		Mineralizer		Reinforcements		Grain Size	
	Type	% Theoretical	Type	Diameter (inches)	Type	Weight (%)	Type	Weight (%)	Type	Ratio of 5μ:20μ:125μ grains
Ranges	Extra high	30	Large	0.140	High	1	High	30	Coarse	2:5:3
	High	20	Medium	0.064	Low	0.5	Medium	15	Reinforced	5:5:0
	Medium	17	Small	0.050	-----	-----	Low	4	Fine	10:0:0
	Low	13	Composite 65% large 35% small	-----	-----	-----	-----	-----	-----	-----

Pore size was altered by using various sizes of spherical burn-out material. The same sizes were used in this development work as for the zirconia. However, one additional variation tried was a mixture of large and small pore sizes.

The thermal shock test procedure was the same as for the zirconia except that a surface heating rate of 40°F/sec was used. The 4000°F thermal shock test results indicated that the higher expansion of thoria, as compared with zirconia, rendered thoria more thermal shock sensitive.

(a) Evaluation of Coatings and Sandwich Structures - Techniques were developed for producing a thin dense slurry coating on the thoria bodies. Although these coatings adhered well, the thermal shock resistance of the structures was not enhanced.

(b) Evaluation of Mineralizer Additions and Reinforcements - Two new variables were introduced in attempts to improve the thermal shock resistance of the thoria bodies. The first was the addition of up to 1% mineralizer (CaO in the form of minus 150 micron size calcined powder) to the thoria grain during batch mixing operations in an attempt to obtain a stronger body by promoting sintering.

The second variable was the introduction of short pieces of dense thoria reinforcements or "fibers," consisting of presintered thoria extrusions approximately 0.05 inch in diameter. These were made by wrapping unfired extruded rod around a 1/4 to 1/2 inch diameter mandrel, clipping off half-turns of the extruded rod, and firing the resulting short pieces. Various firing temperatures and compositions were evaluated for the fibers to obtain optimum firing procedure and composition. Also investigated was the coating of the fibers with a burn-out material to allow a gap for the thoria body to shrink around the fibers. This procedure was found to be unnecessary.

The fibers were mixed into the low density batch at the end of the mixing cycle to avoid breakage. Quantities up to 30% by weight of the low density body were added. It was felt that the fibers would be stronger than the low density body and, in theory, would carry the loads imposed by the thermal stresses. They would also tend to hold the body together if micro-cracking did occur in the low density structure.

A series of nine bodies was made incorporating these two variables. The results of tests on these bodies are shown in Table XVI. The mineralizer and reinforcements improved the thermal shock resistance of the bodies in the better combinations. The best combination was body T-51 with 15% reinforcement and 0.5% mineralizer. Figure 53 shows the structure of this body.

(c) Improved Body - The dense reinforcements, while helping the thermal shock resistance of the body, created machining problems (at McDonnell) due to inhomogeneity. In further development work, a coarser grained body was developed by introducing 125 micron size grain. The new body (T-68) had thermal shock resistance comparable to the body containing reinforcements, and had a density of 125 lb/ft³ (20% theoretical). This body consisted of a ratio of 2:5:3 of 5 micron:20 micron:125 micron grain sizes, 0.05 inch diameter pores, and 0.8 w/o CaO. The T-68 body structure shown in Figure 54, was chosen for manufacturing development in Phases II and III.

The highest attainable thermal shock resistance rating with the thoria was "4" on the scale of "6." Since the nose cap design did not require this material, further development to improve the thermal shock resistance was not undertaken. It was felt that further improvement would be a major effort because the relatively high thermal expansion coefficient of the thoria rendered it inherently thermal shock sensitive.

4.3.2.2 Phase II and III - Reproducibility and Producibility - Body T-68, selected for further manufacturing development, was assigned the number LT5006.

Production techniques were worked out which enabled the reproducible manufacture of the desired body. Initially in this phase, mixing and drying problems occurred, but these were solved in the course of the development. Unlike with zirconia, firing was not a problem in producing the thoria specimens. A total of 27 parts (4-1/2 inches x 2-1/2 inches x 2-1/2 inches) were delivered to McDonnell. Although visual inspection at 2 to 20X showed a few parts with very small cracks; cracking of parts or reproducibility was not a problem in the thoria work. The properties of the LT5006 specimens produced in Phases II and III are shown in Table XVII.

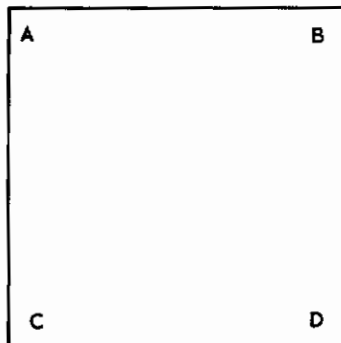
During the Phase III work, twenty specimens (2-1/2 inches x 2-1/2 inches x 4-1/2 inches) were produced, and further work was then halted at the request of McDonnell as sufficient specimens were delivered to meet all material requirements. One inch cube samples were cut from these parts and thermal shock tested at McDonnell to 4000°F at surface heating rates of 50°F/sec and 25°F/sec. It was found that the thoria failed by thermal shock even at 25°F/sec and; therefore, was not suitable for full scale component applications.

Text continued on page 79

**TABLE XVI - RESULTS OF MINERALIZER AND REINFORCEMENT
ADDITIONS TO LOW DENSITY THORIA BODIES**

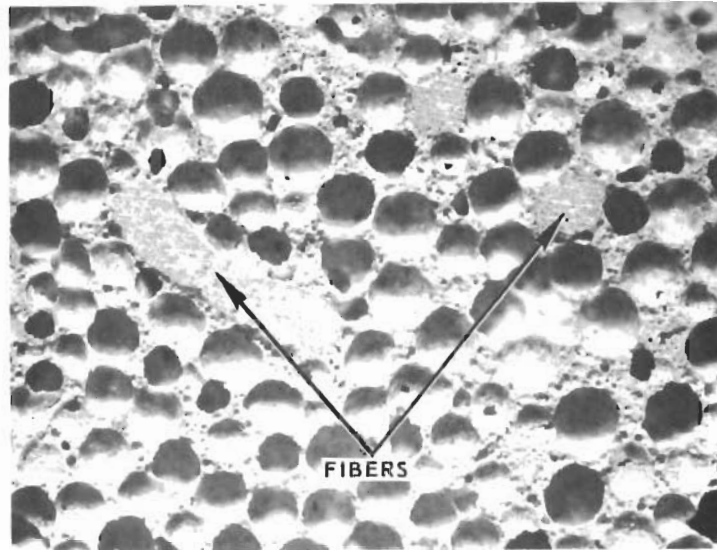
0%		MINERALIZER (CaO) WEIGHT - % 0.5%		1%		REINFORCEMENT (-0.050" DIAMETER ThO ₂ "FIBERS") WEIGHT - %
T-34	25	T-41	26	T-46	31	
830	1	990	1.5	1160	3	0%
T-47	22	T-51	24	T-57	20	15%
510	1	380	4	160	3	
T-58	19	T-54	22	T-55	22	30%
190	3	210	3	60	3	

NOTE: PORE SIZE OF ALL BODIES = 0.05" DIAMETER



- A BODY NUMBER
- B PERCENT THEORETICAL DENSITY
(THEO. DENSITY - 624 LB/FT³)
- C CRUSHING STRENGTH (PSI)
- D THERMAL TEST RATING:

- 0 = BROKE IN MANUFACTURE
- 1 = CRACKED APART IN 4000°F TEST
- 2 = BADLY ERODED IN TEST
- 3 = PIECES LOOSE AFTER TEST OR PUNKY, MEDIUM EROSION
- 4 = CRACKS THROUGH BODY OR MILD EROSION
- 5 = SURFACE CRACKS ONLY OR VERY SLIGHT EROSION
- 6 = UNAFFECTED



MAG: 5X

FIGURE 53 - PORE STRUCTURE AND ThO_2 "FIBERS" IN BODY T-51

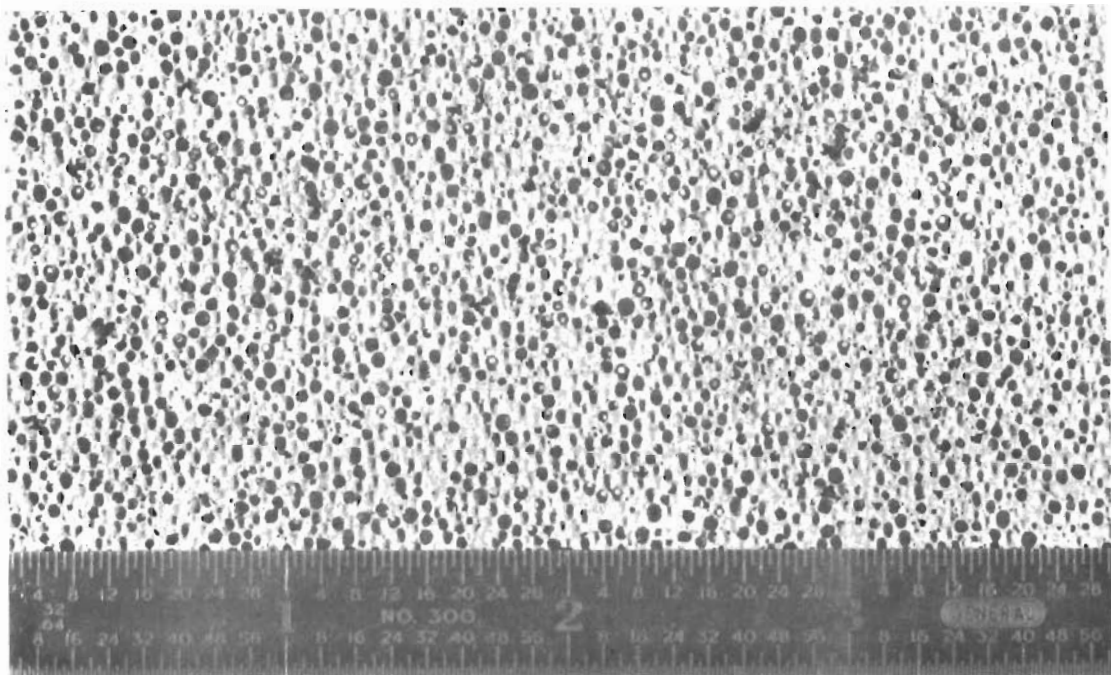


FIGURE 54 - NORTON, PHASE II, LOW DENSITY ThO_2 , $\rho \sim 125 \text{ LB/FT}$
(BODY T-68)

TABLE XVII - PROPERTIES OF PHASES II - III THORIA BODIES

Specimen Identification	Bulk Density (lb/ft ³)	Crushing Strength @ RT (psi)	4000°F Thermal Shock Test Results	
			Thermal Drop (°F/in.)	Thermal Shock Resistance of Body Structure
Phase II, Lot 1	128	550	---	4
Phase II, Lot 2	121	---	---	4
Phase II, Lot 3	135	510	1760	4
Phase III	124	450	1750	4

In summary, the inherent physical properties of thoria precluded, within the scope of this project, the production of a low density material which was completely resistant to heating rates of 25°F/sec. The developed material cracked and was weakened by this heating condition but did not exhibit spalling. This material was superior, however, in structure uniformity, strength, and thermal shock resistance to any low density thoria available at the beginning of this project. It could be reproducibly manufactured and probably would have application under less severe surface heating conditions. This thoria material was not utilized in the building of full size components in this program.

4.4 CHEMICALLY BONDED REFRACTORY OXIDE DEVELOPMENT

In addition to the improvement and development by a subcontractor of sintered low density ceramics, the development of chemically bonded ceramics (alumina, zirconia, and thoria) of low and high density was carried on at McDonnell over a time span of six months. This time span was dictated by subscale module fabrication scheduling.

The advantage of chemically bonded ceramics over the sintered variety is that the former allow in situ fabrication of components, which can decrease attachment steps and problems. The disadvantage of chemically bonded ceramics is that they generally are of lower strength and are less stable chemically and dimensionally than their sintered counterparts. The chemically bonded ceramic development work was conducted at McDonnell, since this phase was so closely related to component fabrication and because of past applicable experience.

High density chemically bonded ceramics were studied because preliminary designs indicated that these materials would probably be required for surfacing or attaching low density sintered or chemically bonded ceramics.

4.4.1 Applicable Experience

For over a year prior to the initiation of this project, McDonnell had conducted in-house development studies on chemically bonded, low and high

density ceramics. The majority of these studies were concerned with zirconia, but some work was also done with alumina and thoria. Over 250 compositions were prepared and evaluated in this work to study types of bonding agents and techniques of inducing porosity. This work is summarized here because of its applicability to this project.

Table XVIII lists many of the bonding agents studied by using varying quantities for bonding fused or calcined, partially stabilized, -325 mesh zirconia. Some work was also done on grain sizing effects. All samples were qualitatively evaluated for strength after curing at 1000°F and for refractoriness and thermal shock resistance by torch testing to 4000°F at a surface heating rate of 50°F/sec. The conclusions of this study were as follows:

(a) Acid bonds - The fluorine-containing acids were unpleasant and somewhat dangerous to work with although giving fairly good bonds. H₂SiF₆ was the best of these acids. HNO₃, HCl, and H₂SO₄ gave low bond strengths but the H₂SO₄ bonded bodies had good thermal shock resistance.

TABLE XVIII - CHEMICAL BONDING AGENTS FOR ZIRCONIA

Acid Bonds	Silicate Bonds
H ₃ PO ₄	Potassium Silicate (Liquid)
H ₃ PO ₄ + ZrO ₂ Paste	Potassium Silicate (Powdered)
H ₃ PO ₄ + Zircon	Potassium Silicate + Na ₂ SiF ₆
H ₃ PO ₄ + Hydrous ZrO ₂	Potassium Silicate + Zr Pyrophosphate
H ₂ SiF ₆	Potassium Silicate + Zr(SO ₄) ₂
H ₂ SO ₄	Potassium Silicate + K ₃ PO ₄
H ₂ SO ₄ + Hydrous ZrO ₂	Potassium Silicate + Na ₃ PO ₄
H ₂ SO ₄ + Zr Pyrophosphate	Potassium Silicate + K ₂ CO ₃
H ₂ SO ₄ + AlPO ₄	Potassium Silicate + KNO ₃
H ₂ PO ₃ F	Sodium Silicate (Liquid)
H ₂ PO ₃ F + NH ₄ H ₂ PO ₄	Sodium Silicate (Powdered)
HSO ₃ F	Sodium Silicate + Colloidal ZrO ₂
HNO ₃	Sodium Silicate + Zr(NO ₃) ₄
HCl	Ethyl Silicate + Zr Acetate
HCl + MgO	
Miscellaneous Bonds	
NH ₄ H ₂ PO ₄ + AlCl ₃	NH ₄ Zirconyl Carbonate + MgSO ₄
NH ₄ H ₂ PO ₄ + Colloidal Al ₂ O ₃	NH ₄ Zirconyl Carbonate + CaSO ₄
NH ₄ H ₂ PO ₄ + Zr(NO ₃) ₄	Colloidal ZrO ₂
NH ₄ H ₂ PO ₄ + Zr(SO ₄) ₂	Colloidal Al ₂ O ₃
NH ₄ Zirconyl Carbonate	Zircon Bond

The H_3PO_4 seemed the best all around acid bond, yielding bodies with good cured strength, good working properties, and fair thermal shock resistance. The addition of a material like zircon aided setting at low temperatures. Quantities of H_3PO_4 greater than about 5% (based on zirconia content) tended to yield some surface melting and blistering at $4000^\circ F$.

(b) Silicate bonds - Both sodium and potassium silicate, bonded zirconia very well, yielding bodies with good cured strength and good thermal shock resistance. The potassium silicate bonded bodies had better refractoriness. Quantities of K_2SiO_3 greater than about 7% gave some surface melting at $4000^\circ F$.

Use of a setting agent such as Na_2SiF_6 or a carbonate, phosphate, or nitrate was helpful in decreasing bond migration during curing. The powdered sodium silicate plus colloidal zirconia bond was comparable to the potassium silicate bond but with somewhat less bond migration difficulty.

(c) Miscellaneous bonds - $NH_4H_2PO_4$ plus $AlCl_3$ was the best of the miscellaneous binders, with properties similar to the H_3PO_4 bond, as might be expected.

(d) Fused versus calcined zirconia - The fused zirconia seemed to yield bodies of somewhat lower drying, curing, and firing shrinkage than bodies using calcined materials of comparable grain size. The calcined material was somewhat more reactive in bonding, resulting in bodies of higher cured strength.

(e) Grain size - Bodies containing only -325 mesh material had higher shrinkage, poorer thermal shock resistance, and better bond strength than bodies containing coarser fractions.

Preliminary work on attaining low density was performed on many of the zirconia bodies utilized in the chemical bonding studies. Methods studied for attaining low density were mechanical foaming (whipping or beating using a foaming agent), chemical foaming (chemical reaction which evolves gas such as acid + aluminum which evolves hydrogen), burn-out (decomposing volatile component) and low density aggregate (bubble zirconia). The general conclusions from this work are listed below:

(a) Mechanical Foaming - This process was very adaptable to fine grained systems, but required considerable processing refinement to attain stable, reproducible, low density foams. Of the foaming agents tried, Mearl SW2336 (Mearl Chemical Corp.) seemed adequate, and of the organic agents added to influence slip viscosity, methyl cellulose or Burtonite V-7-E appeared to work well.

(b) Chemical Foaming - Most of this work was done utilizing the reaction between aluminum metal powder and acid (buffered or unbuffered) to evolve hydrogen gas. This process seemed difficult to control and reproduce because of its reliance on the rate and uniformity of a chemical reaction.

(c) Burn-out - Of the various burn-out materials tried (including polystyrene, phenolic, graphite, and acrylic), acrylic and polystyrene seemed most promising because of the ease of burning them out cleanly. This process was adaptable to a variety of grain sizes and bonding agents. Reproducibility, density, pore size, and uniformity were dependent on the control of the burn-out material, quantity introduced, particle size, uniformity of dispersion, and techniques for removing (heating rates).

(d) Low Density Aggregate - The density was dependent on the bulk density of the aggregate which in this case was bubble zirconia. At a grain sizing of -8 + 20 mesh, this material had a bulk density of 75 lb/ft³. In general, it was found that addition of sufficient bubble zirconia to a bond system (-325M zirconia plus bonding agent) to lower the bulk density to less than 120 lb/ft³ resulted in a very weak body. The low density aggregate technique had the advantage that the aggregate was a stable material which did not undergo shrinkage during curing and thermal shock testing.

4.4.2 Development Approach

Based on the past in-house development studies, a laboratory work plan was prepared to cover a six-month span. This limited period dictated that the development work be primarily qualitative in nature, and oriented to obtain workable, usable systems as soon as possible and not necessarily optimum, highly refined systems. The overall approach was to develop and refine dense chemically bonded zirconia systems and to apply techniques of attaining low density to these systems. It was felt, and later confirmed, that the knowledge gained working with zirconia systems would be directly, or with minor variations, applicable to alumina or thoria systems. Emphasis was placed on silicate and phosphate bonded systems. The property goals arbitrarily set for the final selected compositions were as listed below:

(a) Adequate Pot Life - 30 minutes minimum after completion of all mixing operations.

(b) Good Working Properties - Capable of being readily formed into usable shapes by casting, troweling, or tamping.

(c) Good Cured Strength - Minimum crushing strength of 200 psi for low density compositions and 4000 psi for high density compositions.

(d) Low Total Shrinkage - Shrinkage after drying, curing, and thermal shock testing as low as possible, preferably less than 4%.

(e) Good Thermal Shock Resistance - No spalling, completely integral, very minor or no cracking, good retained strength.

(f) Adequate Refractoriness - No melting or slumping, little or no surface change.

(g) Density (Low Density Compositions Only) - Alumina, 50 lb/ft³; Zirconia, 120 lb/ft³, Thoria, low as possible.

4.4.3 Laboratory Procedure

Figures 55 and 56 show the types of specimens used in the laboratory work. The small 1 inch x 1 inch x 1/2 inch specimen was used for preliminary screening work to check out bond properties and thermal shock resistance (at 50°F/sec heating rates). All promising compositions were fabricated and evaluated in the 2 inch x 2 inch x 1 inch size. The larger specimen was more indicative of a tile size that might be used in a nose cap, for instance, and served to reveal fabrication problems. Specimens 1 inch in diameter x 1 inch long were prepared for crushing strength determinations.

All specimens were cast or formed in silicone rubber molds which would withstand curing temperatures to approximately 500°F and which were flexible enough to permit easy sample removal with little or no sticking of the sample to the mold. Some wood and stainless steel molds were also utilized, and petroleum jelly was used as a release agent.

In preparing a specimen, all materials (see Table XIX) were carefully weighed out; the dry ingredients mixed by hand; sufficient liquids added to form a stiff plastic mix; and the wet mix trowelled and vibrated by hand into the mold.

In the course of the investigation, it was found that a mix of this consistency was too fluid for fabricating larger shapes. This consistency tended to be highly thixotropic and to allow segregation of binders and liquids; segregation of fine and coarse materials; and drying, curing, and firing shrinkage cracking. A composition of tamping consistency (nearly dry but wet enough to be compacted into a solid mass) was found to minimize this problem and was the forming technique utilized later in the program. Most of the preliminary designs which included the use of chemically bonded, low density ceramics appeared adaptable to the tamping technique of fabrication.

Burn-out compositions were prepared by adding the burn-out material after all liquids had been added. The composition was then thoroughly mixed by hand and additional liquid added, if necessary.

In the case of a mechanical foam, the dry materials were added to the predetermined amount of liquid to form a fluid mix and mixing was done using a propeller-type mixer to achieve foaming (mixing time approximately three minutes). A relatively fluid mix was necessary for preparing a chemical foam as well as for a mechanical foam in order to permit the foaming to take place.

During the preliminary screening work, an arbitrary curing cycle was used which consisted of overnight drying at room temperature, followed by two hours at 200°F, one hour at 500°F, and one hour at 1000°F. All curing was performed in circulating air ovens. Curing rates were such as to attempt to minimize cracking.

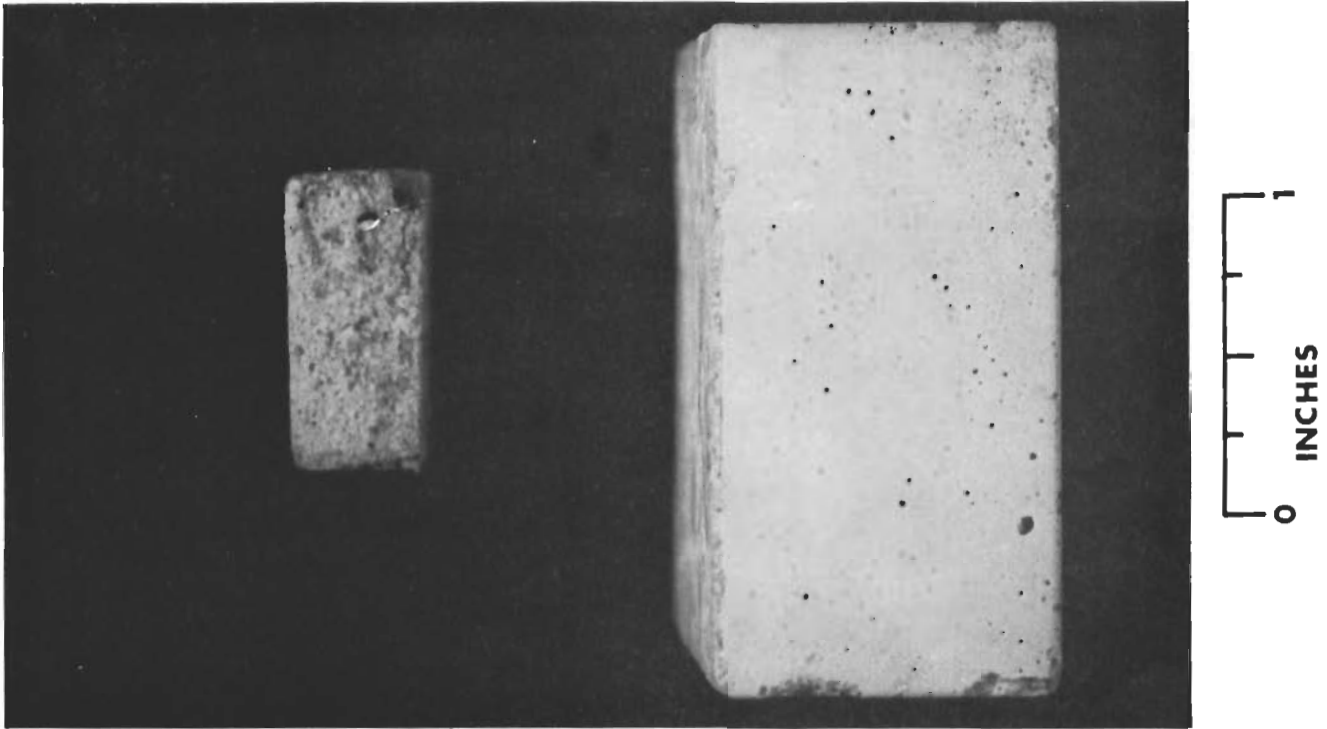


**FIGURE 55 - CHEMICALLY BONDED DENSE (~ 25% POROSITY)
ZIRCONIA SAMPLES - $\rho = 270 \text{ LB/FT}^3$**

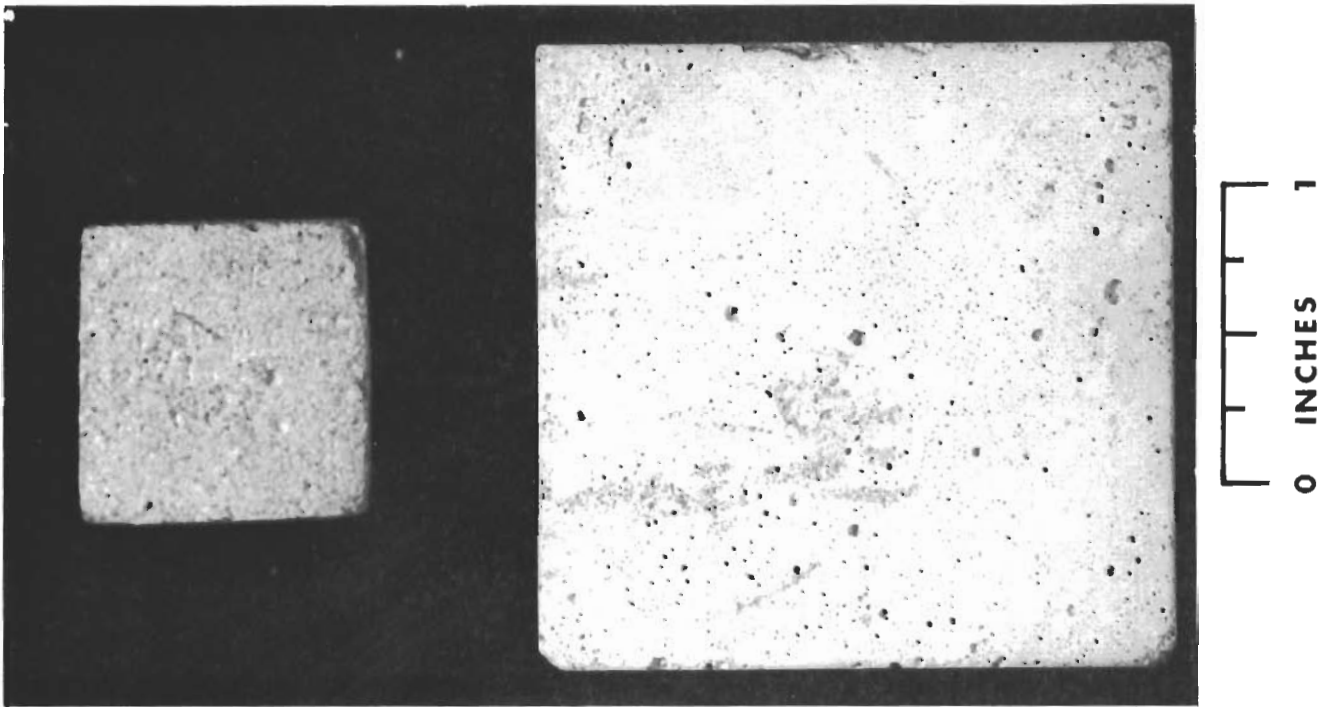


**FIGURE 56 - CHEMICALLY BONDED DENSE (~ 25% POROSITY)
ZIRCONIA SAMPLES - $\rho = 270 \text{ LB/FT}^3$**

As part of the laboratory investigation, more nearly optimum curing cycles were determined by qualitative comparison of samples cured at different cycles and by curing samples to constant weight at various arbitrary temperatures. The latter method was necessary in determining required curing cycles for burn-out compositions.

TABLE XIX - MATERIALS UTILIZED IN CHEMICAL BONDING STUDY

Material	Source
Zirconia	
Zircoa GGC, -65M, partially stabilized (CaO), calcined	Zirconia Corp. of America
Zircoa A, -325M, unstabilized, calcined	Zirconia Corp. of America
Zircoa B, -325M, partially stabilized (CaO), calcined	Zirconia Corp. of America
Zircoa C, -325M, fully stabilized (CaO), calcined	Zirconia Corp. of America
Zirnorite H, 30F, partially stabilized (CaO), fused	Norton Co.
Zirnorite H, 90F, partially stabilized (CaO), fused	Norton Co.
Zirnorite I, 4F, partially stabilized (CaO), fused, bubbles	Norton Co.
Zirnorite I, 325F, partially stabilized (CaO), fused, crushed bubbles	Norton Co.
Zirnorite I, 8F, partially stabilized (CaO), fused, bubbles	Norton Co.
Alumina	
38500 A.W.I.F. Alundum 500F, fused	Norton Co.
38900 A.W.I.F. Alundum 900F, fused	Norton Co.
38 Alundum, 100F, fused	Norton Co.
Alundum 163, 8/72, fused, bubbles	Norton Co.
Thoria	
100F, fused	Norton Co.
325F, fused	Norton Co.
900F, fused	Norton Co.
Chromia	
-325M, C.P.	Fisher Scientific
Bonding Agents	
Kasil 55 Powder, powdered potassium silicate, (28.3% K ₂ O, 70.7% SiO ₂)	Philadelphia Quartz Co.
Kasil 1, potassium silicate solution (8.3% K ₂ O, 20.8% SiO ₂ , 70.9% H ₂ O)	Philadelphia Quartz Co.
Kasil 88, potassium silicate solution (9.1% K ₂ O, 19.9% SiO ₂ , 71% H ₂ O)	Philadelphia Quartz Co.
Star, sodium silicate solution (10.6% Na ₂ O, 26.5% SiO ₂ , 62.9% H ₂ O)	Philadelphia Quartz Co.
K, sodium silicate solution (11.0% Na ₂ O, 31.0% SiO ₂ , 57.1% H ₂ O)	Philadelphia Quartz Co.
E, Sodium silicate solution (8.6% Na ₂ O, 27.7% SiO ₂ , 63.7% H ₂ O)	Philadelphia Quartz Co.
SS20 Powder, powdered sodium silicate (23.3% Na ₂ O, 75.0% SiO ₂ , 1.7% H ₂ O)	Philadelphia Quartz Co.
G, powdered sodium silicate (19.2% Na ₂ O, 61.8% SiO ₂ , 19.0% H ₂ O)	Philadelphia Quartz Co.
Metso Granular, powdered sodium metasilicate pentahydrate (29.5% Na ₂ O, 28.7% SiO ₂ , 41.8% H ₂ O)	Philadelphia Quartz Co.
Phosphoric Acid, (H ₃ PO ₄), 85%	Fisher Scientific
Colloidal Zirconia, aqueous slurry, 20% ZrO ₂ content	Titanium Alloy, Mfg. Div.
Calcium Aluminate Cement, CA-25, 90% -325M	National Lead Co.
Thorium Nitrate, (Th (NO ₃) ₄ · 4H ₂ O)	Aluminum Co. of America Fisher Scientific

TABLE XIX - MATERIALS UTILIZED IN CHEMICAL BONDING STUDY (CONTINUED)

Material	Source
Setting Agents	
Ultrax 1000W, Zircon, (ZrSiO ₄)	Metal & Thermite Co.
Sodium silico-fluoride, (Na ₂ SiF ₆)	Fisher Scientific
Potassium orthophosphate, (K ₃ PO ₄)	Fisher Scientific
Ethyl acetate	Fisher Scientific
Glycerol diacetate	Fisher Scientific
Potassium carbonate, (K ₂ CO ₃)	Fisher Scientific
Sodium orthophosphate, mono-H, (Na ₂ HPO ₄ ·7H ₂ O)	Fisher Scientific
Sodium orthophosphate, di-H, (NaH ₂ PO ₄ ·H ₂ O)	Fisher Scientific
Zirconium Sulfate, (Zr(SO ₄) ₂ ·4H ₂ O)	Titanium Alloy Mfg. Div.
	National Lead Co.
Zirconium pyrophosphate, (ZrP ₂ O ₇)	Titanium Alloy Mfg. Div.
	National Lead Co.
Miscellaneous Materials	
Acrylic powder (burn-out additive)	Fisher Scientific
Polystyrene beads (burn-out additive)	Union Carbide
Naphthalene crystals (burn-out additive)	Fisher Scientific
Methyl cellulose, 400 cps (suspending agent)	Fisher Scientific
Burtonite V-7-E (suspending agent)	Burtonite Co.
Marex (suspending agent)	Kelco Co.
Mearl SW-2336 (foaming agent)	Mearl Chemical Corp.
Triton X-100 (foaming agent)	Rohm & Haas, Inc.
Rodine 82-A (acid inhibitor)	Amchem Products, Inc.
Aluminum powder	Fisher Scientific

(CONCLUDED)

It was desirable that the maximum curing temperature be as low as possible because in the expected application the chemically bonded material would be attached to a metal and it was preferable not to expose the metal to high temperatures, especially for extended time periods. In instances of water cooled metal substructures, the metal was expected to be aluminum. Minimum curing times and temperatures were also desirable to minimize processing time.

After curing, the samples were visually examined and qualitatively evaluated for cured strength, bond migration, cracking during curing, and curing shrinkage. The samples were then thermal shock tested (50°F/sec surface heating rate) using the torch facility shown in Figure 21 and the procedure outlined in Section 4.2. After torch testing, all samples were visually examined and qualitatively evaluated for strength, refractoriness (melting), shrinkage, and cracking (during and after testing).

4.4.4 Chemical Bonding Systems and High Density Compositions

4.4.4.1 Zirconia - In the past work, a composition consisting of 100 g I325F zirconia, 6.2 g Kasil 88, and 7.1 g water had shown good cured and after-torch-test strength. This composition was therefore selected as a starting

point for the investigation of the effects of grain size and crystal habit, bonding agents, setting agents, and curing cycle, as discussed below.

(a) Grain Size and Crystal Habit - Substitution of H3OF or H9OF zirconia for the I325F zirconia was made in approximately 10 g increments all the way to a 100% H3OF or H9OF content. The increase in coarse grain content resulted in an increase in thermal shock resistance and a decrease in cured strength. A grain sizing of 72.8% H3OF and 27.2% I325F was selected as having the best combination of good cured strength, low curing and thermal testing shrinkage, and good thermal shock resistance. One sample of this composition was subjected to four thermal shock cycles without any apparent degradation. Compositions of even coarser grain size were of little interest because of the intended use of the dense compositions as surface coatings.

A composition of 80% H9OF and 20% I325F looked very promising but was not as thermal shock resistant as, and had higher shrinkage than, the mixture containing H3OF. Some investigation was also made of three-component systems (H3OF, H9OF, plus I325F) but the preliminary work did not reveal sufficient advantages over the two component systems to warrant further study of the more complex system.

Substitution of calcined -325 mesh, partially stabilized zirconia for the fused I325F material in the 72.8% H3OF, 27.2% I325F composition (Kasil 88 bonded) resulted in a somewhat better cured strength but less thermal shock resistance (greater cracking due probably to a shrinkage increase). For the same case, substitution of calcined -325 mesh fully stabilized or unstabilized zirconia yielded similar results, with the substitution of unstabilized zirconia yielding much less shock resistance.

(b) Bonding Agent - Phosphoric acid and silicates (see Table XIX) were added in amounts from one to seven percent to the standard zirconia mix (72.8% H3OF, 27.2% I325F) to determine the superior bonding agent, and to determine the minimum quantity of binder required for good cured strength. It was desired to use the minimum quantity in order to obtain a composition of maximum refractoriness.

Quantities of H₃PO₄ greater than approximately 2.2 g per 100 g of zirconia yielded surface blistering during thermal test and quantities less than this gave inadequate cured strength. One sample (2 inches x 2 inches x 1 inch) utilizing 2.2 g H₃PO₄ binder per 100 g zirconia successfully survived three thermal shock tests, with the only damage being some slight surface blistering.

The minimum amount of liquid silicate that could be used was 5 g per 100 g zirconia. In the case of the powdered silicates, the amount was 5.4 g per 100 g zirconia. Liquid colloidal zirconia was utilized with the powdered silicates rather than water, and seemed to improve the bond strength. Of the liquid silicates utilized, the "K" variety yielded the best bond strength and the Metso Granular material was the best of the powdered silicates. Compositions utilizing these two bonding agents had crushing strengths on the order of 8000 and 6000 psi, respectively, while the other silicates

yielded compositions with strengths of about 1000 to 2000 psi. These systems had adequate refractoriness with some slight surface change occurring during thermal shock testing to 4000°F. Potassium silicate bonded systems were somewhat more refractory but of lower bond strength.

(c) Setting Agent - As mentioned in the section on laboratory procedure, problems with bond migration during curing were encountered which were related to composition consistency. Correcting the consistency, however, did not entirely eliminate the problem with the silicates, which have a natural tendency to migrate to the exposed, drying surface. The setting agents listed in Table XIX (except the zircon) were added in amounts of 0, 0.2, 0.3, 0.4, 0.6, 1.0, and 1.5 g to the 100 g batches of the standard zirconia mix which was bonded with 5 g of one of the liquid silicates listed in Table XIX. The glycerol diacetate was added in an amount equivalent to 90% of the alkali content of a particular silicate, and the ethyl acetate was added in the amount of 1.2 cc per cc of liquid silicate. Colloidal zirconia acted as a setting agent and bonding agent with the powdered silicates, and bond migration was not a major problem with this system. Adding the setting agent to the dry zirconia mix, to the silicate binder, and to the water were each tried to determine if one method displayed advantages over the other. No apparent difference was discovered so it was decided to add the setting agent to the dry zirconia mix as this was the simplest and most straightforward method.

In general, the K_3PO_4 seemed to work best as a setting agent with the potassium silicates, and the Na_2SiF_6 worked best with the sodium silicates.

In the previous section, it was mentioned that sodium silicate "K" was selected as the bonding agent. It was determined that 0.4 g Na_2SiF_6 per 5 g of "K" silicate gave the best results with respect to minimum bond migration, adequate pot life, and good cured strength. Setting agent contents greater or less than this resulted in lower strength and increased bond migration.

A Vicat type apparatus (see ASTM C187-58) was utilized to obtain relative measurements of setting time and composition consistency. This apparatus consists of a weighted plunger which penetrates a sample. Holding mixing and fabrication time constant, the amount of penetration at zero time after mixing yields a measure of consistency, and the amount of penetration versus time after fabrication yields a measure of setting time.

Using 0.4 g Na_2SiF_6 setting per 5 g sodium silicate "K," initial setting at room temperature took place in approximately 30 minutes, and a part could be sufficiently set within less than four hours so that it could be removed from a mold. As expected, setting time was greatly influenced by consistency (moisture content) - a wet mix taking considerably longer to set than a drier one. However, at the same setting agent content, the time versus penetration curves for a variety of consistencies would converge at some time period and become the same curve. Therefore, a wetter mix could be utilized to extend the pot life during mixing and still achieve the same working consistency as a drier mix by delaying start of fabrication until the wetter mix attained the desired consistency.

Preliminary work indicated it might be possible to decrease or eliminate the setting agent by use of special drying and curing techniques such as infrared heating and/or humidity controlled drying and curing. Some samples were prepared using these techniques and these samples appeared to be very strong and displayed very little apparent bond migration. However, on breaking these samples, it was discovered they were very weak on the inside while having a strong "skin." This work was not pursued further.

The fact that H_3PO_4 bonded systems did not set until about 400 or 500°F was considered in some cases to be a disadvantage. It was found that setting could be promoted at lower temperatures by adding zircon (see Table XIX) to the composition in an amount equal to the amount of H_3PO_4 used.

(d) Curing Cycle - Curing cycles were determined for the dense zirconia systems in the manner mentioned in the laboratory procedure section. For silicate bonded systems, this cycle consisted of overnight at ambient conditions, 24 hours at 150°F, 2 hours at 200°F, and 2 hours at 300°F. For H_3PO_4 bonded systems, the cycle was the same except an additional 2 hours at 500°F was used. Time at temperature was variable depending on sample cross-section, but the times presented were normally utilized. Curing temperatures as high as 1000°F did not appreciably increase the strength over the 300 and 500°F curing temperatures.

4.4.4.2 Alumina - The knowledge and techniques acquired in working with zirconia were utilized in the alumina work.

(a) Grain Size - Utilizing a composition of 4 g H_3PO_4 , 100 g of 100F alumina, plus water as required, substitutions were made in 10 g increments of 900F or 500F alumina for the 100F alumina. The two most promising compositions were 50 g 100F, 50 g 500F (crushing strength ~7600 psi) and 60 g 100F, 40 g 900F (crushing strength ~5500 psi). Both compositions displayed good cured strength and thermal shock resistance, with the coarser composition having somewhat better thermal shock resistance and lower shrinkage after curing and thermal shock test.

(b) Bonding Agent - Phosphoric acid, liquid sodium silicate type "K," Metso Granular powdered sodium silicate plus colloidal zirconia, and CA-25 calcium aluminate cement were investigated as bonding agents with the 50 g 100F, 50 g 500F alumina composition.

The H_3PO_4 and "K" silicate were found to give the best cured strengths of the bonds tried. Four grams of H_3PO_4 per 100 g alumina and 10 g of "K" silicate (with 0.6 g Na_2SiF_6 setting agent) per 100 g alumina were determined to be the minimum quantities that could be used. Quantities of the Metso Granular (using colloidal zirconia as the liquid instead of water) as high as 15 g per 100 g alumina did not give as good a cured strength as the "K" silicate or the H_3PO_4 . The CA-25 was added at the expense of the 500F alumina in quantities up to 30% of the total mix but did not give as good results as the "K" silicate or H_3PO_4 .

(c) Setting Agent - Instead of 0.4 g Na_2SiF_6 per 5 g "K" silicate as used with bonding zirconia, it was determined that 0.3 g Na_2SiF_6 per 5 g "K" silicate worked best when bonding alumina.

(d) Curing Cycle - Curing cycles determined for zirconia were also utilized here.

4.4.4.3 Thoria - Experience gained with zirconia and alumina was applied to the thoria investigation.

(a) Grain Size - A composition of 4 g H_3PO_4 , 100 g of 100F thoria, and water as required, was used for grain size studies. Substitutions were made in 10 g increments of 325F or 900F thoria for the 100F thoria down to a 50:50 mixture. A composition of 70 g 100F and 30 g 325F was found to have the best combination of properties; i.e., good cured strength (crushing strength ~8000 psi), low shrinkage, and good thermal shock resistance.

(b) Bonding Agent - The grain sizing of 70 g 100F and 30 g 325F thoria was used in the bonding agent studies. Thorium nitrate, Metso Granular (plus colloidal zirconia), sodium silicate "K," and phosphoric acid were the bonding agents used. The use of thorium nitrate as a bond was suggested by the Solar Aircraft work (Reference 3). At phosphoric acid contents of 4 g or greater per 100 g thoria, problems were encountered with bloating during thermal shock testing and even to some extent during curing. The bloating during curing was alleviated by using a H_3PO_4 content of 2 g but some slight surface bloating still occurred during thermal shock testing. Using 2 g H_3PO_4 , the cured crushing strength was ~4500 psi versus ~8000 psi for the 4 g content.

Thorium nitrate was tried in amounts of 5, 7.5, and 10 g per 100 g thoria, and the 5 g content yielded the best cured strength. During curing, the decomposition of the nitrate tended to leave a porous structure. Careful curing procedures were required to control this decomposition to keep from completely disrupting the sample. The thorium nitrate bond was not as strong as the H_3PO_4 (2 g content) bond but did have the advantage of not decreasing refractoriness.

The Metso Granular (plus colloidal zirconia) binder used at 5 g and 7.5 g per 100 g thoria was not as strong as the nitrate bond. Greater quantities were avoided because of refractoriness problems.

Sodium silicate "K" was tried at various contents and 5 g (plus 0.3 g Na_2SiF_6 setting agent) per 100 g thoria was found to be the minimum amount to give an adequate cured strength. The cured crushing strength was ~6500 psi. This composition was selected as the best of those tried as it gave good cured strength, low shrinkage, adequate refractoriness, and good thermal shock resistance. It was not possible to thermal test this composition to the expected use temperature of 5000°F, and as there was some question as to refractoriness at this temperature, it was attempted to heat a 1 inch x 1 inch x 1/2 inch thick sample as high as possible by heating one corner with a small oxyacetylene cutting torch with a concentrated tip. A temperature of 4600°F was achieved, and no detectable surface change was observed.

(c) Setting Agent - As with the alumina, it was determined that 0.3 g Na_2SiF_6 setting agent per 5 g silicate "K" gave the best results with thoria.

Zircon was tried as a setting agent with H_3PO_4 in amounts equal to the H_3PO_4 content. This promoted low temperature setting and decreased bloating during curing and thermal shock testing. However, the samples containing zircon displayed poorer thermal shock resistance.

(d) Curing Cycle - The curing cycles determined for H_3PO_4 and silicate bonded zirconia were also used for the thoria. The curing cycle used for the nitrate bonded thoria consisted of the silicate cycle up to $300^\circ F$, and then 6 hours at $450^\circ F$, 6 hours at $500^\circ F$, and 2 hours at $1000^\circ F$.

4.4.4.4 High Density Surface Coatings - In addition to providing knowledge about chemically bonded ceramics, the work with high density systems yielded compositions for use as surface coatings to densify the surface of porous, low density ceramics. The compositions selected for the surfacing investigation are listed in Table XX.

These compositions were applied on the 2 inch face of 2 inch x 2 inch x 1 inch thick samples of low density zirconia, alumina, or thoria as appropriate, in thickness from 0.01 to 0.12 inch. As shown in Figure 57, the thicker coatings were pre-scored (before curing) to permit controlled cracking during thermal shock testing. To eliminate coating cracking during high temperature exposure, it was necessary to keep the surface coating as thin as possible, normally on the order of 0.02 inch or less. To obtain best coating adherence, it was necessary to pre-wet the low density ceramic with water.

The coatings were qualitatively compared as to ease of application, adherence, shrinkage and crackage during curing, cured strength, and thermal shock resistance. This comparison led to the selection of zirconia composition No. 3, alumina composition No. 2, and thoria composition No. 1. In the H_3PO_4 bonded systems, the H_3PO_4 appeared to migrate to the substrate during drying, leaving the surface coating weakened. The silicate bonded systems set during room temperature drying.

Phosphoric acid did work well in bonding a Cr_2O_3 coating which was brushed on alumina ceramics to increase the emissivity. This composition consisted of 100 g 325M Cr_2O_3 , 4 g H_3PO_4 , and 220 g water. When coating a high density impervious alumina, it was found best to first coat the alumina with H_3PO_4 , leave the acid on for about two minutes, wash, and then paint with a thin coating of Cr_2O_3 .

The surface coatings were cured using the cycles mentioned in the previous sections.

4.4.5 Low Density Compositions

4.4.5.1 Zirconia - The techniques investigated for attaining low density in chemically bonded zirconia compositions were chemical foaming, mechanical foaming, burn-out, low density aggregate (bubble zirconia), and a combination of bubble zirconia - burn-out. This work paralleled the chemical bonding studies to a certain extent, so some of the compositions and curing procedures utilized in the early low density work were not the better ones that evolved later in the chemical bonding study.

TABLE XX - HIGH DENSITY CHEMICALLY BONDED SURFACE COATINGS

ZIRCONIA

<p>① 72.8 g H30F 27.2 g I325F 2 g H₃PO₄ 6 g H₂O</p>	<p>② 72.8 g H30F 27.2 g I325F 5.0 g Na₂SiO₃ "K" 0.4 g Na₂SiF₆ 3g H₂O</p>	<p>③ 72.8 g H30F 27.2 g I325F 5.4 g Metso Granular 7 g Colloidal Zirconia</p>
<p>④ 80 g H90F 20 g I325F 5.4 g Metso Granular 10 g Colloidal Zirconia</p>	<p>⑤ 80 g H90F 20 g I325F 5 g Na₂SiO₃ "K" 0.4 g Na₂SiF₆ 8 g H₂O</p>	

ALUMINA

<p>① 50 g 100F 50 g 500F 2 g H₃PO₄ 20 g H₂O</p>	<p>② 50 g 100F 50 g 500F 10 g Na₂SiO₃ "K" 0.6 Na₂SiF₆ 10 g H₂O</p>	<p>③ 50 g 100F 50 g 500F 10 g Metso Granular 20 g Colloidal Zirconia</p>
<p>④ 60 g 100F 40 g 900F 2 g H₂PO₄ 25 g H₂O</p>	<p>⑤ 60 g 100F 40 g 900F 10 g Na₂SiO₃ "K" 0.6 g Na₂SiF₆ 13 g H₂O</p>	

THORIA

<p>① 70 g 100F 30 g 325F 5 g Na₂SiO₂ "K" 0.3g Na₂SiF₆ 5 g H₂O</p>	<p>② 70 g 100F 30 g 325F 5 g Th(NO₃)₄·4H₂O 10 g H₂O</p>	<p>③ 70 g 100F 30 g 325F 5 g Metso Granular 10 g Colloidal Zirconia</p>
--	---	---

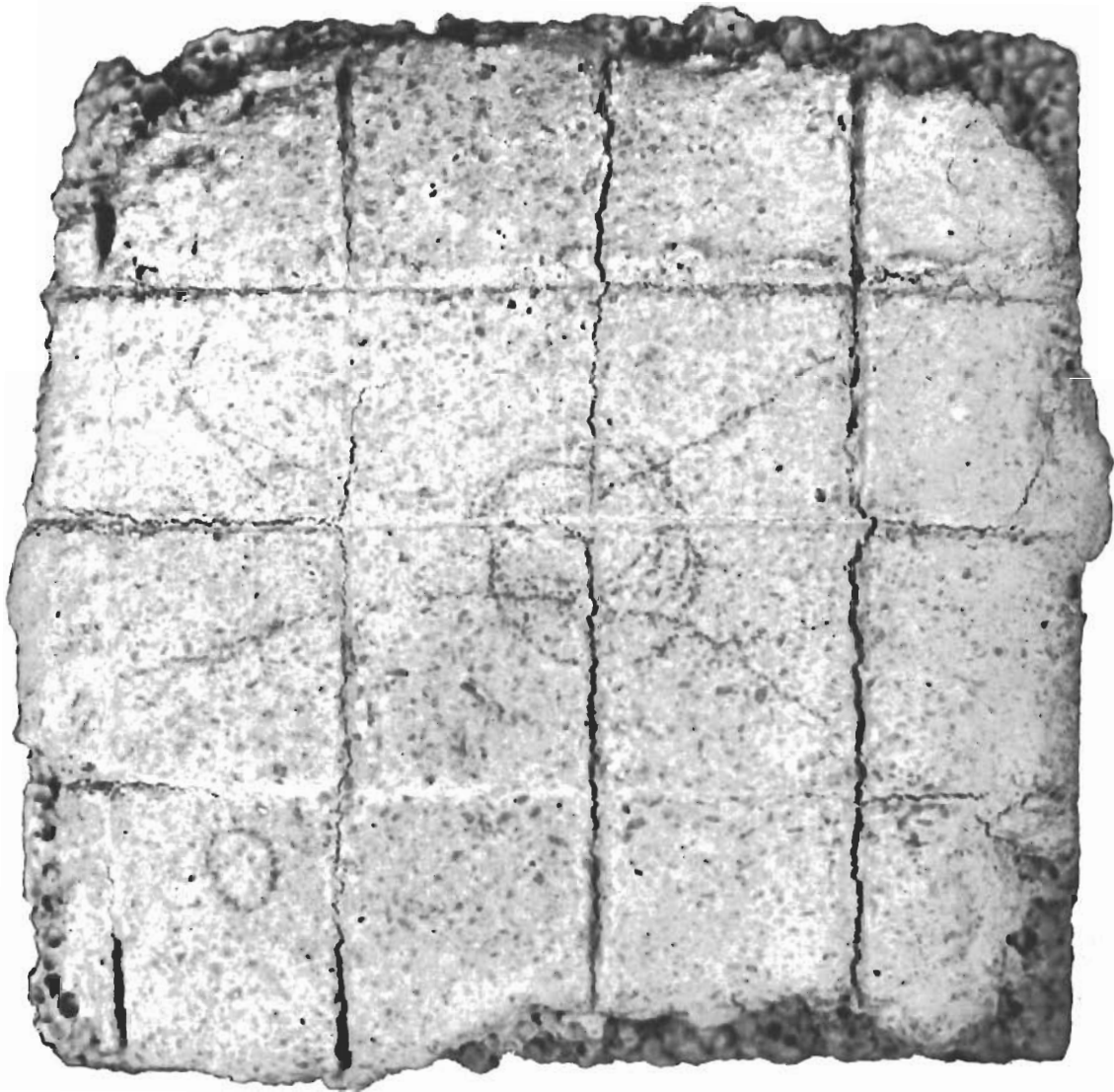


FIGURE 57 - LOW DENSITY SINTERED ZrO_2 WITH CHEMICALLY BONDED, DENSE ZrO_2 SURFACE, AFTER THERMAL SHOCK TEST

(a) Chemical Foam - Because past experience in chemical foaming had displayed control difficulties, only a minor additional effort was expended. A typical composition was 71 g H3OF, 29 g H9OF, 4.8 g H3PO4, 4.8 g zircon, 0.1 g aluminum powder, and 10.7 g of a 3% methyl cellulose solution.

This composition had a density of 155 lb/ft³, low cured strength, fair after-torch-test strength, and fair thermal shock resistance. An increase in acid or aluminum content resulted in decreased density, refractoriness, and shock resistance. The porosity in most of these compositions was fairly large and non-uniform. To slow down the chemical action, use of an acid inhibitor was tried but little improvement in body properties were obtained. This method of attaining low density was dropped early in the program because of the mentioned difficulties.

(b) Mechanical Foam - The foaming agent utilized in preparing mechanical foams was Mearl SW2336 and the bonding agent was a silicate. It was found best to use a viscous liquid in order to produce a stable foam, and aqueous solutions of 1.3% Burtonite V-7-E or 3% methyl cellulose (400 cps) were used for this purpose. Foam density was found to be dependent on solids-to-liquid ratio, with an increase in liquid content resulting in a decrease in density, and an increase in shrinkage during curing and after torch test. Fine grained zirconia (I325F) was used in most of these foams as the fine materials were most readily suspended and foamed. Preliminary work with substitution of coarse grained zirconia (H9OF or H3OF) for the I325F material indicated an increase in foam density and shock resistance, and a decrease in cured strength and shrinkage after torch test. The total shrinkage in fine grained bodies was approximately 10%.

In general, all the mechanical foams at densities of less than 120 lb/ft³ had very poor cured strength. Perhaps 1000°F was too low a curing temperature or the foaming agent and organic-water solution diluted or weakened the chemical bond. The porosity in the mechanical foams was of small pore size and quite uniform.

A typical mechanical foam composition with a density of 100 lb/ft³ which had poor cured strength, good strength after torch test, and fair thermal shock resistance consisted of 100 g I325F zirconia, 8.1 g Kasil 88, 0.9 g Mearl SW2336, 12.8 g of a 1.3% aqueous solution of Burtonite V-7-E, and 0.9 g Na2SiF6. It will be noted that the binder-to-zirconia ratio was higher than in the high density systems. The binder content was increased in an attempt to increase cured strength. In the intended application, low density materials would be coated with more refractory high density materials so it was felt the slight decrease in refractoriness could be tolerated. As with the chemical foaming, the mechanical foaming approach was dropped early in the project due to control difficulties, lack of versatility, and low cured strengths.

(c) Low Density Aggregate (Bubble Zirconia) - The broken particles were separated from the coarse grained bubble zirconia (I4F or I8F); the resulting material was screened to various mesh size ranges; and the bulk density was determined for these ranges. This was done to select a sizing that might yield a composition with a density close to the desired 120 lb/ft³. Table XXI lists the bulk density for the various aggregate sizings.

TABLE XXI - BULK DENSITY vs. MESH Z SIZE FOR BUBBLE ZIRCONIA

Mesh Size Range	Bulk Density (Lb/Ft ³)
- 8M + 20M	75
-20M + 30M	96
-30M + 50M	110
-50M + 70M	129
-70M + 100M	143
-30M + 100M	119
- 8M + 100M	97

The -8 +20 mesh material was selected for study because of its low density and past experience with this sizing. A series of compositions was prepared in which the ratio of I325F zirconia to -8 +20 mesh bubble zirconia was varied to determine the minimum I325F content which would yield a sample having the voids between bubbles filled. It was necessary to fill the voids to obtain a good cohesive structure, and to minimize the I325F content to keep the density low. The Metso Granular-colloidal zirconia bond was used in these compositions.

A composition of 50 g I325F, 50 g -8 +20 mesh bubble zirconia, 5.8 g Metso Granular, and 5.6 g colloidal zirconia, displayed very good cured strength, but had a density of 150 lb/ft³. Figure 58 shows such a sample after torch test. Although some cracking occurred during thermal shock testing, as shown in Figure 58, the sample was intact and only slightly weakened by the thermal shock testing.

Figure 59 shows a sample (after thermal shock testing) of 130 lb/ft³ density which had a composition of 32 g I325F, 68 g -8 +20 bubble zirconia, 5.8 g Metso Granular, and 5.6 g colloidal zirconia. As can be seen, there was insufficient fine zirconia to fill the voids between the bubble zirconia, which resulted in individual bubbles being weakly attached to the matrix, especially in the as-cured state. This sample did display very good thermal shock resistance.

The 150 lb/ft³ density would have to be considered a minimum attainable density with this type of composition. In general, all of the bubble zirconia compositions studied showed very low drying, curing, and after-torch-test-shrinkage, and good thermal shock resistance. Several 2 inch x 2 inch x 1 inch specimens were thermal shock tested twice with very little detrimental effect. The size of the bubbles used (-8 +20 mesh) probably would yield a body with relatively high thermal conductivity compared to another body of like density and smaller pore size. Low thermal conductivity was desirable to minimize the ceramic thickness required to insulate metal substructure.

(d) Burn-Out - Two types of burn-out material were utilized - acrylic powder which burned out at under 1000°F, and -30 +50 mesh or -50 +100 mesh naphthalene powder which volatilized at less than 200°F. Naphthalene crystals were ground with a mortar and pestle and screened to the desired mesh size.

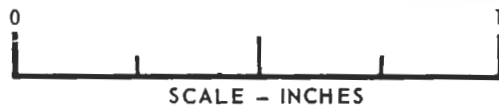
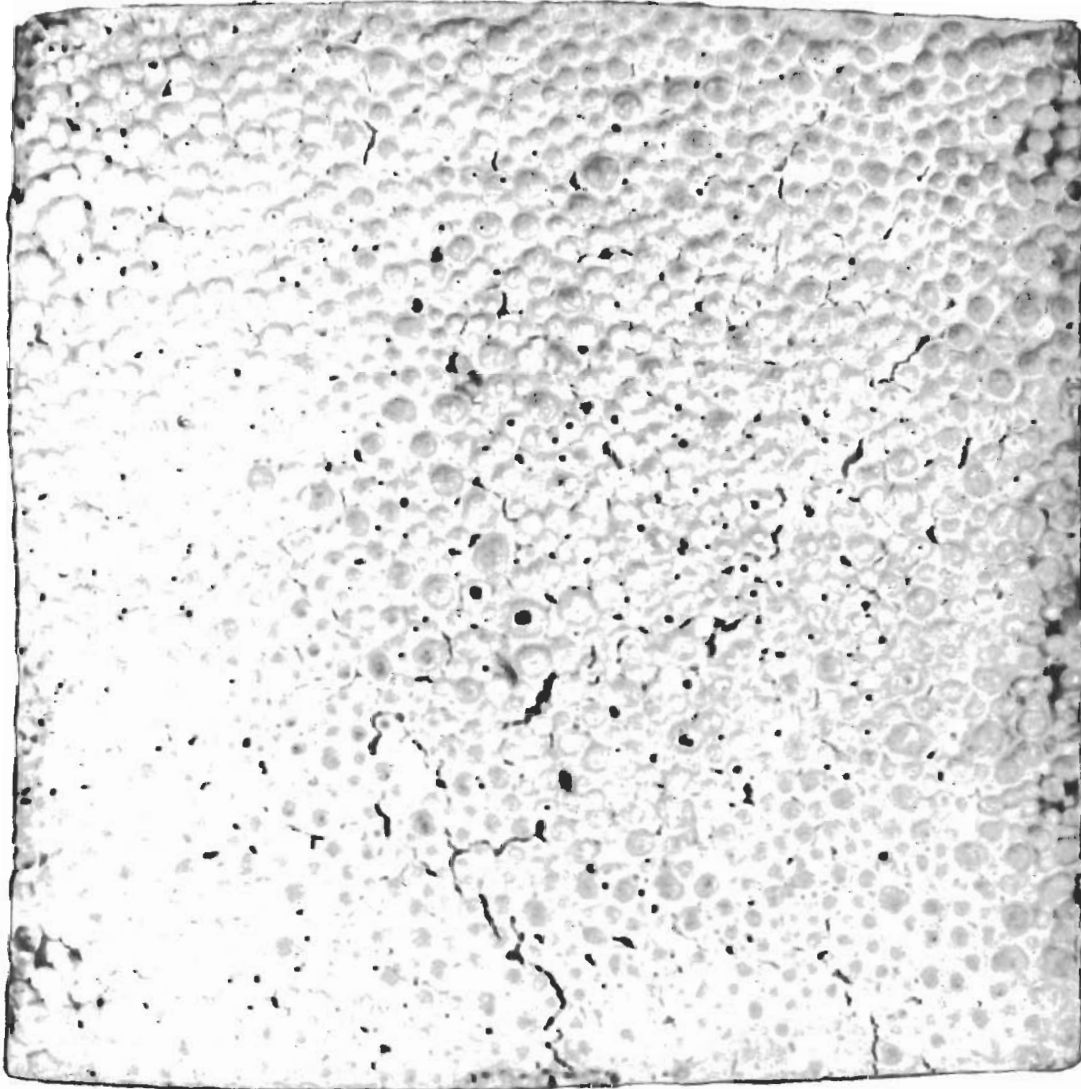


**FIGURE 58 - CHEMICALLY BONDED, BUBBLE ZrO_2
~ 150 LB/FT³) AFTER THERMAL SHOCK TEST**

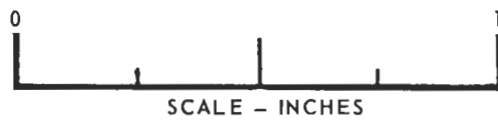
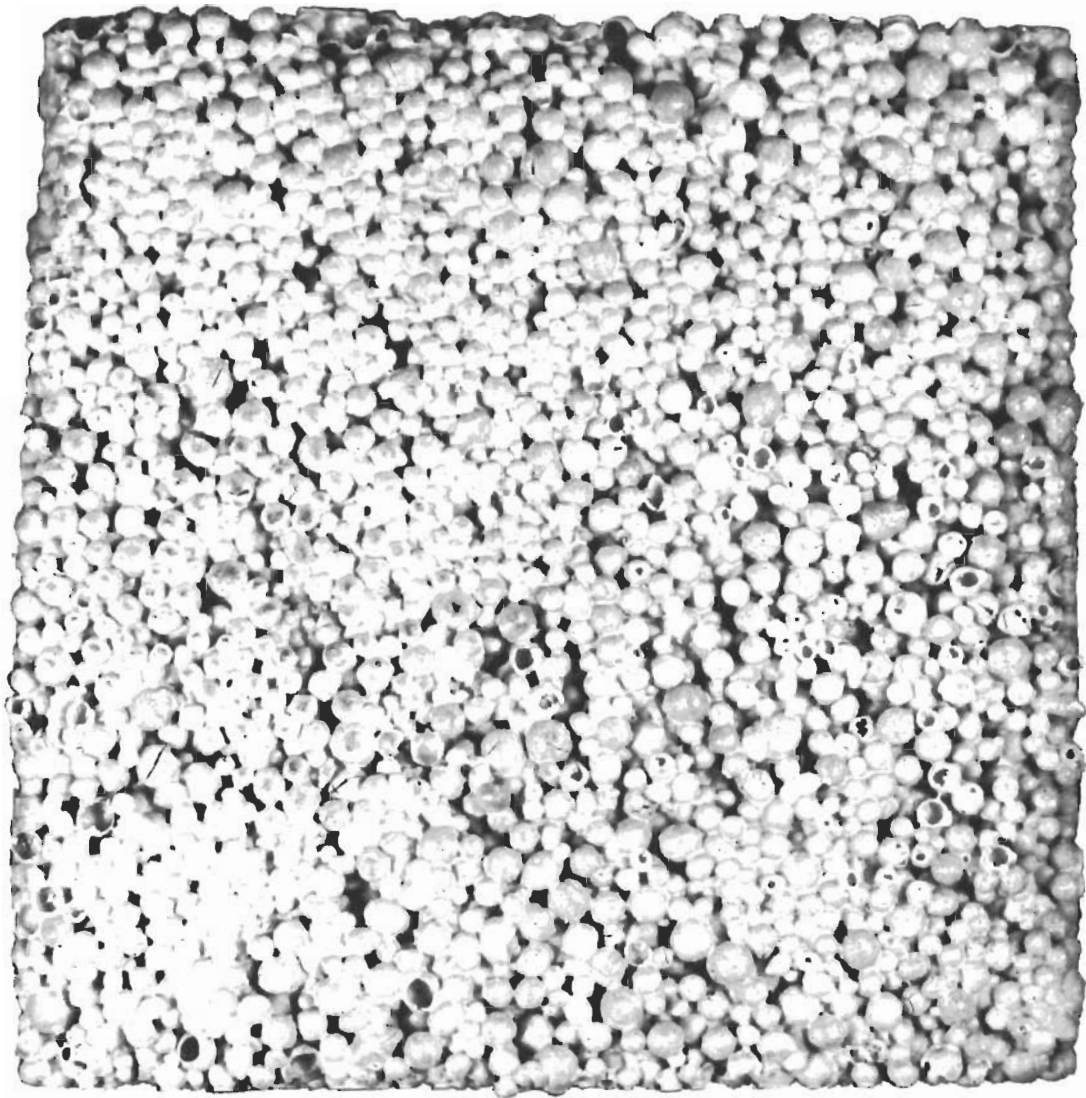


**FIGURE 59 - CHEMICALLY BONDED, BUBBLE ZrO_2
($\rho \sim 130 \text{ LB/FT}^3$) AFTER THERMAL SHOCK TEST**

In the initial work, phosphoric acid, Metso Granular - colloidal zirconia, and Kasil 88 were the bonding agents utilized, with little difference being noted between the three. The phosphoric acid gave poor results with the naphthalene, due apparently to the fact that the naphthalene volatilized before the acid bond set. As with other low density compositions, the ratio of binder to zirconia was increased over that used in high density compositions to increase cured strength.

In an attempt to obtain good cured strength, most of the early work was done with fine grained compositions (I325F). Even so, the cured strength was very low, and these samples had poor thermal shock resistance. Figure 60 shows a fine grained, low density sample after torch testing. This typical sample had a composition of 100 g I325F zirconia, 28.6 g colloidal zirconia, 11.7 g Metso Granular, 51 g acrylic powder, and had an as-cured density of 80 lb/ft³. Much of the cracking was probably related to shrinkage occurring during testing. After torch testing, the heated surface was quite strong, while the back side was still very weak. Figure 61 shows the microstructure and small pore size obtained in this type sample. Higher density compositions (~120 lb/ft³) had better cured strength and better thermal shock resistance.

Using either acrylic powder or naphthalene powder, it was found possible to attain densities as low as 80 lb/ft³, depending on the amount of burn-out used. Both types of burn-out had about the same effect on the cured strength of the low density material.

Considerable difficulty was experienced in determining curing cycles which would remove the burn-out materials without disrupting the ceramic structure. Prior to volatilizing, the acrylic powder softened at some temperature and seemed to undergo a volume expansion. Some of the products of volatilization were apparently combustible, resulting in burning within the sample and/or the curing oven, if volatilization was not carried out at the proper rate. Too rapid a curing cycle did not allow these phenomena to occur slowly enough to prevent disrupting the ceramic structure. Examination of some of the samples showed internal laminations and cracks, apparently caused by the rapid decomposition or physical change of the acrylic.

After several unsuccessful curing cycle trials, fairly satisfactory (not optimum) cycles were determined by checking the weight change of samples during curing. The samples were held at various arbitrary temperatures until a constant weight was attained, indicating no further change occurring at that particular temperature. This work yielded the curing cycles listed below:

(a) Curing cycle for acrylic-containing samples:

Ambient - 18 hours	450°F - 24 hours	650°F - 8 hours
200°F - 5 hours	500°F - 29 hours	800°F - 15 hours
300°F - 2 hours	550°F - 16 hours	1000°F - 73 hours
400°F - 83 hours		

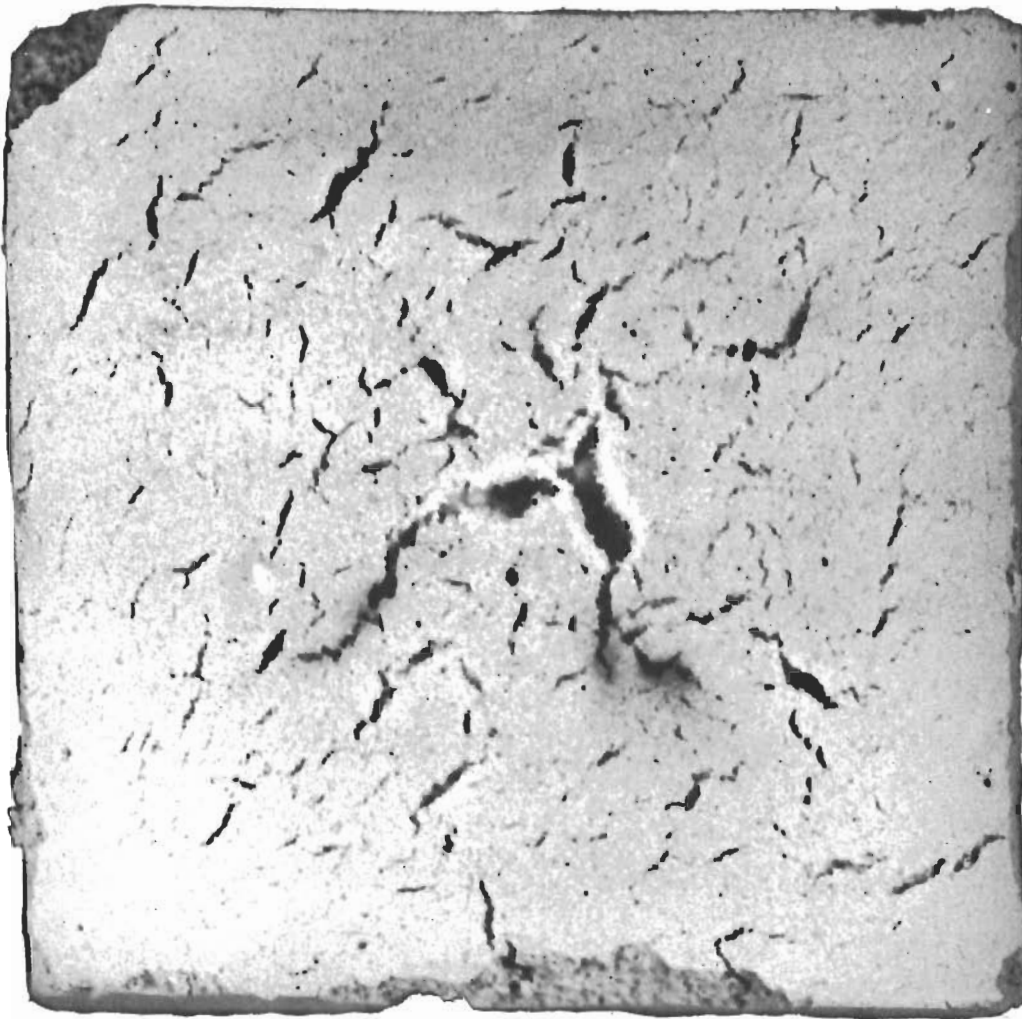
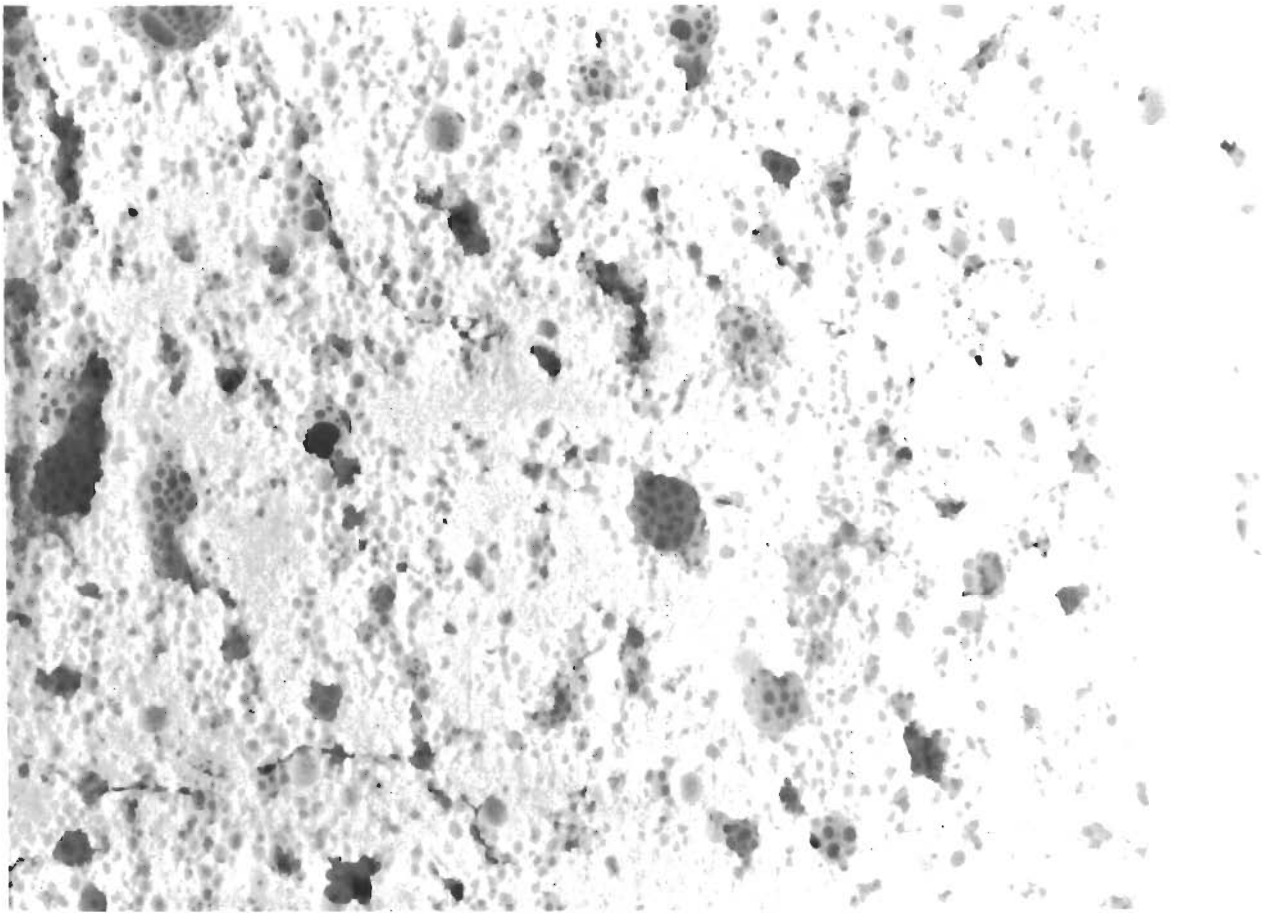


**FIGURE 60 - CHEMICALLY BONDED, LOW DENSITY, BURN-OUT ZrO_2
($\rho \sim 80 \text{ LB/FT}^3$) AFTER THERMAL SHOCK TEST**



MAG - 20X

**FIGURE 61 - CHEMICALLY BONDED, LOW DENSITY, BURN-OUT
ZrO₂ ($\rho \sim 100 \text{ LB/FT}^3$), AFTER THERMAL SHOCK TEST**

(b) Curing cycle for naphthalene-containing samples:

Ambient - 24 hours	150°F - 5 hours	500°F - 1 hour
100°F - 4-1/2 hours	175°F - 91 hours	1000°F - 1 hour
125°F - 22 hours	200°F - 22 hours	

Because little difference was noted in cured strength between specimens containing the two burn-out materials and because the naphthalene was easier to remove, it was decided to drop the efforts with the acrylic and concentrate on the naphthalene. Further work with the naphthalene resulted in the curing cycle below: (Time at temperatures would vary depending on sample cross section, but these times were satisfactory for 2 inch x 2 inch x 1 inch samples).

Ambient - 16 hours (overnight)
150°F - 24 hours
200°F - 72 hours
300°F - 6 hours

It was found that silicate samples cured at 300°F had as good a cured strength as those cured at 1000°F. The previously mentioned difficulties with H₃PO₄ bonded naphthalene containing samples resulted in dropping this bonding agent.

As the work with high density compositions evolved, this knowledge was applied to the burn-out composition studies. It was found that the sodium silicate "K" was the most suitable bonding agent to use with the burn-out composition. Also, the best grain sizing utilized for high density compositions (72.8 g H₃OF, 27.2 g I325F) was found to give the best thermal shock resistance with the burn-out compositions.

Using a composition of 72.8 g H₃OF, 27.2 g I325F, 10 g sodium silicate "K," 0.8 g Na₂SiF₆, and sufficient water for tamping consistency, the content of -30 +50 mesh naphthalene was varied to determine the amount to use to obtain the lowest density compatible with adequate cured strength. It was determined that 35 g of -30 +50 mesh naphthalene was the optimum quantity.

After determining the quantity of burn-out to use, the sodium silicate content was varied to determine the minimum quantity to use and still have adequate cured strength. This amount was found to be 7.6 g sodium silicate "K" (plus 0.6 g Na₂SiF₆) per 100 g of zirconia.

The finally selected composition had a density of 100 lb/ft³ and consisted of 72.8 g H₃OF, 27.2 g I325F, 7.6 g sodium silicate "K," 0.6 g Na₂SiF₆, 35 g -30 +50 mesh naphthalene, and 14 g water. This composition had fair cured strength, good thermal shock resistance, low shrinkage, and adequate refractoriness. Somewhat better cured strength could be achieved by increasing density (decrease in naphthalene content). Figure 62 is a cross-sectional view of this composition after thermal shock testing, and shows the type of porosity achieved in this body.

The use of -50 +100 mesh naphthalene gave a body of lower cured strength than one with -30 +50 mesh naphthalene at the same density level.

(e) Burn-Out - Bubble Zirconia Combination - As both of these individual approaches of decreasing density had shown promise and each had its advantages and limitations, it was decided to combine the two techniques. It was thought the bubbles would potentially allow low density, low shrinkage, and good thermal shock resistance, and the burn-out would permit decreasing the density beyond the lower limit of a straight bubble composition. Potentially, a composition with a density of 120 lb/ft³ or less should be attainable by using a bubble zirconia of such grain size as to have a bulk density of 120 lb/ft³ or less in combination with a fine grained zirconia matrix containing sufficient burn-out material that the bulk density of the matrix would be 120 lb/ft³ or less.

As this work was begun prior to completion of the high density and the burn-out studies, the initial investigations utilized potassium silicate, phosphoric acid, and Metso Granular-colloidal zirconia bonds, and acrylic and naphthalene burn-out. Based on the bubble zirconia studies, the -8 +20 mesh bubbles were utilized in combination with I325F and/or H90F zirconia in a variety of mixtures.

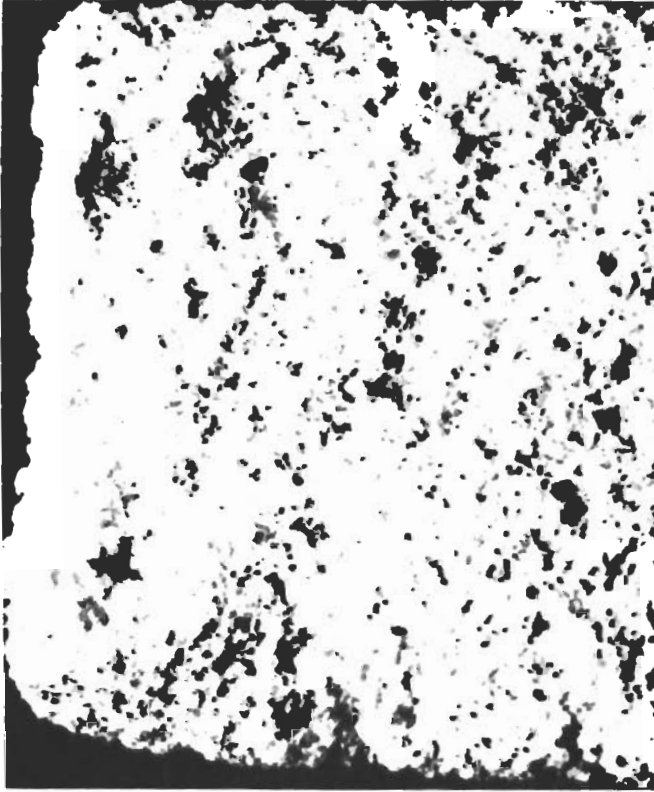


**FIGURE 62 -CHEMICALLY BONDED
BURN-OUT TYPE LOW
DENSITY ZIRCONIA AFTER
THERMAL SHOCK TEST
 $\rho \sim 100 \text{ LB/FT}^3$ (MAG: 3X)**

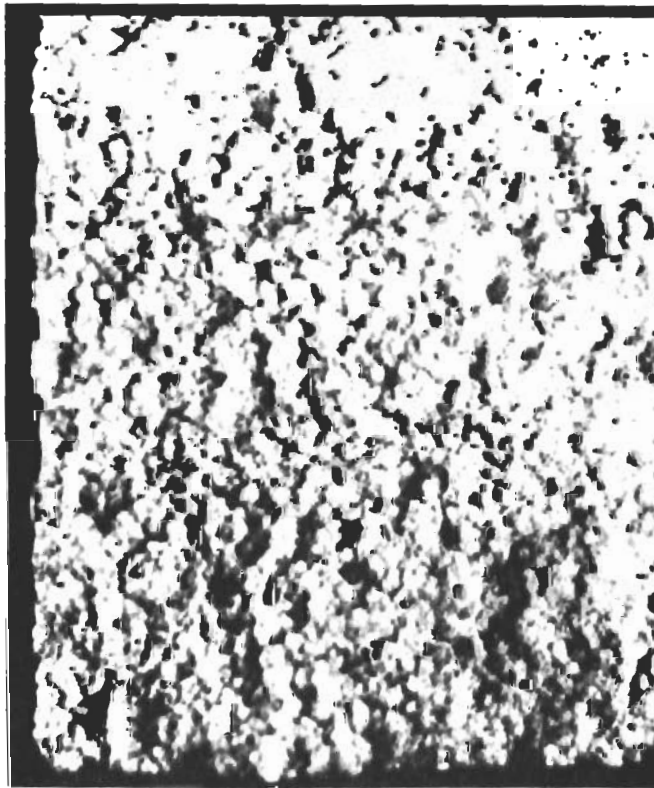


**FIGURE 63 - CHEMICALLY BONDED
BUBBLE-BURN-OUT TYPE
LOW DENSITY ZIRCONIA
AFTER THERMAL SHOCK
TEST
 $\rho \sim 125 \text{ LB/FT}^3$ (MAG:3X)**

A typical composition from these studies consisted of 35 g I325F zirconia, 35 g H90F zirconia, 30 g -8 +20 mesh zirconia bubbles, 11.7 g acrylic powder, 6.6 g Metso Granular, and 10 g colloidal zirconia. This composition had a density of 145 lb/ft³, fair cured strength, good strength after torch test, and good thermal shock resistance. One such sample successfully withstood two thermal cycles (50°F/sec surface heating rate) to 4000°F (10 minutes at 4000°F) without apparent degradation. The density could be decreased by increasing bubbled zirconia or acrylic content but cured strength decreased. However, thermal shock resistance and strength after torch test were still fair down to a density of 100 lb/ft³.

The later burn-out studies led to the use of naphthalene as the burn-out material and sodium silicate "K" plus Na₂SiF₆ as the bonding agent in the burn-out bubble compositions. Similar to the results obtained in the burn-out studies, it was found best to use 7.6 g sodium silicate (plus 0.6 g Na₂SiF₆) per 100 g zirconia and 35 g of -50 +100 mesh naphthalene per 100 g of zirconia in the matrix. The burn-out curing cycle was used for the burn-out bubble compositions.

The -50 +100 mesh naphthalene was used rather than -30 +50 mesh grain in order to yield a smaller pore size in the matrix around the bubbles and thus improve the bonding properties of the matrix. Also, the smaller pore size would tend to decrease thermal conductivity at elevated temperatures. For this same reason, a grain sizing for the bubble zirconia of -30 +100 mesh (bulk density of 119 lb/ft³) was selected over the -8 +20 mesh sizing used in the earlier work.

Both H90F and I325F zirconia were tried singly and in combination as matrix materials with the -30 +100 mesh bubbles. Best cured strength was obtained with the I325F material with no sacrifice in thermal shock resistance. The ratio of I325F to bubble content was varied and the best overall properties were obtained at a ratio of 45 g I325F to 55 g bubbles. The final composition that evolved consisted of 55 g -30 +100 mesh bubbles, 45 g I325F, 7.6 g sodium silicate "k," 0.6 g Na₂SiF₆, 15.8 g -50 +100 mesh naphthalene, and 7.5 g water. This composition had a density of 125 lb/ft³ which was somewhat higher than the 120 lb/ft³ goal, but lower densities (accomplished by an increase in naphthalene content) resulted in an undesired decrease in cured strength. The crushing strength was 600 psi.

Figure 63 is a cross-sectional view of this low density zirconia composition after thermal shock testing, and shows the type of porosity achieved in this class of bodies. The burn-out-bubble bodies had better cured strength, lower curing and firing shrinkage, and better thermal shock resistance than the burn-out bodies of like density.

4.4.5.2 Alumina - Based on the results of the zirconia studies, only two techniques of attaining low density were tried with alumina - burn-out and burn-out-bubble combination. The bonding agent studies with low and high density zirconia and high density alumina formed the basis for the bonding agents used here. Curing cycles used in similar zirconia work were used for the alumina studies.

(a) Burn-Out - Although some preliminary work was done utilizing acrylic and naphthalene burn-outs, and potassium silicates, phosphoric acid, and Metso Granular-colloidal zirconia bonds, most of the investigation was carried out with -30 +50 mesh naphthalene burn-out and sodium silicate "K" (plus Na_2SiF_6) bonding agent. Using this latter combination and the grain sizing determined in the high density alumina study (50 g 500F, 50 g 100F), the naphthalene content was varied to determine the quantity necessary to yield the desired density and cured strength. It was determined that 75 g of naphthalene per 100 g of alumina yielded a density of 55 lb/ft³. Increasing the naphthalene content beyond this yielded lower densities, but at too great a sacrifice in cured strength.

Using a composition of 50 g 500F, 50 g 100F, and 75 g -30 +50 mesh naphthalene, the sodium silicate content was varied to determine minimum quantity for adequate cured strength. It was found necessary to use 10 g sodium silicate "K" (plus 0.6 g Na_2SiF_6) per 100 g of alumina. Higher silicate contents yielded better cured strengths, but questionable refractoriness. The final composition derived was 50 g 500F, 50 g 100F, 75 g -30 +50 mesh naphthalene, 10 g sodium silicate "K," 0.6 g Na_2SiF_6 , and 30 g water. This composition had fair cured strength, low shrinkage and good thermal shock resistance. Some work was done with substitution of 900F for the 500F alumina which did improve cured strength, but increased shrinkage and decreased thermal shock resistance.

(b) Burn-Out-Bubble Alumina - The as-received alumina bubbles were culled to remove broken particles; the resulting material screened to -8 +20 mesh and -30 +72 mesh fractions; and the bulk density of these two fractions determined to be 55 lb/ft³ and 65 lb/ft³, respectively. From these bulk densities, it obviously was not possible to obtain a straight bubble composition at a density level even approaching the 50 lb/ft³ goal.

The -30 +72 mesh fraction of the bubbles was selected for this study because of the smaller pore size and only a slightly higher bulk density than the -8 +20 mesh fraction. As with the burn-out-bubble zirconia composition, -50 +100 mesh naphthalene was the burn-out used. The naphthalene content and bonding agent type and content determined in the burn-out alumina studies were used here. The ratio of -30 +72 mesh bubbles to 500F grain was varied to determine the grain sizing which would give the best overall properties.

This study yielded the following composition: 50 g -30 +72 mesh bubbles, 50 g 500F, 37.5 g -50 +100 mesh naphthalene, 10 g sodium silicate "K," 0.6 g Na_2SiF_6 , and 14 g water. This composition had lower shrinkage and better thermal shock resistance than the straight burn-out composition and had a density of 65 lb/ft³. The cured strength was low even at this density level so it was considered impractical to further reduce density.

This composition was developed consistent with the time schedule of the first phase of the subscale module program (see Section 5.2). A composition of improved cured strength was developed later by increasing the sodium silicate "K" content to 15 g (plus 0.9 g Na_2SiF_6) per 100 g of alumina. The density of this composition was 65 lb/ft³ and crushing strength was 200 psi.

As the increased silicate content made the refractoriness questionable, a reinforced castable alumina subscale module (see Figure 106) was remade and subjected to the 3.0 inch radius leading edge thermal environment. It can be seen in Figure 64 that the module successfully survived the thermal test with no melting or severe cracking.

Crushing strength was increased to 475 psi by grain sizing and naphthalene content changes. This composition consisted of 70 g -30 +72 mesh bubbles, 30 g 900F, 30 g -50 +100 mesh naphthalene, 15 g sodium silicate "K," 0.9 g Na_2SiF_6 , and 12.8 g water and had a density of 65 lb/ft³. The overall properties of this composition were good.

4.4.5.3 Thoria - There was no bubble thoria or low density aggregate thoria available, so only the burn-out technique was used. Based on the zirconia and alumina studies, the -30 +50 mesh naphthalene burn-out was used. Sodium silicate "K" (plus Na_2SiF_6) and thorium nitrate were investigated as bonding agents, and better cured strengths were obtained with the former. The curing cycles were identical to that developed for the burn-out zirconia except for the nitrate bond which was cured an additional 6 hours at 450°F and 6 hours at 500°F. The silicate content was not increased beyond 5 g per 100 g thoria because of the intended 5000°F use temperature and the possible refractoriness problem. The same grain size as evolved in the high density thoria studies was utilized; (70 g 100F and 30 g 325F). Finer grain sizes had better cured strength, but higher shrinkage and poorer thermal shock resistance.

A basic composition of 70 g 100F, 30 g 325F, 5 g sodium silicate "K" and 0.3 g Na_2SiF_6 was used and the naphthalene content was varied to obtain the lowest possible density compatible with good cured strength. This resulted in a composition of 70 g 100F, 30 g 325F, 5 g sodium silicate "K," 0.3 Na_2SiF_6 , 15 g -30 +50 mesh naphthalene, and 6.9 g water which had a density of 200 lb/ft³, good cured strength, low shrinkage, and good thermal shock resistance.

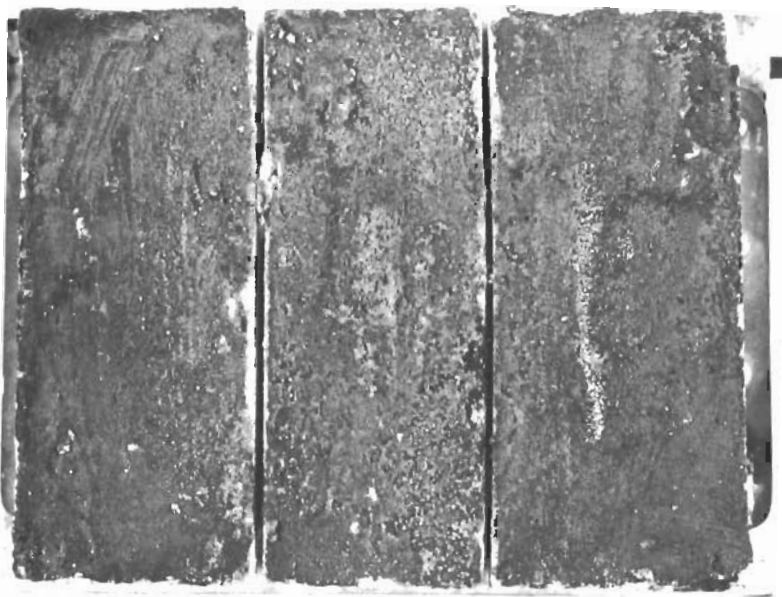
4.4.6 Summary of Chemically Bonded Compositions

Table XXII presents the better compositions developed in this portion of the project, and indicates the utilization of these materials. In general, the materials met the arbitrary goals originally set forth, but in certain cases some property compromises had to be made, especially with respect to density. These compositions had adequate pot life, suitable working properties, satisfactory cured strength, low shrinkage after heating (less than 4% total), good thermal shock resistance, and sufficient refractoriness. Most of the compositions were developed within the six month time limitation to permit utilization in the subscale program, but some composition improvements came after this time period.

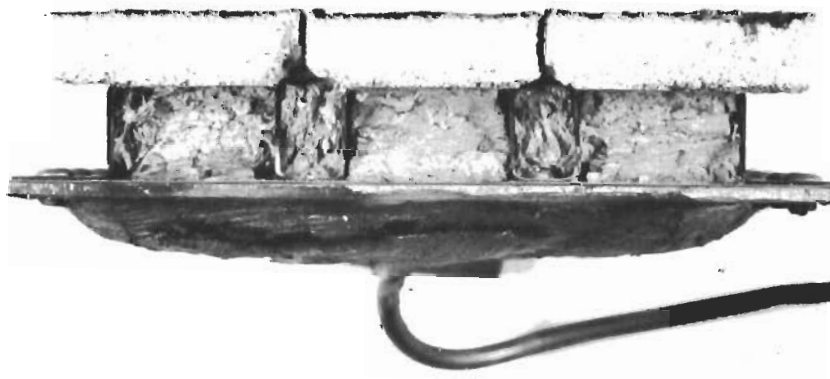
Samples of the better compositions (IA-2, LZ-1, DZ-1, LT-1, DT-1, DC-1) were sent to Southern Research Institute for measurement of thermophysical properties. The sample sizes sent were 2-5/8 inches diameter x 3-3/8 inches long; 5/8 inch diameter x 1/4 inch long; 4 inches long x 3-1/2 inches x 3-1/2 inches; and 1-1/4 inches diameter x 3-1/4 inches long. These samples were fabricated in wood molds as shown in Figure 65. Southern Research Institute (SRI) machined specimens of appropriate sizes from these samples.



(a) BEFORE TEST



(b) AFTER TEST, TOP VIEW



(c) AFTER TEST, SIDE VIEW

FIGURE 64 - REINFORCED CASTABLE Al_2O_3 SUBSCALE, AFTER THERMAL TEST

TABLE XXII - CHEMICALLY BONDED CERAMICS

Type, Number, and Consistency	Composition (Parts by Weight)	Subscale Application	Full Scale Application	Curing Cycle*	Density (lb/ft ³)	Crushing Strength (psi)
High density Al ₂ O ₃ DA-1 Tamping	50 500F Al ₂ O ₃ 50 100F Al ₂ O ₃ 0.6 Na ₂ SiF ₆ 10 Na ₂ SiO ₃ "K" 7.5 H ₂ O	Figures 109, 111, 113	Potting bolt heads in 3.0" R leading edge	A	150	8950
High density Al ₂ O ₃ DA-2 Troweling	50 500F Al ₂ O ₃ 50 100F Al ₂ O ₃ 0.6 Na ₂ SiF ₆ 10 Na ₂ SiO ₃ "K" 10 H ₂ O	Figures 103, 104, 106, 109, 111, 113	Surface coating on 3.0" R leading edge	A	150	---
Low density Al ₂ O ₃ LA-1 Tamping	50 -30+72 bubble Al ₂ O ₃ 50 500F Al ₂ O ₃ 0.6 Na ₂ SiF ₆ 10 Na ₂ SiO ₃ "K" 37.5 -50+100 naphthalene 14 H ₂ O	Figures 103,104, 106	---	B	65	125
Low density Al ₂ O ₃ LA-2 Tamping	50 -30+72 bubble Al ₂ O ₃ 50 500F Al ₂ O ₃ 0.9 Na ₂ SiF ₆ 15 Na ₂ SiO ₃ "K" 37.5 -50+100 naphthalene 9 H ₂ O	Figure 64	---	B	65	200
Low density Al ₂ O ₃ LA-3 Tamping	70 -30+72 bubble Al ₂ O ₃ 30 900F Al ₂ O ₃ 0.9 Na ₂ SiF ₆ 15 Na ₂ SiO ₃ "K" 30 -50+100 naphthalene 12.8 H ₂ O	---	---	B	65	475
High density Cr ₂ O ₃ DC-1 Brushing	100 -325 Cr ₂ O ₃ 4 H ₃ PO ₄ 220 H ₂ O	Figures 103,104,106, 109,111,113, 115,118	Surface coating on 3.0" R leading edge	C	---	---
High density ZrO ₂ DZ-1 Troweling	72.8 H30F ZrO ₂ 27.2 I325F ZrO ₂ 5.4 Matsa-Granular Na ₂ SiO ₃ 7 Colloidal ZrO ₂	Figures 120, 123, 125, 127, 129, 131	Surface coating on 1.5" R leading edge and on ZrO ₂ blocks on 6.0" R nose cap	A	230	8140
Low density ZrO ₂ LZ-1 Tamping	55 -30+100 bubble ZrO ₂ 45 I325F ZrO ₂ 0.6 Na ₂ SiF ₆ 7.6 Na ₂ SiO ₃ "K" 15.8 -50+100 naphthalene 7.5 H ₂ O	Figures 120, 123, 125, 127, 129, 131, 142, 144, 147, 157	Potting bolt heads on 1.5" R leading edge and on 6.0" R nose cap. Potting ZrO ₂ tubes on 6.0" R nose cap	B	125	600
High density ThO ₂ DT-1 Troweling	70 100F ThO ₂ 30 325F ThO ₂ 0.3 Na ₂ SiF ₆ 5 Na ₂ SiO ₃ "K" 5 H ₂ O	Figures 142, 144, 147, 149, 151, 157	Surface coating on 6.0" R nose cap	A	390	6575
Low density ThO ₂ LT-1 Tamping	70 100F ThO ₂ 30 325F ThO ₂ 0.3 Na ₂ SiF ₆ 5 Na ₂ SiO ₃ "K" 15 -30+50 naphthalene 6.9 H ₂ O	Figures 142, 144, 147, 149, 157	Potting ThO ₂ tubes on 6.0" R nose cap	B	200	300

*Curing cycles

(A) Ambient 16 hrs (overnight)
150°F 24 hrs
200°F 2 hrs
300°F 2 hrs

(B) Ambient 16 hrs (overnight)
150°F 24 hrs
200°F 72 hrs
300°F 6 hrs

(C) Ambient 16 hrs (overnight)
150°F 24 hrs
200°F 2 hrs
300°F 2 hrs
500°F 2 hrs

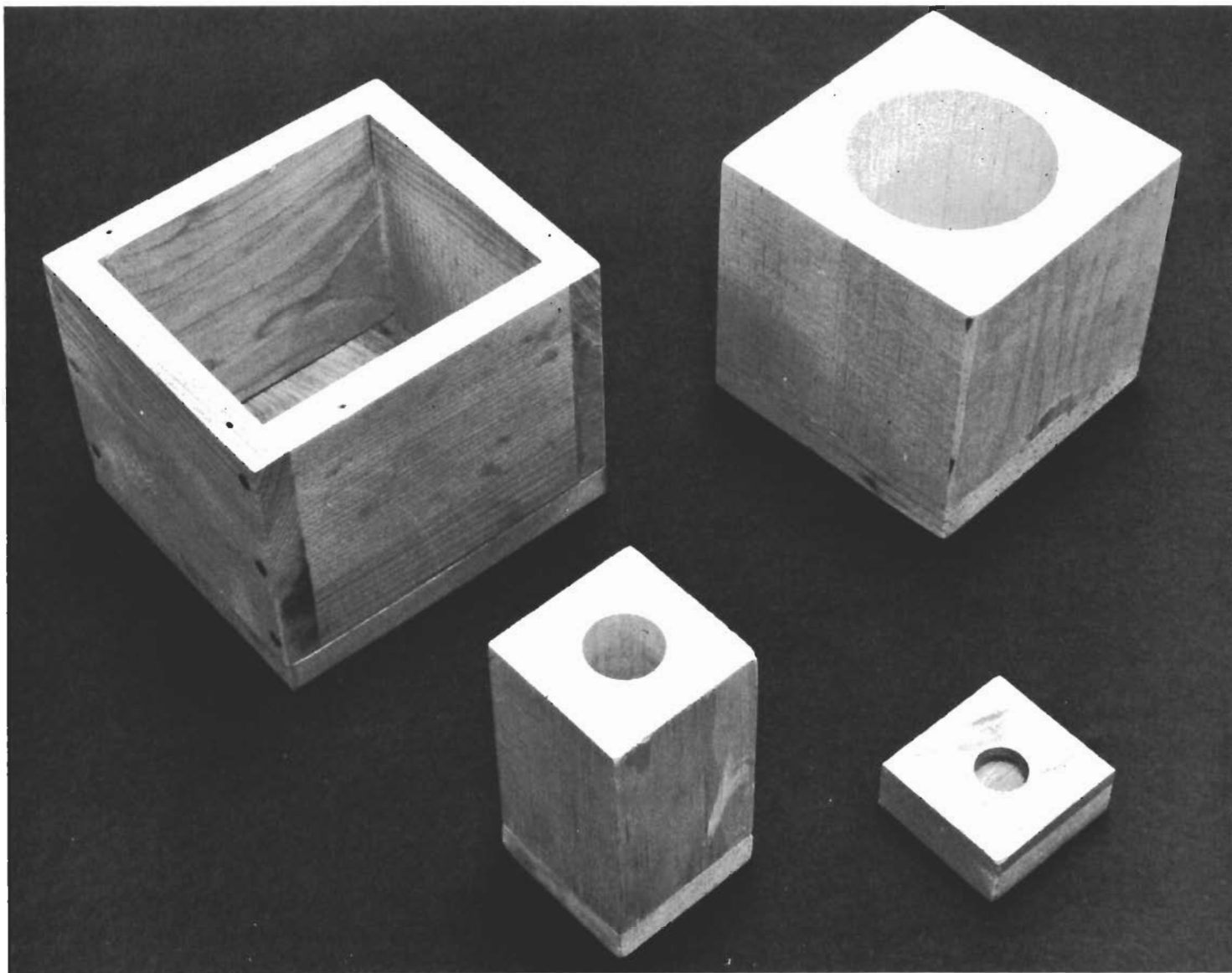


**FIGURE 65 - WOODEN MOLDS FOR MATERIAL PROPERTIES
DETERMINATION SAMPLES**

4.5 DETERMINATION OF MATERIAL PROPERTIES

The thermophysical properties of the ceramic materials utilized in the subscale and full scale components were required for design and for structural and thermal analyses. The major properties necessary were thermal conductivity, heat capacity, total normal emittance, thermal expansion, and modulus of rupture. Depending on the material, data were needed to temperatures of 3400°^o, 4000°^o, and 5000°^oF and in some cases at reduced pressures.

Scheduling requirements dictated the selection of a subcontractor experienced in, and equipped to perform, the measurement of the thermophysical properties of ceramics. Southern Research Institute (SRI) of Birmingham, Alabama, was selected as the subcontractor. Table XXIII lists the properties measured for various materials.

SRI was able to measure all the required properties with a few exceptions due to limitations of the measuring technique or the material. A presentation of those properties measured is made in the following sections. The apparatus and measurement and data reduction techniques that SRI utilized for the specific material property generation are described in Appendix II.

TABLE XXIII - THERMOPHYSICAL PROPERTIES MEASURED

Material (a)	Density (lb/ft ³)	Thermal Conductivity (b)	Thermal Expansion	Heat Capacity	Total Normal Emittance (c)	Modulus of Rupture (d)
LECO X-3306 Al ₂ O ₃	228	---	---	---	X	---
Ipsen ICB-3400 Al ₂ O ₃	34	X	X	---	---	---
Norton RA5058 Al ₂ O ₃	85	X	X	---	---	X
MAC LA-2 Al ₂ O ₃	65	X	X	---	---	X
ZIRCOA Y-714 ZrO ₂	280	X	X	X	X	X
Norton LZ5991 ZrO ₂	95	X	X	---	---	X
MAC LZ-1 ZrO ₂	125	X	X	---	---	X
MAC DZ-1 ZrO ₂	230	---	X	---	---	---
ZIRCOA Y-1193C ThO ₂	460	X	X	X	X	X
Norton LT5006 ThO ₂	125	X	X	---	---	X
MAC LT-1 ThO ₂	200	X	X	---	---	X
MAC DT-1 ThO ₂	390	---	X	---	X	---

Notes:

- (a) For alumina materials, data was obtained in the temperature range of (500° - 3400°^oF).
For zirconia materials, data was obtained in the temperature range of (500° - 4000°^oF).
For thorium materials, data was obtained in the temperature range of (500° - 5000°^oF).
- (b) Data obtained at pressures of 760, 10, 1, 1 x 10⁻¹, and 1 x 10⁻³ mmHg.
- (c) Data obtained in oxidizing atmosphere.
- (d) Deflection at break recorded.

4.5.1 Heat Capacity

The heat capacity data are presented in the curves of Figure 66 for the Zircoa Y-714 zirconia and Zircoa Y-1193C thoria materials. Two specimens of the zirconia and three specimens of the thoria material were run in order to get duplicate data, and good agreement was obtained. The heat capacity of the zirconia material increased from 0.130 Btu/lb/°F at 500°F to about 0.163 Btu/lb/°F at 2000°F, and then became essentially constant to 4000°F. For thoria, the heat capacity increased from 0.050 Btu/lb/°F at 500°F to about 0.098 Btu/lb/°F at 3500°F, and then was essentially constant to 5000°F. These heat capacity values were considered applicable to all zirconia and thoria materials used because of the similarity in chemistry.

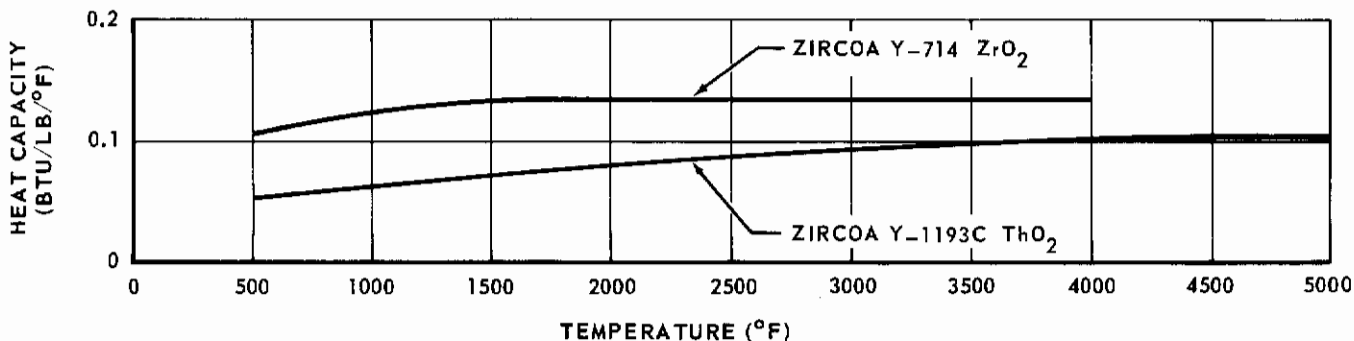


FIGURE 66 - HEAT CAPACITY OF ZIRCONIA AND THORIA

4.5.2 Total Normal Emittance

Figure 67 shows the total normal emittance of LECO X-3306 alumina coated with MAC DC-1 chromium oxide. This coating was developed at MAC and is described in Section 4.4.4.4. The values decreased from 0.65 at 1200°F to a minimum of 0.45 at 2700°F. Above 2700°F, the emittance increased to 0.70 at 3400°F. It was noted upon visual inspection of the specimens after the run, that the chromia had reacted with the alumina to form a coating which varied in color from dark ruby to black. The stability of this system is felt to be limited by either the vaporization of the coating or the reaction of the coating with alumina. With long time exposure, this coating is lost.

The two zirconia materials (Zircoa Y-601 zirconia and MAC DZ-1 zirconia) exhibited total normal emittance values as shown in Figure 68. The MAC developed zirconia had slightly higher values than the commercial zirconia from 1200°F to 3000°F, but above 3000°F the values for the commercial zirconia were higher. The slight variation in the emittance of the two zirconia materials is apparently due to the differing surface characteristics, compositional differences, and accuracy of the experiment. These values are similar in character and magnitude to previous values obtained on zirconia in the Air Force ASSET program.

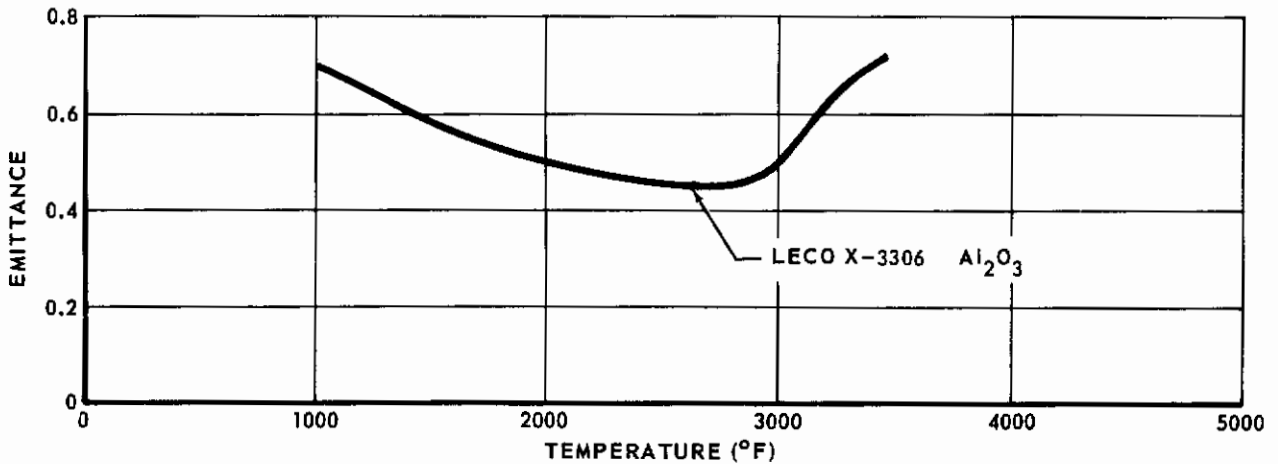


FIGURE 67 - TOTAL NORMAL EMITTANCE OF ALUMINA (Cr_2O_3 - COATED) IN AIR

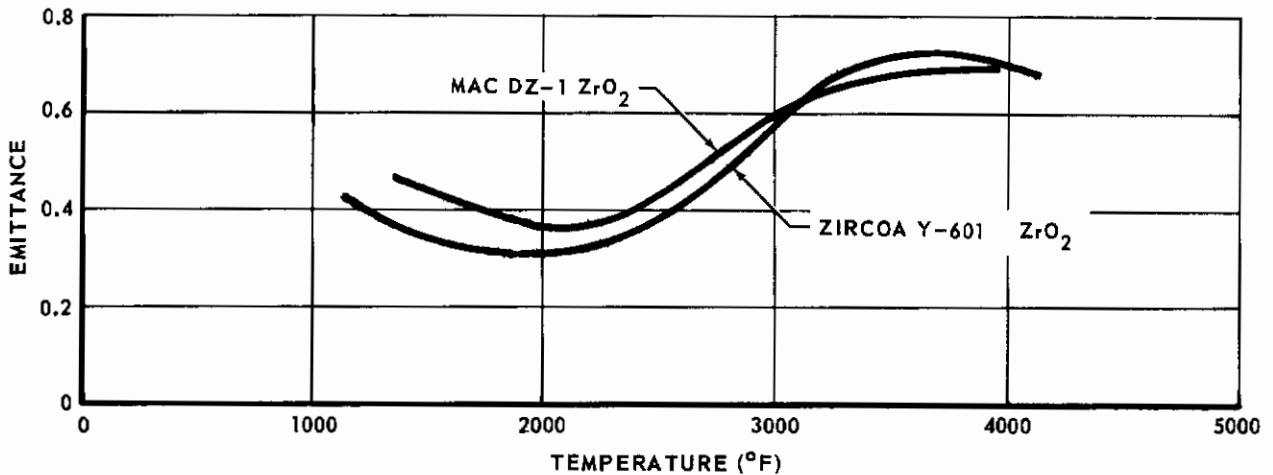


FIGURE 68 - TOTAL NORMAL EMITTANCE OF ZIRCONIA IN AIR

The two thoria materials (Zirconia Y-1193C thoria and a MAC DT-1 thoria) exhibited total normal emittance values as shown in Figure 69. Both thoria materials had similar values up to 3000°F, but between 3000°F and 3800°F, the MAC developed thoria had a lower emittance. As apparent from Figure 69, no values above 4000°F were obtained. In attempting to obtain front face temperatures greater than 4000°F, the heated back surface of the specimen became molten and the specimen was rapidly destroyed.

SRI's procedure for determining emittance is correct only for those materials that radiate as graybodies, since the total emittance is assumed to be equal to the spectral emittance at the pyrometer wavelength of 0.65 microns. The error in emittance values for non-gray materials will vary, depending on the difference between the spectral and total emittance.

From a statistical analysis of the data obtained on past emittance determinations, SRI has concluded that the measurement system used has a probable overall error of about 12% and that fitting the points to a curve reduced this maximum to about 5%. At temperatures in excess of 3600°F,

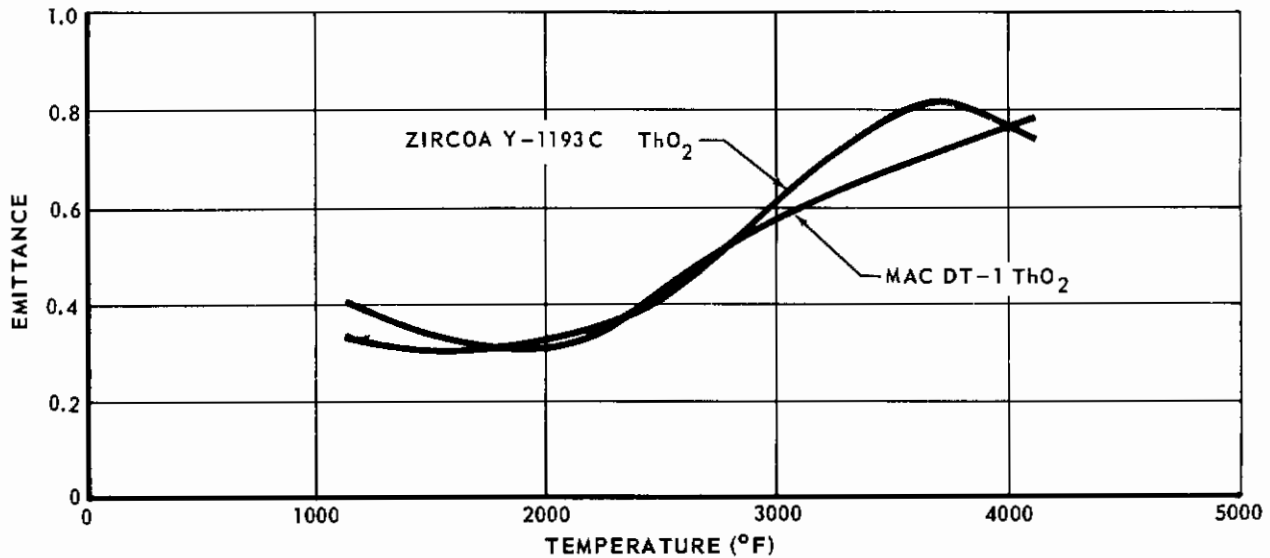


FIGURE 69 - TOTAL NORMAL EMITTANCE OF THORIA IN AIR

where the heated surface of the specimen becomes molten and steady state conditions no longer exist, the error involved is undoubtedly higher. As to utilization, the data generated by SRI above 3600°F should be used with discretion.

4.5.3 Linear Thermal Expansion

The thermal expansion data of three alumina bodies (Norton RA5058, Ipsen ICB 3400, and MAC LA-2) are presented in Figure 70. The thermal expansions of all three were approximately the same up to about 1500°F; however, at 2000°F the MAC chemically bonded alumina began to shrink severely. The Ipsen alumina began its severe shrinkage at about 3200°F, while the Norton body continued to expand to 3400°F. Of the three materials, the Norton body had the highest coefficient of expansion, followed by Ipsen and then MAC. Good agreement was obtained between runs on duplicate specimens for each material.

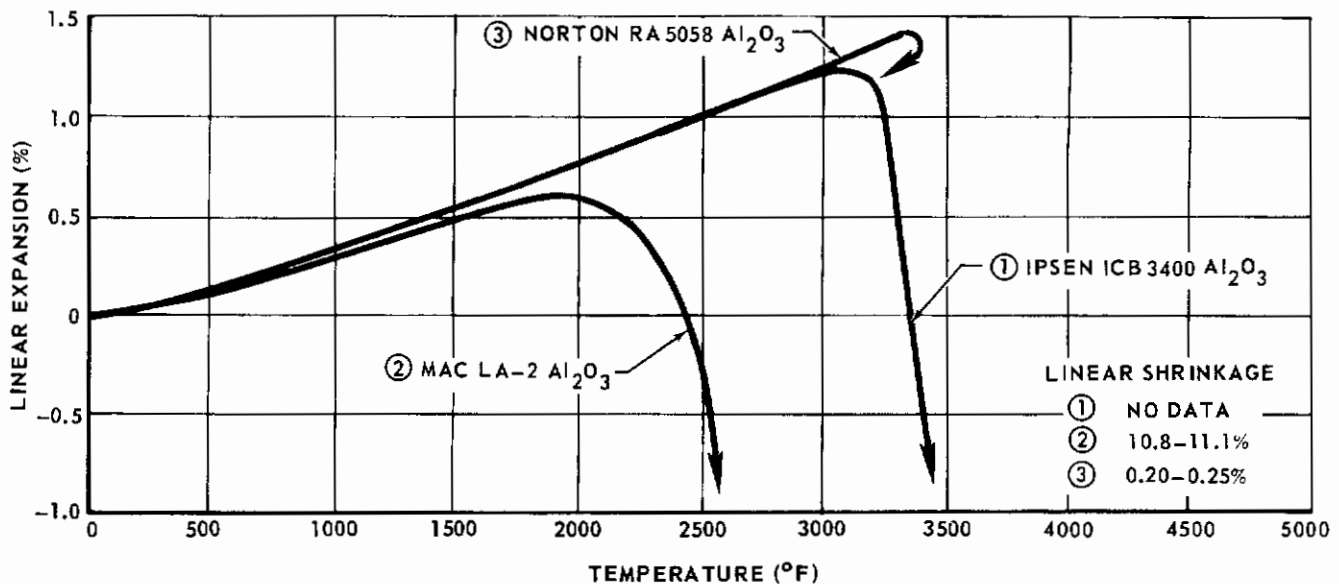


FIGURE 70 - THERMAL EXPANSION OF ALUMINA BODIES

Figure 71 shows the thermal expansion of four zirconia bodies (Norton LZ5991, Zircoa Y-714, MAC LZ-1, and MAC DZ-1). Zircoa Y-714 had the highest expansion, which is comparable to a fully stabilized zirconia body. This body exhibited the most consistent behavior and expanded to about 3900°F before shrinkage began. Of the two MAC zirconia bodies, the low density formulation had the higher expansion; however, this body exhibited the greatest linear shrinkage of all zirconia bodies. Both MAC zirconia formulations began to shrink at 2300 to 2500°F. The data for the three specimens of Norton developed zirconia were in good agreement up to about 1800°F, from which point the duplicate specimens exhibited completely unrelated behavior. One specimen continued to expand; the second began to shrink; and the third shrank, then began to expand again to a temperature where shrinkage began again. This behavior was probably due to a difference in crystallographic stabilization.

The thermal expansion data of four thoria materials (Zircoa Y-1193C, Norton LT5006, MAC LT-1, and MAC DT-1) are shown in Figure 72. The data for all four materials had approximately the same slope, but each began to shrink at a different temperature. The MAC low density formulation began shrinking at 1250°F, the MAC high density at 1850°F, the Norton at 3000°, and the Zircoa at about 4000°F.

The linear shrinkage values given in Figures 70, 71, and 72 are somewhat misleading as to the actual dimensional change which would be expected to occur on an actual heat shield. In the measurements at SRI, the specimens were held at temperatures for three times the theoretical soak time required to eliminate a temperature gradient within the specimen. In the actual heat shield environment, the material is at maximum temperature a relatively short period of time and a large thermal gradient exists through the material thickness. This gradient does not allow the material to shrink as much as indicated from the thermal expansion values. A "dimensional" analysis was made on a one-inch cube using the MAC low density zirconia. The cube was divided into thin rectangular slabs, and the maximum temperature that each slab achieved in a representative heat shield was used along with an effective expansion coefficient to determine the dimensions of the slab upon cooling to room temperature. The resulting dimensional change at the hot surface of the cube was found to be 0.03 inch which is 3% linear shrinkage, instead of the 11% value as shown in Figure 71.

4.5.4 Thermal Conductivity

The thermal conductivity values at atmospheric pressure for three aluminas (Ipsen ICB 3400, Norton RA5058, and MAC LA-2) are presented in Figure 73. Of the three materials, the lowest values were found for the Ipsen alumina and the highest for the Norton. However, above 2250°F, the Ipsen material had a higher conductivity than the MAC alumina. The rate of increase in conductivity with increasing temperature was less for the MAC material than for the other two, probably because the smaller pore size and higher density of the MAC material caused the radiant heat transfer to be less.

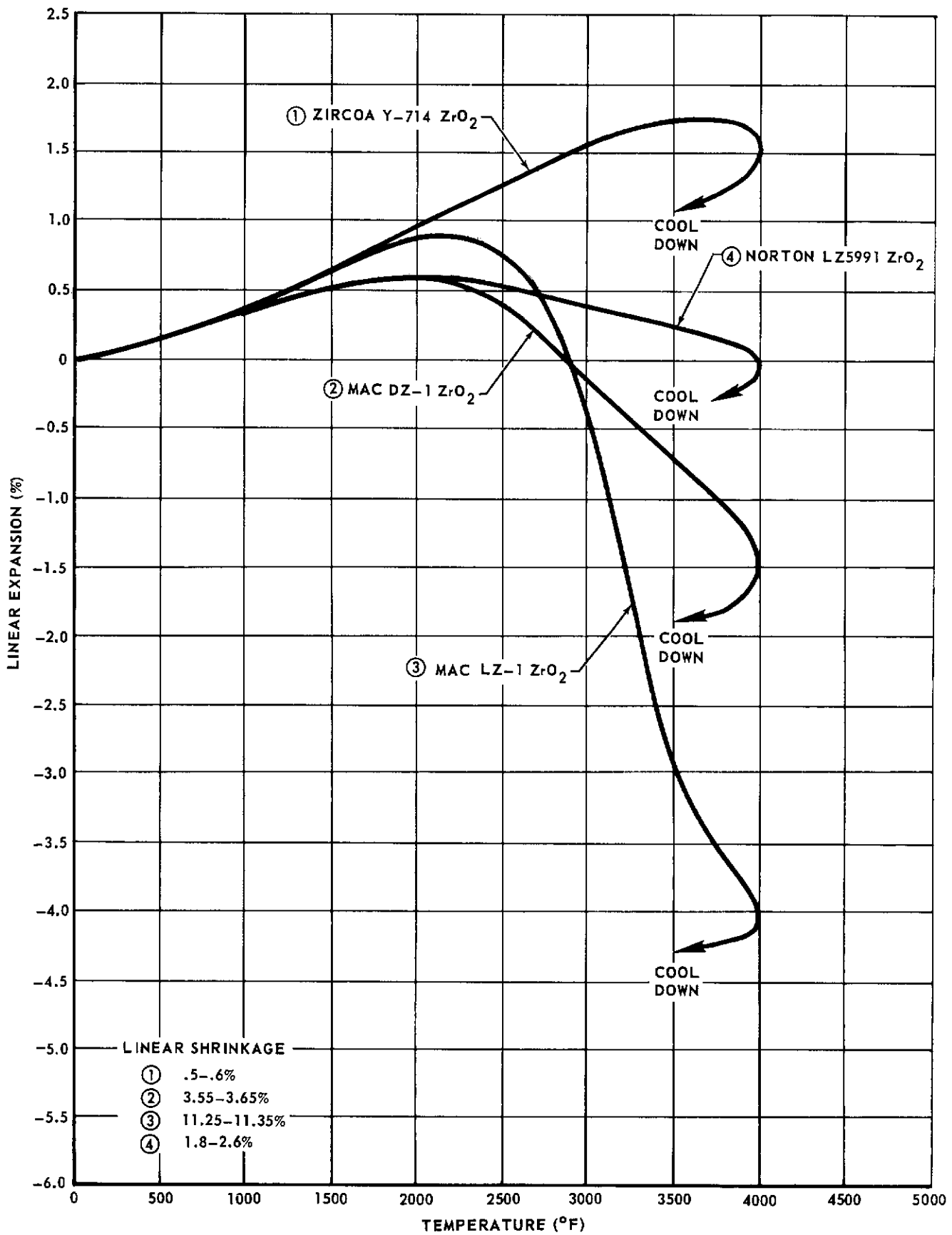


FIGURE 71 - THERMAL EXPANSION OF ZIRCONIA BODIES

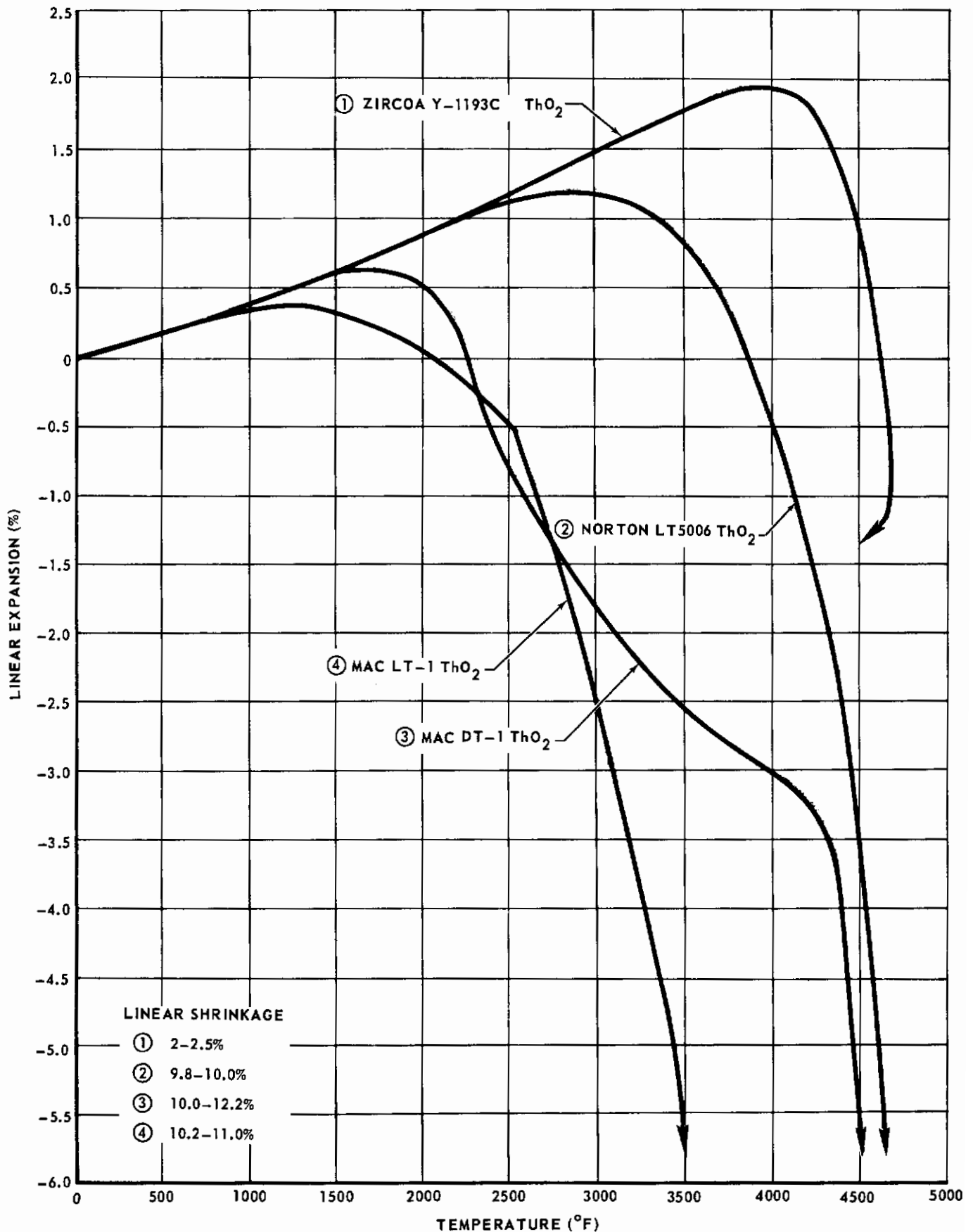


FIGURE 72 - THERMAL EXPANSION OF THORIA BODIES

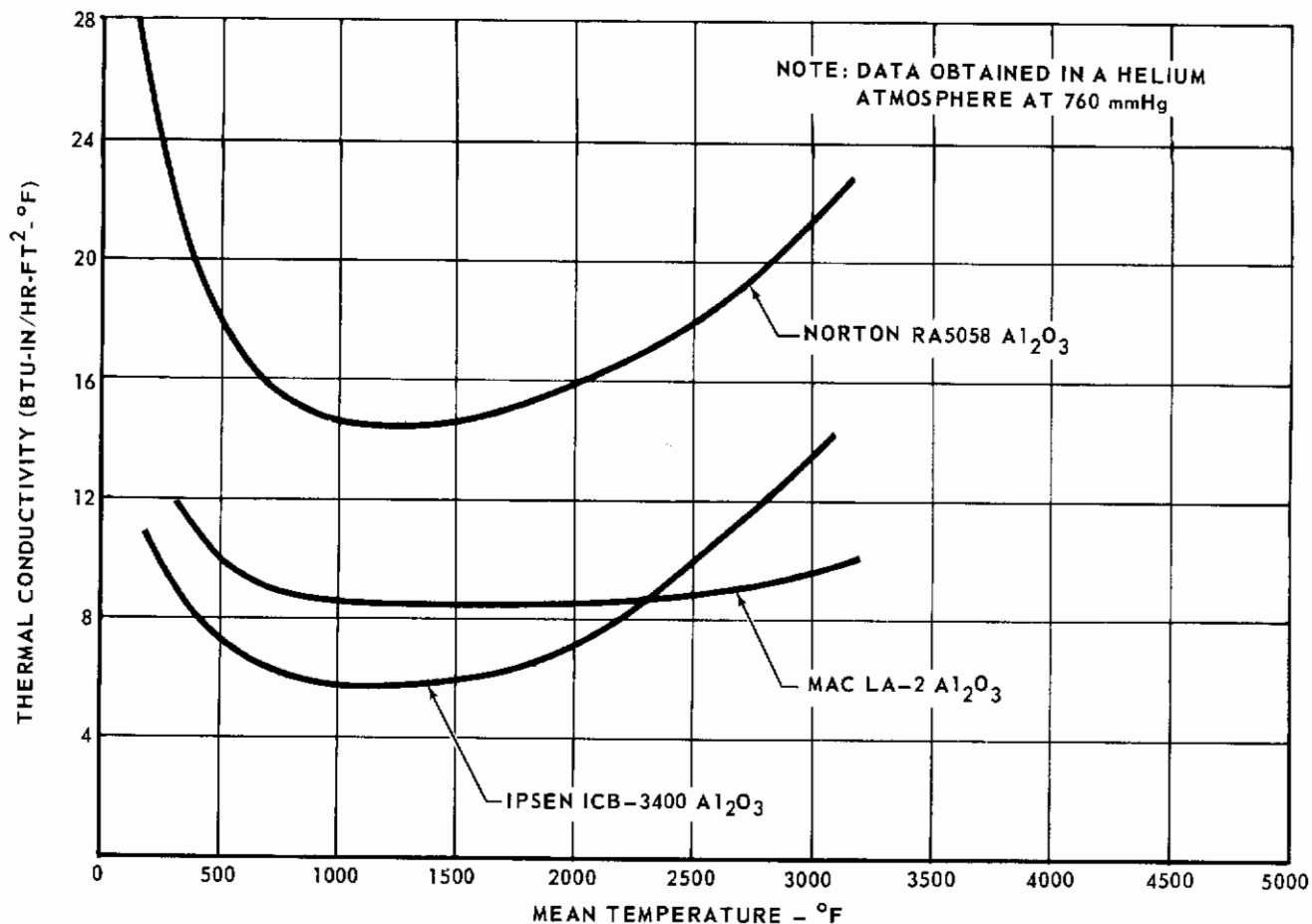


FIGURE 73 - THERMAL CONDUCTIVITY OF ALUMINA BODIES

The thermal conductivity (Btu-in/hr-ft²-°F) of the Ipsen alumina decreased from about 11 at 230°F to a low of about 5.7 at 1300°F, and then began to increase and at 2650°F was about 11. Conductivity of the Norton alumina decreased from about 26 at 190°F to a low of 14.2 at 1250°F and then increased to 20 at 2790°F. Conductivity of the MAC alumina decreased from about 11.8 at 330°F to a low of about 8.2 at 1650°F and then increased to 9.7 at 3030°F.

The thermal conductivity values at atmospheric pressure for three zirconias (Norton LZ5991, Zircoa Y-714 and MAC LZ-1) are presented in Figure 74. At the lower temperatures, the low density bodies had the lower conductivity values, while at the higher temperatures the low density bodies exhibited the higher values. Apparently the increased heat transfer by radiation across pores at the higher temperatures nullified the advantage of the lower densities.

The thermal conductivity (Btu-in/hr-ft²-°F) of the MAC zirconia increased continuously from a low of about 3.0 at 280°F to a high of 13.7 at 3950°F. Conductivity of the Norton zirconia increased from a low of 4.3 at 240°F to a high of 17.9 at 3850°F. Conductivity of the Zircoa zirconia increased from a low of 8.2 at 500°F to a high of 11.3 at 3650°F.

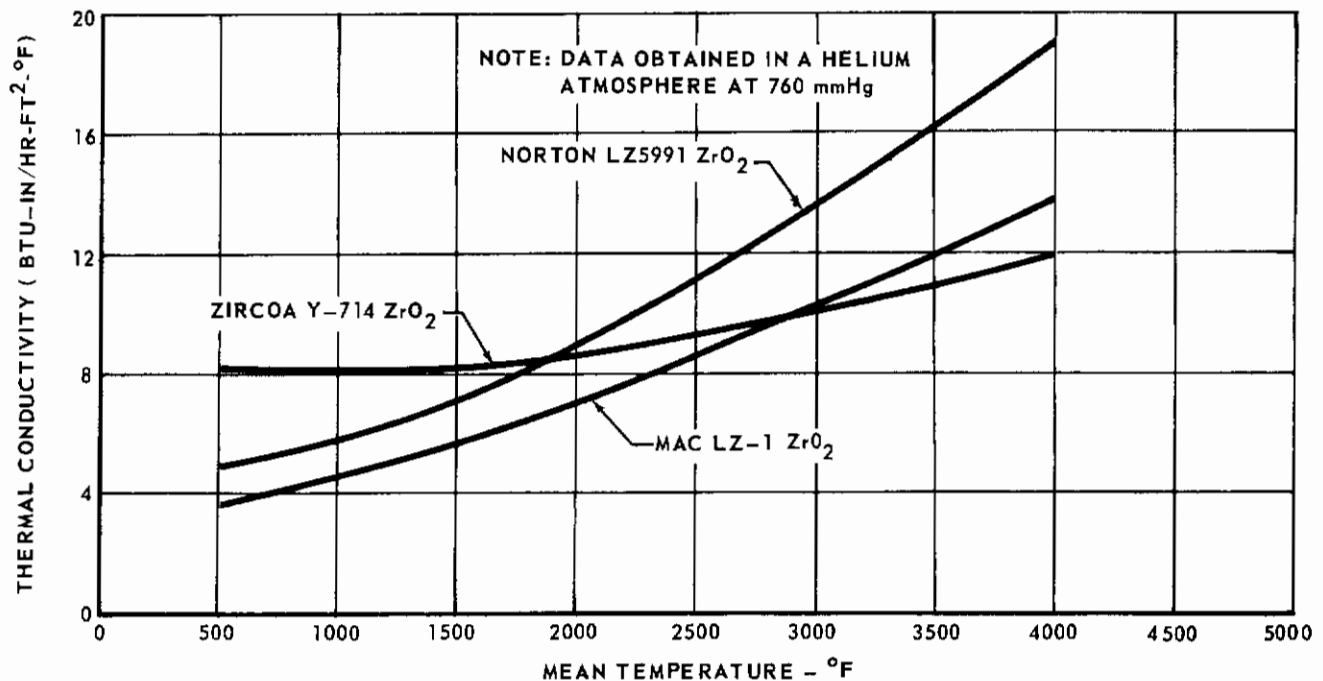


FIGURE 74 - THERMAL CONDUCTIVITY OF ZIRCONIA BODIES

The thermal conductivity values at atmospheric pressure for three thorias (Norton LT5006, Zircoa Y-1193C, and MAC LT-1) are presented in Figure 75. Considerable variation was found for the conductivities of these three materials. In the lower temperature range, the Zircoa material had the highest conductivity value and the Norton and MAC materials were about the same; while at higher temperatures the Norton material had higher values and the Zircoa material lower. This behavior was about the same as for the zirconia, but the differences were more pronounced.

The thermal conductivity (Btu-in/hr-ft²-°F) of the MAC thoria decreased from 9.4 at 500°F to a low of 8.3 at 1000°F and increased to 18.9 at 4100°F. Conductivity of the Norton thoria decreased from about 8.8 at 250°F to a low of 8.2 at 700°F and then increased to a high of 32.2 at 4500°F. Conductivity of the Zircoa thoria decreased continuously throughout the temperature range but tended to level out and become constant above 3700°F. The value at 300°F was 27.7 and at 4500°F was 12.3.

The data at reduced pressure levels (10, 1, 10⁻¹, and 10⁻³ mm Hg) as well as atmospheric for all the materials previously mentioned are shown in Figures 76 through 84. The thermal conductivity of all the materials investigated decreased with decreasing pressure. However, in most cases, the conductivity at any one level of pressure at 10 mm Hg and below differed from the conductivity at another by an amount no greater than normally experienced as data scatter. Consequently, all the reduced pressure data should be depicted as a band. For all the materials, conductivity data at 10 and at 1 mm Hg were obtained to higher mean temperatures than data at 0.1 and 0.001 mm Hg because of volatilization at the lower pressures.

Text continued on page 123

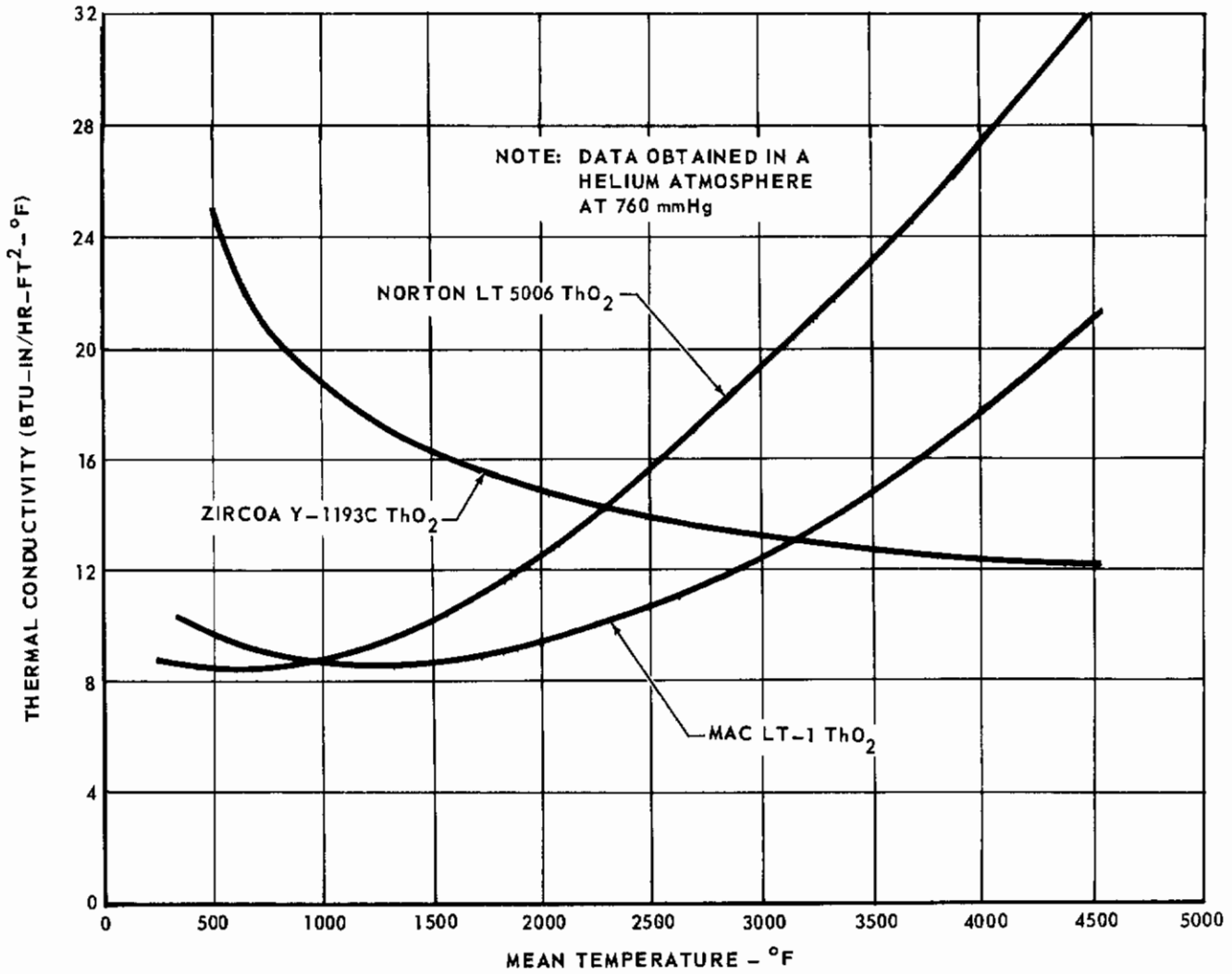


FIGURE 75 - THERMAL CONDUCTIVITY OF THORIA BODIES

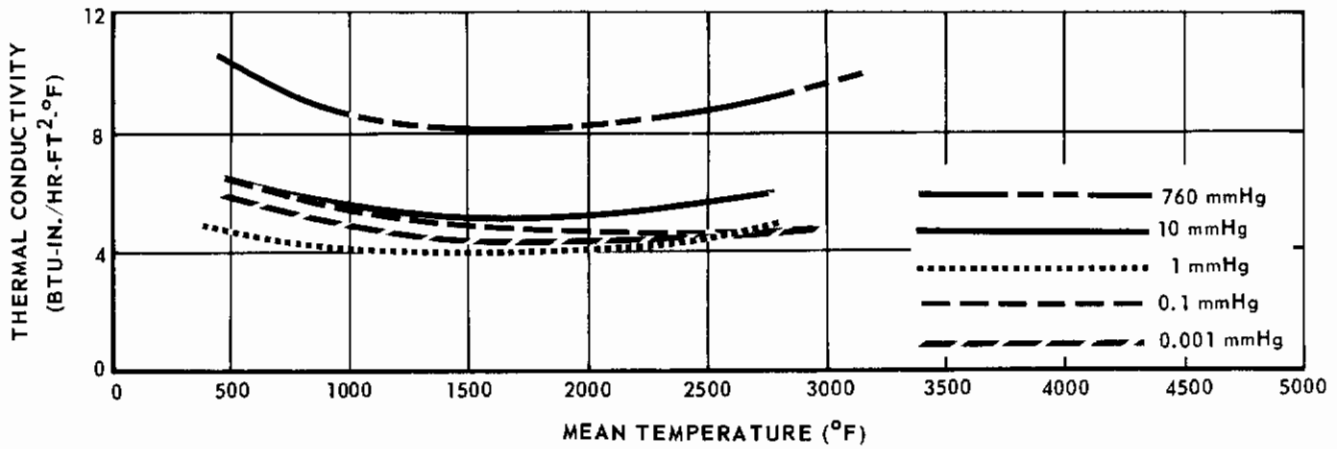


FIGURE 76 - CONDUCTIVITY OF MAC LA-2 Al₂O₃ AT REDUCED PRESSURES

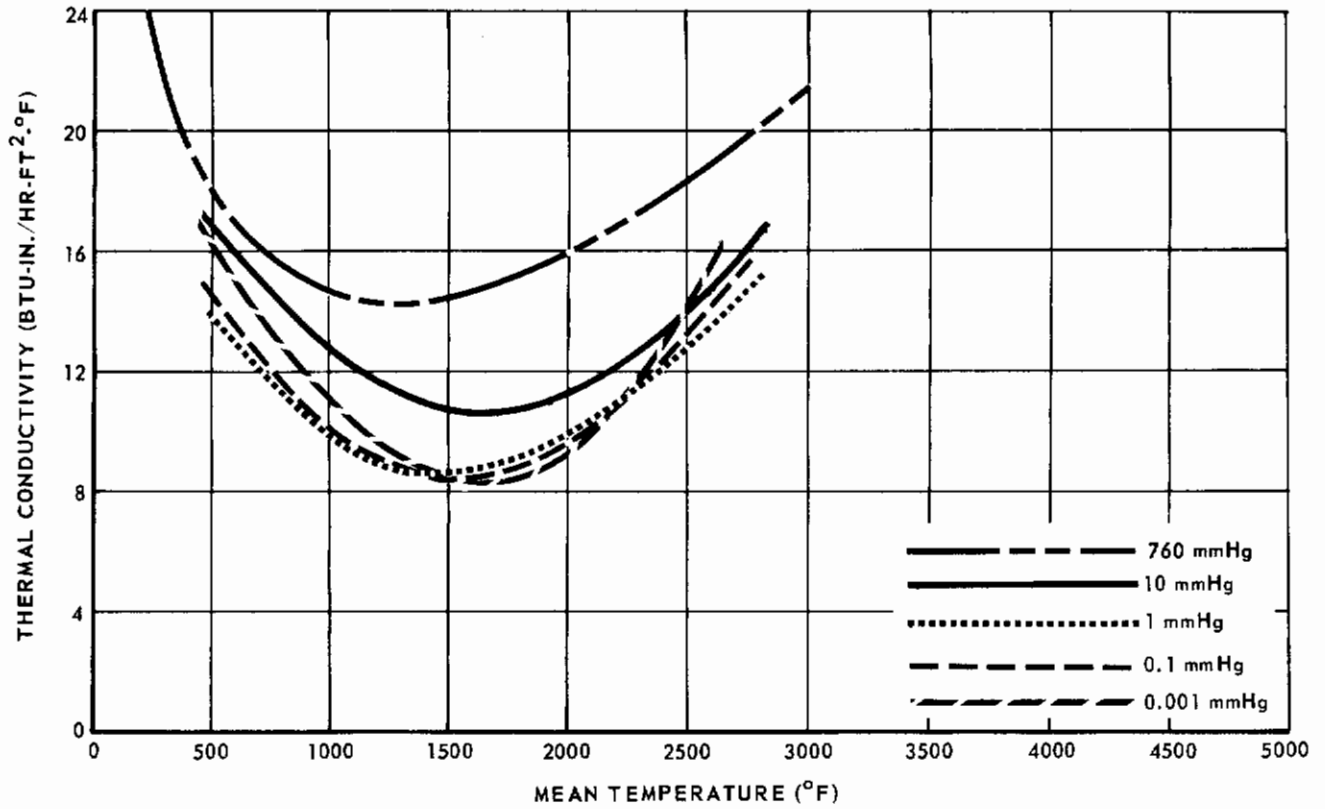


FIGURE 77 - CONDUCTIVITY OF NORTON RA 5058 Al_2O_3 AT REDUCED PRESSURES

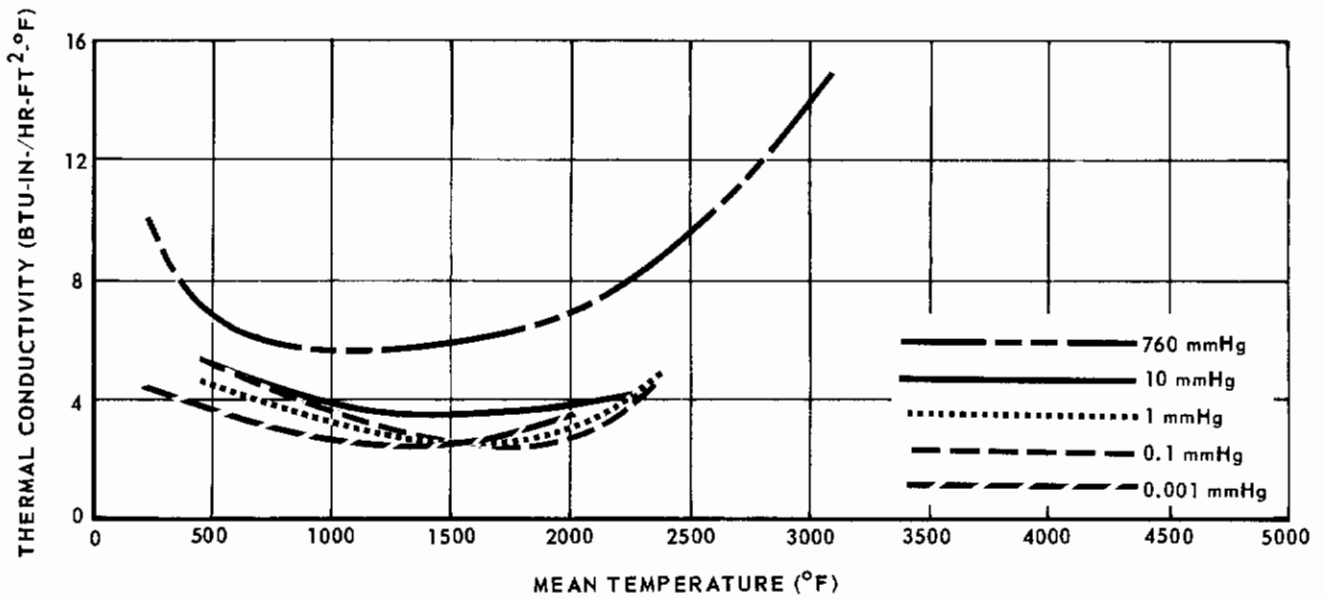


FIGURE 78 - CONDUCTIVITY OF IPSEN ICB-3400 Al_2O_3 AT REDUCED PRESSURES

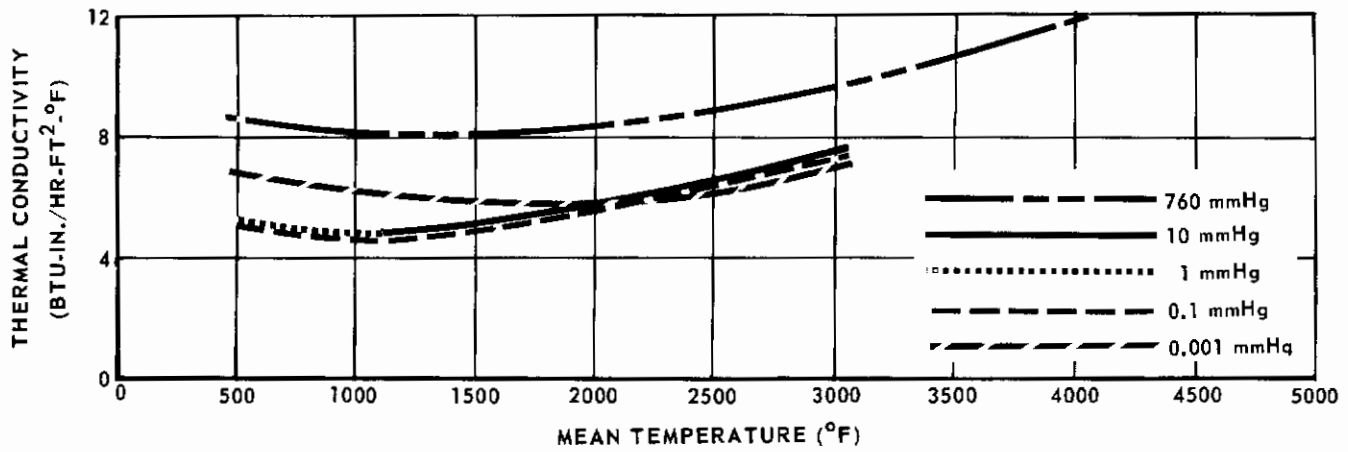


FIGURE 79 - CONDUCTIVITY OF ZIRCOA Y-714 ZrO₂ AT REDUCED PRESSURES

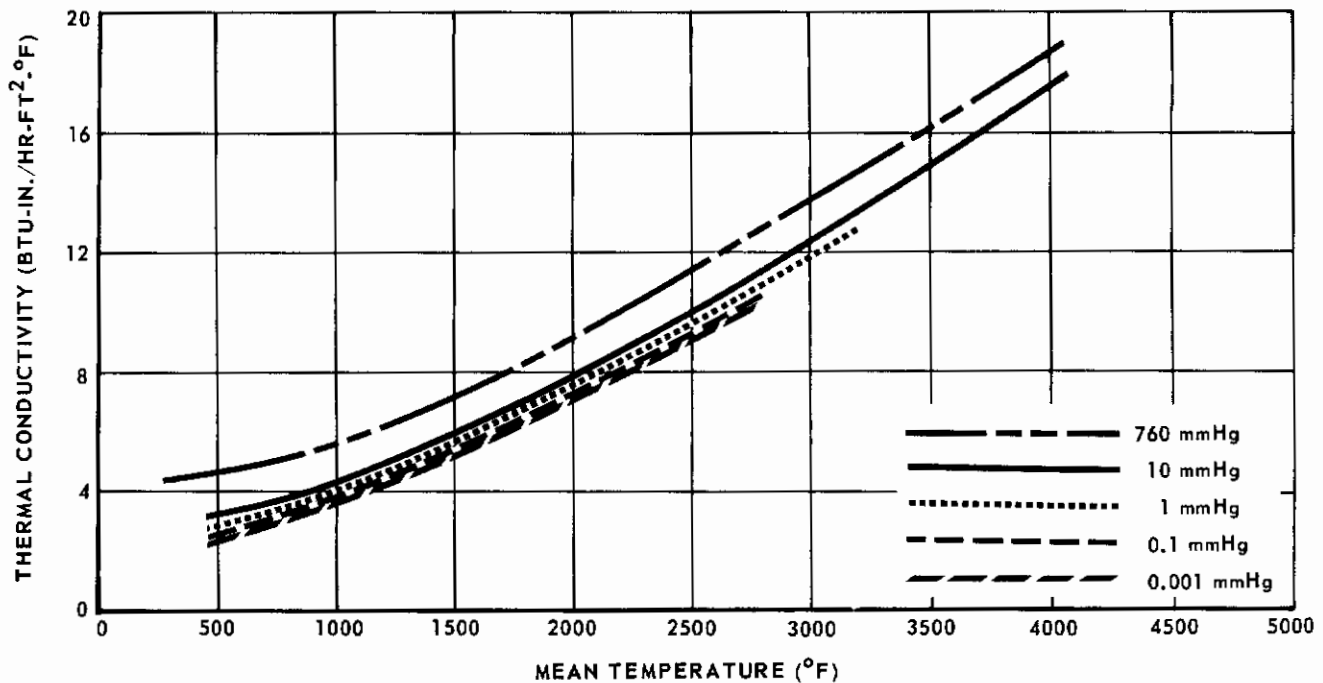


FIGURE 80 - CONDUCTIVITY OF NORTON LZ 5991 ZrO₂ AT REDUCED PRESSURES

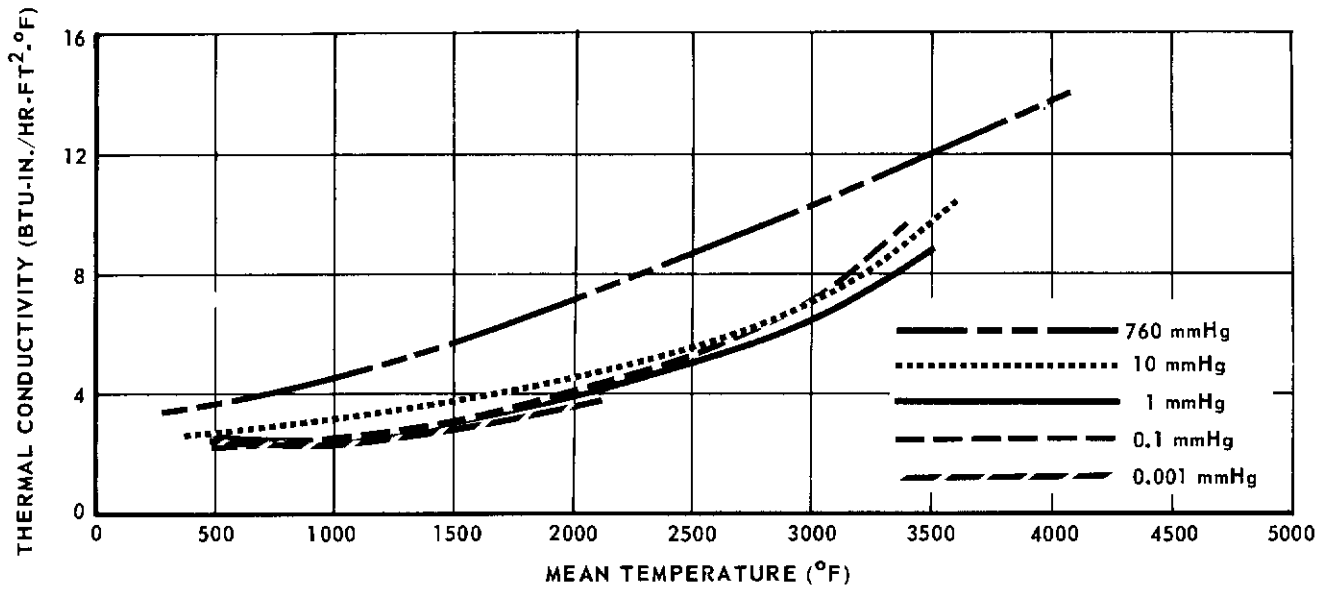


FIGURE 81 - CONDUCTIVITY OF MAC LZ-1 ZrO₂ AT REDUCED PRESSURES

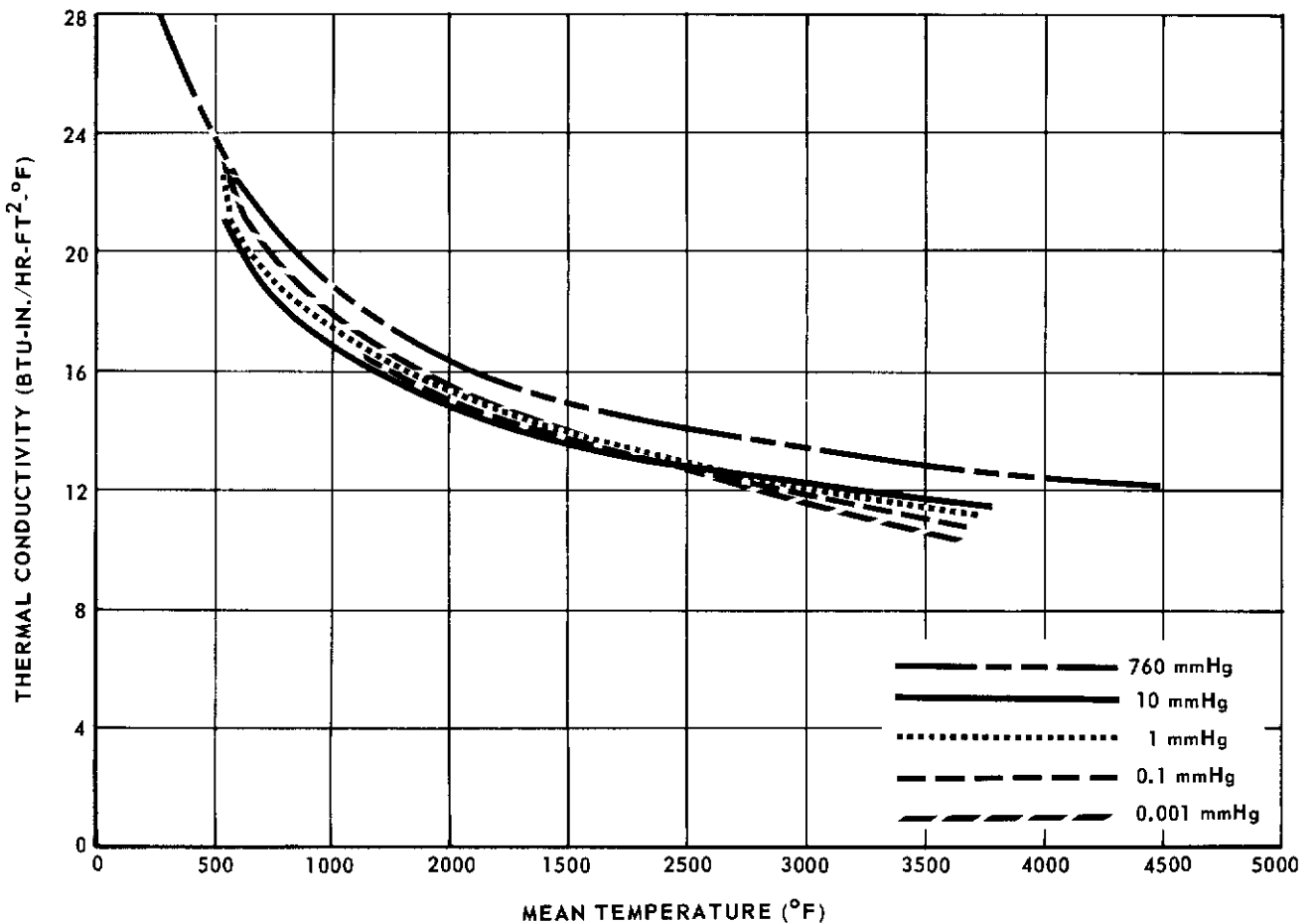


FIGURE 82 - CONDUCTIVITY OF ZIRCOA Y-1193C ThO₂ AT REDUCED PRESSURES

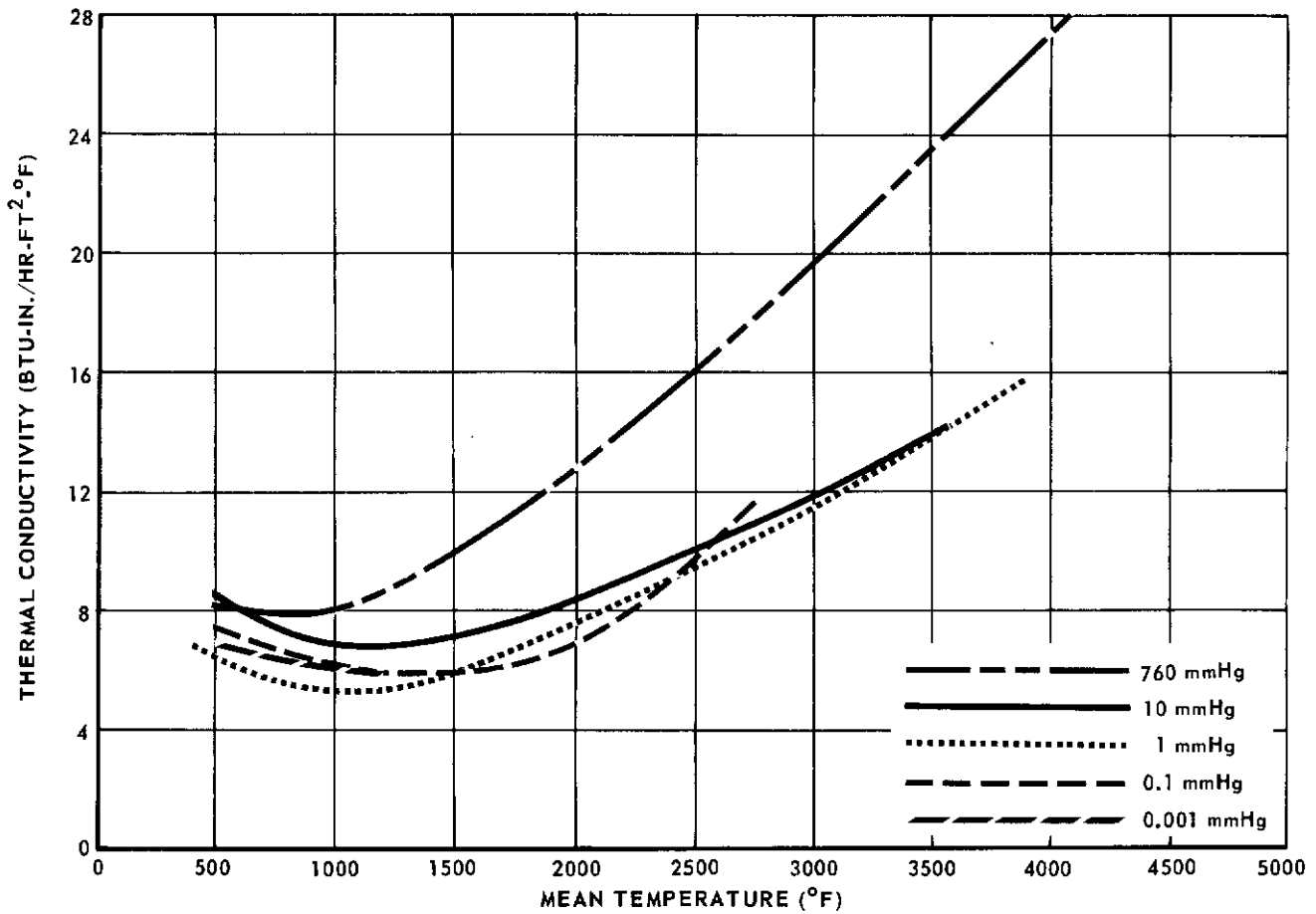


FIGURE 83 - CONDUCTIVITY OF NORTON LT-5006 ThO₂ AT REDUCED PRESSURES

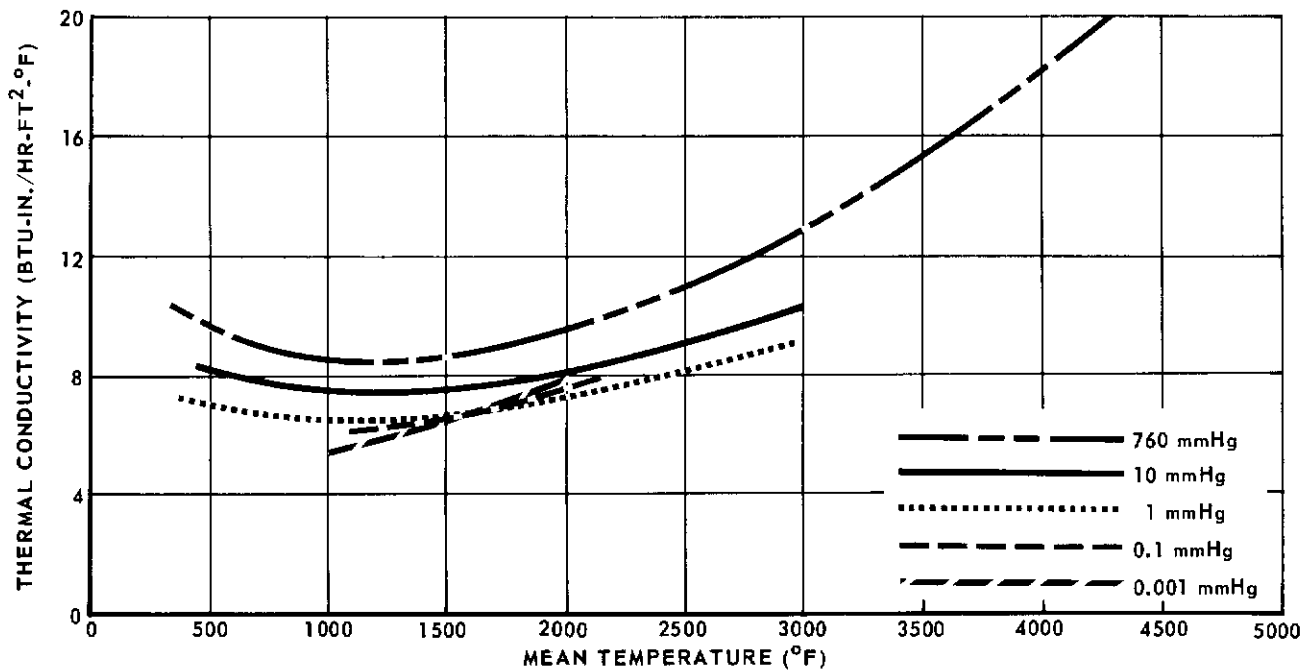


FIGURE 84 - CONDUCTIVITY OF MAC LT-1 ThO₂ AT REDUCED PRESSURES

Reduced pressure data were obtained at all pressure levels to 2700°F mean temperature for the Norton alumina, but vapor formation prevented data determination for the Ipsen alumina at 2300°F and for the MAC body at 2200°F. Reduced pressure data were obtained to about 3500°F for the MAC and Norton zirconias, while 3000°F was the limit for Zircoa. Reduced pressure data were obtained to 3000°F for the MAC thoria body, to 3900°F for the Norton, and to 3400°F for Zircoa.

It should be noted that most of the conductivity measurements were performed in a helium atmosphere. For porous materials, where gas conduction is a mode of heat transfer, it is necessary to be aware of the interstitial gas. Since helium does have a higher conductivity than air, the measured values should be somewhat conservative.

4.5.5 Modulus of Rupture

Composite plots of flexural strength (MOR) and Young's modulus in flexure versus temperature for all the materials are presented in Figures 85 and 86. The mechanical properties for the eight materials varied greatly. At 500°F, the variation between lowest and highest MOR and Young's modulus values was a factor of 10. The overall trend was a general decrease in both strength and Young's modulus with increasing temperature for all the materials.

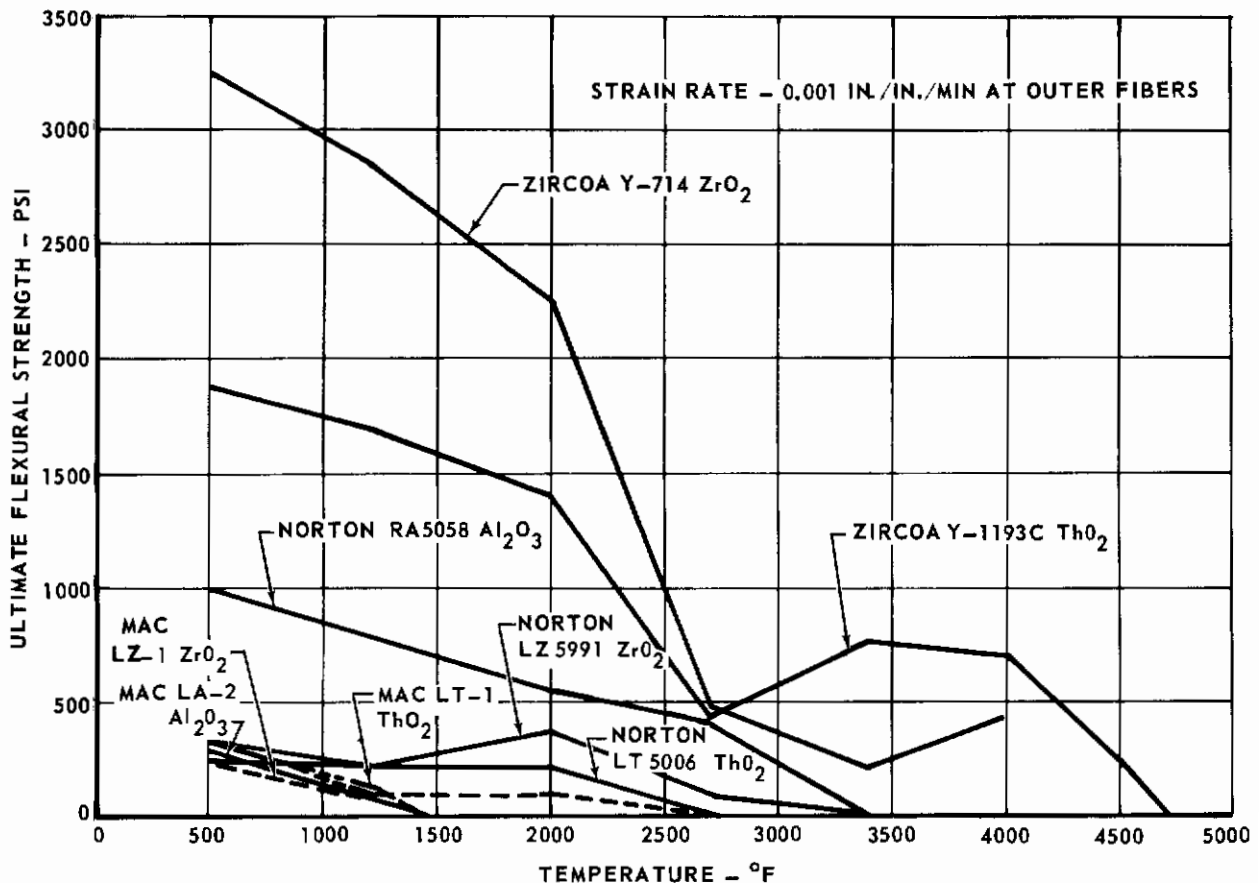


FIGURE 85 - COMPOSITE PLOT OF ULTIMATE FLEXURAL STRENGTH VERSUS TEMPERATURE

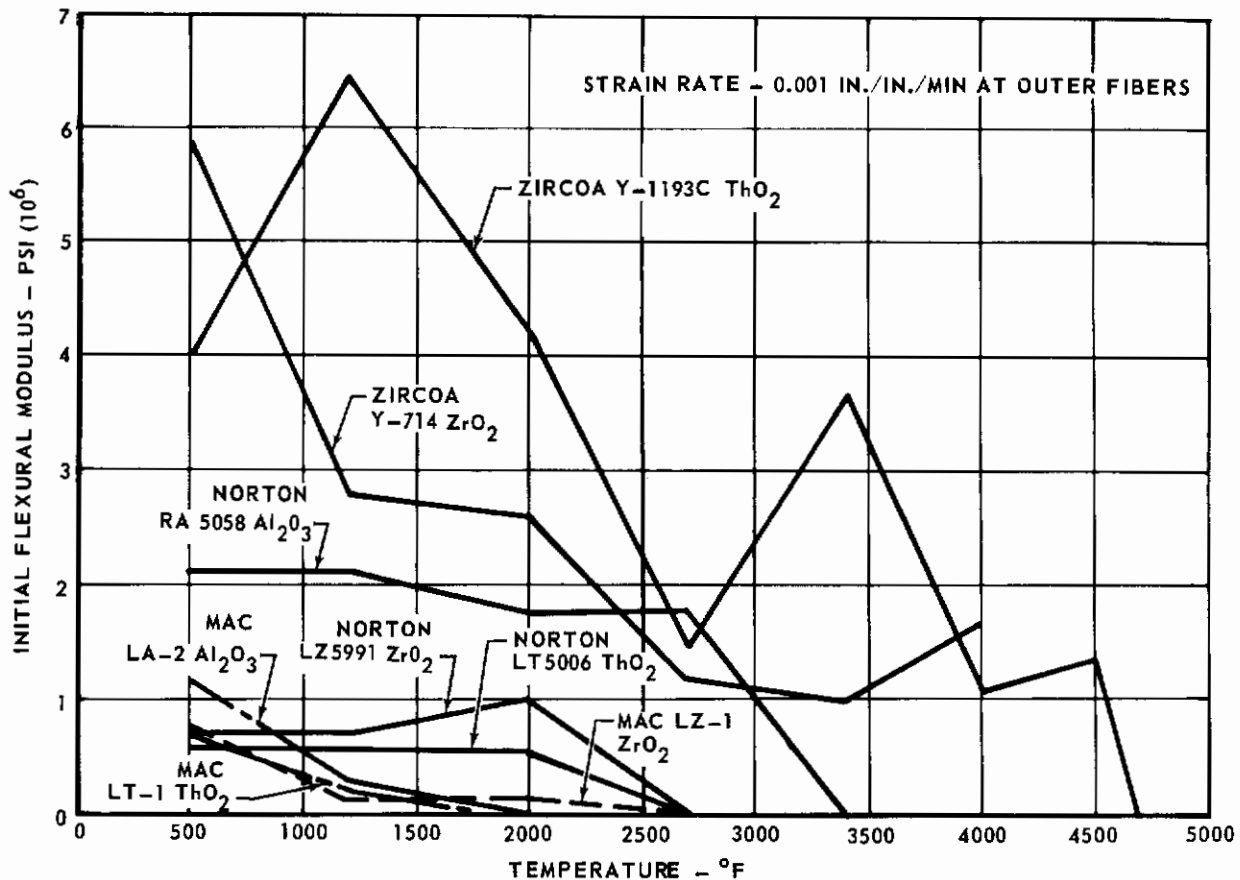


FIGURE 86 - COMPOSITE PLOT OF INITIAL FLEXURAL MODULUS VERSUS TEMPERATURE

As some of the materials approached their upper temperature limit, their strength became extremely low. The very low load required to break or deflect some materials was difficult to measure and the deflection measurement rod penetrated the specimen in some cases. The strengths of such specimens were reported as 0 psi.

The MAC developed low density alumina, zirconia, and thoria behaved in almost an identical manner. The ultimate flexural strength of the three materials decreased from about 300 psi at 500°F to about 0 psi at 2000°F, the zirconia retaining some strength at 2000°F. Young's modulus decreased from about 0.75×10^6 psi at 500°F to about 0 psi at 2000°F, the value for alumina being somewhat higher at 500°F. In addition to low strength, the MAC developed materials exhibited no apparent elastic behavior above about 1200°F. The materials were permanently deformed upon being loaded and unloaded. The behavior of these materials is not completely unexpected, due to their composition. They are all chemically bonded with a silicate binder system and cured at very low temperatures.

The mechanical properties of the Zircoa Y-1193C thoria and the Y-714 zirconia were much higher than for the other materials. These materials were considerably higher in density than the other materials, which accounts for this difference. For each material, the strength and modulus followed the same trend with temperature. Young's modulus was generally higher for

the thoria throughout the temperature range. Flexural strength was higher for the zirconia than for the thoria up to 2700°F and lower at 3400°F and 4000°F.

The Norton low density alumina, zirconia, and thoria behaved in a similar manner; however, the strength and Young's modulus values were considerably higher for the alumina body throughout the temperature range. The Young's modulus of thoria and zirconia decreased to almost 0 psi at 2700°F, and the alumina decreased to 0 psi at 3400°F. The modulus values at 500 to 2000°F were about 2.0×10^6 psi, 0.75×10^6 psi, and 0.5×10^6 psi for the alumina, zirconia, and thoria materials, respectively. The flexural strength was fairly constant with temperature for Norton low density thoria and zirconia, being about 250 psi at 500 to 2000°F. The strength of the thoria dropped to 0 psi at 2700°F, and the zirconia body became 0 psi at 3400°F. The strength of the alumina body decreased almost linearly from about 1000 psi at 500°F to about 0 psi at 3400°F.

4.6 MATERIALS SELECTIONS AND CONTROL FOR FULL SCALE COMPONENTS

The final materials selection was based on an evaluation of the ceramic screening tests, the in-house materials development program, the subcontract materials development effort, the subscale module fabrication and testing (see Section 5.2), materials availability, and the full scale designs.

Table XXIII lists the MAC developed chemically bonded materials which were utilized and the area of application. The commercial materials selected are listed below:

(a) Alumina - 3.0 Inch Radius Leading Edge Ceramic Tiles - Norton RA5058, density 85 lb/ft³ purchased in 9 inch x 4-1/2 inch x 2-1/2 inch bricks.

(b) Zirconia - 1.5 Inch Radius Leading Edge Ceramic Blocks and 6.0 Inch Radius Nose Cap Ceramic Blocks - Norton LZ5991 (developed as part of the program), density ~95 lb/ft³. Purchased in 4-1/2 inch x 2-1/2 inch x 2-1/2 inch blocks.

6.0 Inch Radius Nose Cap Tubes and Pins - Zircoa Y-601, density 280 lb/ft³. Purchased in 5/8 inch OD x 3/8 inch ID x 2 inch long tubes and 1/8 inch diameter x 5/16 inch long rods.

(c) Thoria - 6.0 Inch Radius Nose Cap Tubes - Zircoa Y-1193C, density 460 lb/ft³. Purchased in 1 inch OD x 5/8 inch ID x 1 inch long tubes.

To insure that all full scale components were built from quality parts, attempts were made to set up quality controls for all incoming ceramic materials. Attempts were unsuccessful to utilize radiographic and ultrasonic techniques to detect surface or internal cracks, and small flaws. In fact, no successful techniques evolved for detecting small internal flaws in the ceramics. The fact that all materials were of 20 to 80% theoretical density increased the inspection problem. To detect surface flaws, all incoming parts were visually inspected at 2-20X with optical aids such as microscopes. All cracks were marked and if located in a non-critical area, the part was still considered usable. After machining, all parts were once more inspected and rejected for defects in critical areas.

This inspection for cracks, before and after machining, resulted in the elimination of many of the low density zirconia parts for the 1.5 inch radius leading edge and the nose cap, and some of the high density thoria and zirconia tubes for the nose cap.

Representative samples of any single lot of parts were checked for density. If the samples were 10% off the expected density, the lot was considered substandard.

Representative samples of all materials were thermal shock tested by subjecting one-inch cubes to surface heating rates of 25°F/sec and 50°F/sec to maximum temperature. Samples of roughly the same size and shape as the parts to be used in the full scale components were subjected to the thermal environment of the design that was to utilize the particular parts. For example, low density zirconia samples 3.6 inches x 2.25 inches x 1.2 inches thick and 1 inch thick, and low density alumina samples 3.5 inches x 4.35 inches x 0.9 inch thick were thermal shock tested. Many of these samples were surfaced with chemically bonded materials, as would be the case in the full scale application.

This testing resulted in the selection for the 3.0 inch radius leading edge of RA5058 alumina with a density of 85 lb/ft³ rather than the LA5969 alumina at 80 lb/ft³, because the former was found to have the better thermal shock resistance for the particular batches on hand. The RA5058 material did not show any cracks after test, but was somewhat weakened. The testing indicated thermal shock resistance varied somewhat from brick to brick, indicating a questionable reproducibility and predictability.

As discussed in Section 4.3.1.2, the thermal shock resistance of the low density zirconia produced in the Reproducibility Phase (Phase II) of the subcontract was found to be less than the original material. Although the samples developed small cracks during thermal shock testing, all remained integral and no spalling occurred. As no other material was available, the material lots displaying the better thermal shock resistance were selected for full scale utilization.

Testing of high density thoria tubes revealed this material to have less thermal shock resistance than the material used in the subscale modules. However, scheduling requirements did not permit attempts to obtain better material. During testing, the tubes developed hairline cracks approximately 1/4 of their length from the heated surface, but remained integral. The cracking occurred even when the tubes were potted in chemically bonded low density thoria although this material did not crack. On this basis, it was decided to use a greater depth of the chemically bonded thoria than originally planned (approximately one inch instead of 0.5 inch), to give more insurance against failure in the event the tubes cracked during nose cap testing. Therefore, if the tubes cracked near the mold-line surface, which was the logical place, the nose cap would remain integral and adequately tied together. The increase in thoria content increased the predicted overall density of the nose cap from 168 lb/ft³ to 179 lb/ft³.

Thermal shock testing of the high density zirconia tubes for the nose cap showed this material to be very satisfactory and capable of withstanding the expected thermal environment.

SECTION V

DESIGN, FABRICATION, AND TESTING

The development of a 1.5 and 3.0 inch radius leading edge and a 6.0 inch radius nose cap was performed in three stages. (Section III presents a discussion of the process which led to the selection of these three components.) This step-by-step approach was taken to gain experience in the use of low density ceramics, to utilize the data generated by other program efforts, and to evaluate the largest possible number of design and fabrication approaches. The three stages of development were as follows:

- Stage 1. Basic design concepts and preliminary layouts.
- Stage 2. Subscale design, fabrication, and testing.
- Stage 3A. Design and fabrication of full scale components
- Stage 3B. Full scale component tests.

In the first stage, several basic design concepts utilizing known forms of ceramic materials were conceived and applied to preliminary layouts for full scale components. These initial layouts, in conjunction with the selected re-entry trajectories and material properties from the literature survey roughly established ceramic shield thickness and criteria for substructure materials. The second stage consisted of fabricating and testing subscale modules evolved from the preliminary layouts and basic design concepts. The final stage of the program was the fabrication and testing of three full scale components selected from the subscale phase.

Environmental conditions based on a lifting type re-entry vehicle as discussed in Section III (including a boost and launch phase as well as re-entry) were used for design, analyses, and testing. These conditions are presented in Table XXIV. The time duration for the acoustic environment was not to exceed five minutes while random vibrations could occur for as long as 15 minutes. The glide equilibrium temperatures at the stagnation point were approximately 15 to 20% lower than the maximum peak temperatures and lasted for approximately 25 minutes. The time at temperatures greater than the glide equilibrium temperature ranged from 200 to 300 seconds, depending on the particular component.

5.1 STAGE 1 - BASIC DESIGN CONCEPTS AND PRELIMINARY LAYOUTS

5.1.1 Basic Design Concepts

The basic design concept utilized was a thermal insulating layer of ceramic material over a supporting metal substructure. The ceramic was of sufficient thickness to prevent the metal substructure from exceeding its temperature limit.

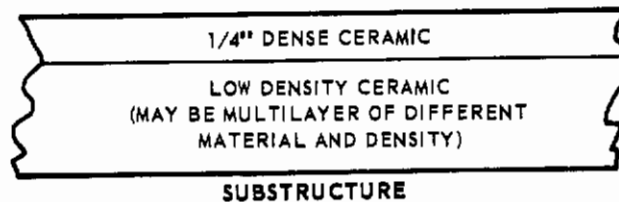
The three basic concepts presented below were an attempt to stratify the ceramic materials into a composite in which their desirable qualities were effectively utilized and their inherent handicaps minimized.

TABLE XXIV - ENVIRONMENTAL CONDITIONS

Description of Components	Thermal Environment*			Dynamic Environment					
	Maximum Surface Temperature (°F)	Avg. Surface Heating Rate (°F/Sec)	Max. Surface Heating Rate (°F/Sec)	Acoustic		Random Vibration		Dynamic Pressure @ Max. Temp. (psf)	Maximum Dynamic Pressure (psf)
				Level (db)	Frequency (cps)	Max. Load (grms)	Frequency (cps)		
3.0 Inch radius leading edge	3400	14	30	155	15 - 9600	6.41	20 - 2000	185	320
1.5 Inch radius leading edge	4000	20	42	155	15 - 9600	6.41	20 - 2000	260	330
6.0 Inch radius nose cap	5000	18	30	155	15 - 9600	6.41	20 - 2000	115	204

* @ Stagnation point

5.1.1.1 Dense Ceramic Tile Over Low Density Ceramic - Figure 87 shows the concept in which relatively dense sintered ceramic tile formed the outer surface and covered a layer of low density foamed ceramic. The dense ceramic was used on the outer surface because it has shown generally greater resistance to thermal shock, surface spalling, and erosion. The low density ceramic was more susceptible to cracking under rapid heating, but was a more efficient thermal insulator and enabled a lower overall composite density. The dense ceramic surface tile appreciably reduced the heating rate at the low density strata, and suitable thicknesses of one or more low density materials were used to maintain acceptable substructure temperatures.



MATERIALS CONSIDERED

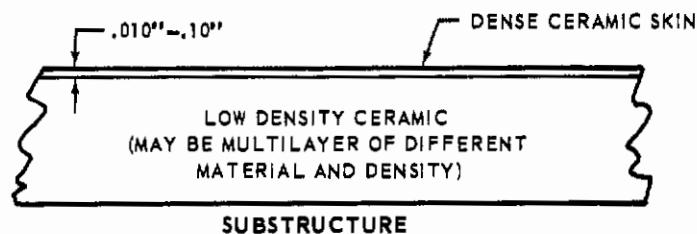
DENSE CERAMIC		LOW DENSITY CERAMIC	
	DENSITY (LB/FT ³)		DENSITY (LB/FT ³)
a) SINTERED ThO ₂	510	a) SINTERED ThO ₂ FOAM	125
b) SINTERED ZrO ₂	269	b) CHEMICALLY BONDED ThO ₂ FOAM	250
c) SINTERED AL ₂ O ₃	200	c) SINTERED ZrO ₂ FOAM	75
		d) CHEMICALLY BONDED ZrO ₂ FOAM	110
		e) SINTERED AL ₂ O ₃ FOAM	30
		f) CHEMICALLY BONDED AL ₂ O ₃ FOAM	50
		g) LOOSE GRAIN OR BUBBLES (ThO ₂ , ZrO ₂ , AL ₂ O ₃)	50-300
		h) FIBROUS BATTS (SILICA)	3 TO 10
		i) COMBINATIONS OF ABOVE	

FIGURE 87- DESIGN CONCEPT OF DENSE CERAMIC TILE COVERING ON A VARIABLE DENSITY CERAMIC

The low density ceramic could be used in a pre-fired or sintered form, or in a chemically bonded form that could be cast and cured in place. The sintered form has greater strength and dimensional stability, but the hardness and the brittle nature of the material complicates fabrication and assembly. The castable form requires special members that entrap and reinforce the castable body.

A variation of this basic concept was produced by substituting loose ceramic bubbles or fibrous insulation for the low density ceramic layer. These materials are more efficient insulators and have lower densities than the foamed ceramics; however, these loose or fibrous materials tend to shrink (sinter) at high temperatures. In addition, the loose materials require provisions for their containment and the fibrous batting requires non-abrading restraints to fix it in the desired location.

5.1.1.2 Dense Ceramic Skin Over Low Density Ceramic - The design concept illustrated in Figure 88 was one in which a low density ceramic material was faced with an integral dense ceramic skin. The dense ceramic was either chemically bonded or sintered to the low density material to improve surface strength, smoothness, and crack resistance.

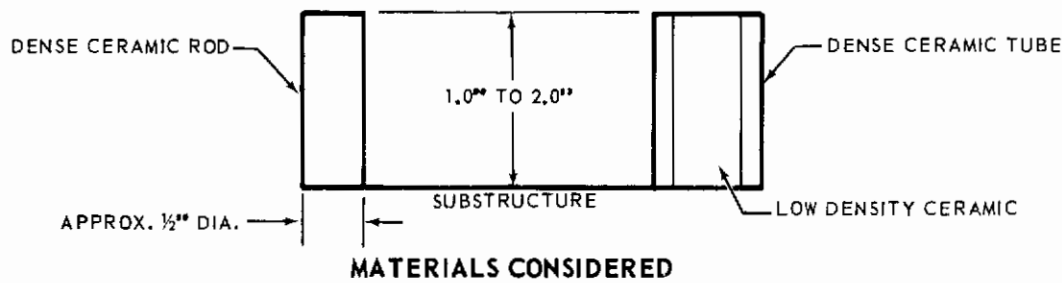


MATERIALS CONSIDERED

DENSE CERAMIC	DENSITY (LB/FT ³)	LOW DENSITY CERAMIC	DENSITY (LB/FT ³)
a) CHEMICALLY BONDED ThO ₂	510	a) SINTERED ThO ₂ FOAM	125
b) SINTERED ThO ₂	510	b) CHEMICALLY BONDED ThO ₂ FOAM	250
c) CHEMICALLY BONDED ZrO ₂	269	c) SINTERED ZrO ₂ FOAM	75
d) CHEMICALLY BONDED AL ₂ O ₃	200	d) CHEMICALLY BONDED ZrO ₂ FOAM	110
		e) SINTERED AL ₂ O ₃ FOAM	30
		f) CHEMICALLY BONDED AL ₂ O ₃ FOAM	50
		g) LOOSE GRAIN OR BUBBLES (ThO ₂ , ZrO ₂ , AL ₂ O ₃)	50-300
		h) FIBROUS BATTS (SILICA)	3 TO 10
		i) COMBINATIONS OF ABOVE	

FIGURE 88-DESIGN CONCEPT OF SKINNED LOW DENSITY CERAMIC

5.1.1.3 Small Dense Ceramic Modules - The third basic concept, shown in Figure 89, was a build-up of relatively small dense ceramic tubes or rods to form the ceramic shield. This concept was particularly suited to a nose cap component where extremely high temperatures produced severe three-dimensional thermal gradients. The individual small module, because of the size of its exposed face, essentially eliminated the effects of thermal gradients except in the thickness dimension. One of the problem areas in this concept was the attachment of the numerous small modules to the substructure.



DENSE CERAMIC		LOW DENSITY CERAMIC	
	DENSITY (LB/FT ³)		DENSITY (LB/FT ³)
SINTERED ThO ₂	510	a) SINTERED ThO ₂	125
		b) CHEMICALLY BONDED ThO ₂	250
		c) SINTERED ZrO ₂	75
		d) CHEMICALLY BONDED ZrO ₂	110

FIGURE 89 - DESIGN CONCEPT OF SMALL MODULES (RODS, TUBES)

5.1.2 Preliminary Layouts

The basic design concepts were translated into preliminary layouts, representative of the leading surface configurations. In addition, several more detailed design and fabrication approaches were established.

It was desirable to operate the substructure at the highest possible temperature to minimize the thickness of the insulating ceramic and thereby achieve the lowest weight composite for the selected long time, high temperature re-entry conditions. Also, hot structure was more compatible with the most likely adjoining wing or nose cap structure. Therefore, the use of coated columbium and molybdenum at temperatures to 2800°F and 3000°F, respectively, was emphasized. Liquid cooled substructure for the 3.0 inch radius leading edge was also investigated.

Attachment of ceramic materials to metallic substructure was accomplished primarily by mechanical means such as ceramic pins, submerged refractory metal fasteners, and entrapment of the ceramic by the substructure. Mechanical attachment was necessary to allow for differential movement between the ceramic and the metal substructure. Differential movement was appreciable because of the large difference in expansion coefficient between the ceramic and metals, the high temperature at the ceramic-metal interface, and the large thermal gradient through the ceramic. Also, because of differential expansion effects, a spring was specified for all pass-through fasteners to maintain desired clamp-up pressure and/or allow deflection of the ceramic element. The ceramics were used as relatively small modular elements to minimize thermal stresses.

The ceramic modules shown on the layouts are for illustration purposes; their actual size was determined by analyses and laboratory testing which simulated the heating rates encountered in re-entry. Aerodynamic considerations required that the faces of the modules be as smooth as possible and that the expansion gaps between the modules be kept to a minimum.

The preliminary layouts were also used to establish basic thermal models for the individual leading surfaces. Analysis of these early models roughly predicted the temperature histories of points at the face of the leading surface and within the composite structure. These predicted temperatures helped to establish the thickness of the ceramic modules and the material requirements for the substructure. In addition, the thermal gradients were used in the structural analyses of the leading surface components.

5.1.2.1 3.0 Inch Radius Leading Edge (Preliminary Layout) - Figures 90 and 91 illustrate two composite designs for a 3.0 inch radius leading edge capable of operating at a peak temperature of 3400°F. These designs incorporated liquid cooled structures.

In Figure 90, the cooling system was limited to the airfoil closure web and the leading edge substructure was cooled by radiation. This technique offered a very simple cooling system which lowered substructure temperatures to a point where conventional super alloys could be used. The leading edge ceramic shield was composed of low density, pre-fired alumina modules keyed to the substructure and attached by a relatively dense ceramic pin and metal spring retainer system. A relatively dense alumina skin covered the exposed face of the modules for surface strength, smoothness, and thermal shock resistance.

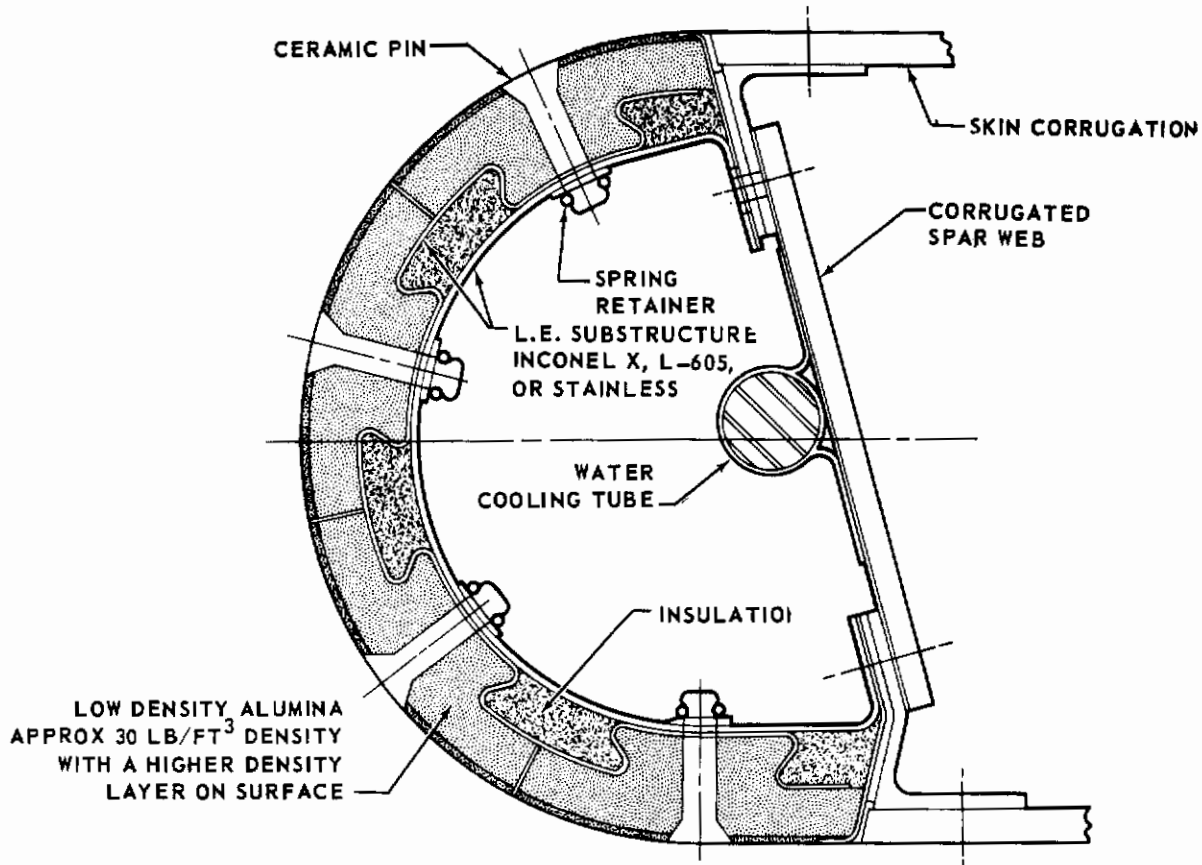


FIGURE 90 - 3.0-INCH RADIUS LEADING EDGE - SINTERED CERAMIC TILE

In Figure 91, the leading edge substructure was formed from a metal sheet which contained integral cooling tubes. Under these conditions, the substructure was kept quite cool and employed more reliable and lighter conventional metals. However, the cooling system was more complex and required more coolant than the system shown in Figure 90. The ceramic shield in this design consisted of chemically bonded low density alumina cast in place about coated molybdenum reinforcing elements which were fastened to metal hat sections built up from the integrally cooled substructure. The extent to which the ceramic shield had to be segmented in order to survive the critical thermal environment was determined by later laboratory testing.

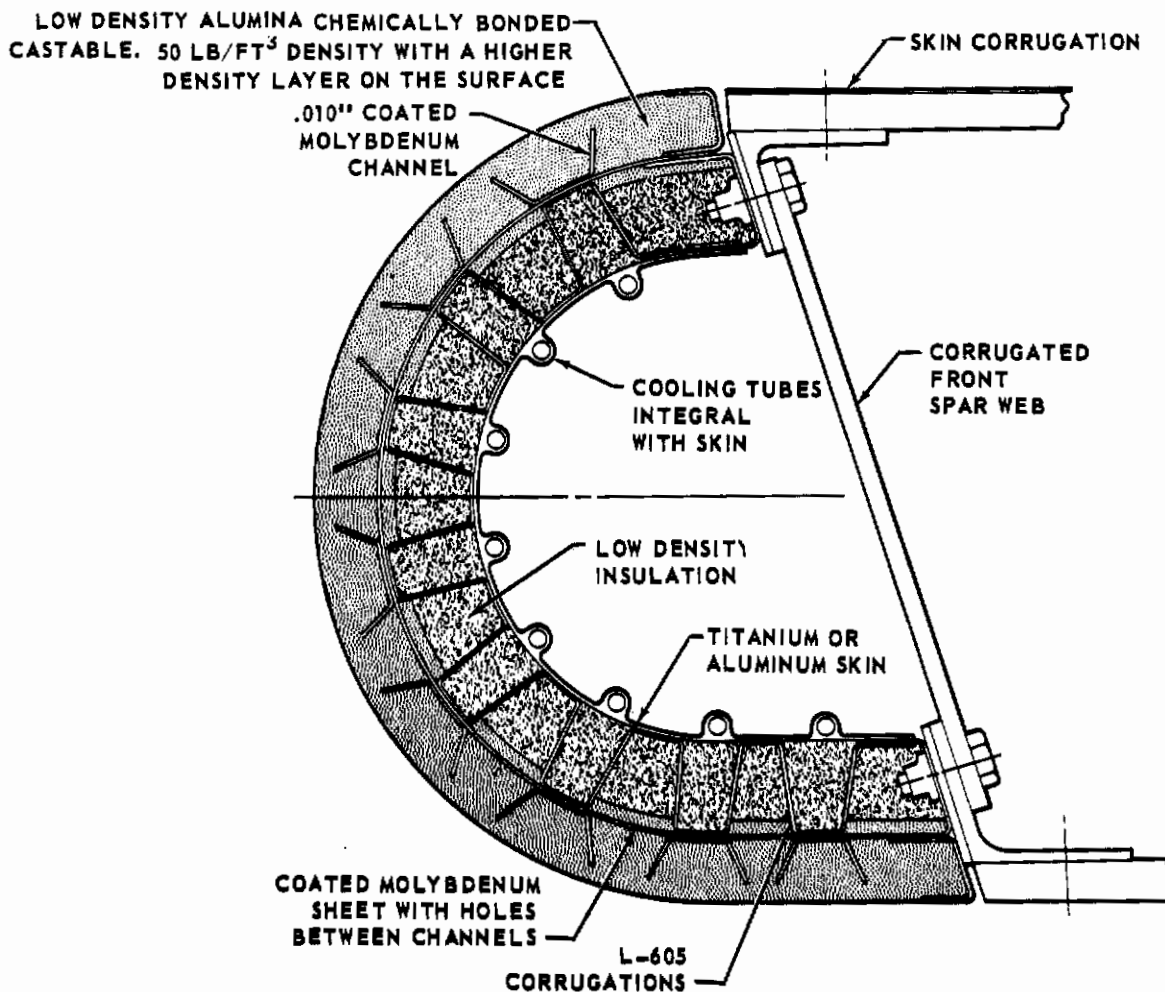


FIGURE 91 - 3.0-INCH RADIUS LEADING EDGE - REINFORCED CHEMICALLY BONDED CERAMIC

Numerous transient temperature histories were calculated during the evolution of the three leading surface components. (A discussion of the analytical techniques employed in the derivation of these temperature histories is presented in Section VI.) A temperature history related to a preliminary layout for a 3.0 inch radius leading edge is presented in Figure 92. This figure is a temperature history of a thermal model which approximates the preliminary design in Figure 90 except that no heat was dissipated from the substructure. Under these conditions, the substructure (at point 43) directly below the stagnation point reached approximately 2700°F near the end of the equilibrium glide (2300 seconds). The greatest temperature difference between the ceramic and the substructure was approximately 2000°F and occurred at the stagnation point at approximately 250 seconds. for. The greatest temperature difference between the ceramic and the substructure was approximately 2000°F and occurred at the stagnation point at approximately 250 seconds.

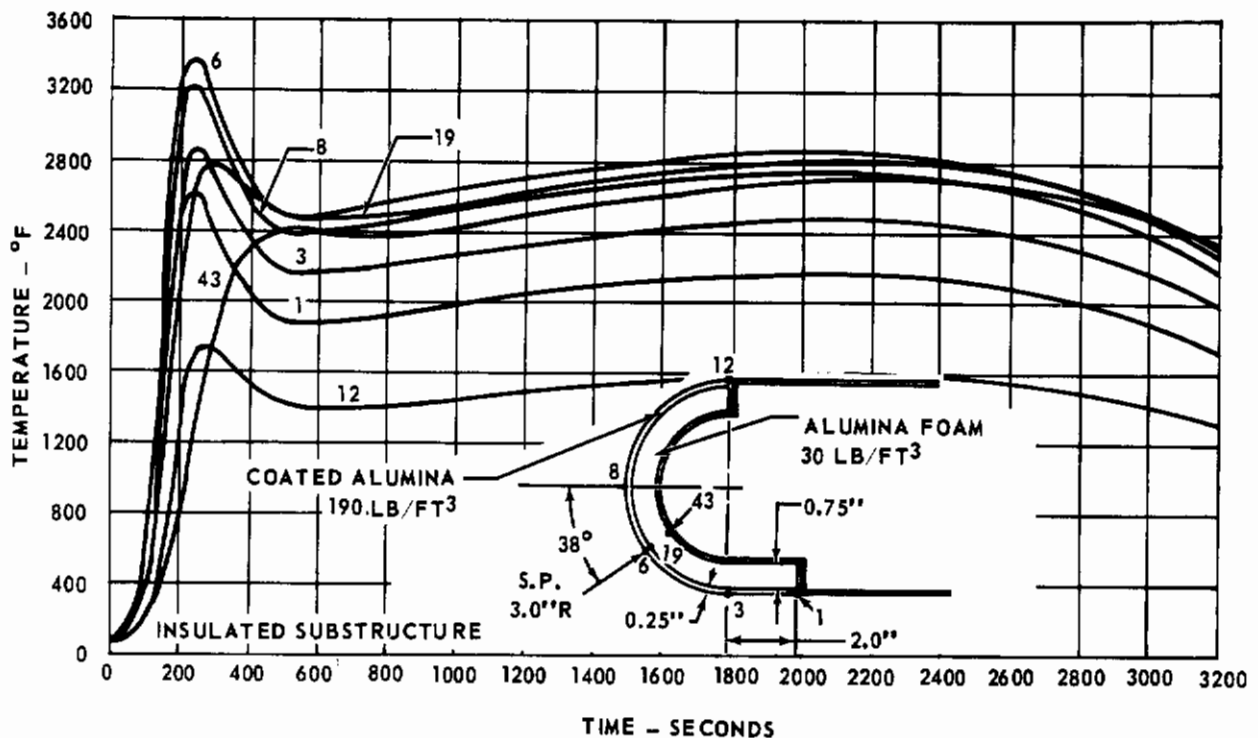


FIGURE 92 - LEADING EDGE TEMPERATURES - TRAJECTORY NO. 2

5.1.2.2 1.5 Inch Radius Leading Edge (Preliminary Layout) - Figures 93 through 95 present the three initial designs for the 1.5 inch radius, 4000°F leading edge. The design in Figure 93 utilized a pre-fired dense zirconia tile over a low density foam zirconia. The ceramic shield was divided into modules which were attached to the substructure by a system which employed relatively dense zirconia rods and metallic spring retainers.

Figure 94 illustrates a reinforced chemically bonded low density zirconia design. The reinforcing elements were restricted to zones which did not exceed 3000°F and the low density chemically bonded zirconia was cast in place around the coated molybdenum reinforcements.

The design in Figure 95 was predicated on the fact that a large non-linear thermal gradient is the fundamental cause of thermal stress failure. The multiple layer design results in reduced gradients for each body in the composite. Pre-fired layers would have to be machined to shape and would be difficult to fit while chemically bonded material, although not as strong, could be cast in place. A burnt out separator material would be used to eliminate any knitting between the casted layers.

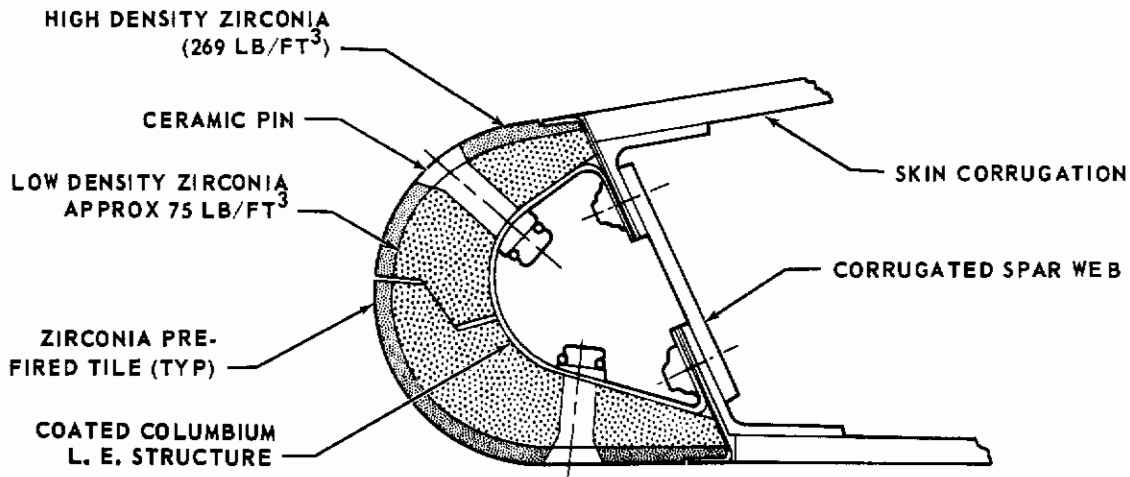


FIGURE 93 - 1.5-INCH RADIUS LEADING EDGE-SINTERED CERAMIC TILE

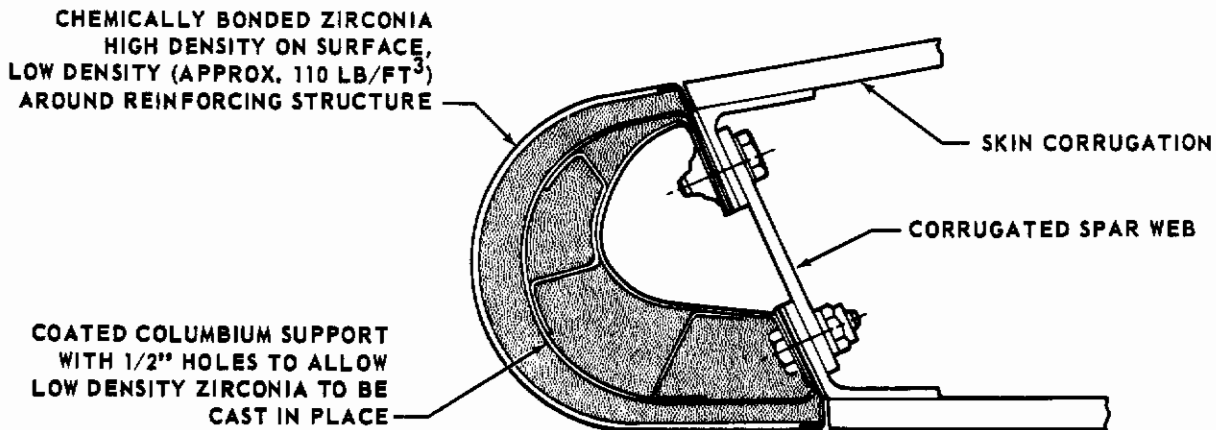


FIGURE 94 - 1.5-INCH RADIUS LEADING EDGE - REINFORCED CHEMICALLY BONDED CERAMIC

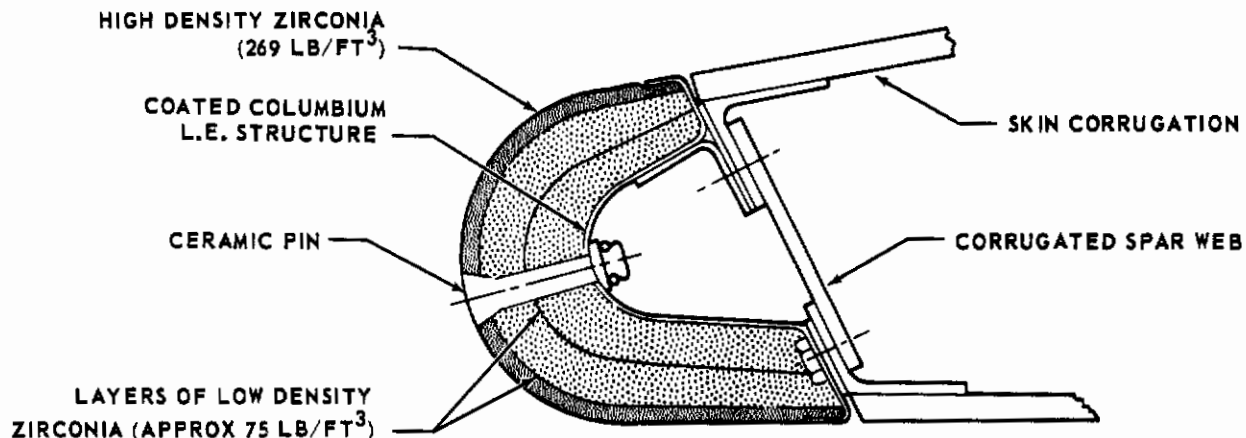


FIGURE 95 - 1.5-INCH RADIUS LEADING EDGE - CERAMIC LAYER

A transient temperature history of a thermal model (see Section VI for thermal analyses) developed in conjunction with the 1.5 inch radius leading edge layouts is presented in Figure 96. The thermal study indicated that a point on the insulated substructure (58), shielded by 1.0 inch of zirconia, reached a peak temperature of 2700°F after 2200 seconds of re-entry. This temperature level was entirely within the capabilities of a coated molybdenum substructure. A more severe problem uncovered by the temperature/time study was the temperature gradient imposed on the ceramic shield. The outer face at the stagnation point (6) at 200 seconds attained a temperature of 3800°F while the temperature at the interior face (58) was approximately 400°F. This 3400°F temperature gradient created a severe thermal stress situation and a sizable thermal expansion difference between the ceramic and the substructure.

5.1.2.3 6.0 Inch Radius Nose Cap (Preliminary Layout) - The preliminary layouts for a 6.0 inch radius nose cap capable of 5000°F are presented in Figures 97 and 98.

Figure 97 illustrates the small dense module concept applied in two forms to a nose cap configuration. In the right half of this figure, the design consisted of dense thoria rods attached to a retaining dome. Each rod had a plug protruding from one end which fit into a hole on the retaining dome. The rod was then retained by flame spraying a ceramic material around the portion protruding through the dome, thereby trapping the rod on the dome. In the left half of Figure 97, the design utilized dense thoria tubes instead of rods. Each tube had a shoulder at its base and was held on the dome by a perforated retainer which fit over the shoulder. In both designs, a chemically bonded low density thoria was packed into the spaces between the tubes or rods. The tube design resulted in the lower composite density due to the greater volume of low density material.

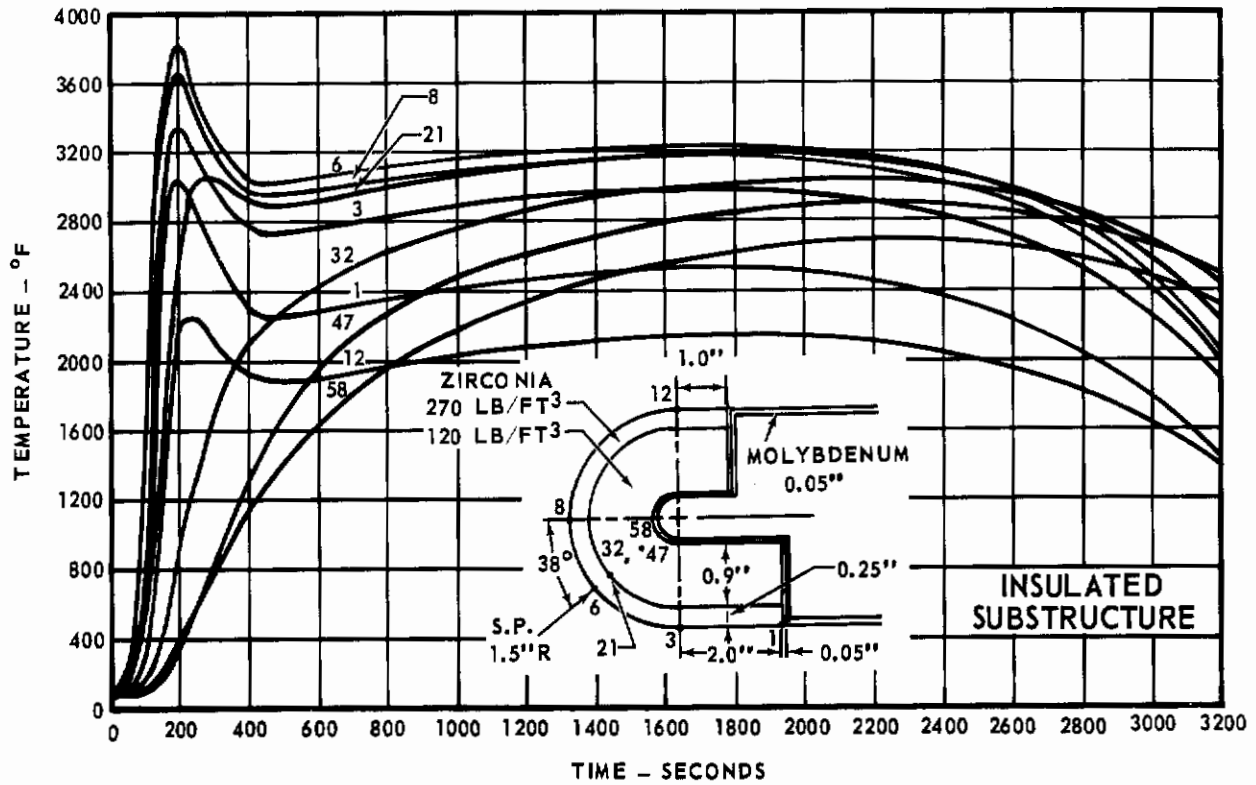


FIGURE 96 - LEADING EDGE TEMPERATURES - TRAJECTORY NO. 1

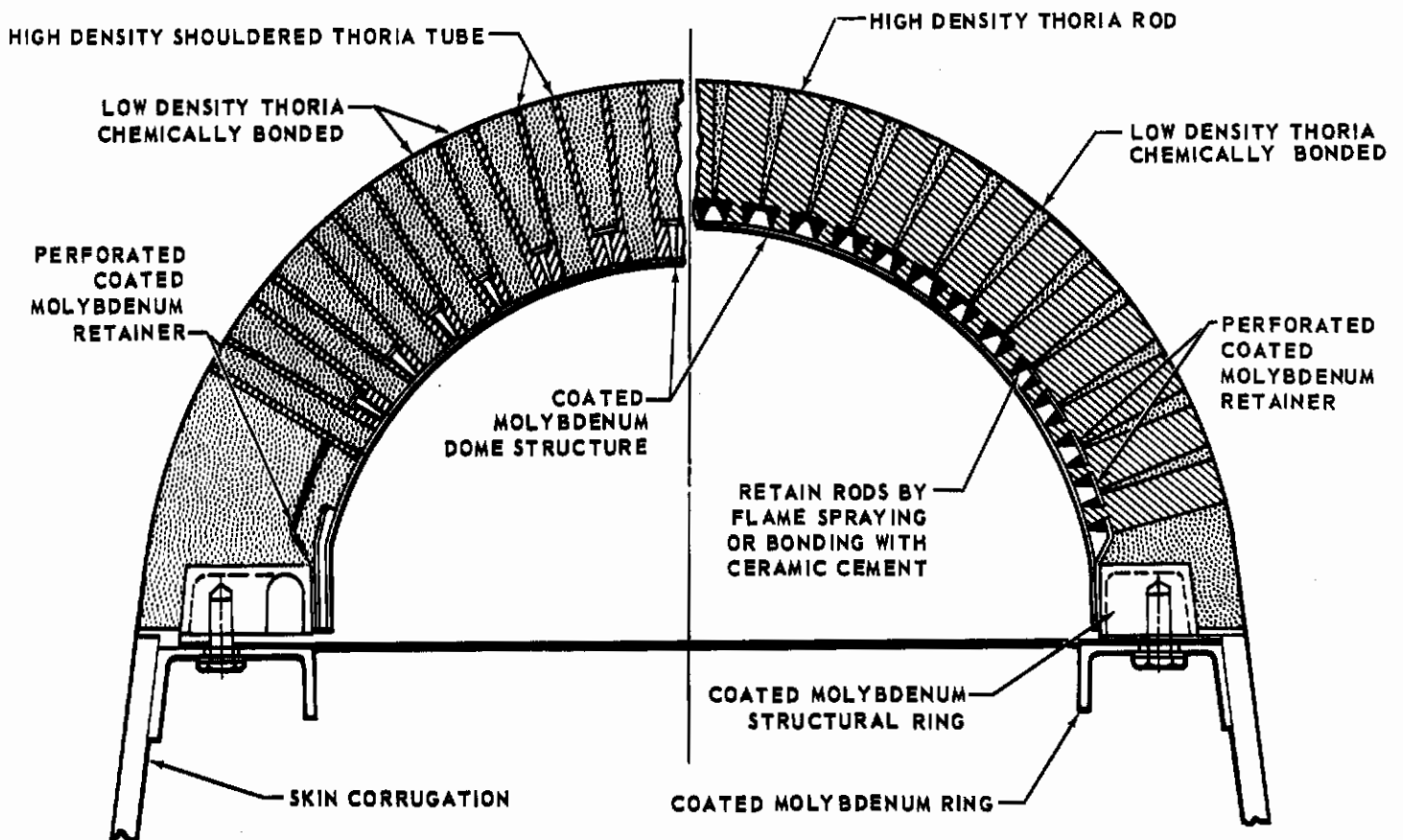


FIGURE 97 - 6.0-INCH RADIUS NOSE CAP - SMALL MODULES - TWO DESIGNS

Figure 98 shows a nose cap construction which used relatively large modules to simplify the attachment problem. However, the enlarged module increased the risk of thermal shock failure. To reduce the density, cavities were bored into the dense thoria modules and filled with chemically bonded low density thoria.

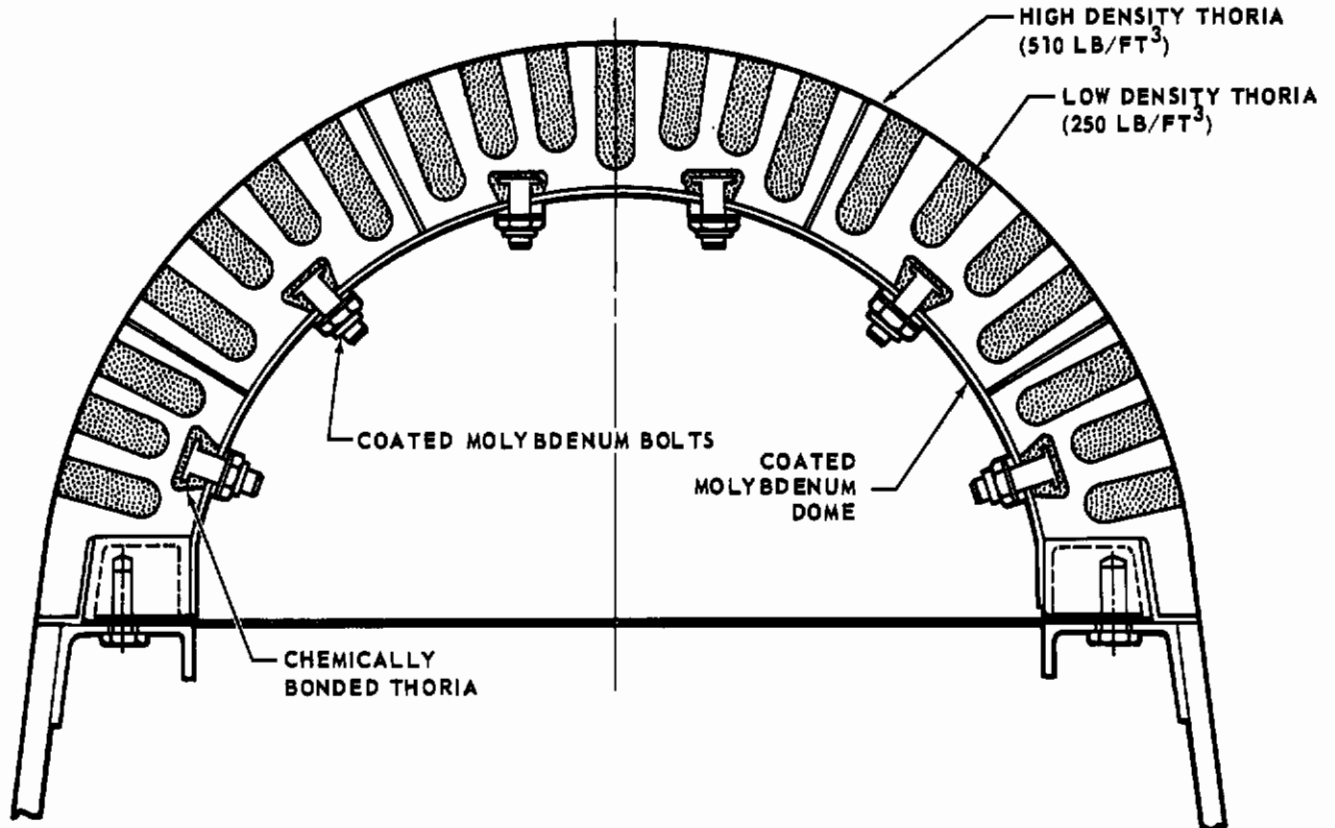


FIGURE 98 6.0-INCH RADIUS NOSE CAP - LARGE MODULE, VARIABLE DENSITY

Figure 99 presents a temperature history for a thermal model which approximated the nose cap designs depicted in the preliminary layouts. The temperature/time study indicated that a 2.35 inch depth of thoria was required at the stagnation point to limit the temperature on the underlying structure (point 96) to a maximum of 2700°F. The study also revealed the severity of the thermal gradient through the thickness of the ceramic shield and the gradient across the face of the cap. After 300 seconds of re-entry, the outer surface at the stagnation point (point 1) peaked at approximately 5200°F; the underlying inner face (point 96) reached approximately 1200°F; and the edges of the outer face (point 80) peaked at approximately 3000°F. Therefore, a 4000°F temperature gradient through the thickness, and a 2200°F gradient across the face of the cap existed.

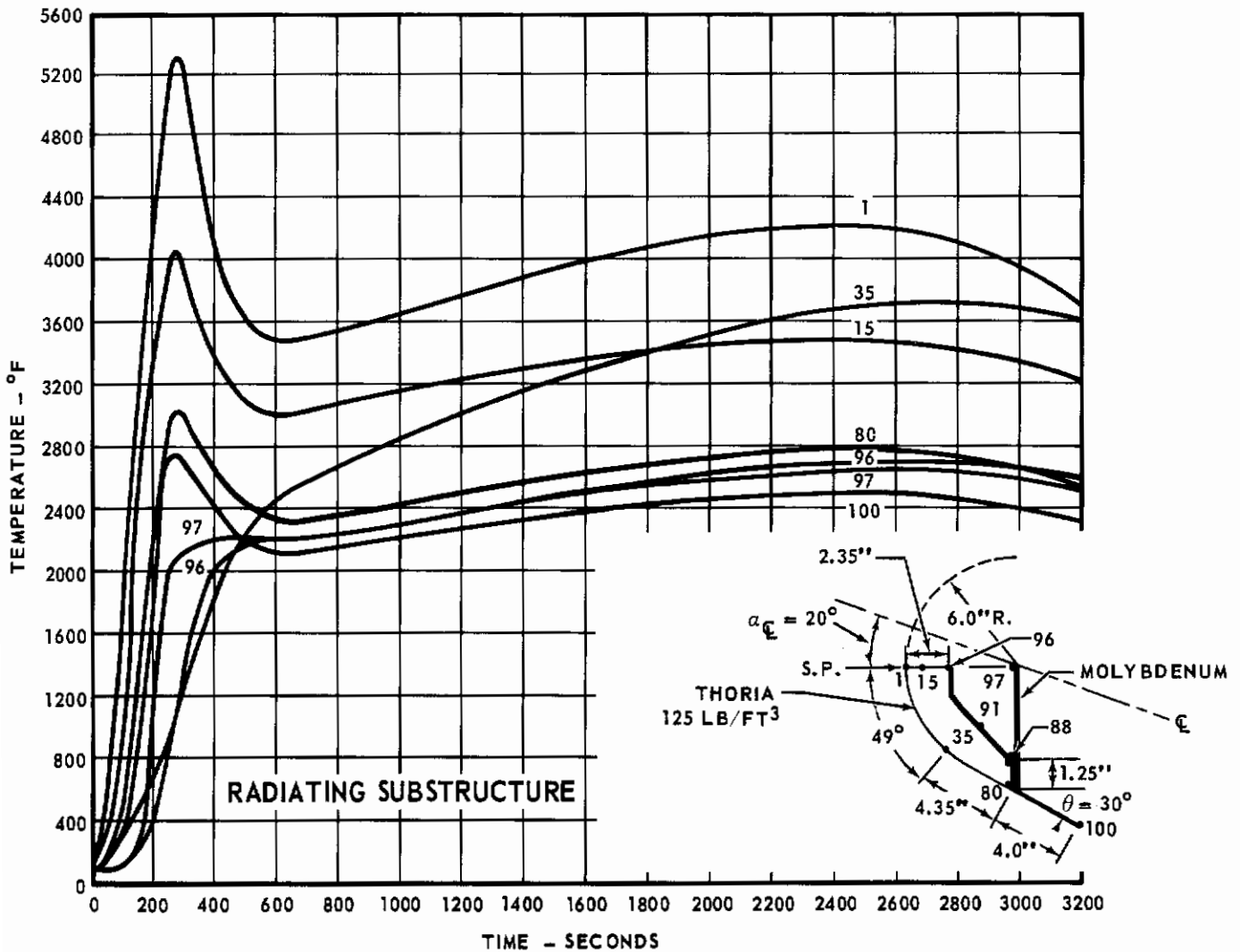


FIGURE 99 - NOSE CAP TEMPERATURES - TRAJECTORY NO. 3

5.2 STAGE 2 SUBSCALE DESIGN, FABRICATION, AND TESTING

Several designs for each full scale component under study were suggested by the basic design concepts, preliminary layouts, and initial thermal analyses. Thermal analysis helped to establish the kind of ceramic, depth of ceramic phase, and substructure metals required by the expected environment of each leading surface component. However, thermal analyses could only offer broad guidelines for other pertinent design decisions. Data were very limited on the mechanical and thermal properties of the numerous types of ceramic bodies possible. This limited property information and the lack of a rigorous analytical treatment for the thermal shock phenomenon hampered the establishment of size limits for the ceramic elements.

Under these circumstances, a test program was undertaken to develop a reliable design for each of the three full scale components. Subscale specimens of the several designs suggested for each component were fabricated and tested to their design environmental conditions. Test results formed the basis for selecting the most promising designs and provided a guide for subsequent improvements to either the design or the ceramic materials.

In general, the subscale specimens consisted of single modules which served as building blocks in a full scale component or of several elements fashioned after a representative cross section of a full scale component. The subscales, however, were built on flat substructures to expedite fabrication and testing. The flat test specimens offered a reasonable facsimile of a critical sector in a given leading surface; and the testing of these specimens produced credible data for selecting and verifying the more outstanding designs, materials, and fabrication methods.

Each subscale was subjected, in order, to a vibration test, acoustical test, and thermal test. The vibration and acoustical tests simulated critical conditions of the launch environment and were conducted at room temperature. In the vibration test, each specimen was subjected to three separate random vibration exposures. The excitations in these runs were mutually perpendicular and their frequencies ranged from 20 to 2000 cps. The root-mean-square acceleration levels versus time in each vibration exposure is given in Figure 100.

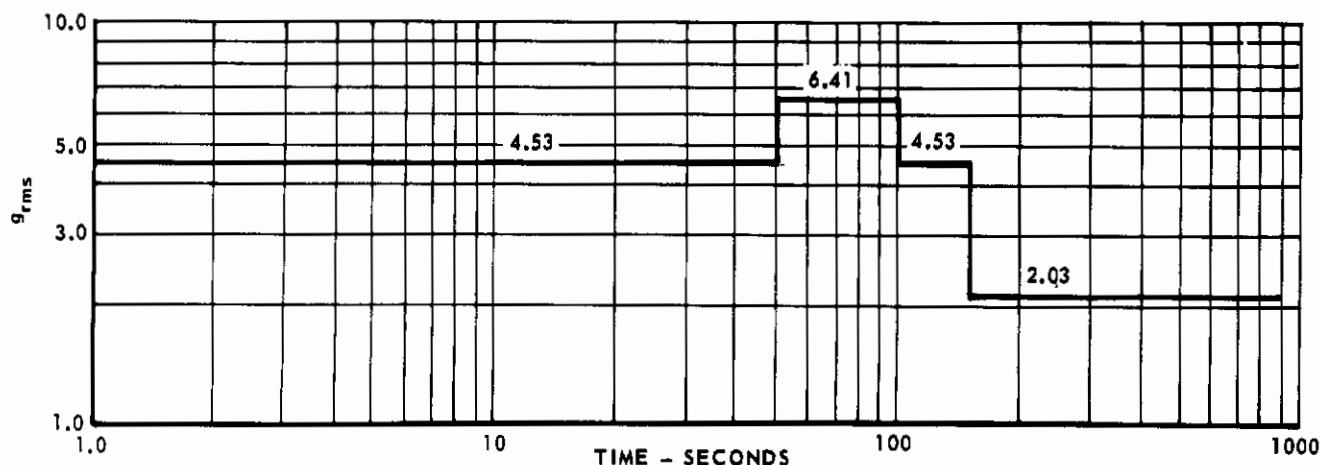


FIGURE 100 - VIBRATION INPUT LEVELS RMS ACCELERATION vs TIME

The acoustical test conducted on each specimen consisted of a five minute exposure to a sound spectrum which ranged from 15 to 9600 cps and attained an overall sound pressure level of 155 db. The acoustical excitation was normal to the top of the specimen. The thermal tests simulated the temperature-time profile which aerodynamic heating would produce at the stagnation point during re-entry. The three temperature-time profiles established for the subscale thermal tests are shown in Figure 101.

Subscale modules were heated with an oxyacetylene torch mounted on a movable cart, as shown in Figure 102. The desired surface temperature-time profile was attained by moving the torch head toward or away from the specimen. Surface temperature was measured with an optical pyrometer and the output was plotted on a T-y recorder. The 6.0 inch radius nose cap modules were tested to a peak temperature of 4300°F instead of the 5300°F shown in Figure 101, as 4300°F was the maximum temperature capability of the oxyacetylene facility. The test was valid for determining thermal shock resistance of the module as

the more severe shock was experienced during heat-up. However, the 4300°F test did not give an indication of the module's refractoriness at higher temperatures. (Test facilities and test setups are described in detail in Appendix I.)

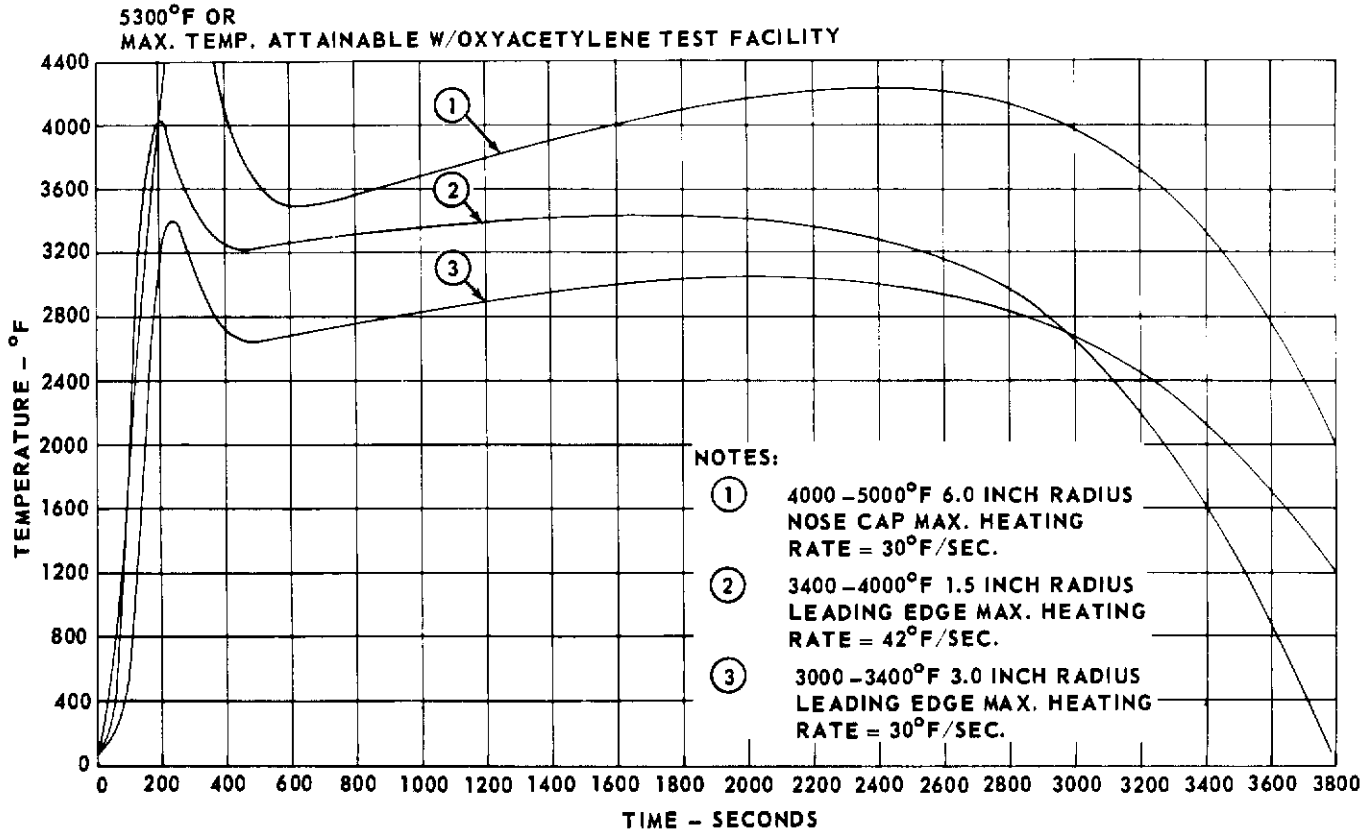


FIGURE 101 - STAGNATION POINT TEMPERATURE HISTORIES

The design concepts that were produced and tested in the subscale phase are discussed below, along with the fabrication methods for ceramic and refractory metal parts and the selection of design concepts for full scale development.

Generally, the major design considerations for each subscale specimen were as follows:

- (a) Ceramic elements kept small.
- (b) Expansion joints required.
- (c) Utilized attachments which induced minimum stress in ceramic modules.
- (d) Spring washers desired for differential movement.
- (e) Stress risers in ceramics minimized.

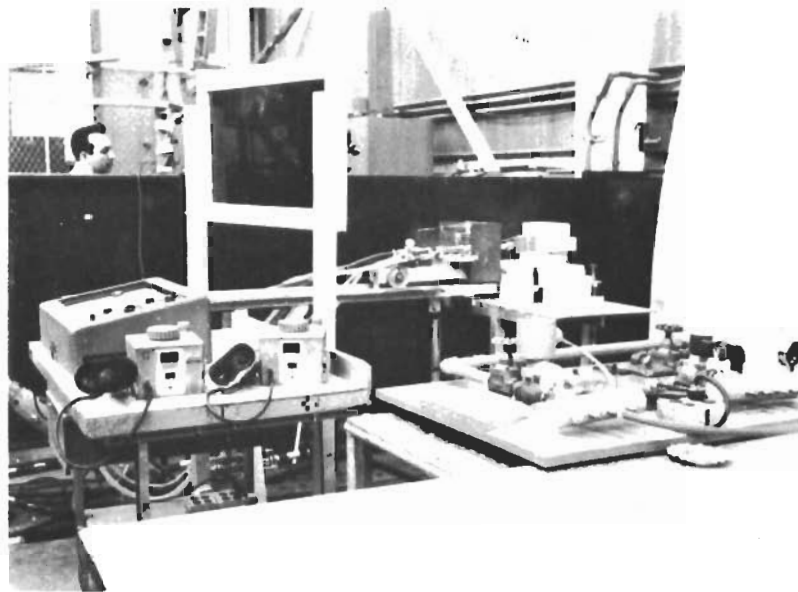


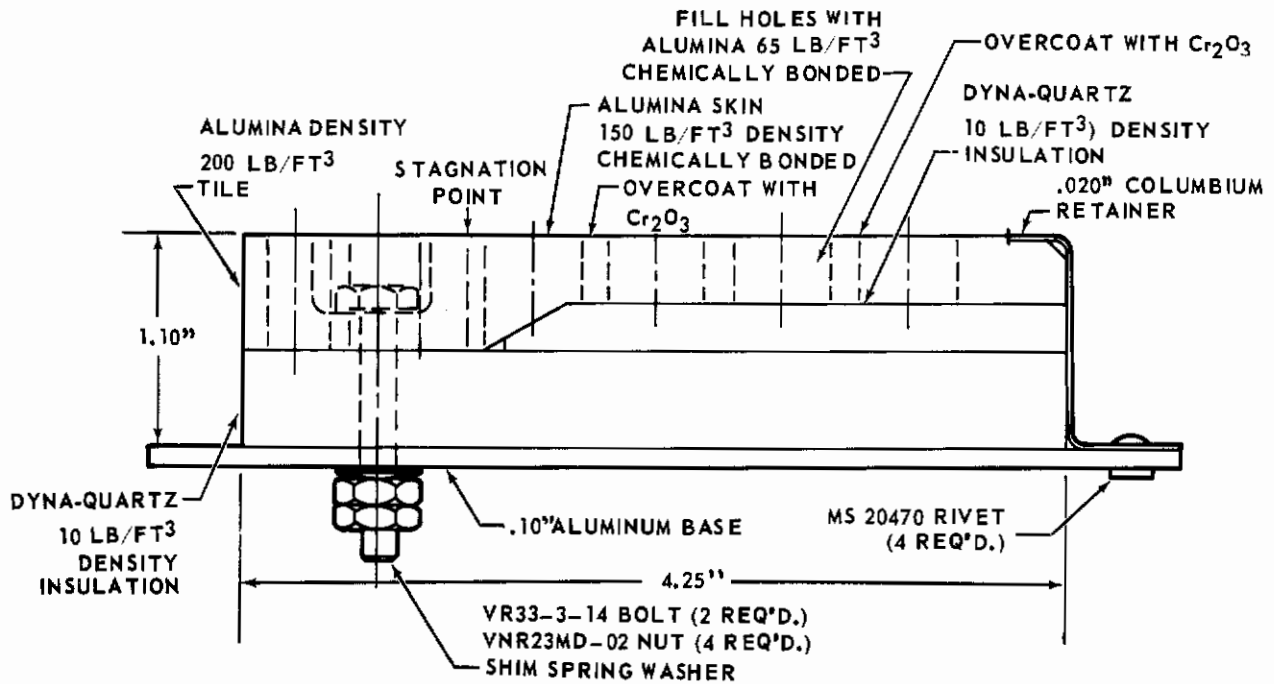
FIGURE 102 - SUBSCALE THERMAL TEST FACILITY

The use of small ceramic elements reduced the thermal stresses while the expansion joints allowed unrestricted thermal growth of the ceramic element. Utilization of spring washers permitted movement of an attachment pin or bolt, which in turn allowed the ceramic member being held to deform or move freely when thermal gradients occurred. To further minimize stress level state at attachment points, allowances were made for differential thermal movement by the use of slotted or oversize bolt holes. Also, where fasteners were in contact with the ceramic, washers were provided to minimize point loading, and low torquing forces were used. To minimize stress risers, rapid changes in ceramic cross-section were avoided where possible and all sharp corners were rounded off or filleted.

5.2.1 3.0 Inch Radius Leading Edge

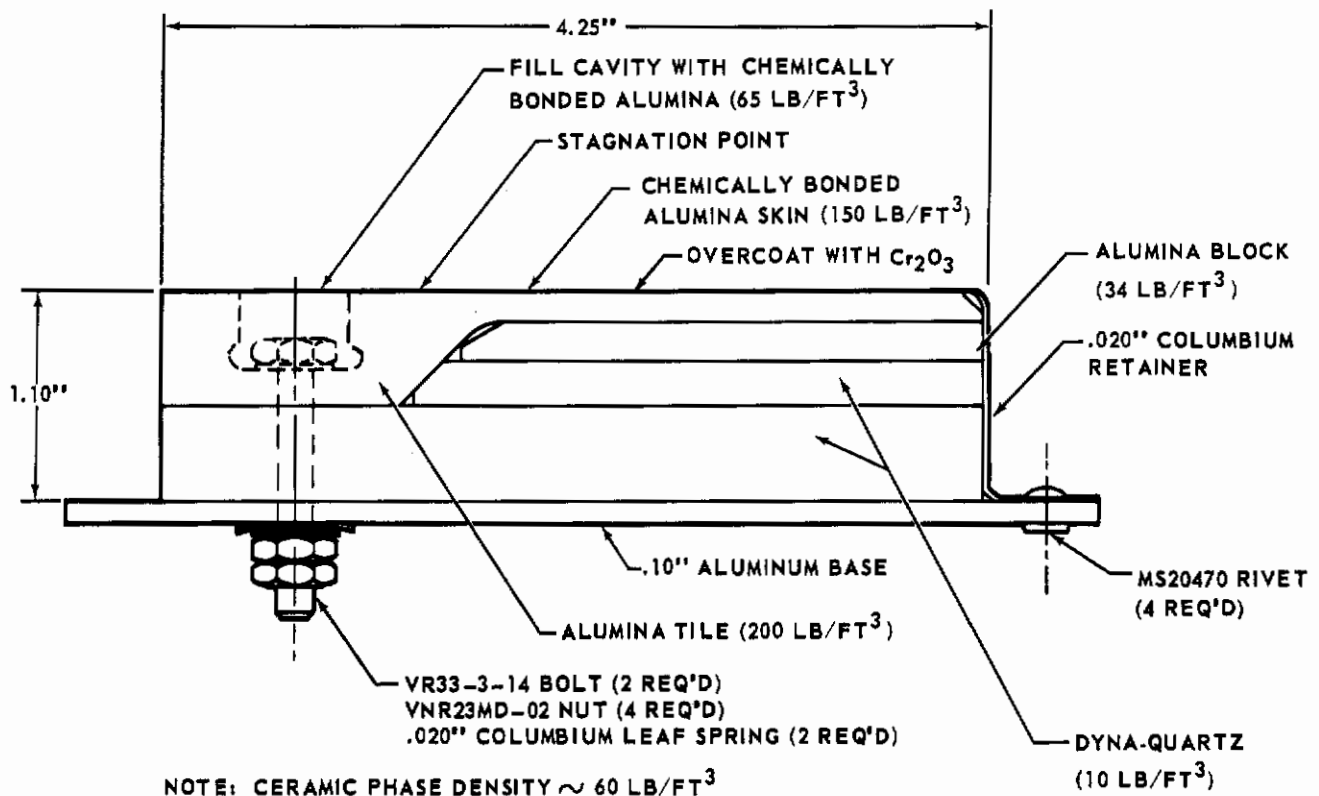
The designs for subscales representing the 3.0 inch radius leading edge were governed basically by the predicted temperatures, the geometry imposed by the 3.0 inch radius, and the 50 lb/ft³ density limit for the ceramic phase of the composite. The predicted peak temperature of 3400°F made it possible to utilize alumina, a relatively common material, at the exposed face.

5.2.1.1 Variable Density Tile Design - Figure 103 shows a subscale specimen which incorporated a variable density tile design concept. A relatively dense alumina facing tile, containing perforations filled with chemically bonded low density alumina was used to cover an insulating stratum which was made of load bearing compact silica fiberboard. The ceramic materials were positioned on the substructure by a coated columbium retainer and two spring loaded coated molybdenum bolts. The substructure on this specimen and several other specimens representing the 3.0 inch radius leading edge consisted of a water cooled aluminum plate. A cooling coil was bonded to the backface of the substructure by a high temperature, silver filled epoxy. This type of substructure was used on several specimens to evaluate water cooled substructure.



NOTE: CERAMIC PHASE DENSITY ~ 61 LB/FT³

FIGURE 103 - 3400°F TEST SPECIMEN - 3.0 INCH RADIUS LEADING EDGE - VARIABLE DENSITY TILE DESIGN



NOTE: CERAMIC PHASE DENSITY ~ 60 LB/FT³

FIGURE 104 - 3400°F TEST SPECIMEN - 3.0 INCH RADIUS LEADING EDGE VARIABLE DENSITY TILE DESIGN, REVISION A

The high density perforated tile proved to be extremely fragile and cracked either in fabrication or during assembly. These failures made it impossible to build a specimen in accordance with the design shown in Figure 103; therefore, a new subscale was designed and produced.

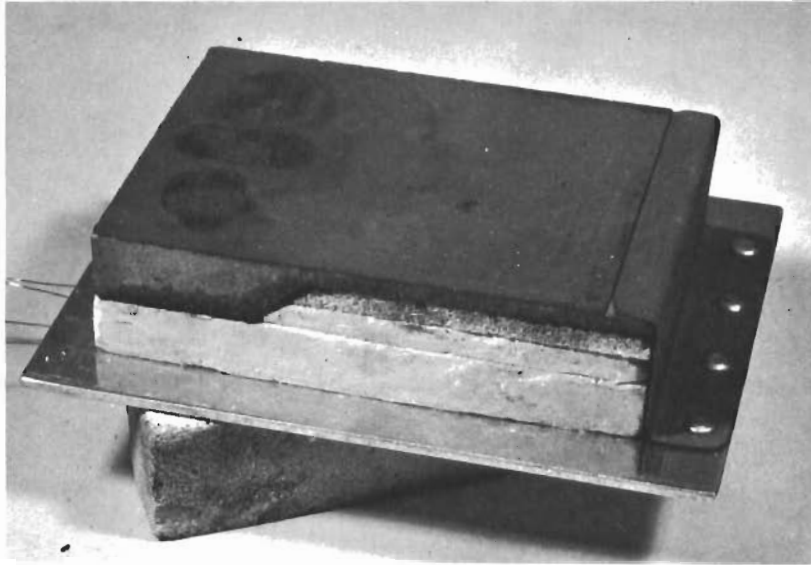
In the revised design, shown in Figure 104, a thin, solid, high density tile was used on the exposed face instead of the original perforated tile. A low density sintered alumina tile was located below the facing tile and the total depth of the two new tiles was slightly greater than the original perforated tile. The remaining features in the new design were identical to the original design except for the type of springs used on the tie-down bolts. The coated molybdenum Belleville spring washer which was used on the original group of subscale specimens had a relatively high spring constant and produced excessive loads in some specimens during thermal deformations. The Belleville washers were replaced by coated columbium leaf springs in all second and third generation designs.

The subscale built to the revised design is shown in Figure 105. The specimen was subjected to the vibration, acoustical, and thermal tests described in Section 5.2. Vibration and acoustical tests produced no visible failures, but the thermal test did affect the ceramic constituents, although not producing failures in the metallic parts.

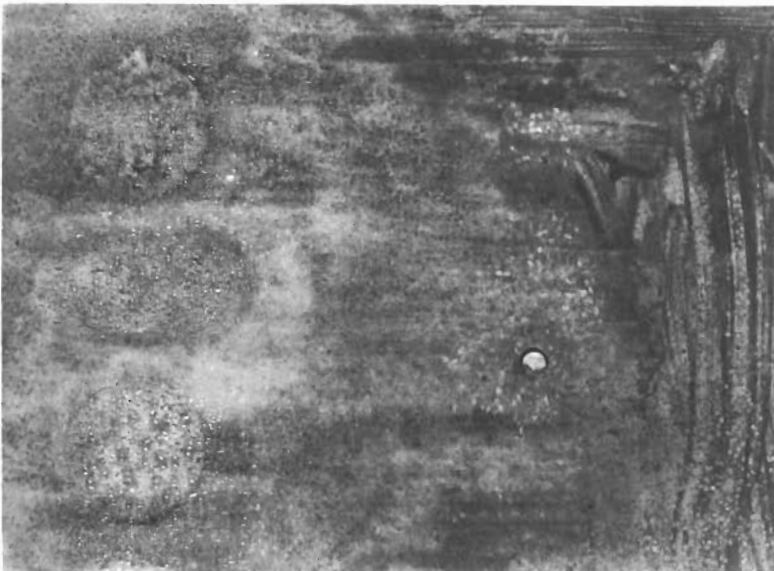
Several localized hairline cracks appeared in the facing tile and a severe fracture (visible in Figure 105) was produced in the low density tile. During thermal test, the facing tile tended to bow and assume a cylindrical shape due to the thermal gradient and expansion. The restriction of this movement by the low density tile, the thermal stresses generated in the facing tile, and the thickness of the facing tile all contributed to the cracking. The coated columbium leaf spring appeared to have functioned satisfactorily without unduly restricting thermal movement of the tile. The insulation and the low density tile suffered some shrinkage, as visible in Figure 105.

These results indicate that the facing tile did not reduce the heating rate to the level required to prevent cracking of the underlying low density tile, which was susceptible to thermal shock failure. In addition, the outer ceramic tiles did not provide sufficient thermal protection for the underlying silica fiberboard and low density tile. A greater thickness of high density tile was not felt practical from a weight or thermal shock standpoint.

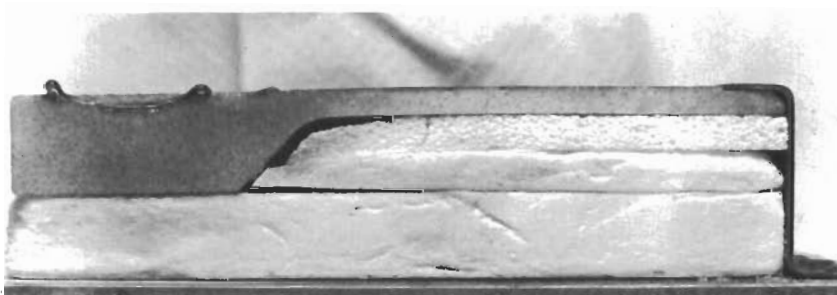
5.2.1.2 Reinforced Castable Alumina Design - A reinforced castable design concept was utilized in the subscale specimen illustrated by Figure 106. In this design, coated columbium wire screen was used for reinforcement and attachment of a cast-in-place chemically bonded alumina. The alumina was in segments separated by thermal expansion gaps. The ceramic shield was supported by coated columbium corrugations to which the coated columbium screen was resistance welded and which were filled with low density insulation. The corrugations were riveted to a structural aluminum plate which was water cooled by the system described in Section 5.2.1.1. Although water cooled substructure created a severe long term temperature gradient in the ceramic shield, the major portion of the gradient was within the nonstructural insulation.



(a) BEFORE TEST



(b) AFTER TEST,
TOP VIEW



(c) AFTER TEST,
SIDE VIEW

**FIGURE 105 - 3400°F TEST SPECIMEN - 3.0 INCH RADIUS LEADING EDGE -
VARIABLE DENSITY TILE DESIGN REVISION A (THERMAL TEST)**

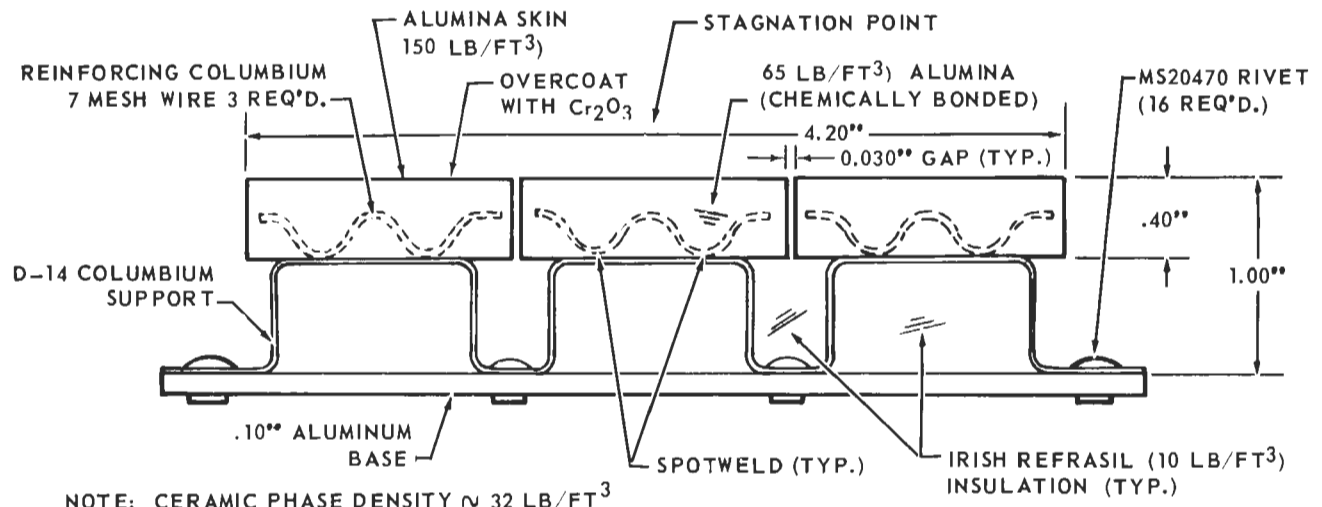


FIGURE 106 - 3400°F TEST SPECIMEN - 3.0 INCH RADIUS LEADING EDGE - REINFORCED CASTABLE ALUMINA DESIGN

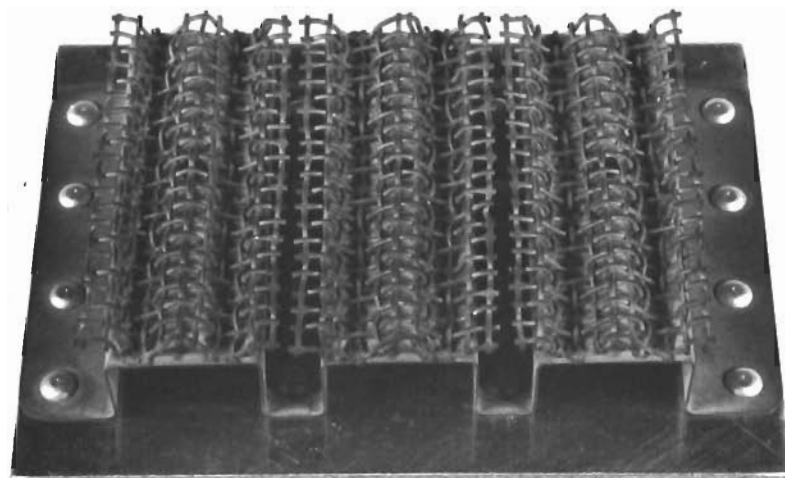
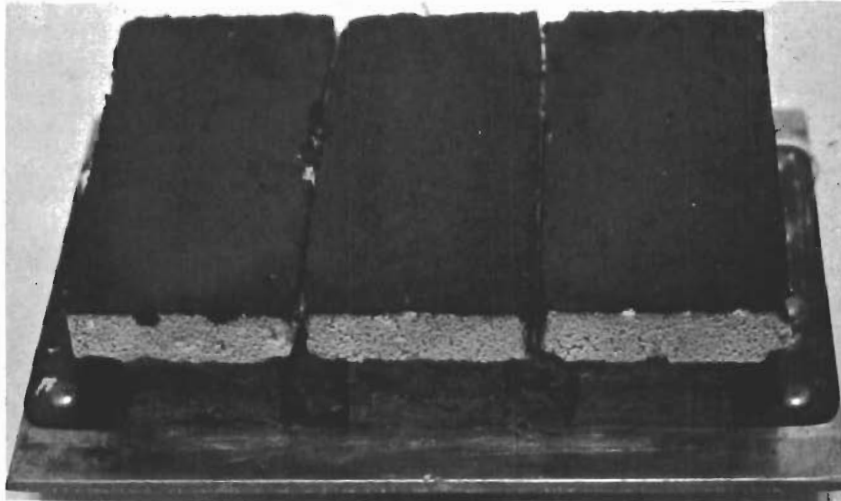
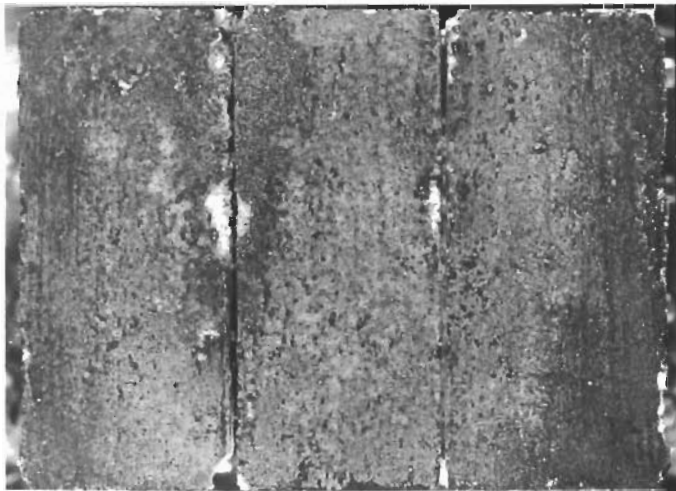


FIGURE 107 - METAL SUBASSEMBLY-3400°F TEST SPECIMEN REINFORCED CASTABLE ALUMINA DESIGN

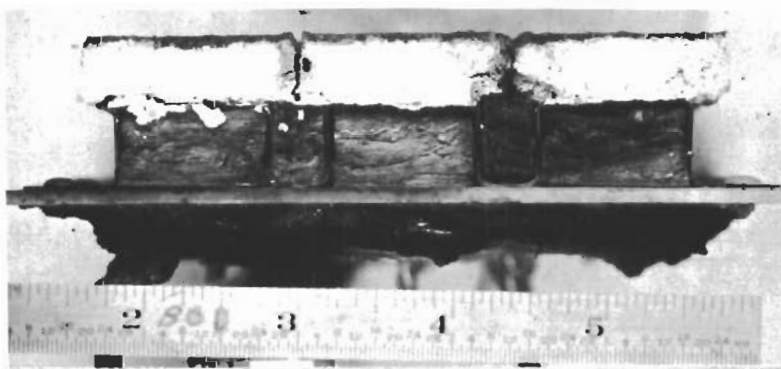
The metallic subassembly for this specimen is shown in Figure 107 and the fully assembled subscale in Figure 108. The subscale survived the vibration and acoustical tests without any detectable failures. On completion of the thermal test, the specimen appeared to be completely intact and crack-free. However, examination revealed that the chemically bonded alumina was very friable and tended to crumble in handling. In Figure 108, crumbled edges and corners are clearly visible. The particular alumina composition utilized was inherently low in strength, even before thermal test.



(a) BEFORE TEST



(b) AFTER TEST,
TOP VIEW



(c) AFTER TEST,
SIDE VIEW

**FIGURE 108 - 3400°F TEST SPECIMEN - 3.0 INCH RADIUS LEADING EDGE -
REINFORCED CASTABLE ALUMINA DESIGN (THERMAL TEST)**

A second reinforced castable specimen was built because an improved chemically bonded alumina was developed. The results of the thermal tests (Figure 64) showed a marked improvement in the strength (both before and after thermal testing) of the new ceramic body, which was again free from cracks and any signs of melting.

5.2.1.3 Tile Design - The subscale specimen shown in Figure 109 was based on a design concept which used a ceramic outer tile over low density fibrous insulation. The tile rested on compact silica fiber pads which were supported by coated columbium members attached to a water cooled aluminum substructure. This cooling system was again identical to the system described in Section 5.2.1.1. The ceramic tile was attached by two spring loaded bolts with heads trapped in ceramic filled recesses in the back of the tile. One bolt passed through a relatively tight hole in the substructure and the second passed through an enlarged hole to allow for differential thermal expansion. This enabled stress-free expansion of the ceramic tile in all directions from the tight fitting hole. The open areas between the facing tile and the substructure were filled with fibrous insulation. The metallic subassembly for this specimen is shown in Figure 110.

The specimen was subjected to the required vibration, acoustical, and thermal tests which did not produce any detectable failures. At the conclusion of the thermal test, the facing tile showed no outward signs of any defects; however, the tile was no longer securely attached to the substructure. The basic cause for the failure lay with the entrapment of the bolts in the tile. The chemically bonded ceramic had failed to fully pack around the submerged bolt heads and/or the elevated temperatures had caused some shrinkage of the castable ceramic.

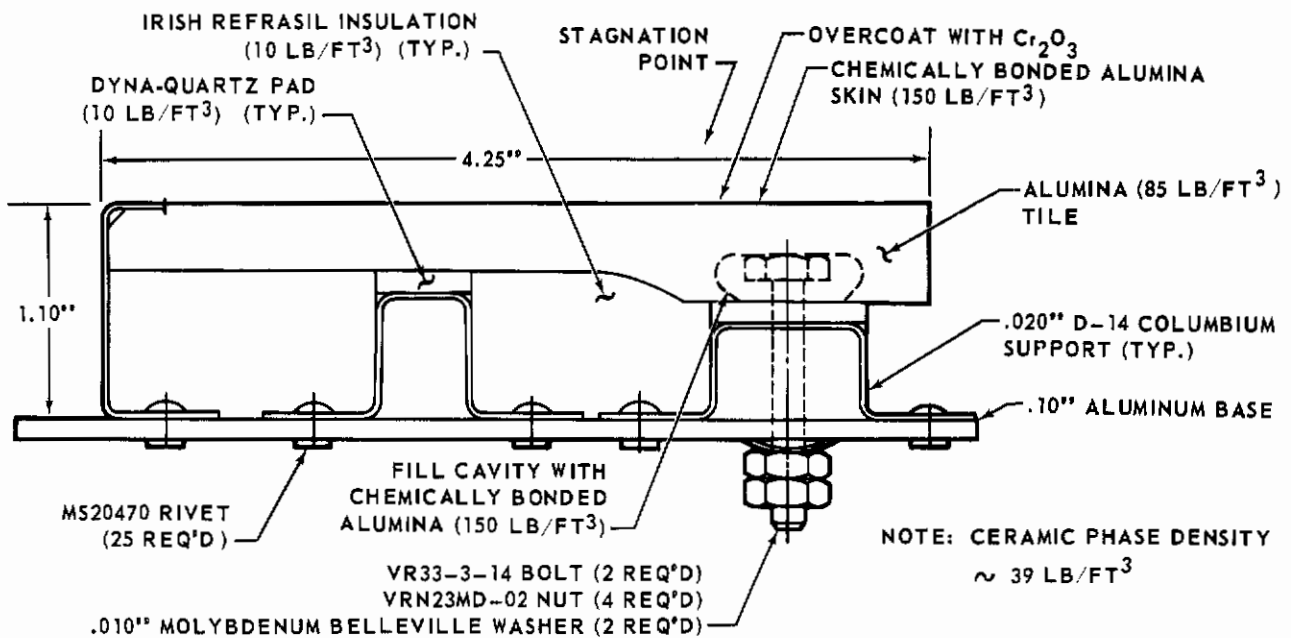


**FIGURE 109 - 3400°F TEST SPECIMEN - 3.0 INCH RADIUS
LEADING EDGE TILE DESIGN**

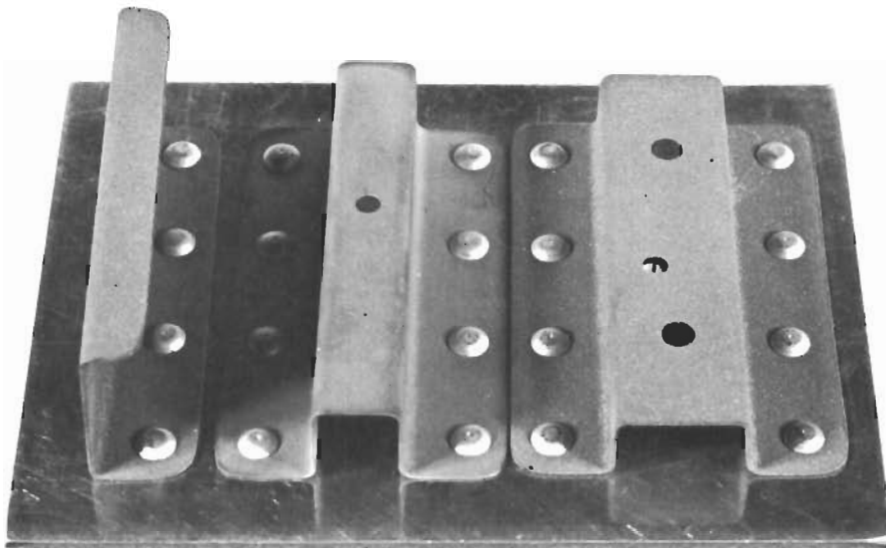


**FIGURE 110 - METAL SUBASSEMBLY - 3400°F
TEST SPECIMEN - TILE DESIGN**

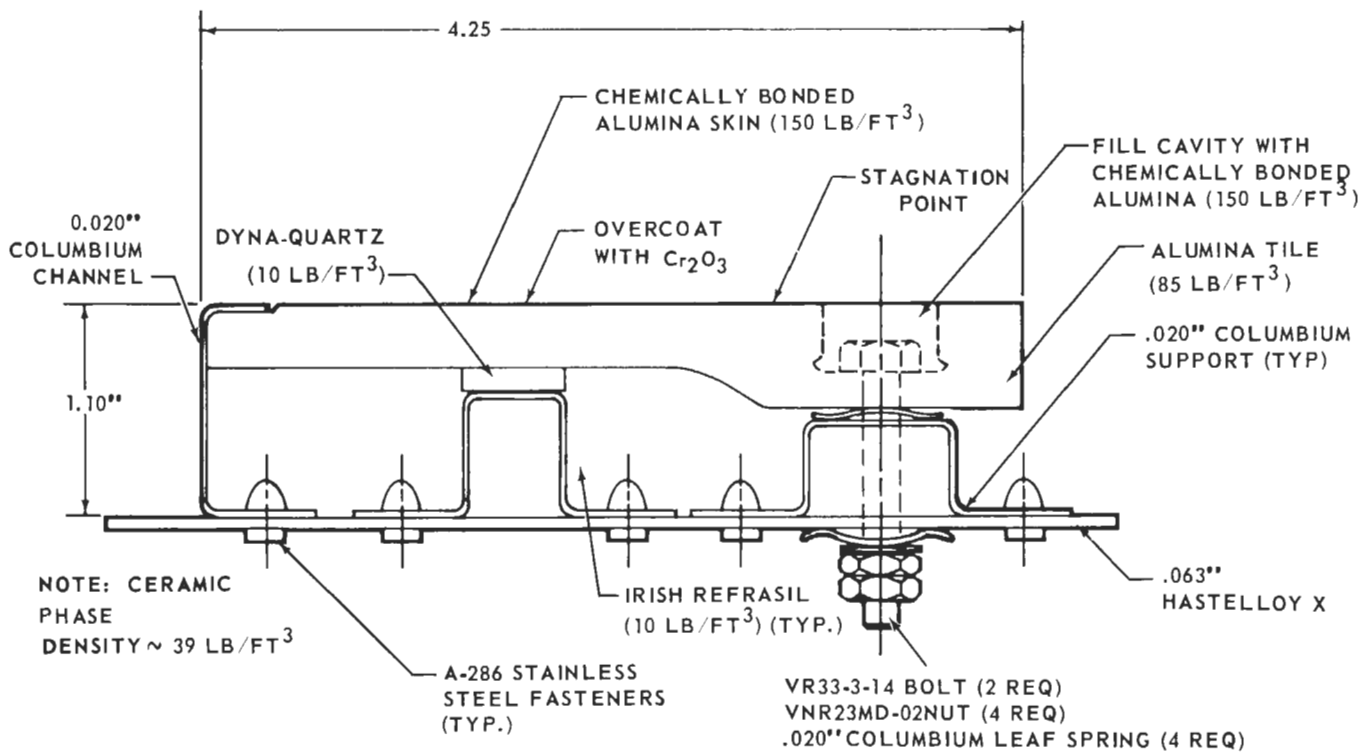


**FIGURE 111 - 3400°F TEST SPECIMEN - 3.0 INCH RADIUS
LEADING EDGE TILE DESIGN REVISION A**

The tile design was revised for the second generation specimen. In the new design shown in Figure 111, the bolts no longer acted as entrapped couplers, but clamped the tile to the substructure. The bolts passed through the tile and their heads were thermally protected by being recessed in undercut counterbored holes which were filled with chemically bonded ceramic. In addition, the Belleville spring washers were replaced by coated columbium leaf springs as discussed earlier. A columbium leaf spring also replaced the compact silica fiber pad that was located at the attaching interface. This substitution provided a more reliable elastic support for the facing tile. This second specimen also did away with the water cooled substructure in favor of a hot super-alloy substructure.

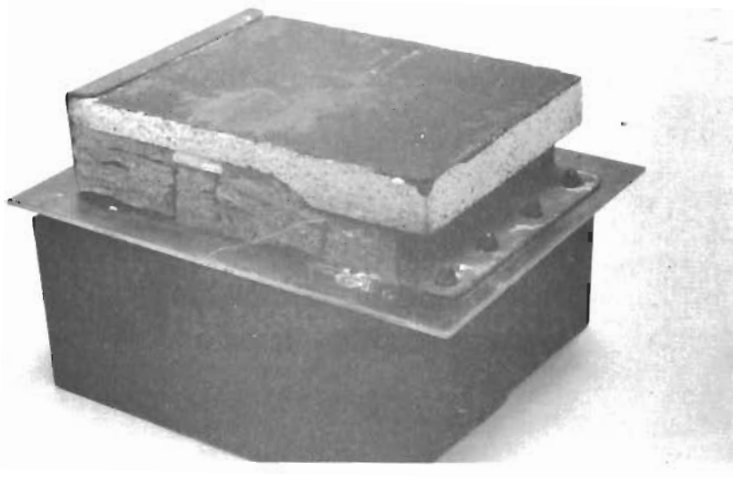
Only the thermal test was imposed on this second generation specimen. The facing tile again exhibited no cracks. However, the tile was again loose and had a very slight permanent bow (see Figure 112). The looseness this time was traced to shrinkage in the compact silica fiber pad at the midspan support. The slight permanent bow was probably due to the bolt attachment system which did not allow the tile to pivot or rotate as required when exposed to the temperature gradient.

The tile design was again modified and a third specimen built for the final group of subscales. This third design, like the second, did not employ a water cooled substructure (see Figure 113). In addition, the midspan support was eliminated and a ledge was introduced to support the free end of the facing tile. The tile attachment holes in the substructure below the columbium support were enlarged to allow the bolts to pivot more freely. For the same reason, the stroke on the attach bolts was increased by double-stacking opposing sets of leaf springs.

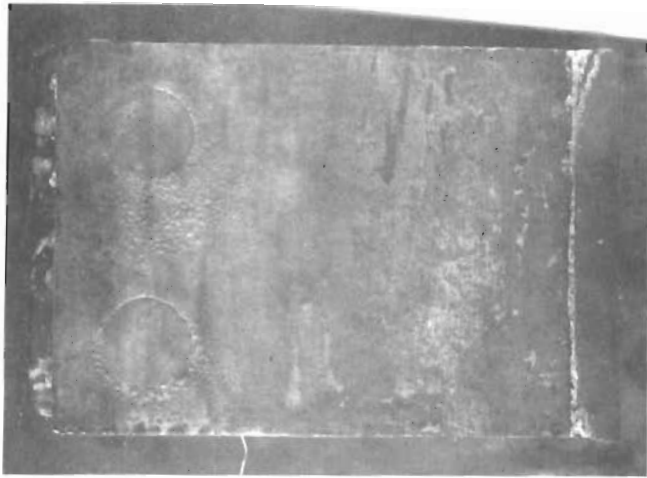
The third generation specimen was subjected to the appropriate thermal test after which the metallic parts showed no defects and the facing tile was straight, crack-free, and firmly attached. Some minor hairline cracks (shrinkage cracks) at the periphery of the potted bolts holes did appear and are visible in Figure 114. This type shrinkage cracking in the chemically bonded alumina was not unexpected and the undercuts in the potting holes trapped the chemically bonded material to assure retention.

5.2.1.4 Pin Tile Design - The subscale specimen shown in Figure 115 used a dense facing tile over a low density sintered ceramic block which was engaged with and supported by coated columbium corrugations. The corrugations were fastened to a structural aluminum plate which was water cooled. Ceramic constituents were attached to the substructure by a spring loaded dense alumina pin which extended from the face of the specimen to the backside of the substructure. The open areas of the corrugations were filled with fibrous insulation. Figure 116 shows the metallic subassembly for this specimen.

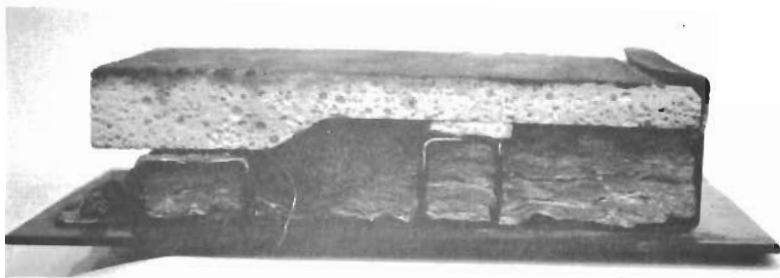
The assembly of this specimen revealed a structural weakness in the 0.25 inch diameter dense alumina pin which was spring loaded and attached by a 0.09 inch diameter molybdenum cross pin. The alumina pin broke at the hole for the cross pin because of the stress concentration and the marginal effective cross section. An interim correction was devised for all first generation pin designs. The cross pin was eliminated and attachment was achieved by casting a ceramic "head" around the pin shank protruding from the backside of the substructure.



(a) BEFORE TEST



(b) AFTER TEST,
TOP VIEW



(c) AFTER TEST,
SIDE VIEW

**FIGURE 112 - 3400°F TEST SPECIMEN - 3.0 INCH RADIUS LEADING EDGE -
TILE DESIGN - REVISION A (THERMAL TEST)**

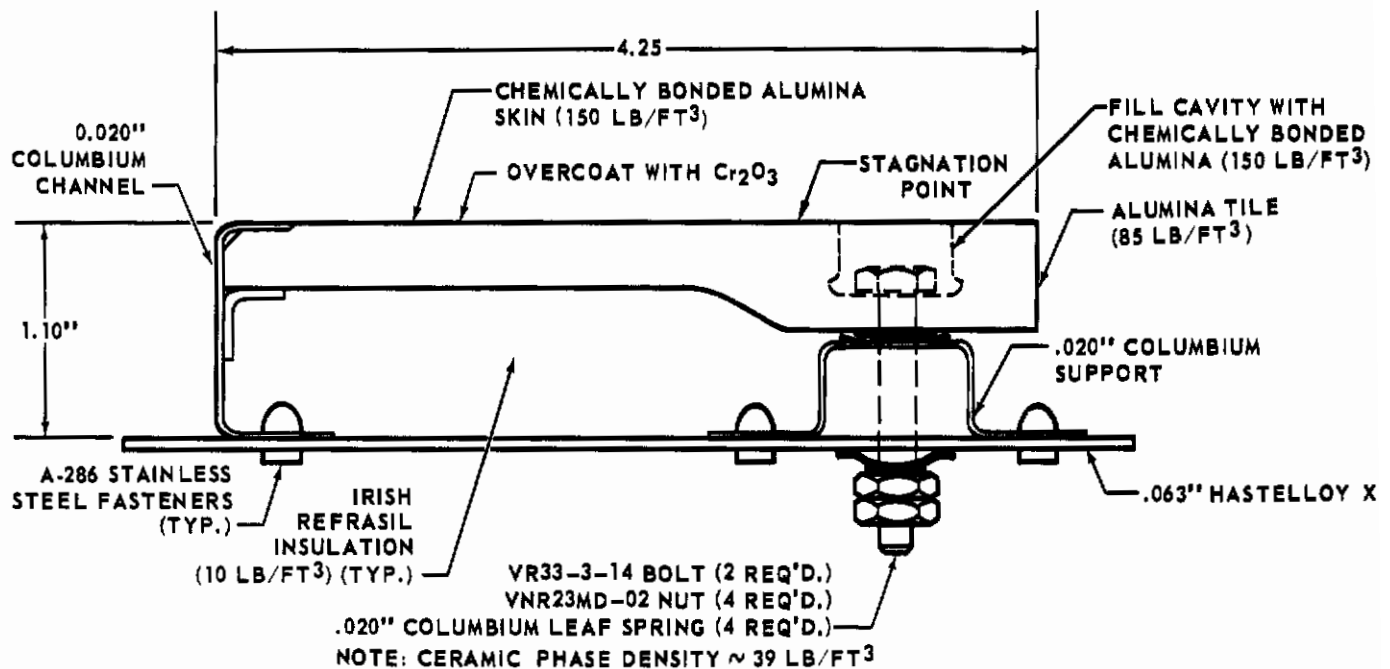
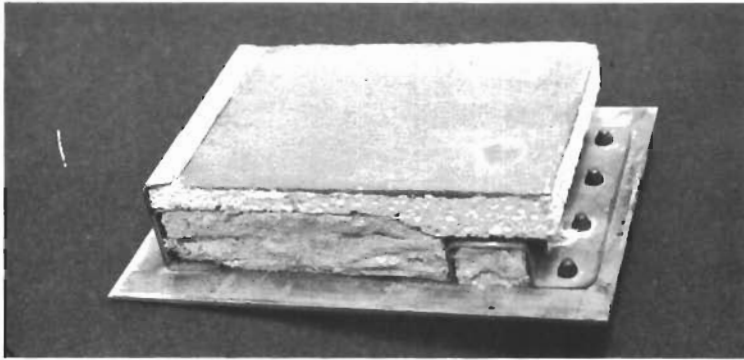


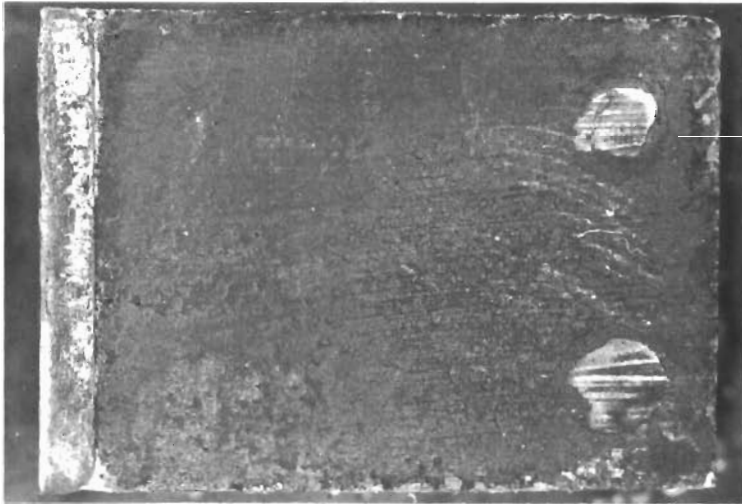
FIGURE 113 - 3400°F TEST SPECIMEN - 3.0 INCH RADIUS LEADING EDGE TILE DESIGN - REVISION B

The specimen survived the initial vibration and acoustical tests without any visible failure. However, the thermal test resulted in several cracks in the low density block and a crack in the facing tile (visible in Figure 117) that radiated from the pin hole. The tile had not separated and was still firmly attached. The cracking in the tile was probably due to the marginal thermal shock resistance of the high density alumina and the expansion restriction imposed by the pin because the Belleville washer did not permit sufficient movement of the pin. The low density block cracked due to low thermal shock resistance and the stress riser effect of the undercuts provided for attachment. The tile did break apart (see Figure 117) in the course of a follow-up vibration test, which was run to determine the severity of the crack.

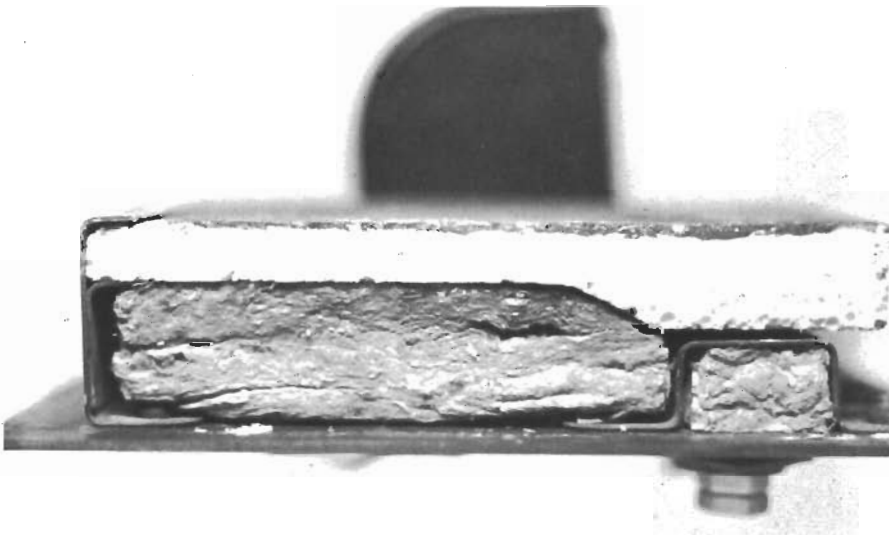
The design was revised extensively for the second generation pin-tile specimen. In the new design, shown in Figure 118, a slightly less dense and more thermal shock resistant alumina was specified for the facing tile and the thickness of the tile was increased to decrease heating rate to the low density block. The low density alumina block was disengaged from the corrugations to eliminate undercuts and thus decrease stress risers; and the former engagement area was filled with a load bearing compact silica fiberboard. The diameter of the attaching pin was enlarged to 0.375 inch to provide adequate strength, and the original Belleville spring washer was replaced by a coated columbium leaf spring. A molybdenum retainer which fitted a reverse taper at the base of the pin was used to engage the enlarged alumina pin. This system eliminated the stress concentration that occurred in the original cross pin design. In addition, the original water cooled substructure was replaced by a radiation cooled substructure.



(a) BEFORE TEST



(b) AFTER TEST,
TOP VIEW



(c) AFTER TEST,
SIDE VIEW

**FIGURE 114 - 3400°F TEST SPECIMEN - 3.0 INCH RADIUS LEADING EDGE -
TILE DESIGN, REVISION B (THERMAL TEST)**

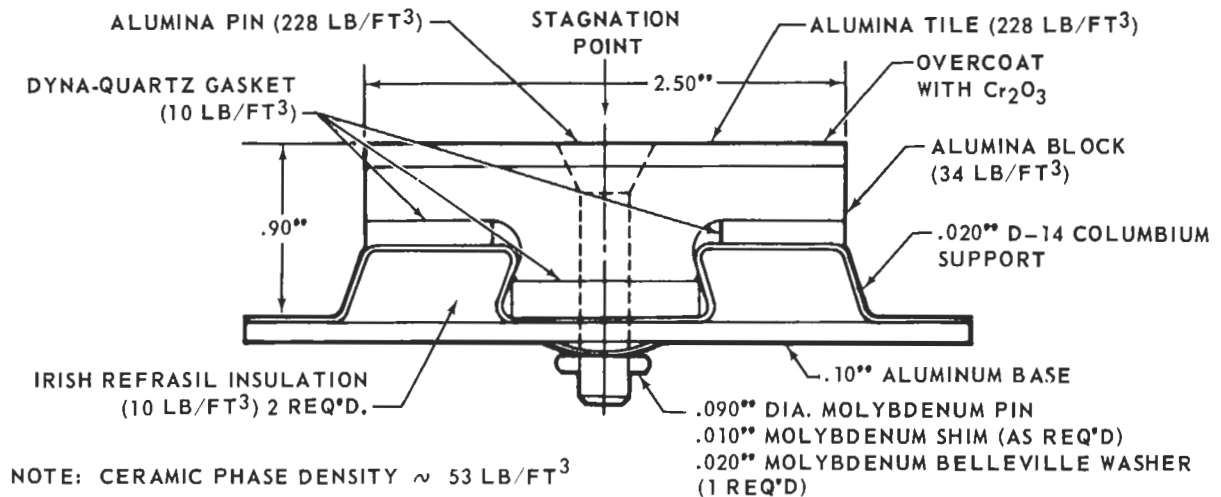
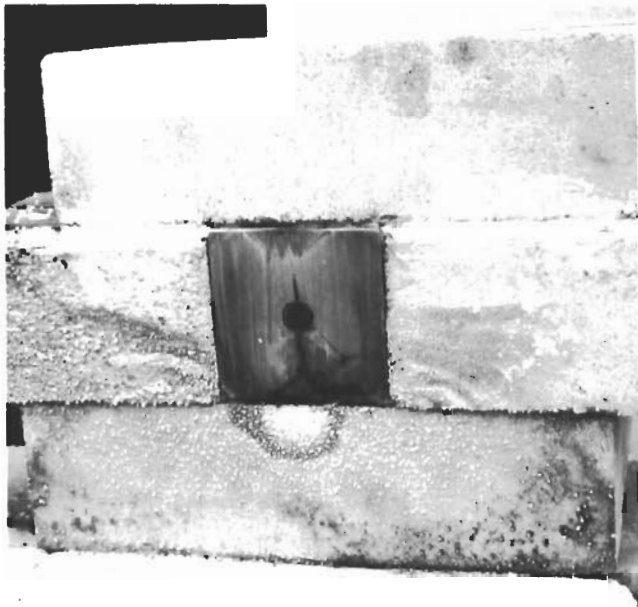


FIGURE 115 - 3400°F TEST SPECIMEN - 3.0 INCH RADIUS LEADING EDGE PIN TILE DESIGN

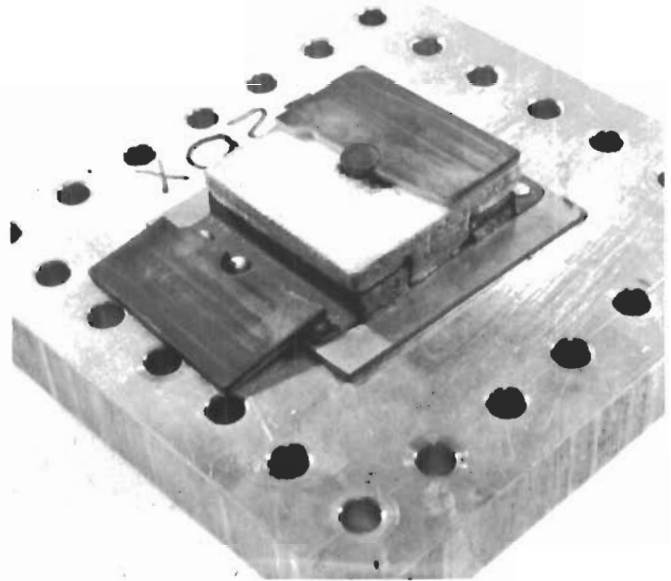


FIGURE 116 - METAL SUBASSEMBLY - 3400°F TEST SPECIMEN - PIN TILE DESIGN

The performance of the original specimen indicated that the thermal test was most critical. Accordingly, the new specimen was only subjected to the appropriate thermal test and the results are barely discernible in the views shown in Figure 119. The exposed faces of the low density block exhibited several non-traversing very fine cracks due to the low thermal shock resistance of this material. The cracks started at an edge and were confined within the immediate vicinity. The head of the pin also suffered a slight crack, which is barely distinguishable in view (b) of Figure 119. This cracking was probably due to pin material strength being insufficient to withstand the tensile loading imposed by the thermally expanding tile.



(a) AFTER THERMAL TEST



(b) VIBRATED AFTER THERMAL TEST

FIGURE 117 - 3400°F TEST SPECIMEN - 3.0 INCH RADIUS LEADING EDGE
- PIN-TILE DESIGN (TEST RESULTS)

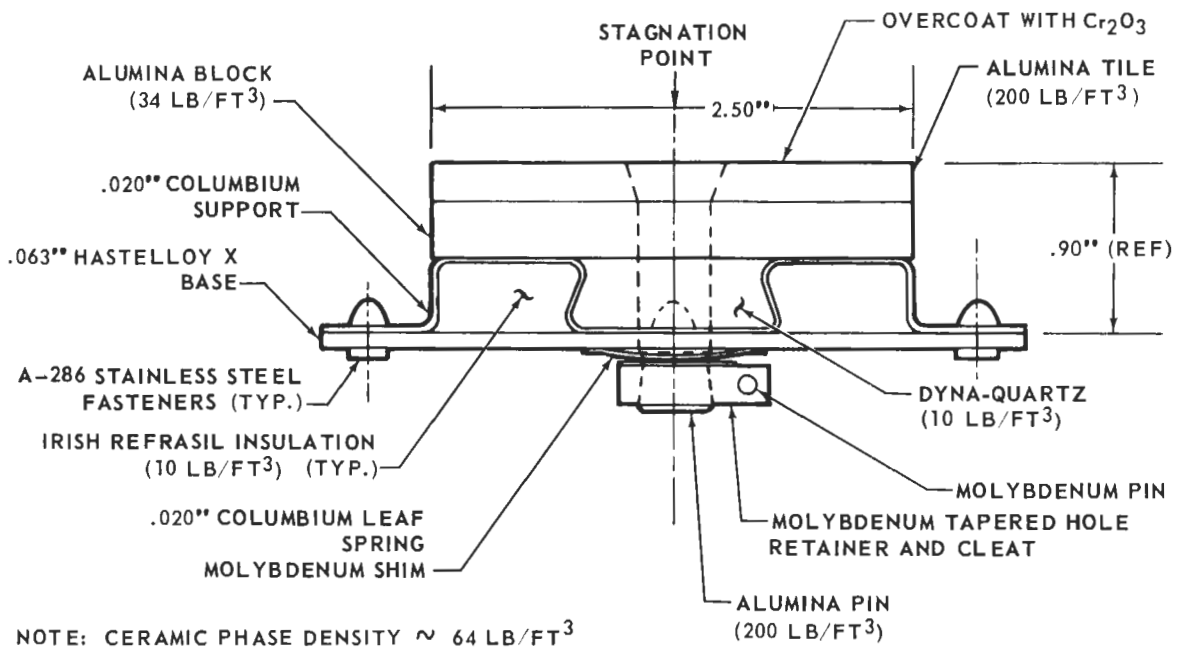
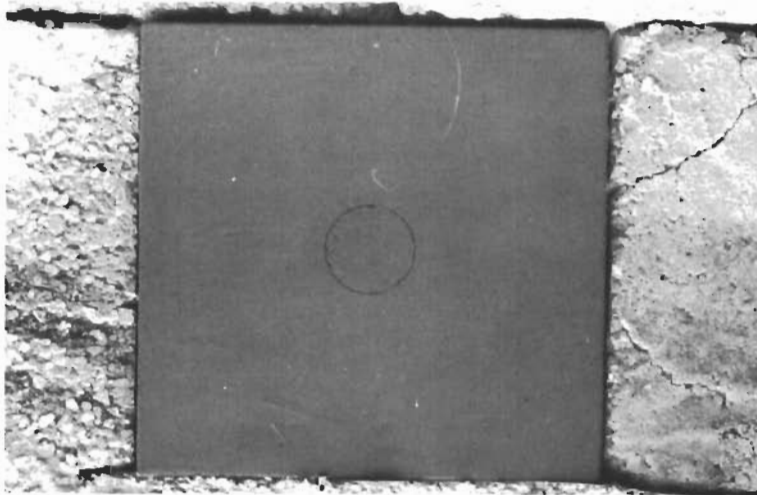
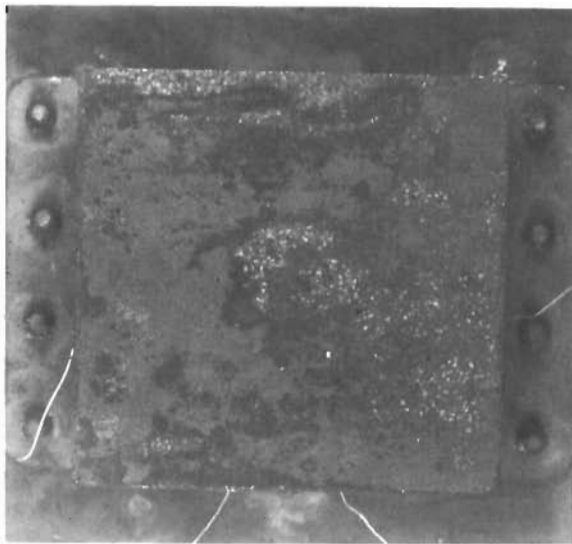


FIGURE 118 - 3400°F TEST SPECIMEN 3.0 RADIUS LEADING EDGE
PIN TILE DESIGN - REVISION A



(a) BEFORE TEST,
TOP VIEW



(b) AFTER TEST,
TOP VIEW



(c) AFTER TEST,
SIDE VIEW

**FIGURE 119 - 3400°F TEST SPECIMEN 3.0 INCH RADIUS LEADING EDGE -
PIN-TILE DESIGN - REVISION A (THERMAL TEST)**

5.2.2 1.5 Inch Radius Leading Edge

The basic design considerations for all subscales representing a 1.5 inch radius leading edge were the temperature-time profile, the 1.5 inch radius envelope, and the 120 lb/ft³ limitation on the ceramic phase density. The predicted peak temperature of 4000°F exceeded the melting point of alumina and made it necessary to use zirconia at the exposed faces. The 1.5 inch radius presented a relatively limited envelope which made it difficult to employ the very low density insulation materials. The desired ceramic phase density limitation necessitated extensive use of the low density zirconias.

5.2.2.1 Key Block Design - A key block design concept was utilized in the subscale specimen illustrated in Figure 120. In this design, two low density end blocks were trapped by coated molybdenum bolts. The substructure for all specimens had no provisions for water cooling. The high density key block of thermal shock resistant zirconia was positioned at the stagnation point where the highest heating rate occurred. The design called for a space between the sides of the key block and the end blocks to allow for the large dimensional tolerances expected. A low density chemically bonded zirconia was packed into these voids and was also used to pot the counterbored attachment holes. The entire subscale was surfaced with a high density chemically bonded zirconia. The coated molybdenum subassembly for the specimen is shown in Figure 121.

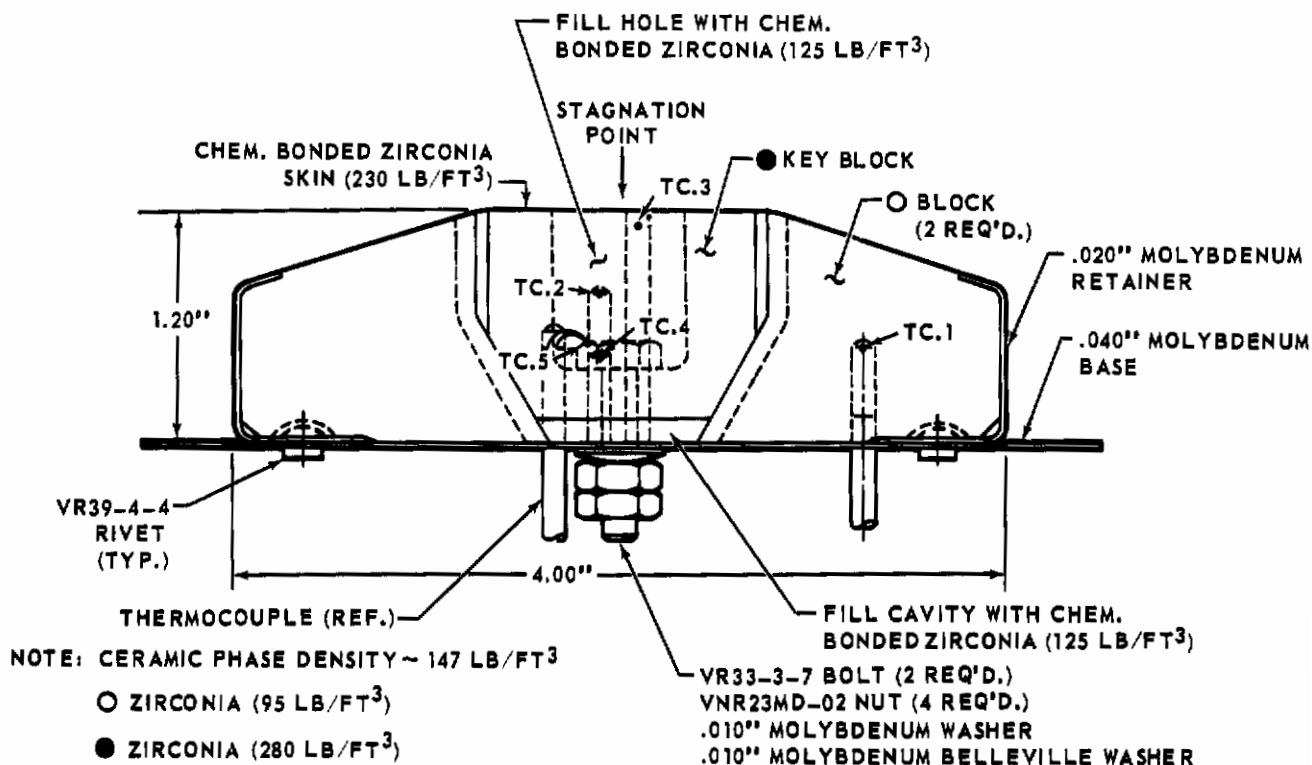
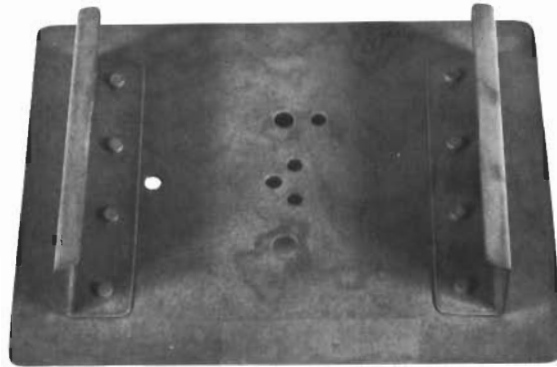


FIGURE 120 - 4000°F TEST SPECIMEN - 1.5 INCH RADIUS LEADING EDGE KEY BLOCK DESIGN

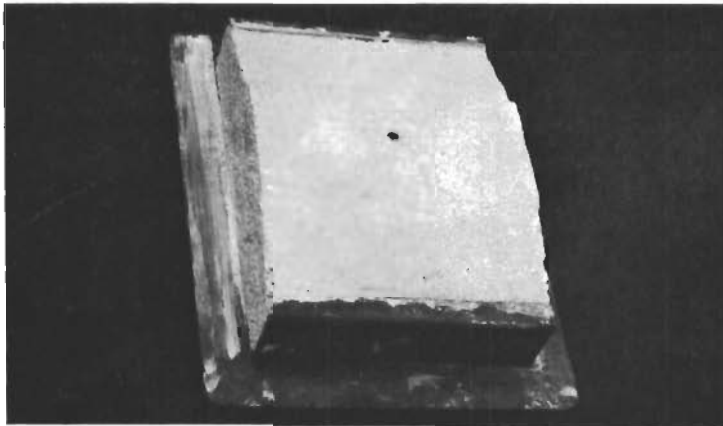


**FIGURE 121 - HIGH DENSITY METAL SUBASSEMBLY -
4000°F TEST SPECIMEN - KEY BLOCK DESIGN**

The specimen survived the prescribed vibration and acoustical tests without any visible failures. The appropriate thermal test however, produced defects which are visible in Figure 122. Thermally induced shrinkage in the low density chemically bonded zirconia packed into the voids between the blocks produced a network of cracks. The greater expansion of the key block (due to higher temperature exposure) in relation to the end blocks probably aggravated these cracks and was responsible for a crack which developed across a corner of one low density sintered end block. A physical tie existed between the key block and end blocks as a result of the chemically bonded zirconia surface coating.

In the second generation key block design, attempts were made to correct the shortcomings which appeared in the original specimen and also to lower the ceramic phase density. A newly shaped key block was the basic change, as shown in Figure 123. This shape change was primarily possible because of the favorable working properties of the newly developed low density sintered zirconia. (Norton MZ-44, see Section 4.3.) Parts made from this zirconia could be readily held to relatively close tolerances. The new material was specified for the end blocks which were fashioned to receive a wedge headed key block without resorting to any chemically bonded zirconia potting. In addition, the new key block design, in common with all second generation designs, specified coated columbium leaf springs for the attachment system in place of the original Belleville spring washers to permit free expansion of attached ceramic parts.

Only the crucial thermal test was performed on the second generation specimen because the original specimen had withstood the vibration and acoustical tests. The results of the second thermal test are shown in Figure 124. There were very slight peripheral separations (due to shrinkage) around the potted bolt holes, but the chemically bonded zirconia plugs were tight and fully intact due to the undercuts in bolt holes. The surface skin opened along the joint between the key block and the end block as expected. This in no way impaired the structural integrity of any ceramic element. However, a crack did appear across a sharp corner (stress riser situation) of the wedge headed key block, apparently from thermal stresses. No failures were noted in any of the metallic components.



(a) BEFORE TEST



(b) AFTER TEST, TOP VIEW



(c) AFTER TEST, SIDE VIEW

**FIGURE 122 - 4000°F TEST SPECIMEN - 1.5 INCH RADIUS LEADING EDGE -
HIGH DENSITY KEY BLOCK DESIGN (THERMAL TEST)**

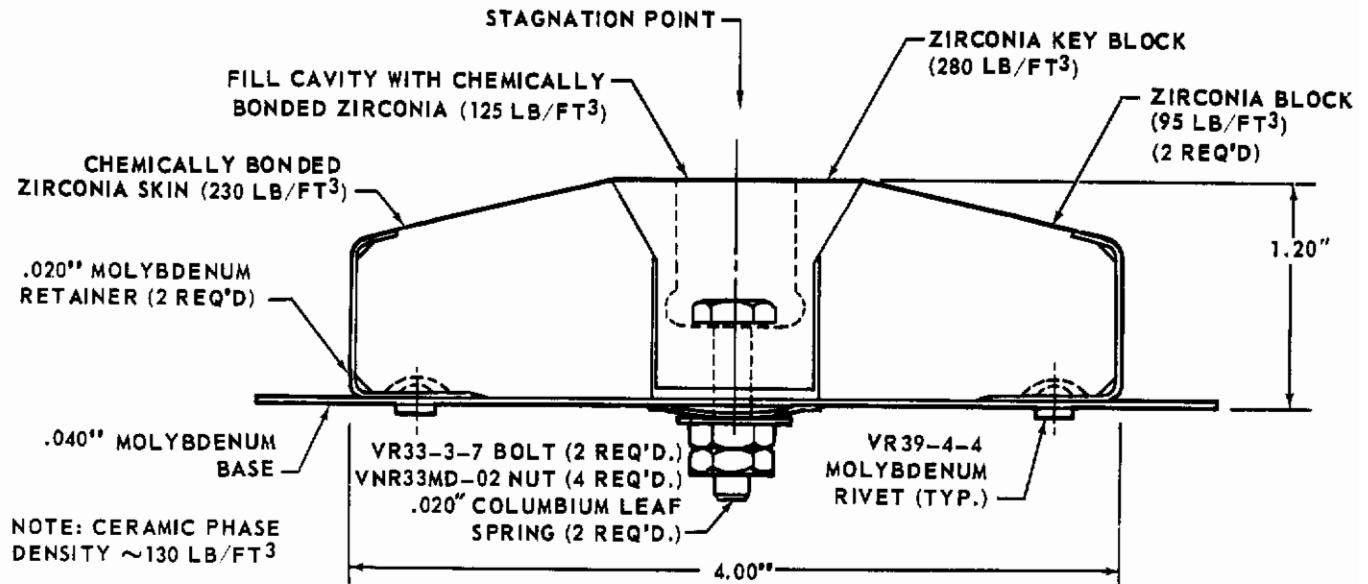
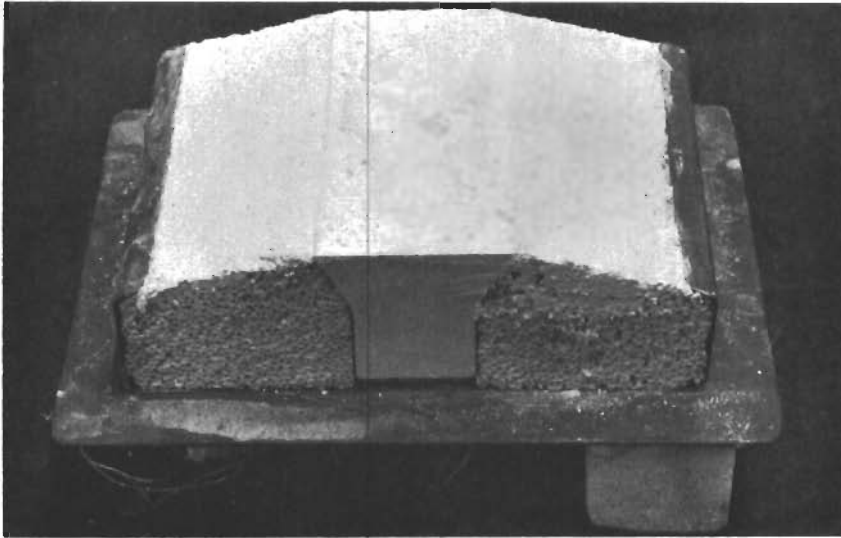


**FIGURE 123 - 4000°F TEST SPECIMEN - 1.5 INCH RADIUS
LEADING EDGE KEY BLOCK DESIGN - REVISION A**

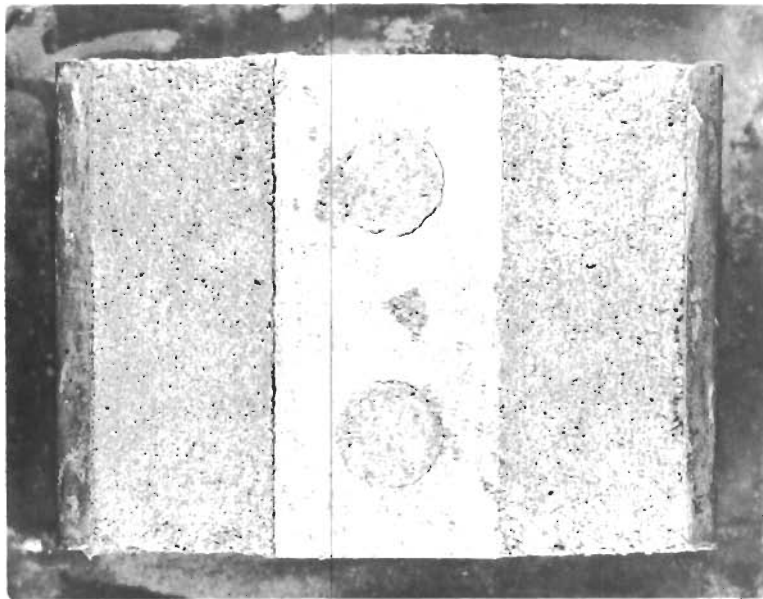
The second generation design was revised slightly to produce a third and final test specimen. The sharp corners on the key block head were eliminated in the third generation design, which is shown in Figure 125. In addition, the low density sintered ceramic previously used in the end blocks was specified for all the blocks. Therefore, the final design had a density of 96 lb/ft³ compared to 130 lb/ft³ for the ceramic phase density in the second generation design.

The third generation key block design was subjected to the appropriate thermal test. The results of this test are shown in Figure 126. The facing skin again parted along the key block/end block joints (as expected) but no cracks or spalls appeared in any of the blocks. This separation of the facing skin at the joints had no effect on the integrity of the ceramic shield.

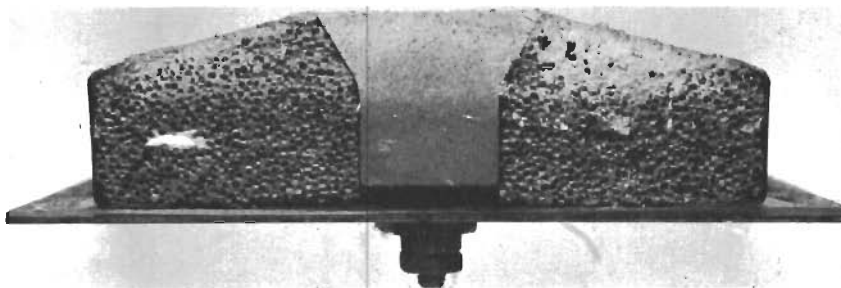
5.2.2.2 Block Design - The design concept illustrated in Figure 127 utilized a one piece block for the full ceramic phase. A full scale leading edge component would consist of several such blocks mounted to a common substructure. The low density block was retained by two spring loaded molybdenum bolts and sat on a compact but resilient, fibrous silica pad to help distribute the clamp-up pressure across the base of the ceramic. One of the two bolt holes in the substructure was slotted to provide for thermal expansion. The porous face of the low density block was surfaced with a dense chemically bonded zirconia skin.



(a) BEFORE TEST

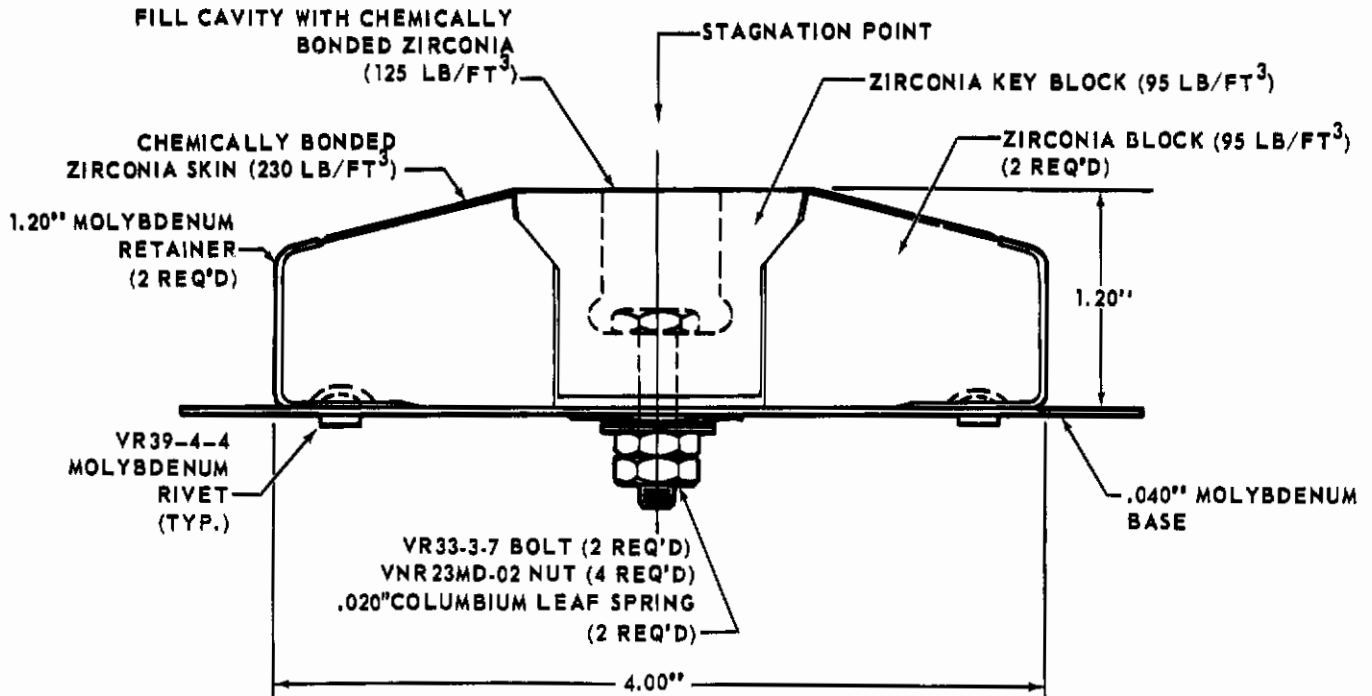


(b) AFTER TEST, TOP VIEW



(c) AFTER TEST, SIDE VIEW

FIGURE 124 - 4000°F TEST SPECIMEN - 1.5 INCH RADIUS LEADING EDGE, HIGH DENSITY KEY BLOCK DESIGN REVISION A (THERMAL TEST)

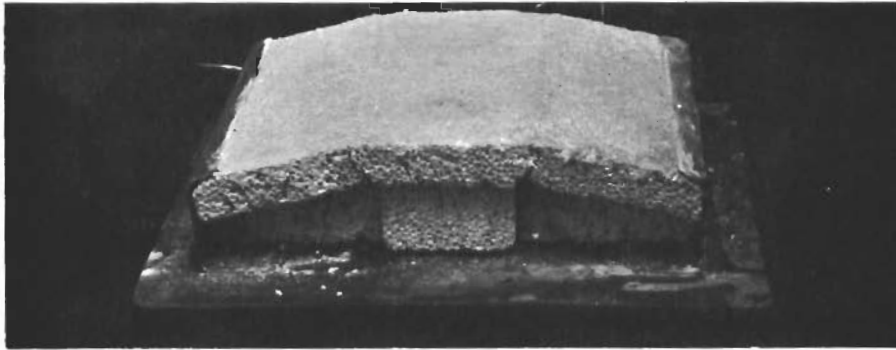


NOTE: CERAMIC PHASE DENSITY $\sim 96 \text{ LB/FT}^3$

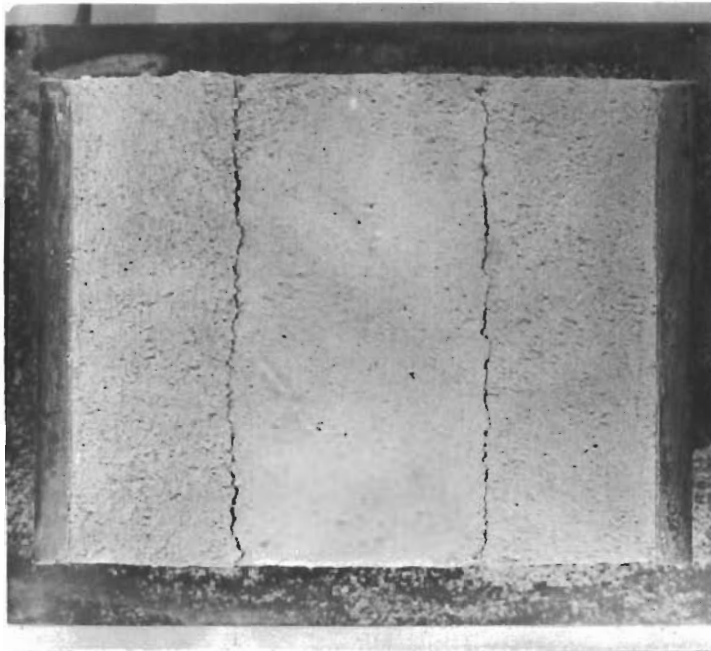
**FIGURE 125 - 4000°F TEST SPECIMEN - 1.5 INCH RADIUS LEADING EDGE
LOW DENSITY KEY BLOCK DESIGN - REVISION B**

The specimen was subjected to the vibration and acoustical test without failure. The prescribed thermal test did result in minor shrinkage cracks at the potted bolt cavities, and in more serious cracking in the body of the block. Figure 128 clearly shows a crack parallel to the exposed face, and several smaller hairline cracks radiating from the base were detected in the actual specimen. This low density zirconia apparently was not sufficiently thermal shock resistant to tolerate the thermal stresses generated in a large monolithic block. The specimen was subjected to a second vibration test to determine the integrity of the cracked ceramic shield. The block remained intact, although there were signs of further localized cracking. The promising thermal shock resistance of the new low density zirconia (see Section 4.3) used in the second generation key block specimen prompted a second try at a one piece block specimen. In the new design, shown in Figure 129, the new low density zirconia was contoured to a 1.5 inch radius block. The attachment for the contoured block was the same as the original block except for the substitution of coated columbium leaf springs for the original Belleville spring washers. The lower spring constant for the leaf springs permitted the removal of the compact silica pad which had experienced some loss of resilience (due to shrinkage) in the initial thermal test.

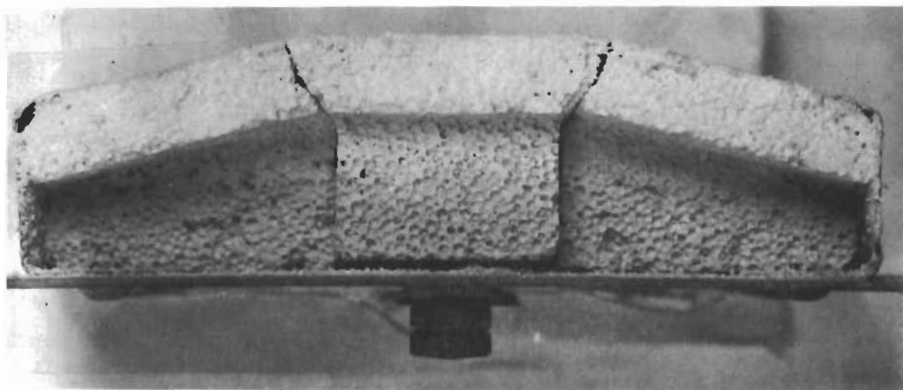
The appropriate thermal test was conducted on this second generation specimen, and resulted in a substantial crack (see Figure 130) which originated at the base but did not penetrate to the outer surface of the block. The failure indicates that the block configuration exceeded size limitations which were critical to thermal shock resistance.



(a) BEFORE TEST



(b) AFTER TEST, TOP VIEW



(c) AFTER TEST, SIDE VIEW

FIGURE 126 - 4000°F TEST SPECIMEN - 1.5 INCH RADIUS LEADING EDGE - LOW DENSITY KEY BLOCK DESIGN REVISION B (THERMAL TEST)

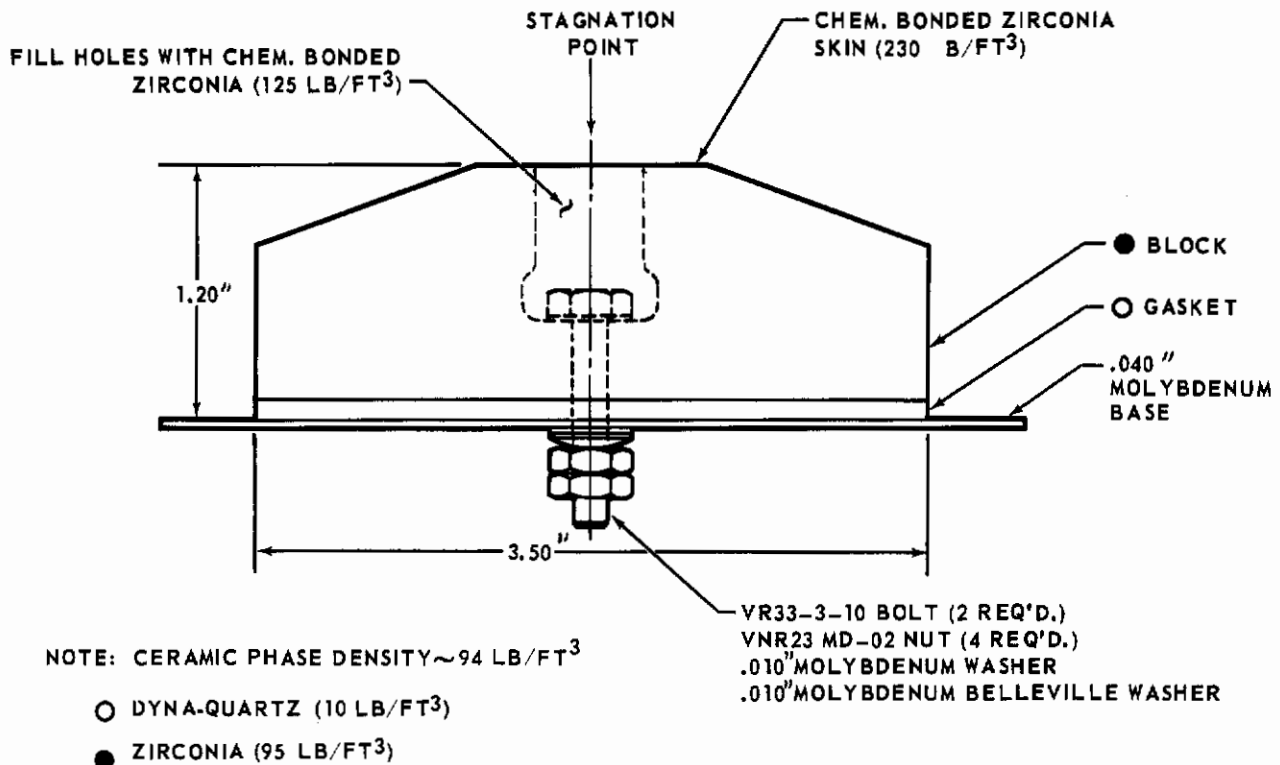
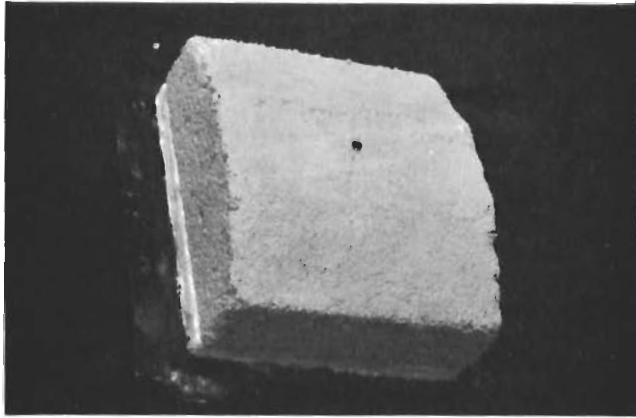


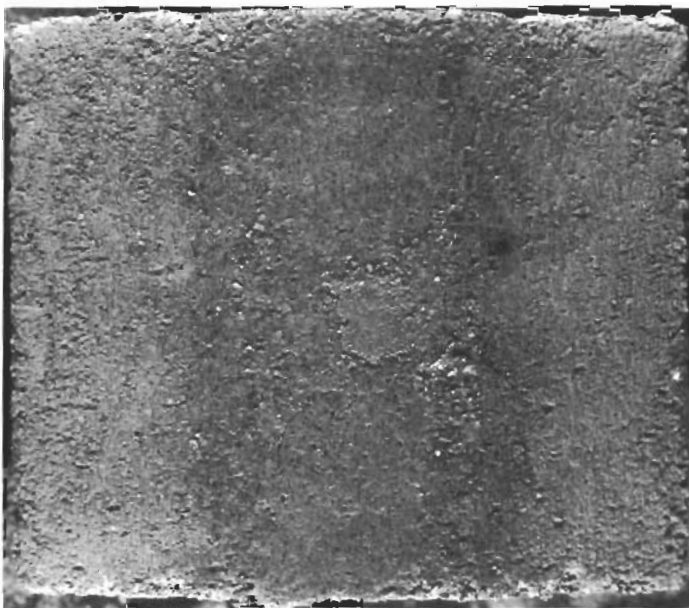
**FIGURE 127 - 4000°F TEST SPECIMEN - 1.5 INCH RADIUS
LEADING EDGE BLOCK DESIGN**

5.2.2.3 Reinforced Chemically Bonded Design - A reinforced chemically bonded design for the 1.5 inch radius leading edge is shown in Figure 131. In this design, a layer of sintered low density zirconia was trapped and covered by a segmented outer layer of reinforced chemically bonded low density zirconia which was faced with a dense chemically bonded zirconia skin. The reinforcements consisted of perforated, coated molybdenum tee sections attached to the substructure at either side of the stagnation line. A spring loaded high density zirconia pin acted as the retention member in the stagnation zone where temperature precluded the use of refractory metal reinforcements. The interim method for engaging the first generation retention pins (see Section 5.2.1.4) was used in the assembly of this specimen. The metallic subassembly for the specimen is shown in Figure 132 and the fully assembled subscale in Figure 133(a).

The vibration and acoustical tests were performed without failure. The specimen was then subjected to the prescribed thermal test, which resulted in a single hairline crack across the apex of a subsurface sintered block (see Figure 133(b)). This crack was possibly caused by the thermal expansion bowing effect of the outer layer of chemically bonded zirconia causing it to bear down on the low strength apex area of the sintered block and cracking it. This low density sintered zirconia was not the improved variety developed in the Norton subcontract. With the exception of the one crack, the specimen was completely intact. The subscale was subjected once again to the vibration and the thermal tests. At the conclusion of the second thermal test the specimen exhibited a crack in one of the chemically bonded segments, which can be seen



(a) BEFORE TEST

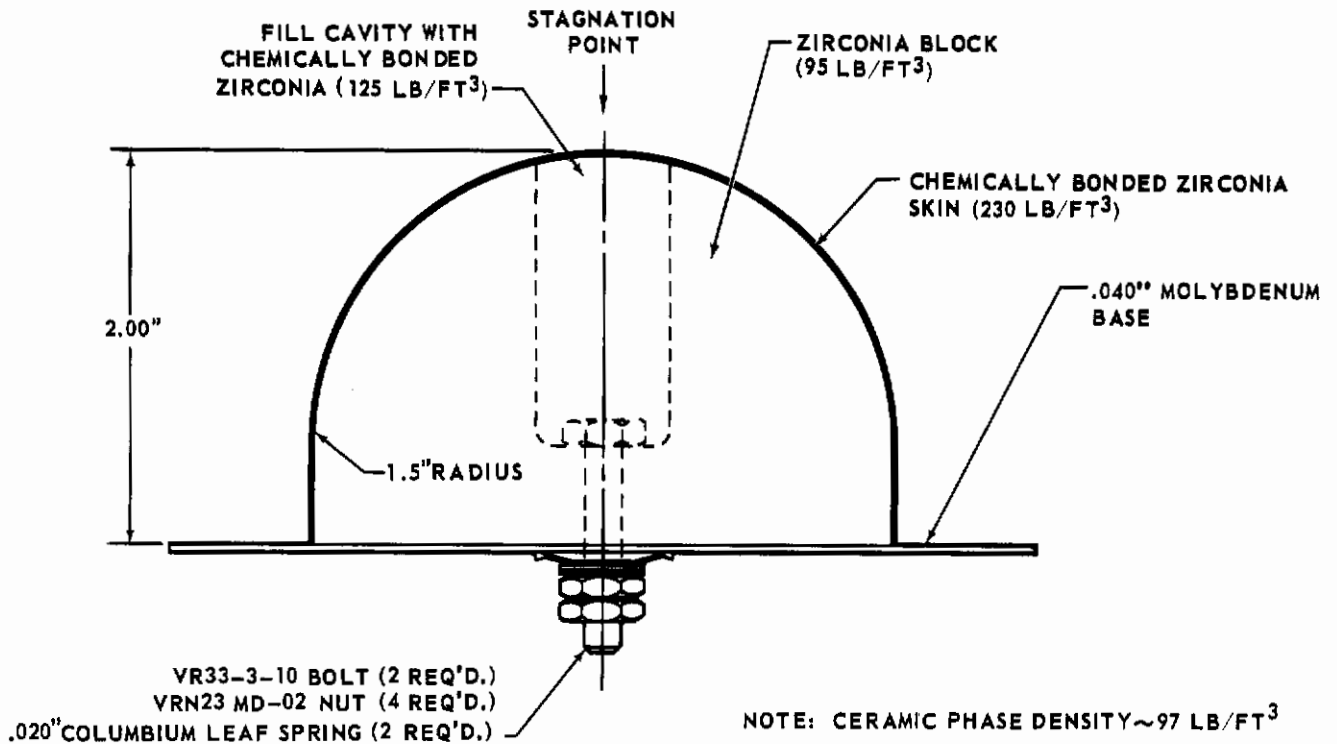


(b) AFTER TEST, TOP VIEW



(c) AFTER TEST, SIDE VIEW

FIGURE 128 - 4000°F TEST SPECIMEN - 1.5 INCH RADIUS LEADING EDGE-BLOCK DESIGN (THERMAL TEST)

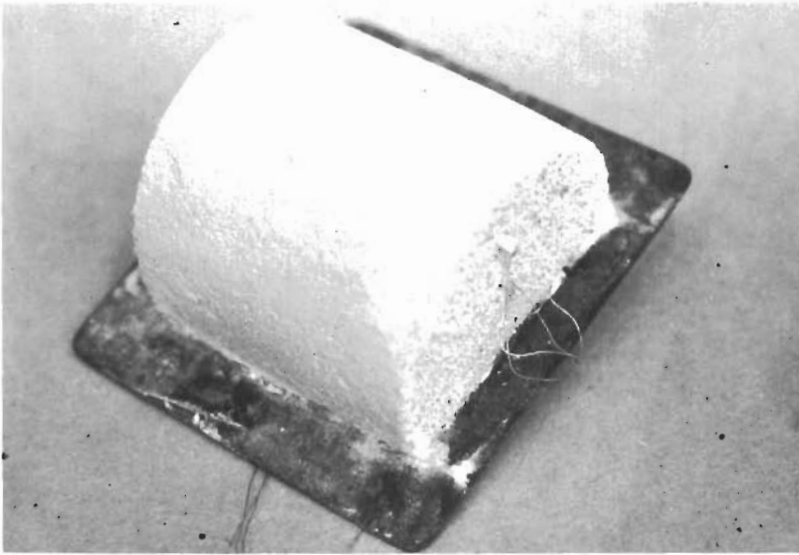


in Figure 133(c). Differential thermal expansion between the coated molybdenum reinforcements and the chemically bonded zirconia in combination with a fold-line from fabrication was probably responsible for this crack. No further cracking was detected in the sintered zirconia blocks, and the specimen was still completely intact and in good condition.

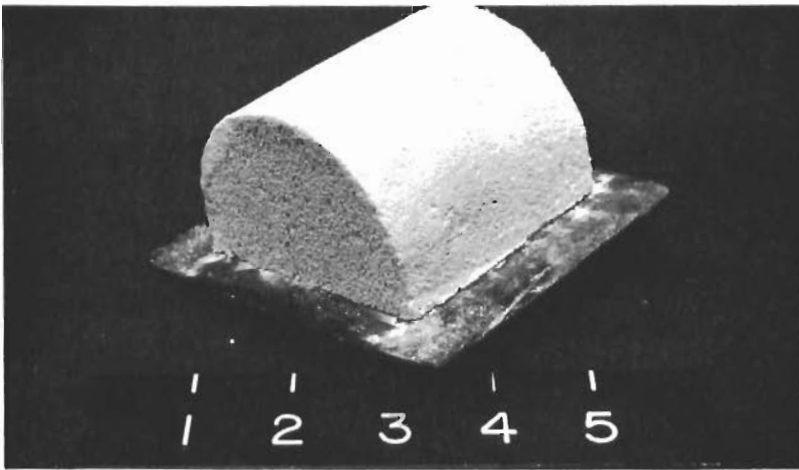
5.2.2.4 Pin-Tile Design - Figure 134 shows a pin-tile design adapted to the 1.5 inch radius leading edge. The design features were identical to the features in the pin-tile specimen which was designed for a 3.0 inch radius leading edge (see Section 5.2.1.4). The differences between the two specimens were in the ceramic materials and the refractory metal used for support. The 1.5 inch radius leading edge specimen employed zirconia and coated molybdenum, while the 3.0 inch radius leading edge specimen employed alumina and coated columbium. In the actual specimen, the zirconia retention pin was not engaged by a cross pin but was retained by a cast ceramic plug due to the experience noted in Section 5.2.1.4.

The zirconia pin-tile specimen survived the vibration and acoustical tests without failures. The thermal test, however, resulted in several defects which are visible in Figure 135. The low density block exhibited numerous fine cracks with several of these located at the shoulder notches. These cracks were due to the low thermal shock resistance of this material (which was not the improved zirconia developed later) aggravated by the stress riser effect of the attachment undercuts. The dense tile and the head of the retaining pin were deformed and some cracks had developed in the tile.

Text continued on page 169



(a) BEFORE TEST



(b) AFTER TEST



(c) AFTER TEST, END VIEW

FIGURE 130 - 4000°F TEST SPECIMEN -1.5INCH RADIUS LEADING EDGE-BLOCK DESIGN-REVISION A (THERMAL TEST)

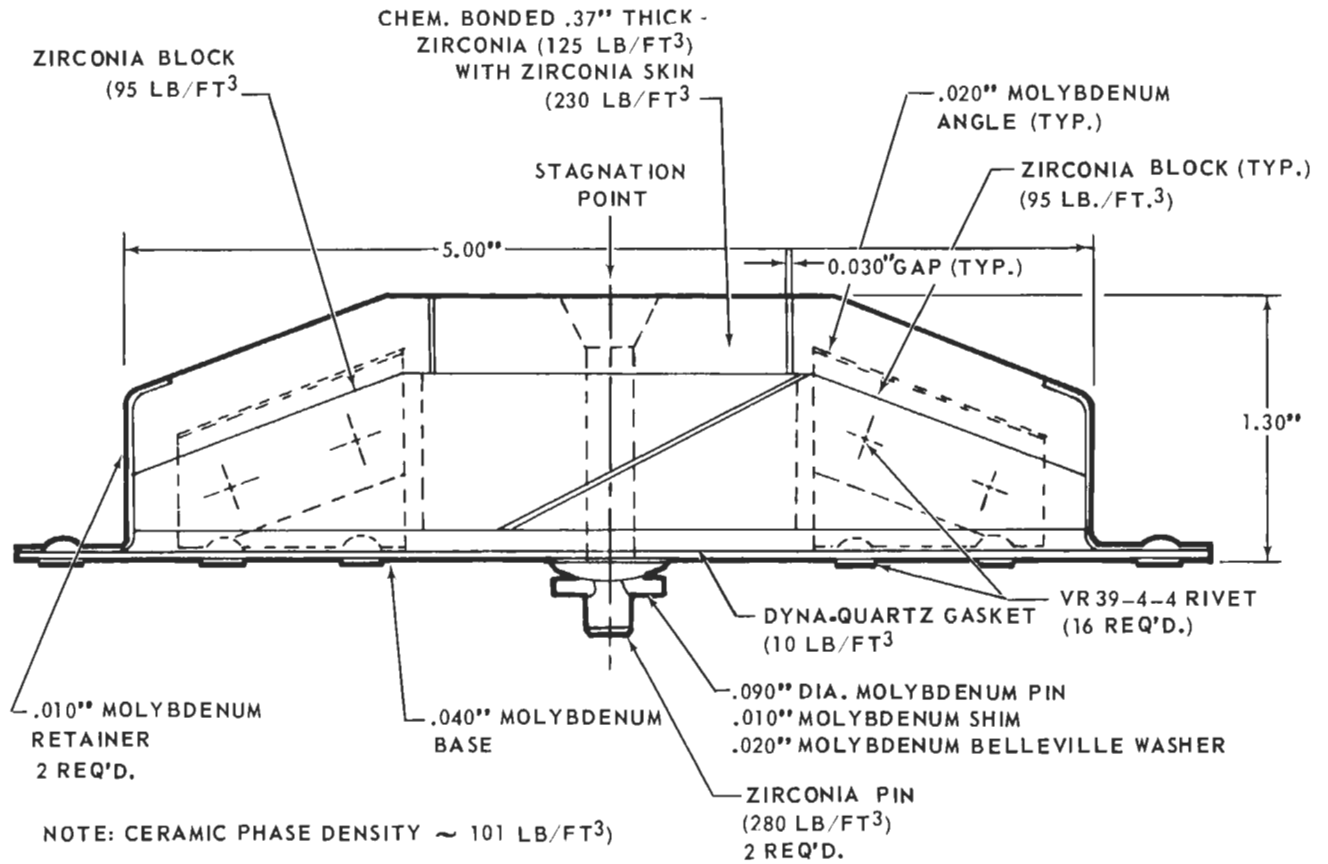
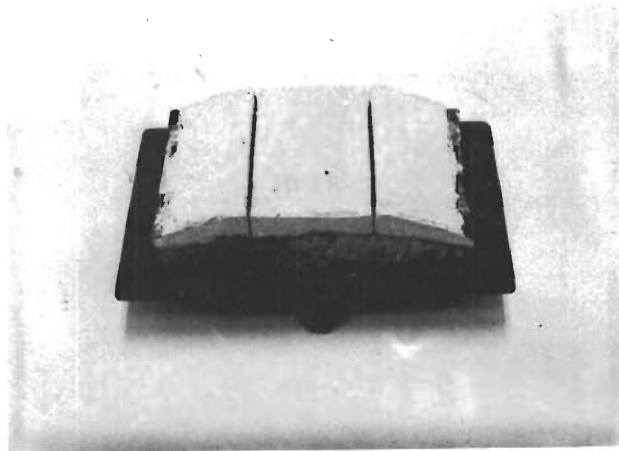


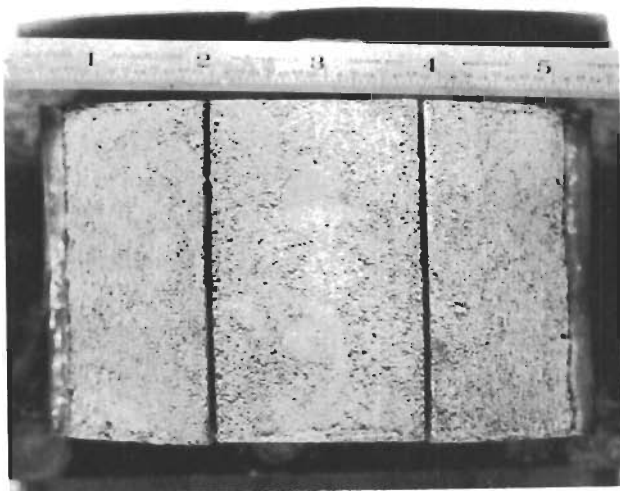
FIGURE 131 - 4000°F TEST SPECIMEN - 1.5 INCH RADIUS LEADING EDGE REINFORCED CHEMICALLY BONDED DESIGN



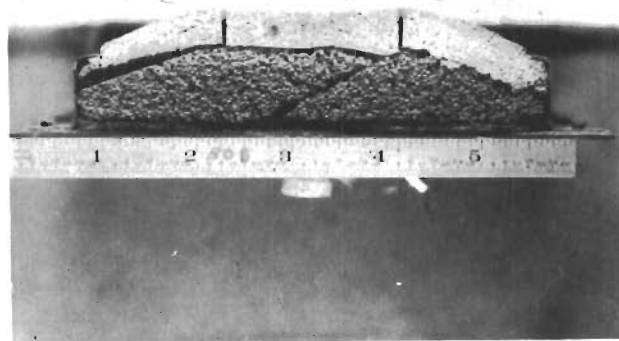
FIGURE 132 - METAL SUBASSEMBLY - 4000°F TEST SPECIMEN REINFORCED CHEMICALLY BONDED DESIGN



(a) BEFORE TEST

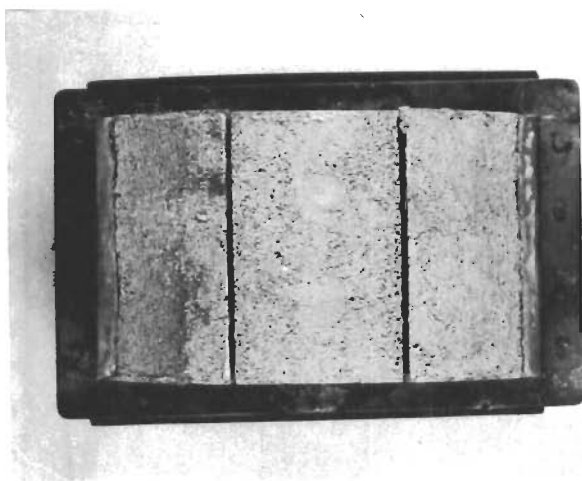


TOP VIEW



SIDE VIEW

(b) AFTER TEST, 1ST CYCLE



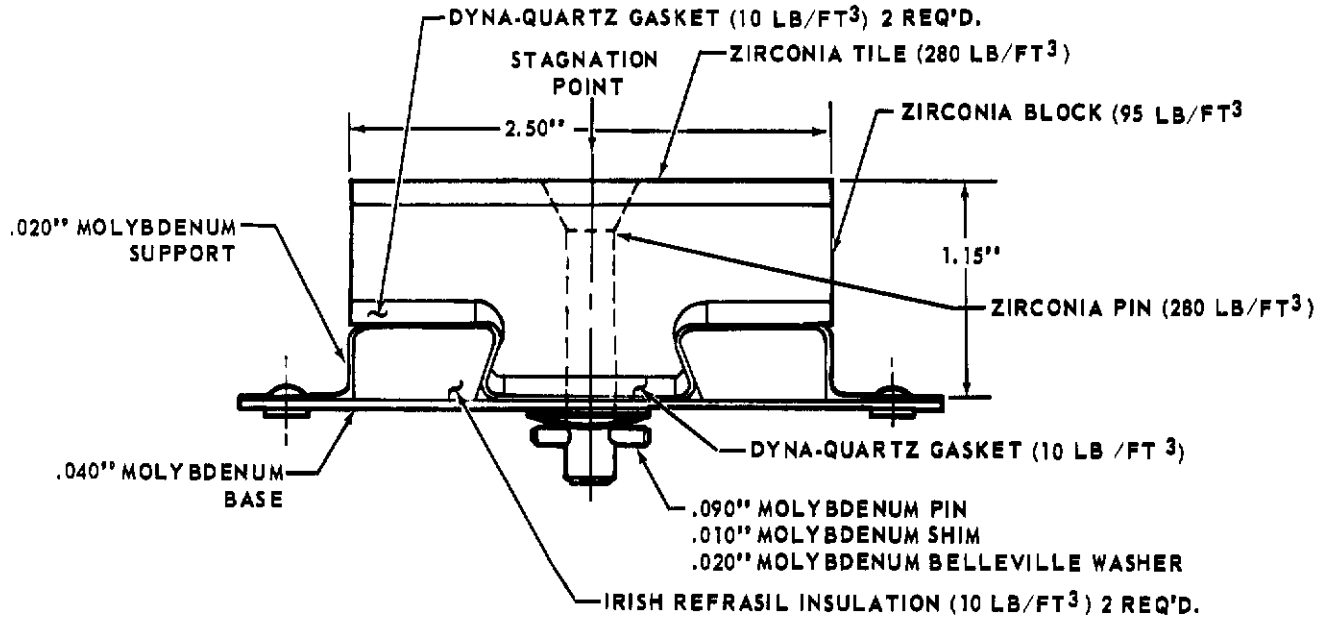
TOP VIEW



SIDE VIEW

(c) AFTER TEST, 2ND CYCLE

**FIGURE 133 - 4000°F TEST SPECIMEN - 1.5 INCH RADIUS LEADING EDGE -
REINFORCED CHEMICALLY BONDED DESIGN (THERMAL TEST)**



NOTE: CERAMIC PHASE DENSITY ~ 92 LB/FT³

**FIGURE 134 - 4000° F TEST SPECIMEN - 1.5 INCH RADIUS
LEADING EDGE - PIN-TILE DESIGN**

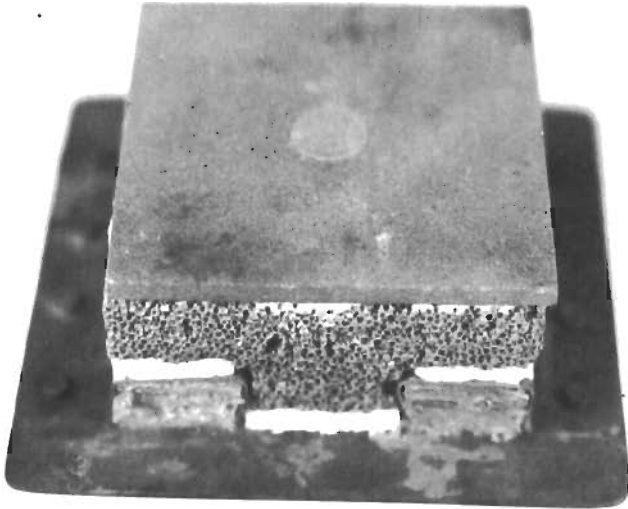
These failures indicated that the spring loaded pin exerted an excessive force when the facing tile bowed in response to the temperature gradient. Therefore, a lower spring constant and/or greater pin stroke was required to allow this bowing to occur in a less restrained manner.

The zirconia pin-tile specimen was redesigned; the design revisions being smaller than those employed in the second generation alumina pin-tile specimen (see Section 5.2.1.4). No material change was specified for the facing tile, but its thickness was increased (see Figure 136) to increase strength and reduce the heating rate to the low density block. The revisions to the low density block and the retention system were identical to those made on the second alumina pin-tile specimen. The new retention system had a reduced spring constant (see Section 5.2.1.4) to reduce the force required to effectively lengthen the grip of the pin.

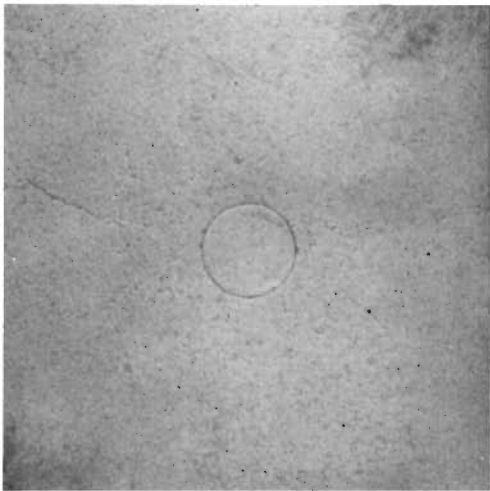
The second zirconia pin-tile specimen was thermally tested and, deformation and cracking of the facing tile and deformation of the head of the retention pin (see Figure 137) occurred again. The underlying low density zirconia block appeared to be unaffected.

These test results suggested that the deformations could also be caused by a "bottom-out" spring. In such a situation, the thermally induced bowing of the facing tile would be opposed by an "immovable" pin. Accordingly, a third specimen was built with a retention system that doubled the allowable stroke. All other design features remained the same. The third specimen was subjected to the thermal test, which resulted in the same failures that occurred in the preceding tests (see Figure 138).

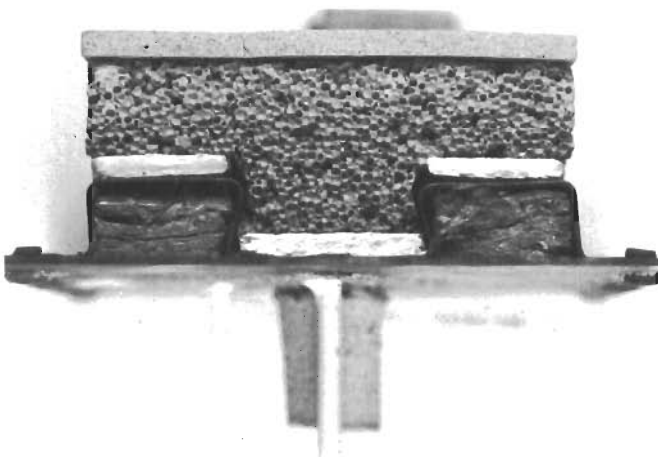
The results of this final test indicated that the high temperature strength



(a) BEFORE TEST

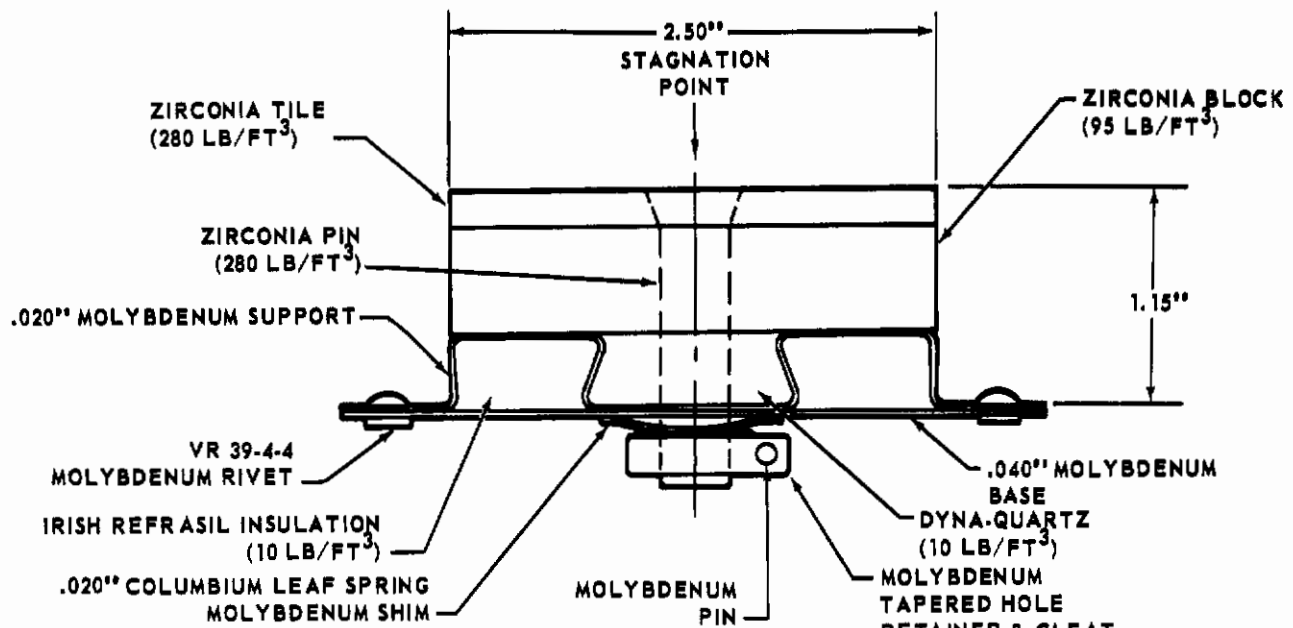


(b) AFTER TEST, TOP VIEW



(c) AFTER TEST, SIDE VIEW

**FIGURE 135 - 4000°F TEST SPECIMEN - 1.5 INCH RADIUS LEADING EDGE -
(THERMAL TEST)**



NOTE: CERAMIC PHASE DENSITY ~ 101 LB/FT³

**FIGURE 136 - 4000°F TEST SPECIMEN - 1.5 INCH RADIUS
LEADING EDGE TILE DESIGN - REVISION A**

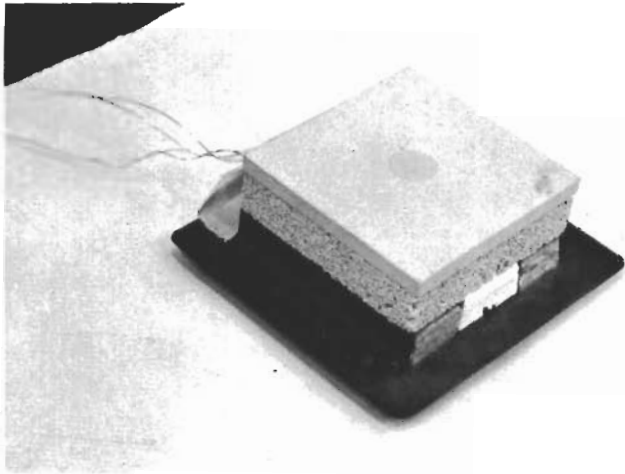
of the zirconia tile was not adequate for the loads which were generated in the pin-tile design. Any further reduction in the spring constant, which might reduce the high temperature loads, would also result in reducing the ability of the specimen to resist the dynamic loads common to the launch environment.

5.2.3 6.0 Inch Radius Nose Cap

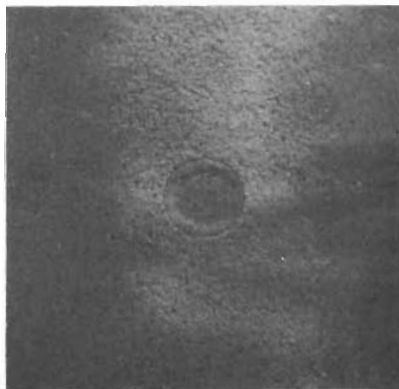
The primary design consideration in all subscales representing the 6.0 inch radius nose cap was the expected peak temperature of 5000°F. Since this peak temperature exceeds the melting point of zirconia, it was necessary to employ thoria in the stagnation point area of the nose cap. This use of thoria precluded a relatively high ceramic phase density since the theoretical density of thoria is almost twice as great as zirconia. Special attention had to be given to the mechanical composition of the shield to minimize the thermal shock and differential expansion problems which the severe thermal gradients induced.

5.2.3.1 Tile Design - The specimen illustrated in Figure 139 utilized a multi-layer design concept to counteract the severe thermal gradients. The ceramic cross-section was layered along those planes which thermal stress analyses had indicated would be the probable failure planes due to thermally induced shearing stresses. In this design, a facing tile of dense thoria was stacked on two blocks of low density sintered zirconia. All the ceramic elements were attached to a molybdenum substructure by a spring loaded, 0.25 inch diameter thoria pin extending to the outer surface of the thoria tile. The thoria retention pin, in the actual specimen, was not engaged by a cross pin as shown in the sketch, but was retained by a cast ceramic plug as discussed in Section 5.2.1.4.

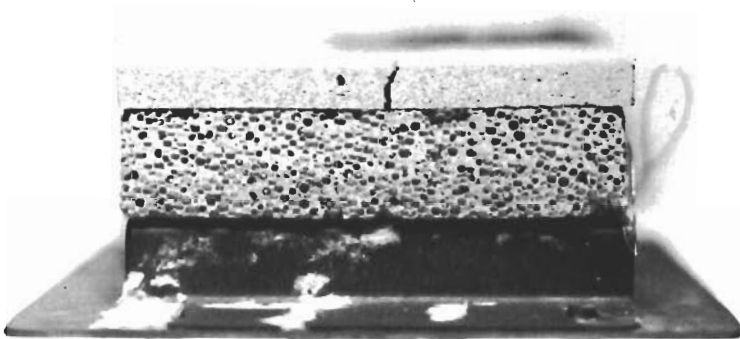
Text continued on page 174



(a) BEFORE TEST

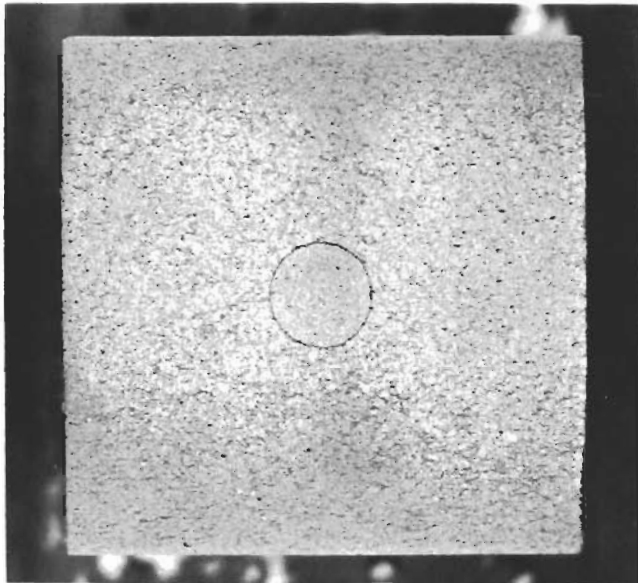


(b) AFTER TEST, TOP VIEW



(c) AFTER TEST, SIDE VIEW

**FIGURE 137 - 4000°F TEST SPECIMEN - 1.5 INCH RADIUS LEADING EDGE -
PIN-TILE DESIGN - REVISION A (THERMAL TEST)**



(a) AFTER TEST, TOP VIEW



(b) AFTER TEST, SIDE VIEW

**FIGURE 138 4000°F TEST SPECIMEN 1.5 INCH RADIUS LEADING EDGE -
PIN-TILE DESIGN - REVISION B (THERMAL TEST)**

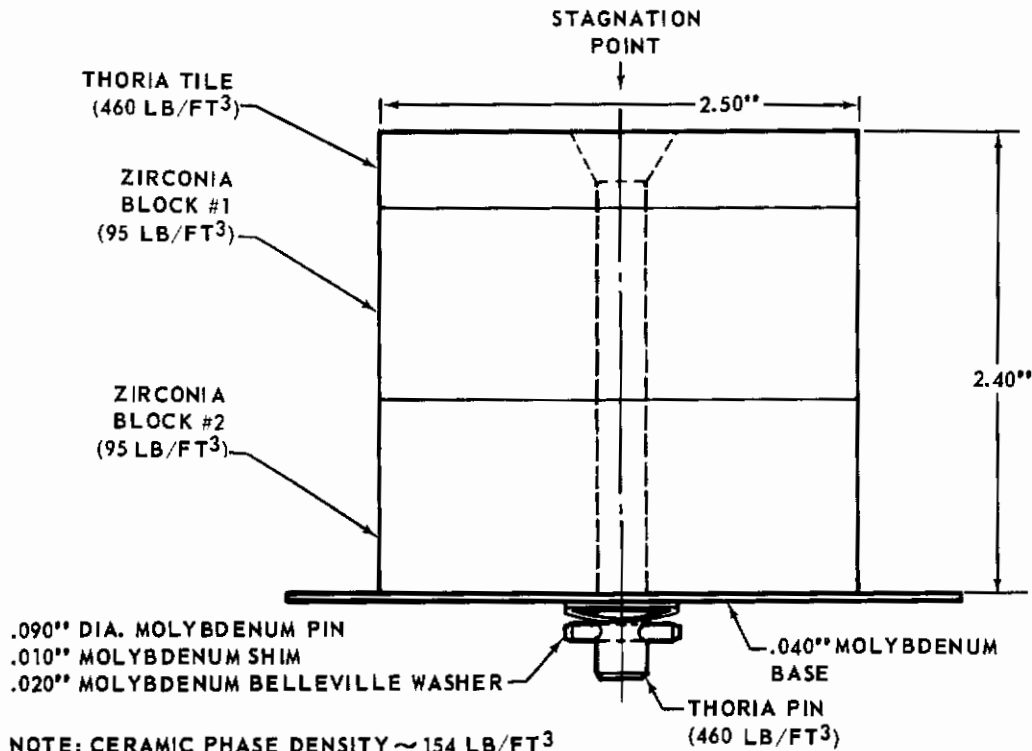
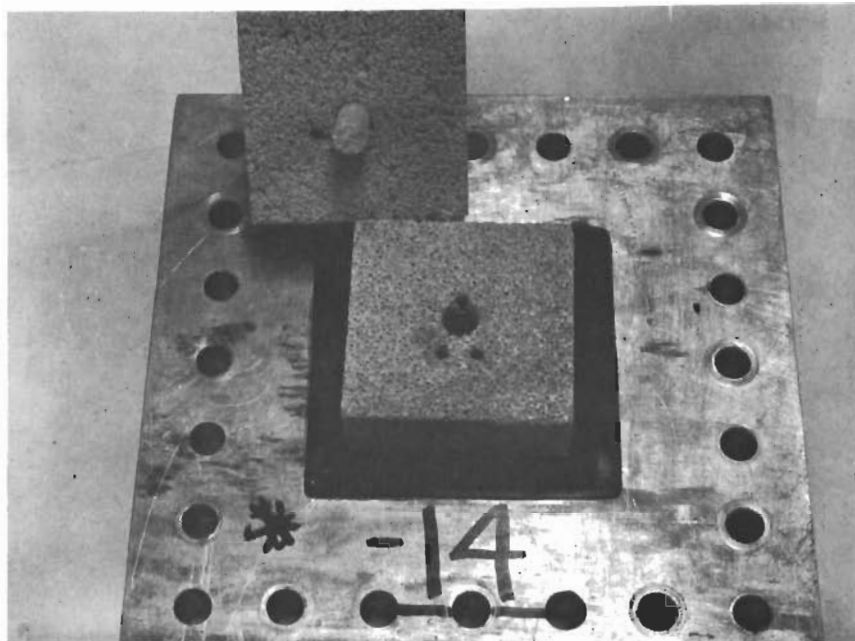


FIGURE 139 - 5000°F TEST SPECIMEN - NOSE CAP - TILE DESIGN

Vibration test of the specimen produced the failure shown in Figure 140. The thoria pin broke near the substructure during a vibration run in which the excitation was normal to the axis of the pin. The specimen was then modified to accept a larger diameter pin (0.375 inch), which was attached by a leaf spring and molybdenum retainer identical to those employed in the second generation alumina Pin-Tile design (see Section 5.2.1.4). This modified specimen withstood the vibration and acoustical tests, but fractures occurred in the facing tile and the thoria pin during thermal testing (see Figure 141). There were no signs of deformation in the tile or the pin, indicating that the failure, if due to loads caused by restriction of thermal expansion movement, occurred at relatively low temperatures. The failure may also have been due to the low thermal shock resistance of the thoria.

A different form of thoria was employed at the exposed face of the second generation specimen. In the new design (see Figure 142), a single block of low density sintered zirconia was attached to the substructure by a spring loaded molybdenum bolt. The upper face of the zirconia block had a cruciform dovetail groove which trapped a cast facing tile composed of chemically bonded thoria. Spool-shaped dense sintered thoria pins were distributed in the chemically bonded thoria for reinforcement.

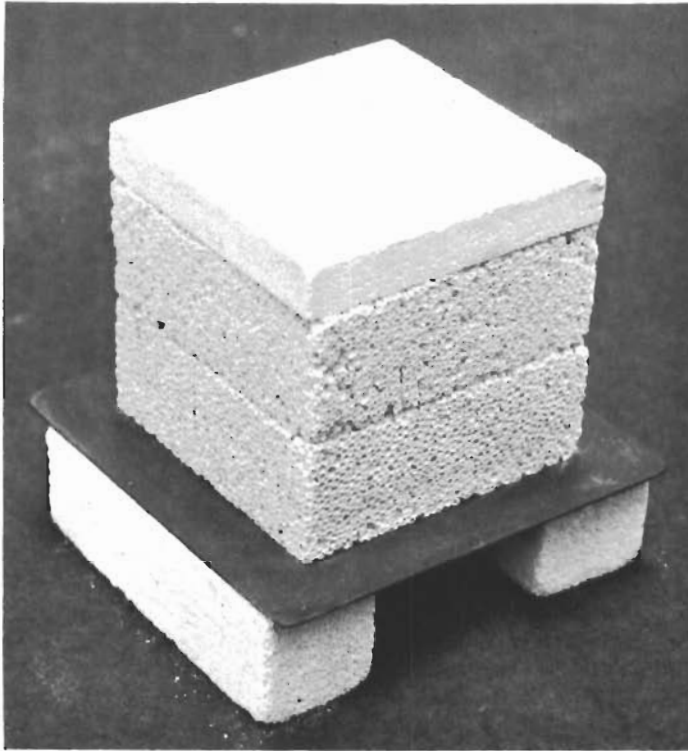
Only the thermal test was imposed on the second generation tile specimen. At the conclusion of the test, the ceramic elements were fully intact but showed some slight hairline shrinkage cracks. Shrinkage of the castable thoria at high temperatures reduced the engagement in the dovetail grooves (which served as the mechanical tie between the tile and the zirconia block), resulting in a limited directional mobility between the thoria facing tile and the zirconia substrate (see Figure 143).



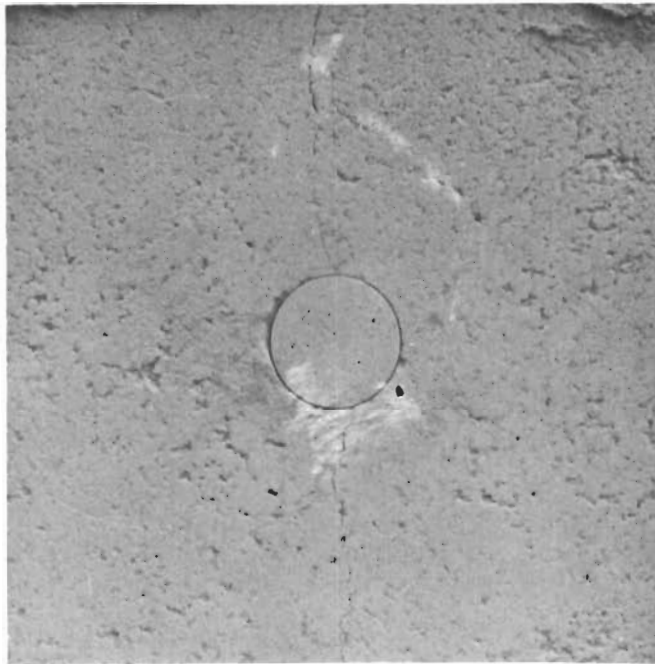
**FIGURE 140 - 5000°F TEST SPECIMEN - NOSE CAP -
TILE DESIGN (VIBRATION TEST)**

5.2.3.2 Tube Reinforced Castable Design - The subscale design shown in Figure 144 was based on the use of small dense ceramic elements to form a thermal shock resistant shield. In this design, dense zirconia tubes were pinned at their bases to coated molybdenum channel clips which were in turn riveted to a coated molybdenum substructure. Dense thoria tubes were fastened to the top of the zirconia tubes by zirconia pins. All the tubes had perforations to entrap the chemically bonded ceramic tamped into all open spaces. A low density castable zirconia was built up until it was 0.50 inch away from the moldline, and a low density castable thoria was then applied to the final half inch. A high density chemically bonded thoria skin was applied to the exposed face of the specimen. The assembled coated molybdenum substructure for this specimen is shown in Figure 145.

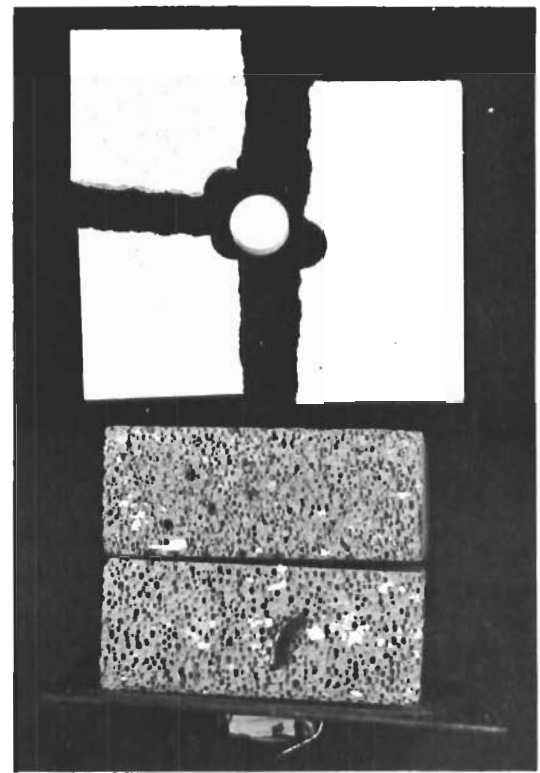
No defects were evident in the specimen at the conclusion of the vibration and acoustical tests. The thermal test produced very minor visible faults. The specimen was fully intact, but the thoria layer had separated from the castable zirconia (see Figure 146(c)). The specimen was sectioned to determine if the layers had shifted or if the reinforcing elements had failed. One thoria tube in the section was cracked but not displaced and the castable thoria had shrunk away from the reinforcing elements (see Figure 146(d)). However, the outer castable layer was integral and adhered tightly to the subscale proper, which indicated that the castable material was still engaged to the perforated reinforcing elements. The evidence demonstrated that the outer thoria layer need not be knitted to the underlying zirconia in order to produce a sound and integral facing tile.



(a) BEFORE TEST



(b) AFTER THERMAL TEST, TOP VIEW



(c) AFTER THERMAL TEST, DISASSEMBLED

FIGURE 141 - 5000°F TEST SPECIMEN - NOSE CAP - TILE DESIGN

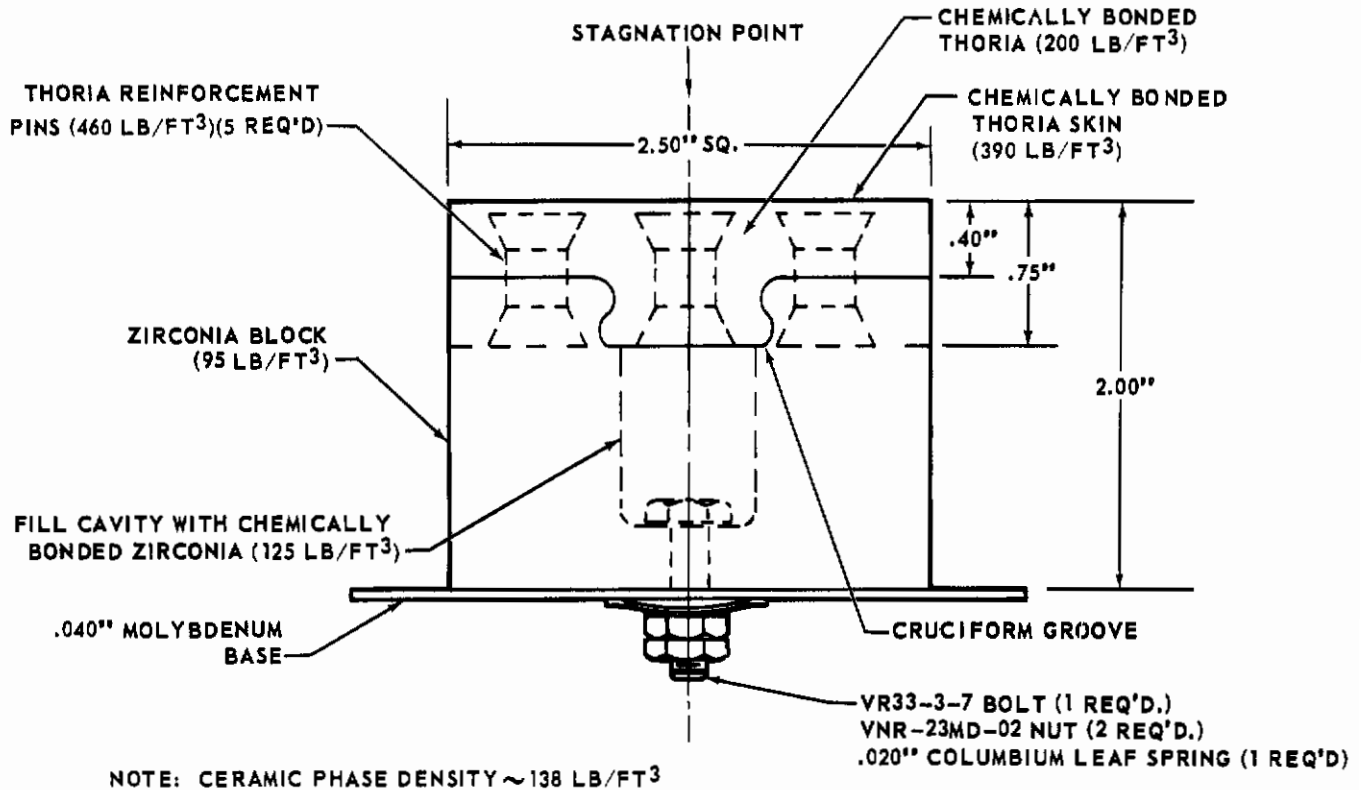


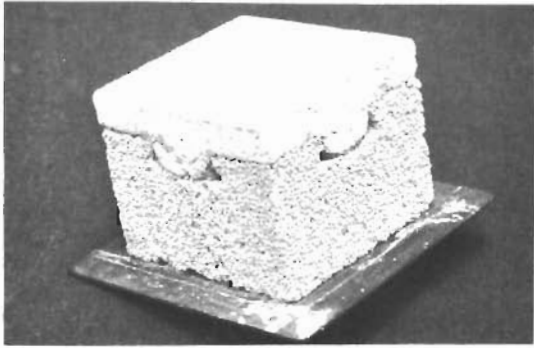
FIGURE 142 - 5000°F TEST SPECIMEN - NOSE CAP TILE DESIGN - REVISION A

The second generation tube reinforced castable design incorporated several changes, as shown in Figure 147. The original thoria tubes pinned to the end of the zirconia tubes were replaced by truncated conical plugs. This change provided a positive retention of the thoria to circumvent the shrinkage noted in the first specimen. In addition, a burn-out material was used to intentionally separate the castable thoria and zirconia layers.

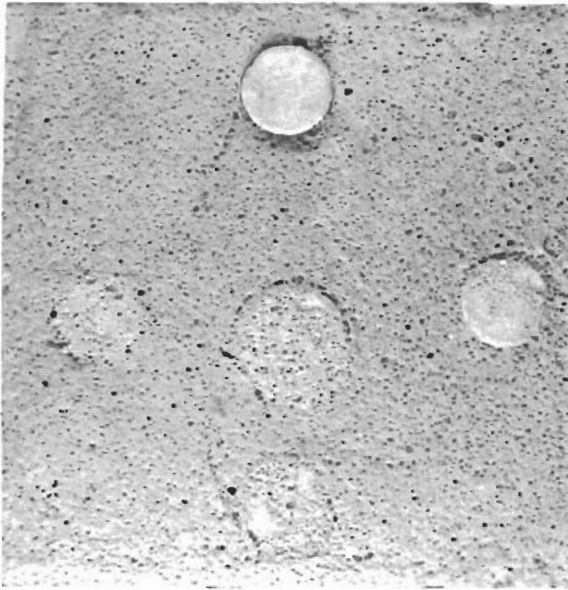
The vibration and acoustical tests were not performed on the second specimen. The results of the thermal test are shown in Figure 148. The distinct layers were fully intact and firmly attached, but some minor shrinkage cracks were evident in the castable bodies. The shrinkage cracks were local and did not traverse any face, and the reinforcing elements in the facing tile appeared to be soundly bound in the castable matrix.

5.2.3.3 Variable Density Block Design - The variable density block concept was evaluated with the subscale specimen illustrated in Figure 149. In this specimen, a perforated high density thoria block was attached to a coated molybdenum substructure by a spring loaded bolt. The holes in the block were filled with a chemically bonded low density thoria to produce a pattern of low density cores in a high density matrix.

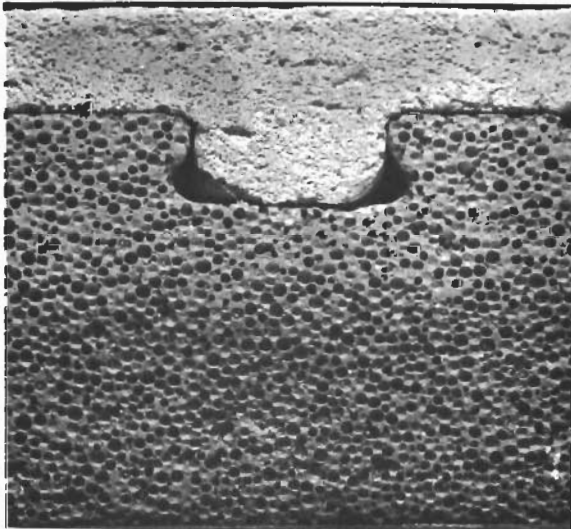
Vibration, acoustical, and thermal tests were performed with the thermal test producing some peripheral separations at the interface between castable cores and the high density block and a continuous crack across the perimeter of the high density block (see Figure 150). This crack was a serious failure since the block provided the only means of attaching the ceramic shield to the substructure. Block failure was attributed to thermal stresses.



(a) BEFORE TEST

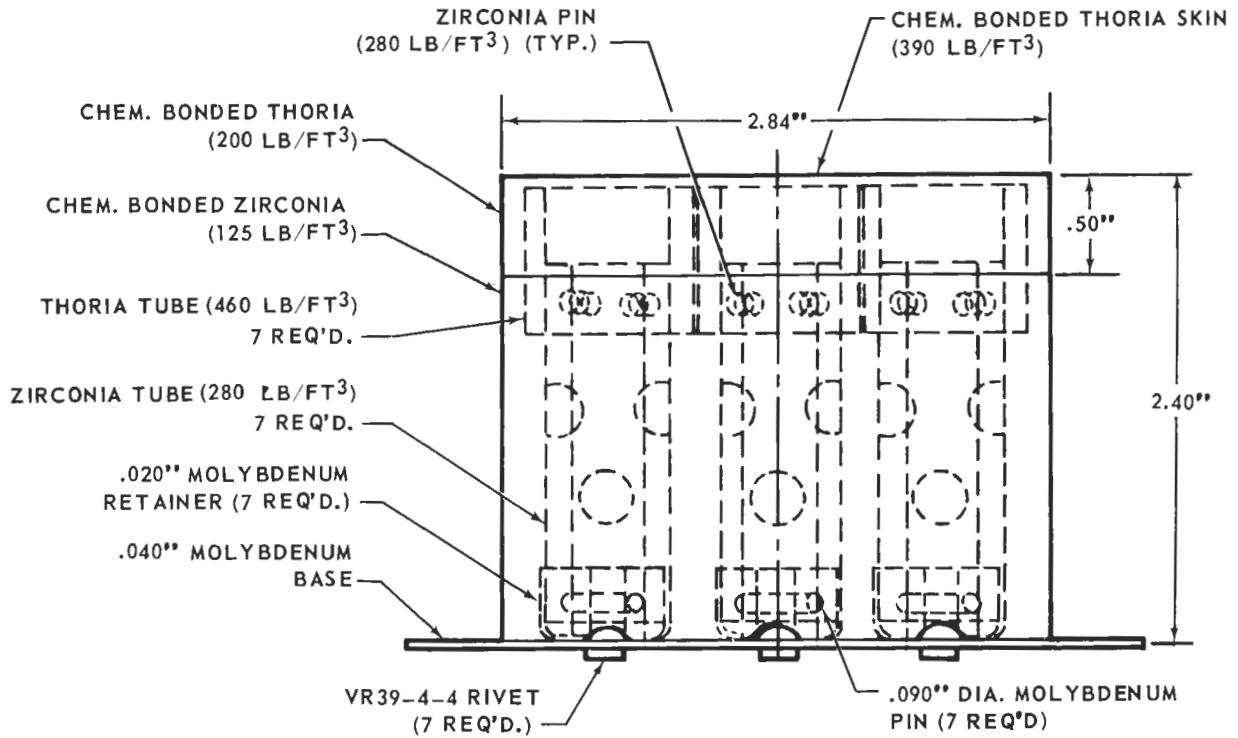


(b) AFTER TEST, TOP VIEW



(c) AFTER TEST, SIDE VIEW

**FIGURE 143 - 5000°F TEST SPECIMEN - NOSE CAP - TILE DESIGN, REVISION A
(THERMAL TEST)**



NOTE: CERAMIC PHASE DENSITY ~ 182 LB/FT³

**FIGURE 144 - 5000°F TEST SPECIMEN - NOSE CAP -
TUBE REINFORCED CASTABLE DESIGN**

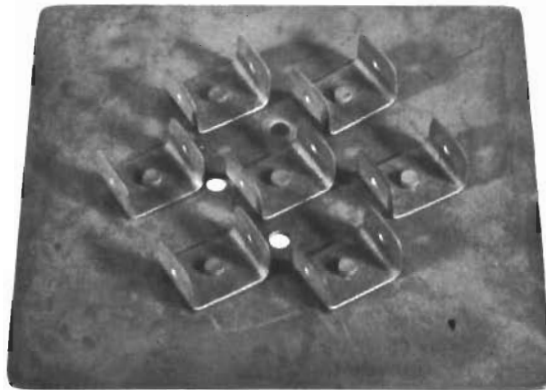
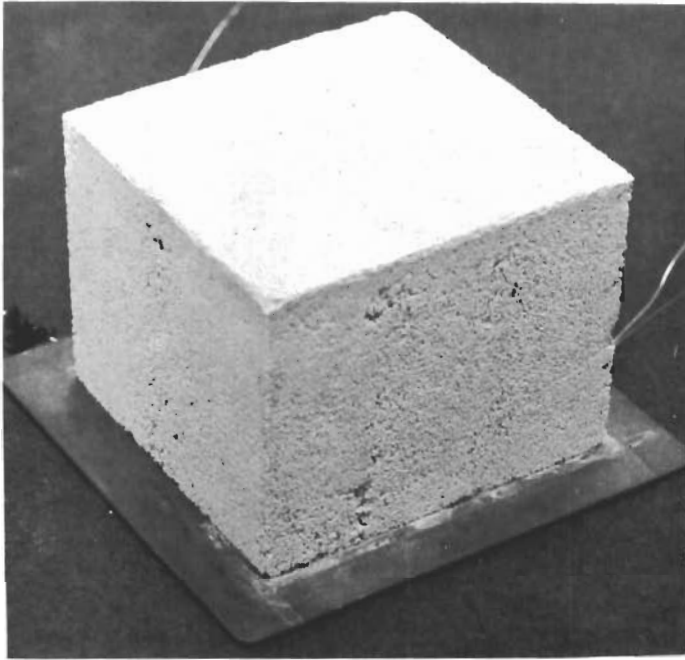
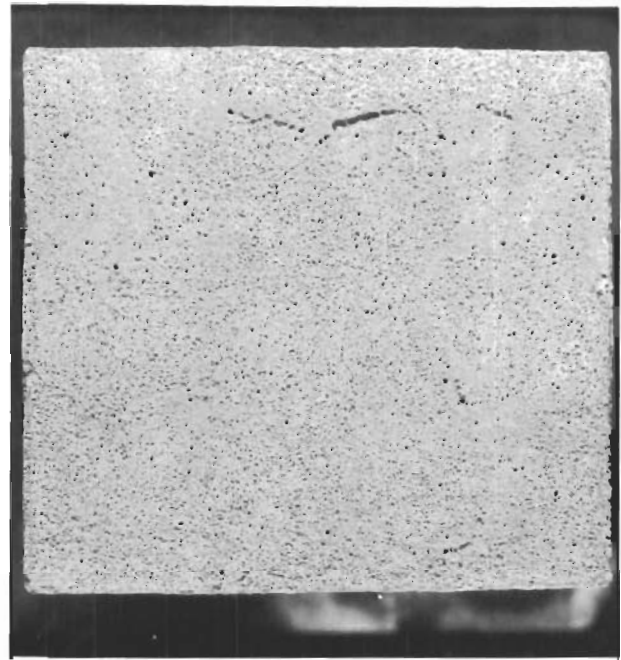


**FIGURE 145 - METAL SUBASSEMBLY - 5000°F TEST SPECIMEN -
TUBE REINFORCED CASTABLE DESIGN**



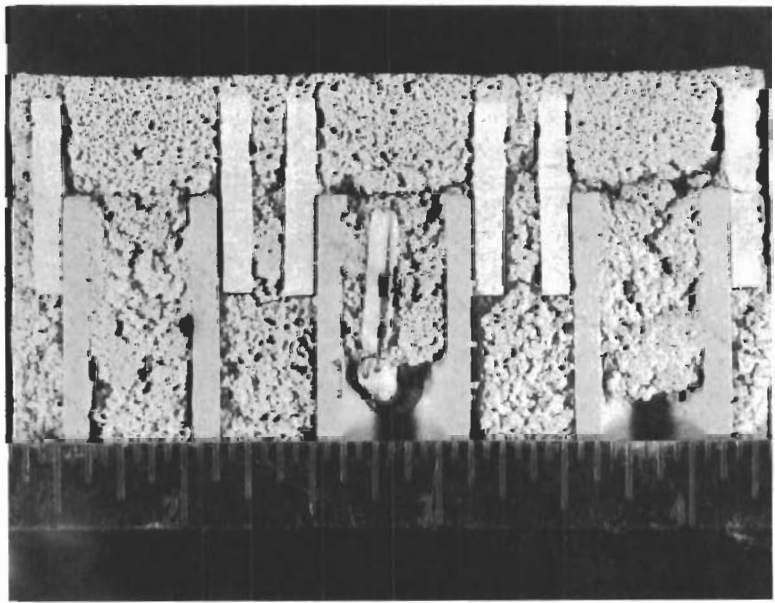
(a) BEFORE TEST



(b) AFTER TEST, TOP VIEW

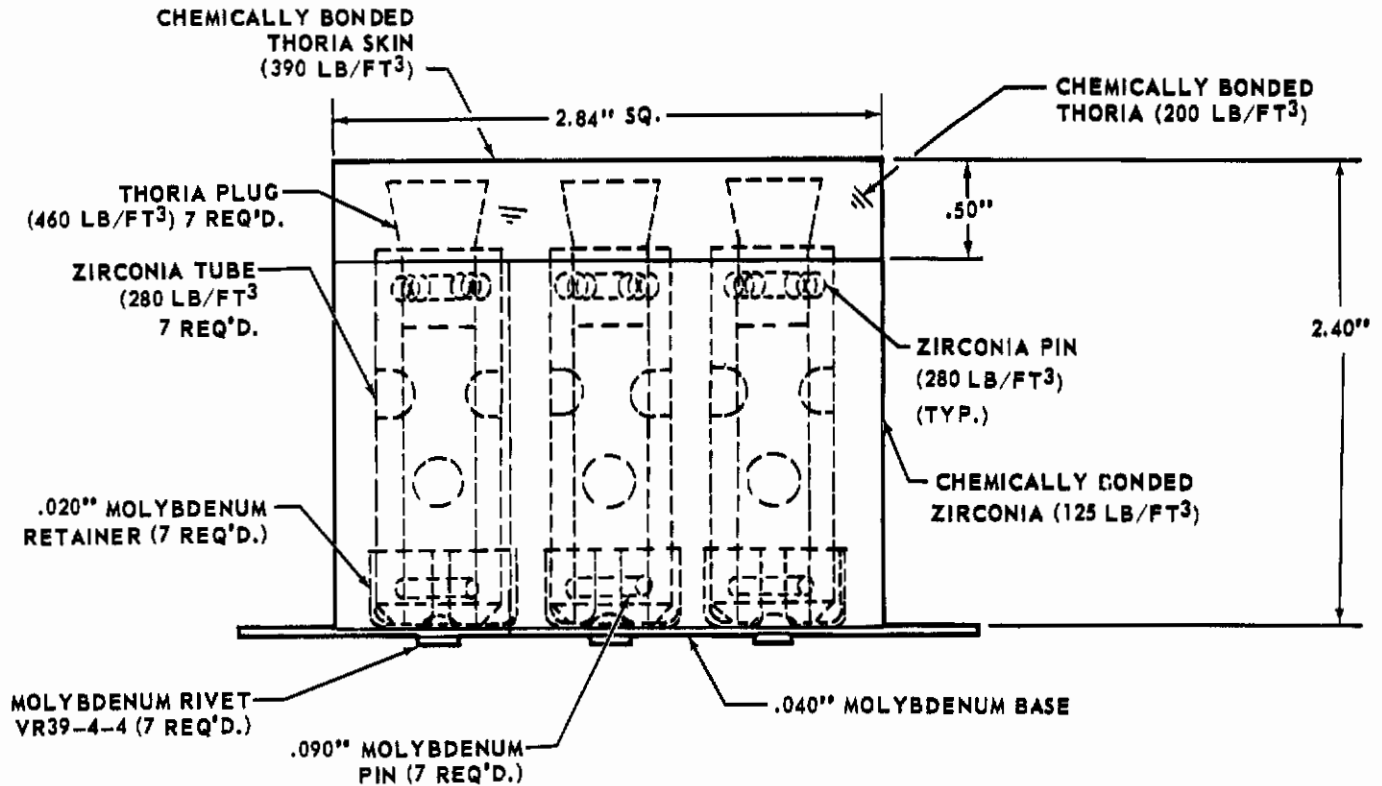


(c) AFTER TEST, SIDE VIEW



(d) AFTER TEST, SECTIONED VIEW

**FIGURE 146 - 5000°F TEST SPECIMEN - NOSE CAP - TUBE REINFORCED CASTABLE DESIGN
(THERMAL TEST)**

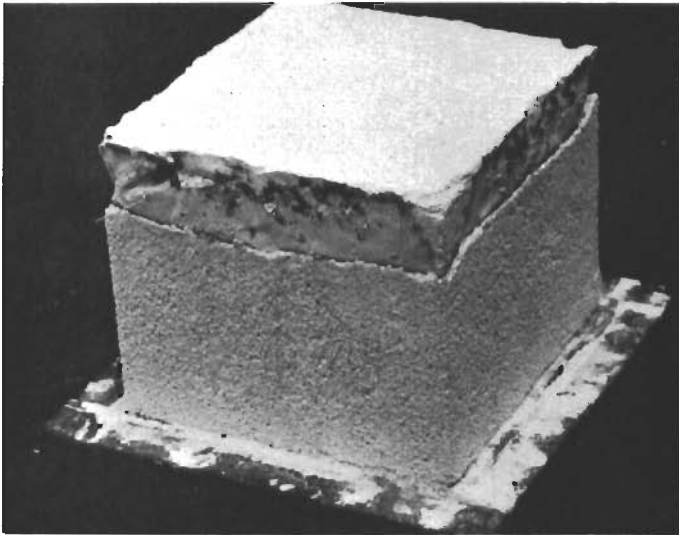


NOTE: CERAMIC PHASE DENSITY $\sim 171 \text{ LB/FT}^3$

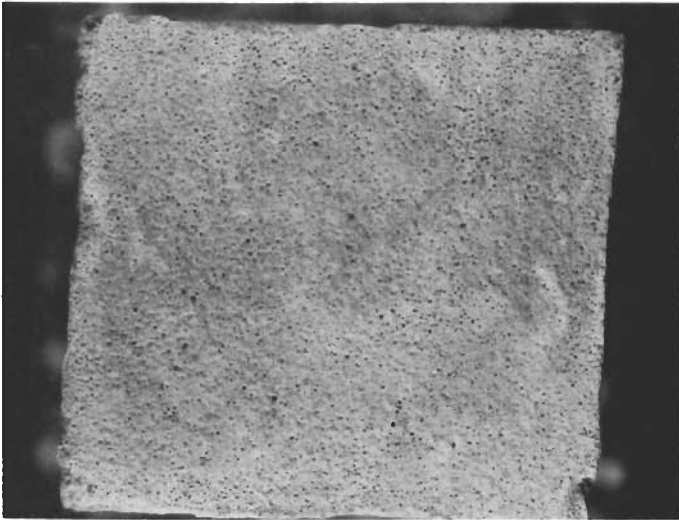
**FIGURE 147 - 5000°F TEST SPECIMEN - NOSE CAP-TUBE REINFORCED
CASTABLE DESIGN - REVISION A**

5.2.3.4 Pre-Loaded Tile Design - The diagram in Figure 151 shows a pre-stressed tile specimen for a 6.0 inch radius nose cap. In this specimen, two low density zirconia blocks were attached on a coated molybdenum substructure and capped with a high density thoria tile. The tile contained an arc-shaped groove which would accommodate a coated tungsten strap with threaded ends. All the components were set in a fixture and the strap drawn against the fixed specimen. The tightly drawn strap compressively preloaded the facing tile by pulling down against it and pulling side fixture bricks in against the tile sides. The strap also held the ceramic elements in position. Chemically bonded high density thoria was trowelled over the strap in the groove to form a thermal shield for the coated tungsten.

Because of the complexity of this setup, this specimen was subjected only to the thermal test, the critical environment for the majority of the test samples. The only visible failure after test was a shrinkage crack across the chemically bonded thoria in the groove (see Figure 152(b)). However, more serious fracture in the dense thoria tile at the groove was found when the setup was disassembled (see Figure 152(c)), and the tile was also warped. Either the pre-loading or the manner of applying pre-load did not improve the thermal shock resistance of the type thoria utilized and promoted tile deformation at elevated temperatures.



(a) BEFORE TEST

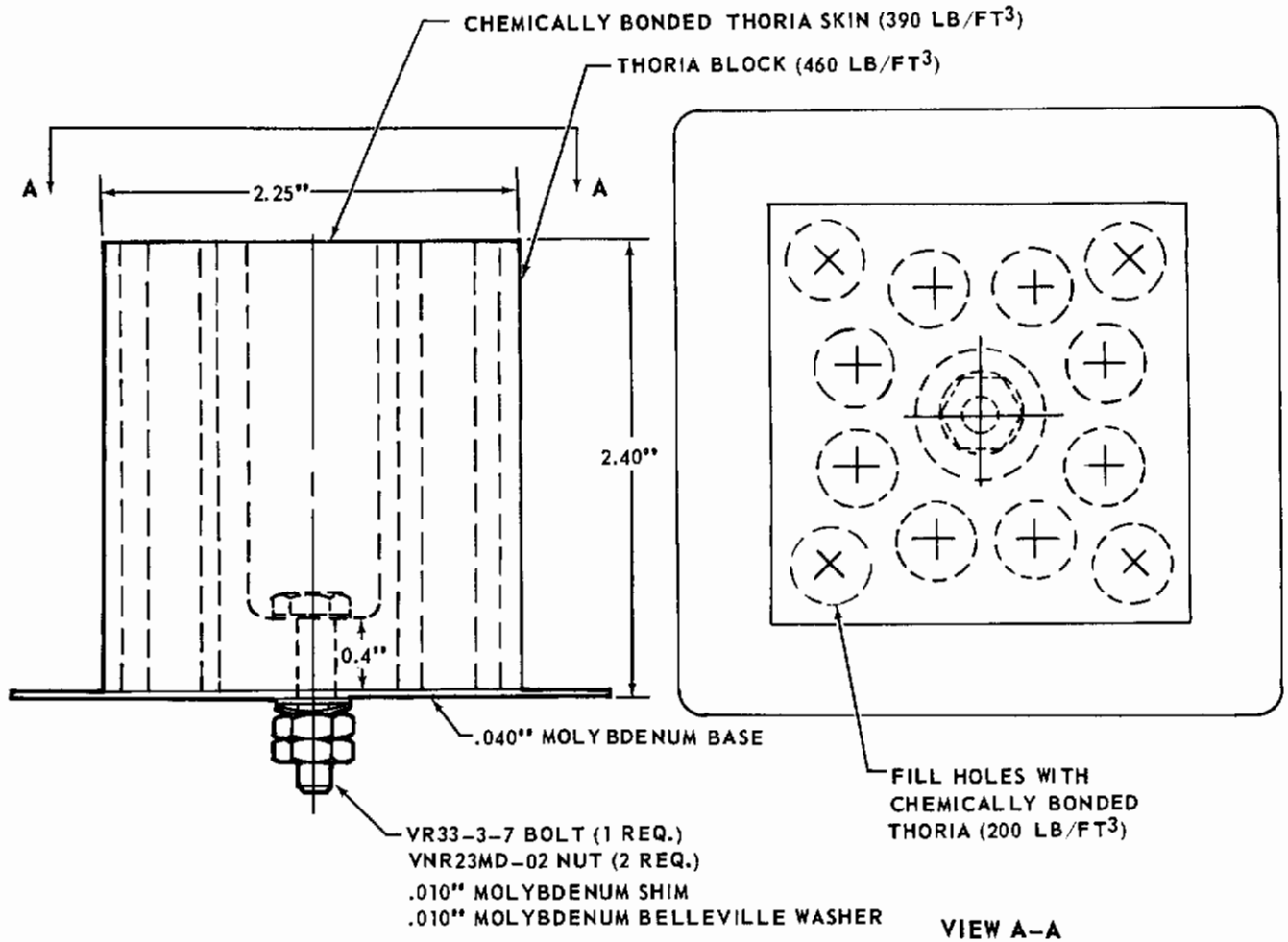


(b) AFTER TEST, TOP VIEW



(c) AFTER TEST, SIDE VIEW

**FIGURE 148 - 5000°F TEST SPECIMEN - NOSE CAP -
TUBE REINFORCED CASTABLE DESIGN, REVISION A (THERMAL TEST)**

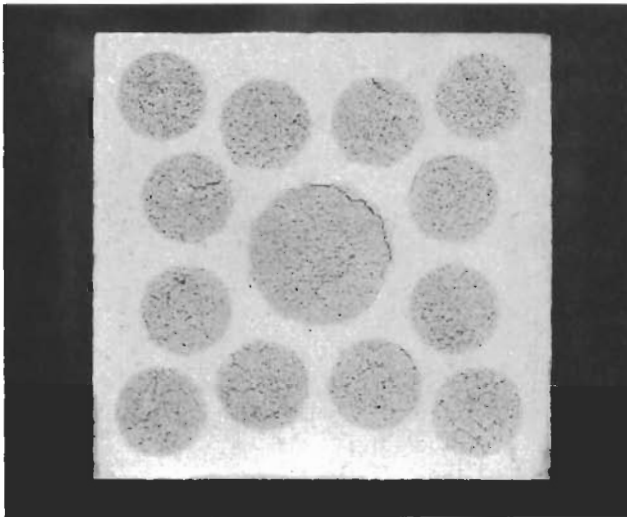


NOTE: CERAMIC PHASE DENSITY ~ 353 LB/FT³

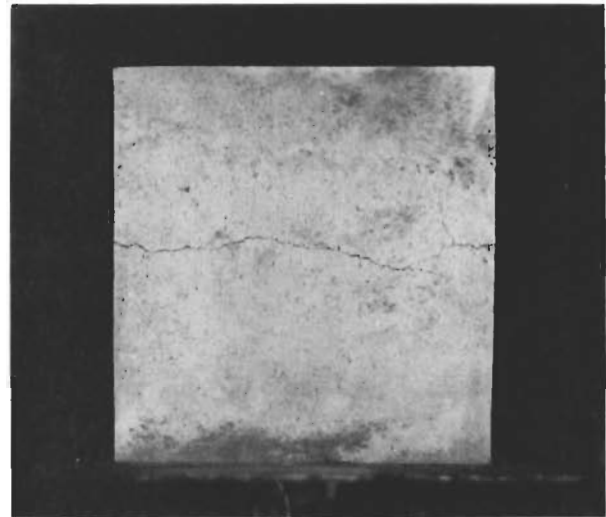
**FIGURE 149 - 5000°F TEST SPECIMEN - NOSE CAP -
VARIABLE DENSITY BLOCK DESIGN**



(a) BEFORE TEST



(b) AFTER TEST, TOP VIEW



(c) AFTER TEST, SIDE VIEW

**FIGURE 150 - 5000°F TEST SPECIMEN - NOSE CAP - VARIABLE DENSITY BLOCK DESIGN
(THERMAL TEST)**

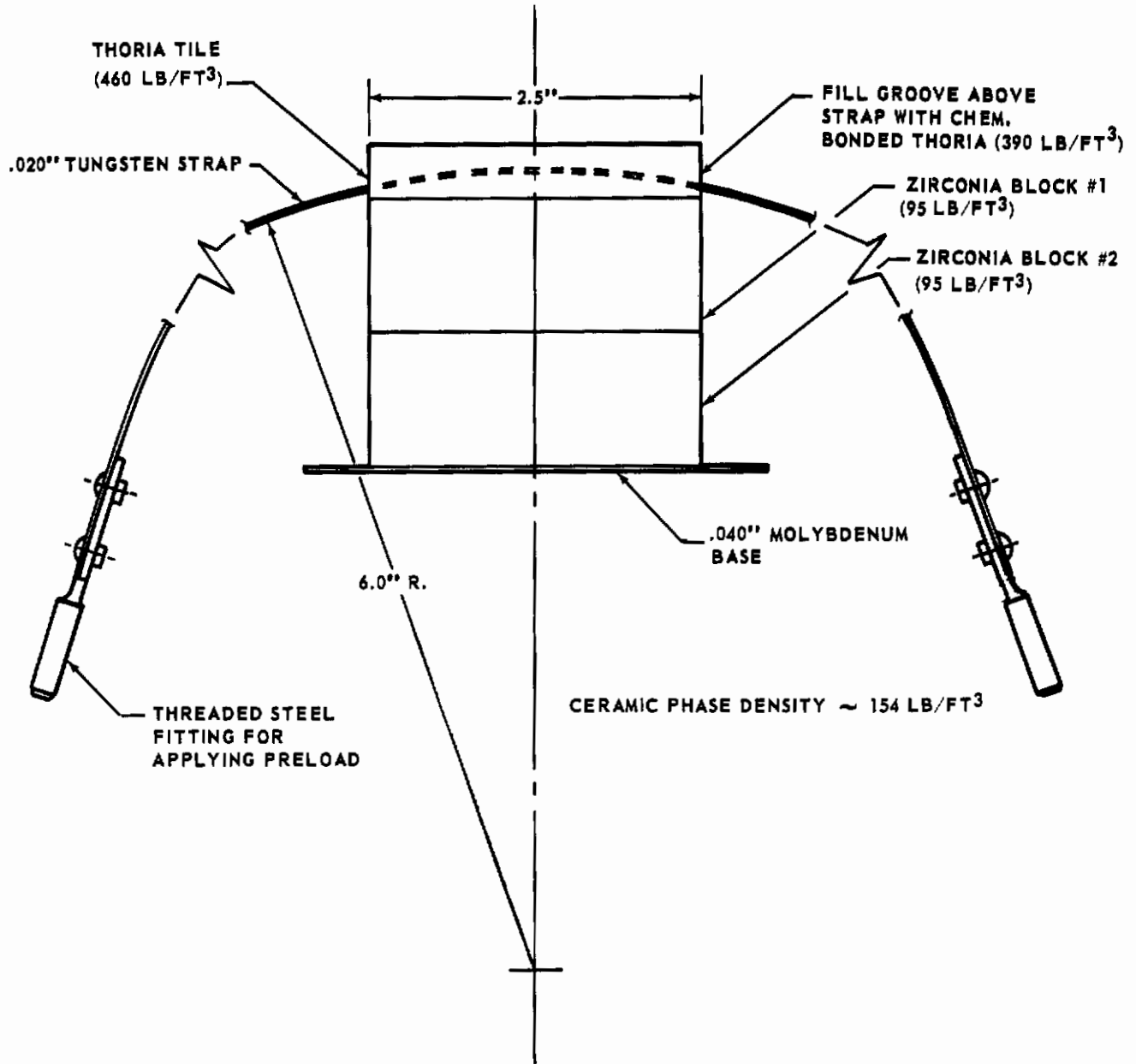
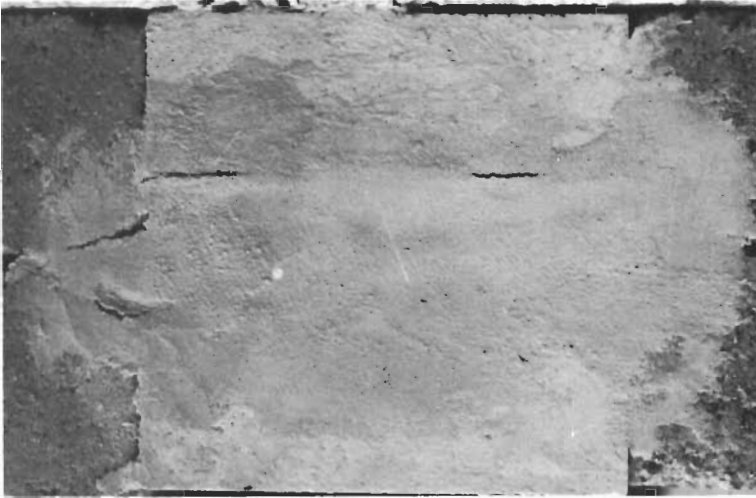
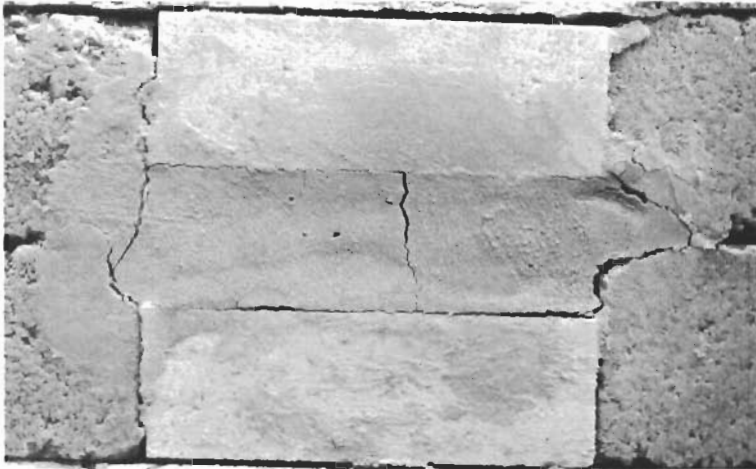


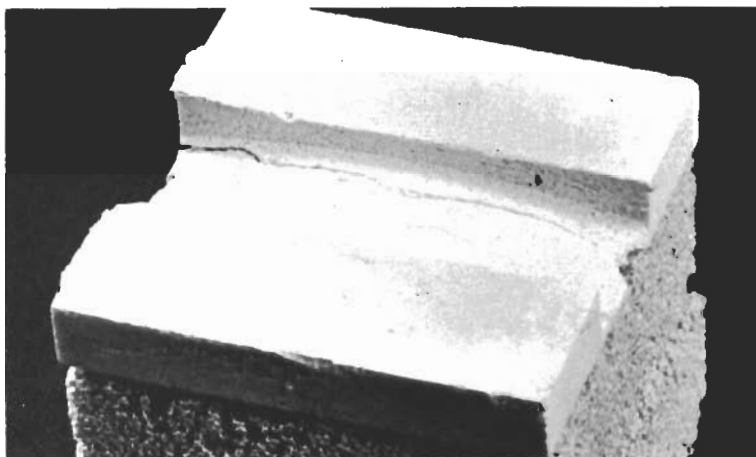
FIGURE 151 - 5000°F TEST SPECIMEN - NOSE CAP PRE-LOADED TILE DESIGN



(a) BEFORE TEST, TOP VIEW



(b) AFTER TEST, TOP VIEW



(c) AFTER TEST, THORIA TILE

**FIGURE 152 - 5000°F TEST SPECIMEN - NOSE CAP - PRE-LOADED TILE DESIGN
(THERMAL TEST)**

5.2.4 Subscale Fabrication Techniques For Ceramics and Refractory Metals

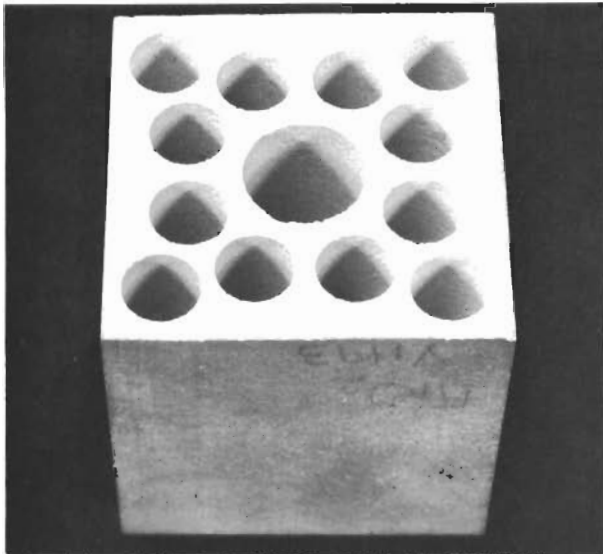
The sintered alumina, zirconia, and thoria parts employed in the subscales were fashioned from raw stock by various grinding processes. It was found that the low density (less than 40% of theoretical) aluminas and zirconias and all thorias could be shaped with silicon carbide grinding tools. However, these tools wore rapidly in working high density alumina and zirconia, and for these materials it was necessary to use diamond grinding tools. Metal bonded diamond grinding wheels with 150 concentration, 120 to 150 grit size and a diamond surface depth of 1/64-1/16 inch were used. Diamond core drills, from 3/32 inch to 5/8 inch diameter, and with abrasive surfaces similar to the wheels, were also used. The larger wheels were 7.0 inches OD and 3/16 inch or 3/8 inch wide. Other diamond wheels included 3/16 inch and 3/8 inch diameter ball wheels and 3/16 inch and 1/2 inch diameter cylindrical wheels. In addition, metal-bonded diamond saws were also employed. One saw (cut-off wheel) was 6.0 inches in diameter by 0.045 inch thick and a second was 8.0 inches in diameter by 0.065 inch thick. A diamond band saw was procured for the full scale program to expedite rough-in work on some contoured surfaces. Some of the diamond tools used are shown in Figure 153.

The brittle nature of ceramics complicated the holding techniques needed in the cutting operations. Early in the program, all ceramic stock was bonded with thermal setting cement to metal blocks which were in turn clamped in the machine. It was later found that most ceramic stock (except for the very low density, low strength ceramics) could be clamped if the clamping surfaces were true and pressures light and uniform.

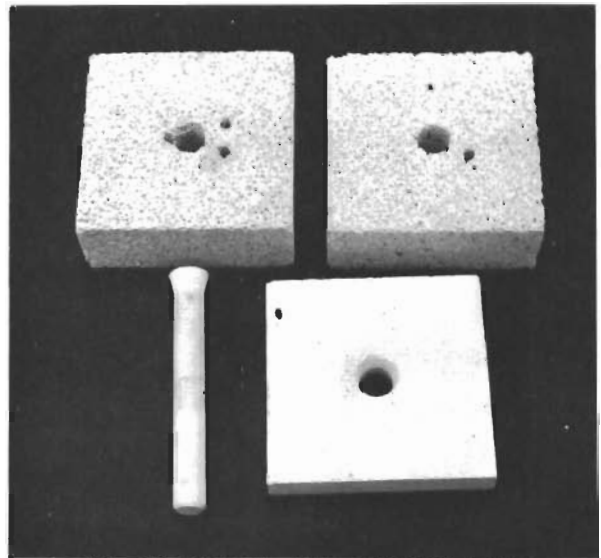
The very low density ceramics (20% theoretical or less) were impregnated with paraffin before grinding to prevent chipping and tearing on the surfaces, edges, and corners. These low density ceramics could also be cut with a silicon carbide wheel, with each pass removing as much as 0.015 inch of material. Tolerances on parts cut from paraffin-filled stock could be held as close as +0.003 inch. However, these techniques could not produce sharp edges in the ceramic materials. In addition, the paraffin loaded the grinding wheels, which required stopping at intervals to clean the wheel by melting the paraffin. The paraffin in the finished part was removed by boiling in water, and as a final clean-up, all parts were baked in an oven at 1600°F to insure that all paraffin and other contaminants were removed.

Diamond tools were used to grind zirconia and alumina with densities that ranged from 40% to 90% theoretical. Maximum material removal per pass on the highest density materials was held to 0.001 inch with very low cross feeds used. All holes in low and high density materials were made with diamond core drills which produced good surfaces and close tolerances. Counterbores were produced using an appropriate core drill and snapping off the core. The bottom of the counterbore was then cleaned-up with a cylindrical grinding wheel. A flood of coolant, consisting of water and a rust inhibitor-lubricant, was used in all grinding operations conducted on the sintered ceramics. This coolant is visible in Figure 154, which shows a surface grinding operation on a low density zirconia. A baking process was used on unfilled finished parts to remove any residual coolant or other contaminants.

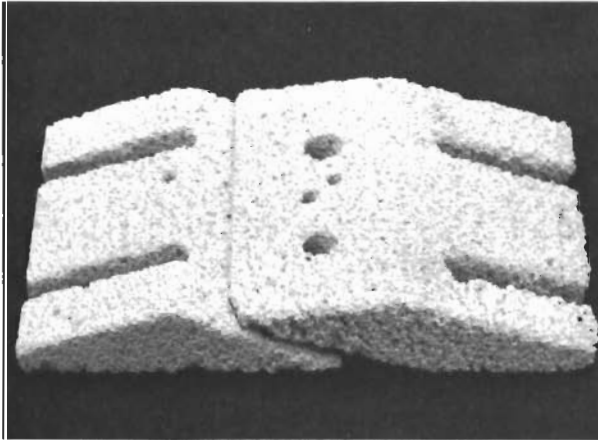
Some of the ceramic parts produced for the subscale specimens are illustrated in Figure 155. The ceramic pins shown in this figure were turned in a



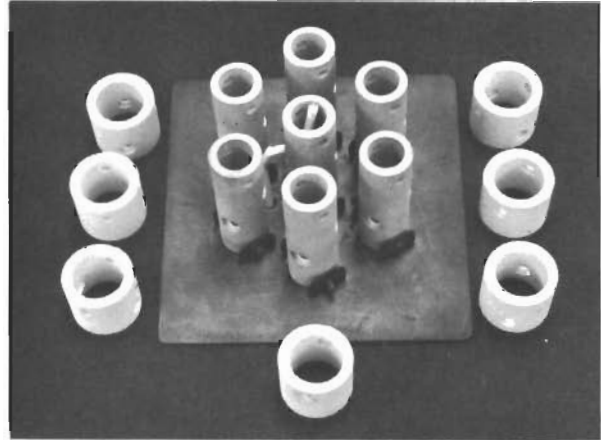
(a) HIGH DENSITY THORIA BLOCK



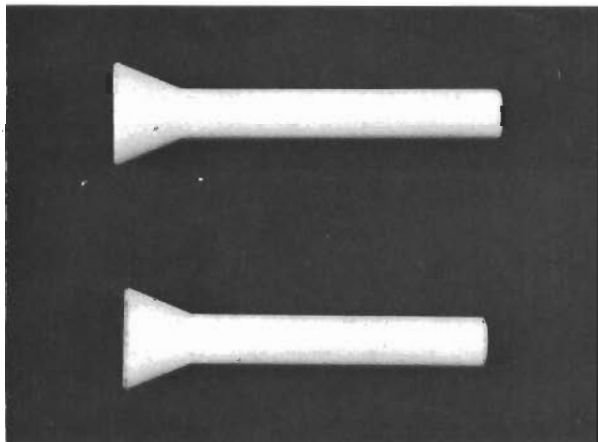
(d) ZIRCONIA AND THORIA FOR THORIA PIN-TILE DESIGN



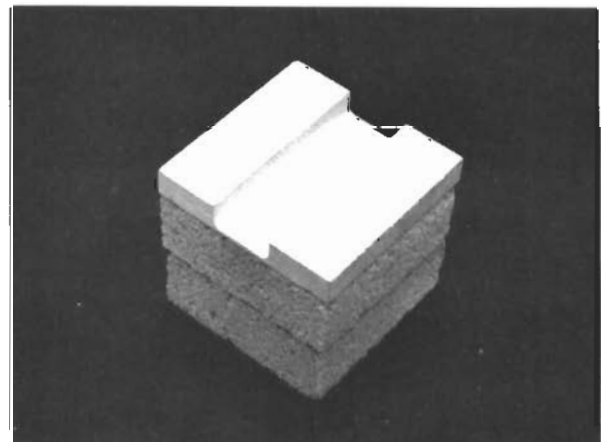
(b) LOW DENSITY ZIRCONIA FOR CASTABLE DESIGN



(e) ZIRCONIA AND THORIA PARTS FOR THORIA TUBE REINFORCED CASTABLE DESIGN



(c) ZIRCONIA PINS



(f) ZIRCONIA AND THORIA PARTS FOR THORIA PRE-LOADED TILE DESIGN

FIGURE 155 - CERAMIC PARTS AFTER MACHINING

lathe which utilized a tool post grinder. The tapers on the pins were made with a 3/16 inch diameter ball wheel. The radiused groove in the tile in Figure 155(f) was produced with the aid of a specially built fixture, which permitted a securely held tile to be rotated on an appropriate arc while the grinding wheel was fed into the tile.

The hemi-cylinder block used on the specimen shown in Figure 130 was ground with the aid of a similar fixture. This type of grinding operation is shown in Figure 156.

Fabrication of subscales which employed chemically bonded castable ceramic revealed that these materials possessed very poor flow characteristics. These materials had to be forced into the voids, cavities, or molds and then thoroughly tamped to insure that the material packed solidly. The fill and tamp process was repeated until the desired level was reached. Stainless steel rods with diameters appropriate for the cavities were used as tamping tools. Stainless steel was also used for molds in fabricating the castable subscales shown in Figures 108, 133, 143, 146, and 148. Petroleum jelly was used to coat the mold surfaces to act as a release agent. The molds were readily broken down after the specimens were cured to the required 300°F. The surface skins required on some subscales were carefully applied by troweling a thin layer of the chemically bonded high density material into and onto the surface of the previously moistened subscale module.

Columbium and molybdenum parts used on the subscales required special fabricating processes which were not necessary for the more conventional metals. Shearing was not used in blanking parts from columbium or molybdenum. The detail columbium parts were sawed from sheet stock and the molybdenum parts were either chemically blanked or milled from stock. Special blanking methods for molybdenum were designed to eliminate delamination at the edges of the part. Sawing, in the case of columbium, was chiefly a measure for conserving the costly material. The edges of all blanked parts were radiused to a minimum of 0.005 inch by hand-sanding or vibratory deburring in preparation for the protective coating. The molybdenum parts were hot formed as required, while the columbium parts were formed at room temperature. All formed parts were thoroughly inspected for cracks, delaminations, and general surface abnormalities, and then cleaned by pickling. All further work on the refractory metal parts was performed under white-room conditions.

The next step for the molybdenum details was a fit-up assembly. All sharp edges produced on the details in this operation were radiused. The details were pickled once again and a silicide oxidation protective coating was applied to the individual parts. Detail parts were assembled and a final silicide repair-coat applied to the assembly. McDonnell silicide coating (L-7) applied by the slurry-diffusion process was used in all cases for molybdenum.

A fit-up operation was also performed in the case of the columbium details and any newly created sharp edges were radiused. Details were pickled and then permanently assembled by welding or riveting. An aluminum slurry (McDonnell LB-2) was applied at all riveted faying surfaces in the assembly. All surfaces of the complete assembly were coated with the aluminum slurry and the fully coated unit was then processed at elevated temperatures to produce an aluminide oxidation protective coating (McDonnell LB-2).

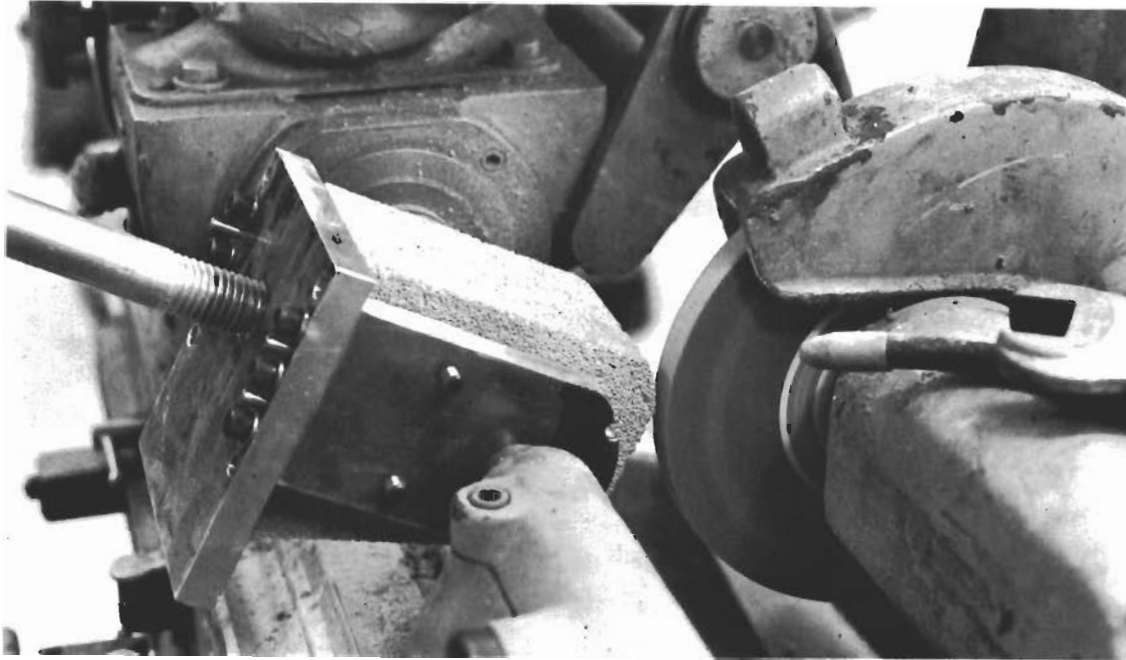


FIGURE 156 - GRINDING OF CONTOUR ON LOW DENSITY ZrO_2 BLOCK

5.2.5 Subscale Program Conclusions

Test results for all subscale specimens are presented in Table XXV. It will be noted that most failures occurred during the thermal tests with almost all specimens successfully surviving vibration and acoustical testing.

The results for the 3400°F subscale specimens show that the 3400°F tile design, revision B (see Figure 113) survived all tests without any critical failures. This subscale also exhibited the fewest and the least significant flaws after test. This design was considered very adaptable to full scale fabrication and assembly, and was selected as the model for the full scale 3.0 inch radius leading edge. The actual ceramic phase density in this successful subscale was 48 lb/ft³, which was very close to the design objective of 50 lb/ft³.

The reinforced castable design proved fairly successful in testing but the strength of the chemically bonded low density alumina utilized was considered too low for handling and assembling purposes for a full scale component. A better low density alumina was developed later but not before full scale designs were already firm. The revised pin-tile design had sufficient cracking after thermal test to consider it marginal for withstanding the thermal trajectory. Difficult fabrication and assembly problems would be expected with this design. The comments for the pin-tile design also apply to the variable density design.

The initial plan for a water cooled substructure for the 3.0 inch radius component was changed in favor of a radiation cooled substructure. This change in plans was due chiefly to a thermodynamic analysis which indicated

TABLE XXV - SUBSCALE TEST RESULTS

Type Module	Ceramic Phase Density (Lb./Fr ³)		Vibration and Acoustic Testing ^(b)	Thermal Testing ^(a)	
	Predicted	Actual		Max. Temp. of Base (°F)	Remarks
(1) 4000°F key block design	147	158	No visible failure	2130 (Insulated backside)	Small shrinkage cracks in chem. bonded ZrO ₂ at all cavities; crack in low density block; see Figure 122. (c)
(2) 4000°F key block design revision A	130	146	Not tested	2250 (Insulated backside)	Small crack in key block; see Figure 124 (c)
(3) 4000°F key block design revision B	96	95	Not tested	2140 (Insulated backside)	Very minor cracks; see Figure 126 (c)
(4) 4000°F block design	94	73	No visible failure (d)	1880 (Insulated backside)	Small shrinkage cracks in chem. bonded ZrO ₂ at bolt holes; crack in block, parallel and close to surface; see Figure 128 (c)
(5) 4000°F block design revision A	101	120	Not tested	2100 (Insulated backside)	Cracks initiating from backside; see Figure 130 (c)
(6) 4000°F reinforced chemical bonded design	101	83	No visible failure	2100 (first cycle) (Insulated backside)	First cycle, crack in low density commercial block, no cracks in chem. bonded ZrO ₂ ; second cycle cracks in end sections of chem. bonded ZrO ₂ . See Figure 133 (c)
(7) 4000°F Pin-tile design	92	78	No visible failure (d)	1720 (Insulated backside)	Tile cracked and deformed; pin head deformed; low density block had various cracks; see Figure 135 (e)
(8) 4000°F Pin-tile design revision A	101	115	Not tested	1850 (Insulated backside)	Tile cracked and bowed; pin head deformed; see Figure 137 (e)
(9) 4000°F Pin-tile design revision B	101	115	Not tested	No instrumentation (insulated backside)	Tile cracked; pin head deformed; see Figure 138 (e)
(10) 5000°F tile design	154	146	Pin broke during vibration near molybdenum base (see Figure 140); no visible failure with new retainer for ceramic pin.	1250 (Free to radiate)	Tile cracked; pin broke near head; see Figure 141 (e)
(11) 5000°F tile design revision A	138	129	Not tested	1125 (Free to radiate)	Shrinkage in chem. bonded ThO ₂ tile; slight cracks; see Figure 143 (f)
(12) 5000°F tube reinforced castable design	182	176	No visible failure	T/C was lost (free to radiate)	Separation between chem. bonded ThO ₂ and ZrO ₂ ; small cracks in ThO ₂ tube; see Figure 146 (c)
(13) 5000°F tube reinforced castable design, Rev. A	171	163	Not tested	950 (Free to radiate)	Slight cracks in chem. bonded ThO ₂ and ZrO ₂ ; see Figure 148 (c)
(14) 5000°F variable density block design	353	350	No visible failure	1000 (Free to radiate)	Crack traversing perimeter ~1 inch below surface; see Figure 150 (f)
(15) 5000°F pre-stressed tile design	154	---	Not tested	1200 (Free to radiate)	Chem. bonded ThO ₂ cracked; tile cracked in groove; see Figure 152 (e)
(16) 3400°F variable density tile design revision A	60	63	No visible failure	475 (Water-cooled)	Small crack in high density tile; catastrophic crack in low density Al ₂ O ₃ ; insulation shrunk; see Figure 105 (c)
(17) 3400°F reinforced castable design	32	32	No visible failure	450 (Water-cooled)	Weak after test; see Figure 108 (f)
(18) 3400°F tile design	39	44	No visible failure	210 (Water-cooled)	Molybdenum bolts loosened; tile had no visible cracks; water seeped into insulation (c)
(19) 3400°F tile design revision A	39	54	Not tested	1550 (Free to radiate)	Plate deformed; insulation shrunk; see Figure 112 (c)
(20) 3400°F tile design revision B	39	48	Not tested	1400 (Free to radiate)	Chem. bonded Al ₂ O ₃ shrunk away from tile; see Figure 114 (c)
(21) 3400°F pin-tile design	53	58	No visible failure; (d) Cracked tile fell off. See Figure 117	170 (Water cooled)	Tile cracked; low density block had various cracks; water seeped into insulation. (Figure 117) (e)
(22) 3400°F pin-tile design revision A	64	56	Not tested	1350 (Free to radiate)	Slight crack in pin; small crack in low density block; see Figure 119 (c)

NOTES:

- (a) Thermal test conditions shown in Figure 101 : Modules 1-9 on Curve 2, Modules 10-15 on Curve 1, Modules 16-22 on Curve 3.
- (b) Test conditions: Vibration - 0.02 g²/cps to 50 sec.; 0.04 g²/cps, 50-100 sec; 0.02 g²/cps, 100-150 sec.; 0.004 g²/cps, 150-900 sec. (Module shaken in three directions)
Acoustic - 155 db above 0.0002 dynes/cm² at 15 to 9600 cps for 5 minutes.
- (c) Component would have functioned satisfactorily for one complete flight.
- (d) Also subjected to vibration only, after thermal testing.
- (e) Component would not have functioned satisfactorily for one complete flight.
- (f) Questionable whether component would have functioned satisfactorily for one complete flight.

that water cooled substructure required 17 pounds of water per hour per foot of leading edge during re-entry. Preliminary weight studies for the full scale component showed that a radiation cooled composite leading edge would weigh approximately 7.0 pounds per running foot. These weight figures show that water cooling, which may be required for the critical compartments of a vehicle, could be employed more efficiently at locations other than at the leading edge substructure.

Test results for the 4000°F subscale specimens indicate that two design concepts, the 4000°F key block design and the 4000°F reinforced chemically bonded design, survived the test environments very well. Neither the pin-tile nor monolithic block concepts were successful. The third generation key block design (see Figure 125) at the conclusion of a single test cycle displayed no significant defects. The reinforced chemically bonded design (see Figure 131) did exhibit a crack in a sub-surface ceramic component at the conclusion of the first test cycle, but the specimen was still intact and serviceable after a second thermal test. The actual ceramic phase densities of the specimens were 95 lb/ft³ for the third generation key block design and 83 lb/ft³ for the reinforced chemically bonded design, both of which were well below the design objective of 120 lb/ft³. A review of the two designs revealed that the key block design required fewer and less complicated ceramic and metallic components and; therefore, could be more readily adapted to the 1.5 inch radius configuration. Also, assembly of the key block design would be simpler. These observations led to the selection of the key block design for the full scale 1.5 inch radius leading edge component.

Test results for the 5000°F subscale specimens showed that the tube reinforced castable designs produced the only reasonably successful specimens. The original tube reinforced castable specimen (Figure 144) and the second generation specimen (Figure 147) exhibited some flaws at the conclusion of the thermal test cycles, but these defects did not threaten the integrity of either composite ceramic shield. Actual ceramic phase densities of 176 lb/ft³ and 163 lb/ft³ were achieved for the first and second generation specimens respectively. These densities were relatively low when considering that a substantial percentage of each specimen was composed of some form of thoria. The first generation design was selected from these two because the thoria tubes would require less grinding than the thoria plugs. Also the first generation design would be easier to assemble as the zirconia-thoria tube assembly could be preassembled before attachment to the metal substructure. The thoria plug-zirconia tube design could not be preassembled because the zirconia tubes could not then be filled with low density chemically bonded zirconia.

There were some reservations about building a full scale tube reinforced castable nose cap. The most serious problem envisioned was the attachment of the numerous reinforcing tubes to the hemispherical substructure. In the tested subscales, the tubes were pinned to channel retainers which were riveted to the substructure. In the full scale component, the pattern and the orientation for the densely packed channel retainers would be very critical since the coupling pins required an open insertion path during the installation of the reinforcing tubes.

A new method for attaching the reinforcing tubes was proposed and the subscale shown in Figure 157 was built to help establish the reliability of

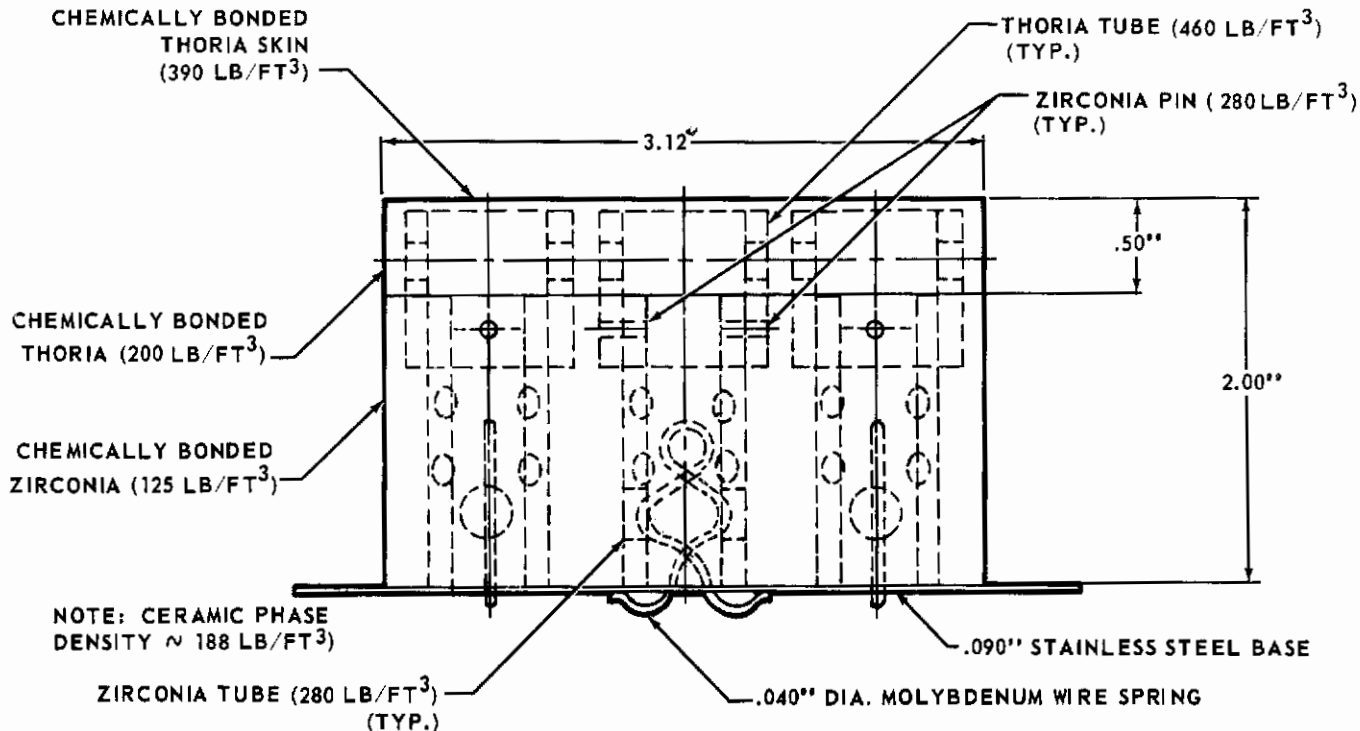


**FIGURE 157 - 5000°F TEST SPECIMEN - NOSE CAP SPRING COUPLED,
TUBE REINFORCED CASTABLE DESIGN**

the concept. On this design, the reinforcing tubes were secured by spring clips made of coated molybdenum wire. In the full scale component, this method of attachment would offer each retention member an open insertion path from the interior of the hemispherical substructure.

Several problems arose during the fabrication of the spring clip subscale specimen. The clips interfered with the tamping procedure and prevented the castable material from fully packing the interior of the reinforcing tubes. In addition, several of the relatively brittle coated molybdenum clips broke in the vicinity of their engaging tangs at the base of the specimen. These failures occurred when a high temperature tape was removed from the base after the specimen was cured. The tape had been applied to the perforated base to contain the uncured castable ceramics during the assembly operation. The vibration and acoustical tests were not performed on this specimen because of the breakage of several springs. The thermal test resulted in no significant damage to the composite ceramic shield and there was no evidence of any further damage to the springs.

The experiences with the spring clip specimen demonstrated once again that the tube reinforced castable design would produce an effective composite ceramic shield. The failures and poor reliability of the coated molybdenum wire spring clips made it necessary to utilize the channel retainer and pin attachment in the full scale nose cap design. To cope with the assembly problem, a pattern with a detailed location and a prescribed orientation for each retainer would have to be established in conjunction with an assembly sequence.

5.3 STAGE 3A DESIGN AND FABRICATION OF FULL SCALE COMPONENTS

The full scale 1.5 and 3.0 inch radius leading edges and the 6.0 inch radius nose cap were designed with the objective of producing representative leading surfaces that would realistically approximate sectors of an operational re-entry vehicle. To this end, each test component included, in addition to the actual leading surface, a structural support stub which represented a small portion of the vehicular body that would ordinarily abut each leading surface. These stubs made it necessary that each leading surface and its mounting provisions be designed within the geometric limits of a representative vehicle. The composition of the actual leading surface was governed by an appropriate design concept which was established in the subscale test program. Construction of the full scale components enabled evaluation of the producibility of the composite ceramic leading surfaces.

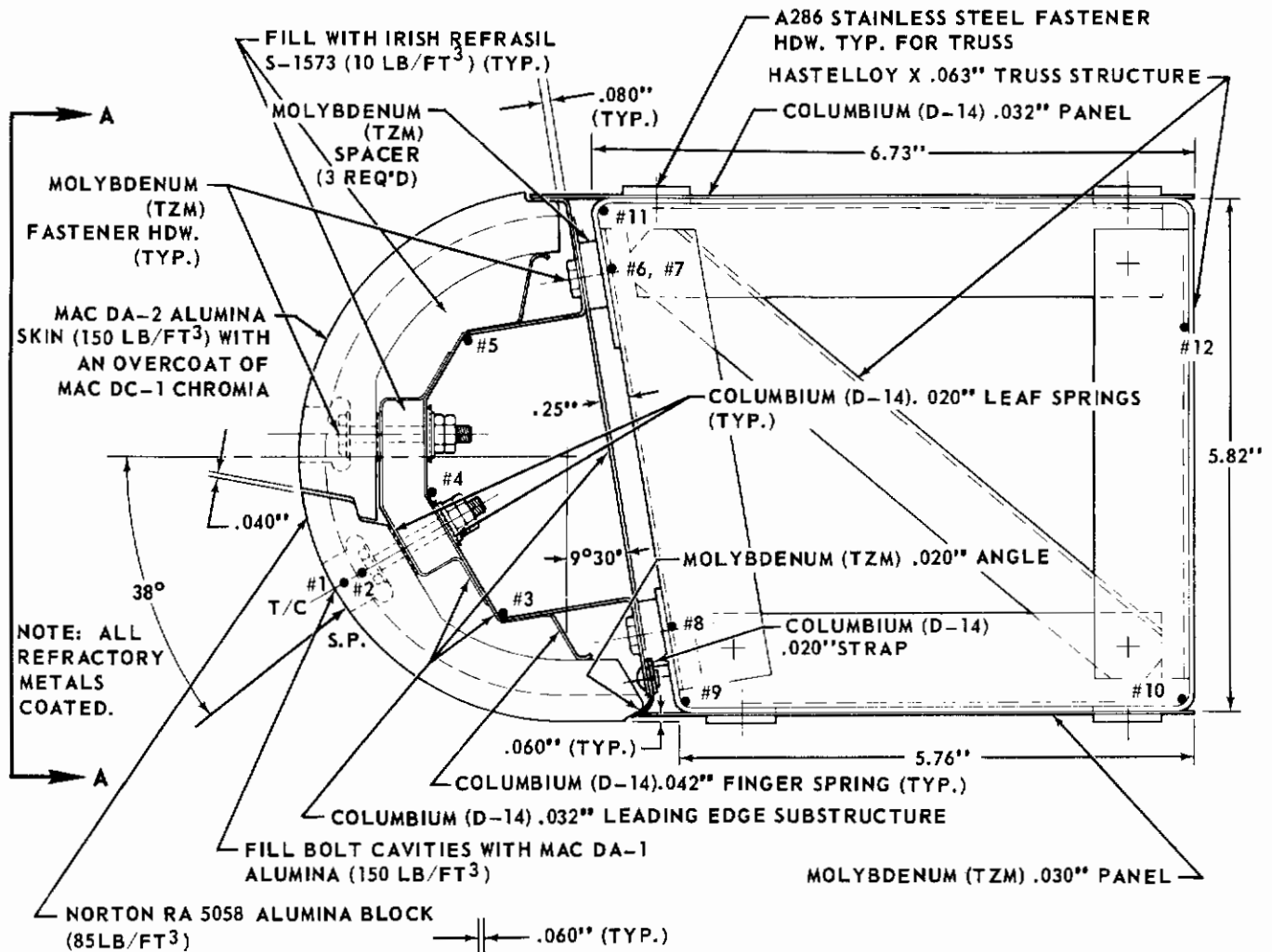
The test program for the full scale components included vibration and acoustical tests to simulate the launch environment, and thermal environment tests to simulate the aerodynamic re-entry heating. In the dynamic test, the resilience in the support structure of the test component helped to duplicate the conditions that would actually prevail in the flight of an actual vehicle. In the thermal tests, the structural stubs helped to approximate the heat exchange that takes place between the leading surfaces and the interior of adjoining vehicular compartments. However, in the test of these full scale components, only the leading surface was fully exposed to the predicted re-entry temperature history and, therefore, the structural stubs did not experience temperatures representative for an actual vehicle. These reduced temperatures allowed the use of super-alloys in the structural stubs instead of refractory metals. In addition, the skin panels on the stubs were made of flat sheet rather than the more representative sandwich panel since the test components were not subjected to flight airloads and thermal gradients.

5.3.1 3.0 Inch Radius Leading Edge Component

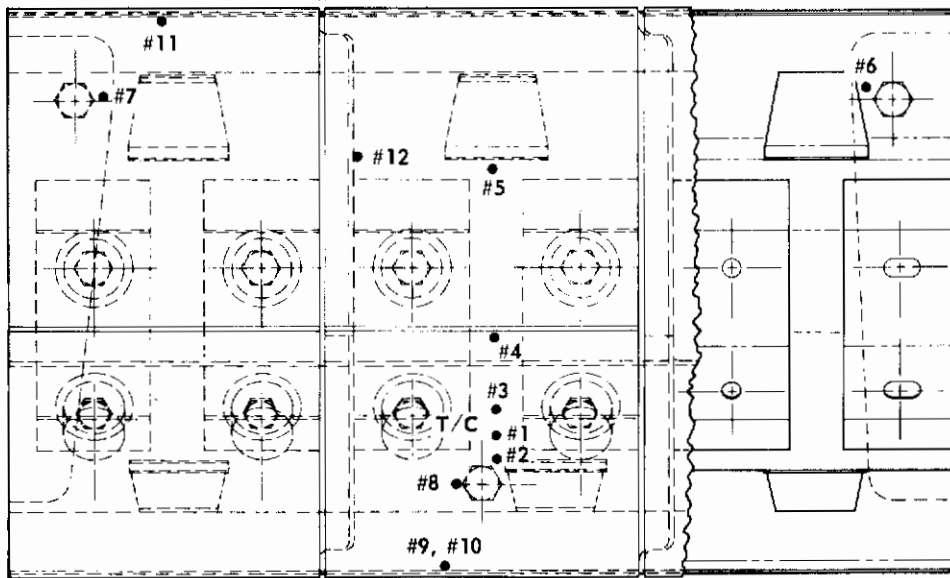
The full scale 3.0 inch radius leading edge component consisted of approximately 10.0 running inches of ceramic shielded leading edge mounted to a like length of closed support structure. The support structure represented the forward portion of a wing or fin and ran from a leading edge spar aft for approximately 6.0 inches to a simulated primary spar. Design and fabrication of this full scale component are discussed below.

5.3.1.1 Full Scale Design - The full scale 3.0 inch radius leading edge component shown in Figure 158 utilized the 3400°F tile design which, on the basis of subscale test results, offered the most promising prospects for this configuration (see Section 5.2.5). Two contoured alumina tiles, each approximately the size of the tile on the subscale specimen, were butted along an axial slip-joint to form a semicircular section of leading edge ceramic. Each tile was retained by two spring loaded bolts, one through a close fit hole in the substructure and the other through a slotted hole. Three of these semicircular sections of ceramic, butting along circumferential slip joints, were mounted on a single unified substructure to form a leading edge segment.

The substructure consisted of a single coated columbium hat section, six coated columbium support brackets, six coated columbium finger springs, two coated columbium tie struts, one coated molybdenum angle (lower retention



T/C #1 & #2
(IR/IR-40 Rh)
T/C #3 THRU #5
(Pt/Pt-10Rh)
T/C #6, #7, #8,
#9, #10, #11, #12
(CHROMEL/
ALUMEL)



NOTE: CERAMIC
PHASE DENSITY ~
57 LB/FT³

VIEW A-A

FIGURE 158 - 3400°F FULL SCALE TEST SPECIMEN
3.0 INCH RADIUS LEADING EDGE

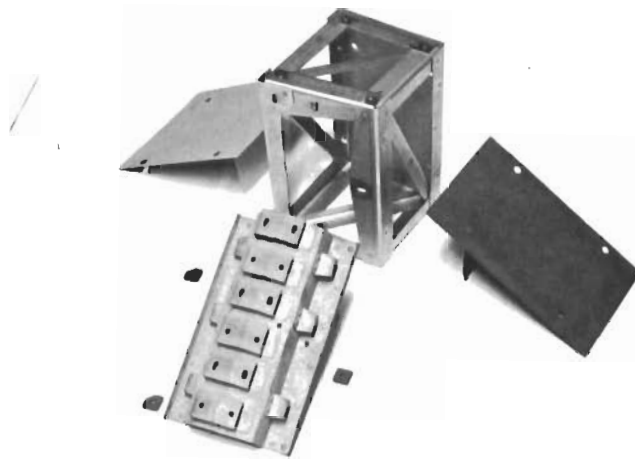
flange) and a coated columbium strap. All of these coated refractory metal elements were assembled into a single unit as shown in Figure 159. The voids between the facing tile and the basic hat section of the substructure were filled with low density silica fiber matt.

The series of holes and slots (see Figure 159(b) for clear view of holes in substructure) used to attach the alumina facing tiles and the slip joints enabled accommodation of a differential expansion between the ceramic and the substructure in an axial direction. The finger springs pressed the unbolted edge of the tiles against a flange of the substructure, thereby maintaining mold-line contour. In addition, the springs deflect as the ceramic tile bows slightly under the influence of a radial temperature gradient. The pivot action produced at the attach joints by this bowing effect is accommodated by the oversize holes in the hat section and by leaf springs situated in the ceramic/substructure interface and under the nut of each bolt. This elastic support minimizes the stresses which the restraining members superimpose upon the ceramic tile when thermal gradients occur.

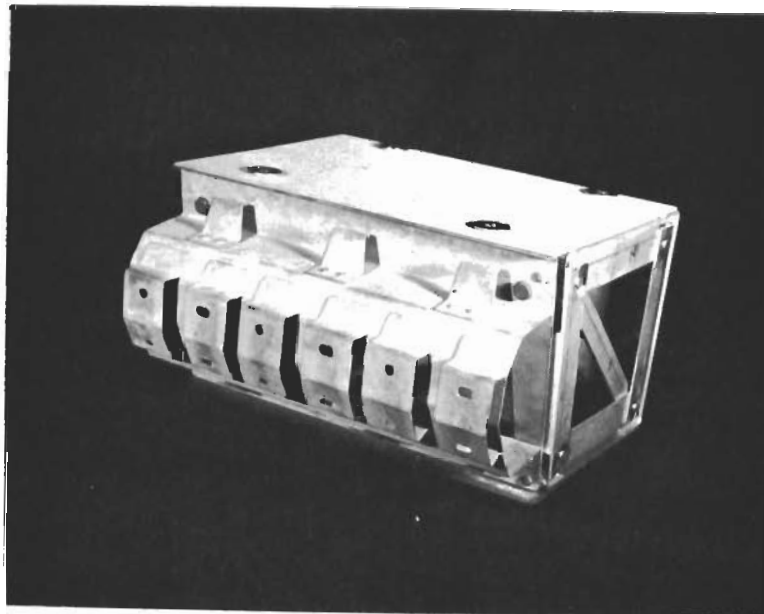
The full leading edge segment (ceramic shield plus coated refractory metal substructure) was attached by three fasteners to the support structure (see Figures 158 and 160). A molybdenum spacer was placed between the substructure and the support structure at each of the three attach points to minimize the thermal conduction path. The two fasteners at the top of the substructure, one at either end, rode in horizontal slots in the support structure. The single center fastener at the bottom of the substructure rode in a vertical slot in the support structure. This arrangement permitted differential linear growth in two directions and also accommodated some degree of curvature change that could be introduced by the thermal gradient across the thickness of the component.

The support structure was made of Hastelloy X, and simple trusses were used for all but one load carrying member. Because of the pin joints and the simple structural elements, a truss can adjust to the differential thermal growth that will arise in a hot structure. A coated columbium skin panel was attached to the top and a coated molybdenum skin panel to the bottom of the truss. Both contained oversize attachment holes for differential growth. These panels helped to close the support structure and create a compartment that would be representative of a section of a wing or fin.

The thermal analyses that were conducted in conjunction with the design effort helped to fashion the full scale component. The final temperature-time histories for some pertinent points in the full scale component are presented in Figure 161. These temperature histories revealed that points on the basic hat section of the substructure (points 18, 93, and 90) would experience a maximum temperature of 2400°F and that a critical point on the support bracket would peak at 2600°F. These temperatures permitted the use of coated columbium for the hat section, brackets, and finger springs. The thermal analysis also showed that the exposed flange of the substructure on the leading edge lower surface would be subjected to a peak temperature of approximately 3100°F for a short duration. This temperature was beyond the upper limit for coated columbium, and necessitated the employment of a coated molybdenum angle at this exposed position. The temperature-time histories were used in a similar fashion to verify the ceramic material selections that were made for the facing tiles and the insulation strata.

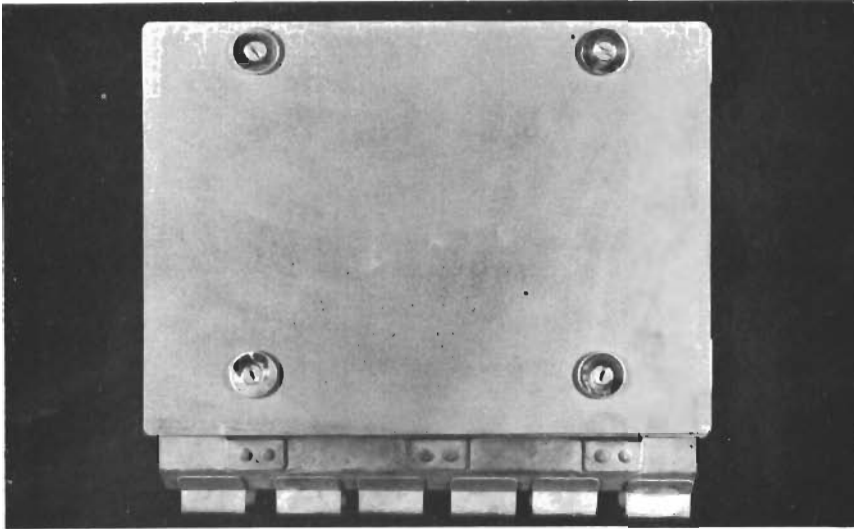


(a) COMPONENTS

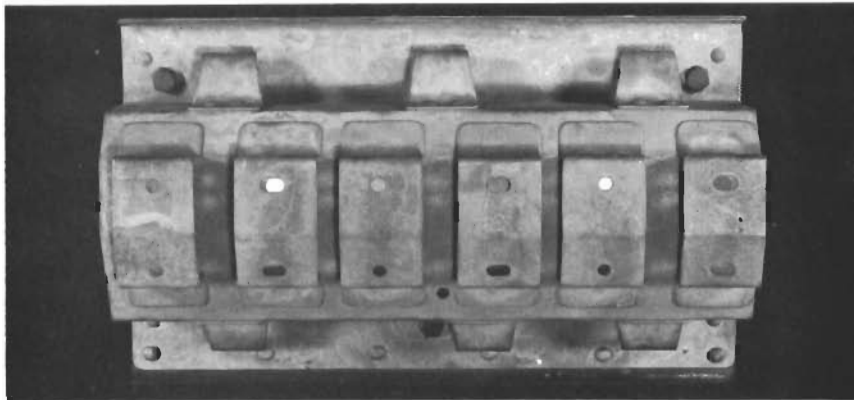


(b) ASSEMBLY

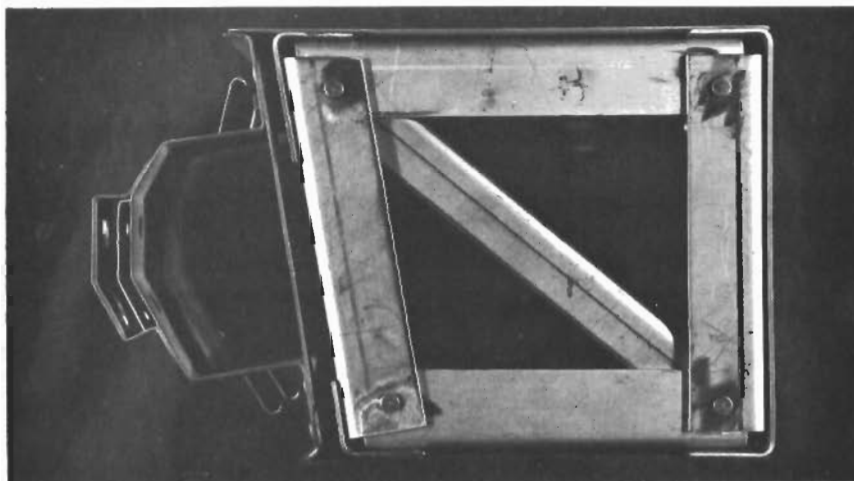
FIGURE 159 - 3.0-INCH RADIUS LEADING EDGE METAL STRUCTURE



(a) TOP VIEW



(b) FRONT VIEW



(c) SIDE VIEW

**FIGURE 160 - METAL ASSEMBLY FOR 3.0-INCH RADIUS LEADING EDGE
IN PROJECTED VIEWS**

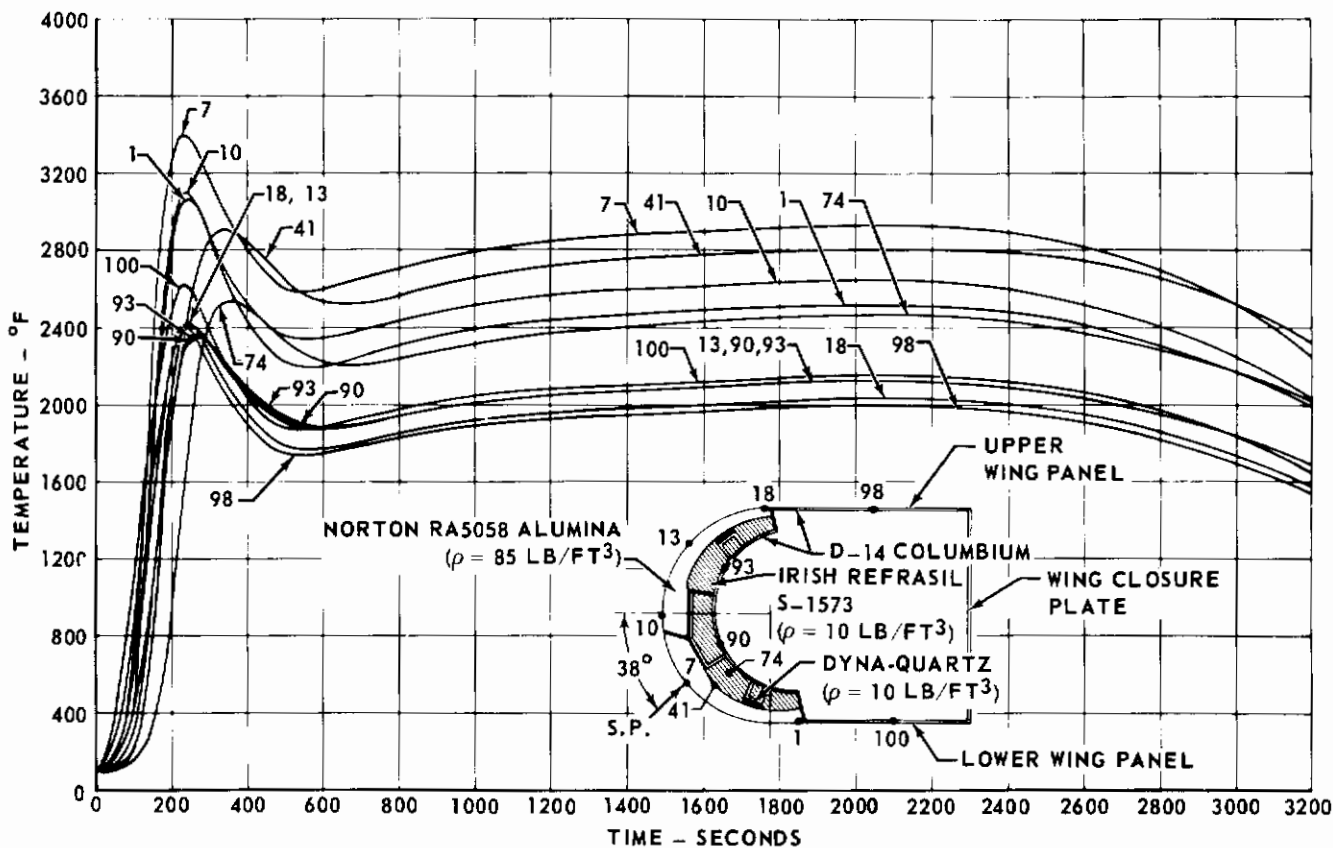


**FIGURE 161 - 3.0 INCH RADIUS LEADING EDGE TEMPERATURES
RADIATING SUBSTRUCTURE**

The temperature-time histories were also used in the structural analytical work performed on the full scale component. These histories established the critical thermal gradients that would be present in the ceramic elements and the working temperatures for the reinforcing substructure. Many of the full scale design features were directed at minimizing the interplay between thermal and restraining stresses and were a direct development of the structural analytical work.

The following areas were examined in detail:

- (a) Stresses in ceramic and metal components due to 20 g loads at room temperature, and due to the maximum airloads at the appropriate temperatures.
- (b) Thermal buckling and crippling of the basic leading edge substructure due to thermal gradients along the surface of the part.
- (c) Performance of the leaf and finger springs at room and elevated temperatures.
- (d) Calculation of the shape of the ceramic elements at elevated temperatures.
- (e) Thermal stress analyses of the ceramic components, utilizing the methods developed in the structural analytical model work.

The results of these examinations were as follows:

(a) The structure will carry the imposed mechanical loads without difficulty.

(b) There is no danger of thermal crippling or buckling of metal parts.

(c) The leaf and finger springs will withstand the design trajectory without permanent deformation and will support the ceramic tiles for the imposed mechanical loads. (It was subsequently determined that the finger springs were excessively stiff at room temperature in the coated condition.)

(d) The point of attachment of the ceramic tiles to the metal substructure must be able to rotate $1\ 1/2^\circ$ during the re-entry heating. The radius of the ceramic tiles is 2.92 inches hot versus 3.0 inches cold.

(e) The maximum tensile stress in the ceramic tiles due to temperature gradients around the circumference of the leading edge was 870 psi at 230 seconds after initiation of the re-entry. The maximum shear stress due to temperature gradients through the thickness of the tile was 2560 psi at 100 seconds after re-entry initiation.

From the allowable strength determined by Southern Research Institute on this ceramic material, the above results would indicate that a thermal stress failure of the ceramic tiles is probable. Since the design insulated the ceramic tiles from any mechanically imposed stress from supporting structure, the possible failure of the ceramic tile is attributable to the material itself. Any improvement in the failure margin of the ceramic tiles must come through more favorable material properties rather than by design technique. In spite of the unfavorable thermal stress predictions, no design or material changes were made because:

(a) The material property determinations and analyses were not complete until the full size component was practically completed.

(b) The subscale specimens of like design and material did not fail (see Section 5.2.2).

(c) The short time elevated temperature material properties were probably more favorable than the properties measured after a longer soak at temperature.

The actual ceramic phase density on the full scale component was 57.0 lb/ft³, which is 7 lb/ft³ greater than the design objective and 9 lb/ft³ greater than the ceramic phase in the subscale specimen. The increase over the subscale can be attributed to the modifications in the facing tile which were imposed by the contoured configuration and the expansion joints. In the full scale component, the ceramic tile thickness was greater in comparison to the low density fibrous insulation thickness. The complete leading edge (substructure, insulation, and ceramic) was 9.87 inches long and weighed 5.5 pounds.

5.3.1.2 Fabrication and Assembly - The Hastelloy X material in the support structure offered no particular fabricating problems and all details were worked by conventional methods. Standard riveting practices were used to join the details into the complete truss assembly.

The blanks for the molybdenum panel and angle were milled from sheet stock and the molybdenum spacers from bar stock. The panel and spacers were drilled and all edges on molybdenum parts were radiused. The angle was hot formed in a brake, all parts inspected for delaminations or cracks, and then cleaned by pickling. The panel and the spacers were then given a silicide oxidation protective coating (McDonnell L-7 coating).

The blanks for the columbium panel and columbium details for the substructure were sawed from sheet stock and all edges were radiused. The basic hat section and the brackets were formed at room temperature on a series of form blocks. The finger springs were shaped at room temperatures in a brake and roller and matched to a check template. All parts were thoroughly inspected for surface imperfections or cracks and then cleaned by pickling. The brackets were positioned on the hat section and spot welded in place. Special fixture blocks were fitted to the hat section and bracket voids of this subassembly to provide the necessary back-up during the drilling of the in-line holes used to attach the ceramic elements.

The finger springs, struts, and molybdenum angle were then fitted to the subassembly and all fastener holes were mate-drilled using proper backup. The finger springs and struts were next riveted to the subassembly with columbium rivets; all open holes in the subassembly, panel, angle, and strap were radiused; and the parts were inspected and pickled again. An aluminide coating (McDonnell LB-2) was then applied to the subassembly, columbium panel, strap, and a group of columbium rivets. A silicide coating (McDonnell L-7) was applied to the molybdenum angle which was then sandwiched between the columbium subassembly and strap, and all items were riveted together. A final aluminide repair coat was applied to the bucked heads of these rivets. The two different diffused coatings may be brought in contact with each other, but the "green" aluminide coating which was applied to the rivets in the repair operation must be restricted to a columbium surface (explaining the function of the columbium strap).

Figure 159 shows the substructure, coated molybdenum spacers (at the sides of the substructure), columbium panel (light colored), truss assembly, and the molybdenum panel. Coated molybdenum bolts and nuts were used in the three bolt joints between the support and substructure assemblies. A locking feature was produced at each bolt joint by using two nuts, the second jamming the properly torqued first nut. Figure 160 shows three views of the completed metallic assembly.

The initial operation in the production of the ceramic tiles consisted of squaring all six sides of the raw alumina brick (9 inches x 4 1/2 inches x 2 1/2 inches) in a surface grinder. The cross-sectional shape of the tile was then laid out on the brick and a diamond band saw used to rough out a tile which was approximately 0.090 inch oversize at all surfaces. In Figure 162, the diamond band saw cutting procedure is shown being checked out on a scrap block of alumina.

The rough tile was next clamped on a turntable and set up on the bed of a vertical mill which was equipped with a 2.0 inch diamond grinding wheel. This setup was used to finish grind the interior surface of the tile. Core drills were then used to produce the attachment holes and counterbores in the tile. Figure 163 shows the setup for the drilling operation.

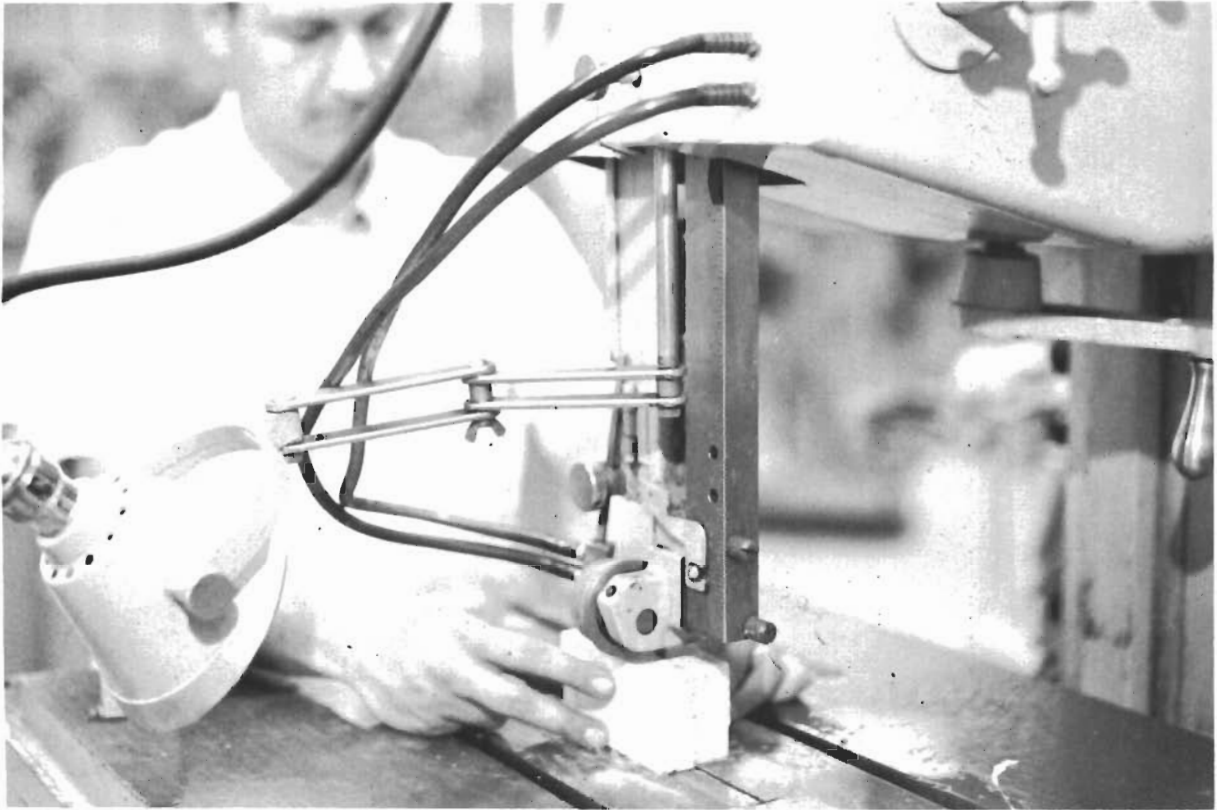


FIGURE 162 - CUTTING LOW DENSITY Al_2O_3 WITH DIAMOND BAND-SAW BLADE



FIGURE 163 - DRILLING LOW DENSITY Al_2O_3 WITH A DIAMOND CORE DRILL

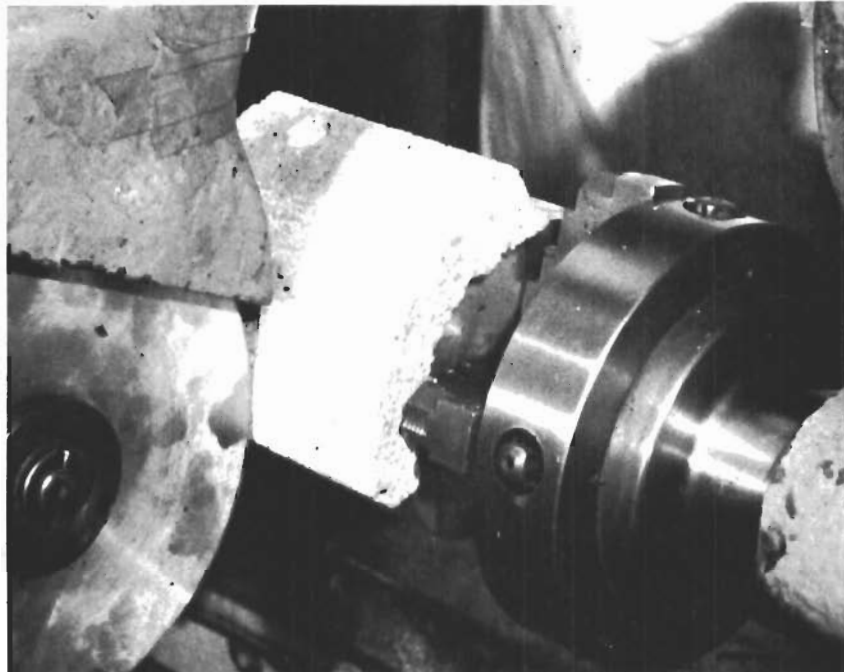


FIGURE 164 - GRINDING CYLINDRICAL SURFACE FOR 3.0 INCH RADIUS LEADING EDGE Al_2O_3 TILE

The finished interior surface of the tile was set on a matching surface in a special fixture, and the tile firmly bolted in place at the counterbored holes. The mounted tile was set in a cylindrical grinder and the outer surface ground to the appropriate arc by rotating the fixture while the grinding wheel was fed into the tile (see Figure 164). The mounted tile was then setup in appropriate positions in a surface grinder and each axial face of the tile ground to the desired shape.

The final operation was to grind the circumferential overlap steps. These surfaces, like the interior surface, were produced in a vertical mill with the aid of a turntable and a small cylindrical grinding wheel. Figure 165 shows two finished tiles butted together at their axial slip joint to form a section of leading edge.

The two small holes stacked radially on the edge of the lower tile in Figure 165 were the entrance points for blind holes that housed two thermocouples which were part of the thermal test instrumentation. The holes were parallel to the surface and extended to a point midway between the attachment cavities. This installation placed the buried thermocouples along isotherms to produce more accurate data.

The installation of the ceramic tiles and insulation on the metallic unit completed the assembly of the 3.0 inch radius leading edge component. Figure 166 shows the component in a partially assembled condition and illustrates the manner in which the insulation was installed. For the test component, the insulation and tiles were assembled to the substructure after it was installed on the support structure. For an actual vehicle, it would

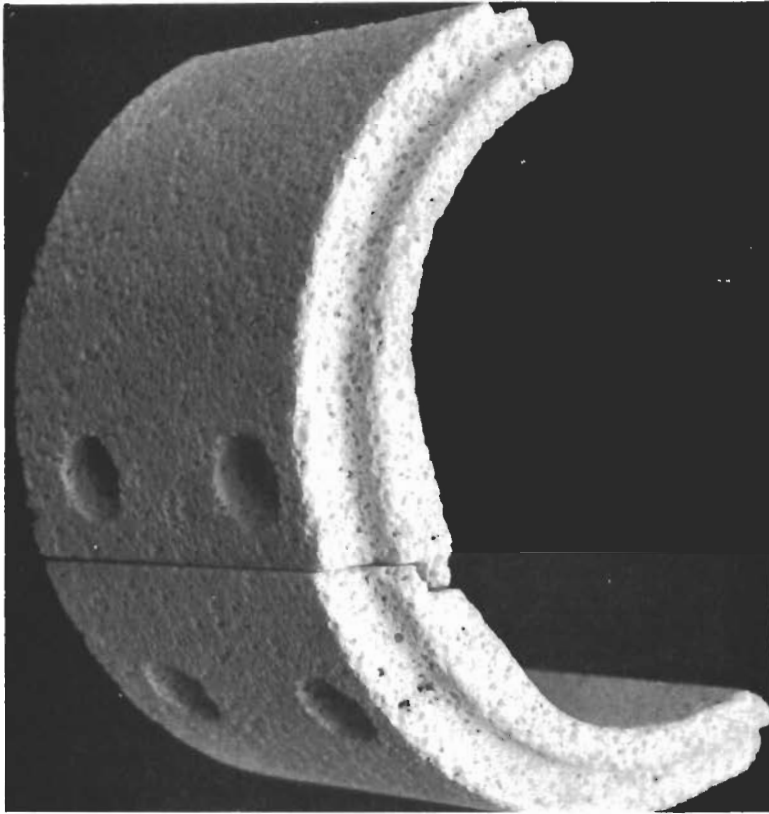


**FIGURE 165 -
LOW DENSITY Al_2O_3 TILES
FOR 3.0 INCH RADIUS
LEADING EDGE**



**FIGURE 166 -
3.0 INCH RADIUS LEADING
EDGE PARTIAL ASSEMBLY,
DISPLAYING INSULATION**

probably be advantageous to assemble standard leading edge segments on the bench for later installation on the vehicle at a convenient stage of assembly. This procedure could be accomplished by replacing the leading edge attaching bolts with studs which would be integral with the substructure.

The installed facing tiles presented a mold-line surface in which no two adjacent tiles exhibited more than 0.02 inch mismatch. The bolt cavities in the tiles were filled with high density, chemically bonded alumina and a thin skin of the same material was applied to the mold-line face, which virtually eliminated the mismatch. (The composition and curing cycle for this alumina are listed in Table XXII.) A final thin coat of chemically bonded chromium oxide was then applied to the mold-line surface to improve the emittance properties. The fully assembled and cured test component is shown in Figure 167.

5.3.2 1.5 Inch Radius Leading Edge Component

The full scale 1.5 inch radius leading edge component, like the 3.0 inch radius component, consisted of approximately 10.0 running inches of ceramic shielded leading edge mounted to a like length of closed support structure. The support structure on this component was built to represent the forward portion of a wing or fin, and consisted of a truss structure that extended from the leading edge aft, for approximately 6.5 inches, to a simulated primary spar. Design and fabrication of this full scale test component are discussed below.

5.3.2.1 Full Scale Design - The successful subscale key block design (see Section 5.2.5) was adapted to a 1.5 inch radius contour and formed the basis for the full scale component design shown in Figure 168. In this component, three sections of sintered low density zirconia, with each section approximating the size of the ceramic elements in the subscale, were mounted on a one piece coated molybdenum substructure to form a leading edge segment. The lower ceramic elements (see Figure 168) were trapped between the key blocks, a flange of the substructure, and the engagement pads, while the key blocks and the upper blocks were attached by spring loaded bolts. Each ceramic block was bolted to the substructure with two bolts, one passing through a close-fit hole in the substructure and the other through a slotted hole, in the pattern shown in Figure 169. Circumferential slip joints between the ceramic sections, in conjunction with the slotted holes, permitted axial growth of the ceramic without the introduction of restraining stresses.

The radial growth in the ceramic elements which occurs at elevated temperatures, was accommodated by the leaf springs in each bolt tie (see Figures 168 and 170). For the key block, the spring permitted the block to move outward as thermal expansion caused growth in the upper and lower blocks. In the upper block, the spring in effect allowed the grip to change in accordance with the thermal growth of the ceramic sandwiched between the nut and the bolt head. As in the case of the 3.0 inch radius leading edge, the springs acted to minimize the loads which the attachments imposed on the ceramic when a thermal gradient occurred.

All the ceramic elements were supported by a relatively simple substructure consisting of a one piece hat section member and two attached engage-

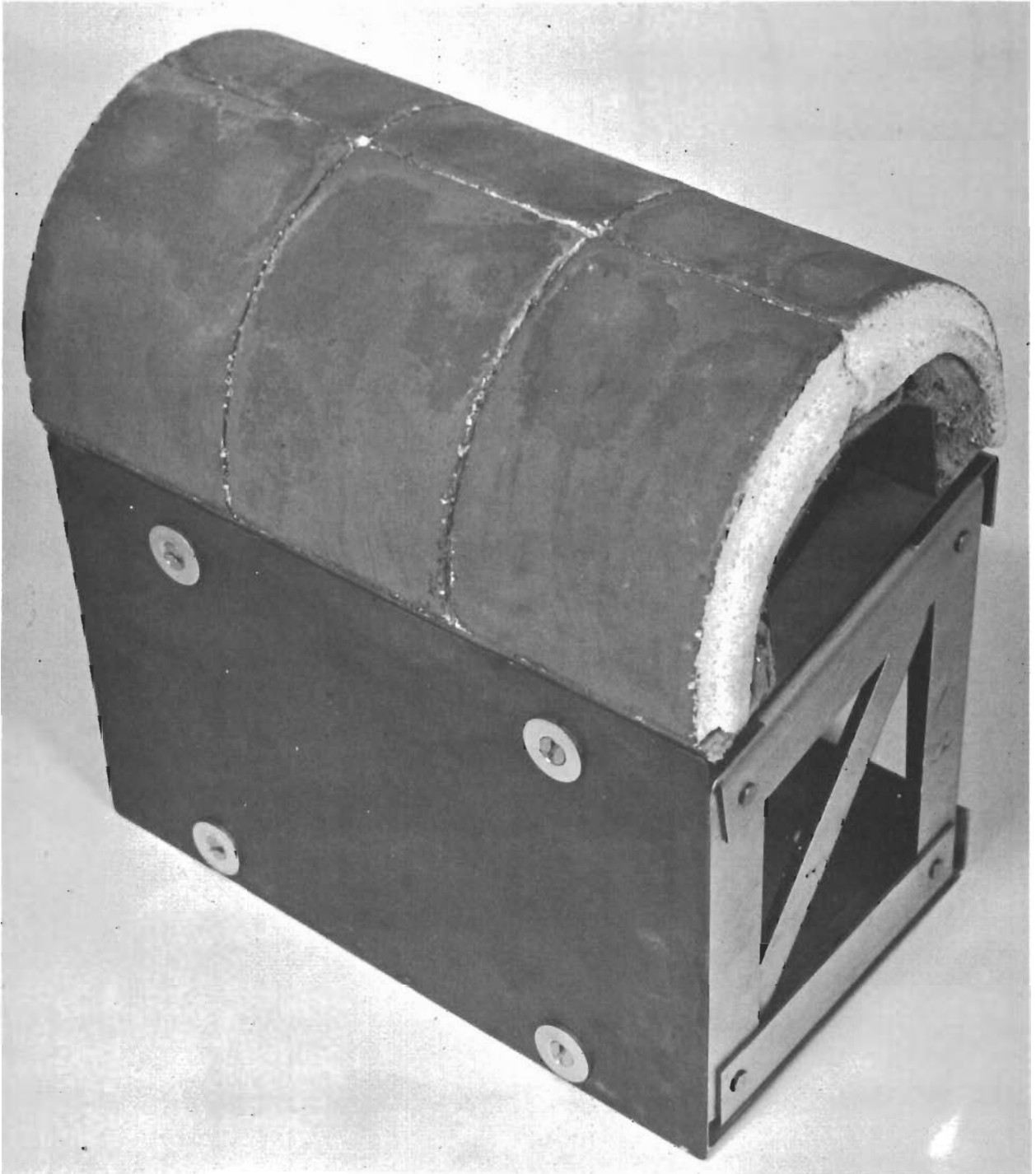
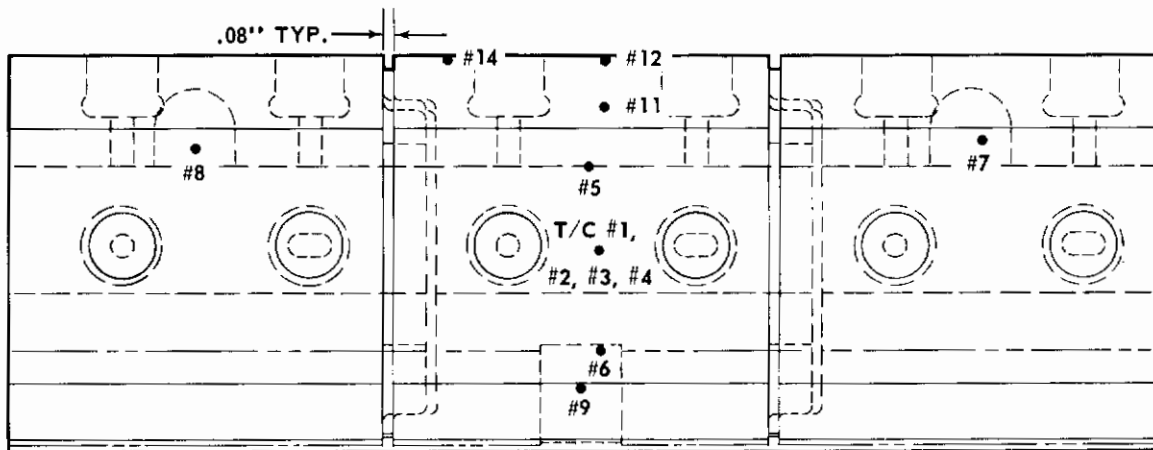
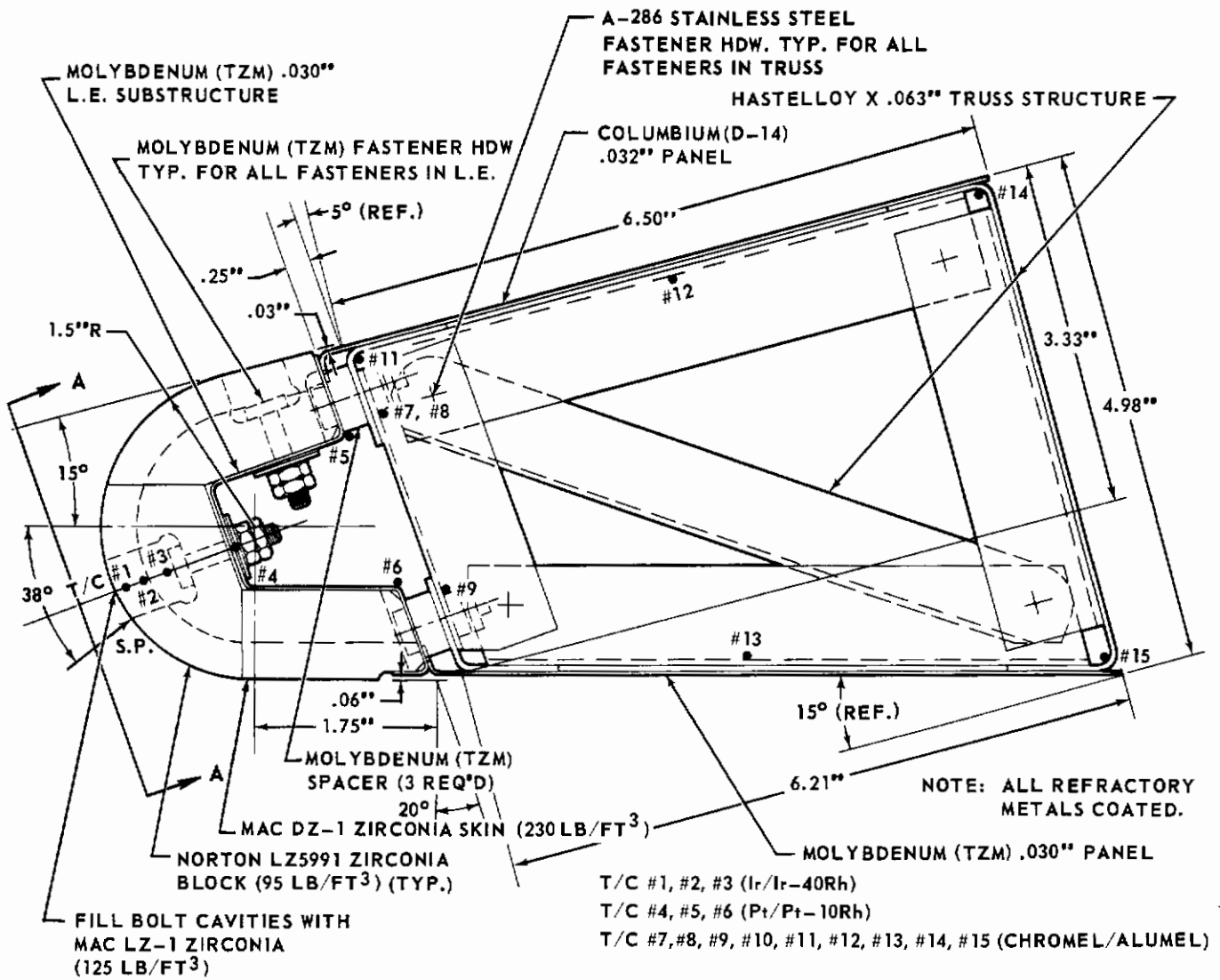


FIGURE 167 - 3.0-INCH RADIUS LEADING EDGE FINAL ASSEMBLY



NOTE: CERAMIC
PHASE DENSITY
~ 96 LB/FT³

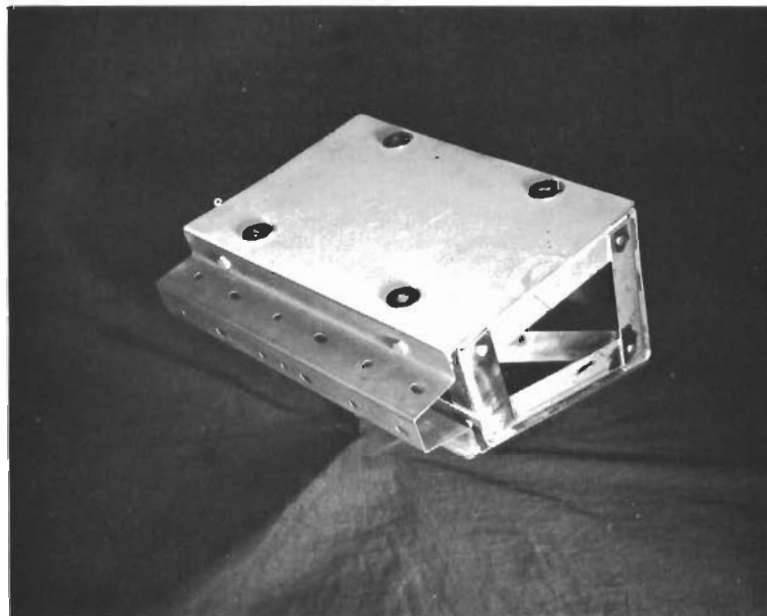
VIEW A-A

ONLY L.E. COMPONENTS ARE
PROJECTED INTO THIS VIEW

FIGURE 168 - 4000°F FULL SCALE TEST SPECIMEN -1.5 INCH RADIUS LEADING EDGE

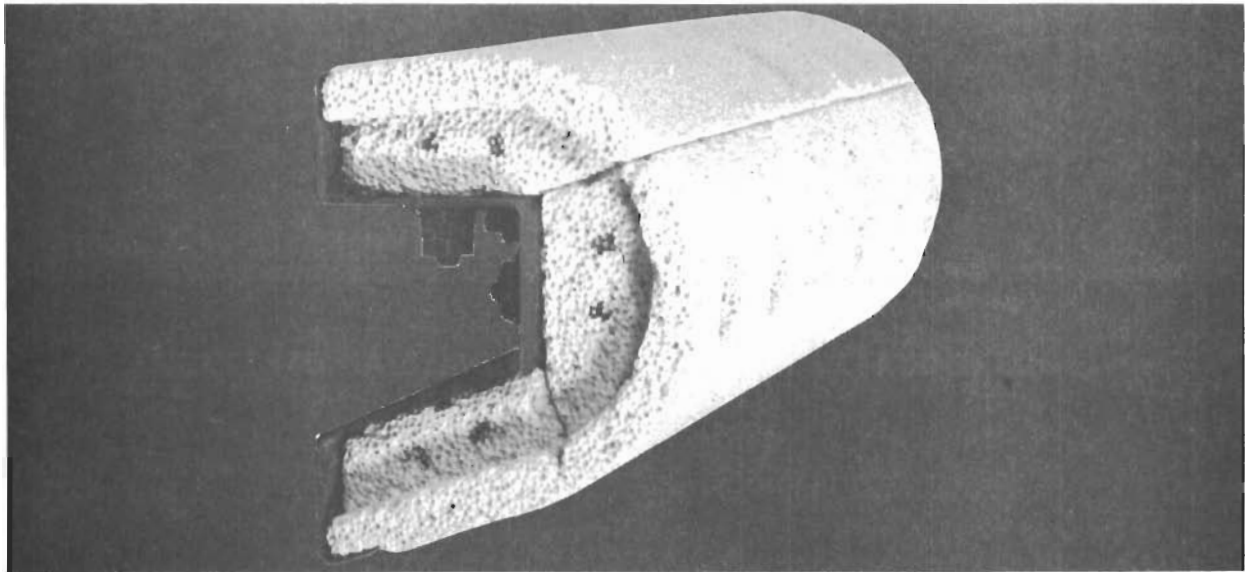


(a) COMPONENTS

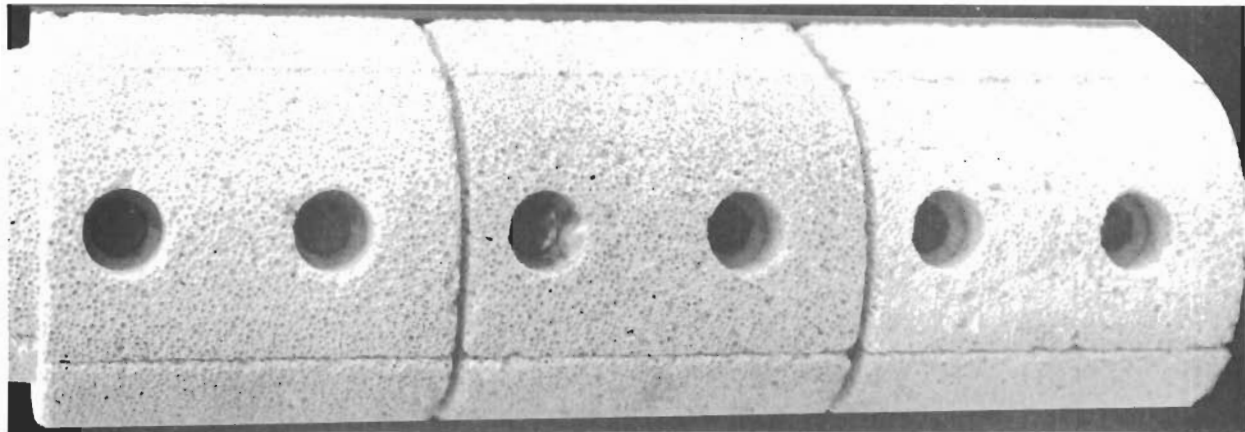


(b) ASSEMBLY

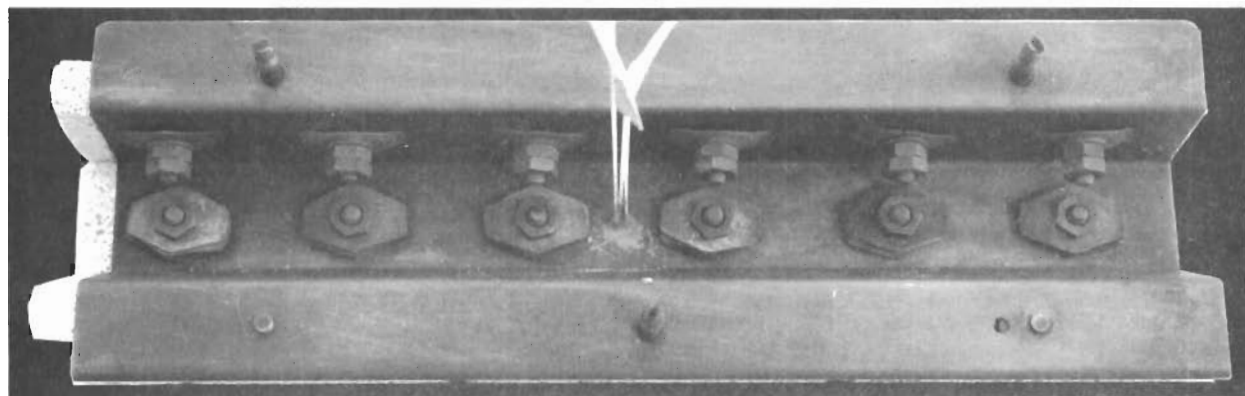
FIGURE 169 - 1.5-INCH RADIUS LEADING EDGE METAL STRUCTURE



END VIEW

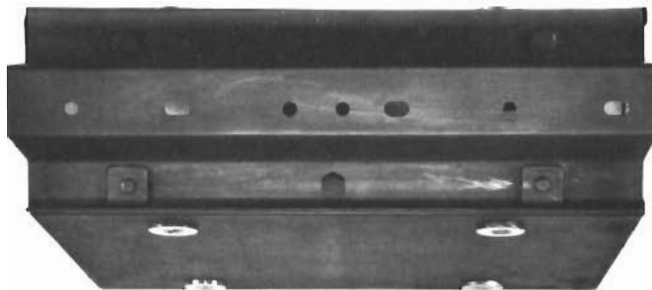


FRONT VIEW

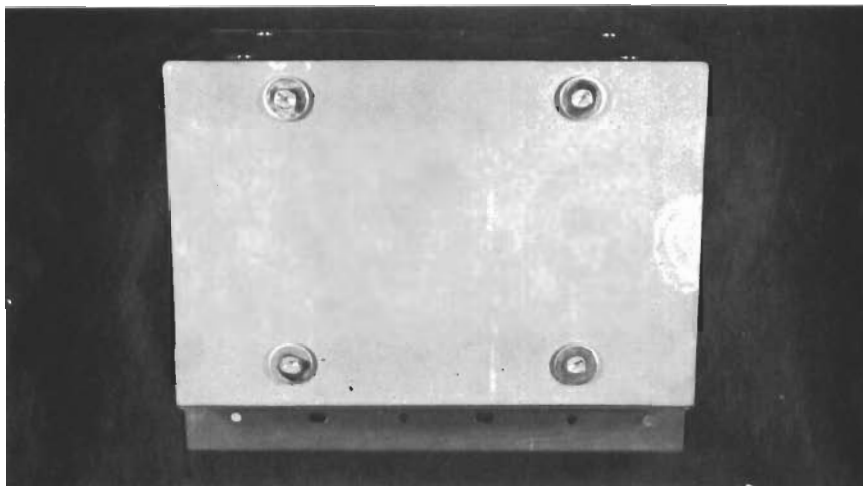


REAR VIEW

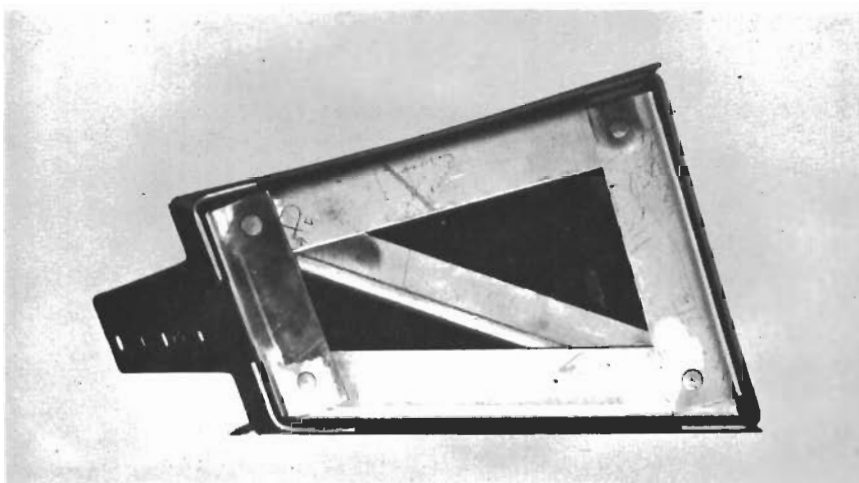
FIGURE 170 - ASSEMBLED 1.5-INCH RADIUS LEADING EDGE



(a) FRONT VIEW



(b) TOP VIEW



(c) SIDE VIEW

**FIGURE 171 - METAL ASSEMBLY FOR 1.5-INCH RADIUS
LEADING EDGE IN PROJECTED VIEWS**

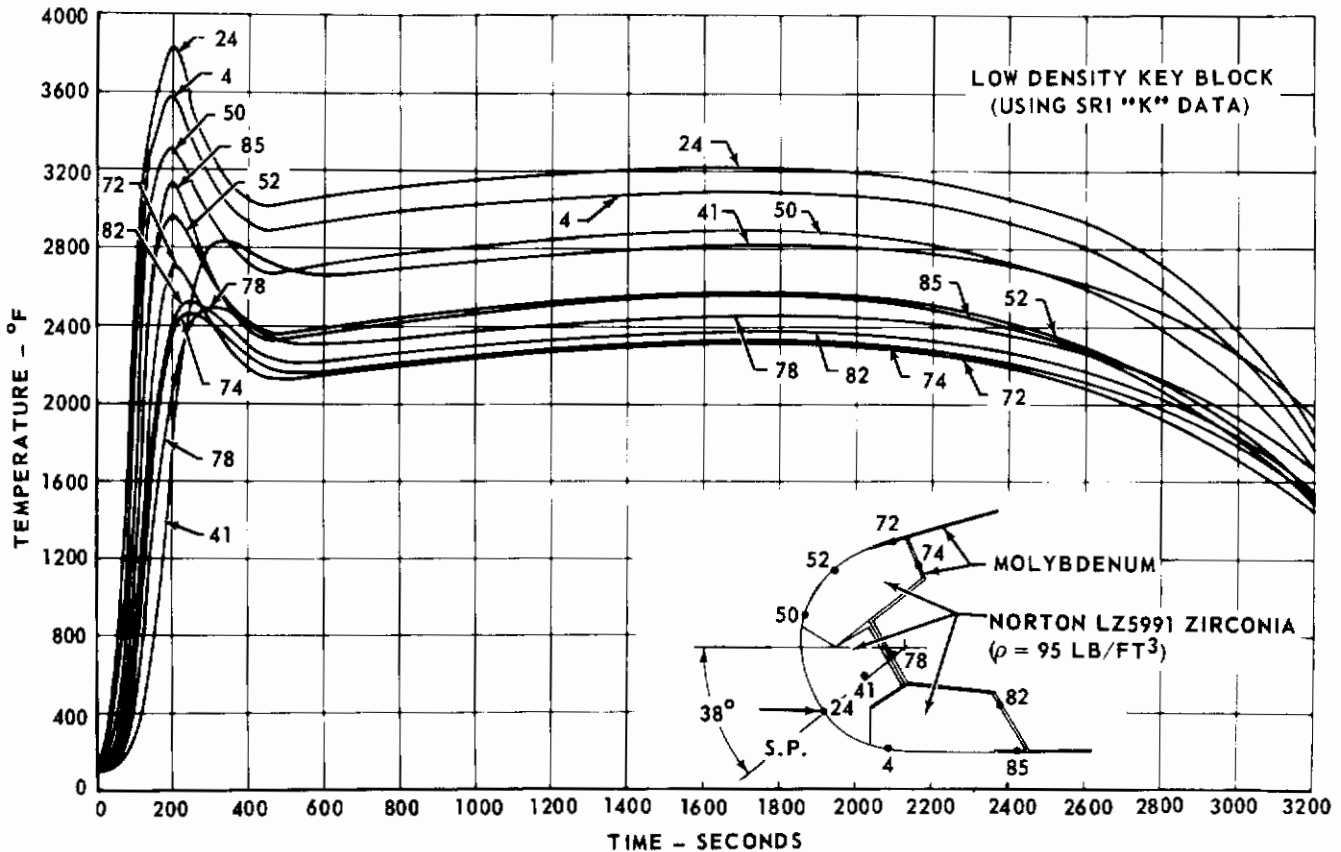


**FIGURE 172 -1.5 INCH RADIUS LEADING EDGE TEMPERATURES
RADIATING SUBSTRUCTURE**

ment pads, all made of coated molybdenum (see Figure 171). The complete leading edge component was attached to the support structure by a three-bolt system which functioned exactly like the system on the 3.0 inch radius component to accommodate differential linear growth and radius change (see Section 5.3.1.1).

The design of the support structure was similar to the design of the support structure for the 3.0 inch radius component. As in that component, the basic truss structure was made of Hastelloy X, and a coated columbium skin panel on the upper face and a coated molybdenum skin panel on the lower face completed the structure.

The final temperature-time histories for pertinent points in the 1.5 inch radius leading edge are presented in Figure 172. These temperature histories show that most substructure temperature (points 74, 78, and 82) do not rise above 2500°F, which would permit the use of columbium. However, the temperature analysis also showed that the exposed substructure flange on the lower face of the leading edge (point 85) would reach a peak temperature of approximately 3100°F for a short duration, which is above the upper limit for coated columbium.

In order to maintain a simple one-piece substructure, which was advisable because of the limited size of the configuration, it was necessary to use coated molybdenum throughout. The temperature histories for points at the surface of the ceramic block are also shown. These temperatures dictated the use of zirconia.

Structural analysis of the 1.5 inch radius leading edge was similar to that of the 3.0 inch radius leading edge. The areas investigated in detail were:

- (a) Thermal crippling and buckling of the coated molybdenum hat section.
- (b) Stresses due to 20 g loads at room temperature and due to airloads at the appropriate temperatures.
- (c) Performance of the leaf springs at room and elevated temperatures.
- (d) Thermal analysis of the ceramic elements utilizing the methods developed in the structural analytical model.

The results of the examination were as follows:

- (a) Thermal buckling and crippling of the hat section will not occur.
- (b) The structure will carry the imposed mechanical loads without difficulty.
- (c) The leaf springs will perform in a satisfactory manner.
- (d) The maximum shear stress due to the temperature gradient through the thickness of the ceramic elements was 1735 psi, 100 seconds after initiation of re-entry.

The actual ceramic phase density for the full scale component was 97 lb/ft³, which was 23 lb/ft³ below the design objective. This low density was due to the extensive use of the low density zirconia (Norton LZ-5991). This zirconia had a density of approximately 95 lb/ft³ and exhibited good thermal shock resistance in the subscale test program. The complete 1.5 inch radius leading edge (substructure plus ceramic) was 9.87 inches long and weighed 3.9 pounds.

5.3.2.2 Fabrication and Assembly - The construction of the Hastelloy X truss structure, like the truss structure on the 3.0 inch radius component, offered no particular problems and was accomplished by conventional methods. The columbium and molybdenum panels for the support structure were, with the exception of one formed stiffening flange on each panel, similar to the panels on the 3.0 inch radius component and fabrication techniques were similar to those described in Section 5.3.1.2. The fabrication techniques for the molybdenum spacers placed between the substructure and the support structure are also described in Section 5.3.1.2.

The blanks for the molybdenum hat section and the engagement pads for the substructure were chemically milled and deburred. All edges on these blanks were radiused by hand sanding to permit application of a continuous

unbroken protective coating. The hat section was hot formed on a series of form blocks and all parts were inspected for delaminations, surface imperfections, and cracks. All parts were cleaned by pickling, and the hole and slot patterns were machined in the hat section using the proper back-up. All open holes in the parts were radiused and all parts were inspected and pickled again. A silicide protective coating (McDonnell L-7) was then applied to the individual parts. Coated molybdenum rivets were used to hot rivet the engagement pads to the hat section. A final silicide repair coating (McDonnell L-7) was applied to the assembly, especially in the area of the bucked rivets.

Figure 169 shows the substructure, molybdenum spacers (at the sides of the substructure), columbium panel (light colored), truss assembly, and the molybdenum panel. As in the 3.0 inch radius component, coated molybdenum bolts and nuts were used for joining the support structure and the leading edge substructure, and two nuts were used on each bolt to provide a locking feature. Figure 171 shows three views of the metal portion of the test component.

The initial operation in producing the ceramic elements consisted of squaring all six sides of the raw zirconia brick ($4\frac{1}{2}$ inches x $2\frac{1}{2}$ inches x $2\frac{1}{2}$ inches) in a surface grinder. The bricks that were supplied for use on the full scale components in conformance with the Reproducibility and Producibility Phases of the Norton subcontract were of lower quality than the bricks supplied for the subscale specimens. The bricks for the full scale component were larger than those for the subscales, had less uniform porosity, more voids and cracks, and exhibited varying inconsistent thermal shock resistance. Quality control tests were instituted to aid in the selection of the best available brick. These control tests established the material lots that possessed the best thermal shock properties and only those bricks in the approved lots were used.

The rough envelope for each ceramic element was cut from a squared brick with a surface grinder using a diamond cut-off wheel. These units were ground again to square all faces and thereby produce certain basic flat surfaces in each ceramic block. The oblique faces on each block were then ground in a surface grinder with the aid of an angle plate and sine bar. The semi-finished blocks were set up on a special fixture to locate the bolt holes, which were then drilled by a diamond core drill in a drill press. The counterbores were cut by an appropriate core drill which was run into the proper depth, the core broken loose, and a cylindrical abrasive wheel used for clean-up. The undercut at the base of each counterbore was produced by a $3/16$ inch ball grinder.

The three semi-finished blocks that form a complete key block section were bolted or trapped on a special fixture which was then set up in a cylindrical grinder. The outer surface was ground to the appropriate arc by rotating the special fixture while the grinding wheel was fed into the tile. This grinding operation was similar to the operation used on the 3.0 inch radius component which is displayed in Figure 164.

The final operation was to grind the circumferential overlap steps in the edges of the ceramic blocks. This operation was accomplished in a vertical mill equipped with a cylindrical grinding wheel while the ceramic parts, still mounted on the special fixture, were clamped to a turntable set up on

the bed of the mill. The finished ceramic blocks are shown installed on the substructure in Figure 170. As indicated by this figure, the 1.5 inch radius leading edge was assembled independent of the support structure. In this instance, the geometric limits of the support structure restricted access to the bolts for the ceramic attachment. As stated in the discussion on the 3.0 inch radius component, completely assembled leading edge segments are probably the most desirable units for an actual vehicle. They could be made as standardized replaceable units to simplify original assembly and subsequent servicing.

Figure 170 also shows the leads from the three thermocouples which were embedded in the central key block. The two thermocouples nearest to the surface were installed so that they paralleled a cylindrical surface element. Thus, the thermocouple lay along an isotherm to produce more representative data. A parallel installation could not be made for the third thermocouple and it had to be installed perpendicular to the surface elements.

The fully assembled 1.5 inch radius leading edge is shown in Figure 173. The ceramic blocks exhibited mismatches of approximately 0.02 inch at the mold-line surface. However, after a skin of high density chemically bonded zirconia (Table XXII) was applied, all abrupt discontinuities were eliminated and a surface comparable to more conventional leading edges was achieved. The cavities for the attaching bolts visible in Figure 170 were filled with low density chemically bonded zirconia. The high density skin was applied over the entire leading edge after the filled cavities were cured.

5.3.3 6.0 Inch Radius Nose Cap

The full scale 6.0 inch radius hemispherical nose cap consisted of an outer layer of composite ceramic attached to and supported by a coated molybdenum substructure. This component was mounted to a cylindrical support structure which approximated a section of adjoining vehicle and extended from a nose cap mounting ring to a second body ring 10.0 inches to the rear. Design and fabrication of this full scale component are discussed below.

5.3.3.1 Full Scale Design - The critical central area of the full scale nose cap shown in Figure 174 was based on the 5000°F tube reinforced castable design. Several subscale specimens made to this design survived the testing in reasonably sound and serviceable fashion (see Section 5.2.5). The composite castable shield was built up from a coated molybdenum dome bearing 80 molybdenum channel retainers which were riveted to the hemisphere in a prescribed pattern. A high density perforated zirconia tube was placed in each channel retainer and anchored to the retainer by a coated molybdenum pin. For installation reasons, the center zirconia reinforcing tube was installed last and pinned to a threaded molybdenum stud which bolted to the molybdenum dome. Perforated high density thoria sleeves, all with external tapers, were coupled to the top of the zirconia tubes by zirconia pins. The thoria sleeves extended beyond the zirconia tubes and served to reinforce and retain the thoria stratum of the composite shield. A low density castable zirconia was packed into and around the zirconia reinforcing tubes to form a hemispherical shell with a depth that extended from the molybdenum dome to the bottom of the thoria tubes. A segmented stratum of low density castable thoria was placed on top of the zirconia stratum and formed the outer shell of the composite. A final skin of high density castable thoria applied to the

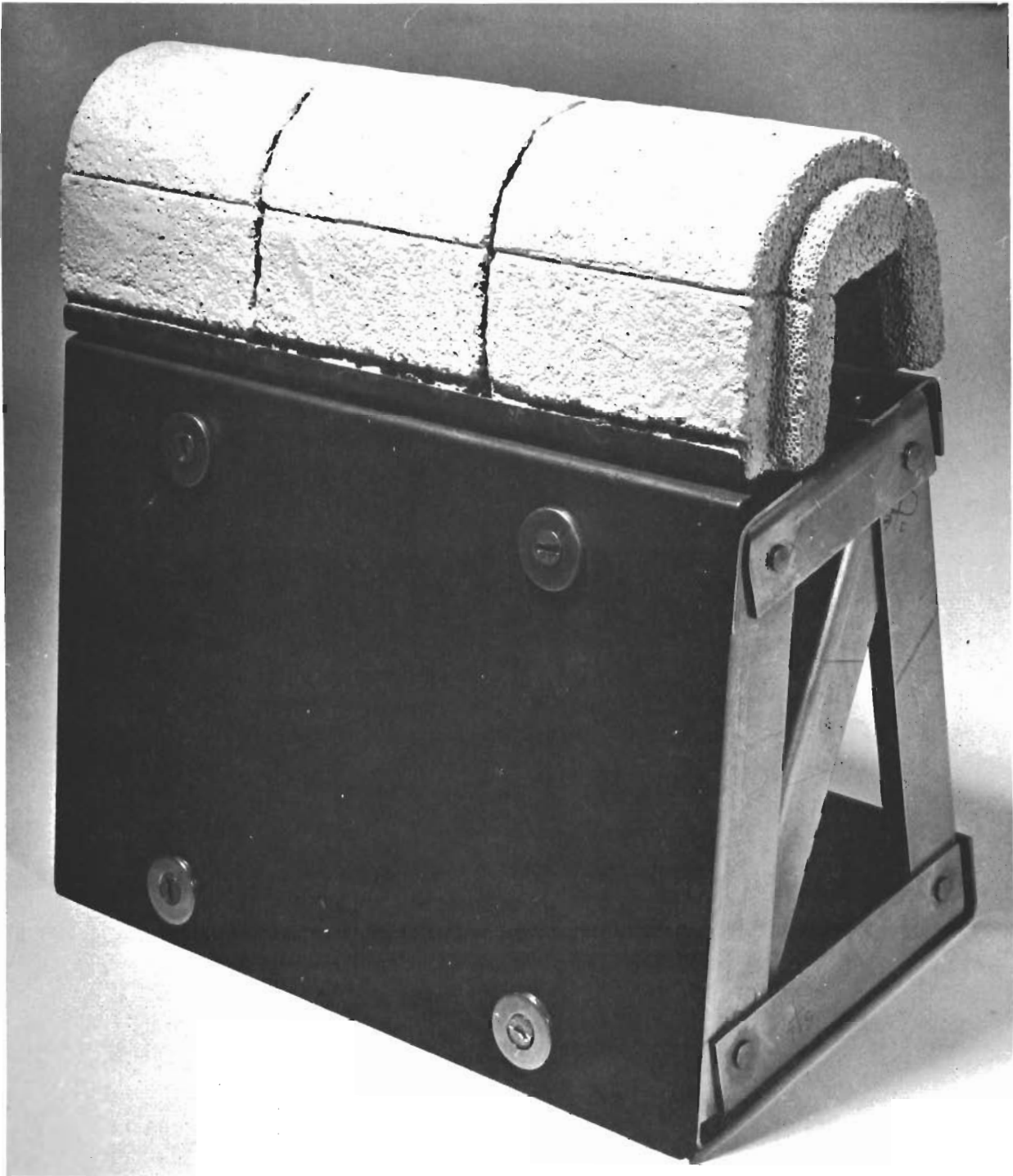


FIGURE 173 - 1.5-INCH RADIUS LEADING EDGE FINAL ASSEMBLY

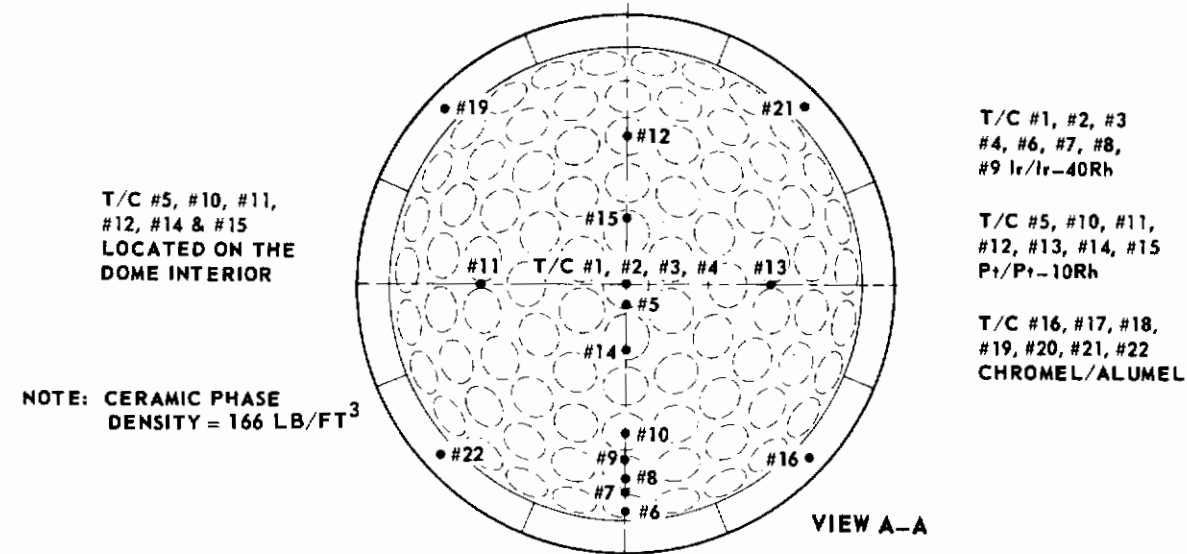
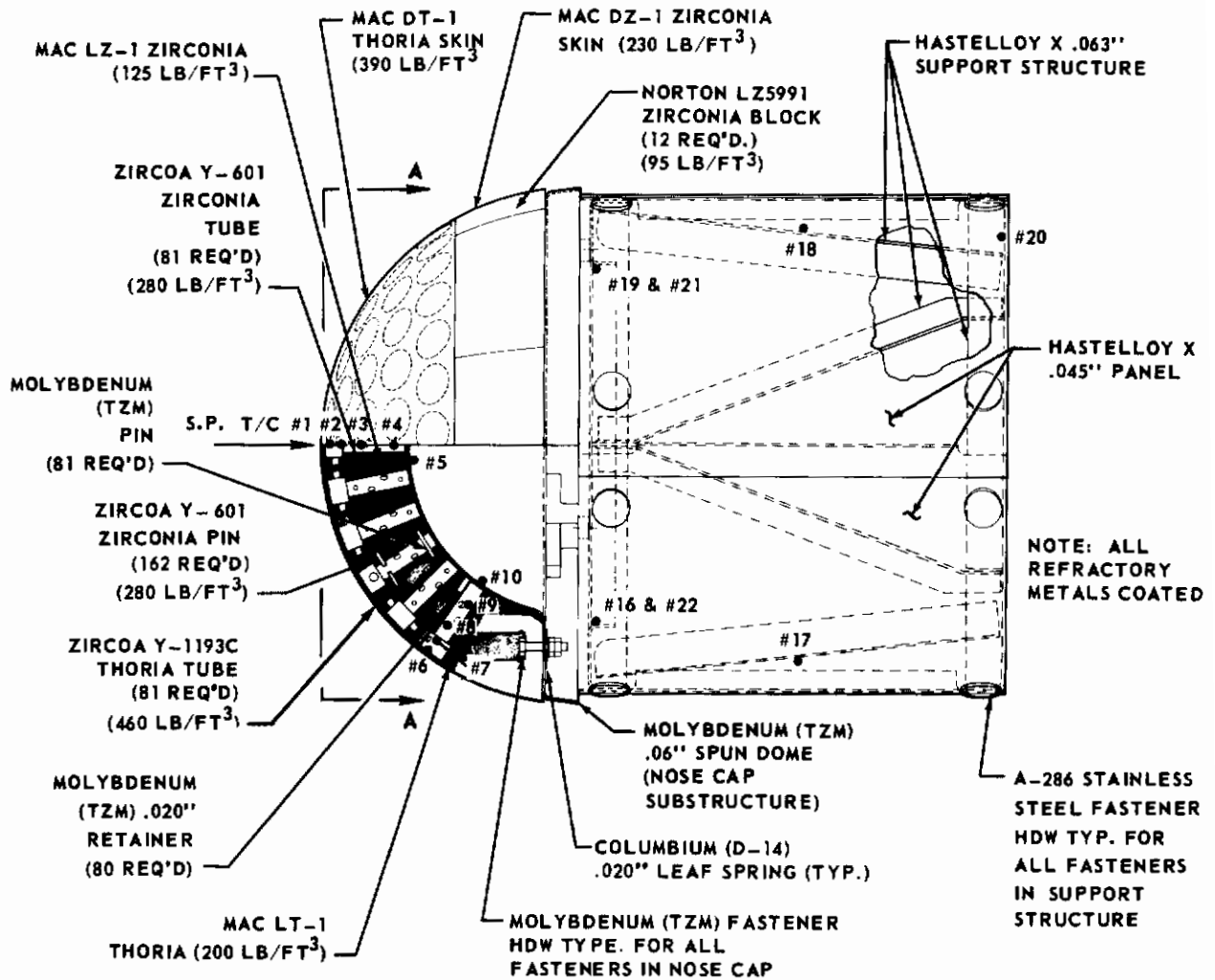


FIGURE 174-5000°F FULL SCALE TEST SPECIMEN
6.0 INCH SPHERICAL RADIUS NOSE CAP

exposed face of the composite completed the ceramic shield in the critical area of the hemisphere.

A ring of low density sintered zirconia blocks (Norton LZ-5991) surrounded the central composite ceramic shield and covered the base of the hemisphere. The sintered blocks were separated from the castable composite by a burn-out divider, and each block was attached to the base (which was formed by a flange of the molybdenum dome) with a spring loaded bolt. The counterbores in the zirconia blocks were filled with low density castable zirconia. Four coated molybdenum fittings, each containing a tapped hole, were bolted to the face of the molybdenum flange and provided the attachment points for the nose cap. The exposed face of the porous sintered ceramic was finished with a skin of high density castable zirconia.

The nose cap was attached by four coated molybdenum bolts which rode in radial slots located in the forward ring of the support structure. This arrangement accommodated a differential thermal expansion between the nose cap and the support structure. The support structure itself consisted of two annular rings tied together by truss members and skinned with floating panels, all made of Hastelloy X. This construction accommodated the differential axial and radial expansions which the support structure underwent.

Due to the complex material arrangement in the composite ceramic shield, a thermal model for the complete nose cap was not developed. Instead, an analysis was conducted for a thermal model that consisted of one tube assembly which was subjected to the stagnation point heating rate. Since the model did not account for circumferential heat loss by conduction or losses from the back side of the molybdenum dome, the resulting temperature histories as presented in Figure 175 are conservative. This analysis showed that the retainers and substructure (points 56 and 65, respectively) reached 3100°F (the limiting temperature for coated molybdenum) at the very end of the re-entry. The zirconia, as represented by point 25, did not exceed 3850°F, which is well within the thermal capabilities of the material. The temperature analysis also showed that the thoria reached a peak stagnation temperature of 5070°F.

A thermal analysis was also conducted for a tube assembly located at the outer extremity of the central composite shield and located 55° away from the stagnation point. The surface temperature at this spot was calculated to be 3700°F and accordingly, all temperature histories for points on this radial tube assembly were lower than those on the stagnation tube assembly. This surface temperature also showed that the low density zirconia blocks which formed the base of the hemisphere would not exceed an acceptable temperature limit.

Structural analysis of the 6.0 inch radius nose cap was accomplished upon the assumption that the chemically bonded thoria and zirconia acted merely as fillers and contributed nothing to the strength of the nose cap. With this assumption in mind, the following were investigated in detail:

- (a) Stresses due to 20 g loads at room temperature; airloads were considered not critical by inspection.
- (b) Thermal crippling of the dome flanges.

(c) Thermal stresses in the tube assembly.

The results of this examination were as follows:

(a) The tube assemblies would carry the 20 g loads from the entire nose cap without failure.

(b) There was no danger of thermal crippling of the dome.

(c) From a computer program, the thorium tubes had the following critical stresses at 270 seconds after initiation of re-entry:

Hoop Tension Stress	2620 psi
Transverse Shear Stress	3250 psi

The actual ceramic phase density on the nose cap was 166 lb/ft³. This relatively low overall density was due chiefly to the use of low density sintered zirconia in the less critical areas of the hemispherical shield. The actual total weight of the nose cap was 33.0 pounds, including substructure.

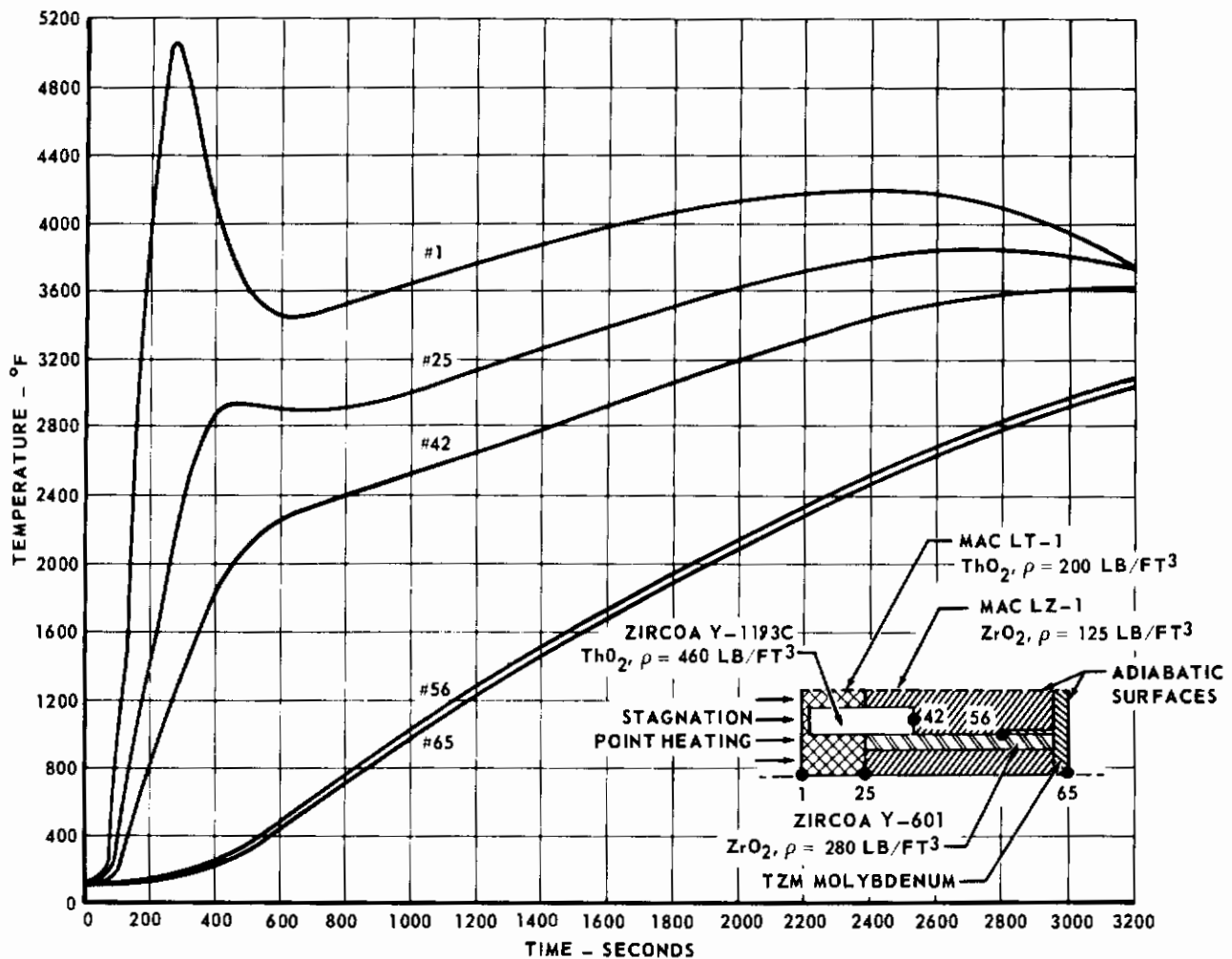


FIGURE 175 - 6.0 INCH RADIUS SHIELD NOSE CAP TEMPERATURES

5.3.3.2 Fabrication and Assembly - The detail parts for the cylindrical Hastelloy X support structure were produced by conventional methods and assembled by fusion welds as well as rivets and threaded fasteners. The assembled support structure, with four coated molybdenum spacers positioned at radial slots in the forward ring, is shown in Figure 176. These spacers were similar to those used in the other components.

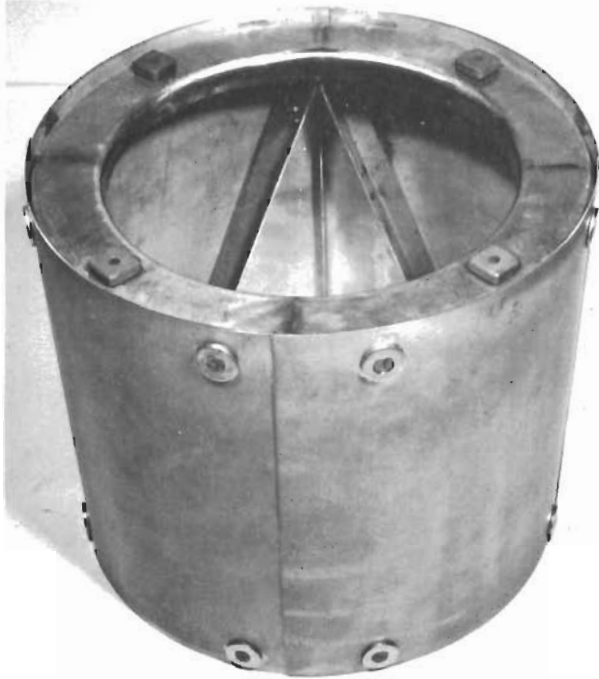
The molybdenum dome, which was the basic unit in the nose cap substructure, was spun to the specified shape by a subcontractor and delivered without any machining required. The compound curved surface and highly formed flanges on the dome (see Figure 176) illustrate the progress that has been made in refractory metal fabrication technology. At McDonnell, a plastic liner was laid up on the interior of the blank dome and the protected cavity filled with plaster to provide the proper back-up for drilling fastener holes. The filled dome was set up in a jig borer on a rotary tilting table to sink the holes required in the hemispheric surface. After this operation, the back-up material was removed and all holes in the flange that formed the base of the dome were drilled with the aid of special tooling for accurate location. The edges of all drilled holes were then radiused to insure a continuous unbroken protective coating over the entire part.

The molybdenum channel retainers which attach to the dome were chemically blanked and hot brake formed to rough shape. They were then finish formed on dies in a Sheridan-Gray hot sizing press. These special procedures were required to produce molybdenum parts which were free from delamination and cracks. The formed retainers were then drilled with the aid of a drill jig which provided the necessary back-up and accuracy.

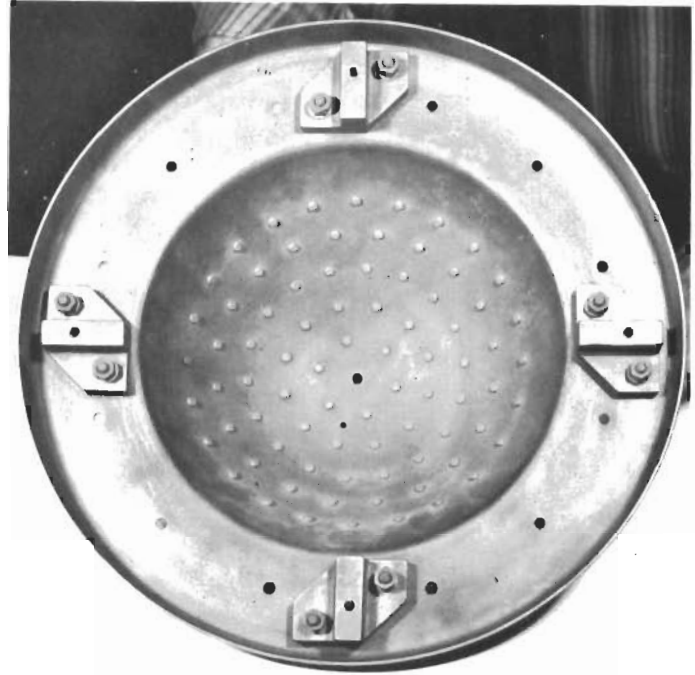
After all edges on the drilled retainers were radiused, retainers and dome were given an initial protective silicide coating (McDonnell L-7). Coated molybdenum rivets were then used to hot rivet the retainers to the dome. Each rivet was maintained at approximately 600°F as it was squeezed to assure the formation of a full upset head with a minimum of cracks. The orientation of each retainer was carefully controlled to comply with the pattern established to insure access for all pins used in attaching the reinforcing ceramic tubes. The riveted unit was again coated to provide oxidation protection for any surface which might have suffered coating damage during the riveting operation.

Four fittings used in mounting the nose cap to the support structure were milled from molybdenum bar stock. Coordinated tooling was used to machine the attach holes and tapped mounting hole in each fitting. A silicide coating (McDonnell L-7) was applied to each fitting after all edges were radiused and the finished fittings were attached to the partially assembled dome with coated molybdenum hardware. The resulting substructure assembly is shown in Figure 176 together with the assembled dome positioned on the support structure.

The first step in fabricating the low density zirconia blocks that made up the ceramic ring at the base of the nose cap was to square all six sides of the raw zirconia brick (4 1/2 inches x 2 1/2 inches x 2 1/2 inches) in a surface grinder. The zirconia brick used for these blocks was the same as that used for the 1.5 inch radius leading edge. As noted in Section 5.3.2.2, all later shipments of the zirconia material exhibited various faults; there-



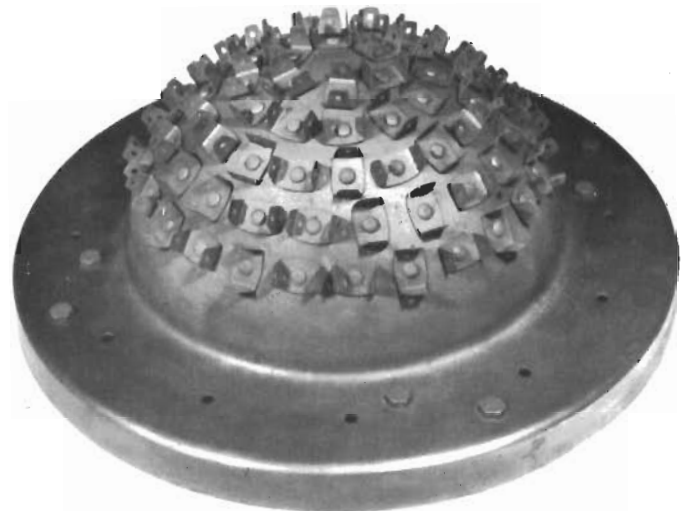
(a) METAL SUPPORT STRUCTURE



(b) MOLYBDENUM SUBSTRUCTURE
BOTTOM VIEW



(c) METAL ASSEMBLY



(d) MOLYBDENUM SUBSTRUCTURE
TOP VIEW

FIGURE 176 - 6.0-INCH RADIUS NOSE CAP SUPPORT STRUCTURE AND SUBSTRUCTURE

fore, the best available bricks were selected for the nose cap blocks. After squaring the brick, core drills were used to cut one through hole and one shallow clearance recess, as required, in a face of the brick. The hole was then used for bolting a pattern plate to the brick and a diamond band saw was used to rough-out the shape of the block. The block was then bolted to an angle plate and the wedge faces were finish ground in a surface grinder.

The blocks were next assembled into a ring on a special fixture which was attached to a turntable. The turntable, bearing the fixture and modules, was set up in a Bridgeport vertical mill, and a 5.0 inch diameter silicon carbide wheel was used to grind the interior of the ring, as shown in Figure 177. Next the head of the mill was inclined as required and a bevel was ground from the base to the inside face of the ring. The blocks were removed and a counterbore was cut for each fastener hole with an appropriate core drill. The blocks were reinstalled on the fixture in the turntable, with bevel face down. The head of the mill was again inclined to a prescribed angle and the conical face of the ring was finish ground. The ring at the conclusion of this operation is shown in Figure 178.

The blocks were next assembled into a ring on a fixture that provided rotation in two directions. This fixture was also installed on the Bridgeport mill and the exterior spherical surface was generated by the grinding wheel as the ring was rotated in two planes. The setup for this final operation on the zirconia blocks is shown in Figure 179.

The high density zirconia and thoria reinforcing tubes were set in drill fixtures, and diamond core drills were used to cut the perforations. The tubes were next set up in a cylindrical grinder and cut to the proper length with a 7.0 inch diameter cut-off wheel. The chamfer on the zirconia tubes and the taper on the thoria tubes were also produced in a cylindrical grinder. In these operations, the head of the cylindrical grinder was swiveled to produce the proper angular relationship between the part and the grinding wheel.

All of the ceramic and metallic parts for the nose cap are shown in Figure 180. In Figure 180, the low density sintered zirconia blocks are arranged in a ring at the base of the assembled dome and their molybdenum attach hardware are lined up in the foreground. The long perforated zirconia reinforcing tubes and their coupling molybdenum pins are shown on the right side of the dome and the tapered thoria tubes and their coupling zirconia pins on the left.

The first step in the assembly of the composite shield was to install and fasten the sintered zirconia blocks on the base of the dome. The void between the inside face of the sintered zirconia ring and the dome was then packed with a low density castable zirconia. Next the dense thoria and zirconia tubes were pinned together and the preassembled reinforcing units were attached to the dome in a predetermined sequential order which had been established to provide access for the assembly operations. A separator was installed on the conical face of the base ring and the nose cap at this stage of assembly, as shown in Figure 181(a).

The next step was the build-up of the castable zirconia stratum in the critical area of the dome. Low density castable zirconia was tamped into and around the zirconia tubes until the stratum reached the base of the thoria

Text continued on page 244

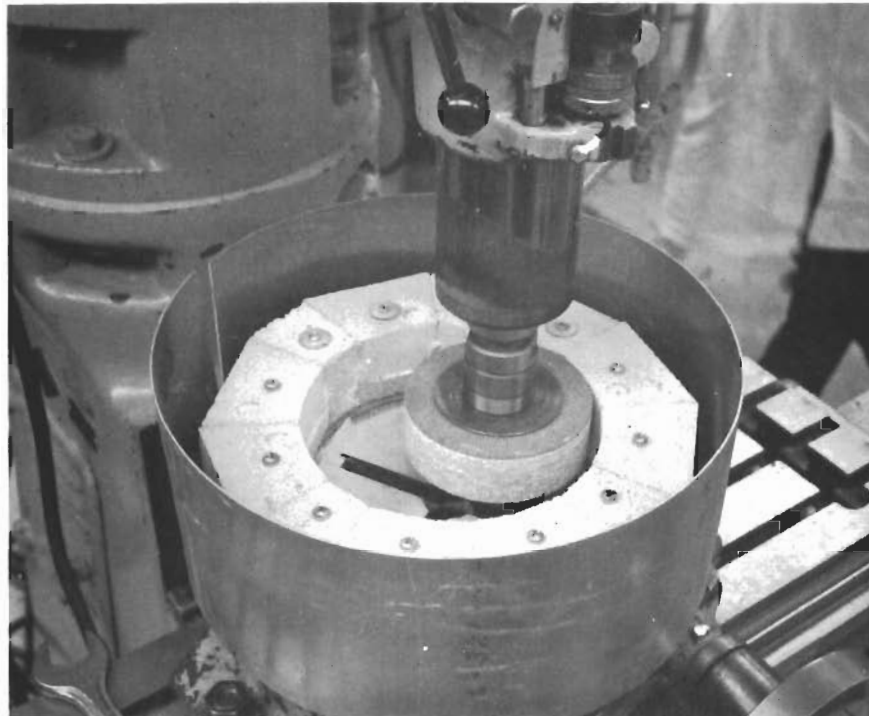


FIGURE 177 - GRINDING INTERIOR OF SINTERED ZIRCONIA RING FOR 6.0 INCH RADIUS NOSE CAP

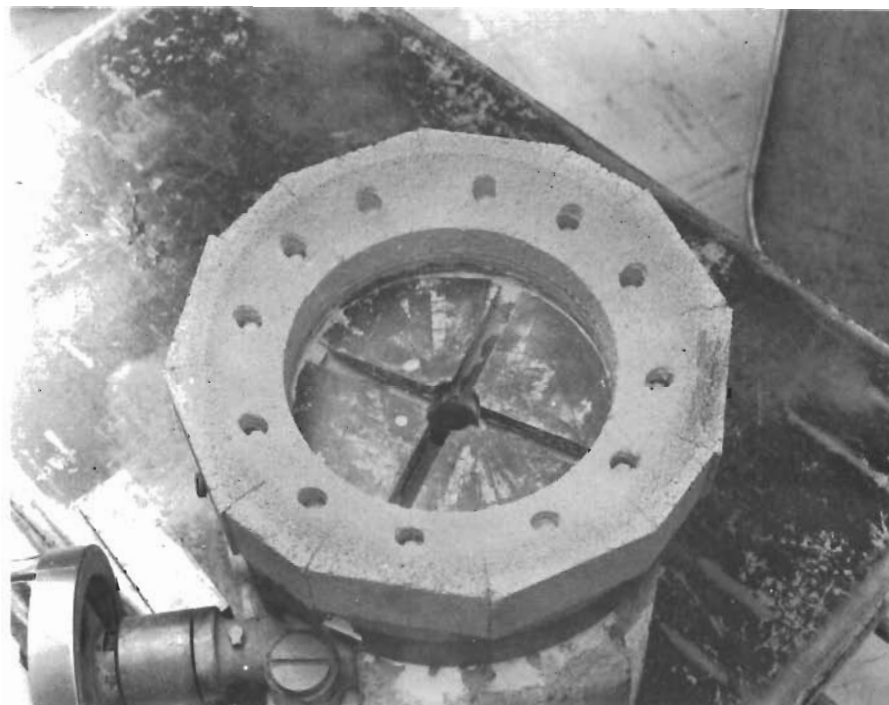


FIGURE 178 - CONICAL FACE ON SINTERED ZIRCONIA RING FOR 6.0 INCH RADIUS NOSE CAP AFTER GRINDING

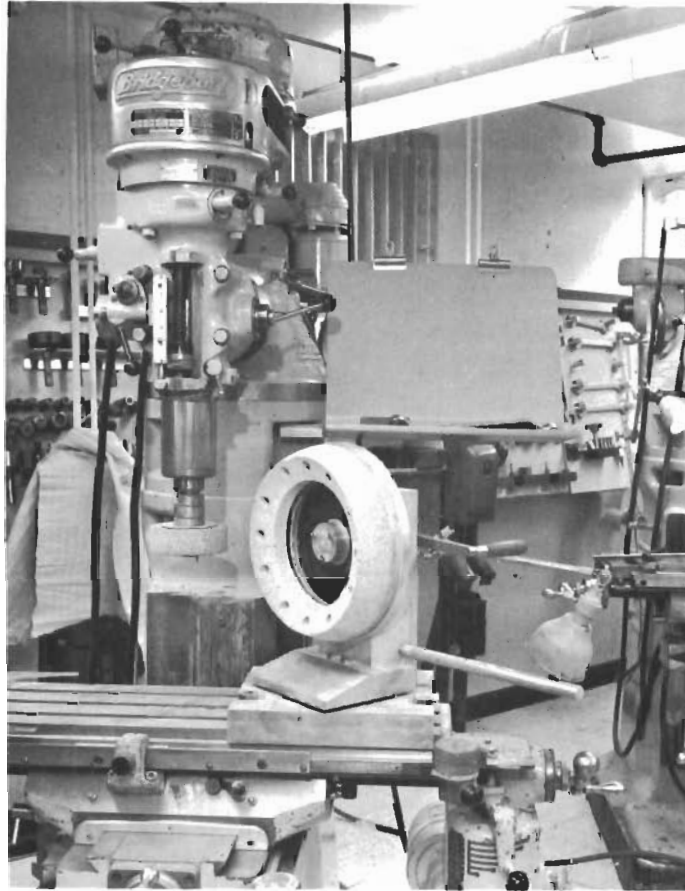


FIGURE 179 - GRINDING EXTERIOR OF SINTERED ZIRCONIA RING FOR 6.0 INCH RADIUS NOSE CAP

tubes. The castable stratum was allowed to cure for 24 hours at room temperature, and the separators which segment the thoria portion of the cap were then installed. The assembly at this point is shown in Figure 181(b). The low density castable thoria was then applied over the zirconia and tamped into and around the thoria tubes until a full contour was achieved. Both layers of castable material were fully cured in a cycle consisting of 24 hours at room temperature, 48 hours at 150°F, 120 hours at 200°F, and 48 hours at 300°F.

Once fully cured, the nose cap was set up on its special fixture in the Bridgeport mill and ground to final contour, as shown in Figure 182. Special precautions were necessary in this finish operation because the low moisture resistance of the chemically bonded materials required grinding without any liquid coolant. As shown in Figure 182, the vertical mill was enclosed in a plastic tent equipped with a vacuum intake to collect the radioactive thoria dust produced in the grinding operation.

After grinding, a thin skin of dense chemically bonded zirconia was trowelled into the exposed face of the sintered zirconia ring. The remaining exposed surface of the thoria hemisphere was thinly skinned with a high density castable thoria and the nose cap was then cured (curing cycle A, Table XXII). The fully assembled and completely cured nose cap is shown in Figure 183.

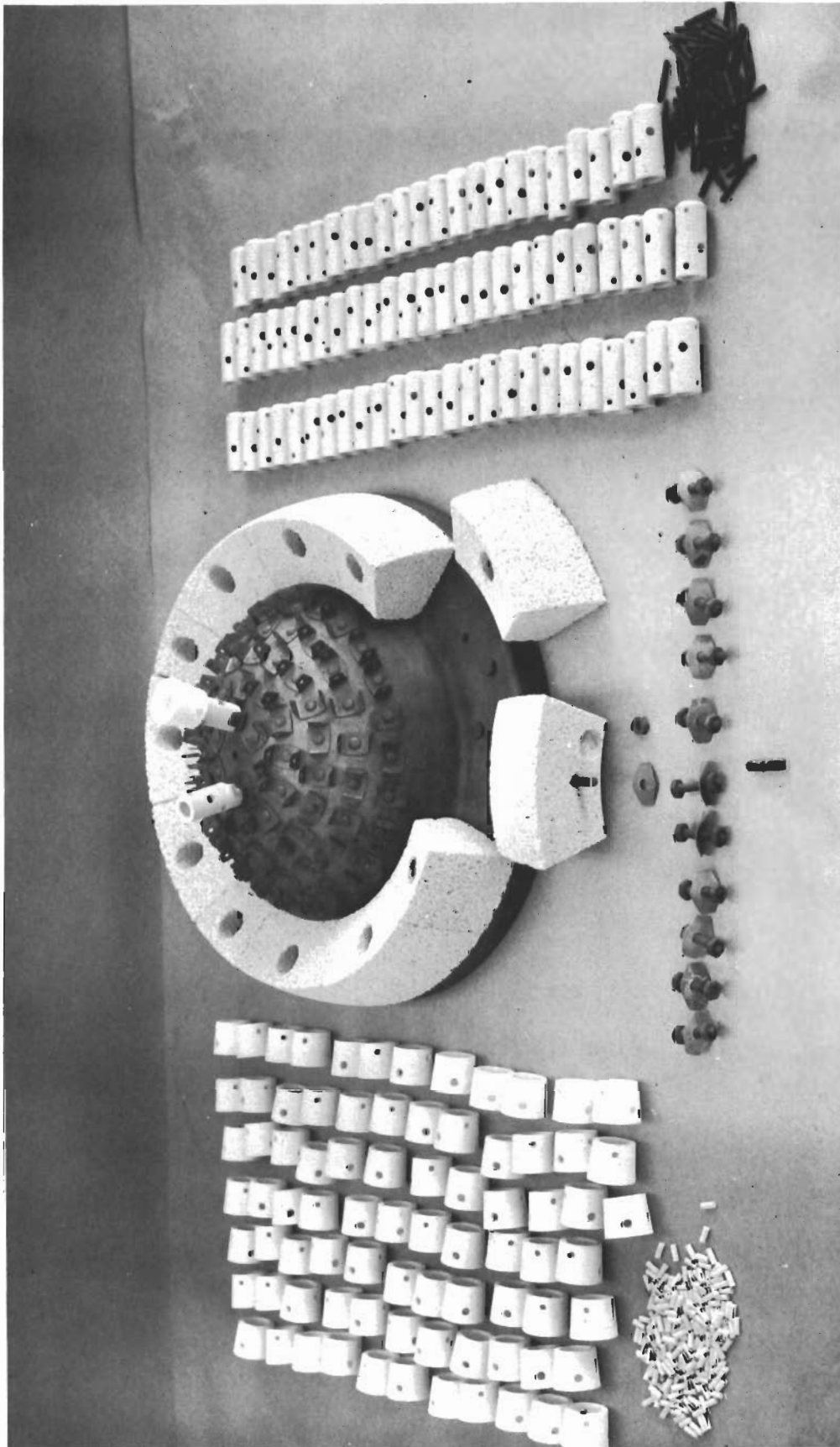
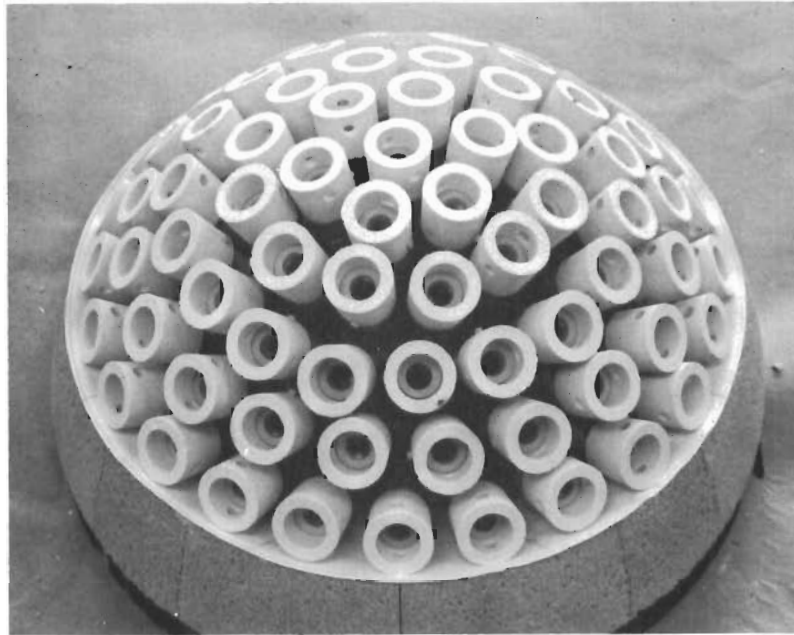
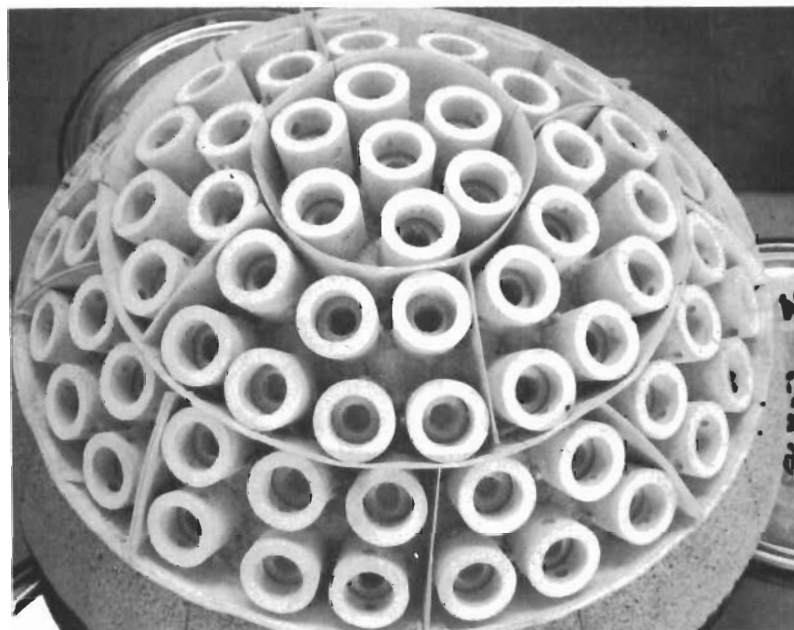


FIGURE 180 - COMPONENTS FOR THE 6.0-INCH RADIUS NOSE CAP



(a) BEFORE APPLICATION OF CASTABLE ZrO_2 AND ThO_2



(b) BEFORE APPLICATION OF CASTABLE ThO_2 ;
CASTABLE ZrO_2 IN PLACE

FIGURE 181 - 6.0-INCH RADIUS NOSE CAP CERAMIC ASSEMBLY



FIGURE 182 - FINISH GRINDING ON 6.0 INCH RADIUS NOSE CAP



FIGURE 183 - FINISHED 6.0 INCH RADIUS NOSE CAP

5.4 STAGE 3B FULL SCALE COMPONENT TESTS

The test program included vibration and acoustic tests which simulated the critical launch or ascent conditions, and thermal tests which simulated the critical re-entry heating conditions. Each full scale component was first subjected to the vibration tests and then to the acoustic tests. Both tests were conducted at room temperature. After the dynamic tests, each component was subjected to the representative temperature-time profile. (Appendix I presents a detailed description of the test facility, test procedures, and steps taken to control test conditions.)

5.4.1 Vibration and Acoustic Tests

In the vibration tests, each component was bolted at its structural base to a heavy plate rigidly attached to an electromagnetic exciter system. Each component was subjected to vibration runs in which the excitation was directed along the three mutually perpendicular axes of the component. Each vibration run (like the subscale test program described in Section 5.2) consisted of random vibrations in the 20 to 2000 cps range administered in a schedule of root-mean-square acceleration levels versus time. An accelerometer attached to the heavy base plate was used to monitor the scheduled input acceleration levels, which included a maximum 6.41 g rms level.

The acoustic test was also conducted in three stages to subject each component to excitations directed along the three mutually perpendicular axes of the component. Each stage of the test consisted of a five minute exposure to a sound spectrum which ranged from 15 to 9600 cps and attained an overall sound pressure level of 155 db. A modulated air stream acoustic transducer, terminated with an exponential horn, was used as a noise source in the test and the acoustic environment was monitored by a calibrated high intensity microphone, positioned at the side of the component.

5.4.1.1 3.0 Inch Radius Leading Edge - No failures occurred to the 3.0 inch radius leading edge component during any of the three vibration runs, although in the last run, a set of nuts shook loose from one of the three leading edge attachment points. Despite the loss of these nuts, the test was carried to completion without damage. From the performance of the remaining two attachment points and from the performance of other attachment points in subsequent tests, the most probable cause for the loss of the nuts was an improperly tightened jam nut.

After the attachment point was resecured, the component was subjected to the full acoustic test without failure. No repairs or modifications were required on the leading edge component at the conclusion of these dynamic tests, but some additional instrumentation was installed in preparation for the thermal environment test.

5.4.1.2 1.5 Inch Radius Leading Edge - Response accelerometers located at the leading edge/support interface, in addition to the input monitoring accelerometer on the base plate, were used in the vibration tests on the 1.5 inch leading edge component to determine the effect of the resiliency of the support structure. The component underwent a vibration run in which the excitation was normal to the base (and leading edge interface) and a run in which the excitation was normal to the plan view of the component, with-

out any failures. With the excitation normal to the base, the response accelerometers indicated that the acceleration level at the interface was $4\frac{1}{2}$ times as great as the input acceleration. With the excitation normal to the plan view, the acceleration level was amplified by approximately two times.

During the final vibration run in which the excitation was normal to the component cross-section, a single cast zirconia plug shook loose from among the 12 filled cavities in the ceramic elements (see Figure 184). The test was completed despite the loss of the plug, and the response accelerometers indicated a magnification level of approximately 200% during this final test run. At the conclusion of the vibration tests, no failures, other than the cast plug, were visible in the full scale component.

A study of the plug failure indicated that the mouth of the undercut at the base of the fastener cavity was obstructed to a significant degree by the bolt head, impairing the entrapment of the cast plug. The obstructing bolt head either hindered the flow of castable material into the undercut or reduced the effective surface between the protrusion and the body of the plug. One solution to the entrapment problem in future designs would be an enlargement in the undercut mouth. A more difficult and expensive solution would be to make the counterbore a reverse taper hole, which would prevent loss of the plug even if it cracked.

The open cavity was refilled with castable zirconia and after the plug was fully cured, the component was subjected to the acoustic tests. No failures occurred and the component, after the installation of additional instrumentation, was ready for the thermal environment test.

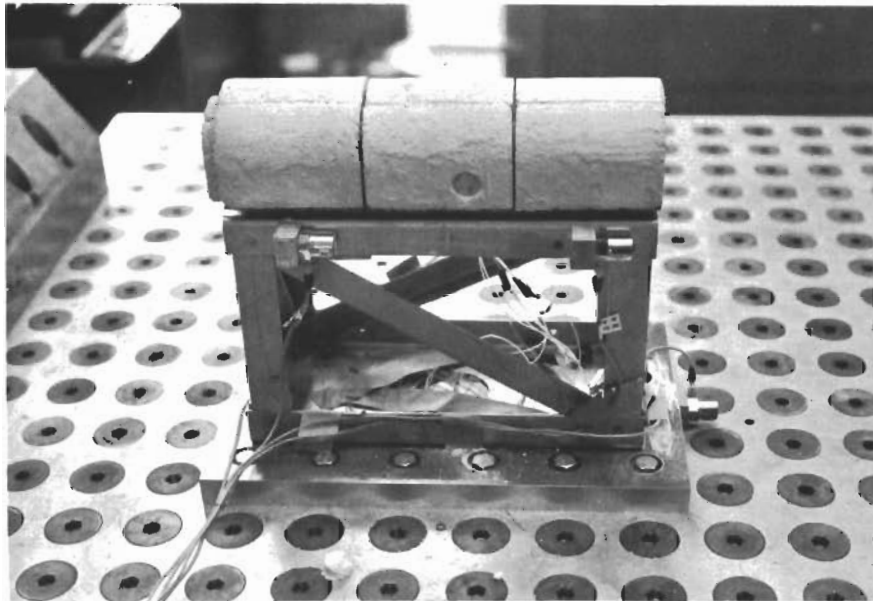


FIGURE 184 - FAILURE AS A RESULT OF VIBRATION OF THE 1.5-INCH RADIUS LEADING EDGE

5.4.1.3 6.0 Inch Radius Nose Cap - In the initial set up for the vibration tests, a response accelerometer was installed at the nose cap/support interface and an input monitoring accelerometer was installed at the heavy mounting plate which coupled the base of the component to the shaker. The component was first subjected, in sequence, to two complete vibration runs in which the excitation occurred in mutually perpendicular directions which were parallel to the base of the nose cap. In both of these tests, the acceleration response of the interface was approximately 2 1/2 times as great as the acceleration input levels at the base. These conditions subjected the nose cap to a maximum acceleration level of 15 g.

A study of the nose cap, following these tests, revealed that the segments of the aft row of the thoria faced modules had loosened and opened very slight clearances at the segment dividers. The segments were completely integral but each segment could be forced to move to some degree in directions parallel to the face of the hemisphere. Since this movement was very slight, no modifications were attempted for the final vibration test in which the excitation was perpendicular to the base of the nose cap.

In the final vibration setup, an exploratory run, which reached 2 g peak at the base of the support, indicated that the support structure in perpendicular excitation amplified the acceleration input some 600% at certain frequencies. Thus, if inputs were monitored at the base, it was possible to subject the nose cap to peak acceleration levels in excess of 36 g. In an actual vehicle installation, amplifications of this order could not be tolerated, and steps would be required to alter the structure and reduce the directional flexibility. However, in this project, the design of the actual nose cap and not the support structure was the primary objective and the support structure was not reworked. To hold the g loads to realistic levels, the test was performed with inputs monitored at the nose cap/support interface and not at the base of the support.

At the conclusion of the last vibration test, the nose cap was examined thoroughly. The segments which had been affected originally gave no indication of further deterioration, but all of the remaining segments had opened slight clearances at the dividers. In addition, there was a crack across a corner of one segment and a circular break in the surface of an adjoining segment (see Figure 185). Both of these segments were located in the middle row of the thoria-containing segments. Some random minor chipping occurred at the segment boundaries. The unit, in the condition noted above, was subjected to three acoustic test runs, which produced no further visible deterioration in the nose cap.

A localized exploratory incursion to the face of the castable zirconia layer was undertaken to seek an explanation for the very limited segment mobility produced in the vibration tests. The castable thoria layer around the corner crack in the one segment was chiseled away until one complete thoria reinforcing tube was fully exposed. The pins coupling the thoria tube to the zirconia tube were extracted and the thoria tube removed. The excavation and the removed parts are shown in Figure 186.

The coupling pins were stuck tightly in the zirconia tube but the holes in the thoria tubes were sufficiently large to permit the thoria tube to rock (even in the plane of the pins) very slightly. Neither the thoria tube

nor the coupling pins gave any indication of failure. However, there were clear indications that the perforated zirconia tube was no longer keyed to the castable zirconia matrix. The tube could be rolled clockwise or counterclockwise, rocked, and pushed in and out, all within the slight limits allowed by the specified clearance at the pin joint which coupled the zirconia tube to the substructure dome. Thus, even within the plane of the coupling pins, the reinforcing elements acted as limited pin-ended links between the thoria layer and the rest of the nose cap and permitted the minimal mobility observed at the face of the hemisphere. The basic cause for this undesirable situation appeared to be the very slight clearance permitted in the fit at the pin joints.

A very close fit was maintained in the pin joints of the completely successful tube reinforced subscale specimen which served as a model for the full scale nose cap. Because of the tight fit, attachment of the seven reinforcing tubes involved in the flat subscale specimen was difficult. The full scale component required 81 reinforcing tubes distributed over a hemispherical surface. These conditions, in the light of the experience on the subscale component, seemed to present an intolerable assembly situation if tight pin joints were used in coupling the tubes to the substructure. Accordingly, a looser fit was specified and the design relied on the engagement between the perforated tubes and the castable zirconia matrix to immobilize the reinforcing elements. Vibration test results clearly indicated that the matrix was taxed beyond its abilities and that a more rigid joint was necessary.

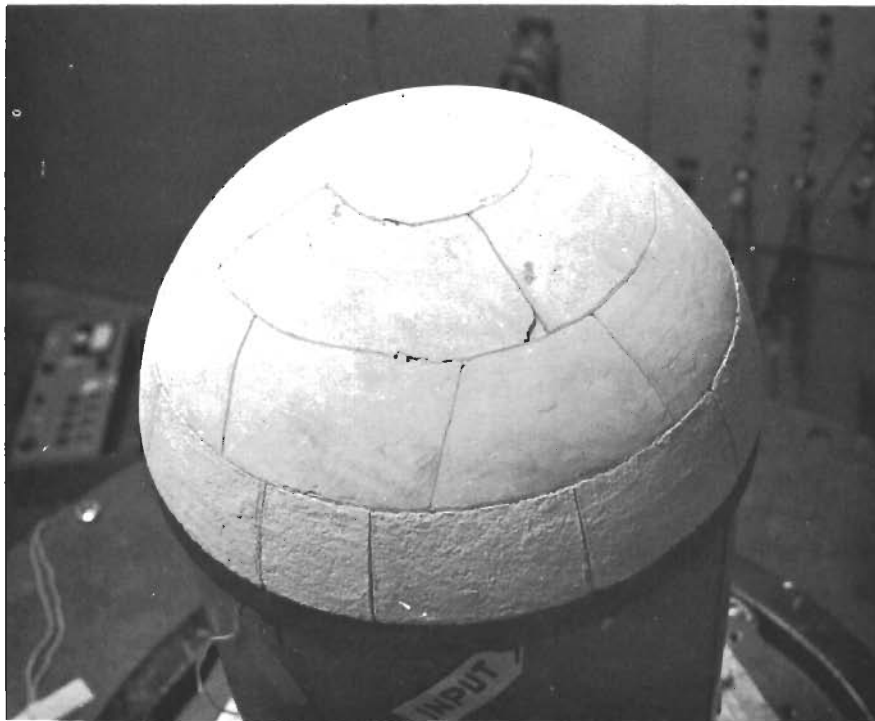
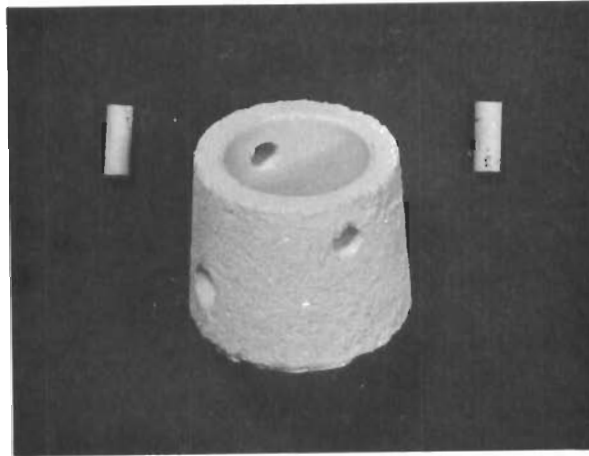
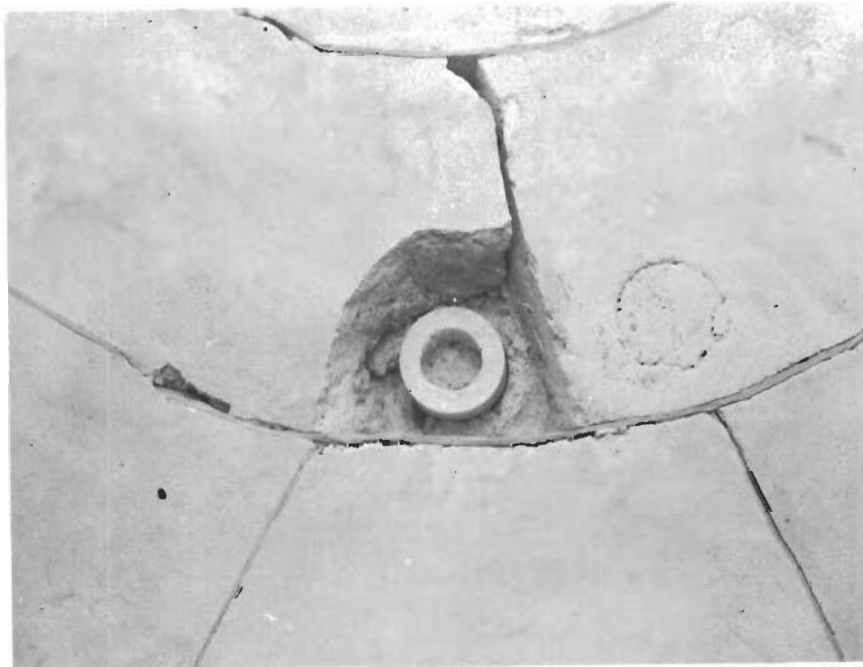


**FIGURE 185 - FAILURE AS A RESULT OF VIBRATION OF
THE 6.0 INCH RADIUS NOSE CAP**



b. REINFORCING THORIA TUBE AND ZIRCONIA PINS REMOVED FROM NOSE CAP.



a. EXCAVATION IN NOSE CAP

**FIGURE 186 - EXPLORATORY STUDY OF NOSE
CAP VIBRATION FAILURE**

Actual assembly work on the full scale nose cap demonstrated that access to the pin joints was not the problem visualized in the planning stage. The assembly sequence devised in conjunction with the careful orientation of the retainer clips had established unobstructed paths for inserting the coupling pins. Consequently, tight fitting joints on the full scale component would not have been complicated by access problems and assembly difficulties would not have been any greater than those experienced on the subscale work.

The investigations indicated that the reinforcing elements were integral and fully coupled to the substructure and that the castable zirconia matrix was continuous and intact, but disengaged from the perforations in the zirconia tubes. The visible face of the nose cap indicated that all but two segments of the thoria layer were intact and fully integrated with the internal reinforcing thoria tubes. In essence, the composite ceramic shield was essentially intact and completely serviceable from a thermal standpoint. Therefore, a few cracks and the void created in the course of this investigation were repaired in preparation for the thermal test. The one thoria tube was reinstalled and low density castable thoria was tamped into the surrounding cavity. A facing was applied at the circular crack and at the chipped areas. This repair work was fully cured and additional instrumentation was installed on the component in preparation for the thermal environment test.

5.4.2 Thermal Tests

For the thermal test, each full scale component was installed on a special setup which established the proper orientation of the given leading surface with respect to a mobile burner head. This burner head consisted of specially designed MAPP-OX gas burners in an arrangement that depended on the unit under test. The desired temperature-time history for each component was achieved by positioning the burner head and/or controlling gas pressures in response to the T-y read-out of a monitoring pyrometer sighted on the stagnation point and a thermocouple bonded on the surface at the stagnation point. The surface thermocouple (chromel/alumel) provided temperature readings up to 2500°F, beyond which the optical pyrometer was utilized. Additional surface temperatures were determined with manually operated L & N optical pyrometers. Thermocouples (Ir/Ir-40% Rh, Pt/Pt-10% Rh, and chromel/alumel) were located in and on the full scale components, including within the ceramic structures, to determine subsurface temperatures during test.

The temperature-time histories specified for the leading edge components included histories at windward and leeward surface elements in addition to the stagnation line. The arrangement of the torches related the windward and leeward histories to the stagnation line history. The temperature-time histories used for the thermal test of the 3.0 inch leading edge and the 1.5 inch leading edge are presented in Figures 187 and 188. The 6.0 inch radius nose cap was tested to the time-temperature profile given in Figure 189 except that a maximum peak temperature of 4500°F was utilized.

5.4.2.1 3.0 Inch Radius Leading Edge - Twelve thermocouples were placed on or in the leading edge structure at various locations. Two Ir/Ir-40% Rh thermocouples placed in the ceramic structure were damaged during installation of the leading edge on the support sting and did not function during the test. Surface temperatures at 24 locations were determined with manually operated L & N optical pyrometers.

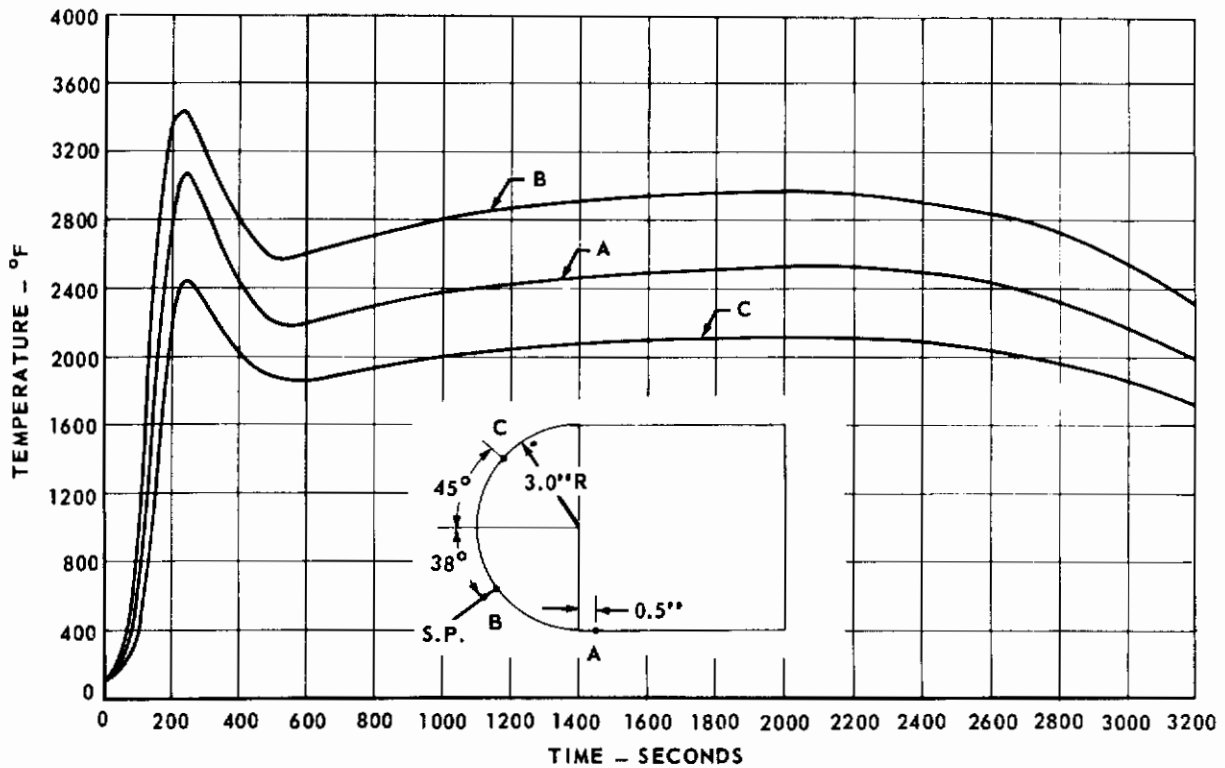


**FIGURE 187 - THERMAL TEST CONDITIONS FOR FULL SCALE
3.0-INCH RADIUS LEADING EDGE**

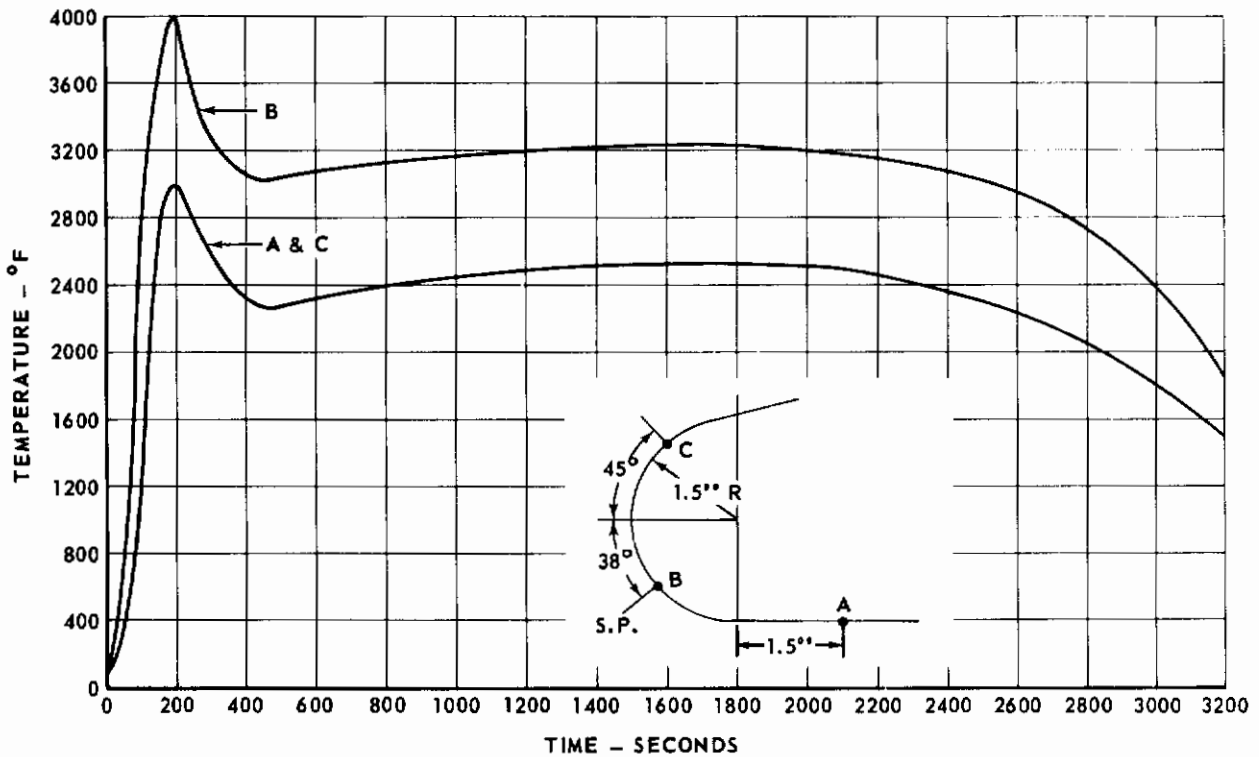


**FIGURE 188 - THERMAL TEST CONDITIONS FOR FULL SCALE
1.5-INCH RADIUS LEADING EDGE**

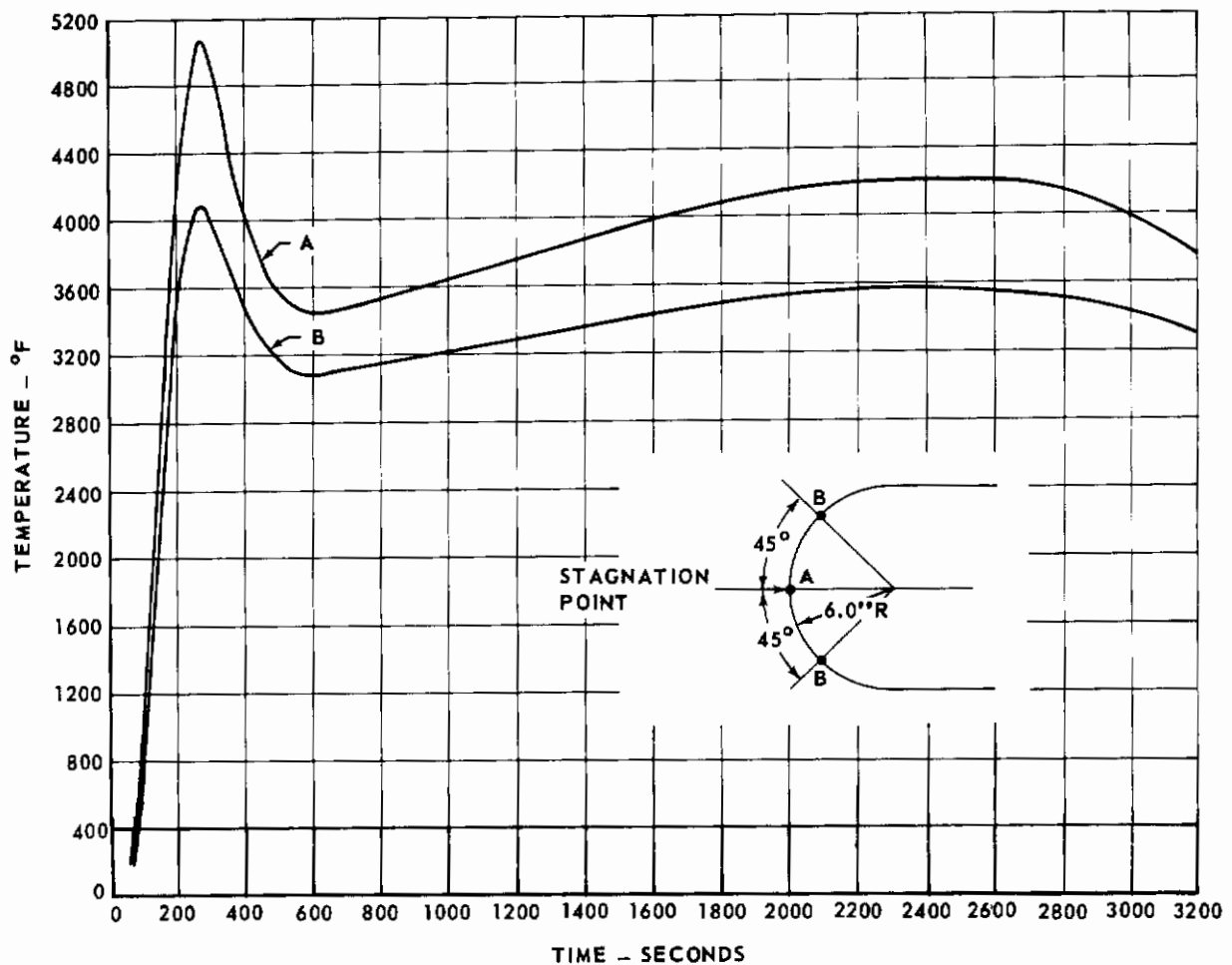
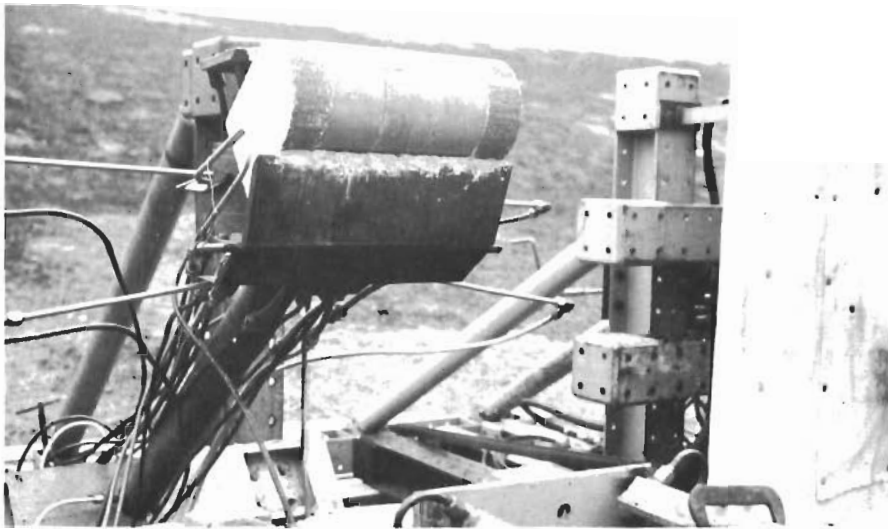


**FIGURE 189 - THERMAL TEST CONDITIONS FOR FULL SCALE
6.0 INCH RADIUS NOSE CAP**

During the approximately one hour thermal test, the thermocouples indicated that none of the metal substructure, including the columbium, exceeded 1500°F. The water cooled external protection shields (see Figure 190(a)) apparently provided cooling of all metal parts.

The surface temperature readings indicated that the desired thermal trajectory was attained at the stagnation line, but hot spots present along the isotherm caused temperature variations of approximately 200°F. The peak temperature of the isotherm at the lower aft edge of the ceramic tiles was about 400°F lower than desired, but the temperature during the glide region was as intended. The peak temperature of the isotherm 83° up from the stagnation line was about 400°F higher than planned and the temperature during glide was about 200°F higher.

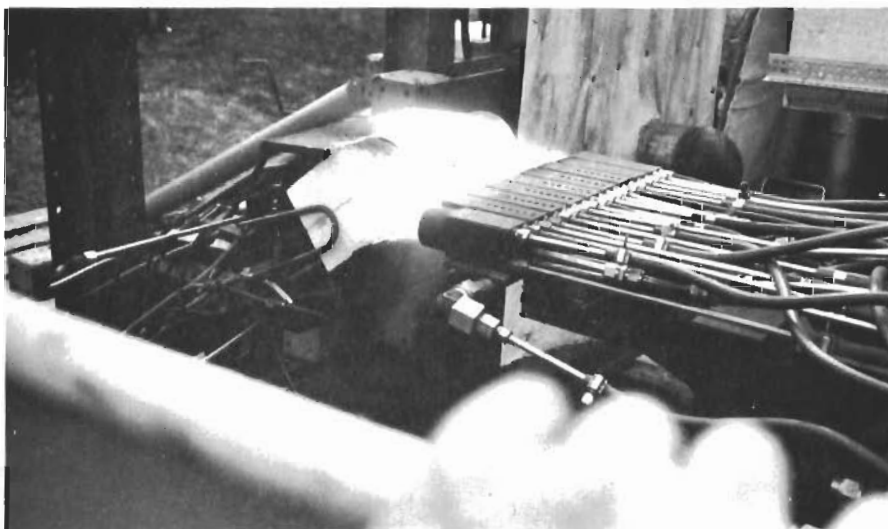
Figures 190(b) and 190(c) show the test in progress. Although not discernible in these pictures, excessive edge heating along the vertical expansion gaps occurred. The horizontal gaps closed very early in the test but the vertical gaps never completely closed. The pressure and high velocity of the MAPP-OX flame coupled with some non-uniformity along the isotherm and the fact that the vertical gaps did not close as designed, contributed to the high edge heating and subsequent melting in these gaps



(a) COMPONENT IN TESTING POSITION



(b) COMPONENT DURING HEAT-UP



(c) COMPONENT AT 3400°F

FIGURE 190 - MAPP-OX THERMAL TESTING OF 3.0 INCH RADIUS LEADING EDGE

Figures 191 and 192 show the leading edge after test. Although many cracks can be seen in the alumina tiles, no spalling occurred and the leading edge remained integral. Figure 192(c) shows the end fixture brick, which remained intact although cracked. The crack pattern (indicative of shear failure) paralleling the curved surface occurred at approximately the thickness of the leading edge tiles, which would indicate that the proper tile thickness was utilized to prevent shear cracking. No surface paralleling cracks were evident in the tiles after test. The cracks in the lower tiles appeared early in the test, while the cracks in the upper tile were not discernible until approximately half way through the test. The melting in the vertical gaps started at or near the time peak temperature was attained. On removal of one of the tiles, it was discovered that the flame had penetrated the gap and that melting of the insulation had also occurred. Most of the chromia coating on the hotter portions of the leading edge was lost or reacted with the alumina, except in the area of the surface thermocouple where excess chromia existed. Loss of chromia did not occur to this extent in the subscale module testing.

The loss of the chromia coating would result in an emittance of less than the 0.7 value for which the controlling pyrometer was compensated. This could have yielded overheating because the temperatures fed into the controller would have been lower than was actually the case, thus calling for more heat. The dynamic condition and/or the atmosphere of the MAPP-OX burners could have caused some of the chromia to be lost, causing the temperatures to be exceeded and resulting in loss of more chromia by vaporization. Exceeding the 3400°F peak temperature for a long period of time would result in a chromia-alumina reaction as did occur and could cause melting or softening of the alumina as occurred at the cracks.

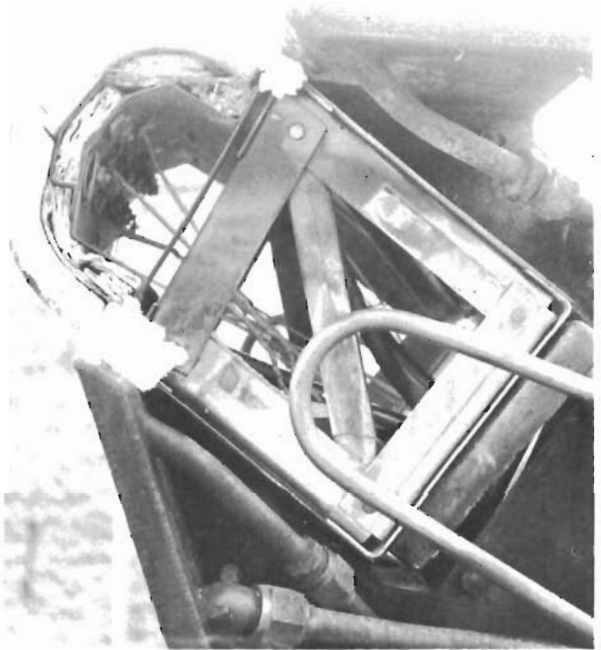
The cracking of alumina tiles did not occur in the subscale module program or in the thermal shock testing of incoming materials. In the subscale program, the tiles were thinner which would make them more thermal shock resistant. Size, configuration, and handling considerations necessitated use of thicker tiles on the full scale leading edge. However, samples 3.5 inches x 4.35 inches x 0.9 inch thick (which simulated the full scale tile size) survived thermal shock testing.

It is felt that the cracking of the alumina tiles was aggravated by the columbium retaining springs which were much stiffer as-fabricated than calculated, because of the stiffening effect of the oxidation protective coating. These springs probably restricted movement of the alumina tiles by thermal growth, adding restraining stresses to the thermal stresses. Unknown configuration effects (curved tiles versus flat) also could have contributed to the failure of the tiles, as would have irreproducibility of materials. The melting and flame penetration in the expansion joints indicated that some heating of the tiles from front and back surfaces had occurred which would have increased thermal stresses.

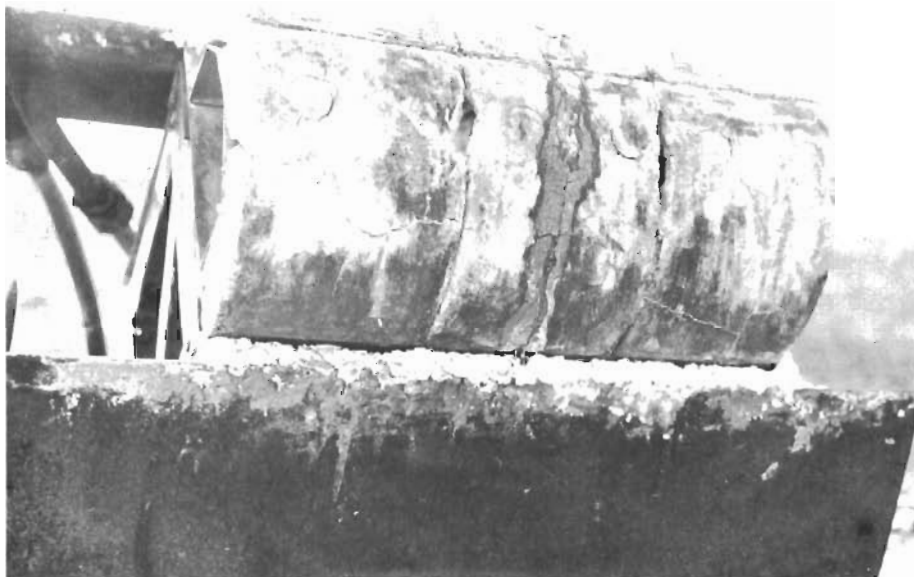
In summary, it would appear that use of a material of superior thermal shock resistance and strength would be in order, closer control of test temperature and environment would be desirable, redesign of the retaining springs is necessary, and the vertical expansion gaps should be smaller. The dynamic conditions (pressure, velocity, and noise) of the MAPP-OX test were more severe than the expected flight conditions. The flame pressure and probable peak temperature overshoot promoted melting in the expansion gaps.



(a) LEFT SIDE VIEW



(b) RIGHT SIDE VIEW



(c) FRONT VIEW

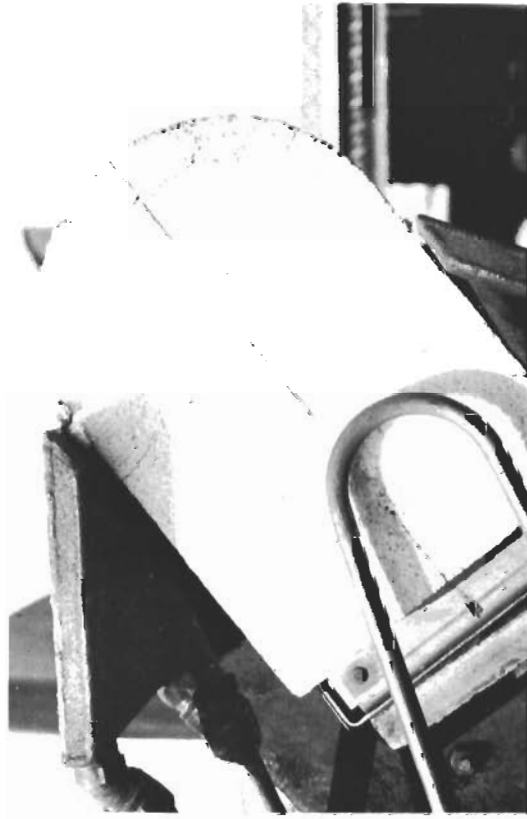
FIGURE 191 - 3.0 INCH RADIUS LEADING EDGE AFTER THERMAL TEST



(b) FRONT VIEW



(a) FRONT VIEW



(c) LEFT SIDE VIEW, END CLOSURE BRICK

FIGURE 192 - 3.0 INCH RADIUS LEADING EDGE AFTER THERMAL TEST

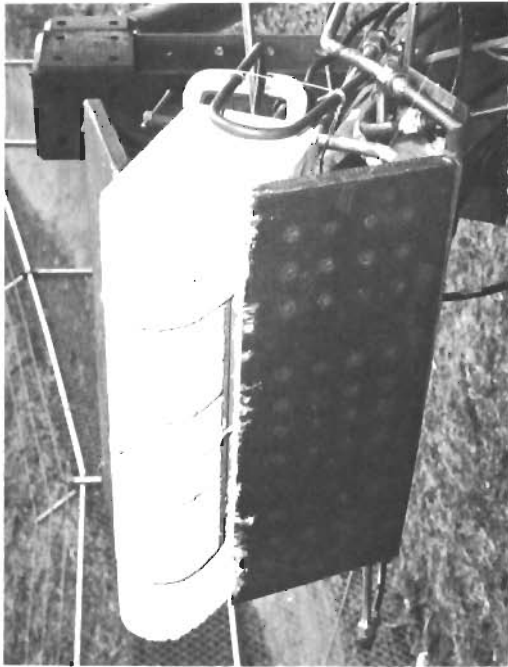
The use of the external water cooling shields created a much cooler substructure than designed for, which in turn created a greater and less linear thermal gradient through the ceramic, increasing thermal stresses. The use of smaller ceramic tiles would lessen the thermal shock problem but increase fabrication and attachment problems. It should be noted again that the subscale module of similar design and like material survived thermal testing essentially unaffected.

5.4.2.2 1.5 Inch Radius Leading Edge - Fifteen thermocouples were mounted on or in the leading edge structure, including three Ir/Ir-40% Rh thermocouples in one of the zirconia blocks. Surface temperatures were monitored at 37 locations by use of manually operated L & N optical pyrometers. Figure 193(a) shows the leading edge prior to test.

After approximately 240 seconds of the thermal test, the end fixture brick on the right side failed, permitting the flame to penetrate behind the zirconia blocks and into the metal structure. This resulted in localized melting of the Hastelloy X support structure and oxidation of the coated molybdenum substructure. At this time, the MAPP-OX burners were immediately shut off, resulting in rapid cooling of the zirconia structure. Prior to complete failure of the end brick, it had cracked sufficiently to permit penetration of enough heat into the metal structure and down the support sting to melt the thermocouple terminal blocks in the sting. This eliminated the thermocouple readings, and at this time air cooling to the Hastelloy X structure was turned on as a precautionary measure. The end fixture brick on the left side failed at or shortly before burner shut-off.

By 240 seconds, the leading edge had been exposed to the peak temperature of 4000°F and the temperature was being reduced, having gotten to ~3600°F (see Figure 188). Pyrometer readings up to this time indicated the isotherm 83° up from stagnation was about 500°F higher than expected when the stagnation line was at peak temperature. At the same time, the isotherm on the lower edge of the leading edge was about 700°F higher than anticipated. The temperature uniformity along isotherms looked very good with no severe hot spots even at the expansion gaps. The stagnation line, time-temperature profile was produced as desired.

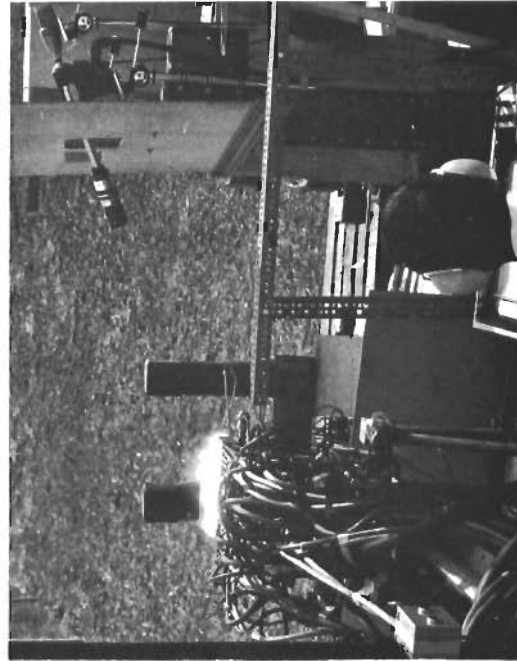
Figure 193(b) shows the very early stages of heating where a corner of the end fixturing brick is already missing. In Figure 193(c), the bright sparks above the leading edge and to the far right of it are pieces of the end brick that are spalling off. In Figure 194(a), the end brick has not yet cracked. Although difficult to see, the end brick has cracked in Figure 194(b) and the flame has penetrated into the metal structure. In Figure 194(c), a corner of the left side end fixturing brick has spalled away and the penetration of heat into the metal structure can be detected. Shortly after this last picture was taken, the right side end brick fell away at the crack noted in Figure 194(b), allowing the flame to enter and destroy part of the metal structure. At this time the test was halted.



(a) COMPONENT IN TESTING POSITION

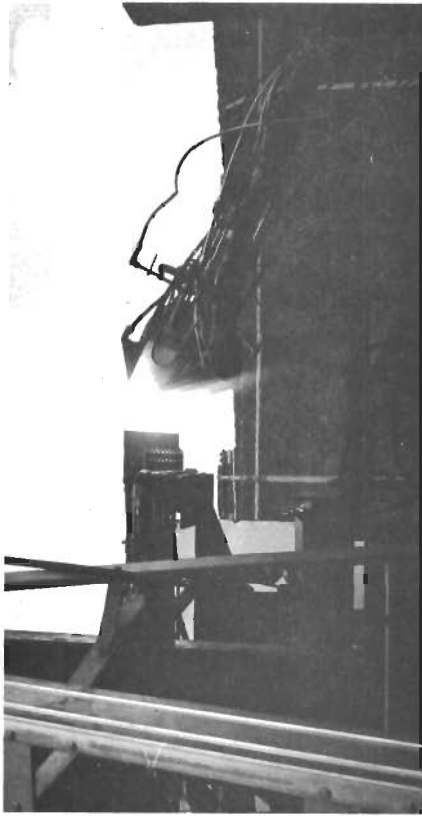


(b) COMPONENT DURING TEST, END BRICK CORNER MISSING

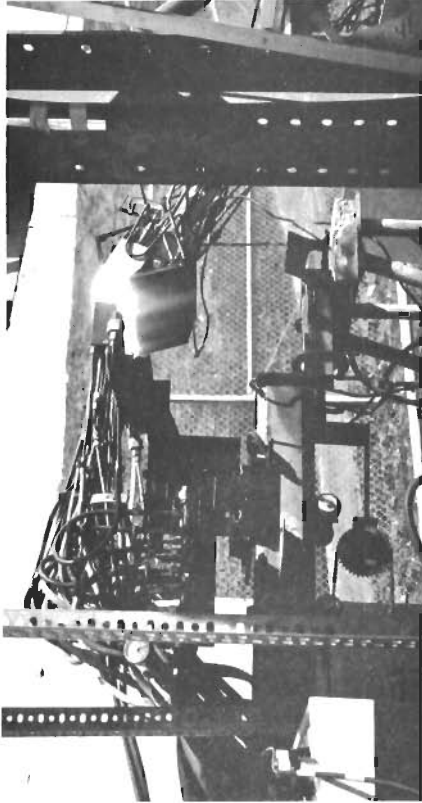


(c) COMPONENT DURING TEST, END BRICK SPALLING

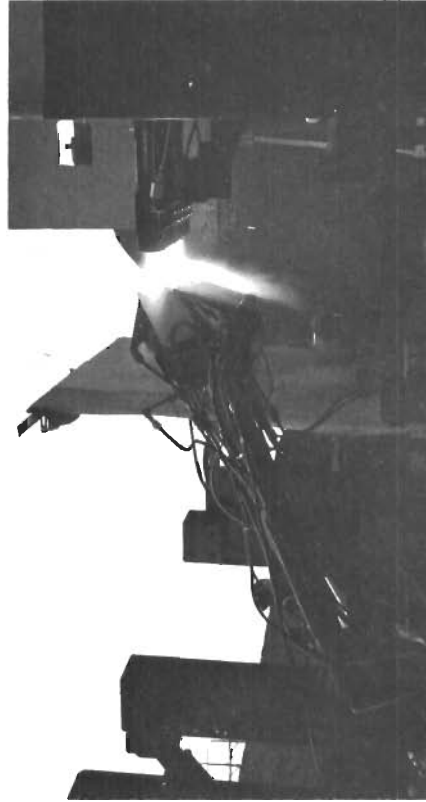
FIGURE 193 - MAPP-OX THERMAL TESTING OF 1.5 INCH RADIUS LEADING EDGE



(a) COMPONENT DURING TEST



(b) COMPONENT DURING TEST, END BRICK CRACKED



(c) COMPONENT DURING TEST, FLAME ENTERING SUBSTRUCTURE

FIGURE 194 - MAPP-OX THERMAL TESTING OF 1.5 INCH RADIUS LEADING EDGE

Figure 195 shows the leading edge after test. The zirconia blocks on the right side can be seen to be barely hanging on to some remaining molybdenum structure and one zirconia block is missing because the metal structure beneath it was completely destroyed. In Figure 195(d) the left side fixture brick is missing. This occurred at a time close enough to test shut-off that there was not sufficient heat penetration in this area to damage the substructure.

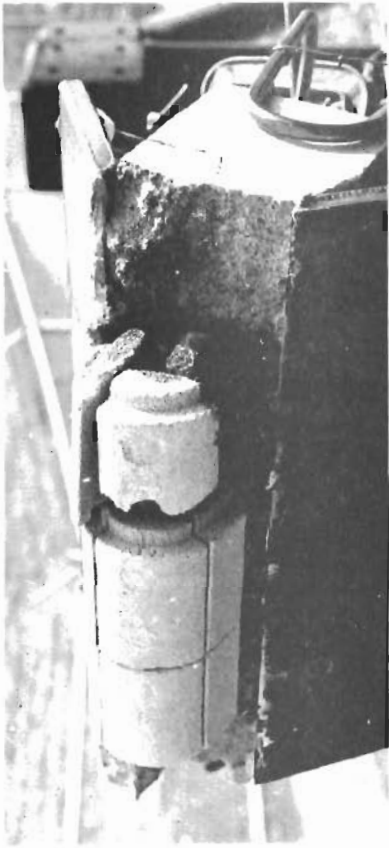
Figure 195 shows the central and left section of zirconia blocks to be intact, with little effects from the testing other than small shrinkage cracks around the potting material in the bolt holes and a few hairline cracks elsewhere. The shrinkage cracks were expected and accounted for by using undercuts in the bolt holes. The other cracks were sufficiently minor as to be discounted.

As the test lasted until after the peak temperature was attained, the leading edge was tested to the most severe thermal shock condition of the thermal trajectory; i.e., surface heating rates up to $42^{\circ}\text{F}/\text{sec}$. In reality, it was subjected to an even more severe thermal stress condition than intended because of the very rapid cooldown. Since the zirconia parts used on the leading edge proper apparently survived the severe thermal shock, it is expected they would have survived the complete hour test. During the remainder of the test, the only expected change would have been some additional shrinkage of the chemically bonded materials.

It is concluded that the partial failure of the 1.5 inch radius leading edge was due to failure of the fixturing, which could be corrected by use of a more thermal shock resistant material such as high density zirconia or by placing additional actual leading edge sections at the ends. The low density zirconia used in fabricating the leading edge was the most thermal shock resistant of the material on hand, but not as good in this respect as laboratory tests had shown it possible to make. It is believed that a leading edge utilizing the present design and state-of-the-art low density zirconia would survive the expected flight environment.

5.4.2.3 6.0 Inch Radius Nose Cap - Twenty-two thermocouples were mounted in or on the nose cap structure, including eight Ir/Ir-40% Rh thermocouples in the ceramic structure which were damaged during installation of the nose cap onto the test stand and did not function during the test. The Pt/Pt-10% Rh thermocouples on the molybdenum indicated a maximum temperature of about 2300°F during test. The chromel/alumel thermocouples on the Hastelloy X support structure indicated a maximum temperature of about 1400°F .

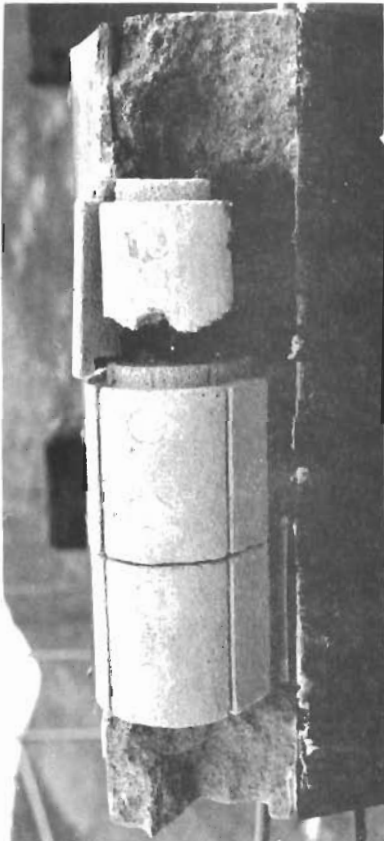
Surface temperatures were determined at 28 points, using manually operated L & N optical pyrometers. These readings indicated the isotherm 45° off of stagnation point was about 200°F lower in temperature than anticipated. The thermal trajectory at the stagnation point was reproduced as desired except that a peak temperature of about 4600°F rather than the desired 4500°F was attained. The 4500°F was to be used instead of the originally planned 5000°F because tests indicated the chemically bonded low density thoria could not resist the dynamic conditions of the MAPP-OX flame at temperatures above about 4500°F . Except for nose cap surface discontinuities, the surface heating was quite uniform on isotherms around the nose cap periphery. The discontinuities were due to nose cap failure as discussed below, which caused the test to be halted after approximately 20 minutes duration rather than the planned one hour run.



(b) RIGHT FRONT VIEW



(d) LEFT FRONT VIEW



(a) FRONT VIEW



(c) LOWER FRONT VIEW

FIGURE 195 - 1.5 INCH RADIUS LEADING EDGE AFTER THERMAL TEST

Figures 196, 197, and 198 show the nose cap during thermal test. In Figure 196(b), the dense thoria tubes are barely visible in the low density thoria matrix as the density difference in the materials causes a different response to heat input. Edge heating can be seen around the first peripheral joint. The sparks above the nose cap in Figure 196(d) indicate the loss of very small amounts of low density thoria in the joint area adjacent to the right of the stagnation point, at about 4300°F. In Figure 197(a), the chemically bonded thoria that bonded the chromel/alumel thermocouple to the surface has spalled away. The other pictures in this sequence illustrate the nose cap failure by erosion of the low density thoria and subsequent failure of many of the high density thoria and zirconia tubes and some of the low density zirconia blocks. The nose cap is undergoing cool-down in Figure 198(d), and a leak in the water cooled shield is evident. The nose cap failure shows here.

Figure 199 shows the nose cap immediately after completion of test. Most of the low density, chemically bonded thoria eroded away, exposing the low density chemically bonded zirconia. The cracks in the low density zirconia were due to shrinkage and not unexpected. If the outer layer of thoria had held up, this cracking would not have even been visible. Some slight melting of this zirconia occurred in the area close to the stagnation point as it was exposed to temperatures of about 4500°F; far higher than intended. Cracks are evident in the low density sintered zirconia blocks and part of one block in the lower right hand corner fell off. As mentioned previously, this zirconia was considered substandard in thermal shock resistance but was the best available. It probably would have survived with only minor cracking if the thoria had not failed. When the low density thoria was lost, the high density thoria and zirconia tubes were exposed to direct flame impingement and failed from thermal and/or mechanical shock.

The nose cap failure began at the first expansion joint to the right of the stagnation point and propagated from there. In the early part of the test, failure had been confined to the right side of the cap but later in the test continued to other areas. Figure 199(a) shows the left side of the cap to be in better condition than the rest of the cap.

It is believed that the nose cap failed from a combination of design, materials, and test condition shortcomings. The number of high density thoria tubes per unit area left the low density thoria at the joint areas poorly supported. In these areas, the outside diameters of many of the tubes almost touched the joint edges, leaving only a thin layer of the low strength, low density thoria to bond around the tube to the rest of the low density thoria matrix. Any shrinkage cracking of the low density thoria in this area would have left it further weakened.

The dynamic conditions (high velocity, high noise, and high pressures) of the MAPP-OX burners probably contributed to the initial failure of the low strength thoria, and undoubtedly promoted the surface erosion from this point to the rest of the cap. Actual inflight re-entry conditions would not be this severe. Once the failure started, high localized heating occurred which would tend to increase thermal stresses and promote failure. Surface erosion was not a problem in the oxyacetylene subscale testing at temperatures up to about 4300°F but this testing was at comparatively low noise, pressure, and velocity levels (more comparable to flight conditions). MAPP-OX testing of

Text continued on page 250



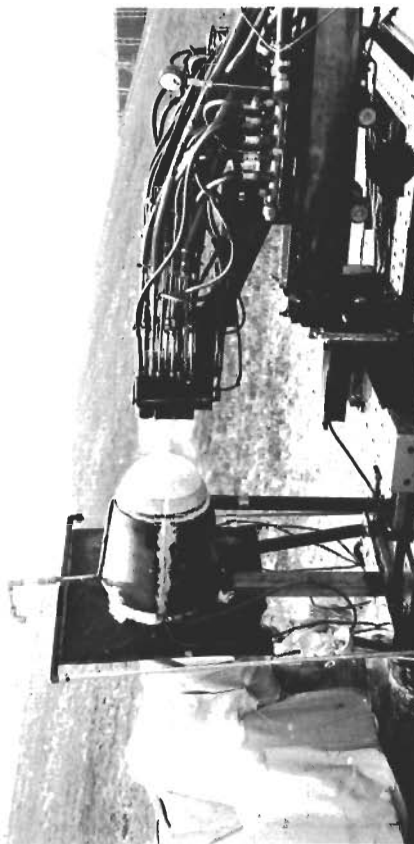
(a) COMPONENT IN TESTING POSITION



(b) COMPONENT DURING HEAT-UP

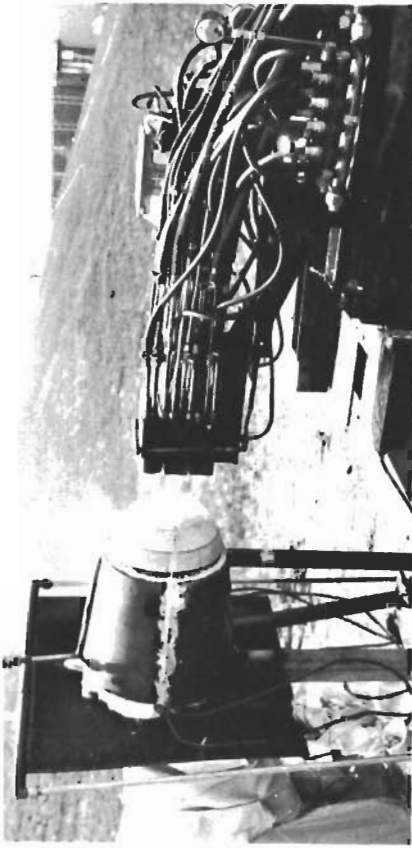


(c) COMPONENT DURING HEAT-UP



(d) COMPONENT DURING HEAT-UP, EROSION STARTING

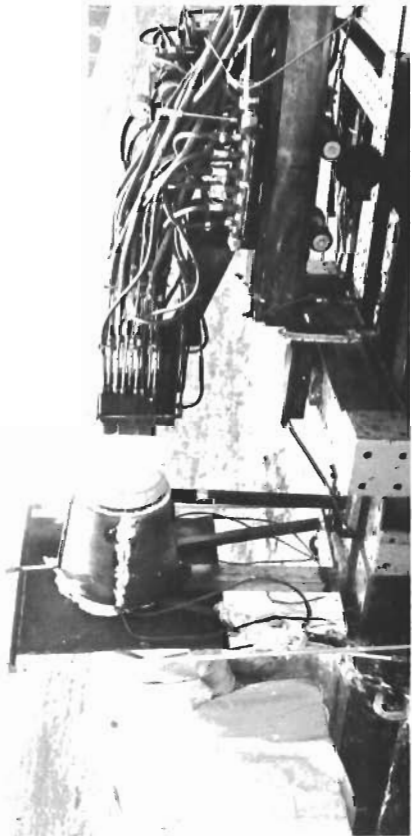
FIGURE 196 - MAPP-OX THERMAL TESTING OF 6.0 INCH RADIUS NOSE CAP



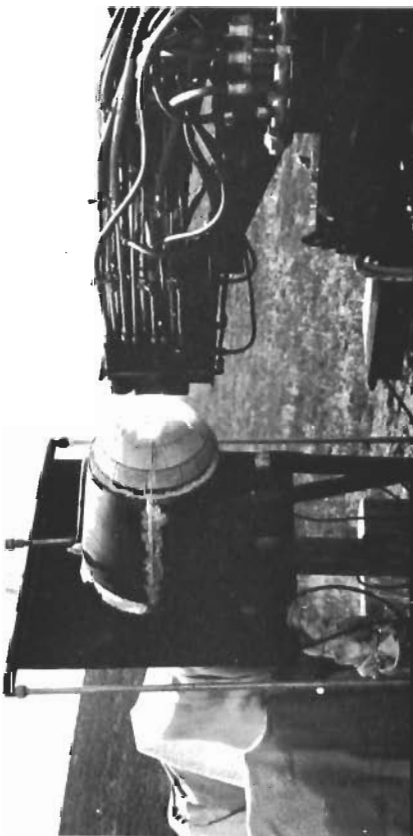
(b) COMPONENT DURING HEAT-UP



(d) COMPONENT AT 4600°F

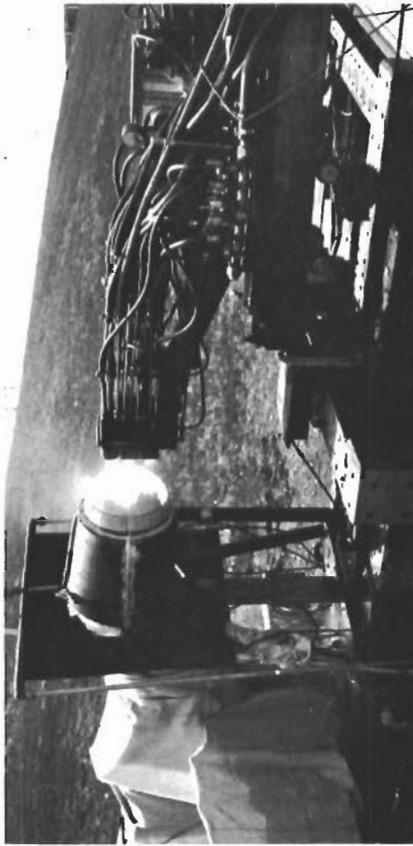


(a) COMPONENT DURING HEAT-UP

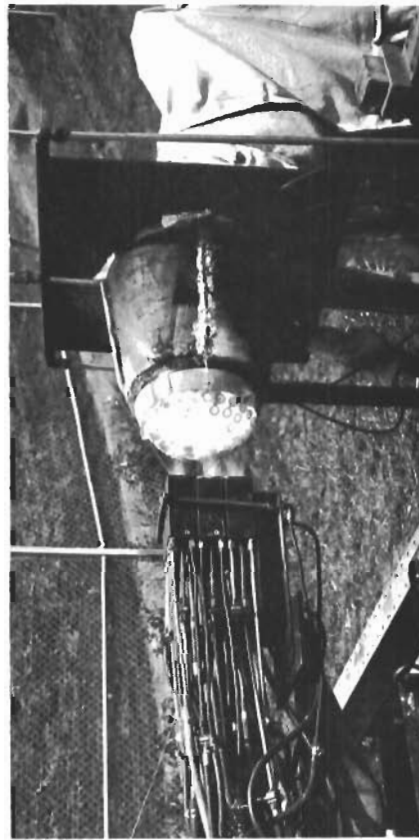


(c) COMPONENT AT 4600°F

FIGURE 197 - MAPP-OX THERMAL TESTING OF 6.0 INCH RADIUS NOSE CAP



(b) COMPONENT DURING GLIDE



(d) COMPONENT DURING COOL-DOWN

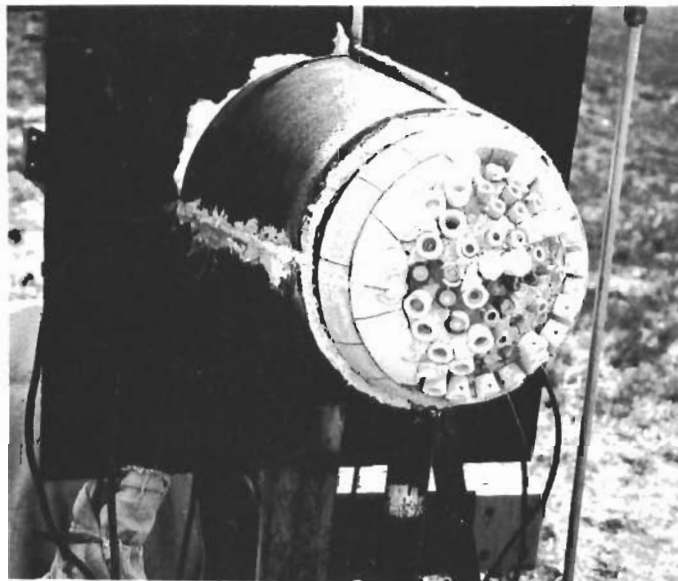


(a) COMPONENT AT 4600°F

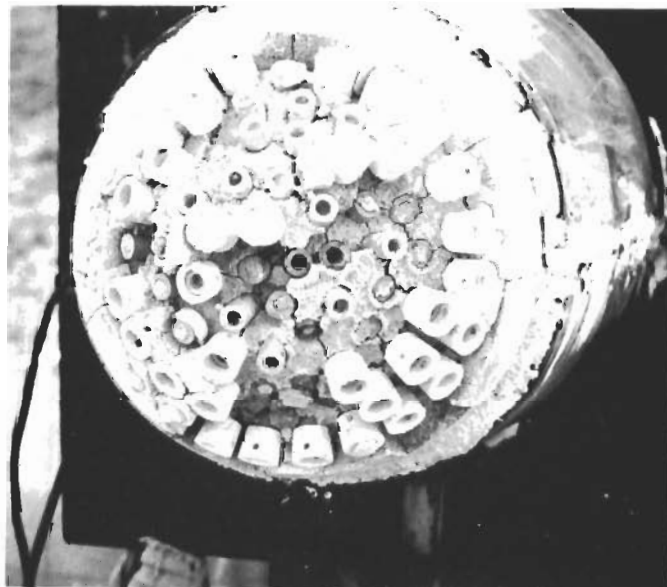


(c) COMPONENT DURING GLIDE

FIGURE 198 - MAPP-OX THERMAL TESTING OF 6.0 INCH RADIUS NOSE CAP



(a) LEFT FRONT VIEW



(b) RIGHT FRONT VIEW

FIGURE 199 - 6.0 INCH RADIUS NOSE CAP AFTER THERMAL TEST

low density chemically bonded thoria samples to about 4500°F had indicated this material would withstand this condition but no unsupported edges existed in the type of sample tested. Laboratory thermal shock testing to 4000°F had indicated the low density thoria and the high density zirconia to have good thermal shock resistance and the high density thoria and low density sintered zirconia to be less thermal shock resistant.

Some possible solutions, singly or in combination, to the nose cap failure are as follows:

(a) Use of a higher strength, higher density chemically bonded thoria outer layer.

(b) Elimination of the outer layer expansion joints to give more self-support to the outer thoria layer and then allow it to assume a natural craze-crack pattern during use.

(c) Decrease the number of high density tubes per unit area to allow a more continuous low density thoria matrix to eliminate weak areas as near joints.

(d) Replace the high density thoria tubes with tapered plugs as were used in the one subscale module (Figure 147) for the same reasons as (c) above. However, the thoria plugs would require better thermal shock resistance than the material used in the past. This design would also be slightly more difficult to fabricate since the thoria plug-zirconia tube assembly is more difficult to preassemble than the present design.

(e) Use test conditions that more closely simulate the expected environment. Considerable effort was expended to achieve this simulation, but it was not within the scope of the project to carry the work to optimization of test conditions.

SECTION VI

THERMAL ANALYSES

6.1 METHODS OF ANALYSIS

The methods of thermal analysis employed to obtain temperature gradients and surface temperature distributions for the ceramic leading edges and nose cap are discussed below. These methods represent an integration of theory and experimental data obtained from heat transfer tests on Project ASSET, a winged lifting type hypersonic vehicle developed by McDonnell under Contract No. AF33(616)-8106. Aerodynamic heat inputs for the two leading edges and the nose cap were based on the trajectories presented in Section 3.3.

6.1.1 Leading Edge Thermal Analysis

The basic thermal analysis method utilized to predict the transient temperatures on the leading edges was Lees' approximate equation for laminar stagnation line convective heating, reduced by a sweep correction factor equal to $\cos^{3/2}$ of the effective sweep angle. The effective sweep angle was determined from the relation $\lambda_e = \sin^{-1}(\sin \lambda \cos \alpha)$, where λ is the sweep angle and α is the angle of attack.

Experimental heat transfer data obtained on an ASSET wind tunnel model indicated that the stagnation line heating rate decreased as the distance along the leading edge (measured from the nose) increased. The amount of this reduction from the theoretical value was based on the ASSET configuration, and for other vehicle designs the deviations from theory might be somewhat different.

Preliminary analysis on the 1.5 inch radius leading edge showed only a 58°F increase in the maximum temperature at the stagnation line when employing 100% of Lees' equation rather than the lower value indicated from the ASSET data. As a result, analyses on the leading edges employed Lees' approximate equation without incorporating a reduction due to the effects of body station and angle of attack. (The early analyses performed in Section III used 91% of Lees' approximate equation.) Figure 200 presents the ratio of surface to stagnation line heat flux plotted versus distance from the stagnation line. This distribution was used in the analyses.

As shown by Figure 200, aerodynamic disturbances such as lateral slots or aft facing steps produce increases in the local heat flux of up to 30% more than the smooth value. Therefore, at the junction between the leading edge and the lower surface panel, an increase of 30% in the heating rate was included in all analyses to account for flow discontinuity. It was expected that the small gaps between ceramic tiles would cause only slight, if any, increase in local heat flux. The increase in heating due to surface gaps was faired linearly into a smooth distribution at a distance of one inch downstream from the gap.

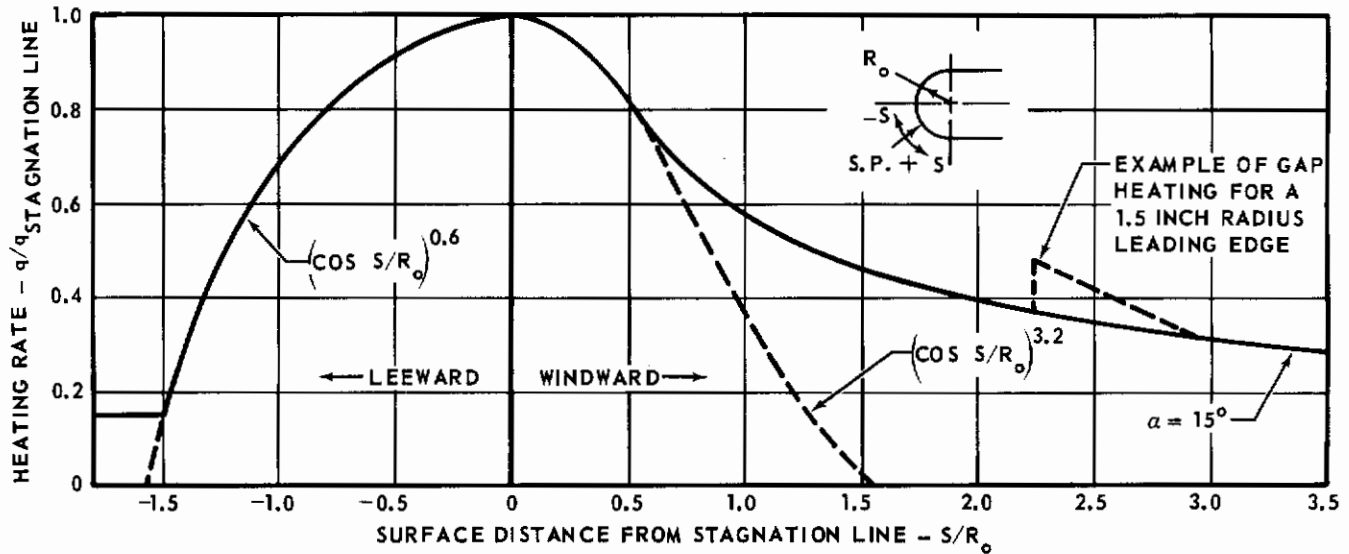


FIGURE 200 - LEADING EDGE HEATING RATE DISTRIBUTION

6.1.2 Nose Cap Thermal Analysis

Design temperatures for the nose cap were based on 82% of Lees' approximate equation for laminar stagnation point convective heating. The 82% factor was according to wind tunnel tests conducted on the ASSET vehicle. The heating rate distribution around the nose cap was varied according to $\cos^{3/2} \theta$, where θ is measured from the stagnation point. Figure 201 presents a typical surface heating rate distribution that was chosen for the nose cap. A 30% increase in heating due to the step at the junction of the ceramic modules and the coated molybdenum substructure was included in the transient temperature analyses, as illustrated in Figure 201.

6.1.3 Transient Heating Computer Programs

6.1.3.1 Two-Dimensional Program - Temperature analyses of the various heat shield design concepts utilized a computer program developed by McDonnell for solving any two-dimensional heat transfer problem. This program, designed for use on the IBM 7094 digital computer, is written in the backward finite difference method and employs either a cartesian or cylindrical coordinate system. Depending upon the complexity of a given configuration, as many as 100 elemental temperature nodes may be used and any combination of the following modes of heat transfer may be represented:

- (a) Conduction
- (b) Convection
- (c) External surface radiation to space
- (d) Internal surface radiation to surrounding elements
- (e) Interface conductance
- (f) Heat storage

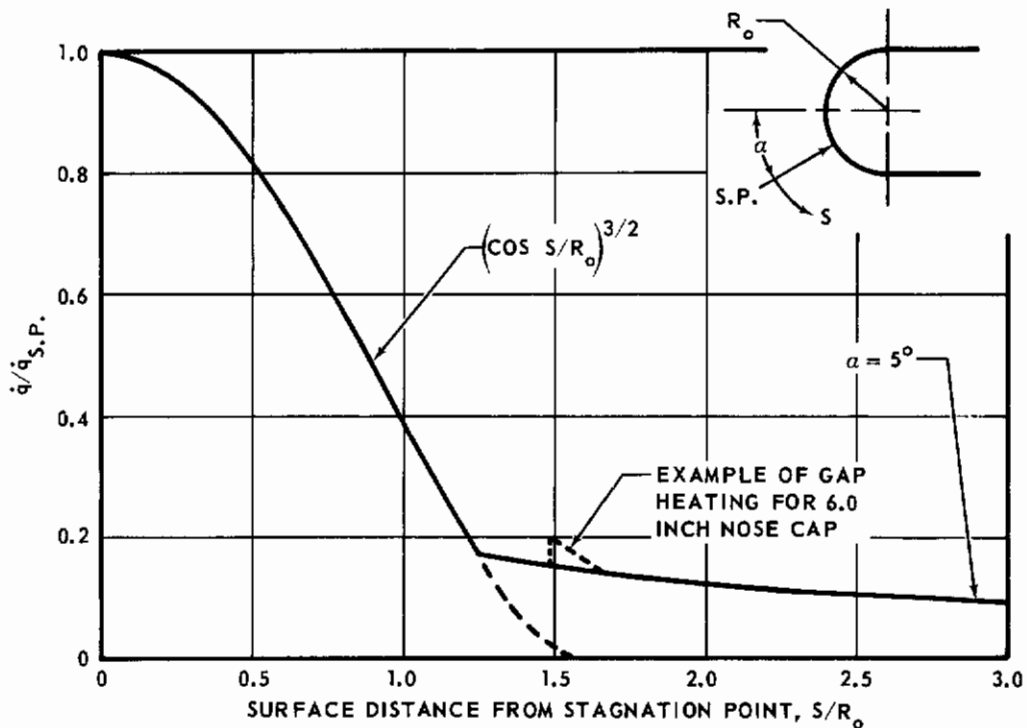


FIGURE 201 - NOSE SURFACE HEATING RATE DISTRIBUTION

Material properties such as thermal conductivity, emittance, and specific heat were varied as a function of temperature. Aerodynamic heating rates were calculated by Eckert's reference enthalpy method (Reference 4) for non-stagnation point areas, or by Lees' approximate equation (Reference 2) for stagnation areas, or specified as heat transfer coefficients and adiabatic wall temperatures. Atmospheric parameters such as pressure, temperature, and density were normally included as curve data which are functions of altitude per the 1959 ARDC model atmosphere. Real gas effects were checked by a separate program which calculates thin skin and equilibrium temperatures by Eckert's method using the transport properties of high temperature air from Reference 5.

To approximate a given configuration with a thermal model, temperature nodes were located at all boundaries such as heated surfaces, at the interfaces between dissimilar materials, and throughout the model at desired locations in a rectangular grid network. Each node represented a heat balance element defined by the intersections of the perpendicular bisectors of the lines connecting adjacent nodes. Temperatures for each node were calculated and printed out for every specified time increment. Truncation errors which may result in any finite difference solution were virtually eliminated by using small time steps and avoiding large-sized temperature nodes.

The limiting features of this particular program are the number and location of temperature nodes. In complex structural configurations such as the final components developed in this project, more flexibility in constructing the thermal model was necessary; however, in many applications this program is entirely adequate.

6.1.3.2 Three-Dimensional Program - During the course of this project, McDonnell developed another transient heating program which eliminated most of the limitations of the two-dimensional program described above. This new three-dimensional program incorporated all the features of the older program and was much less restrictive. Written in a highly universal format, this program will consider any mode of heat transfer desired and permits an arbitrary location of temperature nodes. Thus, for a given problem, fewer temperature nodes are necessary using the new program, while at the same time more accuracy in duplicating the actual physical configuration is obtained.

However, in developing this program, some sacrifices had to be made in return for the overall improvements. Due to the universal nature of this program, the amount of input data and calculations to be supplied by the user is much greater than with the simpler two-dimensional program. In addition, changes to a basic thermal model configuration cannot be made without a large amount of new input data. For these reasons, the effects of small changes in the design of the full scale components after the basic configuration was established were not investigated by constructing new thermal models. The amount of time required to obtain new temperatures which would differ only very slightly from those already calculated, was not considered worthwhile.

6.2 THERMAL MODELS FOR FULL SCALE COMPONENTS

Figures 202 through 207 present six thermal models which were employed to calculate transient temperatures for the full scale components.

6.2.1 3.0 Inch Radius Leading Edge

Figure 202 shows a thermal model of an early configuration of the 3.0 inch radius leading edge. This model was used in conjunction with the two-dimensional transient heating program described in Section 6.1.3.1. As shown in the figure, the design consisted of a 0.25 inch thick layer of dense alumina ($\sim 190 \text{ lb/ft}^3$) backed up with a 0.75 inch thickness of fibrous silica insulation. Two coated columbium channel sections riveted to the coated columbium substructure were used to support the alumina tiles. Pads of heat-shrunk silica fiber insulation provided a cushion between the channels and ceramic tile. This thermal model provided temperature gradients around the circumference of the leading edge and temperatures throughout the composite structure. The model represents a cylindrical shell of unit depth.

Figure 203 shows the thermal model used to predict the temperatures on the final design configuration of the 3.0 inch radius, 3400°F leading edge component. This model was used in conjunction with the three-dimensional transient heating program described in Section 6.1.3.2. Although only a two-dimensional analysis was made, the use of the new program permitted a more exact simulation of the actual physical geometry of the component. Radiation heat exchange between the ceramic tiles and within the wing cavity (backside of substructure and wing surfaces) was accounted for in this model. The variation in thickness of the alumina tiles was also accounted for. This variation in thickness could not be simulated with the older computer program.

It should be noted that the final design configuration of the 3.0 inch radius leading edge differed slightly from the thermal model shown in Figure 203. A cross-sectional drawing of the final configuration is shown in Figure 158 and a

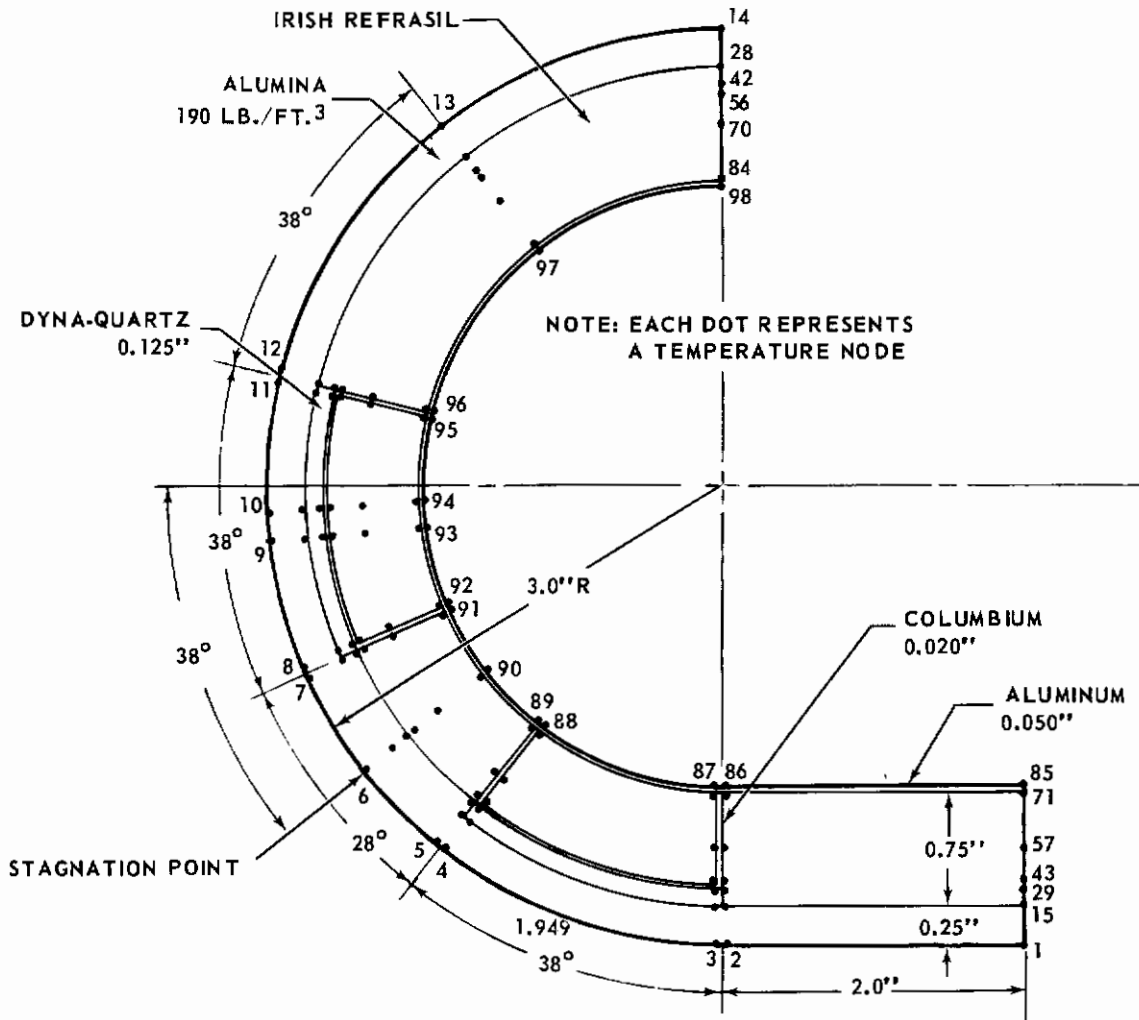


FIGURE 202 - LEADING EDGE THERMAL MODEL

description of the design details is presented in Section 5.3.1.1. Comparison of the thermal model with the final leading edge assembly reveals the following differences:

- (a) The thermal model neglected the bolts attaching the alumina tiles to the coated columbium hat sections.
- (b) In the final design, leaf springs were added between the hat sections supporting the tiles and the ceramic tiles.
- (c) The coated columbium substructure was changed from a cylindrical section to more of a squared channel.
- (d) The thickness of the alumina tiles was increased in all areas.
- (e) The lap joint between the upper and lower tiles was modified.

The effects of these differences on the calculated temperatures were thought to be slight and are discussed in Section 6.3.1.2.

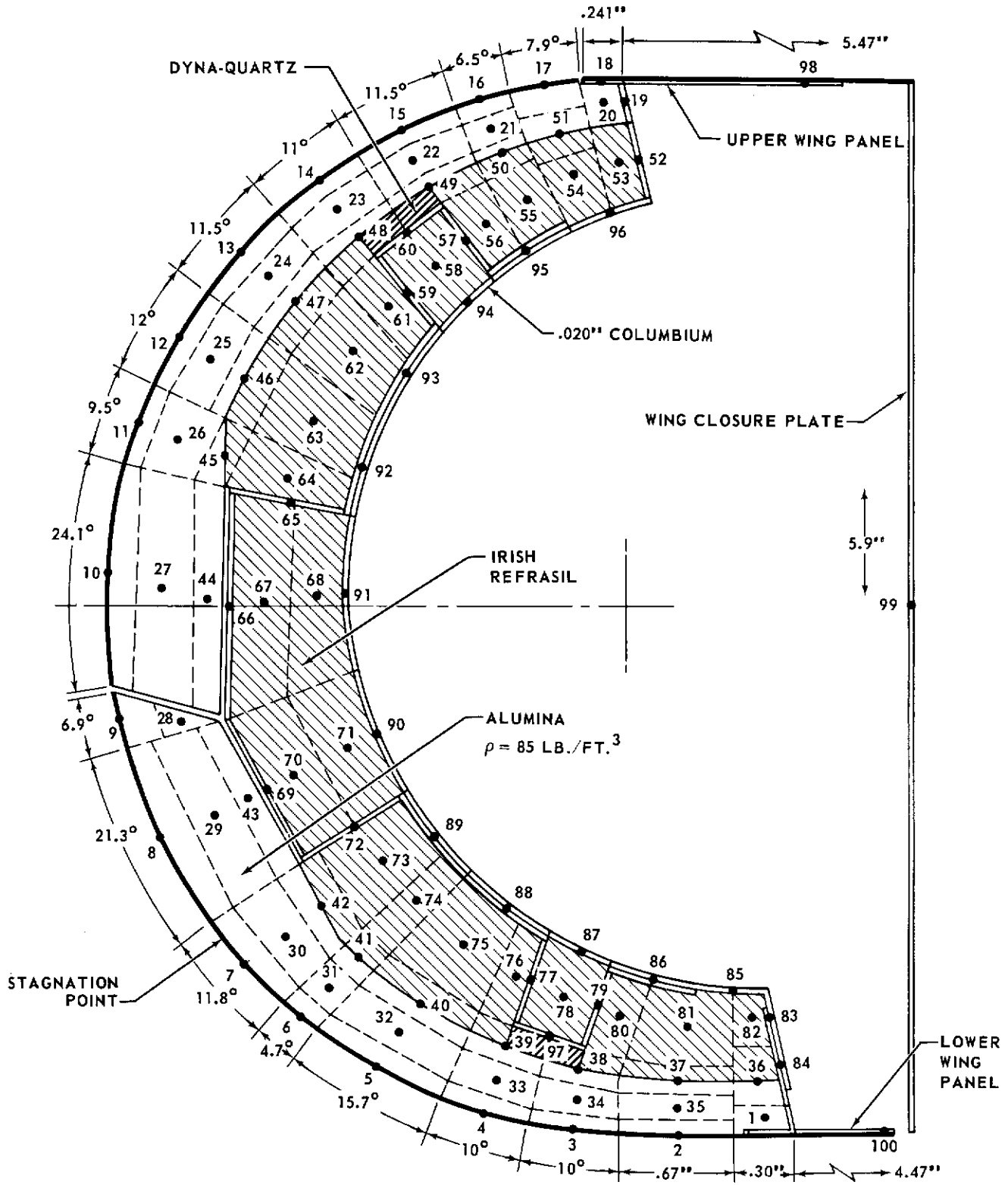


FIGURE 203 - 3.0 INCH RADIUS - 3400°F LEADING EDGE THERMAL MODEL

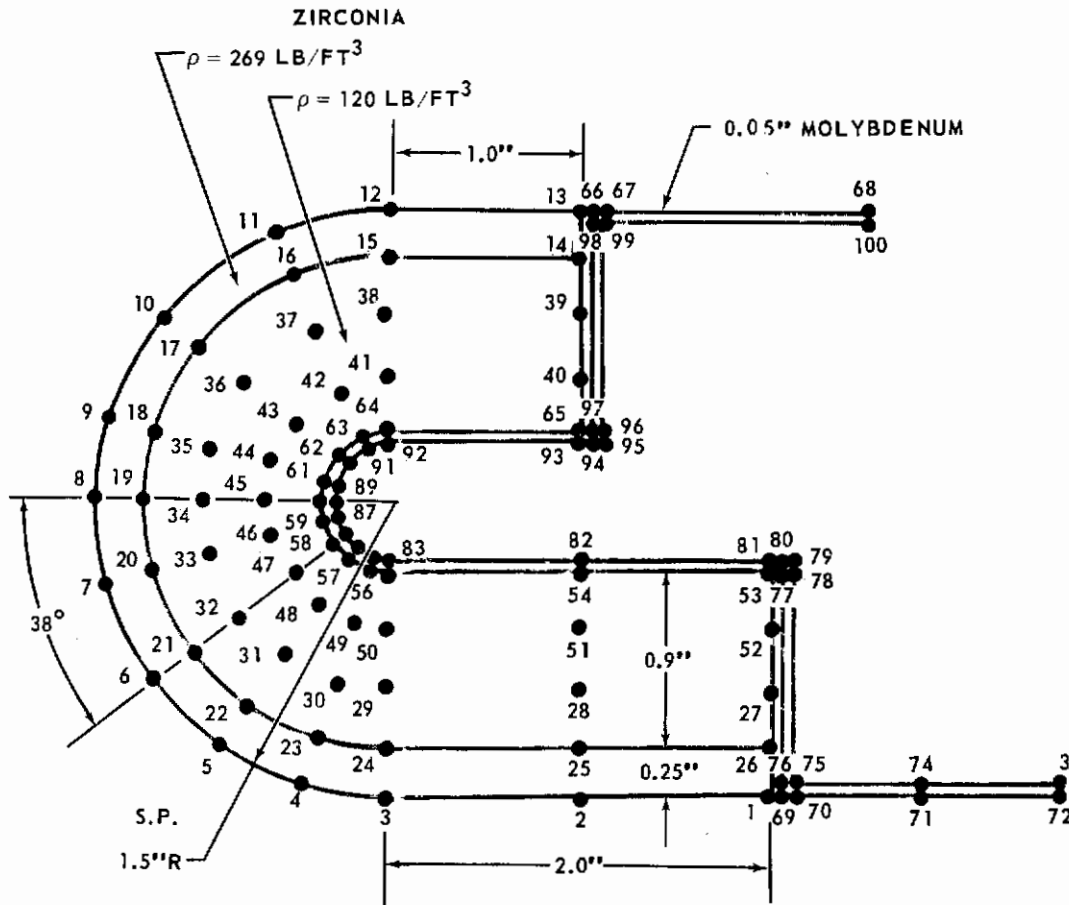


FIGURE 204 - 1.5 INCH RADIUS LEADING EDGE THERMAL MODEL

6.2.2 1.5 Inch Radius Leading Edge

Figure 204 shows a thermal model of a 1.5 inch radius leading edge which was used early in the program to obtain temperature information. This design consisted of a 0.25 inch thick layer of dense zirconia ($\sim 269 \text{ lb/ft}^3$) over a layer of low density zirconia ($\sim 120 \text{ lb/ft}^3$). The two-dimensional program discussed in Section 6.1.3.1 was used in conjunction with this thermal model.

Figure 205 shows the thermal model that was employed for analysis of the final design configuration. Analyses using this model were made with the three-dimensional transient heating program. A description of design details of this component is presented in Section 5.3.2.1. Figure 168 shows a cross-sectional view of the final configuration. The thermal model differed from the actual hardware as follows:

- (a) Attachment bolts were neglected.
- (b) The key block was smaller.
- (c) The substructure was more open.

The effects of these differences on the computed temperatures were expected to be very slight.

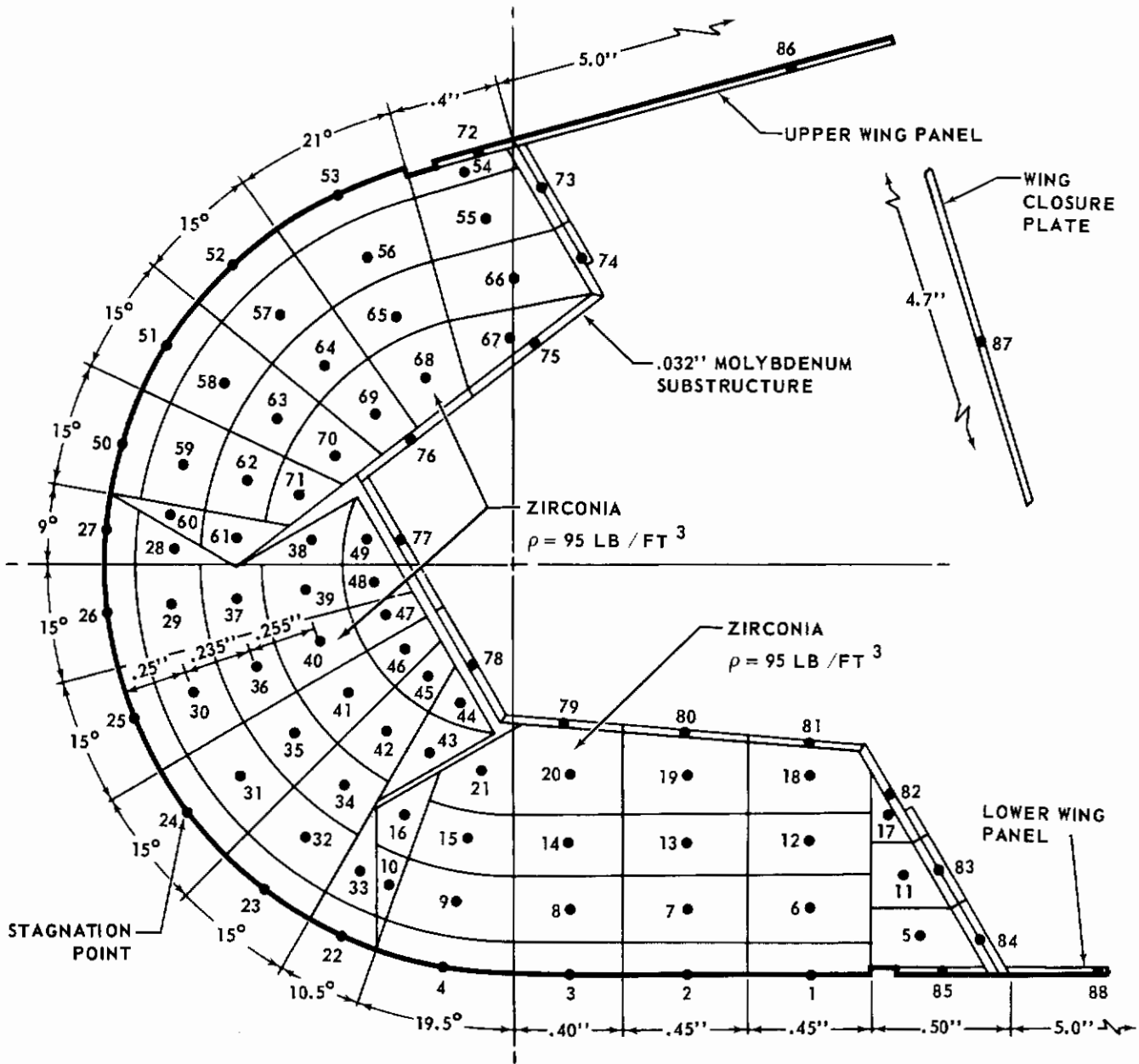


FIGURE 205 - 1.5 INCH RADIUS - 4000°F LEADING EDGE THERMAL MODEL

6.2.3 Nose Cap

Figures 206 and 207 show two thermal models which were used to calculate temperatures for the 5000°F nose cap. Both of these models were employed in conjunction with the two-dimensional transient heating program described in Section 6.1.3.1. Both models were treated as bodies of revolution generated by revolving the sections shown about their respective centerlines.

Figure 206 shows a cross-section of a nose cap consisting of a coated molybdenum dome covered with a varying thickness of thoria. The purpose of this model was to provide temperature gradients through the ceramic material, determine the maximum temperature of the substructure (molybdenum dome), and provide circumferential temperature gradients for a typical re-entry trajectory (shown in Figure 17). The substructure in this model was simulated by the cross hatched area shown in Figure 206.

After the final design configuration had been decided upon, the thermal model shown in Figure 207 was used to obtain temperature information. This model represented a cross-section of a typical tube assembly and was used to calculate temperatures at the stagnation point and at the aft row of tubes (55° away from the stagnation point). Due to the complex nature of the nose cap design, a thermal model representing the complete nose cap could not be developed since the two-dimensional heating program treats the model as a body of revolution. The only type of nose cap which could be completely analyzed was a true body of revolution. The three-dimensional program was capable of handling any type of model, although where the surface and substructure temperatures were of primary interest, the model shown in Figure 207 was considered adequate. Obviously, circumferential conduction effects from adjacent tubes were not included in the temperature analyses using this model. For this reason, the temperatures obtained for the stagnation point tube assembly were slightly conservative and those obtained for the 55° location were slightly low.

6.3 RESULTS OF TEMPERATURE ANALYSES

The following sections present the results of the temperature analyses made on the three components. These analyses utilized the trajectories and material properties presented in Sections 3.3 and 4.5, respectively, with exceptions as noted.

6.3.1 3.0 Inch Radius Leading Edge

6.3.1.1 Preliminary Design Analyses - Figure 208 presents transient temperature histories for a 3.0 inch radius, 3400°F leading edge with the effects of internal radiation neglected. The thermal model was composed of a 0.15 inch layer of dense alumina ($\sim 190 \text{ lb/ft}^3$) over a 0.75 inch thickness of alumina foam ($\sim 30 \text{ lb/ft}^3$). The outer shell of alumina was coated with chromium oxide to maintain the surface emittance at a constant value of 0.7.

Figure 209 presents transient temperature histories for a 3.0 inch radius leading edge consisting of columbium channels with 0.125 inch fibrous silica pads employed to support a 0.25 inch layer of dense alumina ($\sim 190 \text{ lb/ft}^3$) over 0.75 inch of fibrous silica. A detailed sketch of this thermal model is presented in Figure 202. A water cooled substructure maintained at 200°F was included. Results indicated that a water cooled substructure had negligible effect on the surface temperature. Also, the maximum temperature of the columbium channels was found to be only 2140°F , indicating that the cooled substructure had an appreciable effect on this component because of its direct contact with the substructure.

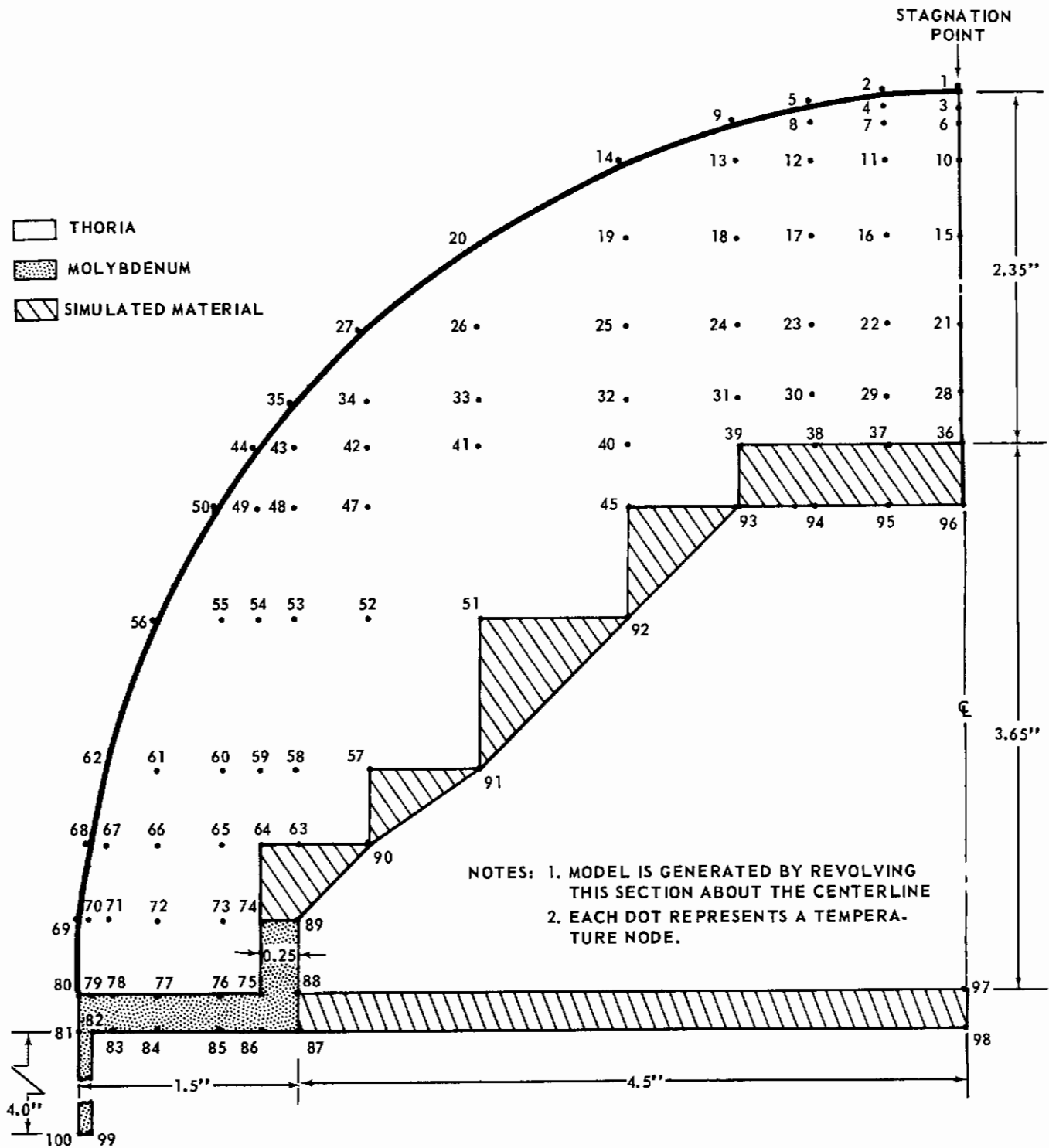


FIGURE 206 - NOSE CAP THERMAL MODEL- 6.0 INCH RADIUS

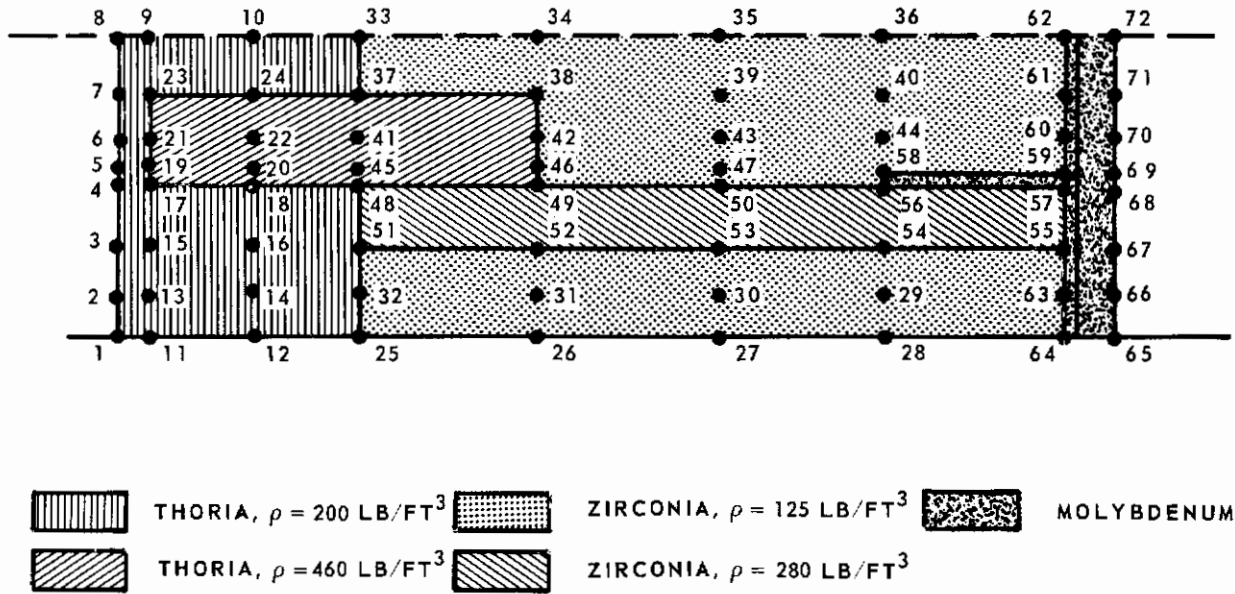


FIGURE 207 - THERMAL ANALYSIS MODEL FOR REINFORCED CASTABLE TUBE DESIGN FOR 6.0 INCH RADIUS NOSE CAP

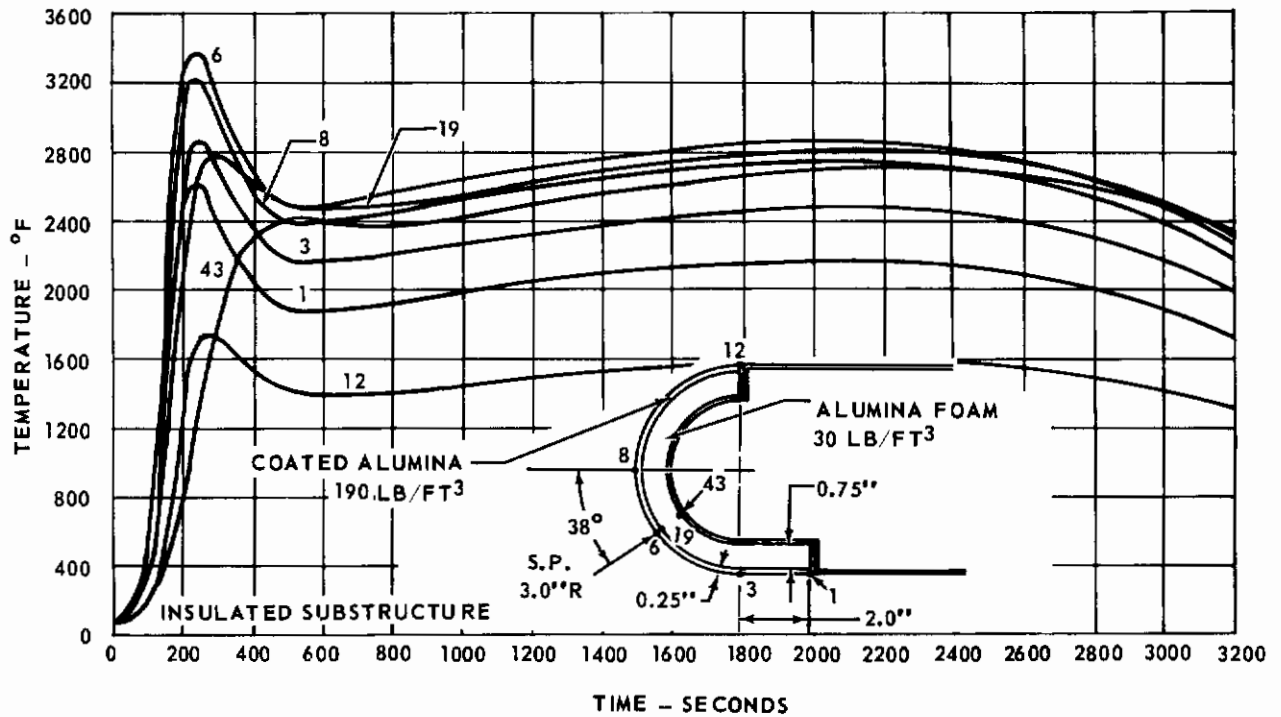


FIGURE 208 - LEADING EDGE TEMPERATURES - TRAJECTORY NO. 2

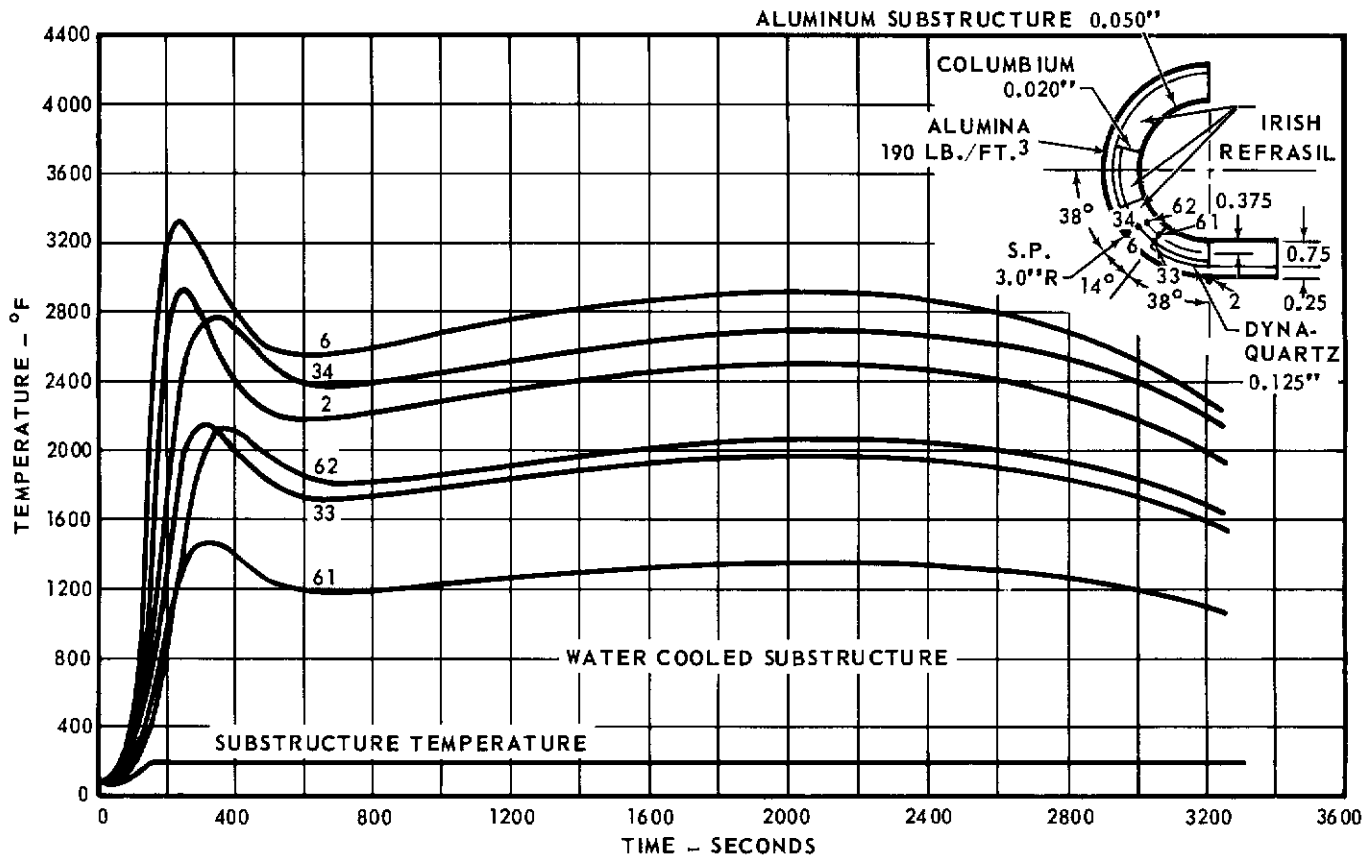


FIGURE 209 - LEADING EDGE TEMPERATURES TRAJECTORY NO. 2

The amount of water necessary to cool the aluminum substructure was calculated to be about 17 pounds per hour per foot of length. This value was based on the near steady state conditions which exist at 2000 seconds after initial re-entry and assumed that the water could be boiled. Although this value is somewhat conservative, it shows that a water-cooled substructure located so close to the heated surface was heavy. To determine if a non-cooled super-alloy substructure could be employed, the thermal model used for the water cooled design was re-analyzed with the substructure being perfectly insulated on the back side. The results of this analysis showed that with a 0.25 inch thick layer of dense alumina (~ 190 lb/ft³) at the surface backed with 0.75 inch of fibrous silica, a maximum substructure temperature of 2680°F was obtained. A subsequent analysis, where the thickness of the insulation was increased by 0.25 inch, resulted in much lower temperatures during the early portion of the trajectory, although the substructure still reached a maximum temperature of 2600°F.

The analyses described above were conducted on preliminary designs of the 3.0 inch radius leading edge component and employed the transient heating program described in Section 6.1.3.1.

6.3.1.2 Final Design Analyses - After considerable design changes were incorporated, additional temperature analyses of the 3.0 inch radius leading edge were made utilizing the thermal model shown in Figure 203 and the transient heating program discussed in Section 6.1.3.2. Three separate cases were considered:

- (a) With no radiation heat exchange between leading edge substructure and wing panels (insulated substructure).

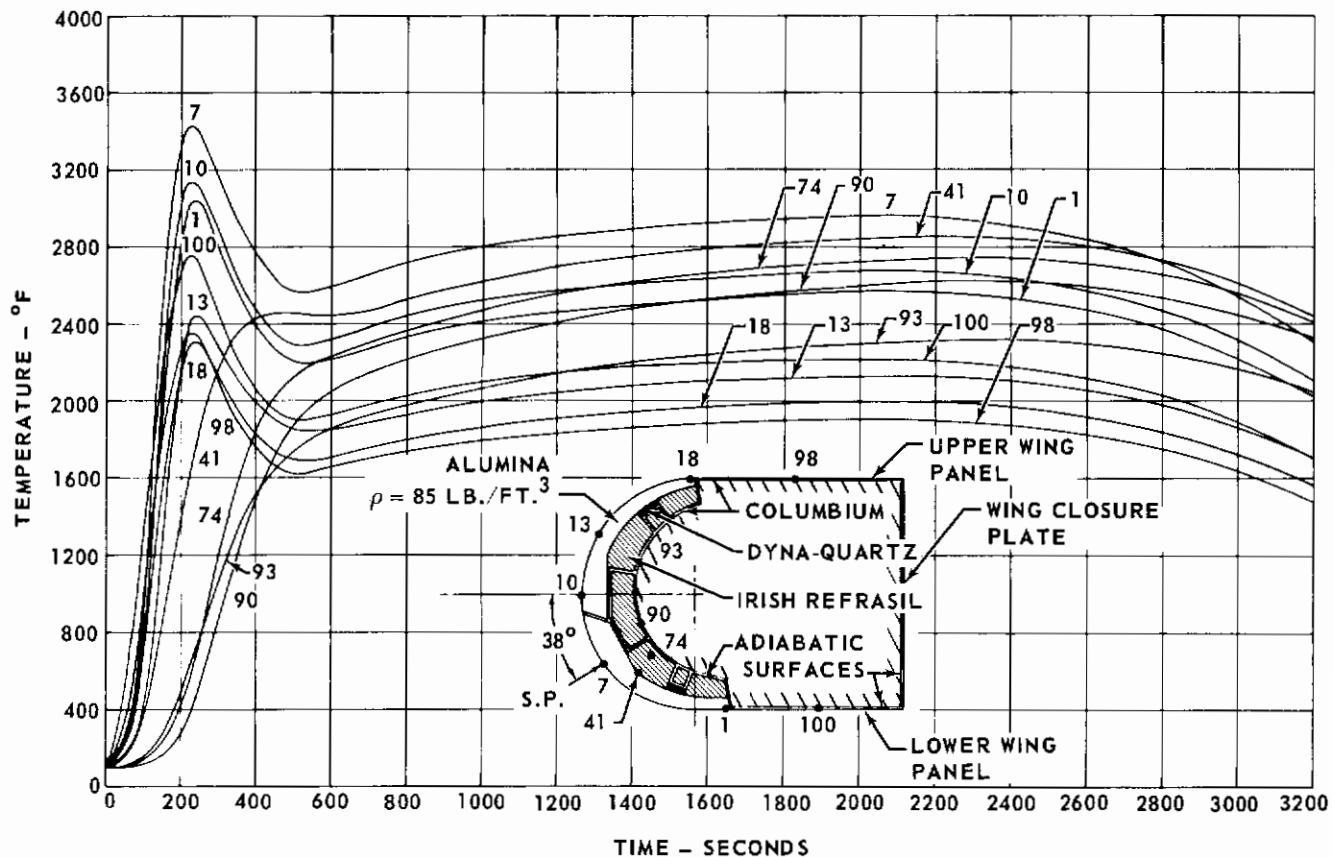
(b) With radiation heat exchange between leading edge substructure and wing panels.

(c) With radiation heat exchange between the substructure and a wing closure plate located about 10 inches aft of the substructure maintained at 200°F by water cooling.

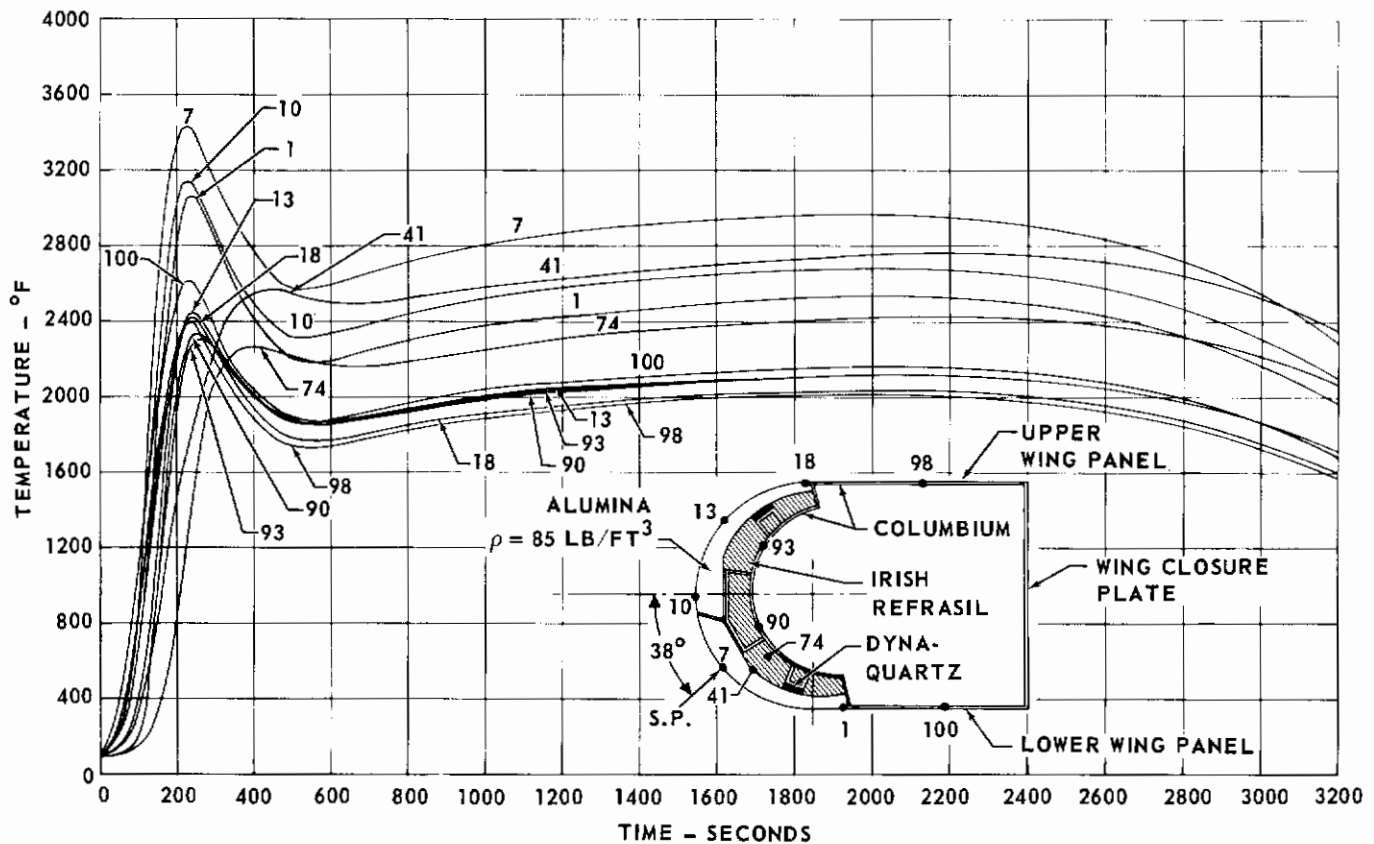
Figures 210, 211, and 212 present temperatures at various locations for these analyses. A surface emittance of 0.7 was used for the coated alumina tile. Maximum temperatures at a few points of interest are summarized in Table XXVI.

TABLE XXVI - MAXIMUM TEMPERATURES OF 3.0 INCH RADIUS LEADING EDGE

Location	Temperature (°F)			
	Stagnation Point #7	Substructure #90	Backside of Tile #41	Insulation #74
Insulated Substructure	3420	2620	2850	2740
Radiating Substructure	3420	2330	2760	2410
Remotely Cooled Substructure	3420	1480	2650	2130



**FIGURE 210 - 3.0 INCH RADIUS LEADING EDGE TEMPERATURES
INSULATED SUBSTRUCTURE**



**FIGURE 211 - 3.0 INCH RADIUS LEADING EDGE TEMPERATURES
RADIATING SUBSTRUCTURE**

Close comparison of the substructure temperature in Figures 210 and 211 revealed that without internal radiation exchange (insulated substructure), the substructure initially was much cooler than the lower wing panel (point 100). Later in the trajectory, however, the insulated substructure was significantly hotter than the wing panel. When radiation exchange was included, the substructure reached its maximum temperature early in the trajectory and then always was cooler than the lower wing panel. This was because the lower wing panel was, in effect, a large "thin skin" and closely followed its associated equilibrium temperature. The amount of heat lost by the lower wing panel by internal radiation was a relatively small portion of the total heat received by the wing panel from convection, but represented a large heat input to the substructure. The net effect was a considerable change in the substructure temperature history and little change in the lower wing panel temperature.

Figure 212 presents the results of an analysis which included radiation heat exchange from the back side of the substructure to a water cooled wing closure plate maintained at 200°F. The upper and lower wing panels were assumed to be perfectly insulated. The resulting substructure temperature of 1480°F was considerably cooler than in either of the two analyses discussed above. For the case considered, approximately two pounds of water per hour per foot of length were needed to maintain the wing closure plate at a temperature of 200°F. An earlier analysis, discussed in Section 6.3.1.1, showed that water cooling the substructure directly would require 17 pounds of water per hour per foot of length. Thus, water cooling

the structure adjacent to the wing section and letting the leading edge substructure lose heat by internal radiation was more practical than cooling the substructure directly. At the time these analyses were initiated, the final design included the columbium hat sections and cylindrical substructure as shown in Figure 203. It should be noted that the bolts holding the alumina tiles to the substructure have been neglected. Subsequently, changes were made in the final design configuration, so that the hat sections were replaced with spring fingers attached to the substructure. The substructure itself was changed to more of a channel than a cylindrical section.

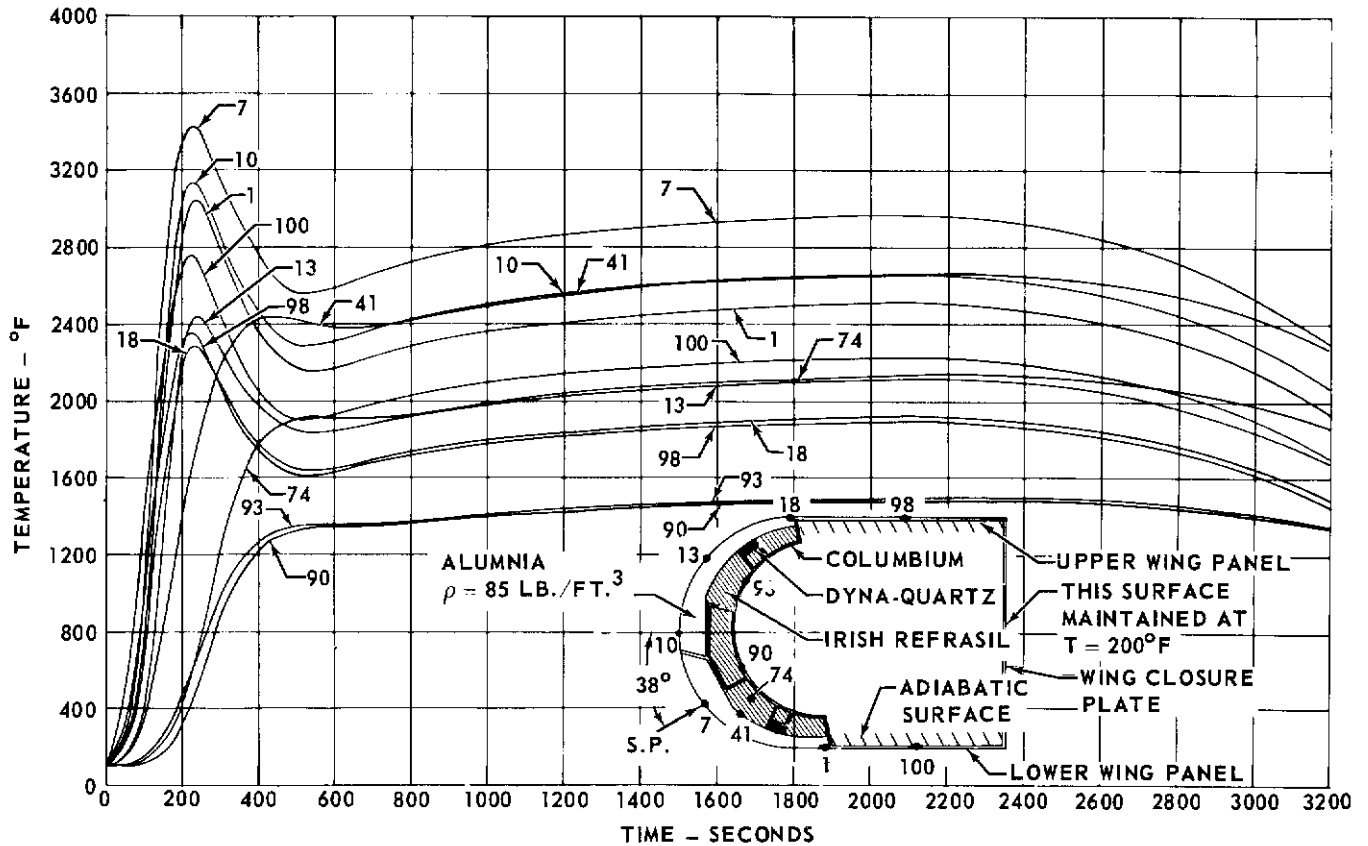


**FIGURE 212 - 3.0 INCH RADIUS LEADING EDGE TEMPERATURES
COOLED SUBSTRUCTURE**

Although the net effect of these changes with respect to the resulting temperatures could only be determined by using a new thermal model, a few conclusions could be drawn. Since the conduction paths from the surface to the substructure through the columbium hat sections had been removed and the radiation view factor from the wing panels to the substructure was less (since the substructure was more closed than before), lower substructure temperatures would be obtained for a radiation exchange case. No significant changes in the surface temperatures would be expected.

Since the thermal conductivity of low density alumina as measured by SRI was considerably higher than the values previously used (Table I), another analysis was made to determine the effect on the leading edge temperatures. The data generated by SRI for Norton RA5058 (~85 lb/ft³) as shown in Figure 73 was used for

this purpose. The results of this analysis for the case with a radiating substructure are shown in Figure 213. Comparing these results with Figure 211 shows that the back side of the ceramic tile and the midpoint of the insulation increased about 50°F during the steady state portion to maximum temperatures of 2800°F and 2460°F, respectively. During the initial re-entry dive, the temperature of the back side of the tile increased 350°F to a maximum of 2910°F. The midpoint of the insulation increased 280°F to a maximum of 2540°F. Slight decreases (less than 50°F) in outer surface temperatures were obtained.

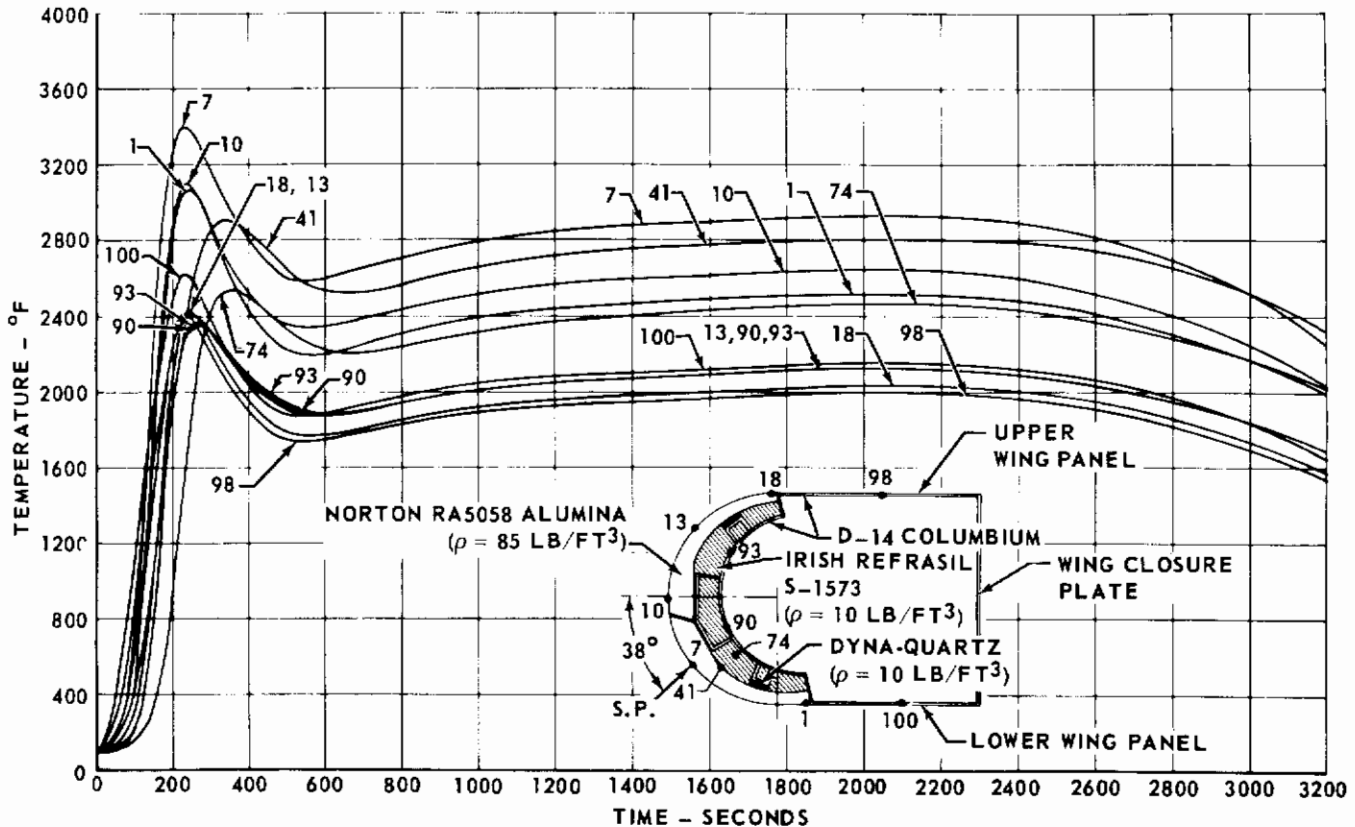


**FIGURE 213 - 3.0 INCH RADIUS LEADING EDGE TEMPERATURES
RADIATING SUBSTRUCTURE**

6.3.2 1.5 Inch Radius Leading Edge

6.3.2.1 Preliminary Design Analyses - Figure 214 presents temperatures for a preliminary design of the 1.5 inch radius leading edge. The thermal model used in this analysis is shown in Figure 204 and consisted of a 0.25 inch thick layer of dense zirconia (~269 lb/ft³) over a layer of low density zirconia (~120 lb/ft³). Maximum temperatures at the stagnation point and on the substructure were 3820°F and 2280°F, respectively. The maximum design temperature of 4000°F at the stagnation point was not obtained because a slightly lower emittance value was used in the early trajectory work discussed in Section III.

Prior to thermal conductivity measurements on zirconia at SRI, the effect of higher thermal conductivity values than those being used was investigated. For this purpose, the thermal model shown in Figure 204 was re-analyzed using conductivity values four times greater than those employed in the first analysis.

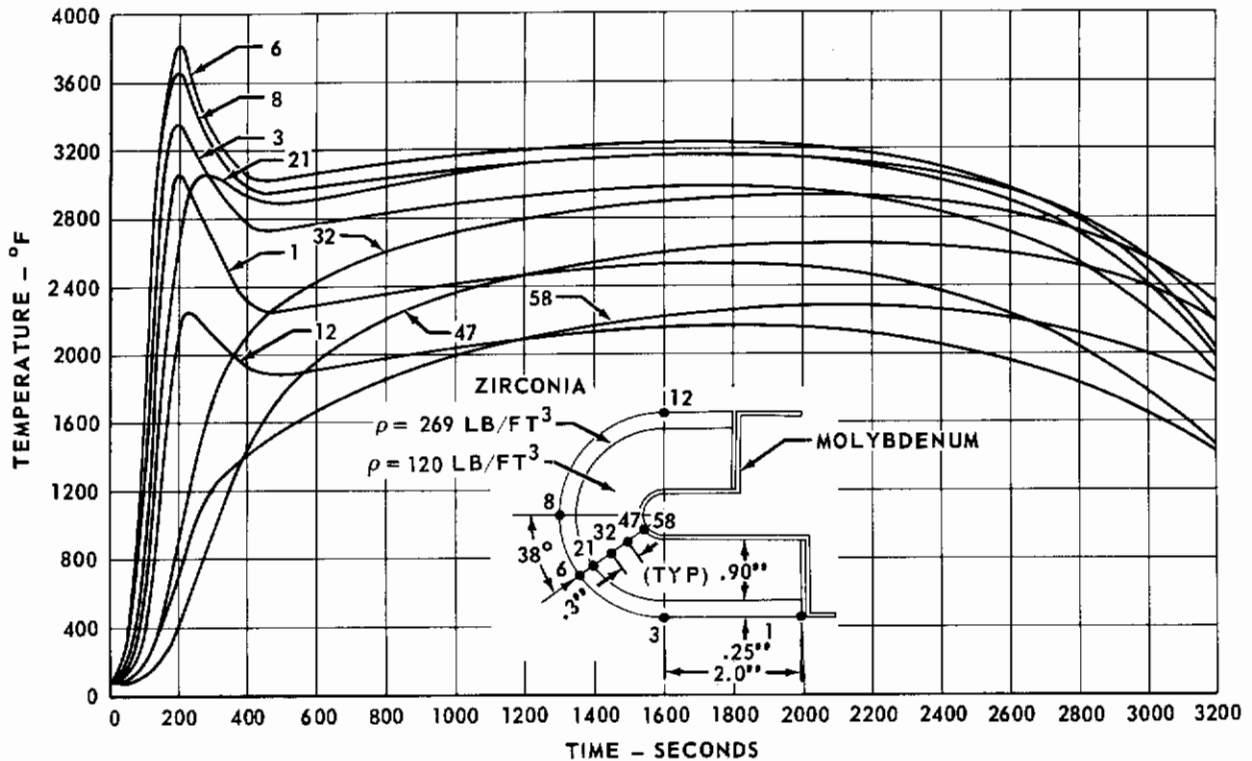


FIGURE 214 - THERMAL ANALYSIS OF A 1.5 INCH RADIUS LEADING EDGE CONFIGURATION

The resulting temperatures from this re-analysis are shown in Figure 215. The most significant effect was on the substructure temperature, which increased from 2280°F to 2660°F. Surface temperatures decreased less than 100°F and interior locations showed increases on the order of 200°F in peak temperature.

6.3.2.2 Final Design Analyses - After the final design of the 1.5 inch radius leading edge component was fairly well established, temperature analyses were made using the thermal model shown in Figure 205 and the transient heating program discussed in Section 6.1.3.2. The results of these analyses are presented in Figures 216 through 218.

Figure 216 shows temperatures at various locations through the 1.5 inch radius leading edge using a high density (~280 lb/ft³) zirconia key block and low density (~95 lb/ft³) zirconia for the other blocks. Figure 217 shows temperatures at the same locations using low density (~95 lb/ft³) zirconia for all three blocks. Radiation heat exchange between the substructures and the upper and lower wing surfaces was accounted for in both of these analyses. Figure 218 shows temperatures obtained on the low density (~95 lb/ft³) zirconia design incorporating the SRI thermal conductivity data from Figure 74. The maximum temperatures obtained at various locations are summarized in Table XXVII.

TABLE XXVII - MAXIMUM TEMPERATURES OF 1.5 INCH RADIUS LEADING EDGE

Location	Temperature (°F)		
	*High Density Key Block	*Low Density Key Block	Low Density Key Block (SRI Data)
Stagnation Point (Node No. 24)	3760	3910	3830
Substructure (Node No. 78)	2370	2310	2500
Midpoint of Key Block (Node No. 41)	2750	2680	2840
Lower Block (Node No. 85)	3130	3140	3130
Upper Block (Node No. 79)	2710	2720	2710

*Based on thermal conductivity data from Table 1 (estimated values)

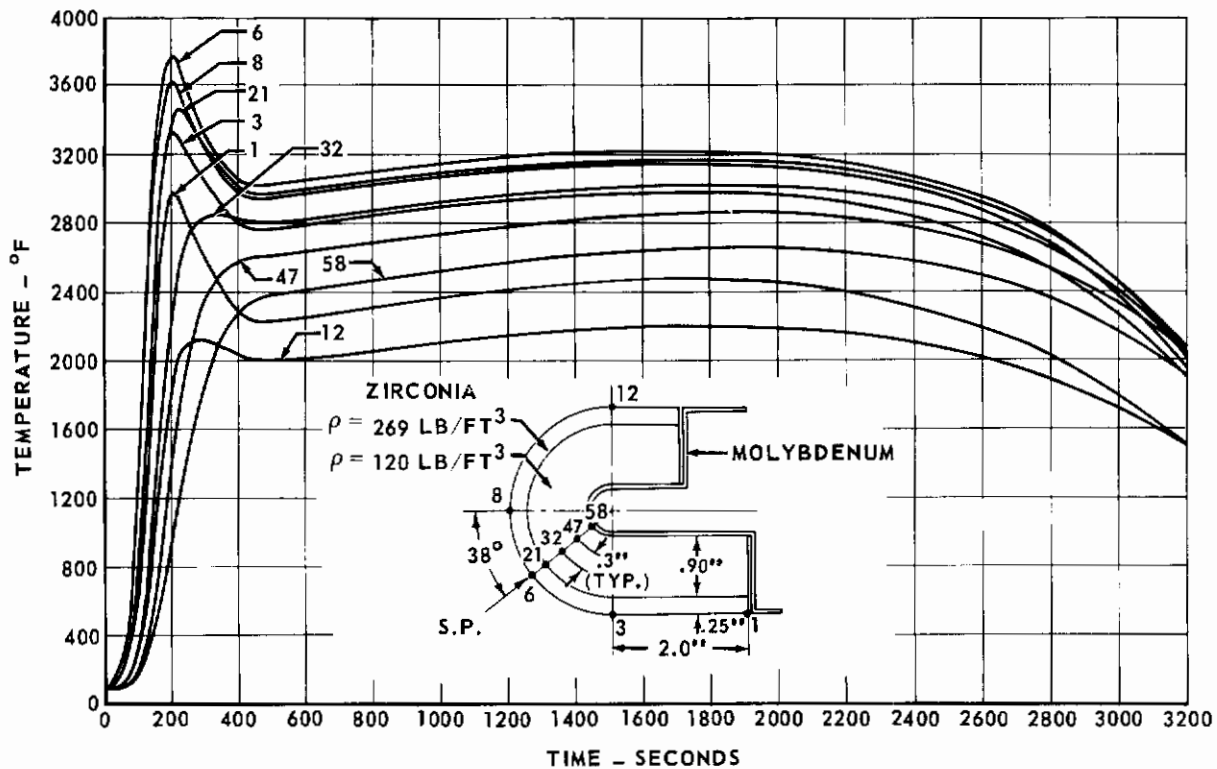


FIGURE 215 - THERMAL ANALYSIS OF A 1.5 INCH RADIUS LEADING EDGE CONFIGURATION ("K" FACTOR = 4.0)

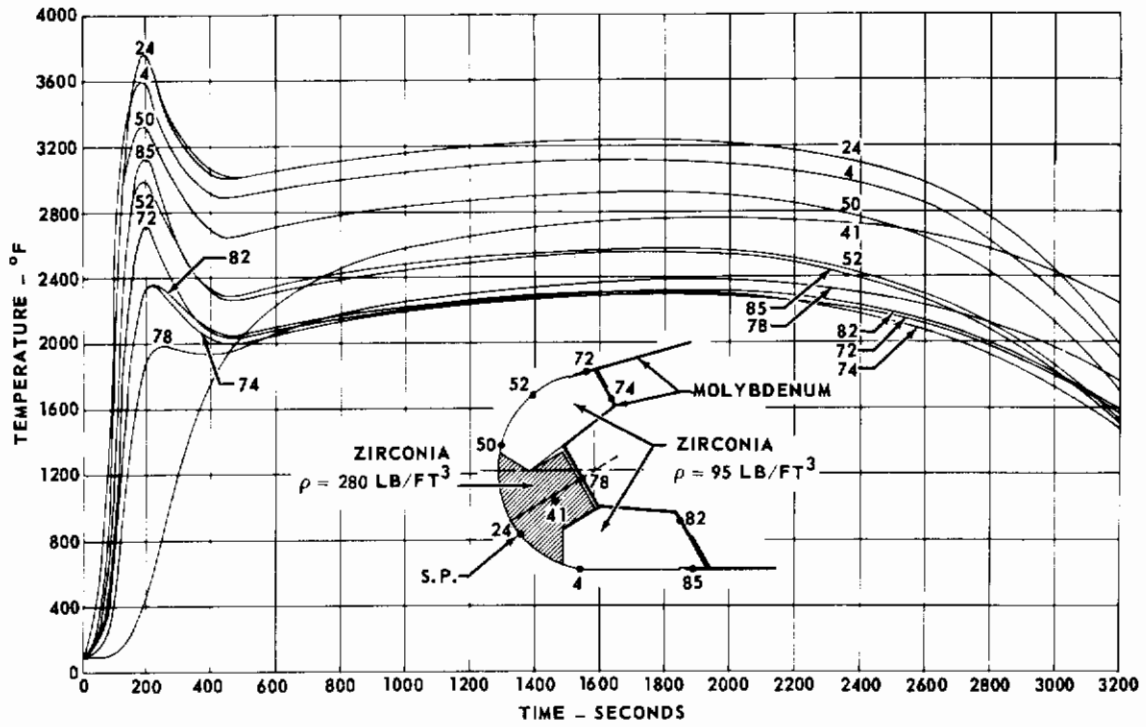


FIGURE 216 - 1.5 INCH RADIUS LEADING EDGE TEMPERATURES RADIATING SUBSTRUCTURE

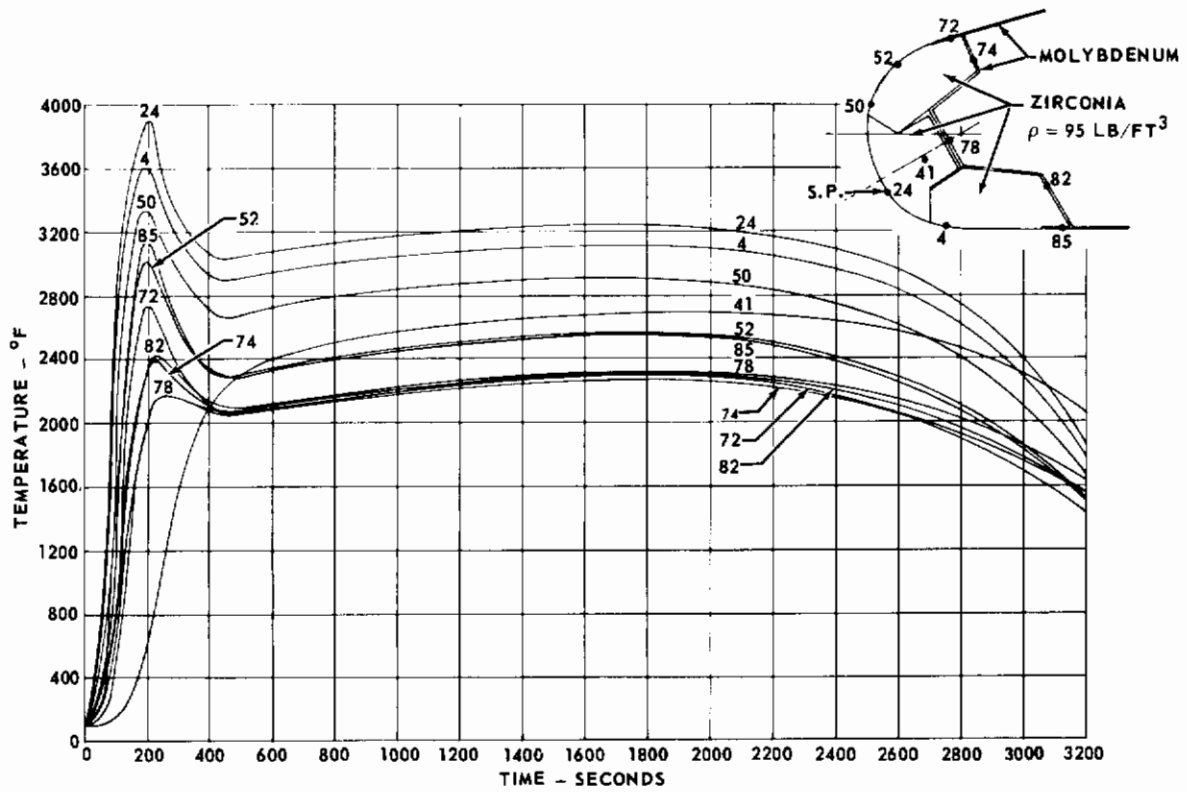
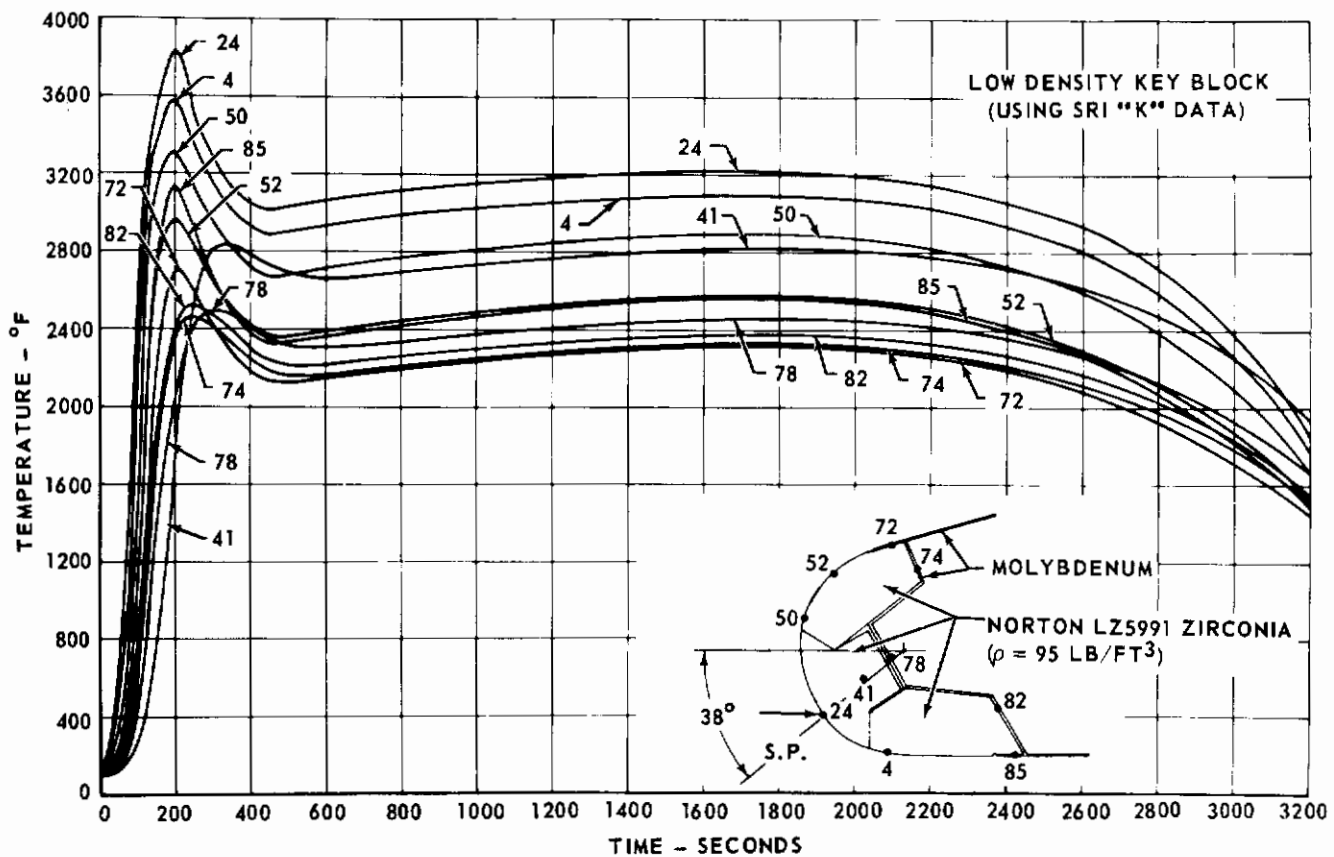


FIGURE 217 - 1.5 INCH RADIUS LEADING EDGE TEMPERATURES RADIATING SUBSTRUCTURE



**FIGURE 218 - 1.5 INCH RADIUS LEADING EDGE TEMPERATURES
RADIATING SUBSTRUCTURE**

6.3.3 Nose Cap Temperatures

6.3.3.1 Preliminary Design Analyses - Temperature analyses of a preliminary design for the 6.0 inch radius nose cap were made using the thermal model shown in Figure 206 and the transient heating program discussed in Section 6.1.3.1. This model was representative of an early design configuration which consisted of a thick layer of thoria supported by a coated molybdenum substructure. Included in the thermal model was a molybdenum back plate which simulated a bulkhead. A portion of the adjoining vehicle body was also simulated by including four inches of a molybdenum panel. Analyses were made with and without radiation heat exchange between the substructure and the bulkhead and using low density thoria ($\sim 125 \text{ lb/ft}^3$) thermal properties. The results of these analyses are presented in Figure 219 for the insulated substructure case and in Figure 220 for the case where radiation was included.

The maximum stagnation point temperature of 5300°F obtained from these analyses was 300°F higher than desired because of the values used for the emittance of thoria. In determining the trajectory for the nose cap component, an emittance of 0.4 was used for all temperatures and a maximum equilibrium temperature of 5160°F was obtained. Conduction losses and heat sink effects were expected to result in the desired surface temperature of 5000°F . The actual emittance values used in these analyses, however, reached a minimum value of 0.3 above 5000°F . Subsequent analyses of the nose cap employed a constant emittance value of 0.4 for temperatures above 5000°F .

TABLE XXVIII - MAXIMUM TEMPERATURES OF 6.0 INCH RADIUS NOSE CAP
Preliminary Design

Location	Temperature (°F)			
	Insulated Substructure		Radiating Substructure	
	Time = 300 Sec.	Time = 3200 Sec.	Time = 300 Sec.	Time = 3200 Sec.
Stagnation Point (Node No. 1)	5300	3730	5300	3720
Tangency Point (Node No. 80)	2560	2280	2560	2260
Substructure (Node No. 96)	640	3000	1000	2360
Substructure (Node No. 91)	900	2700	1150	2340
Bulkhead (Node No. 97)	580	2360	1750	2260

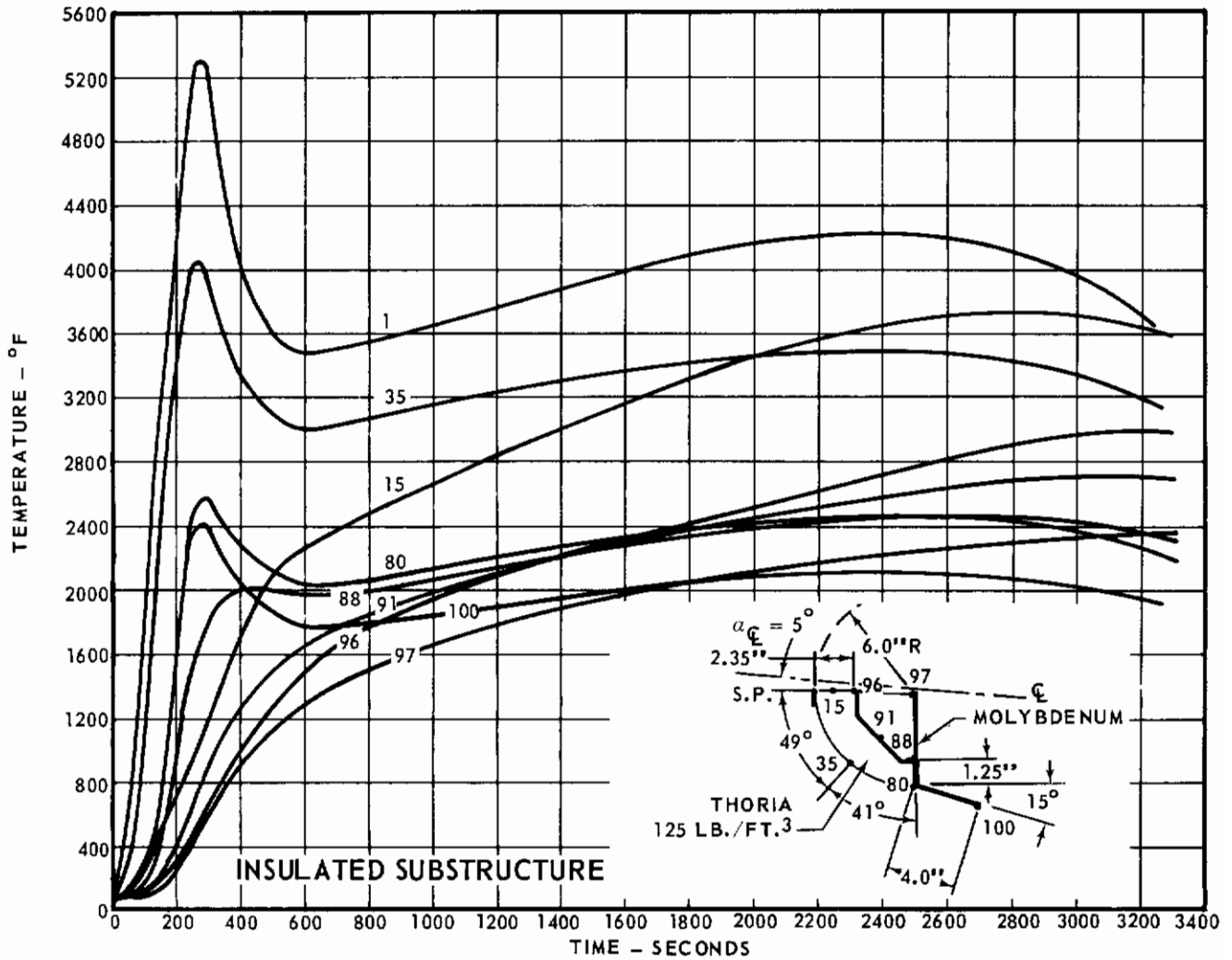
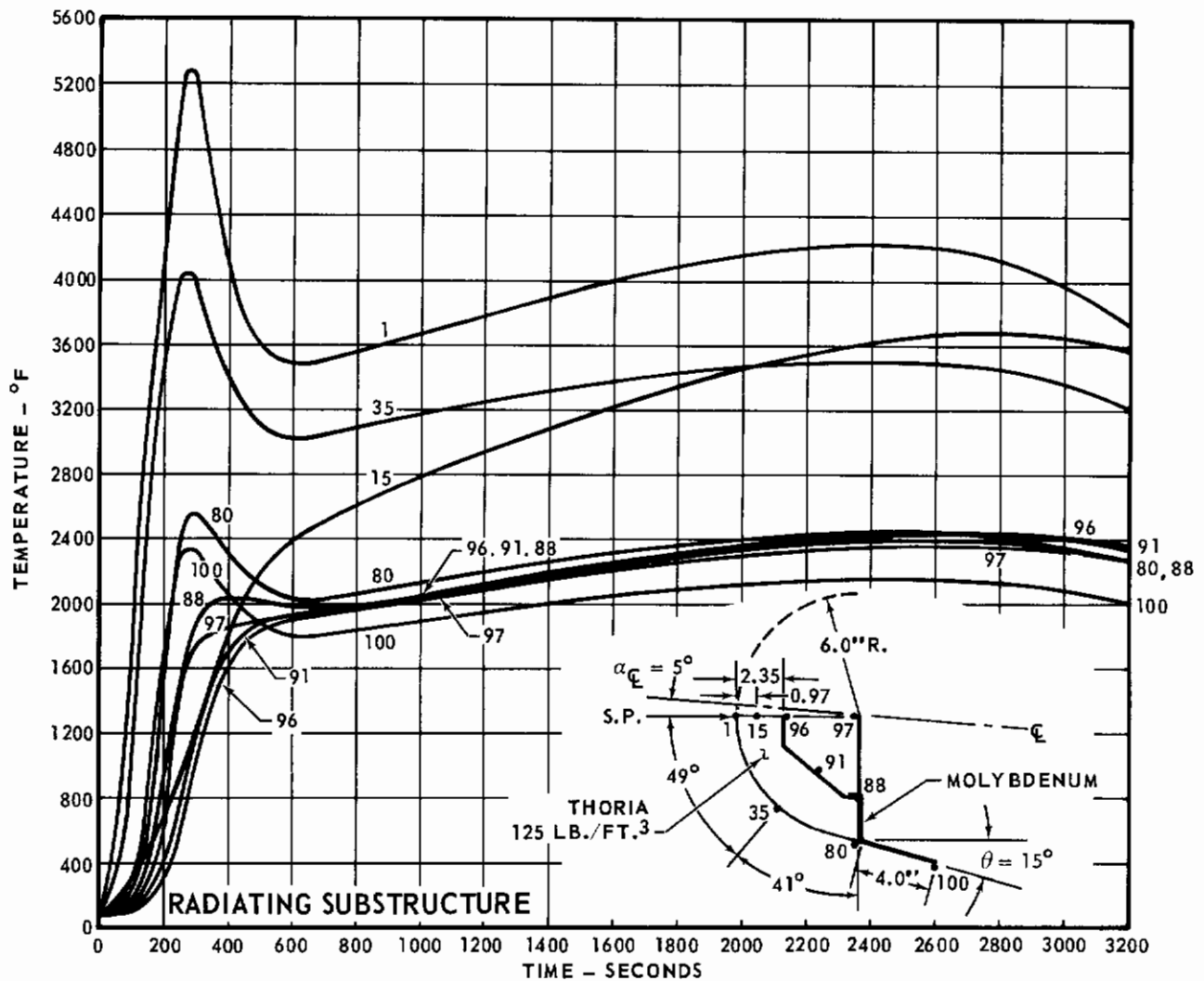


FIGURE 219 - NOSE CAP TEMPERATURES - TRAJECTORY NO. 3



Temperatures obtained at various points in the nose cap for the two analyses discussed above are summarized in Table XXVIII.

6.3.3.2 Final Design Analyses - Figure 180 shows all of the ceramic and metallic parts used in the final design configuration of the 6.0 inch radius nose cap. In addition to the parts shown, two layers of castable ceramic (one of zirconia and one of thoria) were used as a fill between the equally spaced tube assemblies. The end product was a very complex arrangement for heat transfer analysis.

In determining the ability of the ceramic material to withstand the re-entry environment, detailed temperature distributions through individual tube assemblies were considered more valuable than approximate temperature information which would result from an analysis of the complete nose cap. The previous preliminary analyses indicated that the substructure would not exceed the maximum temperature capability of a coated molybdenum substructure with a ceramic overlay thickness of about 2.35 inches. For this reason, temperature analyses based on one complete tube assembly were considered satisfactory, although somewhat conservative since circumferential conduction effects and radiation from the back side of the sub-

structure were not accounted for. The thermal model shown in Figure 207 and the transient heating program discussed in Section 6.1.3.1 were used to obtain temperatures on the nose cap component.

Two analyses were made, one corresponding to the tube assembly at the stagnation point and one corresponding to a location 55° from the stagnation point. The results of these analyses are presented in Figures 221 and 222 for the stagnation point and 55° location, respectively. Maximum temperatures calculated at various points are shown in Table XXIX.

Circumferential conduction through the nose cap and substructure and radiation exchange within the interior of the component would reduce the temperatures obtained for the stagnation point tube assembly and increase those obtained for the 55° location. Thus, the true temperature of the metallic tube retainers and substructure should be well within the capabilities of coated molybdenum.

6.4 THERMAL ANALYTICAL MODEL

Appendix III presents a discussion of the various factors which are involved in determining the overall heat transfer coefficient of a porous material. The effect of transmissivity on the net exchange of energy through a porous material was examined analytically and it was determined that nearly all of the transmitted energy is absorbed within the first five adjacent planes of pores.

6.5 INSTRUMENTATION OF FULL SCALE COMPONENTS

Thermocouples used to measure temperatures on the full scale test components consisted of the following types:

- (a) Iridium/Iridium - 40% Rhodium for temperatures up to 3800°F .
- (b) Platinum/Platinum - 10% Rhodium for temperatures up to 3100°F .
- (c) Chromel/Alumel for temperatures up to 2500°F .

6.5.1 Installation of Thermocouples

The iridium thermocouples (B and S gage 38) were insulated with 1/32 inch outside diameter double-bore ceramic tubing and were installed in the ceramic portion of each component. Thoria thermocouple tubing was used in the stagnation point region of the nose cap, and alumina tubing was used on both leading edge components and at the 55° location on the nose cap. The iridium thermocouples on the two leading edge components were installed in small holes drilled in the ceramic parallel to the outer surface. The leads were then brought through a hole drilled from the back side at an angle to the surface and intercepting an attachment bolt hole. This manner of installation was employed to minimize the effects of conduction losses down the thermocouple.

Platinum thermocouples were used on all three full scale test components to measure the substructure temperature. To prevent a reaction between the disilicide coating on the refractory metal substructure and the platinum, calcium aluminate cement was applied both to the thermocouple junctions and locally to the backside of the substructure. Sauereisen #63 cement was then used to secure the thermocouples in place.

TABLE XXIX - MAXIMUM TEMPERATURES OF 6.0 INCH RADIUS NOSE CAP

Location	Temperature (°F)	
	Stagnation Point	55° from Stagnation Point
Outer Surface (Node No. 1)	5060	3680
Top of Zirconia Tube (Node No. 25)	3840	3040
Bottom of Thoria Tube (Node No. 42)	3620	2870
Molybdenum Retainer (Node No. 56)	3090	2400
Substructure (Node No. 65)	3050	2370

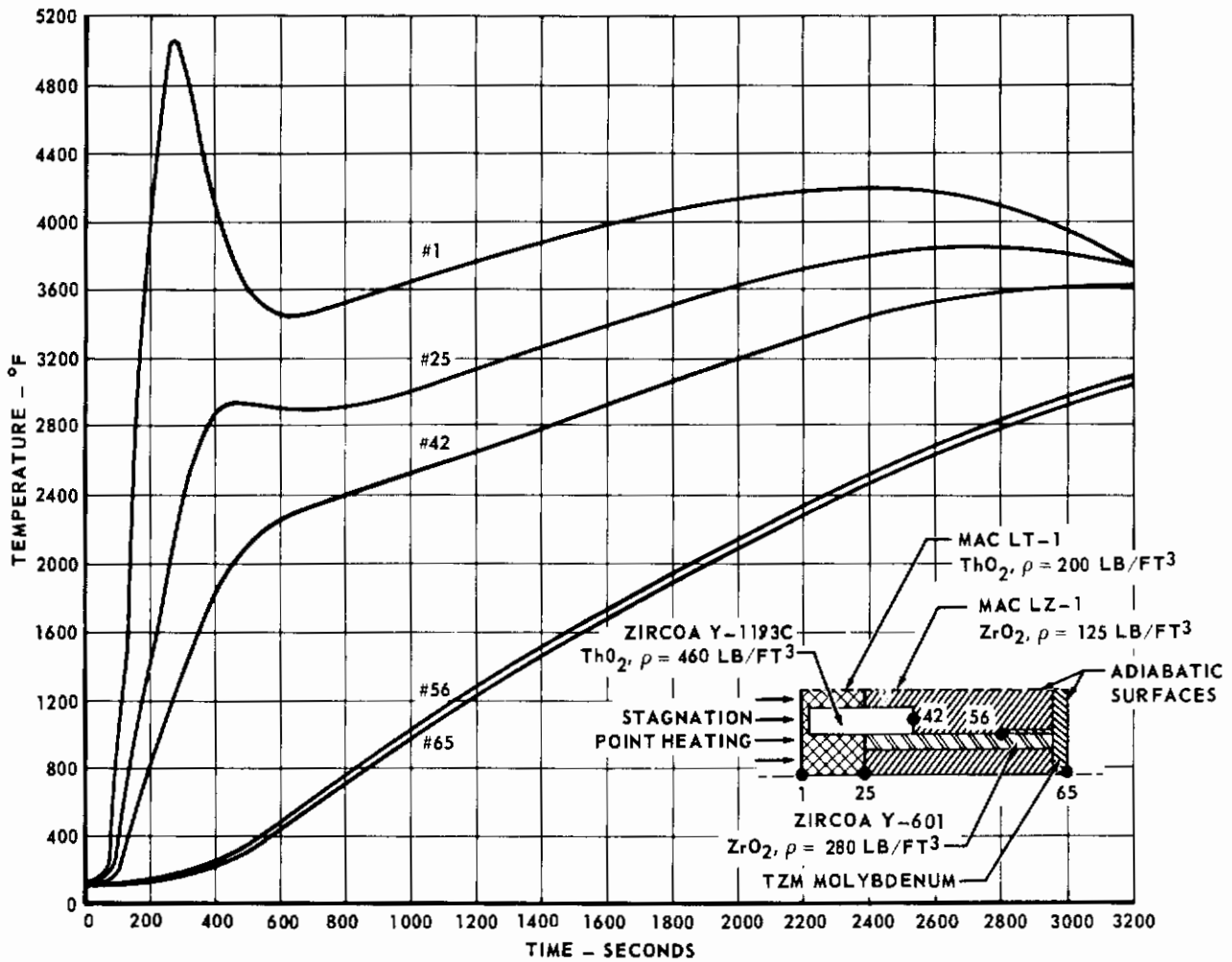
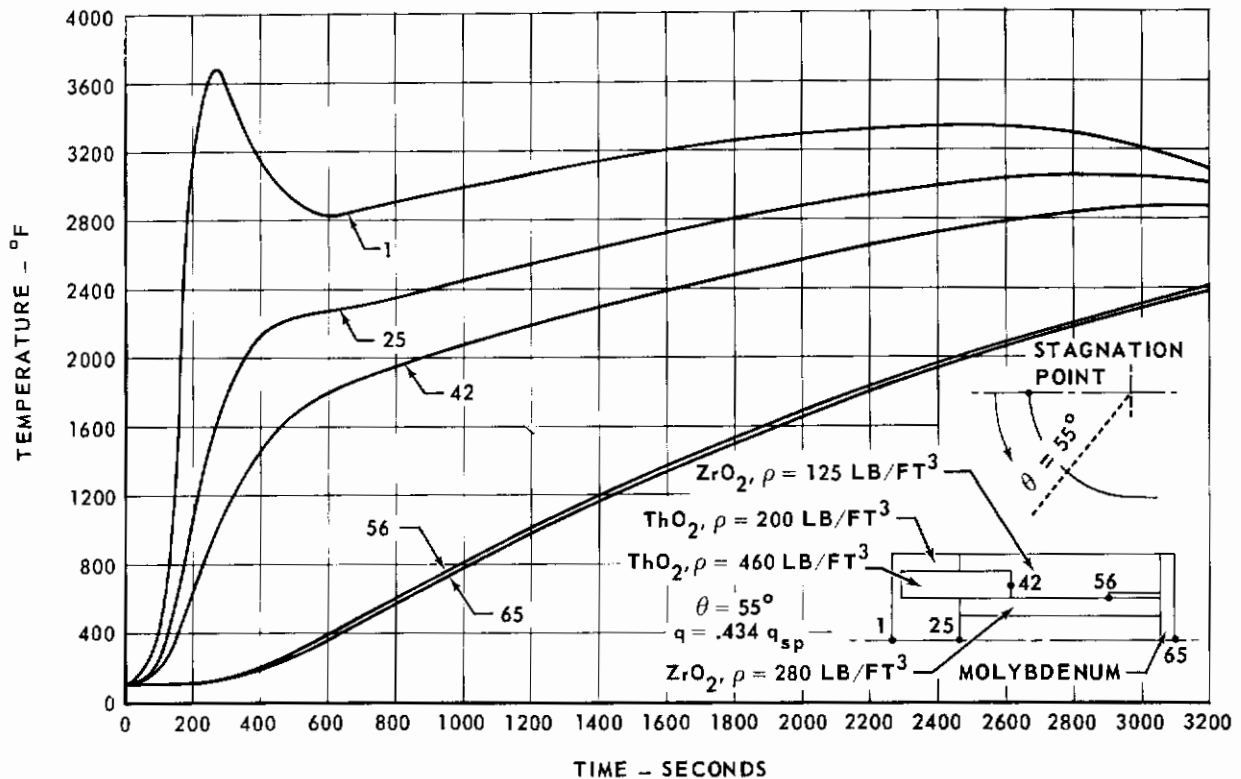


FIGURE 221 - 6.0 INCH RADIUS SHIELD NOSE CAP TEMPERATURES



Copper lead wire was used with both the iridium and platinum thermocouples. The transition to copper wire occurred approximately two feet back from the truss assembly in the case of the iridium thermocouples and approximately three feet back for the platinum thermocouples. A chromel-alumel thermocouple was used to monitor the temperature of the transition point so that appropriate corrections to the thermocouple readings could be made.

Chromel-alumel thermocouples were used to measure temperatures at various locations on the super-alloy support structures. These thermocouples were spot welded in place and protected with alumina insulating tubes for a distance extending beyond the back of the truss structure.

The locations of the iridium and platinum type thermocouples are shown in Figures 158, 168, and 174 for the 3.0 inch radius leading edge, 1.5 inch radius leading edge, and nose cap, respectively.

6.5.2 Calibration of Iridium Thermocouples

The two iridium type thermocouples located in the 3.0 inch radius leading edge and the three located in the 1.5 inch radius leading edge were installed with the wire in the as-drawn state. Since the wire should have been annealed prior to using it as a thermocouple, calibration tests were necessary. For this purpose, two tests were employed, one using a 2000°F furnace and one using an oxyacetylene torch as the heat sources.

In the first test using the furnace, the iridium thermocouple was compared to both a platinum/platinum - 10% rhodium reference thermocouple and a chromel/alumel thermocouple. The effects of Sauereisen #63 cement were also determined by using a total of six thermocouples, three with cement and three without. The results of this test showed that the as-drawn iridium thermocouple output was higher than for an annealed thermocouple. No undesirable effects of the Sauereisen cement were noted for any of the three types of thermocouples.

The second test using the oxyacetylene torch consisted of three thermocouples (iridium, platinum, and chromel/alumel) with the beads joined together with a platinum wire and then covered with Sauereisen. The thermocouples were placed in a groove in a zirconia brick which was then filled with castable zirconia. The thermocouple junctions were located approximately 0.01 inch beneath the exposed surface, which was then heated with the torch. A maximum temperature of 3000°F was obtained during this test.

The results of these two tests are shown on Figure 223. The true temperature was assumed to be that indicated by the platinum thermocouple. As shown in this figure, the deviation of the as-drawn iridium thermocouple increase slightly as the temperature increased. These data were used to correct the temperature readings from the iridium thermocouples in the two leading edge components. The iridium thermocouples in the nose cap needed no correction applied since the wire was annealed before installation.

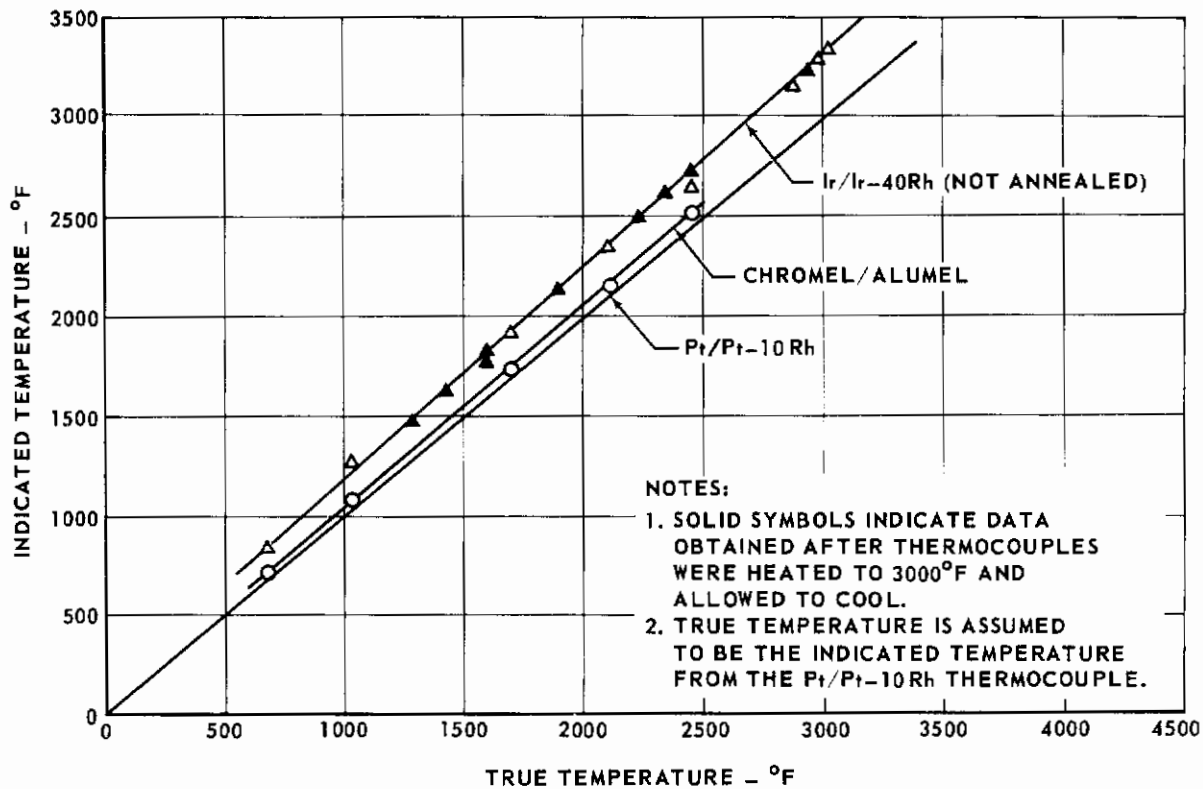


FIGURE 223 - THERMOCOUPLE COMPARISON

SECTION VII

STRUCTURAL ANALYSES

This section summarizes the structural and analytical effort performed in support of the design (both subscale and full scale) and the materials development phases. Various investigations were made, both theoretical and experimentally, to analyze designs and to determine stress levels in ceramic materials under specified conditions. Details of the structural analytical study are presented in Appendix IV.

7.1 METHODS UTILIZED

Standard structural analyses techniques were utilized for the subscale modules and the full scale components. The stresses considered were those imposed by the vibration loading (up to 20 g), maximum airloads, thermal gradients, and differential thermal expansion. Consideration was also given to the need to support deadweight, which was insignificant except in the case of the full scale 6.0 inch radius nose cap.

As part of the structural analyses, the performance of all springs (such as the Belleville washers, leaf springs, and the finger springs in the 3.0 inch radius leading edge) was determined at room and elevated temperatures to establish spring stiffness and stroke. This analysis took into consideration the expected thermal growth of applicable components.

The thermal stress analyses of the ceramic parts utilized techniques developed in the structural analytical model work (see Paragraph 7.2 and Appendix IV) and also took into consideration the change in shape of the ceramic parts due to thermal exposure.

Data generated in the thermophysical property measurement phase of this project (see Section 4.5) were utilized in the analyses of the ceramic parts.

7.2 ANALYTICAL MODEL

The ceramics utilized in this project were from 20 to 80% of theoretical density and had relatively low strength and low modulus of elasticity. Most of these materials had a microstructure consisting of a gradation of grain sizes interspersed with porosity, and were so-called "thermal shock resistant bodies." It is commonly hypothesized that these bodies resist catastrophic thermal shock failure because they micro-crack locally, and macro-cracking does not propagate due to the crack-stopping ability of the loosely knit, porous microstructure. That is, these type ceramics display a certain amount of "give" or "yield" to thermal stress.

This work was performed in an attempt to devise an analytical method of predicting the behavior of a ceramic material when exposed to high surface heating rates (from one side only). The result of this work was an analytical expression or combination of expressions into which appropriate material properties and thermal environmental conditions could be inserted. These expressions were used to solve for the stress levels generated in the ceramic by the given thermal environment or for the maximum surface heating rate a given ceramic could withstand.

The overall approach to the derivation of these expressions consisted of assuming uniform heating from one side only of an unrestricted, free-to-expand slab of ceramic and studying the cross-section of the slab as made up of many freely expanding small slabs or elements. The stresses generated were dependent on the non-linearity of the thermal gradient through the ceramic slab thickness which, due to the resulting non-linear thermal expansion, created a non-equilibrium, geometric incompatibility at the ends of the small elements making up the slab thickness. Transient heat transfer analysis was used to describe the thermal gradients as a function of heating rate and material properties, and expressions were derived to describe the resulting stresses. Data generated by the thermophysical property measurements performed at SRI (see Section 4.5) were utilized in these expressions to predict the thermal shock failure of given ceramics.

The analytical model work indicated that thermal stress failure could be governed by tensile strength or shear strength of the material, depending on material thickness. If a material were relatively thin, failure would be by tensile stress and if the material were relatively thick, failure would be by shear stress. Also when the stress states at edges and corners were considered, the probability of a shear failure mode was even greater. It appeared that in most of the component configurations for this program, shear failure would be the dominating mode of failure. To satisfy the needs of the analytical model expression, it was necessary to know the allowable shear strain, allowable shear stress, and modulus of rigidity of a given ceramic body.

Most investigators in the past have not been concerned with the properties of ceramics in shear (especially in relation to thermal shock resistance). Since allowable shearing strain data were not available from the literature for most of the materials applicable to this project, a mechanical testing program was conducted. The mechanical testing consisted of subjecting a specimen (1 inch diameter x 2 inches long) to pure shear by applying a torque to one end of the specimen while the other end remained static. The apparatus used is shown in Figure 224. It consisted primarily of a torquing fixture, mechanical drive system, deflection measurement system, and instrumentation for the continuous recording of load and deflection. A specimen of circular cross-section was utilized so that plane sections would remain plane and radii in the cross sections would remain straight lines as the bar was twisted. The torque was applied such that a strain rate of 0.001 in/in/min was obtained at the outer surface of the specimen. All testing was performed at room temperature.

The shearing stress at the outer surface at failure was calculated by the following equation:

$$S_s = \frac{Tr}{J} \quad (2)$$

where

S_s = shearing stress at surface

T = torque

r = radius of bar

J = polar moment of inertia of bar

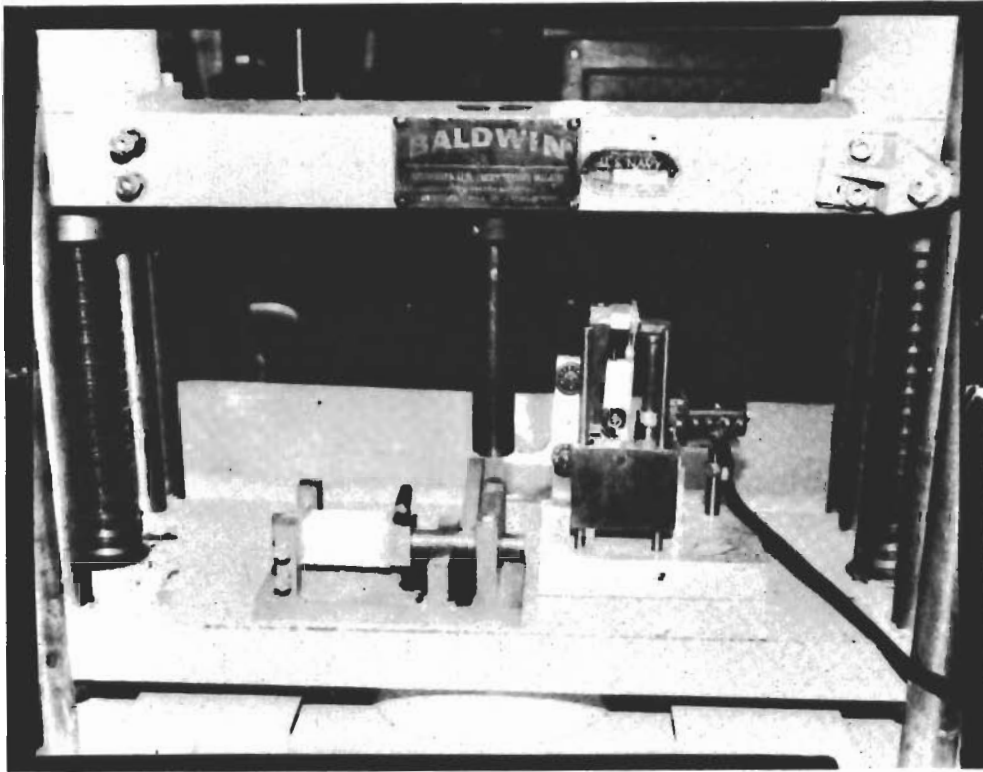


FIGURE 224 - SHEAR TEST FIXTURE

The shearing strain at the outer surface at failure was calculated by the following equation:

$$\gamma = \frac{r\beta}{l} \quad (3)$$

where

- γ = shearing strain at surface
- r = radius of bar
- β = angle of twist expressed in radians
- l = length of bar

In accordance with the assumption that the unit shearing stress is proportional to the unit shearing strain, the modulus of rigidity was calculated.

At a point in a bar under torsion, the shearing stress acting in the circumferential direction is accompanied by an equal shearing stress acting in the longitudinal direction, parallel to the axis of the bar. These shearing stresses cause normal stresses on diagonal planes. The maximum normal stress (diagonal tension and compression) occur on planes at 45° with the planes of shearing stress and have intensities equal to that of the shearing stress. The diagonal

tension is of importance in connection with torsion testing of materials weaker in tension than in shear, since failure is often evidenced by the development of a crack along a helix inclined at 45° to the axis of the bar. This type of failure was evidenced as shown in Figure 225 and was the predominating mode of failure in samples tested. (Data were discarded from samples which failed at the ends.) From this then, the ultimate tensile stress is the same as the shearing stress at failure. Therefore, using an assumed Poisson's ratio, modulus of elasticity and maximum tensile strain could be calculated.

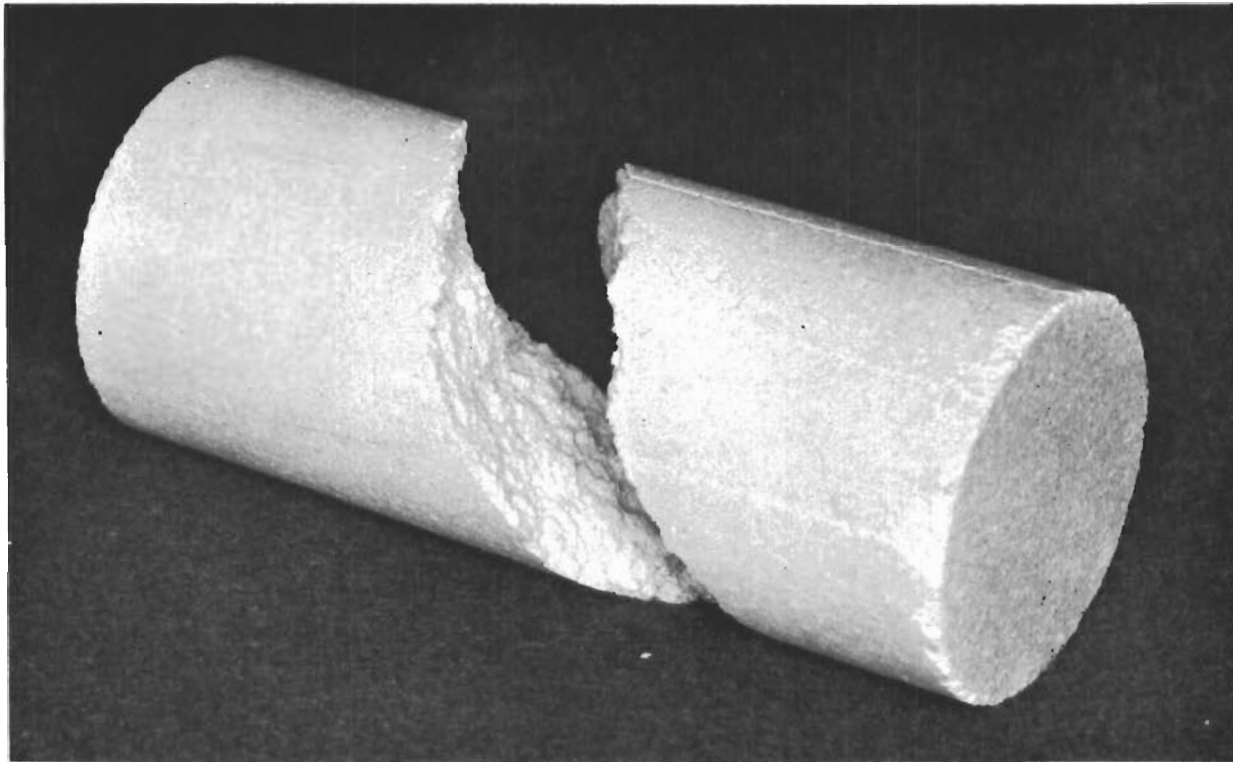


FIGURE 225 - DIAGONAL TENSION FAILURE

The data generated are shown in Table XXX. The scatter in the data ranges from 6% to 25%, with the most scatter being for the Norton developed low density zirconia (LZ 5991). This is not unreasonable, since the material tested came from a lot which was not homogeneous. All specimens were inspected before test for surface defects and micro-cracks, but could not be inspected for internal flaws. The modulus values presented are very low with respect to related high density (96-99%) ceramic oxides and do not agree with the normally extrapolated values which take into account the porosity effect on modulus.

Young's modulus for Zircoa Y-714 zirconia calculated from modulus of rigidity was a factor of 10 less than the values measured by SRI and discussed in Section 4.5.5. A Poisson's ratio of 0.25 was used in the calculation. The discrepancy can only be accounted for by the difference in techniques used to obtain the data.

Thermal shock tests at various heating rates utilizing specimens with various thickness to heated surface area ratios were conducted in an attempt to correlate theory with actual thermal shock results. Although incomplete, this testing did indicate that the thermal shock failure of a given material and specimen size might be predictable by the expressions derived in this study. Much more thorough analyses and testing would be necessary to fully confirm this.

TABLE XXX MECHANICAL PROPERTIES

Ceramic Material	Density (lb/ft ³)	Maximum Shear Stress* (psi)	Maximum Shearing Strain (in/in)	Modulus of Rigidity (psi)
Al ₂ O ₃ :				
Ipsen ICB 3400	34	320	0.0032	9.9 × 10 ⁴
Norton RA 5058	85	490	0.0033	1.5 × 10 ⁵
Norton RA 5213	190	1850	0.0088	2.1 × 10 ⁵
ZrO ₂ :				
Norton LZ 5991	95	180	0.0028	6.4 × 10 ⁴
Zirconia Y-714	280	1980	0.0117	1.7 × 10 ⁵
ThO ₂ :				
Norton LT 5006	125	160	0.0024	6.8 × 10 ⁴
Zirconia Y-1193C	460	1450	0.0063	2.3 × 10 ⁵

* Shearing stress at failure (also can be denoted as ultimate tensile stress)

NOTE: Torsion Testing Performed at Room Temperature and at strain rate of 0.001 in/in/min.

(Note: Page 282 is a blank page)

SECTION VIII

CONCLUSIONS

The conceptual vehicle utilized in this project and the associated flight environments and heat shield configurations are representative for manned, orbital, lifting re-entry vehicles. Therefore, the conclusions should be applicable to a variety of vehicles of this general class.

(a) The thermal shock resistance of high density ($\geq 60\%$ of theoretical) ceramics is related to microstructure as well as inherent material properties. Ceramics with a microstructure consisting of a gradation of grain sizes (generally with relatively coarse sizes predominating), interspersed with porosity possess better thermal shock resistance than like ceramics of very fine, uniform microstructure and practically zero porosity.

(b) One of the best processes for achieving low density in sintered ceramics is the burn-out method. The uniformity, size, and amount of porosity is dependent respectively on the uniformity of dispersion, the size, and the quantity of burn-out material; thereby enabling good control and versatility. It is also adaptable to a complete spectrum of ceramic microstructures, including the thermal shock variety discussed in (a) above. The burn-out material can be readily and completely removed, leaving an uncontaminated ceramic.

(c) In the present state-of-the-art, the practical lower limit of density for sintered low density ceramics is approximately 20% of theoretical density, based on strength, pore size, and thermal shock resistance considerations.

(d) The degree of stabilization of sintered zirconia ceramics (percentage of zirconia in the cubic crystal habit) is dependent on the stabilization additive content, with a 3.12 w/o calcia content yielding a 50% stabilization. Sintered low density zirconia ceramics of this stabilization are more thermal shock resistant than similar materials of higher stabilization; due apparently to the lower thermal expansion coefficient of the former.

(e) A sintered, partially stabilized (50% cubic) low density (95 lb/ft³ or 26% of theoretical) zirconia with a crushing strength of 590 psi and a pore size of 0.05 inch diameter can be produced which will withstand surface heating rates to 50° F/sec to a peak temperature of 4000° F with no spalling, surface erosion, or macro-cracking. This material is useful in fabricating composite heat shield structures.

(f) Considerable difficulties are encountered in reproducibly manufacturing the low density zirconia described in (e) above. Extreme care must be exercised in the compounding, mixing, fabricating, drying, and firing operations.

(g) A sintered, low density (125 lb/ft³ or 20% of theoretical) thoria with a crushing strength of 550 psi and a pore size of 0.05 inch diameter can be produced and reproducibly manufactured, but this material will not withstand surface heating rates of 25° F/sec.

(h) Chemically bonded low density alumina (65 lb/ft^3 or 26% of theoretical), zirconia (125 lb/ft^3 or 32% of theoretical), and thoria (200 lb/ft^3 or 32% of theoretical) ceramics can be produced which are capable of withstanding surface heating rates of 50°F/sec to a peak temperature of 3400°F for the alumina, 4000°F for the zirconia, and 4500°F for the thoria. The respective room temperature crushing strengths for these materials are 475, 600, and 300 psi.

(i) One of the best processes for producing low density in chemically bonded ceramics is the burn-out process. The discussion in (b) above also applies here and, in addition, this process has the advantage of not diluting or affecting the chemical bond. The chemical bond should set up at a temperature below the volatilization temperature of the burn-out material so the bonded structure is not disrupted during volatilization. Naphthalene powder is a very suitable burn-out material as it volatilizes cleanly and readily at very low temperatures ($< 200^\circ\text{F}$). A practical lower limit of density for chemically bonded burn-out ceramics is approximately 20-25% of theoretical in the present state-of-the-art.

(j) The combination burn-out, low density aggregate process of attaining low density in chemically bonded ceramics offers the advantages listed in (i) above and, in addition, offers the advantage of greater dimensional stability at elevated temperatures. A practical lower limit of density for these ceramics is approximately 25-30% of theoretical in the present state-of-the-art

(k) Chemically bonded high density alumina (150 lb/ft^3 or 60% of theoretical), zirconia (230 lb/ft^3 or 63% of theoretical), and thoria (390 lb/ft^3 or 63% of theoretical) can be produced which are capable of withstanding the surface heating conditions mentioned in (h) above. The respective crushing strengths for these materials are 8950, 8140, and 6575 psi.

(l) The chemically bonded, low density thoria discussed in (h) above is incapable of withstanding high air loads and shearing forces at temperatures above 4500°F . Unlike the chemically bonded low density thoria, the high density form discussed in (k) above is usable to temperatures as high as 4900°F .

(m) One of the best materials for use in chemically bonding low and high density materials is water soluble sodium silicate in conjunction with a chemical setting agent. The ratio of silicate to ceramic is dependent on desired strength and refractoriness (approximately 5 w/o of sodium silicate proved satisfactory in this program). Phosphoric acid is also a useful bonding agent but does not have the advantage of room temperature setting of the silicate, and has a tendency to promote blistering and bloating at elevated temperatures.

(n) The low and high density thermal shock resistant ceramic materials can be readily shaped by conventional grinding techniques and equipment, including readily available silicon carbide and diamond grinding wheels and tools. Where possible, grinding should be performed wet, using flood cooling techniques. Care must be exercised in part-holding techniques and

in control of rate of material removal (in-feeds, cross-feeds, down-feeds). The ability to hold tight tolerances is dependent on texture of ceramic material and quality of tooling.

(o) For the ceramic materials investigated in this project, thermal conductivity of the low density materials is lower than for the high density materials at low temperatures (less than 2500°F); however, the inverse is true at higher temperatures (greater than 2500°F). It is apparent that at high temperatures, increasing the porosity (decreasing the density) does not necessarily lower the thermal conductivity. However, the thermal conductivity times density product (a measure of insulating efficiency) is always lower for the low density ceramics.

(p) The ultimate flexural strength of the ceramic materials investigated in this project decreases with increasing temperature, and a significant reduction in strength occurs above 2500°F. The higher density materials are much higher in strength than the low density materials. As to low density ceramic materials, the fired materials and the chemically bonded materials are comparable in strength at low temperatures (less than 500°F); however, as temperature increases, the chemically bonded ceramics lose their strength more rapidly.

(q) The chemically bonded ceramics developed in this project undergo severe shrinkage beginning at about 2000°F when the entire specimen is soaked at a given temperature for long times. However, in heat shield applications the exposure time at very high temperatures is relatively short and a temperature gradient exists through the ceramic because it is heated from one side only. In these applications, total shrinkage is low and occurs primarily at the heated surface.

(r) Designs which impose the minimum restraint on the ceramic parts significantly improve the capability of the ceramics to survive rapid heating. Means of minimizing the restraint include the use of minimum size ceramic elements, adequate expansion joints, and attachment methods which allow the ceramic to expand or change shape freely.

(s) Use of a water cooled substructure is not practical for a high L/D vehicle (long re-entry times) due to the large amount of water required. If water cooling is necessary for equipment, etc., it will be necessary to utilize it at a location other than the leading surface substructure. The cooled substructure also results in large thermal gradients through the ceramic heat shield, creating greater thermal stresses. Use of a hot substructure employing coated molybdenum or columbium is more efficient from a weight standpoint, creates lower thermal gradients through the ceramic, enables the use of a minimum thickness of ceramic, and is more compatible with radiation cooled adjoining wing or body structures.

(t) Typical launch vibration and acoustical environmental conditions are not critical for properly designed ceramic composite heat shields.

(u) Re-entry produces high surface heating rates and subsequent large thermal stresses in the ceramic heat shield parts and is the most critical and difficult environment for the ceramics to withstand.

(v) Analytical expressions have been derived which indicate that the behavior of ceramics exposed to thermal shock conditions can be predicted. Preliminary testing indicates a correlation between theory and practice.

(w) Full scale composite ceramic heat shield components as large as 6.0 inch radius nose caps can be readily designed, fabricated, assembled, and environmentally tested, with some reservations with respect to thermal testing. A successful 1.5 inch radius, 4000°F leading edge design was developed. Promising designs evolved for a 3.0 inch radius 3400°F leading edge and a 6.0 inch radius 5000°F nose cap, but both require further design and ceramic material improvements.

(x) A thermal test facility that adequately reproduces the necessary re-entry environmental conditions for testing full size leading surfaces is not available. A test facility that creates an environment substantially more severe than the re-entry conditions can unduly influence test results. At a given temperature or heating rate, oxyacetylene torches provide a closer flight simulation than existing MAPP-OX burners, and the former are less damaging to components being tested.

SECTION IX

RECOMMENDATIONS

Recommendations for ceramic composite structures for heat shield application are listed below:

(a) The effort to reproducibly manufacture the sintered low density zirconia developed herein should be pursued. Other desirable improvements in this material would be lower density, smaller pore size, better strength, and even greater thermal shock resistance.

(b) Sintered, high strength, small pore sized, thermal shock resistant, low density ($\leq 25\%$ of theoretical) varieties of alumina and thoria should be developed.

(c) The analytical techniques derived in this project for predicting the thermal stress behavior of ceramics require further study and correlation of theory and practice. Such techniques in their final form would prove extremely beneficial in component design and material selection for heat shields.

(d) In future ceramic heat shield designs, where weight is no problem, the high density ($\leq 60\%$ of theoretical) forms of ceramics should be utilized because in general they have superior strength and thermal shock resistance compared to the low density materials.

(e) Future ceramic heat shield designs should allow for thermal growth and deformation of ceramic parts and differential expansion between ceramics and metal members to minimize restraining stresses on the ceramics. This can be accomplished by techniques such as utilizing spring loaded fasteners and adequate expansion gaps. The composite heat shield designs developed in this project have merit and the 4000°F , 1.5 inch radius leading edge should be considered a usable item in its present form. As with any first generation designs, additional effort should be expended on minor design modifications, fabrication of additional units, and further environmental testing to confirm past results and improve reliability.

(f) Future programs concerned with ceramic heat shields should take into consideration scale-up factors from subscale to full scale components and should provide for an intermediate prototype stage of development. Where economically feasible, multiples of full scale components should be fabricated to allow for mishaps such as test fixture failure. Ideally, a redesign, fabrication, and test phase should follow initial full scale testing to permit refinements in full scale designs.

(g) A test facility for full scale components which can accurately simulate the temperature, time, total pressure, and surface shearing stress associated with re-entry is required for effective testing. Temperature distribution over the surface of the ceramic is very important. The MAPP-OX thermal test facility developed in this project has considerable merit, but additional development is required.

(Note: Page 288 is a blank page)

APPENDIX I

ENVIRONMENTAL TEST PROCEDURES AND EQUIPMENT

1. VIBRATION AND ACOUSTIC TESTING

Vibration and acoustic tests were conducted on eleven subscale ceramic modules and three full scale components. The purpose of these tests was to determine the relative ability of the different subscale modules to withstand a given dynamic environment and to determine the effect of this environment on the final full scale components. These tests simulated critical conditions during boost and re-entry phases of lifting re-entry vehicles.

For the vibration testing, each subscale module was bonded to a one inch thick aluminum plate using a low temperature organic adhesive, while each full scale component was bolted to a heavy plate. The plate was then rigidly attached to an electromagnetic exciter system. For each subscale module and full scale component, a crystal accelerometer was cemented to the plate to monitor acceleration inputs. In addition, crystal accelerometers were cemented to the plate to monitor acceleration inputs. In addition, crystal accelerometers were cemented adjacent to the attachment points of the 1.5 inch radius leading edge and the 6.0 inch radius nose cap. Typical vibrational test setups are shown in Figures 226 and 227.

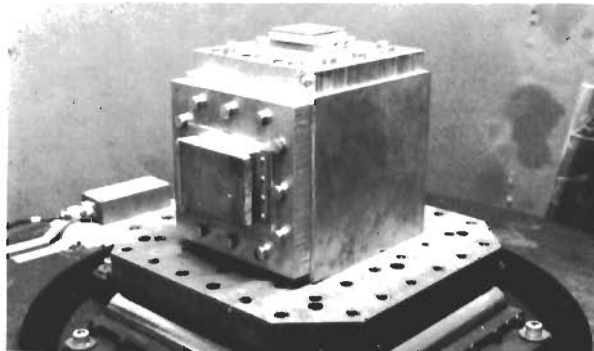


FIGURE 226 - TYPICAL VIBRATION TEST SETUP

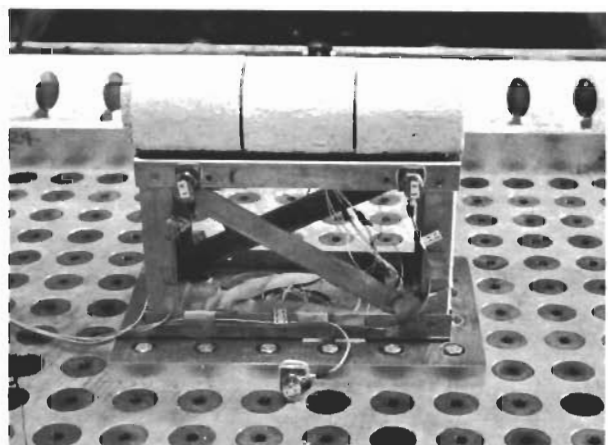
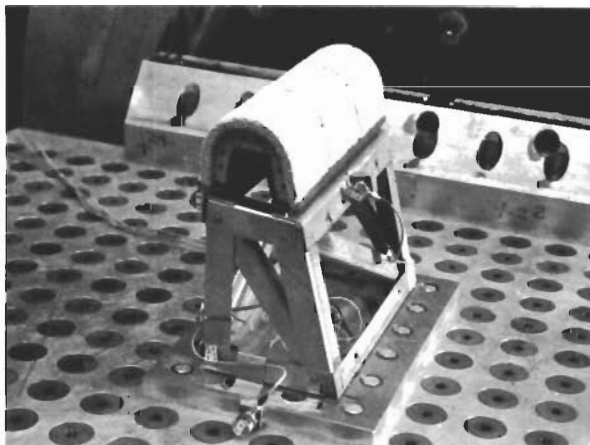


FIGURE 227 - VIBRATIONAL TEST SETUPS FOR THE 1.5-INCH LEADING EDGE

Provisions were made so that vibrational excitation was applied to the specimen in each of three mutually perpendicular directions. Vibrational testing in each direction consisted of the root-mean-square acceleration levels shown in the time schedule of Figure 228. The power density spectrums of these root-mean-square acceleration levels are presented in Figure 229. All input accelerations were controlled at the heavy aluminum mounting plate with the exception of the longitudinal direction of vibration of the 6.0 inch radius nose cap (normal to the base of the nose cap). In this case, input acceleration levels were controlled at the substructure of the nose cap and testing was discontinued after 160 seconds.

Both input and response acceleration data were recorded on magnetic tape throughout vibration testing of the 1.5 inch radius leading edge and the 6.0 inch radius nose cap. Power spectral density analyses were subsequently performed using a parallel filter analyzer. No data were recorded during vibration testing of the 3.0 inch radius leading edge or any of the subscale modules.

After vibrational testing and post-test inspection, each subscale module and full scale component was placed at the mouth of an exponential horn for acoustic testing. A modulated air stream acoustic transducer was used as a noise source. For the subscale modules, the acoustic excitation was normal to the top of specimen, while for the full scale components the excitation was along each of the three vibrational test axes. One test direction was omitted on the 6.0 inch radius nose cap. A calibrated high intensity microphone was positioned near the specimen to monitor the sound pressure level. Typical acoustic test setups are shown in Figures 230 and 231.

The acoustic testing consisted of subjecting each test specimen to an overall sound pressure level of 155 db over a frequency range of 15 to 9600 cps for five minutes per test direction. In some instances, the overall sound pressure levels were determined by the limitations of the test facility. Octave band analyses of the sound fields for each specimen tested were obtained.

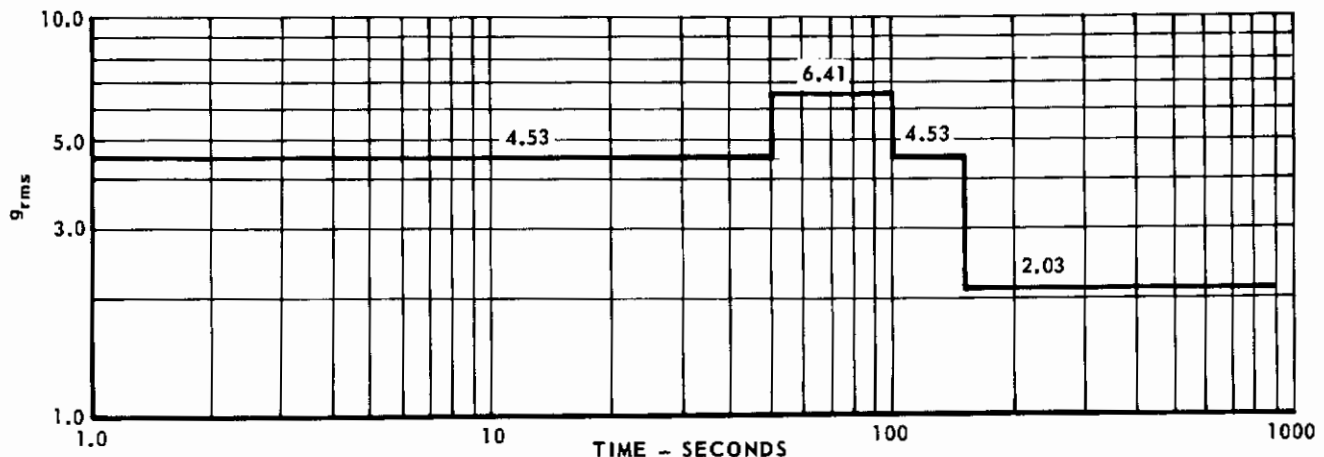


FIGURE 228 - VIBRATION INPUT LEVELS RMS ACCELERATION vs TIME

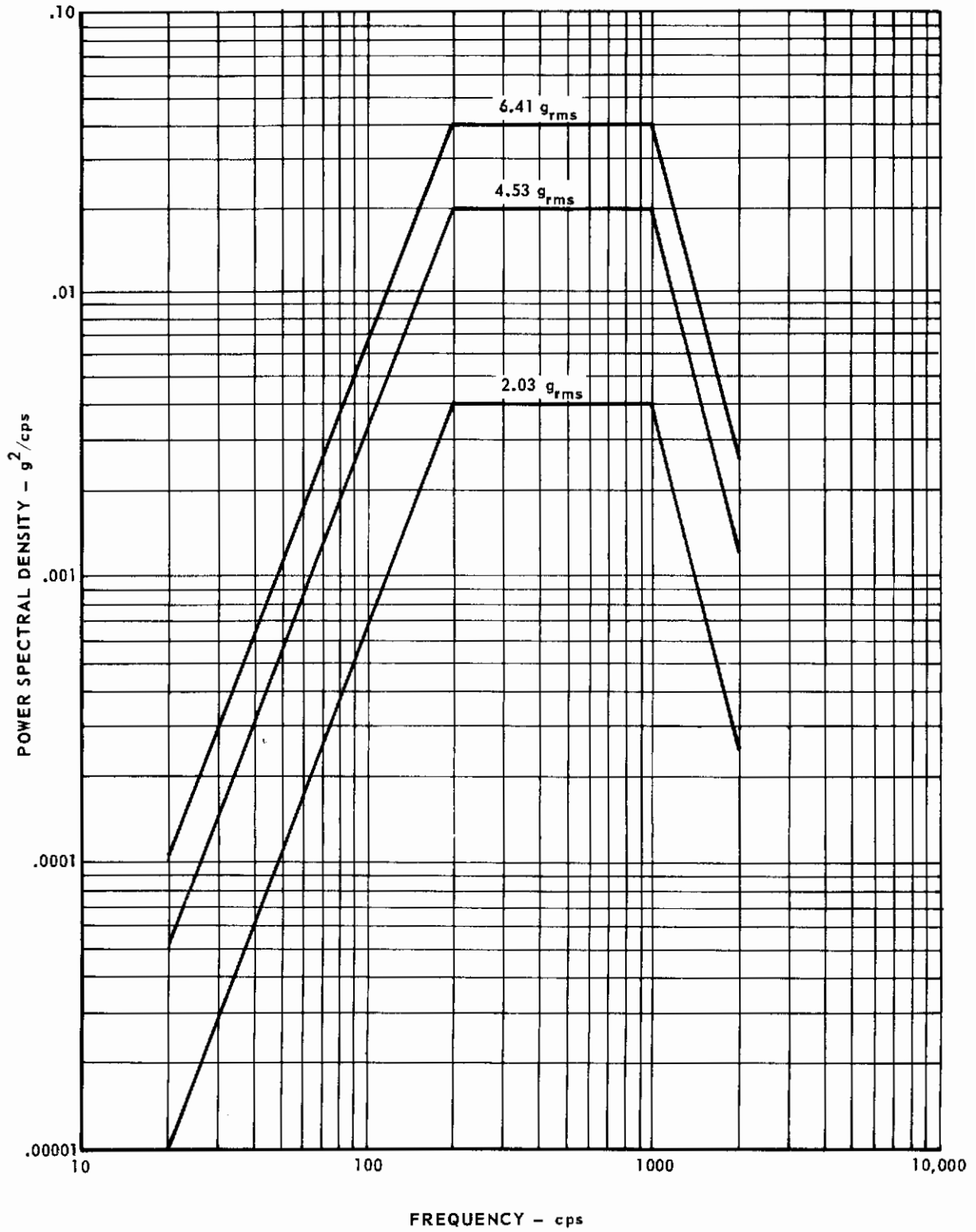


FIGURE 229 - VIBRATION INPUT PSD CURVES

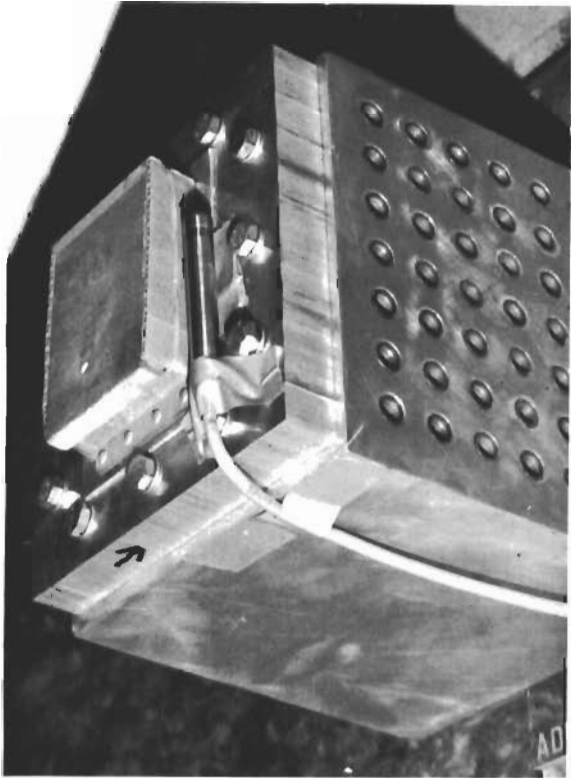


FIGURE 230 - TYPICAL ACOUSTIC TEST SETUP, MOUNTING UNDER HORN

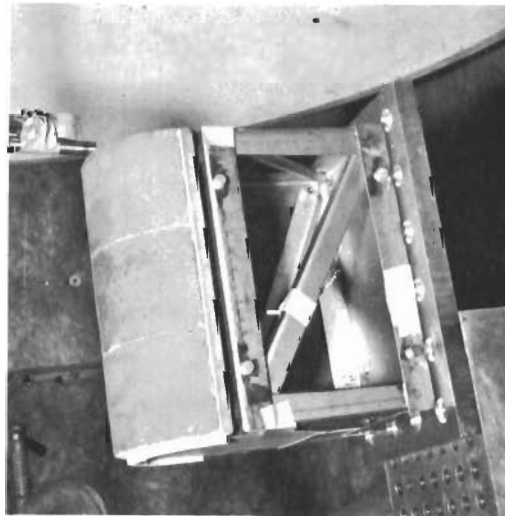
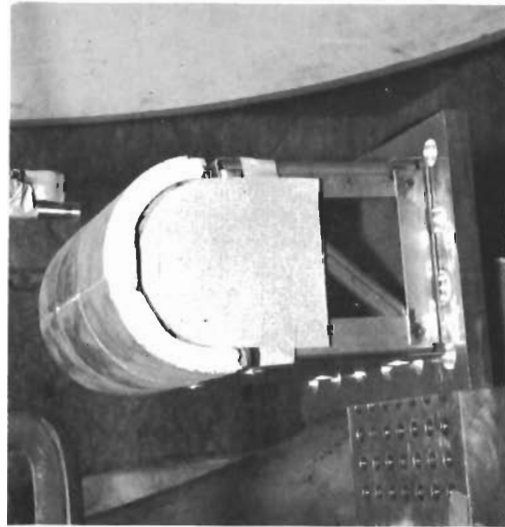
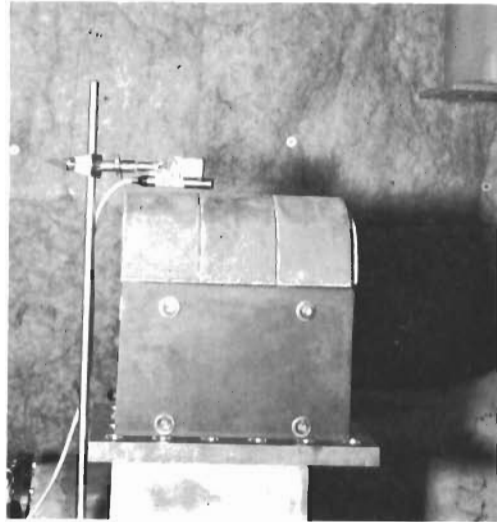


FIGURE 231 - ACOUSTIC TEST SETUPS FOR THE 3.0-INCH RADIUS
LEADING EDGE IN THE THREE ORIENTATIONS

2. SUBSCALE THERMAL TESTING

The thermal environmental tests were performed on all subscale modules. These tests were to simulate the aerodynamic heating produced during the re-entry phase of a typical lifting re-entry vehicle.

Each test specimen was thermally guarded (surrounded) by zirconia bricks (Norton RZ5601) to eliminate as much edge heating as possible. The zirconia bricks were slotted such that the metallic substructure of each subscale module would fit into the slots, letting each subscale module stand vertically. Figure 232 shows a typical thermal test setup.

Depending on the type of ceramic subscale module, the backside was water cooled, insulated with Fiberfrax, or left free to radiate to ambient conditions. Each subscale component had thermocouples inserted at various depths and also attached to the backside of the metallic substructure. These thermocouples were read out on an Electronic #17, 12-channel recorder which permitted continuous reading of all thermocouples. Figure 233 shows the backside of an installed specimen complete with water cooling and instrumentation.

The specimens were heated with an oxyacetylene torch equipped with a large rectangular head, which is also shown in Figure 233. The torch was mounted on a movable cart, which was surrounded by a water cooled copper plate. The torch head was mounted so that it would produce a vertical stagnation line isotherm and the flame was oxidizing. The stagnation line surface heating rate (temperature-time profile) was monitored by a recording optical pyrometer (Thermodot, Model TO-6T-70) together with a T-y recorder. The desired temperature-time profile was pre-plotted on the T-y recorder and the specimen to torch distance was varied to duplicate the desired profile. Figure 234 shows the overall arrangement of the thermal test facility.

Each specimen was subjected to its respective surface temperature-time history as shown in Figure 235. However, the thoria subscale specimens were subjected to a maximum temperature of 4300°F, the limit of the oxyacetylene torch facility. The recording optical pyrometer was corrected for emittance to duplicate the above stagnation point history. The value used in all instances was 0.7.



FIGURE 232 - TYPICAL THERMAL TEST SETUP

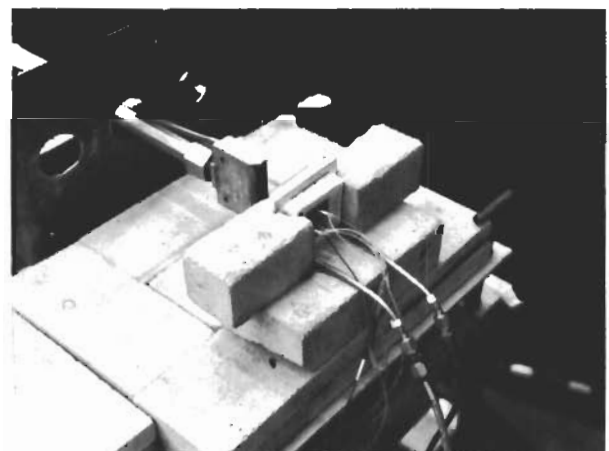


FIGURE 233 - TEST SPECIMEN WITH BACKSIDE WATER-COOLED IN THERMAL TEST FIXTURE

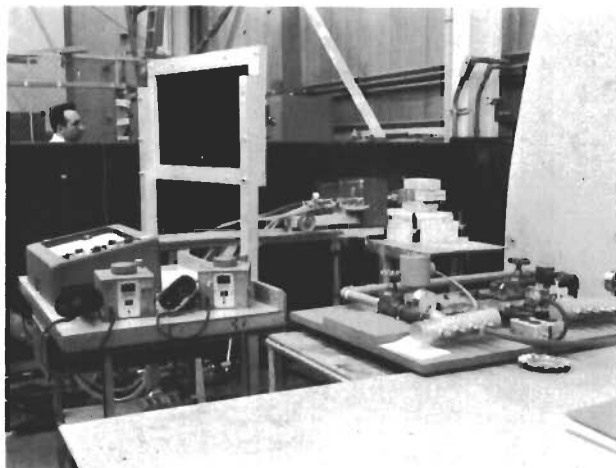


FIGURE 234 - SUBSCALE THERMAL TEST FACILITY

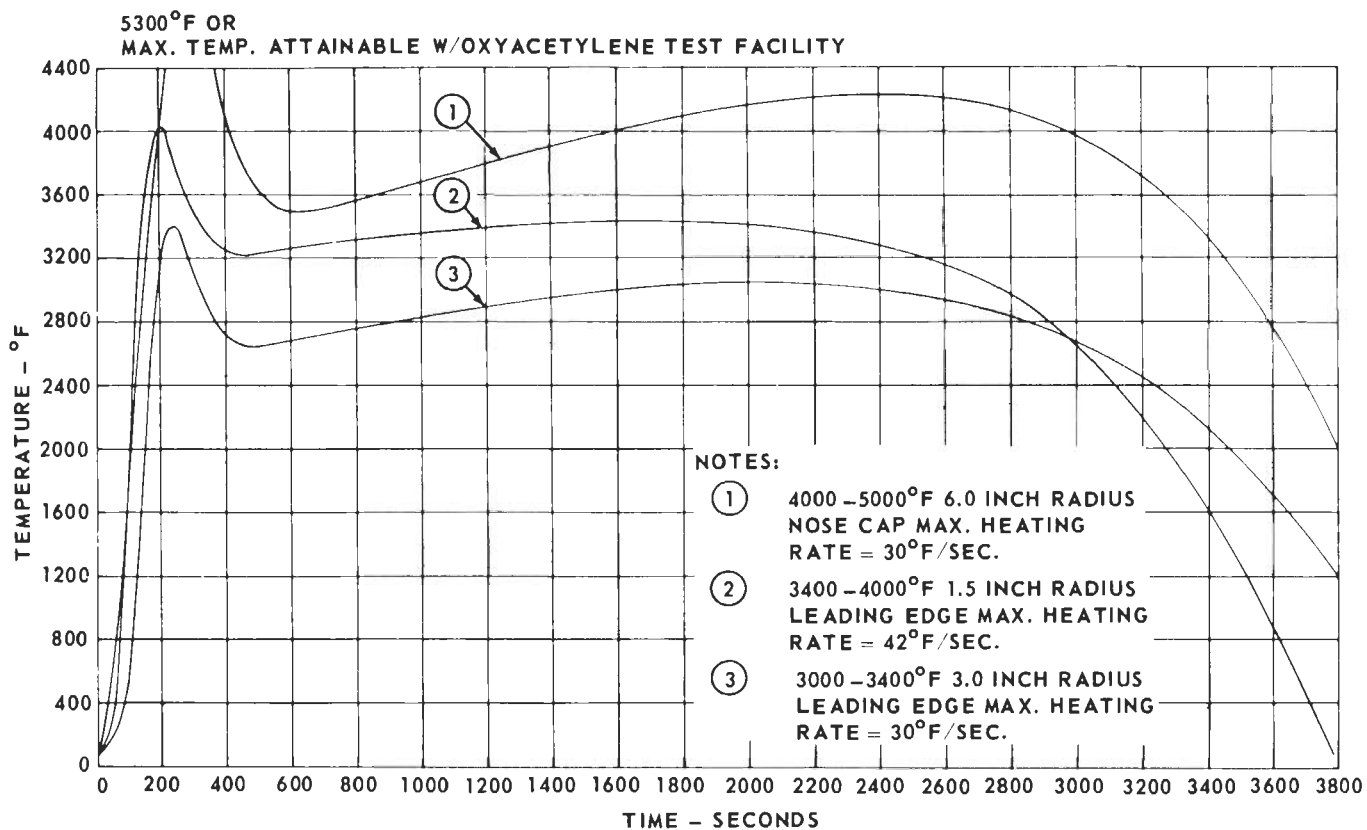


FIGURE 235 - STAGNATION POINT TEMPERATURE HISTORIES

3. FULL SCALE THERMAL TESTING

The oxyacetylene facility used in testing the subscale modules was replaced with a MAPP-OX facility (methyl-acetylene-propylene-propadiene gas, manufactured by Dow Chemical Co., and oxygen). Some of the reasons for selection of MAPP as a replacement for acetylene are listed below:

(a) MAPP can be stored as a liquid in a large tank rather than in many small gas cylinders as necessary for acetylene. Very large quantities of gas would be needed to perform a one hour thermal test on the full scale components.

(b) MAPP is much more stable than acetylene and, therefore, safer to handle in the large quantities required.

(c) Using adequate preheaters, operating pressures as high as 250 psig were possible as compared to a maximum of 15 psig for acetylene. To obtain temperatures in excess of 4400°F over large areas and meet the desired time-temperature profile, it was felt that high gas mass flows would be required and thus high operating pressures.

An 8000 gallon MAPP tank and a 45,000 cubic foot oxygen highway trailer were acquired. This quantity of oxygen was sufficient for a one hour run while maintaining pressures as high as ~150 psig. The MAPP supply was more than sufficient to meet the needs of the entire program. Preheating of the MAPP, when required, was accomplished by covering the tank with a crude tent and injecting hot air that was preheated with a 12 KW heater. With this setup, MAPP pressures of ~60 psig could be maintained at ambient temperatures around 30°F.

At the time MAPP was selected, no commercially available burners for MAPP-OX use existed. Conventional oxyacetylene burners and developmental MAPP-OX burners supplied by two torch manufacturers gave very poor heat distribution and were considered completely unsatisfactory. It was necessary, therefore, to undertake a burner development program in order to be able to perform the desired thermal testing. Since the bulk of this development work was carried out under McDonnell sponsored research programs; the design of the burner nozzles is considered proprietary.

The first burners developed were found to impose very high pressures on a test specimen (16 psi or greater). These burners operated at supersonic exit gas velocities and generated high noise levels. Subsequent development evolved a burner that developed approximately two psi pressure and operated at subsonic gas velocities at typical gas pressures of 40-50 psig MAPP and 60-80 psig oxygen. The noise level was still high with rough measurements indicating on the order of 135 db or greater. This burner utilized a nozzle with a flame exit diameter of ~5/8 inch. Similar nozzles with a flame exit diameter as large as ~2-1/4 inches were eventually developed, utilizing design principles established in the small nozzle development. Figure 236 illustrates test firing of a large burner.

It appeared that as large a nozzle as desired could be readily designed and fabricated and that these nozzles could be built to operate at a variety of pressure conditions. Even at the low exit pressure of two psi, it appeared that these burners would be capable of attaining the desired maximum surface temperatures during actual tests, as indicated by the ease with which calcia stabilized zirconia brick could be melted (estimated melting temperature of ~4700°F). Some

very preliminary work was done with electrical augmentation of the burner to further increase heat output, but scheduling requirements forced termination of this approach. All the burners developed were water cooled, as it was expected that the burner-to-sample distance during test would be relatively small.



FIGURE 236 - TEST FIRING OF 2¼ INCH DIAMETER MAPP-OX BURNER

Burners utilizing the 5/8 inch diameter nozzles were selected for testing the leading edges. The burners were designed so that any desired number could be stacked together in a variety of configurations to give the type of heating pattern needed. Nozzles could be readily removed and replaced for cleaning purposes or O-ring replacement. Nine of these burners were grouped to parallel the specimen stagnation line and extend past the ends to give uniform heating along the entire length of the leading edge. The nine burners were mounted on a movable carriage patterned after the apparatus used in oxyacetylene thermal testing of subscale modules. This permitted control of sample surface temperature by manually cranking the carriage toward or away from the sample. Each burner was fed by separate MAPP and oxygen lines from manifolds. Water cooling was similarly supplied. Figure 237 shows the mounted burners during a test firing.

Initial burner runs were made on a stack of high density zirconia brick (Norton RZ5601). These runs indicated an uneven isotherm along the stagnation line (hot spots on the brick), the cause of which was traced to the gas manifolding. Circular manifolds were installed which supplied each burner with gases at like pressures, and minimized the hot spots.

In additional runs, the uneven burning occurred again and this time was traced to nozzle O-ring deterioration and nozzle contamination. Subsequently, it was made a standard practice to regularly clean the burners. The O-rings appeared to degrade

due to the heat and were replaced with higher temperature O-rings. Also, the nozzles were redesigned so the O-rings were relocated to a cooler area of the burner. After some experience, it was possible for a trained operator to detect the uneven burning by visual observance of the burners while running instead of having to heat up a sample and observe the hot spots. The uneven burning problem was essentially overcome except for the idiosyncracies of individual burners due to slight manufacturing variations within standard tolerances. At one point in the development, the burners were mounted on a pneumatic oscillating device that cycled the burners back and forth parallel to the stagnation line to even out the heating. This device was found unnecessary when the burners were operating properly.

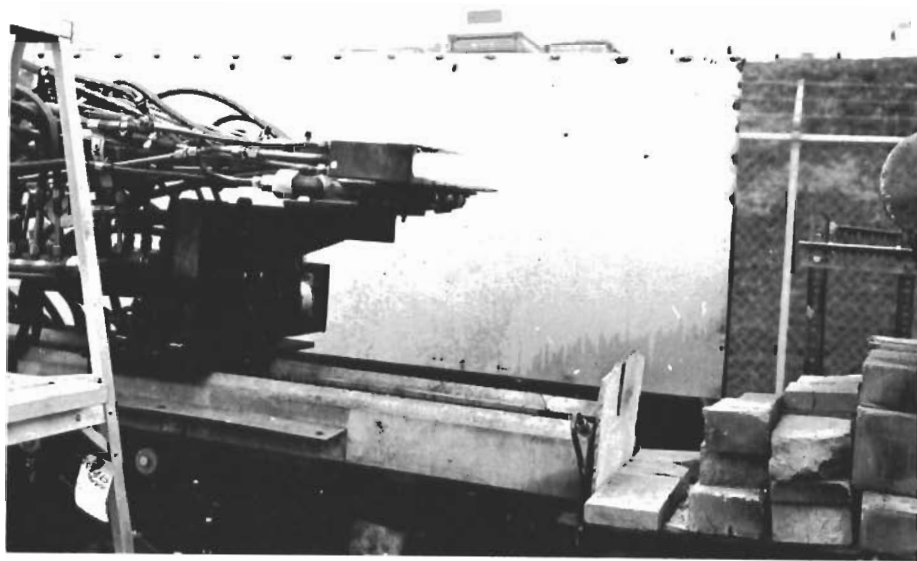


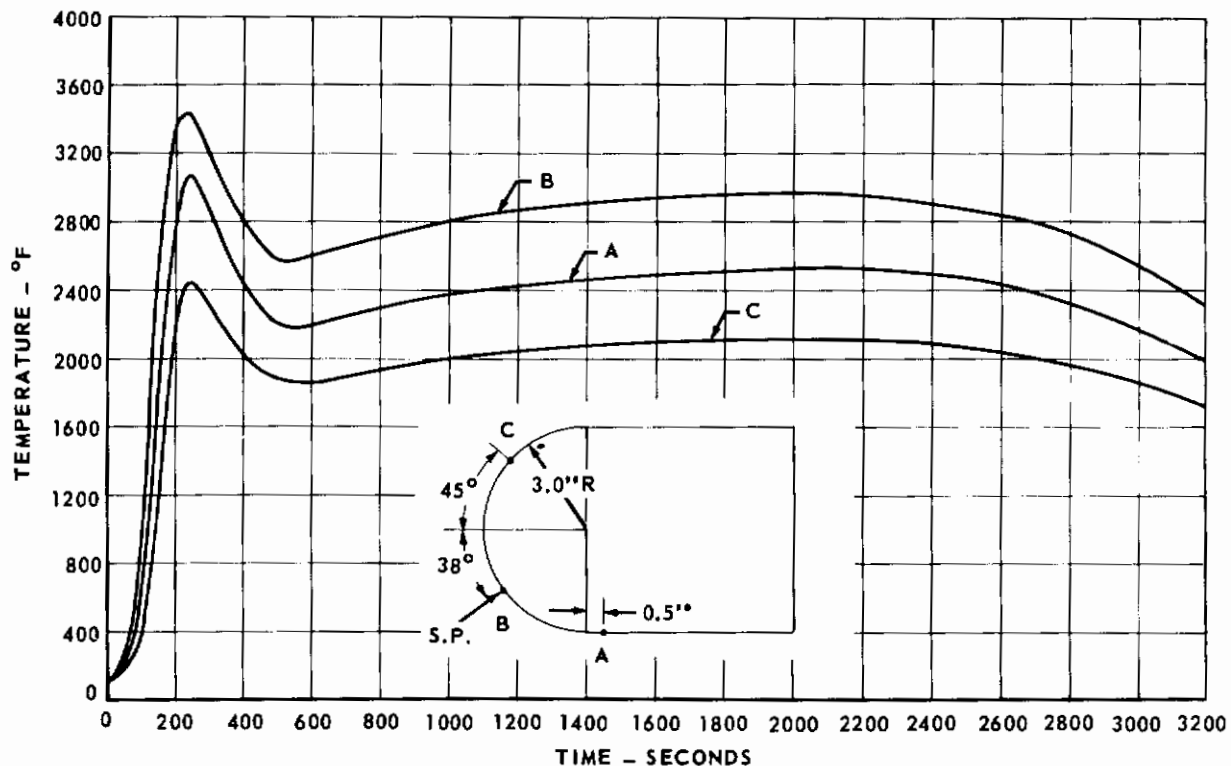
**FIGURE 237 - TEST FIRING OF NINE BANKED
5/8 INCH DIAMETER MAPP-OX BURNERS**

Dummy models of the two leading edges were fabricated from low density alumina and zirconia bricks. These dummies were mounted on a water cooled sting identical to that to be used in full scale testing. The sting placed the sample at the proper angle and height in relation to the burners, with the burners constituting the stagnation line. Water cooled protection shields clamped the dummies to the sting. The shields were designed so they could be used on the actual leading edges also, as preliminary runs indicated it would be necessary to protect the Hastelloy X support structures and instrumentation from overheating. For the same reason, the attach base plate where the leading edge support truss would be bolted onto the sting was water cooled. (In an actual vehicle, the support structure would be made of a material such as coated molybdenum or columbium that would withstand downstream heating. As this program was concerned with the building and testing of the leading surface, it was more economical to provide cooled support structure even though this would increase the severity of the testing somewhat by tending to create greater thermal gradients through the ceramic.)

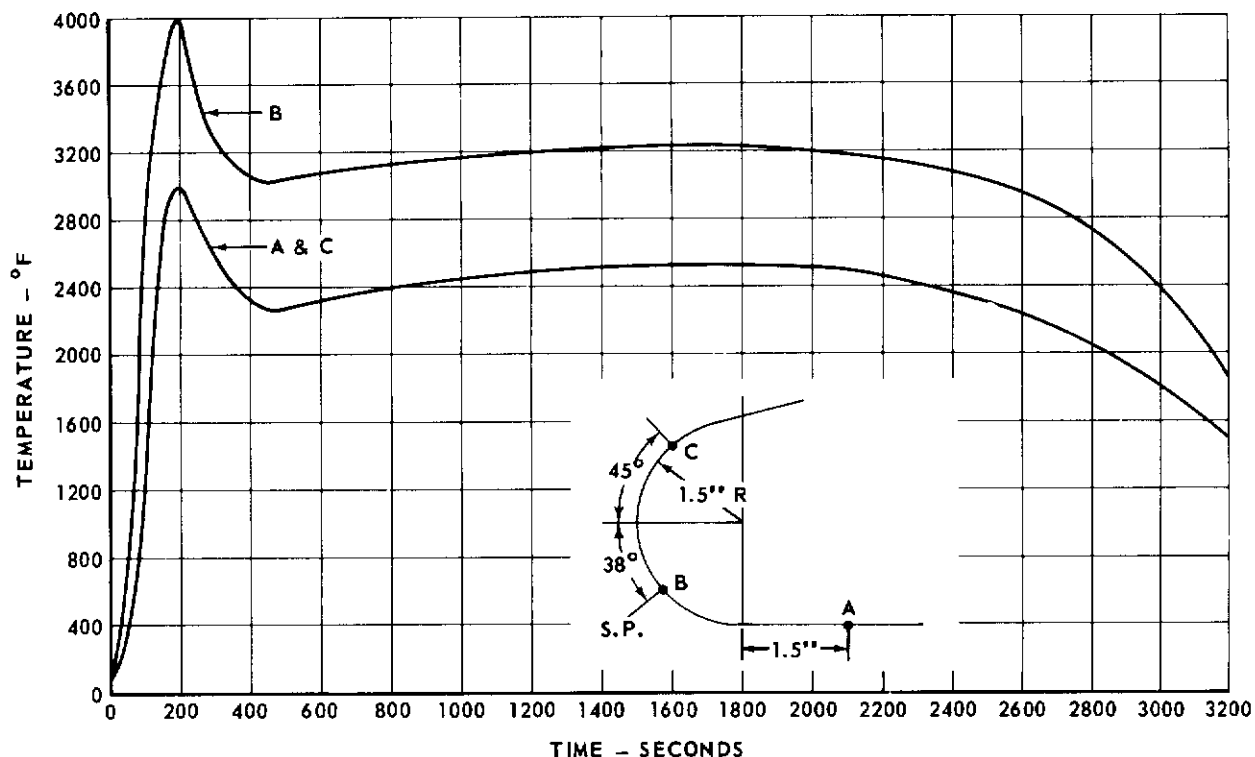
Preliminary runs were made on these dummy models to establish test procedures for use with the full scale components and to determine if the desired test environment would be attainable. Figures 238 and 239 show the desired surface temperature-time profiles for the leading edges at the stagnation line and at points on the periphery. Pressure probe checks indicated static pressure levels of approximately two psi at the gas pressure settings needed to attain the peak temperatures of 3400°F and 4000°F.

Figure 240 shows the thermal testing of dummy leading edges. The water cooled shields and sting mentioned previously can be seen in these pictures. The stagnation line heating pattern was considered sufficiently uniform for testing. Temperature gradients around the periphery were checked with a manually operated L & N optical pyrometers and found to essentially satisfy the requirements of Figures 238 and 239. If the gradients had been higher than desired, it was planned to bank supplemental burners above and below the bank of nine stagnation line burners. If the gradients had been too small, burner redesign would have been required.

For temperature control purposes, it had been planned to utilize a Thermo-Dot recording optical pyrometer as was done with the oxyacetylene subscale testing. However, this instrument was found to be sensitive to the MAPP-OX flame and it was necessary to use a Pyro 650 recording optical pyrometer. This instrument would not sense temperatures below 2500°F, so for control below this temperature a chromel-alumel thermocouple was bonded to the sample surface. The thermocouple would burn away harmlessly at elevated temperatures.



**FIGURE 238 - THERMAL TEST CONDITIONS FOR FULL SCALE
3.0-INCH RADIUS LEADING EDGE**

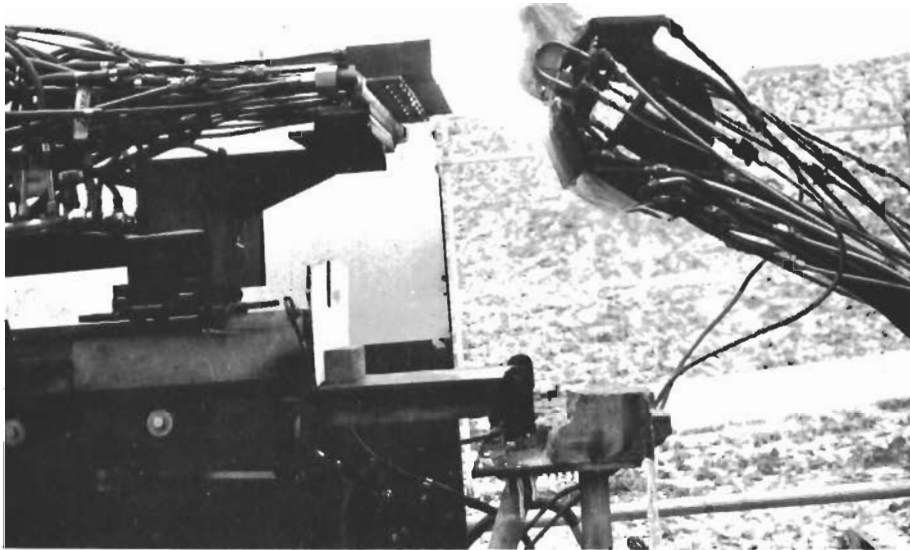


**FIGURE 239 - THERMAL TEST CONDITIONS FOR FULL SCALE
1.5-INCH RADIUS LEADING EDGE**

The test procedure then was to place a heat shield in front of the specimen, light off the burners, regulate and check burners for smooth operation, remove the heat shield, and manually move the burners toward the specimen at a rate to obtain the stagnation line surface temperature vs time curve (Figures 238 and 239). Temperature was sensed by a thermocouple up to 2500°F and the Pyro 650 beyond 2500°F, with the signals from these sensors fed into a T-y plotter which had the desired time-temperature profile pre-plotted on it. Temperatures of other areas were determined with thermocouples (Ir/Ir-40% Rh, Pt/Pt-10% Rh, and chromel/alumel) and manually operated optical pyrometers.

During runs on the dummy models, it was determined that better surface temperature control could be obtained by moving the burners to a point where the surface temperature was 400-500°F less than the peak temperature and then proceeding to obtain the remainder of the thermal profile by manual regulation of the MAPP and oxygen pressures. This proved to work quite well, and the desired time-temperature profiles were readily attainable.

After sufficient runs were made on the dummy models to establish procedures, capabilities, and proficiency, tests were run on the full-scale leading edges. Figure 241(a) shows the 3.0 inch radius leading edge mounted on the sting ready for testing. All thermocouples within and on the sample were led down the water cooled sting to be connected to multi-channel automatic recorders. The surface temperature control thermocouple (on center of leading edge) was bonded to the



(a) SIDE VIEW



(b) FRONT VIEW

FIGURE 240 - MAPP-OX THERMAL TESTING OF DUMMY LEADING EDGES

surface with McDonnell chemically bonded chromia which was cured in place with a heat gun. Thermocouples were placed on the Hastelloy X support structure and in the event the temperature exceeded 1500°F, provisions were made to supply air cooling to the support structure. This provision was made on all the full scale components.

In Figure 241(b), the Pyro 650 and an L & N optical pyrometer can be seen as well as the T-y recorder used for temperature-time profile control by the crank operator. Another T-y recorder was provided for the gas pressure regulation operator.

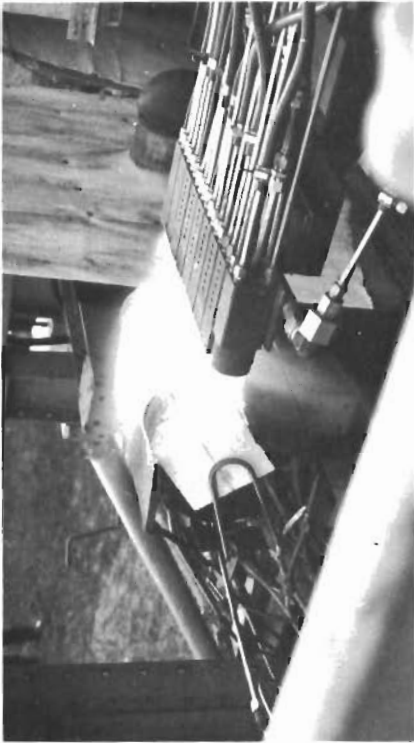
Figure 241(a) shows the low density alumina end brick fixtures which were fabricated to conform to the leading edge shape. These brick fixtures closed the end openings of the test components and simulated additional leading edge surface that would be present in an actual case. The brick fixtures were clamped in place by water cooled U-shaped stainless steel tubes as shown in Figure 241. The gaps between the water cooled shields and the leading edge structure were filled with Fiberfrax insulation and Sauereisen #63 cement.

Figures 241(c) and (d) show the test in progress. Figure 241(c) shows the leading edge during heat-up and 241(d) shows the component at peak temperature. Burner-to-sample distance was approximately six inches in the latter picture. During heat-up, hot spots were noted, especially at the tile joints. However, at peak temperature the surface temperature looked much more uniform.

The test setup and procedures were essentially the same for the 1.5 inch radius leading edge as for the 3.0 inch radius leading edge. To attain the peak surface temperature of 4000°F, a sample-to-burner distance of approximately four inches was necessary. Figure 242 (a) shows the 1.5 inch radius leading edge mounted in place prior to test. The end openings of the structure were closed with low density zirconia brick ground to match the leading edge contour and surfaced with McDonnell chemically bonded zirconia. As with the 3.0 inch radius leading edge, the gaps between the water cooled shields and the leading edge structure were filled with Fiberfrax insulation and Sauereisen #63 cement. Figures 242 (c) and (d) show the test in progress. Although difficult to discern in these pictures, the uniformity of surface heating along isotherms was very good.

Testing procedures for the 6.0 inch radius nose cap were similar to those for the two leading edges, but the test setup varied somewhat. Figure 243 illustrates the desired time-surface temperature profile. Since it was considered too costly and time consuming to fabricate dummy nose caps for testing checkout purposes, a water cooled, 6.0 inch radius copper hemisphere was built, into which calorimeters were inserted at various locations around the periphery, including the stagnation point. It was intended to determine heat flux versus sample-to-burner distance and versus time, at various nose cap locations and relate this to the desired time-temperature profile. Calculations had indicated that hypothetical flight conditions would subject the nose tip to a hot wall heat flux of 215 Btu/ft²-sec at the stagnation point.

One large burner similar to the one shown in Figure 236 was initially evaluated as the heat source. Several runs were made on the calorimeter setup with resulting erratic results, due apparently to deficiencies in the calorimeter and/or dummy nose cap design. During these runs it was indicated that the large burner would require some additional design refinement for completely satisfactory use and that the large single burner might yield too great a temperature gradient around the nose cap surface.



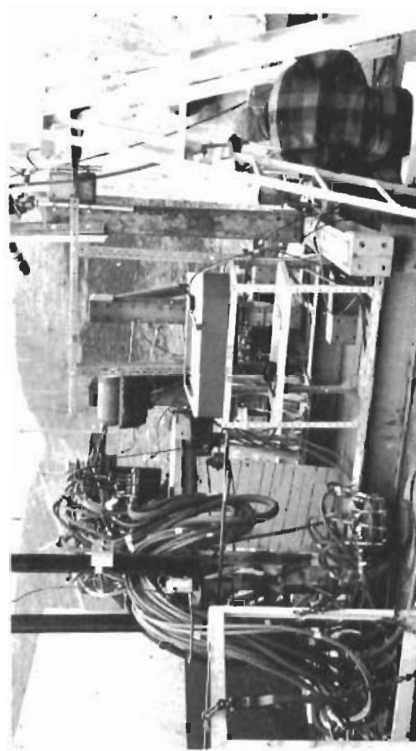
(c) TEST IN PROGRESS



(d) TEST IN PROGRESS

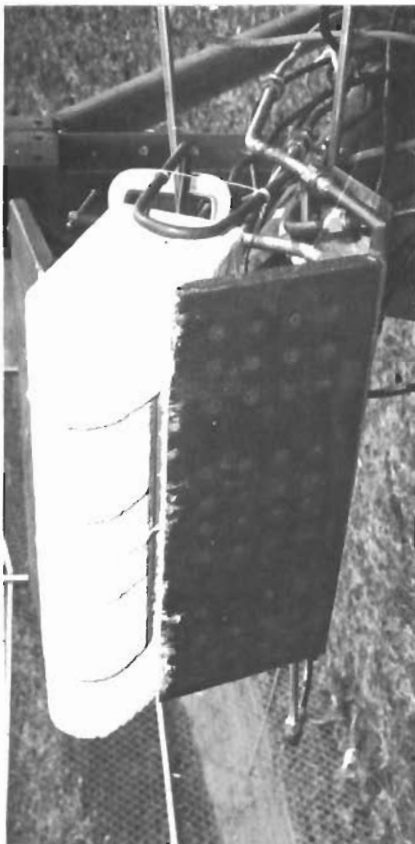


(a) COMPONENT IN TESTING POSITION

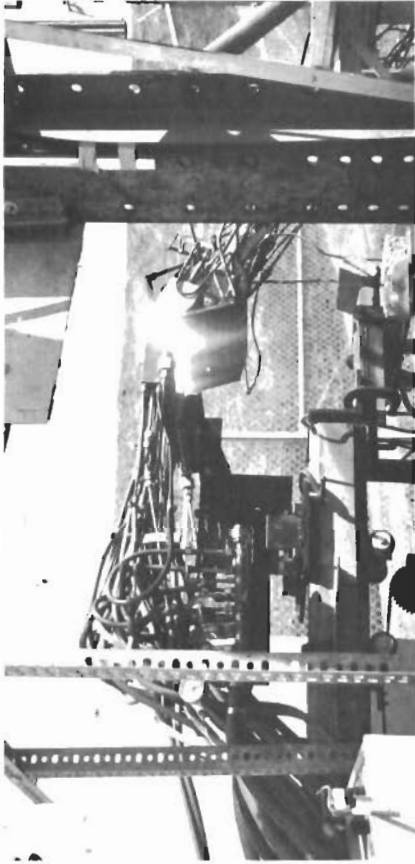


(b) INSTRUMENTATION IN POSITION

FIGURE 241 - MAPP-OX THERMAL TESTING OF 3.0 INCH RADIUS LEADING EDGE



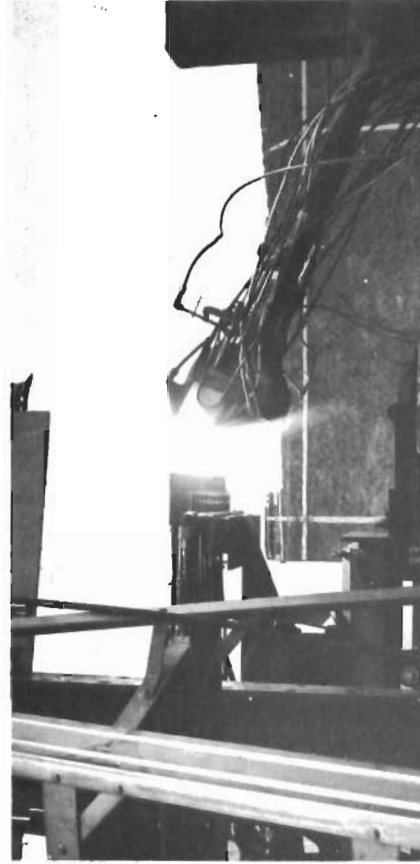
(a) COMPONENT IN TESTING POSITION



(c) TEST IN PROGRESS



(b) INSTRUMENTATION IN POSITION



(d) TEST IN PROGRESS

FIGURE 242 - MAPP-OX THERMAL TESTING OF 1.5 INCH RADIUS LEADING EDGE

Scheduling requirements dictated the cessation of further efforts with the calorimeter and with the large burner. It was decided to use the nine burners used on the leading edge tests and stack them in a 3 x 3 square pattern. Preliminary runs with this setup on a flat "wall" of zirconia brick indicated very uniform temperature distribution. High temperature capability was indicated also, as temperatures up to 4900°F were read optically on melting zirconia brick. The center nozzle in the 3 x 3 burner stack was modified slightly to increase temperature capability somewhat over the other burners, as the center burner would heat the nose cap stagnation point.

There was some question as to the refractoriness and high temperature strength of the McDonnell chemically bonded thoria at 5000°F, as it had never actually been tested to that temperature under the MAPP-OX burner conditions. It was decided to subject low density thoria samples to the expected test environment using the 3 x 3 burner setup to further check material capabilities prior to testing the nose cap. Thoria samples 2 inches x 2 inches x 1 inch thick, were surrounded on all four sides by surfaced Norton low density thoria, backed up with Norton high density zirconia brick, and the samples subjected to the first 20 minutes of the nose cap thermal profile (see Figure 243), except that the peak temperature utilized was 4500°F or 4700°F. Plans were to try a variety of peak temperatures. As seen in Figure 244, the low density chemically bonded thoria was unable to withstand the 4700°F temperature under the MAPP-OX burner conditions of high gas velocity, noise, and pressure (dynamic conditions more severe than expected in flight).

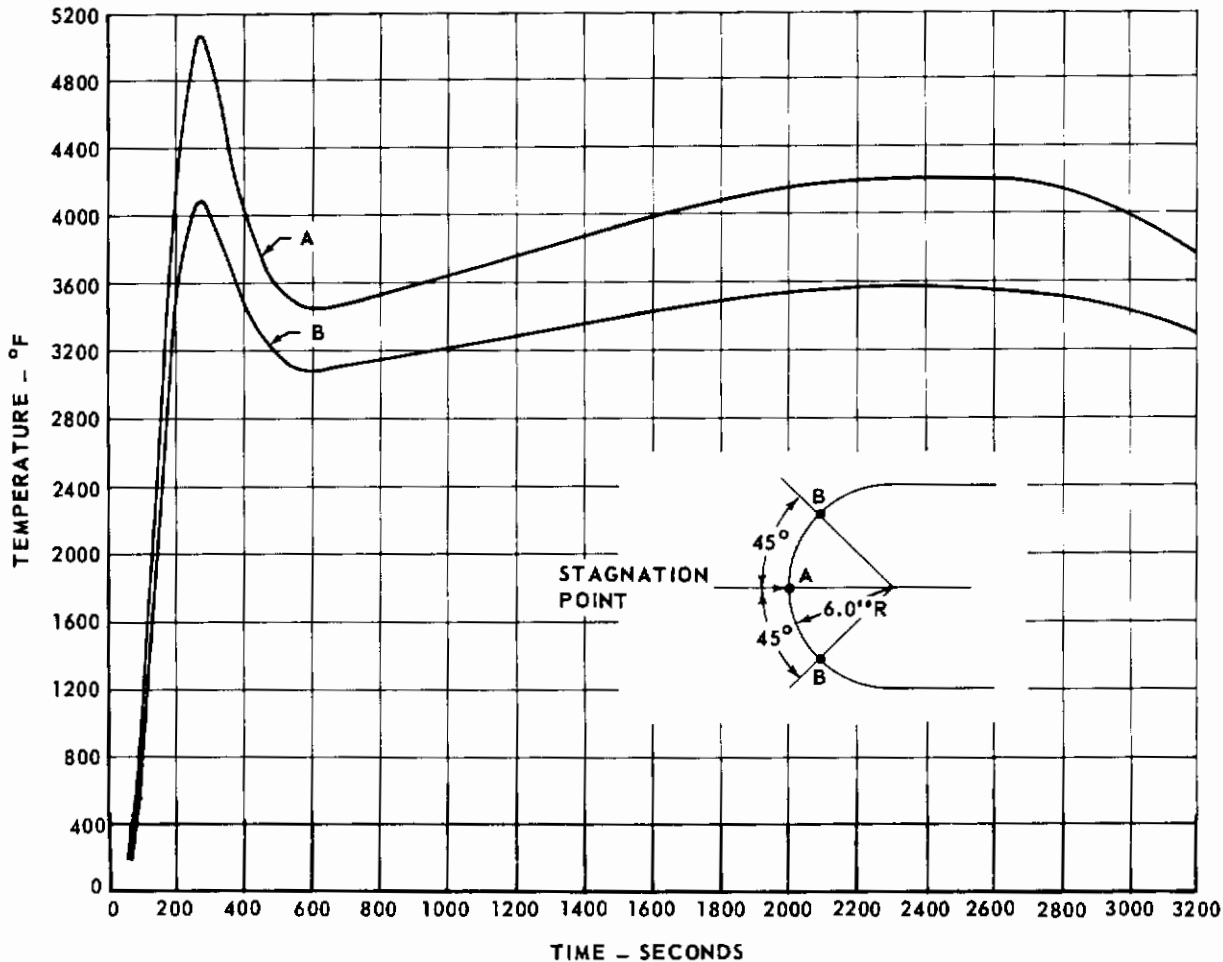


FIGURE 243 - THERMAL TEST CONDITIONS FOR FULL SCALE 6.0 INCH RADIUS NOSE CAP



**FIGURE 244 LOW DENSITY CHEMICALLY BONDED
THO₂ (MAC LT-1) AFTER THERMAL TEST AT 4700°F**

Close examination of this sample indicated that rather than actually melting, it had appeared to soften and be deformed. The McDonnell high density thoria coating on the adjacent Norton sintered low density thoria did not reveal this behavior nor did the sintered thoria (although the latter cracked severely).

Another similar test was run using a peak temperature of 4500°F. Post-test examination of the McDonnell low density thoria indicated it would withstand this condition. Therefore, it was decided to test the nose cap to only 4500°F, using the same thermal trajectory shown in Figure 243 but with the lower peak temperature.

Figure 245 shows the nose cap in place prior to test with the chromel/alumel couple bonded to the stagnation point with McDonnell chemically bonded high density thoria and the gaps under the water shield filled with Fiberfrax insulation and Sauereisen #63 cement.

Figure 246 shows the test in progress and the water soaked asbestos covering over the thermocouple leads can be seen. The desired thermal trajectory including surface temperature gradients was attained in this test. Minimum sample-to-burner distance was approximately four inches.



FIGURE 245 - 6.0 INCH RADIUS NOSE CAP READY FOR THERMAL TEST

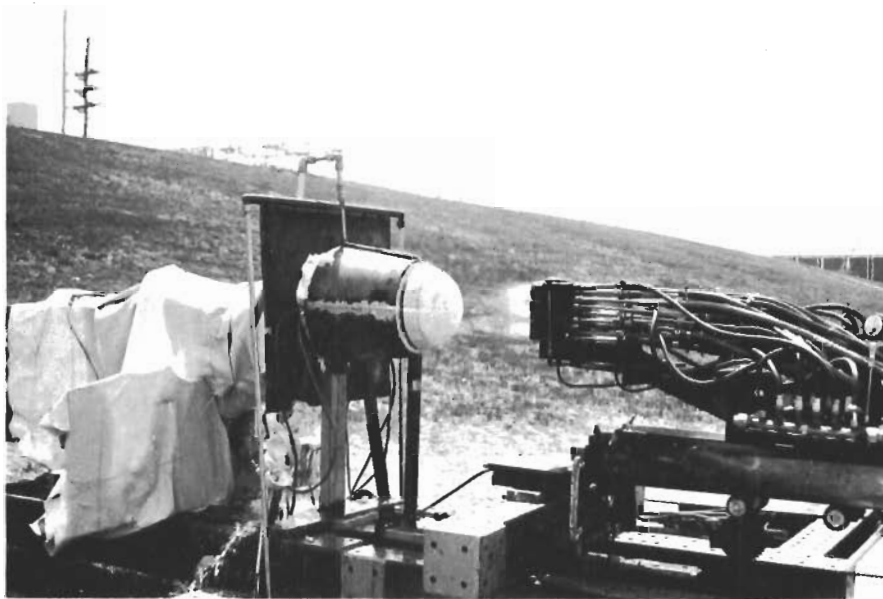


FIGURE 246 - MAPP-OX THERMAL TESTING OF 6.0 INCH RADIUS NOSE CAP

APPENDIX II

THERMOPHYSICAL PROPERTY MEASUREMENT METHODS AND APPARATUS

(Excerpts from Southern Research Institute final report to McDonnell Aircraft Corporation, titled "Some Thermal and Mechanical Properties of Several Aluminas, Zirconias, and Thorias.")

1. HEAT CAPACITY TO 5000°F

The specific heat is determined in the Southern Research Institute drop-type ice calorimeter as shown in Figures 247, 248, and 249.

The specimen should be about 3/4 inch in diameter by about 3/4 inch long and can be assembled by stacking thinner discs. The specimen is enclosed in a drop basket and heated in a furnace with a thin-walled, tubular, resistance heater made from graphite. After bringing the specimen to temperature, it is dropped into an ice calorimeter in which the cup is surrounded by an ice mantle. As the ice melts, the volume change draws mercury from a calibrated manometer tube. The travel of the mercury is a measure of the volume change resulting from the melting ice. The ice is melted by the heat from the dropped specimen. The heat capacity of the specimen is then measured directly by the mercury displacement.

The flutter valve immediately above the cup is a major feature and blocks off radiation losses from the specimen up the drop tube. This heat is then conducted to the cup wall and ice mantle.

After calibrating the cup against synthetic sapphire, the basket and system operation were calibrated. Separate basket calibration minimizes the radiation error accompanying drop techniques. Indeed, these errors are only about 0.5% as reported by Furukawa et al (Reference 6) and not nearly as severe as many investigators would suggest.

Either a helium or an argon environment can be employed. Nitrogen has been used on occasion.

2. TOTAL NORMAL EMITTANCE TO 5000°FGeneral

Emittance is measured by comparing the energy received by a radiometer from the sample to that received from a blackbody cavity maintained at the same temperature.

The equipment may be divided into three main parts: the induction heating furnace, the radiometer, and the temperature measurement equipment. Figure 250 shows a picture of the complete equipment.

Description of Apparatus

A cross section of the apparatus is shown in Figure 251. The specimen (1) is supported in the center of the flat concentrator induction

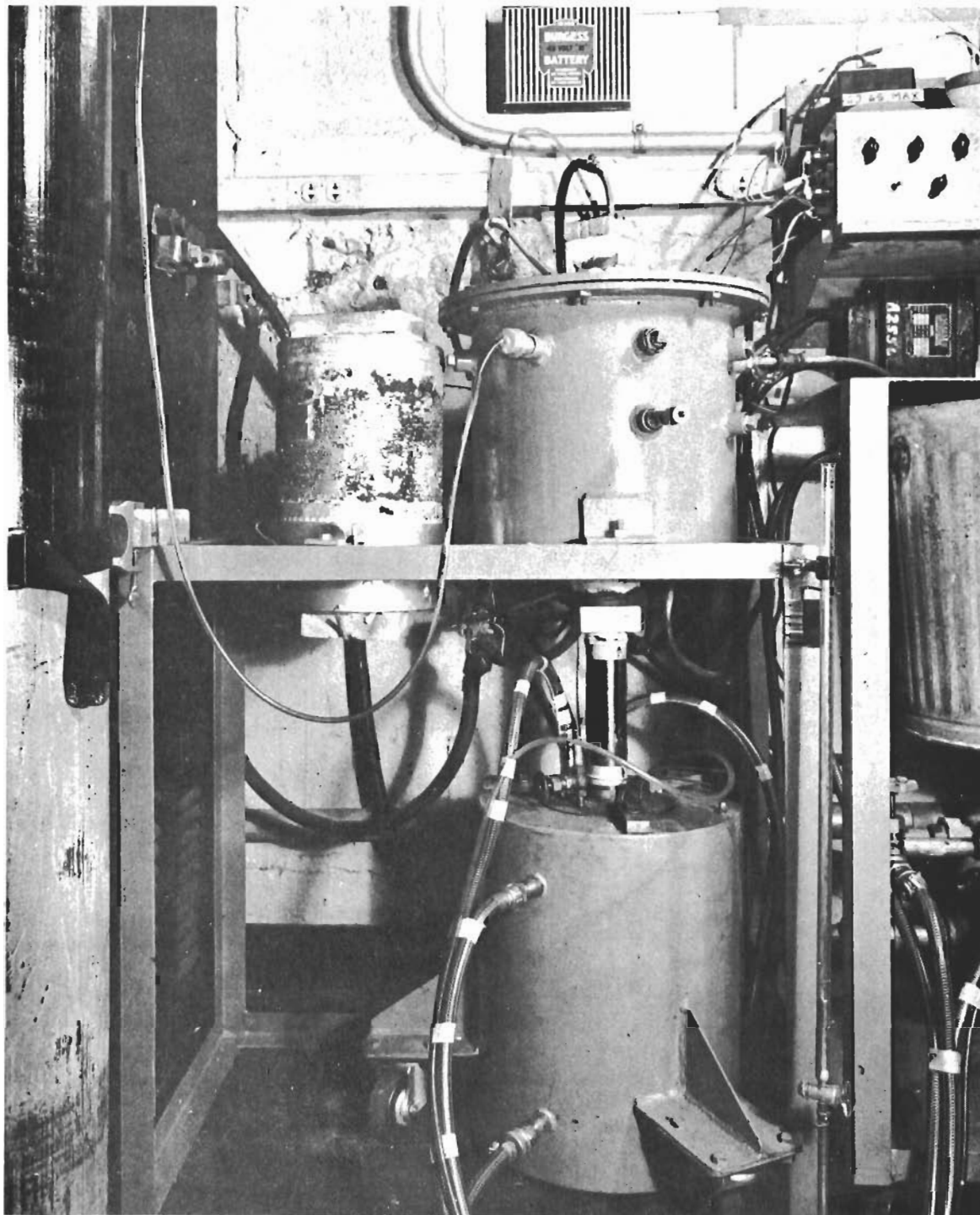


**FIGURE 248 -HEAT CAPACITY EQUIPMENT WITH
DROP SHIELD TUBE IN PLACE**

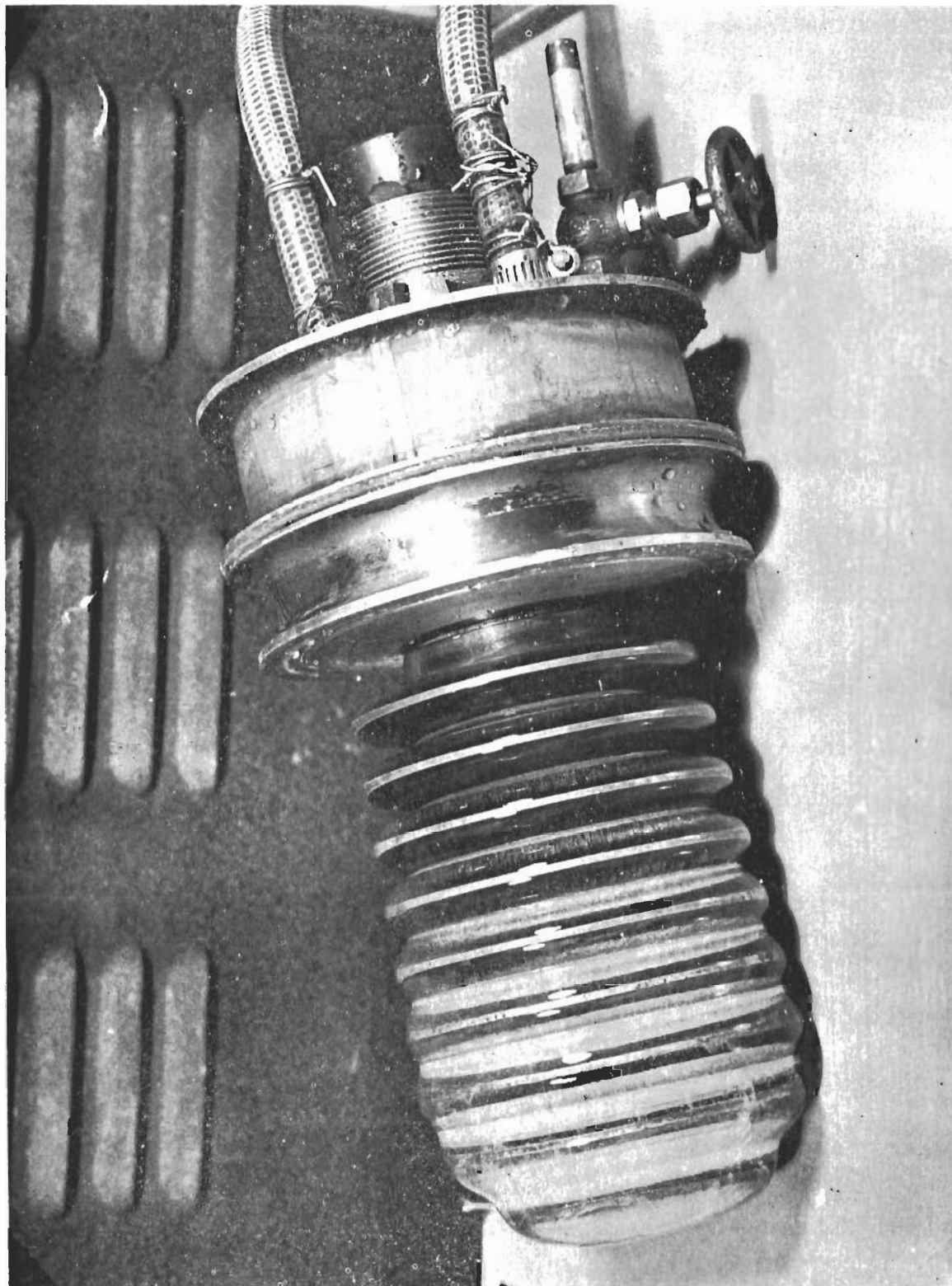


FIGURE 249-ICE MANTLE IN HEAT CAPACITY ICE CALORIMETER

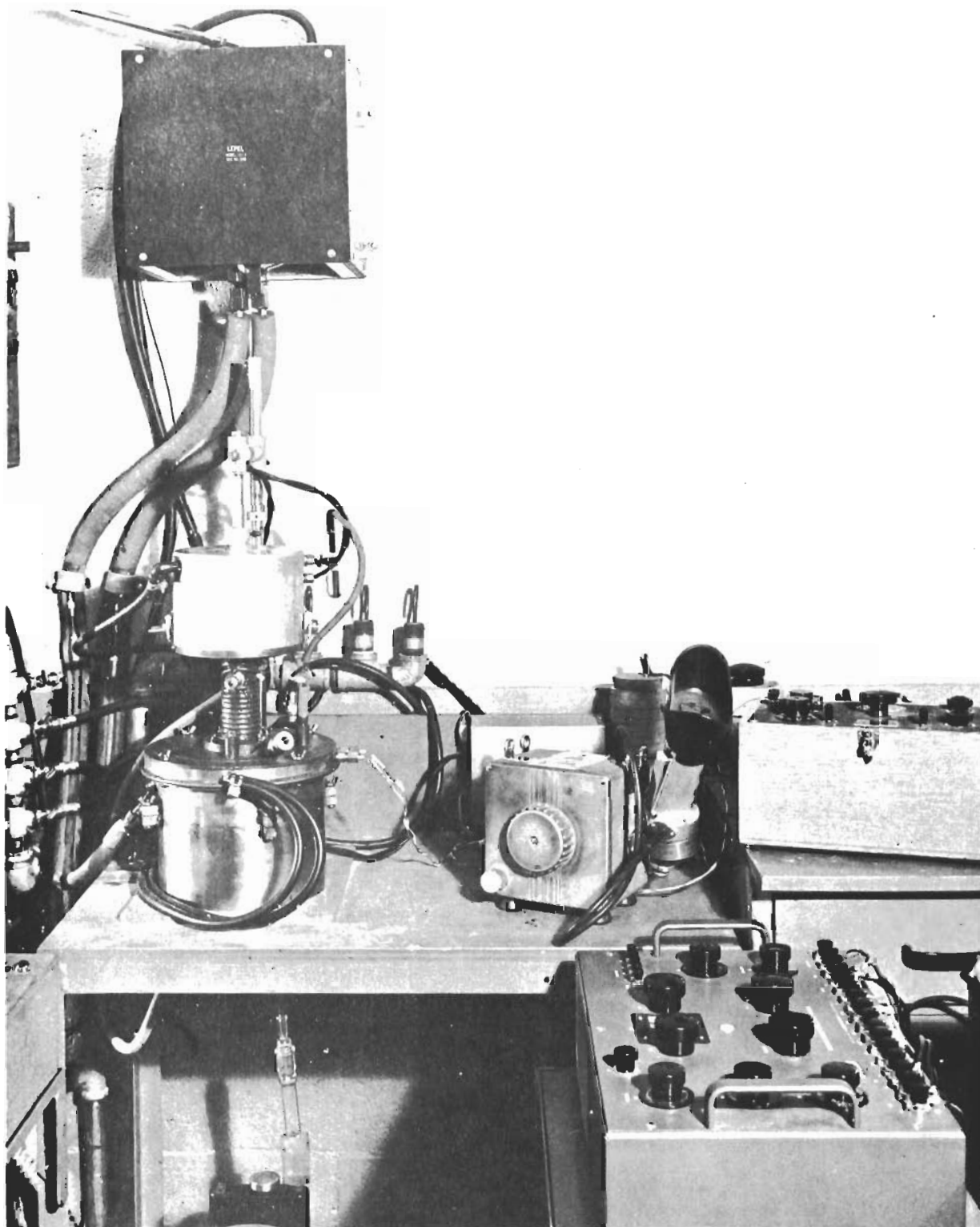


FIGURE 250-APPARATUS FOR MEASURING TOTAL NORMAL EMITTANCE

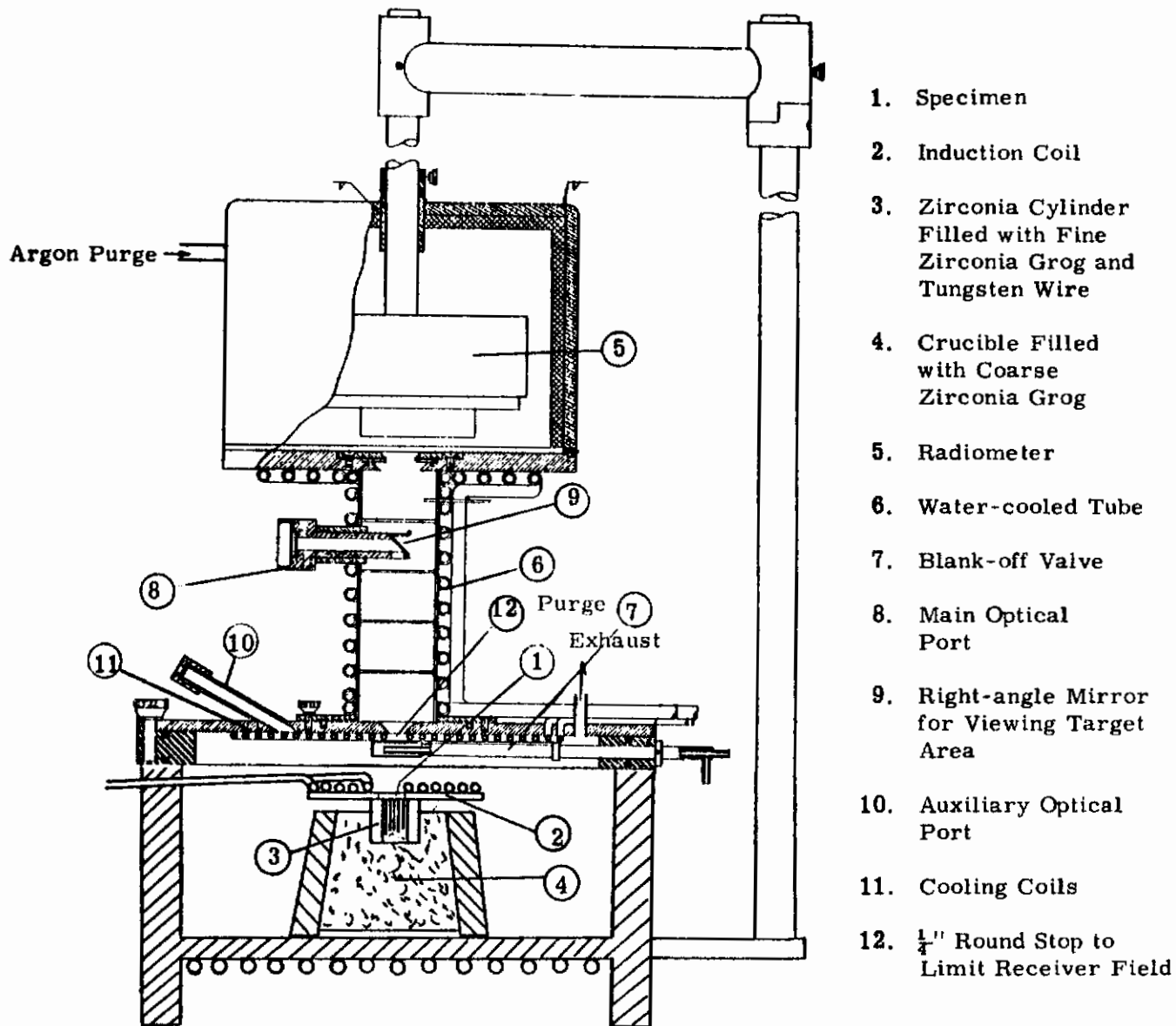


FIGURE 251-CROSS SECTION OF EMITTANCE APPARATUS WITH FLAT COIL FURNACE.

coil (2) by a zirconia cylinder filled with fine zirconia grog and tungsten wires (3). The zirconia cylinder rests on a crucible filled with coarse zirconia grog (4). The radiometer (5) views the specimen from directly above through a water cooled tube (6). A water cooled optical valve (7) is used to blank off the specimen from the radiometer. Optical temperature readings are taken through the main port (8), which may be pushed in to view the specimen through a mirror (9) from directly above. When radiometer readings are being taken, the main port is pulled out and away from the line of sight of the radiometer. Auxiliary port (10) is used to view the specimen directly as a check for the main port. Both viewing ports contain sapphire windows. The portion of the furnace above the specimen (11) is water cooled to eliminate any possibility of energy being reflected back onto the specimen surface. The emittance furnace is built of steel and sealed with O rings so that a vacuum may be attained.

The radiometer (Figure 252) was constructed according to Snyder (Reference 7) and Gier (Reference 8) with some modifications. The receiver element consists of approximately 160 turns of No. 40 AWG bare constantan wire (104 turns per inch) wound around a plastic insulator strip about 2 inches long x $1\frac{5}{8}$ inch wide x $\frac{5}{16}$ inch thick. Silver was electroplated in several stages onto the constantan coil so that two $\frac{1}{8}$ inch wide lines of silver-constantan junctions, $\frac{1}{2}$ inch apart, were formed on the same side of the coil and across all of the wire turns. The remainder of the entire coil was silver plated. Each of the two lines of junctions was covered with a thin, narrow strip of black paper. One of these junction lines is designated as the active or "hot" junction and is placed to receive energy from the sample. The other is shielded and termed the passive or "cold" junction.

In order to shield the element from extraneous radiation, a cylindrical housing is placed immediately around the thermopile. The front of the housing contains a rectangular opening $\frac{1}{4}$ inch by $1\frac{1}{2}$ inch to allow the element to "see" the specimen. The actual limiting of the receiver field is accomplished by this rectangular slit and the $\frac{1}{4}$ inch round stop (12) just above the specimen. Additional stops in the water cooled tube were installed as an added insurance to further minimize spurious reflections. The radiometer views the specimen directly. This eliminates the possibility of dirty lenses affecting the reading and, also, eliminates the spectral selectivity of the different types of materials used as windows.

The voltage generated by the receiver is measured with a Type K-3 Leeds and Northrup potentiometer in conjunction with an L&N Type 2430 DC galvanometer of 0.43 microvolts per millimeter deflection sensitivity. Temperatures are measured with a Leeds and Northrup portable potentiometer.

The receiver element was calibrated against a carbon-filament lamp of known radiation (Lamp No. C584, calibration by the National Bureau of Standards and reported in NBS Report 132737 A, July 1, 1952) and demonstrated a sensitivity of 8.66 Btu/hr/sq ft/millivolt.

The radiometer was also checked against an Eppley thermopile with 12 bismuth-silver junctions and a 1-mm quartz window and agreed within 10%

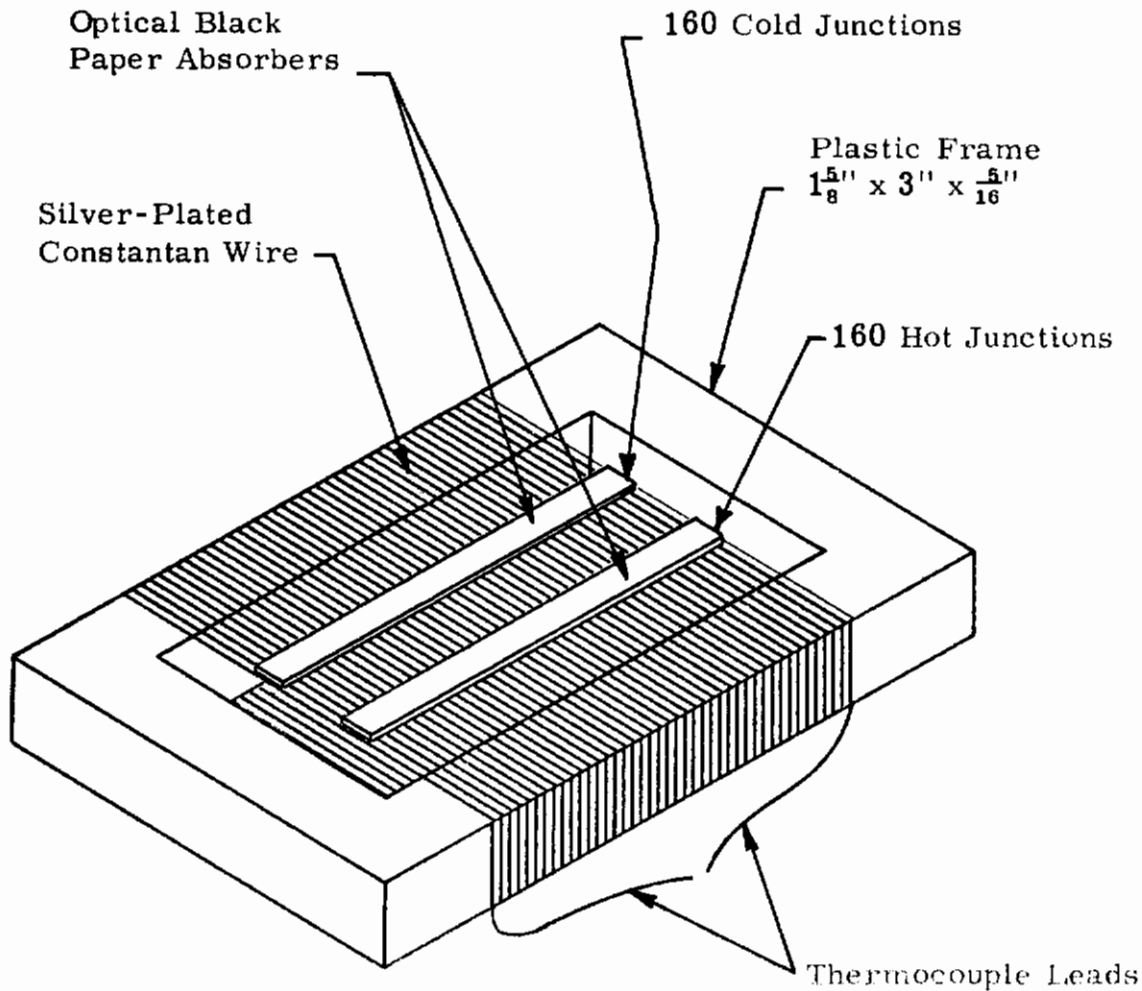


**FIGURE 252 - SCHEMATIC OF 160 - JUNCTION THERMOPILE
IN EMITTANCE EQUIPMENT.**

scatter of data points. By factory calibration the sensitivity of the Eppley thermopile is 0.048 microvolts/microwatt/sq cm.

The optical pyrometers used are I&N catalog type 8622 calibrated in accordance with the International Critical Table of 1948 for an emittance of unity.

Calibration Procedure

To calibrate the radiometer for blackbody radiation, a blackbody cavity with a 6 to 1 aspect ratio made from graphite was used. The blackbody cavity was insulated by zirconia grog and lampblack placed in the annulus between the blackbody and the load coil as shown in Figure 253.

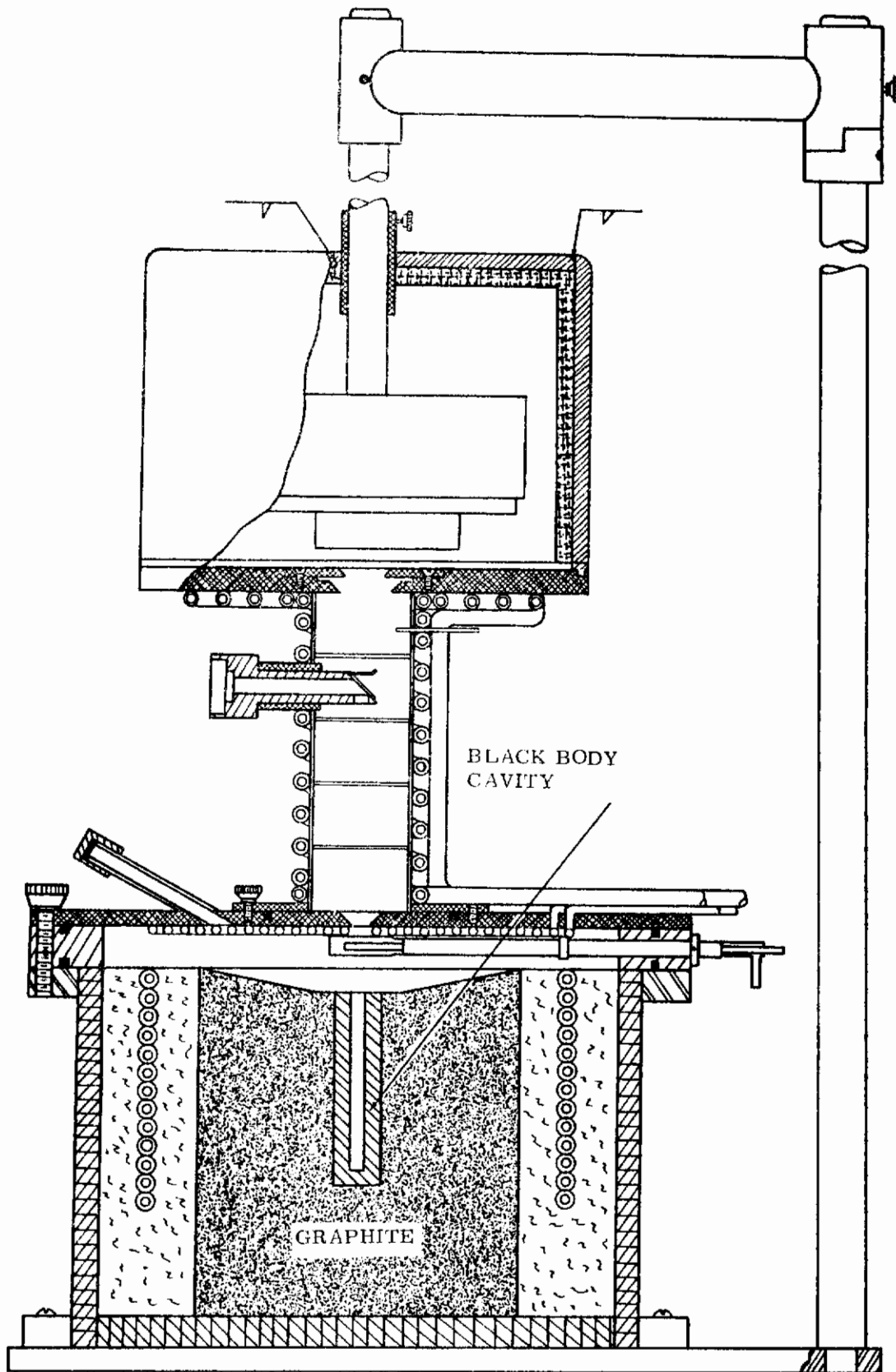


**FIGURE 253-CROSS SECTION OF
EMITTANCE APPARATUS WITH BLACK BODY FURNACE**

The accurate determinations of the specimen and blackbody temperatures are essential to good data. For the cavity-type blackbody, the temperatures are determined relatively easily by (1) thermocouples placed in the bottom of the cavity; (2) thermocouples dropped into the cavity; and (3) optical pyrometer observations. Up to 3000°F, agreement to within 15°F has been obtained regularly between these three readings. Above 3000°F the agreement between tungsten-rhenium couples and the optical pyrometer has been generally within 50°F or the repeatability of this type of thermocouple. Actually, the optical readings have no error other than those of the instrument calibration and the human error, which appears to provide a readout scatter of about 20°F at 4000°F.

Radiometer output versus temperature for blackbody radiation is plotted in Figure 254. Notice that the output is essentially linear from 2500°F to 5000°F with a slight curvature below 2000°F. As in house standards, the emittance of 304 stainless steel, tarnished tungsten, and graphite were measured (Figure 255). The emittance of the stainless steel ranged from 0.15 at 700°F to 0.67 at 2000°F. These values are in close agreement with the literature values. The sanded CS graphite also checked out closely with the literature with values from 0.95 to 0.98.

Operating Procedures

The specimen is placed directly on the surface provided by the zirconia tube, grog, and tungsten wires. However, if the material of interest cannot be heated inductively, tungsten and tantalum heating discs are placed under the specimen with the specimen in contact with the tungsten disc.

The furnace is then evacuated to 15 mm of Hg and filled with high-purity, dry argon. This operation is performed at least twice to assure an inert atmosphere. Throughout the run a slight pressure is maintained in the furnace by an argon purge, which is brought in through the radiometer enclosure and exhausted from the furnace housing as shown in Figure 251. In addition to maintaining an inert atmosphere, the purge flow tends to keep fumes away from the radiometer.

The temperature of the specimen is raised and maintained at the desired point by transferring energy to the specimen through the induction coil. About three hours are required to complete a single run with the temperature increasing stepwise but in uniform intervals. At each temperature level a radiometer reading is taken in conjunction with the temperature readings.

To obtain the radiometer reading, the following procedure is followed: As the specimen is heated, the blank-off valve is shut so that the thermopile can see no impulse. When the specimen temperature reaches steady state, a zero reading is obtained for the thermopile output. This reading is usually in the order of + 0.02 millivolts. The blank-off valve is then opened, and the thermopile output increases several fold in a few seconds. The reading levels off as heat is transferred down the wires to the cold junction. The radiometer output is taken at the peak reading immediately after steady state. The net reading for that temperature is then obtained as the difference between the zero and steady-state reading.

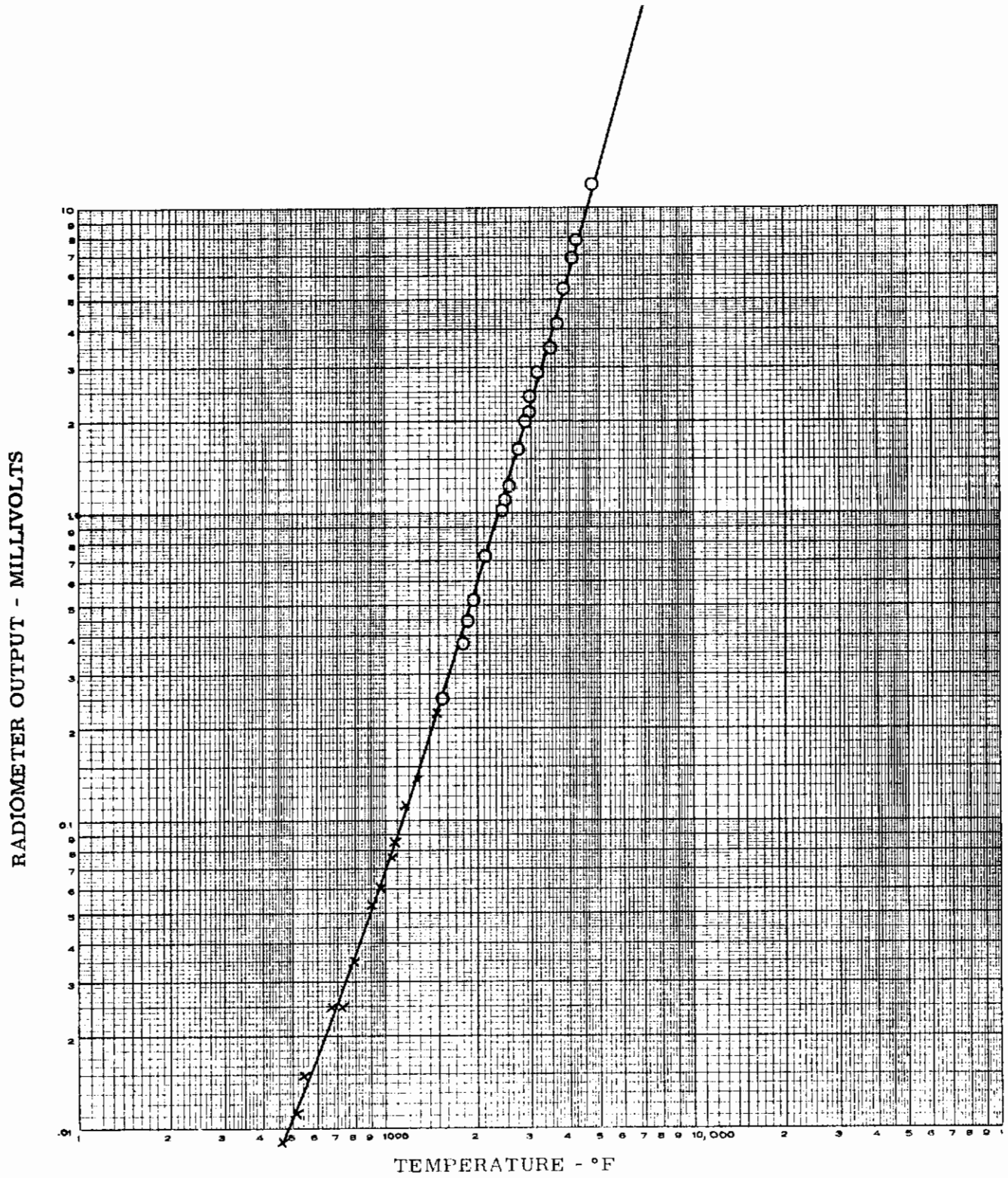


**FIGURE 254-RADIOMETER
OUTPUT vs TEMPERATURE FOR BLACK BODY RADIATION.**

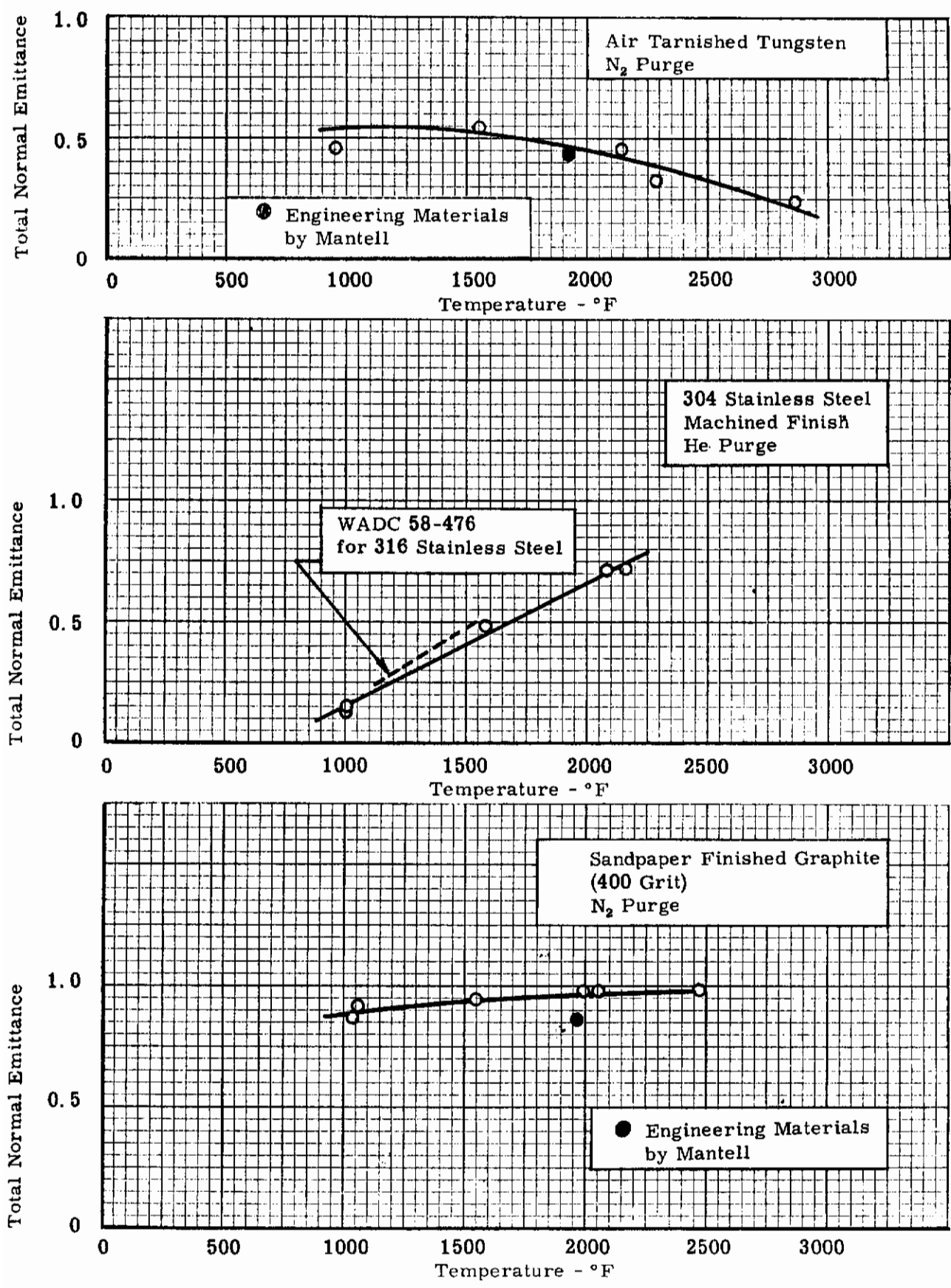


FIGURE 255-CALIBRATION STANDARDS FOR TOTAL NORMAL EMITTANCE

If the blank-off valve were left open, the thermopile output would decrease slowly with time. After about 10 minutes, this reading might decrease by 50%; however, if the blank-off valve were shut and a new zero reading obtained, the difference between this new output and zero reading would be about the same as the original readings. The variation might be about 5 to 10%. The shift in readings is a result of the heating of the cold junctions.

The purge to the radiometer housing has no influence on the readings within the ranges at which the purge is operated. To determine this limit, the purge rate was increased to about 10 times the normal metered reading, and a small shift in readings of less than 1% was noted.

The temperature of the specimen is monitored by (1) thermocouples mounted directly on the target surface (usually held in place by a small zirconia pad) and (2) optical pyrometer readings on the target surface. Low temperature readings were made with thermocouples; however, in the intermediate temperature range from 1600°F to 2700°F a cross check was made between the thermocouple readings and the optical readings. The high-temperature measurements are made with an optical pyrometer. A main-port optical and an auxiliary-port optical-temperature reading are taken at each temperature level. The auxiliary-port temperature is normally used only as a check; however, if conditions warrant, such as a dirty main-port window or mirror, the auxiliary-port value may be used. Usually very good agreement is maintained between the main-port and auxiliary-port optical readings.

Emittance Calculation

The optical temperature readings must first be corrected to obtain true temperatures. The main-port reading is corrected for the sapphire window and mirror while the auxiliary-port reading is corrected for the sapphire window and the angle at which the port views the specimen. The corrections are shown as curves in Figure 256.

After assuming an arbitrary-initial, emittance value, the brightness temperature is corrected for this assumed emittance (see Figure 257). The blackbody output is then read at this "true" temperature from Figure 254. The ratio of the observed specimen radiometer output to the blackbody output is calculated and is the emittance of the material at that temperature. If the assumed emittance is correct, the calculated value will agree with it; if not, the calculated value must be used as the former assumed value and the process repeated until the assumed emittance value agrees with the calculated value. This iterative process will converge on the correct emittance value assuming graybody distribution of most of the energy at the particular temperature. The above process was programmed for analysis by a digital computer.

Error Analysis

The above procedure for determining emittance is strictly correct only for those materials that radiate as graybodies, since the total emittance is assumed to be equal to the spectral emittance at the wavelength of the pyrometer. This approximation was used above to convert the brightness temperature to true temperature.

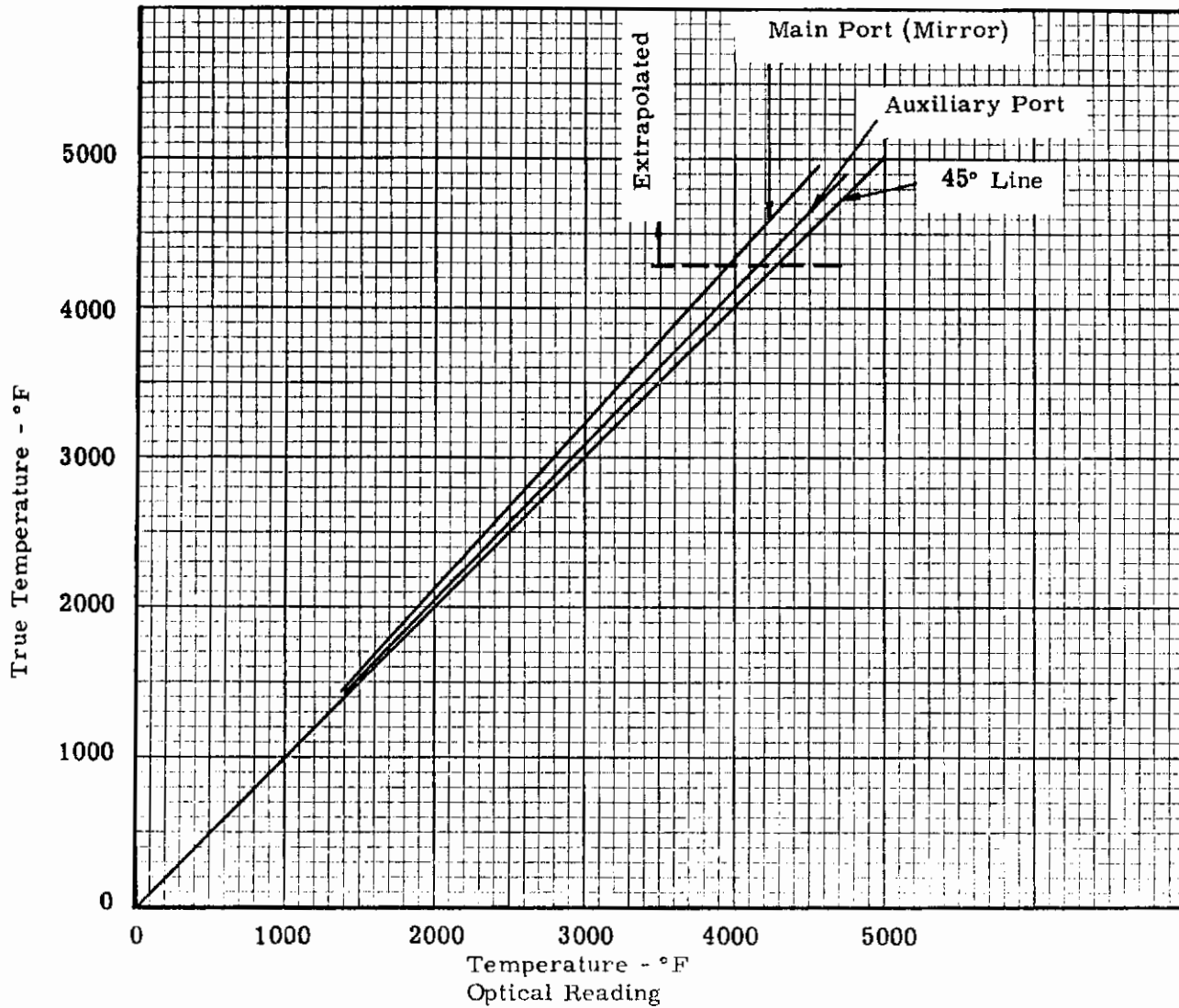


FIGURE 256—CORRECTION FOR MIRROR AND SAPPHIRE WINDOW IN EMITTANCE APPARATUS.

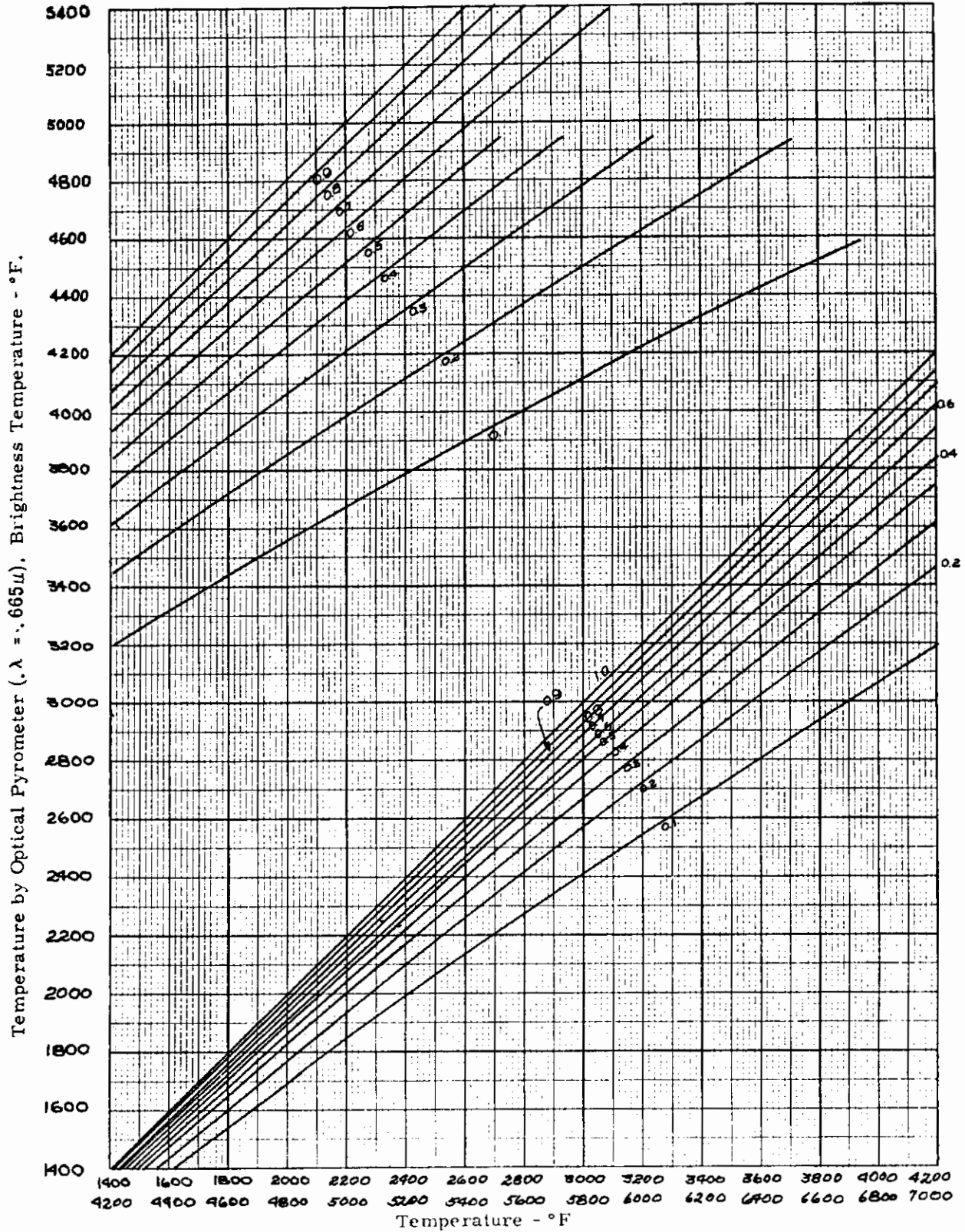


FIGURE 257-CORRECTION FOR BRIGHTNESS TEMPERATURE TO TRUE TEMPERATURE.

The error in emittance values for nongray materials will vary depending on the difference between the 0.665 microns spectral and the total emittance, and the distribution of radiant energy within the particular spectrum. If the deviation from graybody becomes very great at temperatures up to 2500°F, it is indicated by the thermocouple measurements. On materials of low emittance, such as tungsten, the emittance values calculated by this procedure could be in error by as much as 20% at the highest temperatures. However, it is believed that for most materials, the accuracy is within 10%. Several things indicate that the accuracy of the emittance values is good. First, the radiometer output versus temperature curves are orderly and almost linear with only normal data scatter. Second, the data obtained on two samples of the same material are in close agreement. Third, the values of emittance for the check samples agree very well with the literature (see Figure 255).

A statistical analysis of the data accuracy is of interest. Generally, the probable error in each blackbody reading is about 4%, and the probable error in each specimen reading is about 8%. If the data points are used to calculate emissivity, the maximum probable error would then be about 12%. The curve-fitting approach undoubtedly reduces this maximum to about 5%. As a general conclusion, the accuracy of the measuring system is well within the range of variation as is experienced by different finishes on the same material, the changing chemistry of the surface at the high temperatures, surface temperature measurements, and other variables.

3. THERMAL EXPANSION TO 5000°F

Thermal expansion is measured in a graphite tube dilatometer (Figure 258) developed by SRI for performance to 5000°F. The specimen required is about 3/4 inch in diameter and 3 inches long, although the exact size can vary somewhat if it appears desirable from the standpoint of specimen availability. Specimens 3/4 inch in diameter and only 1/4 inch thick can be evaluated, but with a reduced precision. Discs can be stacked to provide more length in many cases. Of course, specimens can always be pinned together from smaller pieces to provide both length and columnar strength.

In the dilatometer, the specimen rests on the bottom of the cylinder with a graphite extension rod resting on the specimen to extend to the top of the cylinder. When required, tungsten pads are inserted at the ends of the specimen to eliminate graphite diffusion from the dilatometer parts into the specimen. This entire assembly is inserted into a 5000°F furnace.

The motion of the specimen is measured by a dial gage attached to the upper end of the cylinder with the stylus bearing on the extension rod. The system accurately indicates total motions of 0.0001 inch - or less than 0.00004 inch per inch of specimen.

Graphite makes a good dilatometer tube and cylinder for operation up to over 5000°F. This material has good strength and known thermal properties. The apparatus has been calibrated against both graphite and "A" nickel. The major difficulty with dilatometer equipment is in unknown temperature

gradients. The long helix heater minimizes the possibility of gradients down the specimen, and the graphite calibration permits detection of any unknown gradients up to 5000°F. Actually, the errors resulting from temperature gradients are less than 1% and overall accuracy is to less than 5% error. Zero returns are regularly to within 0.0005 inch per inch out of 0.030 inch per inch travel.

SRI has designed, built, and calibrated the equipment to do this work. Data have been generated for many specimens including ATJ graphite, tungsten, carbides, borides, nitrides, oxides, and silicates. Materials have been carried to their destruction point of over 5100°F, and short excursions have been made to over 5300°F.

Either a helium or an argon environment can be employed. Nitrogen has been used on occasion. The equipment will permit operation at hard vacuums, but this procedure is rarely used.

4. RADIAL INFLOW APPARATUS FOR MEASURING THERMAL CONDUCTIVITY TO 5000°F

The thermal conductivity was determined using the larger SRI radial inflow apparatus designated and described as GFE in ASD TDR 62-765 with vacuum equipment as shown in Figures 259 and 260. The modified water calorimeter, shown in cross section in Figure 261, was used in which the normal 1/2 inch spacing of the thermocouples has been increased to one inch. This was done to increase the temperature change between the thermocouples and thereby to offset the reduced precision normally found for the low heat inflows associated with the low conductivity materials and larger specimens evaluated in this work.

Thermocouples were used to measure the radial gradient in the specimen at up to 2000°F. Above 2000°F, optical pyrometers were used. A cross section drawing of the furnace and specimen is shown in Figure 262.

To provide the required pressure levels of 760 mm, 10 mm, 1 mm, 0.1 mm, and 0.001 mm, a Welsh mechanical vacuum pump of 15 cfm capacity was used in conjunction with a National Research Corporation HS4-750 diffusion pump. No major difficulty was experienced in attaining and holding the required pressure levels at temperatures below 3000°F. However, at temperatures over 3000°F, particularly for the aluminas, the rate of outgassing of the specimen imposed the limit on the pressures attainable. No serious problem was encountered with the graphite furnace parts at the temperature and pressure levels investigated; the outgassing of the graphite was in every case much less than that of the specimen.

The remainder of the equipment consisted primarily of a recirculating water system for the calorimeter and gages for monitoring system pressure. Two types of vacuum gages were used, depending on the pressure level; first, a Dubrovin gage for the higher pressures of 10 mm and 1 mm, and, second, a Cenco 94156 McLeod gage for the lower pressures.

The specimen configuration, as shown in Figure 263, consisted of a cylinder 2-1/2 inches outside diameter by 3/4 inch inside diameter by 3 inches long, with six holes or wells for temperature measurement. A photograph of a typical specimen is shown in Figure 264. The specimen was placed in the

furnace between graphite cylinders filled with thermanomic carbon. These cylinders acted as guards to minimize axial heat flow and to maintain a constant radial temperature gradient within the specimen. The top cylinder was fitted with graphite sight tubes aligned with the temperature wells in the specimen.

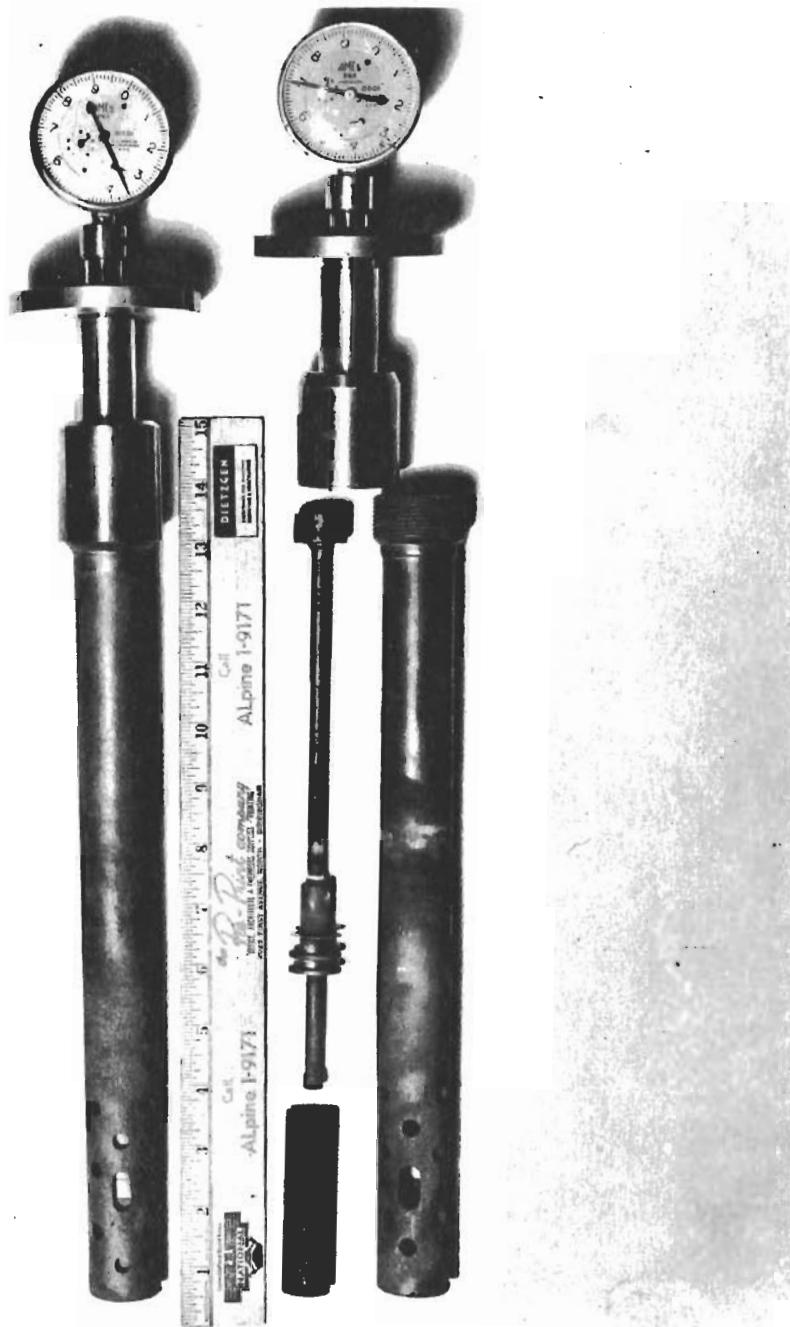


FIGURE 258—GRAPHITE DILATOMETER TUBES FOR MEASURING THERMAL EXPANSION TO 5000°F

Text continued on page 331

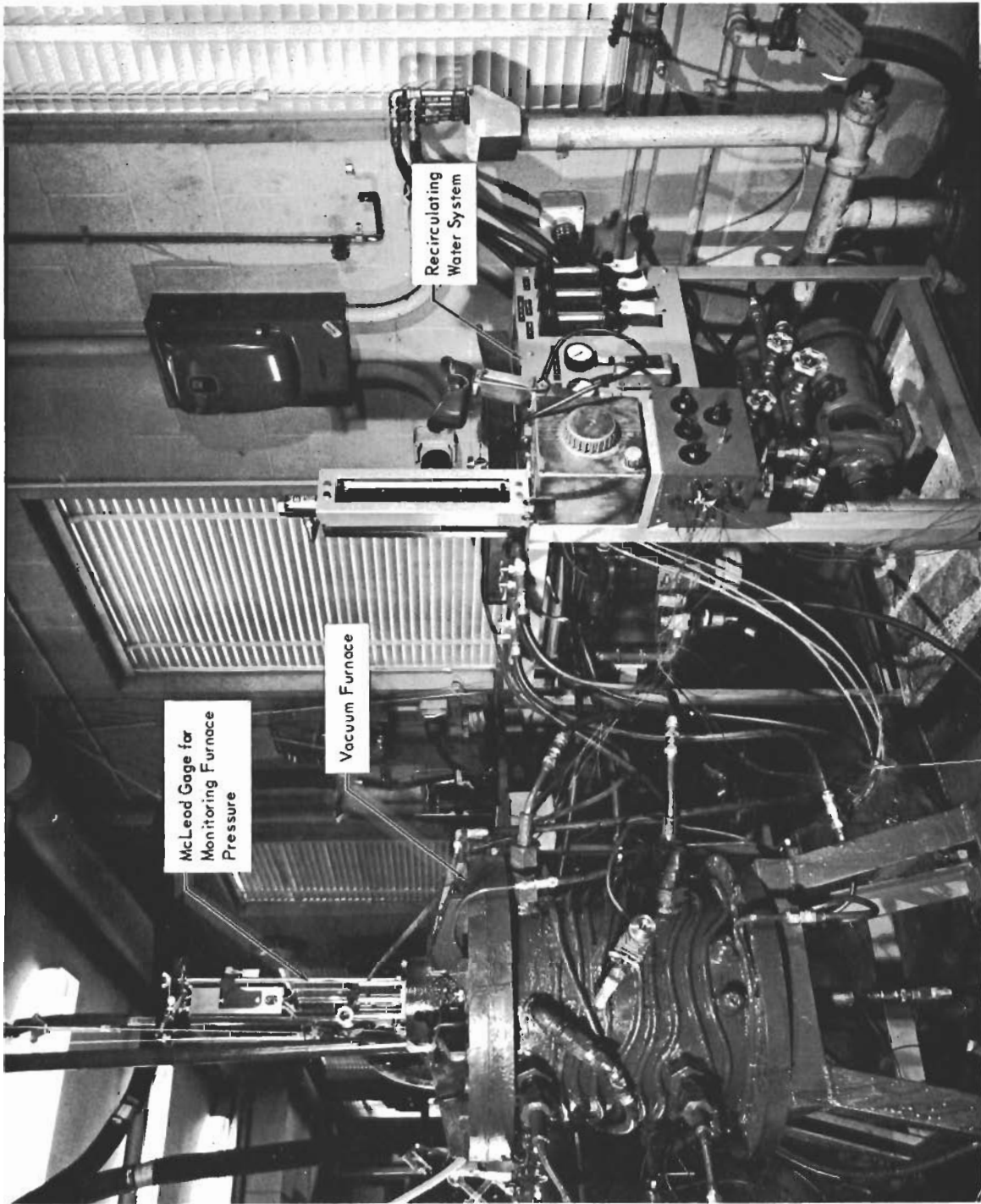


FIGURE 259—RADIAL INFLOW THERMAL CONDUCTIVITY APPARATUS

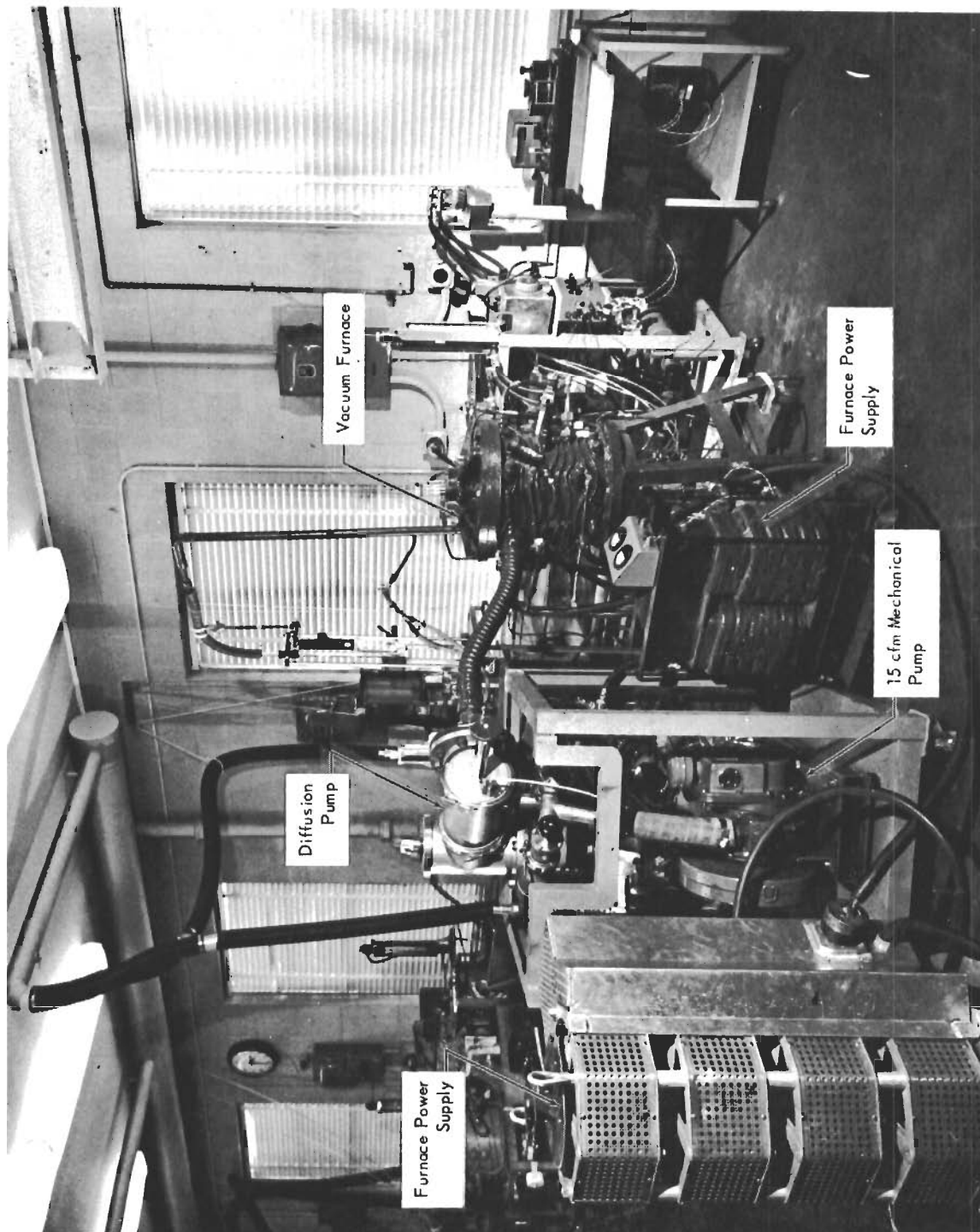


FIGURE 260--RADIAL INFLOW THERMAL CONDUCTIVITY APPARATUS

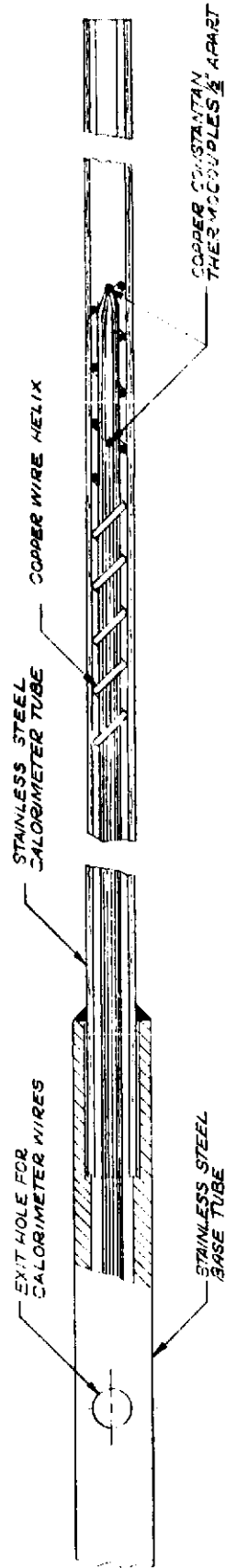
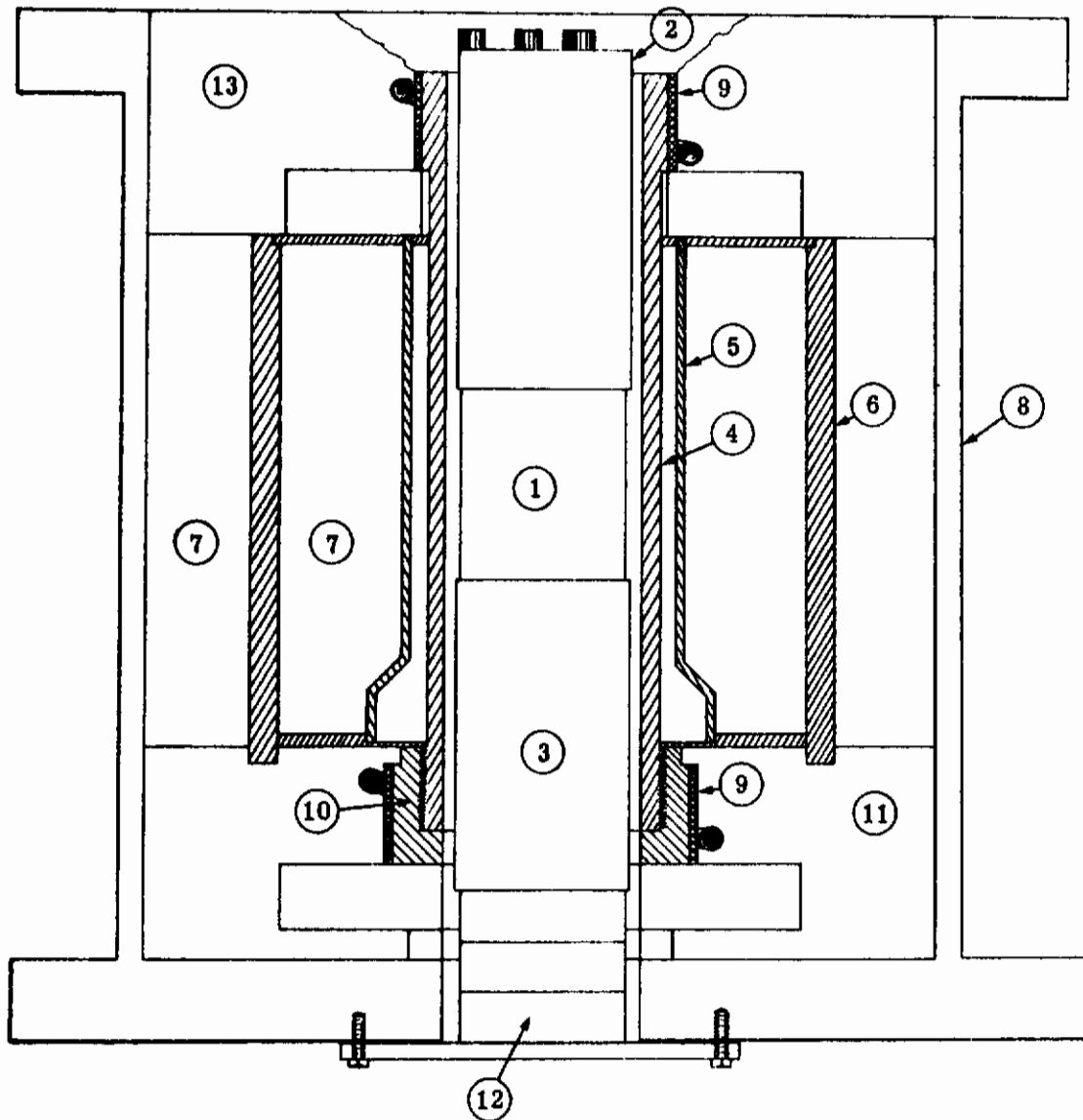
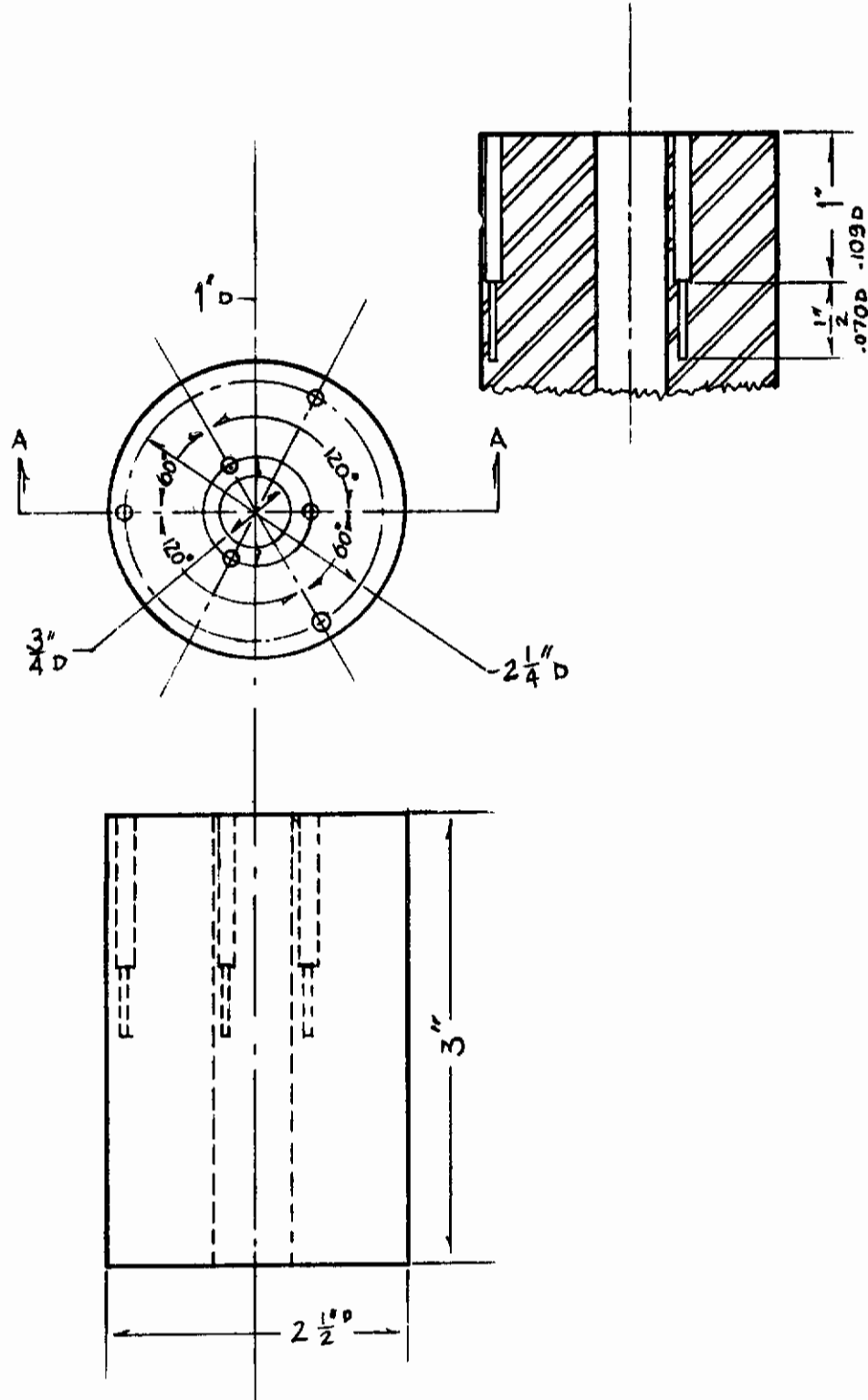


FIGURE 261—CROSS SECTION OF WATER CALORIMETER



1. Specimen
2. Graphite cylinder fitted with 6 graphite sight tubes aligned with holes in specimen
3. Bottom guard cylinder and specimen support
4. Graphite heater tube
5. Inner graphite liner
6. Outer graphite liner
7. Annulus filled with Thermatomic carbon insulation
8. Steel furnace shell
9. Copper water cooled electrodes
10. Graphite electrode insert threaded to accept heater tube
11. Zirconia grog insulation
12. Alsimag spacers
13. Fiberfrax

FIGURE 262—CROSS SECTION OF VACUUM FURNACE FOR DETERMINATION OF THERMAL CONDUCTIVITY



**FIGURE 263—THERMAL CONDUCTIVITY SPECIMEN FOR
RADIAL INFLOW APPARATUS**

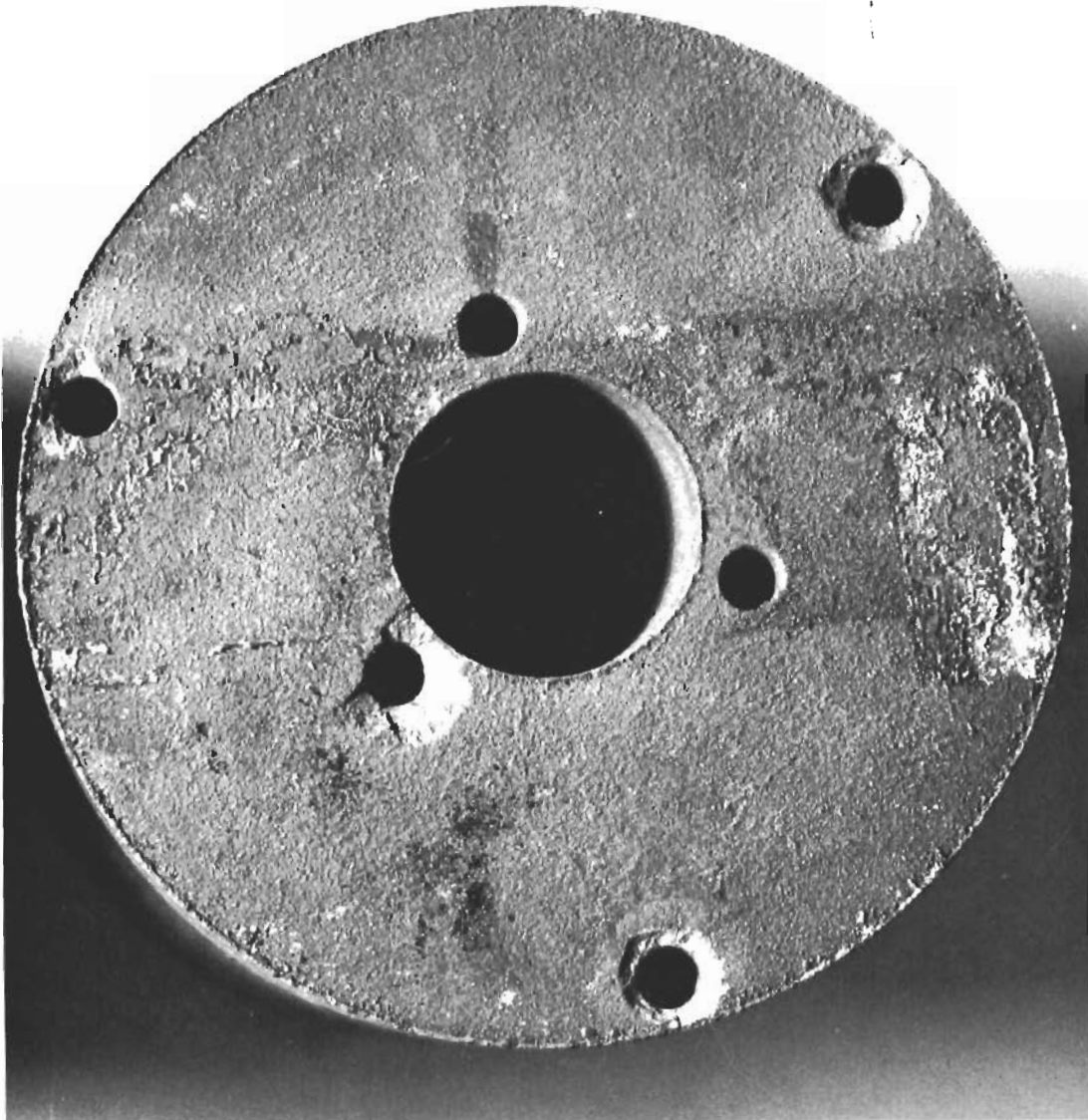


**FIGURE 264—SPECIMEN USED FOR DETERMINATION OF THERMAL
CONDUCTIVITY IN THE RADIAL INFLOW APPARATUS**

The annulus between the specimen and the calorimeter was packed to provide a medium for heat transfer from the inside diameter of the specimen to the outside diameter of the calorimeter tube. The packing material used was either graphite lathe dust or sifted zirconia grog. The graphite dust was used at the lower temperatures to provide the maximum heat flow and the zirconia was used at the higher temperatures to reduce the heat flow to prevent swamping of the calorimeter and to reduce the temperature gradient so that a higher mean temperature could be obtained. The packing material also acted as a centering medium. For the more porous specimens a graphite liner was pressed into the specimen to prevent the fine packing dust from filling the pores near the inside diameter. In some instances, the pores were so continuous that the dust would have filled the temperature measuring wells.

During a run the following data were recorded: (1) power input, (2) specimen outer face temperature, (3) temperature in each of the six temperature wells in the specimen, (4) temperature of the water in the calorimeter at two points 1 inch apart axially within the specimen center, (5) the flow rate of the water through the calorimeter, and (6) furnace pressure. Several readings (four to six) were made at each general temperature range to establish data scatter, to eliminate the error due to stray points, and to confirm the proper influence of water flow rates through the calorimeter.

All thermocouple readings were measured on either a Leeds and Northrup K-2 or K-3 type null-balance potentiometer used in conjunction with a galvanometer of 0.43 microvolts per mm deflection sensitivity. All optically measured temperatures were read on a Leeds and Northrup type 8622 optical pyrometer. The flow rate of the water was measured with a Brooks Instrument Company flowmeter.

The thermal conductivity values were computed from the standard relation of:

$$K = \frac{Q l}{A \Delta t} \quad (1)$$

where Q was the heat flow to the calorimeter within the specimen gage section and was calculated from the relation,

$$Q = M C \Delta t_w \quad (2)$$

in which:

- M = flow rate of the water, lb/hr
- C = specific heat of the water (taken as 1 Btu/lb/°F)
- Δt_w = temperature rise of the water as it passed through the 1 inch gage section, °F

Also, in the equation for calculating the thermal conductivity:

- Δt = temperature drop across the specimen gage length, °F (taken as the temperature difference between the average of the inner and outer temperature wells)
- l = specimen gage length, (0.625 inch)
- A = the log mean area through which the Q was flowing (0.03363 ft²)

A sample calculation follows:

- H₂O flow = 6.8 gph
- H₂O Δt = 2.27 °F
- T mean = 327 °F
- Specimen t = 258 °F

Solving for Q gives:

$$Q = MC\Delta t_w = \frac{(6.8) \text{ gal} (8.33) \text{ lb} (1) \text{ Btu} (2.27)^\circ\text{F}}{\text{hr} \quad \text{gal lb } ^\circ\text{F}}$$

$$Q = 128.6 \text{ Btu/hr}$$

Solving for K gives:

$$K = \frac{Q l}{A \Delta t} = \frac{(128.6) \text{ Btu} (0.625) \text{ in.}}{\text{hr} (0.03363) \text{ ft}^2 (258)^\circ\text{F}}$$

$$K = 9.26 \text{ Btu/hr/ft}^2/^\circ\text{F/in.}$$

The mean temperature at each point was taken as the average of the hot and cold hole averages when the temperatures in the holes were measured with thermocouples and known to be true temperatures. When the hole temperatures were measured with an optical pyrometer, some losses were present due to the small hole diameter and the length of the sight path. As a result, it was necessary to calculate the mean temperature at the diameter of the log mean area. This was accomplished by equating the heat flow through that section of the specimen extending from the log mean radius between the temperature holes and the outer face to the heat flow through that section between the two temperature measuring holes. The solution of this equation yielded the equation:

$$T_{\text{mean}} = T_{\text{OF}} - 0.60 \Delta t \tag{3}$$

where

- T_{OF} = outer face temperature of the specimen, °F
- Δt = temperature differential between the two specimen temperature holes, °F

At the mean temperature of 2000°F it was necessary to vary the standard procedure somewhat. At this mean temperature the temperature in the outer holes was above the serviceable limit of the chromel-alumel thermocouples used. Also, the temperatures in the inner specimen holes were lower than could be read accurately with an optical pyrometer. The specimen temperature gradient was determined from the difference in the outer face temperature of the specimen read with an optical pyrometer through the calibrated port and the specimen inner hole temperatures read with thermocouples. Both of these sites provided readings that were absolute and not relative. This procedure increased the specimen gage length to 0.75 inches and increased the log mean area to 0.03571 ft². The calculation of the thermal conductivity was then made as explained previously. No difficulties were encountered using this technique, and good agreement was obtained with the data at the adjacent temperature levels found using the standard procedures.

The radial inflow data was extended to the top temperatures by calculating the temperature losses in the temperature measuring holes and using the section of the specimen between the outer face of the specimen and the outer temperature hole as the gage section. To apply the correction, the temperature loss was added to the experimentally measured temperature of the outer hole, and this adjusted hole temperature was subtracted from the outer face temperature to obtain a Δt. This method for obtaining a higher mean temperature was only partially successful.

Error Analysis

A calculation of the uncertainty in the thermal conductivity was made using the variables in the equation for the thermal conductivity and the following relation:

$$e_k = \left[\left(\frac{\partial k}{\partial m} e_m \right)^2 + \left(\frac{\partial k}{\partial \Delta t_w} e_{\Delta t_w} \right)^2 + \left(\frac{\partial k}{\partial \Delta t_s} e_{\Delta t_s} \right)^2 + \left(\frac{\partial k}{\partial \Delta l} e_{\Delta l} \right)^2 + \left(\frac{\partial k}{\partial g} e_g \right)^2 \right]^{\frac{1}{2}}$$

which can be reduced to the dimensionless form:

$$\frac{e_k}{k} = \left[\left(\frac{e_m}{m} \right)^2 + \left(\frac{e_{\Delta t_w}}{\Delta t_w} \right)^2 + \left(\frac{e_{\Delta t_s}}{\Delta t_s} \right)^2 + \left(\frac{e_{\Delta l}}{\Delta l} \right)^2 + \left(\frac{e_g}{g} \right)^2 \right]^{\frac{1}{2}} \quad (4)$$

where

- e = error in the particular quantity denoted by the subscript
- k = thermal conductivity
- m = mass flow rate of the water through the calorimeter, lb/hr
- Δt_w = t of the water between the two calorimeter thermocouples, °F
- Δt_s = temperature gradient across the specimen gage length, °F
- Δl = specimen gage length, inches
- g = gage length of the calorimeter thermocouples, inches

For a randomly selected set of data and using the errors in the individual variables as shown:

- $m = 56.6$ lb/hr, obtained from a flowmeter which can be read to 0.1 gal/hr or an uncertainty of about 0.83 lb/hr
- $\Delta t_w = 10.62^\circ\text{F}$, obtained from thermocouples with an uncertainty of about 0.005 millivolts or for the water temperatures involved about 0.22°F
- $\Delta t_s = 1393^\circ\text{F}$, obtained from optical pyrometer readings to within about 20°F
- $\Delta l = 0.625$ inch, obtained from micrometer readings to about 0.005 inch
- $g = 1.000$ inch, the gage length of the calorimeter accurate to within 0.010 inch

The uncertainty in the thermal conductivity was found to be:

$$\frac{ek}{k} = 0.032 = 3.2\% \quad (5)$$

This value of uncertainty of 3.2% is considerably lower than the probable error of 6.82% calculated from the standard deviation of the McDonnell zirconia as shown in Table XXXI. At the higher temperatures the sintering of the specimen with the accompanying gage length changes probably introduced more scatter, thereby increasing the standard deviation and the observed probable error. The value of the 6.82% probable error agrees well with similar analyses made for data obtained recently here in other programs.

A more detailed discussion of the error analysis of the thermal conductivity is contained in Reference 9.

5. A COMPARATIVE ROD APPARATUS FOR MEASURING THERMAL CONDUCTIVITY TO 1500°F

The SRI comparative rod apparatus (Figures 265 and 266) is used to measure thermal conductivities of a wide variety of materials from -300°F to 1500°F . This apparatus consists basically of two cylindrical reference pieces of known thermal conductivity stacked in series with the cylindrical specimen. Heat is introduced to one end of the rod, composed of the references and specimen, by a small electrical heater. A cold sink or heater is employed at the opposite end of the rod as required to maintain the temperature drop through the specimen at the preferred level. Cylinders of zirconia may be inserted in the rod assembly to assist in controlling the temperature drop. Radial losses are minimized by radial guard heaters surrounding the rod and consisting of three separate coils of 26 gage Kanthal wire wound on a 2 inch diameter alumina core. The annulus between the rod and the guard heaters is filled with diatomaceous earth. Surrounding the guard is an annulus of diatomaceous earth enclosed in an aluminum shell.

TABLE XXXI
THE PROBABLE ERROR THAT CAN BE ANTICIPATED IN THE THERMAL
CONDUCTIVITY /DATA OBTAINED IN THE RADIAL INFLOW APPARATUS

Curve Value	Data Point	Deviation of Data Point from Curve	Percent Deviation from Curve	Percent Deviation Squared
9.7	9.9	+0.2	+2.06	4.4.24
9.7	9.8	+0.05	+0.51	0.26
9.9	9.6	-0.3	-3.03	9.18
11.6	9.3	-2.3	-19.82	392.83
11.7	9.1	-2.6	-22.22	493.73
11.7	9.2	-2.5	-21.36	456.25
11.7	8.8	-2.9	-24.78	614.05
10.7	10.4	-0.3	-2.80	7.84
10.6	9.6	-1.0	-9.43	88.92
10.7	10.0	-0.7	-6.54	42.77
10.3	9.8	-0.5	-4.85	23.52
12.5	14.2	+1.7	+13.60	184.96
12.6	14.3	+1.7	+13.49	181.98
12.6	14.8	+2.2	+17.46	304.85
12.7	14.8	+2.1	+16.53	273.24
3.7	4.2	+0.5	+13.51	182.52
3.7	4.2	+0.5	+13.51	182.52
3.7	4.0	+0.3	+8.10	65.61
3.7	4.0	+0.3	+8.10	65.61
4.9	5.1	+0.2	+4.08	16.65
4.9	5.0	+0.1	+2.04	4.16
4.9	4.9	0.0	0.00	0.00
4.9	5.0	+0.1	+2.04	4.16
4.9	4.9	0.0	0.00	0.00
7.2	7.4	+0.2	+2.77	7.67
7.2	7.4	+0.2	+2.77	7.67
7.2	7.3	+0.05	+0.68	0.46
7.2	7.3	+0.05	+0.68	0.46
9.2	8.6	-0.6	-6.52	42.51
9.2	8.7	-0.5	-5.43	29.48
9.2	8.5	-0.7	-7.60	57.76
9.3	8.6	-0.6	-6.45	41.60
10.7	11.4	+0.7	+6.54	42.77
10.7	11.5	+0.8	+7.47	55.80
10.7	11.7	+1.0	+9.38	87.24
10.7	11.4	+0.7	+6.54	42.77
13.4	12.9	-0.5	-3.73	13.91
13.5	12.7	-0.8	-5.92	35.05
13.5	12.7	-0.4	-3.05	9.30
13.4	14.0	+0.6	+4.47	19.98
13.5	13.7	+0.2	+1.48	2.19

$$\Sigma X^2 = 4096.47$$

$$\text{Standard deviation} = \sqrt{\frac{\Sigma X^2}{n-1}}$$

$$= \sqrt{\frac{4096.47}{40}}$$

$$= 10.11\%$$

$$\text{Probable error} = 0.6745 \text{ Standard deviation}$$

$$= 6.82\%$$

1. Basic data is the thermal conductivity at temperature ordinates.
2. Data used were for McDonnell low density zirconia at 760 mm.

The specimens and references (see Figure 267) are 1 inch diameter by 1 inch long. Thermocouples located 3/4 inch apart in radially drilled holes measure the axial temperature gradients. Thermocouples located at matching points in each guard heater are used to monitor guard temperatures, which are adjusted to match those at corresponding locations in the test section.

In operation, the apparatus is turned on and allowed to reach steady state. The guard and rod heaters are adjusted to minimize radial temperature gradients between the rod and guard sections consistent with maintaining equivalent functions of K_r times T in the references. Temperatures are measured on an I&N Type K-3 potentiometer, and the temperature gradients calculated. A typical temperature profile in the test section is shown in Figure 268.

The thermal conductivity of the specimen is calculated from the relation:

$$K_S = \frac{K_1 \Delta T_1 + K_2 \Delta T_2}{2} \frac{\Delta X_S}{\Delta X_R} \quad (6)$$

where K_1 and K_2 are the thermal conductivities of the upper and lower references; ΔT_1 , ΔT_2 , and ΔT_S are the temperature gradients in the upper and lower references and specimen, respectively; ΔX_S and ΔX_R are the distances between thermocouples in the specimen and references.

Note that for purely axial heat flow, the products $K_1 \Delta T_1$ and $K_2 \Delta T_2$ should be equal. Due to imperfectly matched guarding and other factors, this condition is seldom attained in practice; therefore, the average of the two values is used in the calculations. Their difference is maintained as small as possible, usually within 5% of the smaller.

For identical specimens, the ratio $\Delta X_S / \Delta X_R$ should be unity but may vary due to the uncertainty in hole locations. To prevent introducing an additional error in calculations, ΔX is determined as follows: The depth of the hole is measured by inserting a snugly fitting drill rod in the hole, measuring the projecting length and subtracting it from the total length of the rod. The slope, or angle the hole makes with the perpendicular to the specimen axis, is determined by making measurements to the face of the hole and the outer end of the drill rod with respect to a datum plane, using a dial gage. From these measurements, the location of the bottom of the hole can be calculated.

For reference materials, Armco iron or copper are used with high conductivity specimens, 316 stainless steel with specimens of intermediate conductivities, and teflon, Pyroceram 9606, or pyrex with low conductivity specimens. Extensive calibration of the apparatus, using these reference materials as standards, has yielded accuracies to about 5% error, when sufficient care is exercised to maintain closely matched temperatures between the guard and test sections. Even with careless matching, the error is only about 10% so the system is not particularly sensitive to minor imbalances.

To establish the accuracy of the apparatus some initial runs were made on 316 stainless steel, using Armco iron as the reference. The data, shown in Figure 269, are somewhat higher than those reported by Lucks and Deem

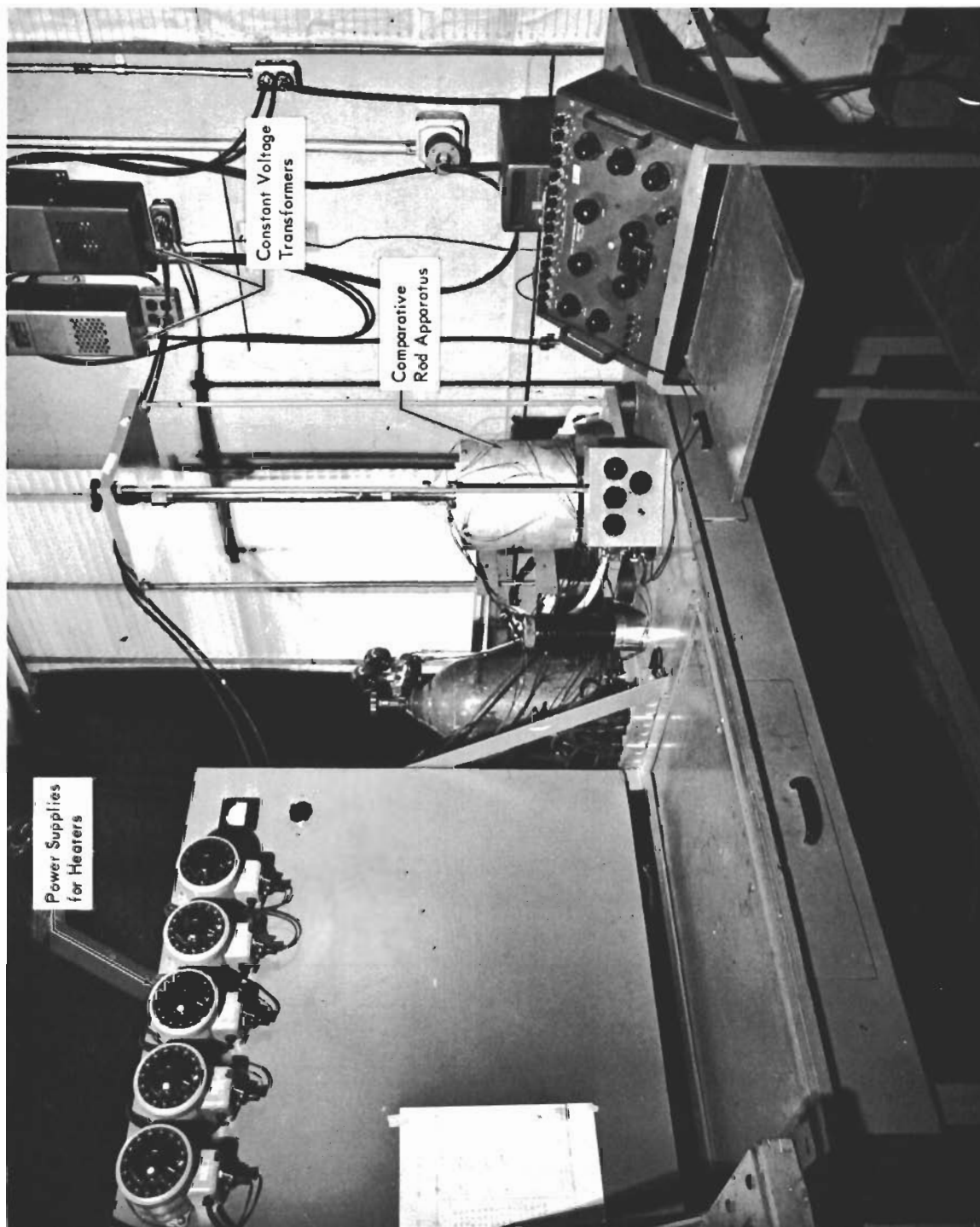


FIGURE 265—COMPARATIVE ROD THERMAL CONDUCTIVITY APPARATUS

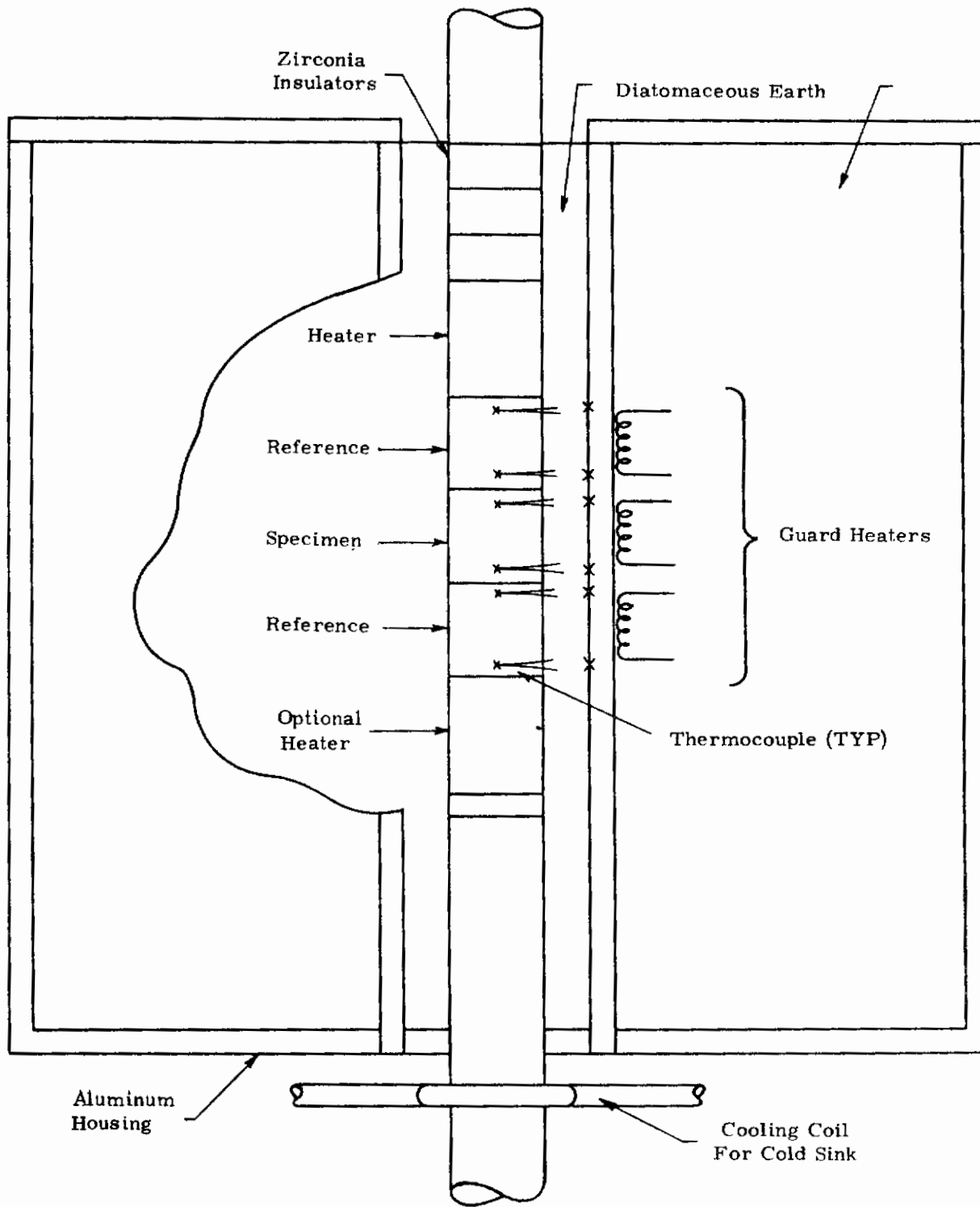
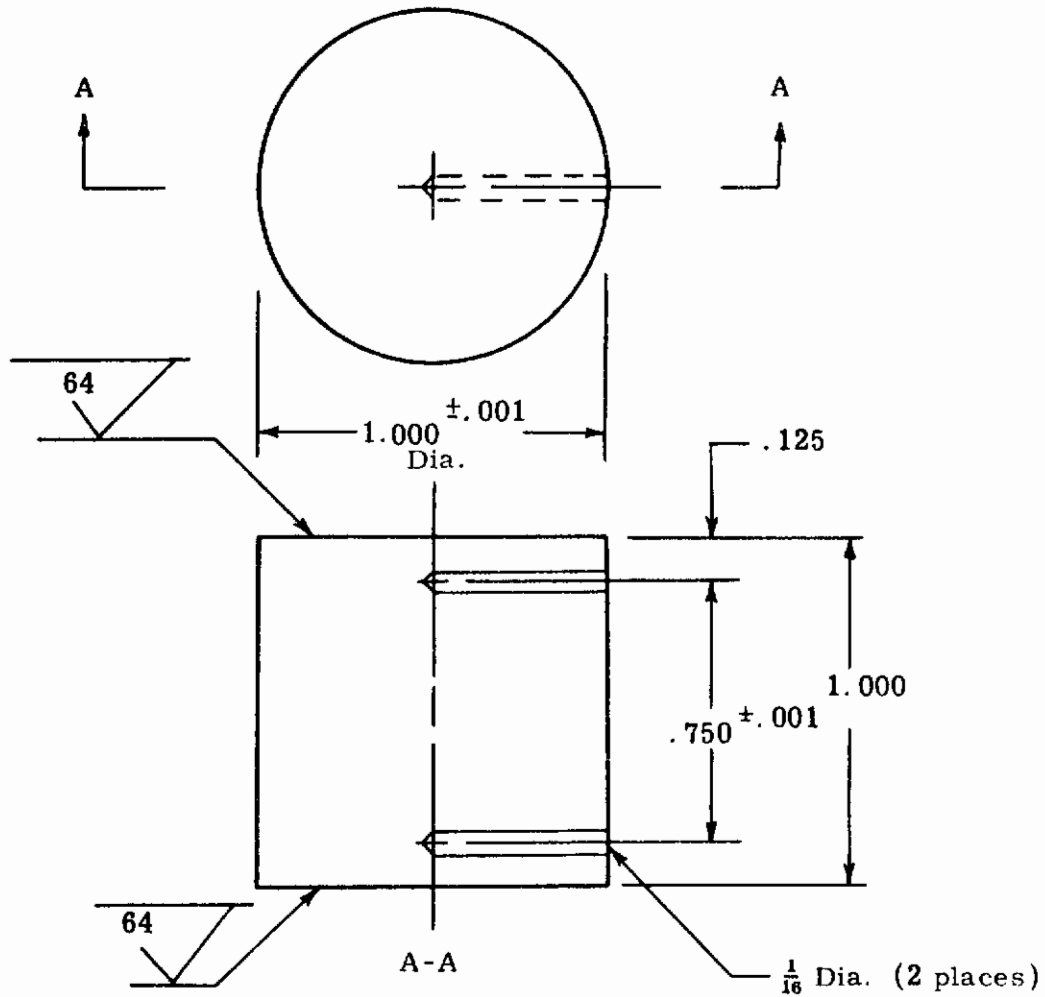


FIGURE 266—SCHEMATIC OF COMPARATIVE ROD THERMAL CONDUCTIVITY APPARATUS



- Notes: 1. Tolerances $\pm .003$ unless otherwise noted.
 2. Upper and lower surfaces to be flat and \perp specimen \varnothing_L within .001 TIR.

FIGURE 267—SPECIMEN CONFIGURATION FOR COMPARATIVE ROD THERMAL CONDUCTIVITY APPARATUS

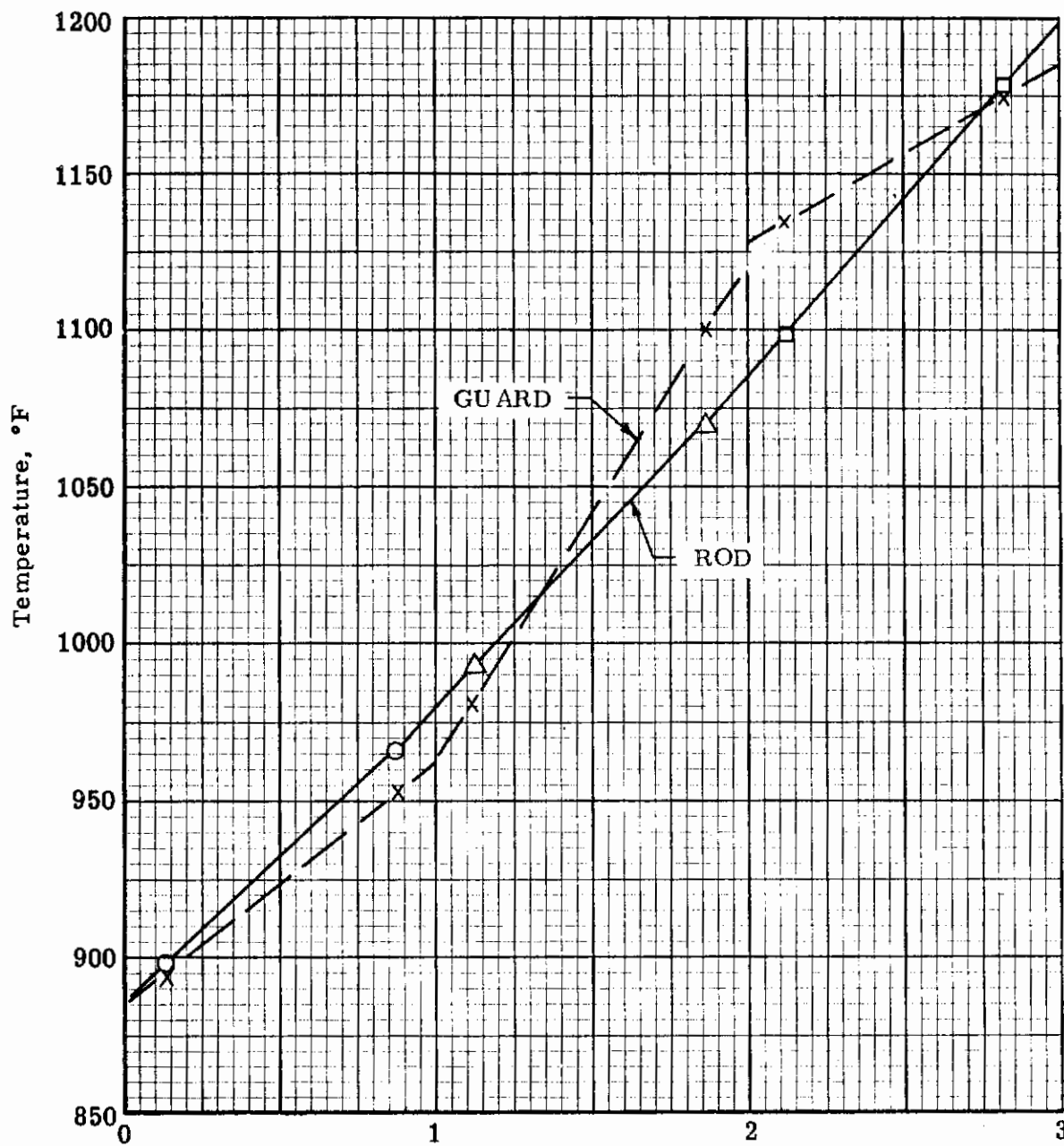


FIGURE 268—TYPICAL TEMPERATURE PROFILE IN TEST SECTION

(Reference 10), but agree well with values reported by several steel manufacturers. Note that the data scatter is less than 5%. The data on stainless steel were confirmed by evaluating Armco iron, using 316 stainless steel as reference. These data are shown in Figure 270 in comparison with values reported by Powell (Reference 11), who compiled his curve from the data of numerous investigators, and estimated its accuracy to be within $\pm 2\%$ over the range from 0° to 1000°C . The comparative rod data for Armco iron, which were computed using the solid curve of Figure 269 for the thermal conductivity of the stainless steel reference, agree with Powell's data within 5%, thus confirming the data obtained for stainless steel.

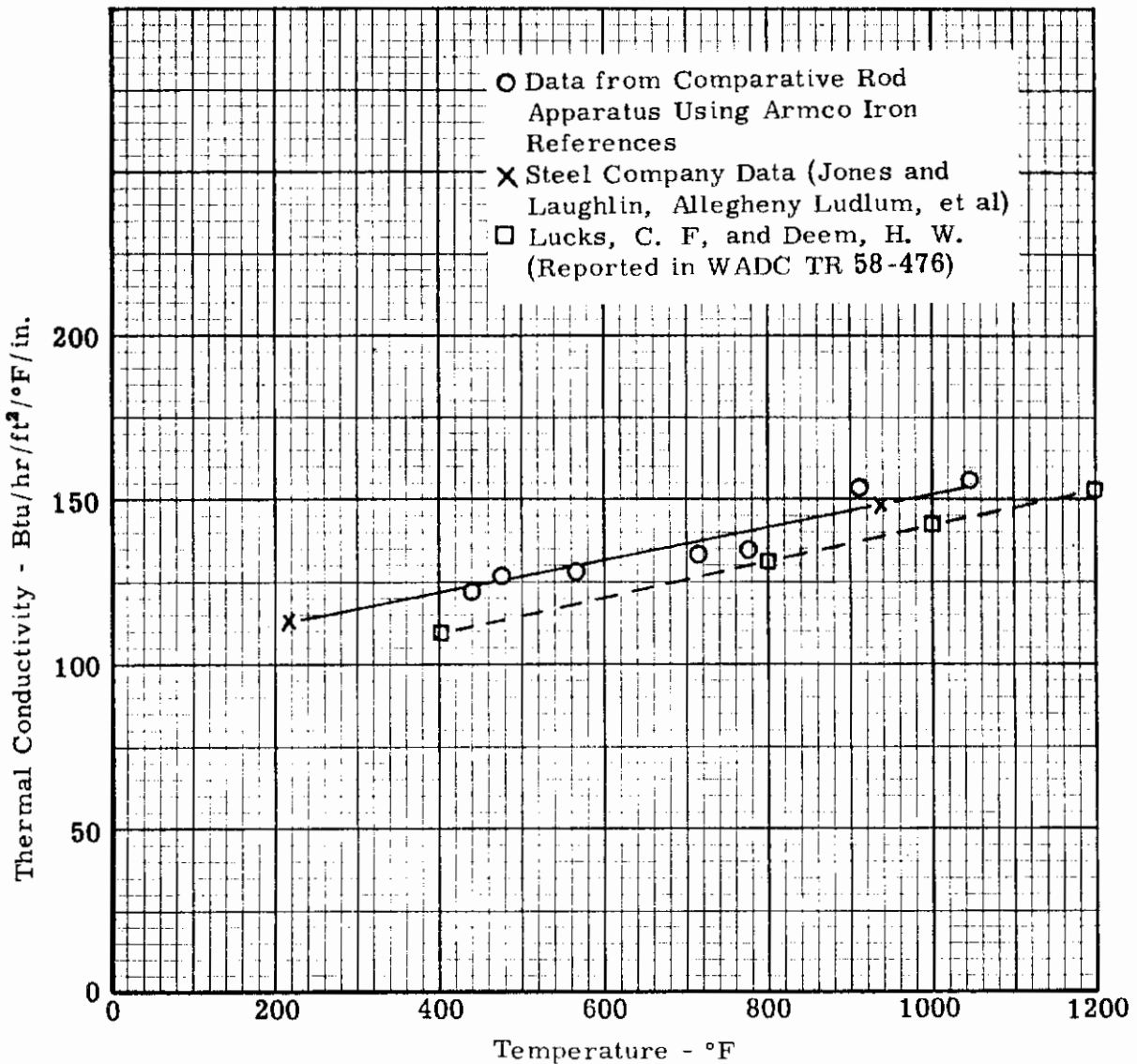


FIGURE 269-THERMAL CONDUCTIVITY OF TYPE 316 STAINLESS STEEL

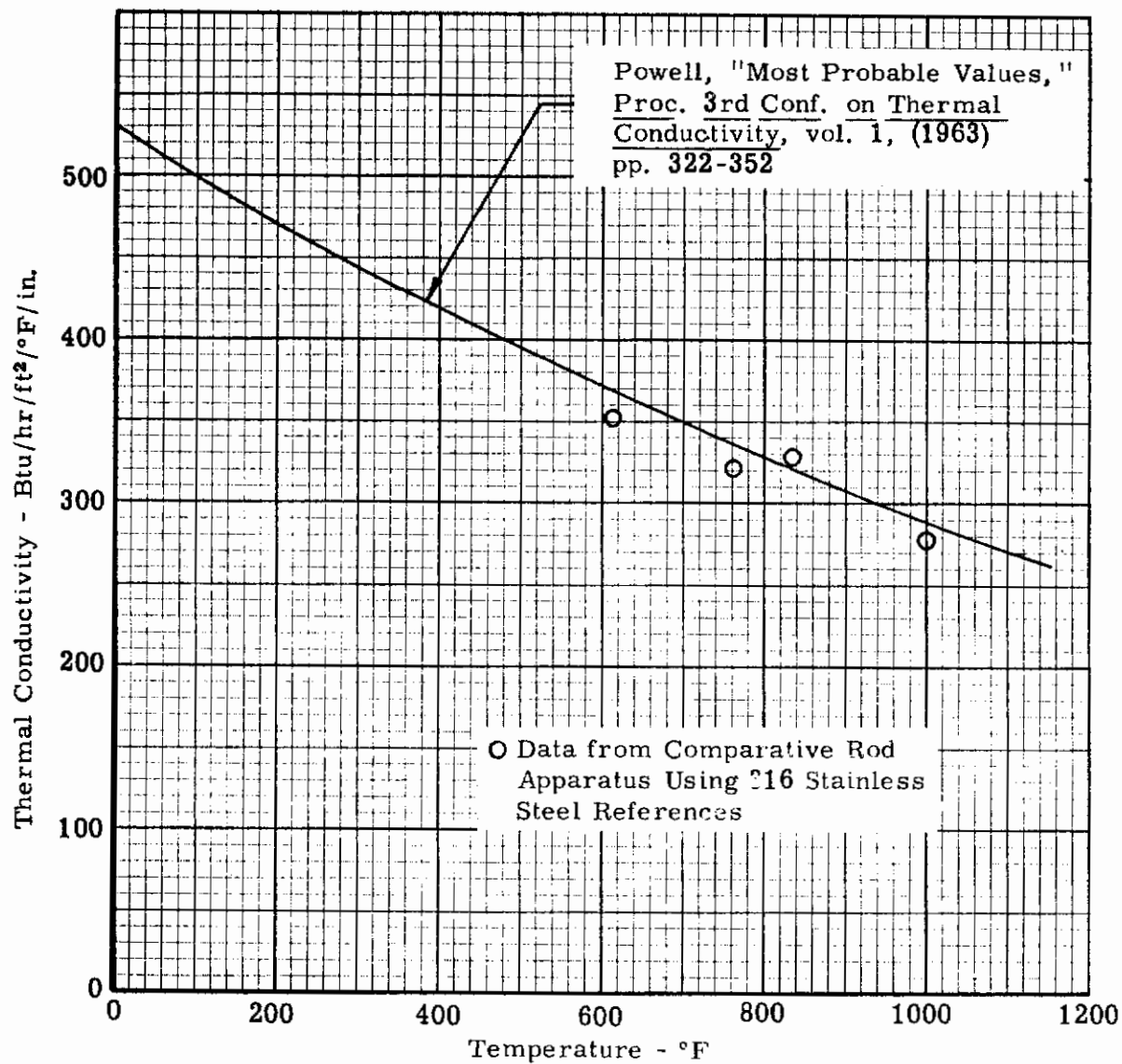


FIGURE 270-THERMAL CONDUCTIVITY OF ARMCO IRON

Some additional data obtained on the comparative rod apparatus are shown in Figures 271 and 272. Figure 271 shows thermal conductivity data for ATJ graphite, with grain, using Armco iron as the reference material. These data show excellent agreement with earlier data obtained here and by other sources (References 12, 13, and 14). The maximum scatter of the comparative rod points was about 5%.

Figure 272 shows data for thermocouple grade constantan obtained on the comparative rod apparatus using Armco iron references, and on Southern Research Institute's high temperature radial inflow apparatus. Note the excellent agreement. These data also show close agreement with data obtained by Silverman (Reference 10) on an alloy of very similar composition.

6. MODULUS OF RUPTURE

Apparatus

The apparatus used to determine the modulus of rupture (MOR, ultimate flexural strength) and the flexural modulus is shown in Figure 273. It consisted primarily of a large high temperature furnace, a load train, a mechanical drive system, a deflection measurement system, and instrumentation for the continuous recording of load and deflection. A third span or four point system was used.

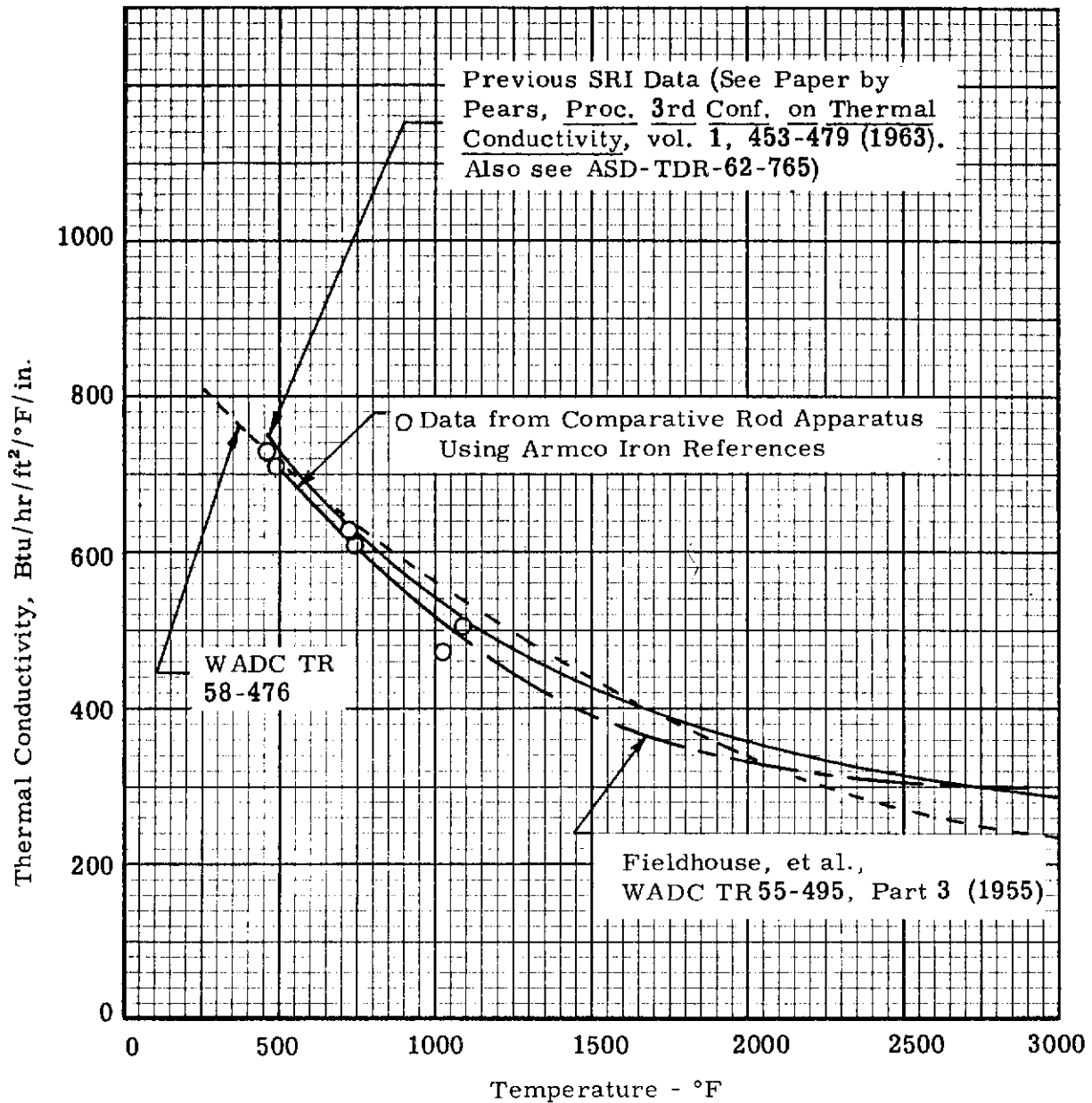


FIGURE 271—THERMAL CONDUCTIVITY OF ATJ GRAPHITE, WITH GRAIN

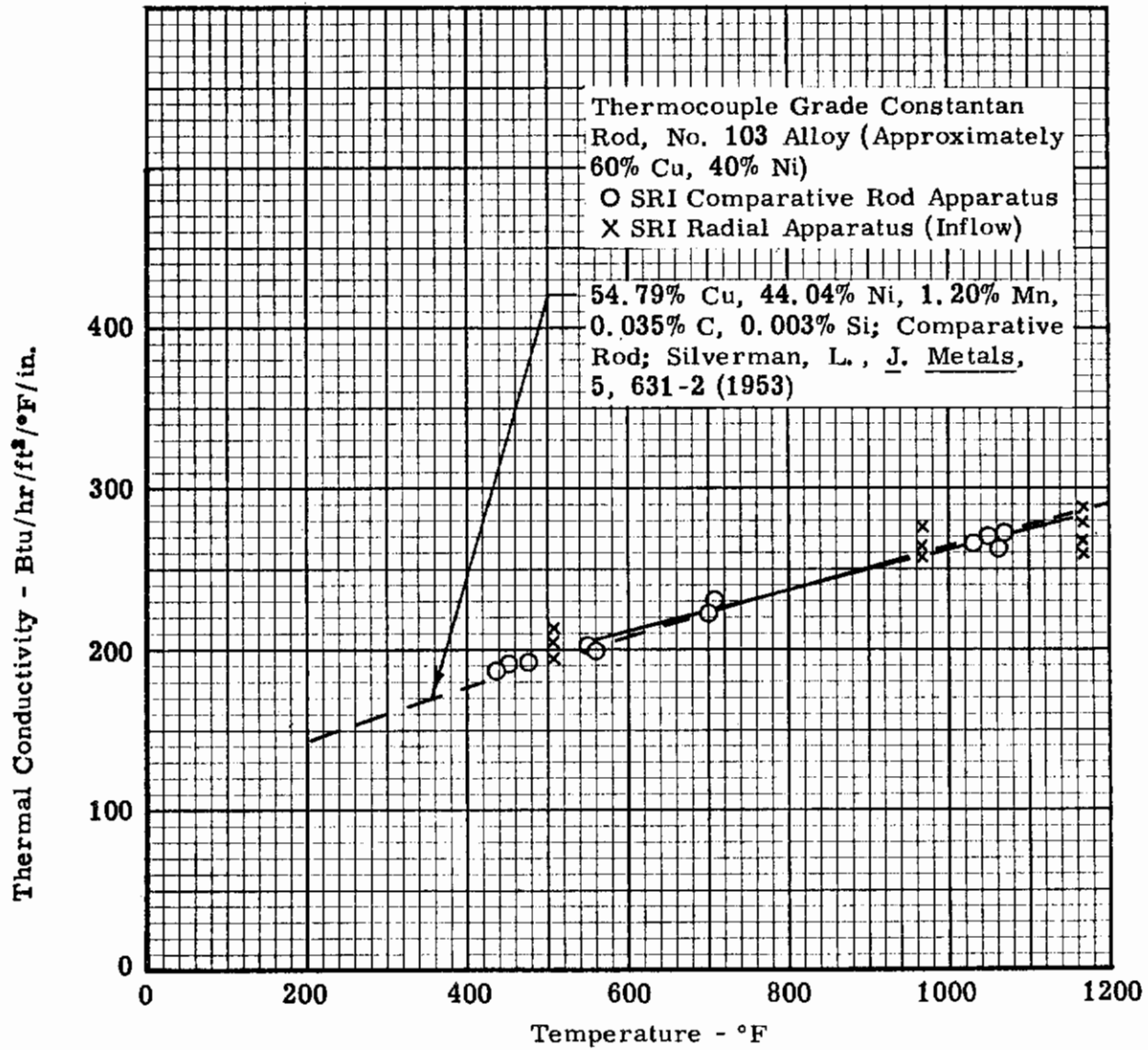


FIGURE 272—THERMAL CONDUCTIVITY OF THERMOCOUPLE GRADE CONSTANTAN ROD

The load train was designed primarily to the recommendations of ASTM C 78-59. It consisted of several components, primarily (1) a stainless steel drive shaft, (2) a graphite push rod, (3) a graphite flexural arm, (4) the specimen, (5) an adapter block, (6) a graphite loading rod, (7) a stainless steel spacer, and (8) a load cell. The main objectives of the load train design were to provide precision alignment and to eliminate friction within the load train.

The stainless steel drive shaft was internally threaded to receive the threaded shaft of the gear reducer. The drive shaft was not permitted to rotate, thus the rotation of the gear reducer shaft caused the drive shaft to move in the journal. The movement of the drive shaft in turn caused the load to be transmitted to the specimen by the push rod and flexural arm.

The push rod was mated to the flexural arm by a spherical socket which prevented any torque from being applied to the specimen. The flexural arm contained two 3/8 inch radii slots which held two slotted graphite rods 3/8 inch diameter x 7/8 inch long. The specimen was contacted on the opposite side by two knife edges positioned in slots within the adapter block. The knife edges and the slotted rods within the flexural arm were easily replaceable when damaged. The load was transmitted to the load cell by way of the flexural block, a graphite push rod, and a stainless steel spacer. A ball joint was employed at the load cell.

The following steps were taken to ensure good alignment and to eliminate friction in the load train. Both journals were machined to close tolerances and good surface finishes and were precisely aligned (within 0.010 inch) before being secured into position. The push rods were machined for close fits in the journals. All mating parts were machined flat and perpendicular (with the exception of the ball joints). The static friction was measured and found to be less than one pound.

The mechanical drive system consisted of a gear reducer that was chain-driven by a variable speed electric motor. The electric drive was a 3/4 horsepower Bodine Type J56 with a Type SH-257E speed control. The motor and control unit were capable of a speed range of 10-1725 rpm.

The deflection measurement system was designed to monitor the motion of the midpoint of the MOR specimen, while compensating for any relative movement of the specimen and load train components (Δ see Figure 27⁴). A 1/8 inch diameter graphite rod (deflection rod) pressed against the midpoint of the MOR specimen. The small rod was spring loaded and moved in a graphite tube (deflection tube) which was also spring loaded. The deflection tube extended into the center of the flexural block and acted as a reference for the movement of the deflection rod. Both the graphite deflection rod and tube were fitted into similar parts of stainless steel in the cooler extremity of the furnace. A differential transformer was connected to the deflection tube through a linkage such that the entire differential transformer moved with the deflection tube. A deflection lever was attached to the transformer linkage with a pivot at its midpoint. Thus, as the specimen deflected, the deflection rod moved the deflection lever and caused an equal movement of the plunger of the differential transformer. The differential transformer transmitted a signal to an X-Y recorder that was proportional to the midpoint deflection. If the flexural block or load train shifted in either direction, the deflection tube and the differential transformer moved the same amount, and no change in deflection was transmitted to the recorder.

The deflection as measured by this system was corrected for the deformation of the knife edges in the adapter block and the deformation of the flexural block due to bending. The correction was established at room temperature on a Tinius-Olsen universal machine and adjusted with temperature for the variation of elastic modulus of the flexural block. The correction was linear with load and was applied with a high degree of accuracy, because (a) the deformation of the parts was small in relation to the deformation of the specimen, (b) the maximum load in any of the parts was well below 20% of ultimate, (c) the elastic modulus of the material was constant at the operation temperatures, and (d) the parts were made of a graphite for which the elastic modulus is well documented here.

The correction as applied to the deflection measurement was less than 10% for most of the runs. However, the Zircoa materials had unusually high elastic moduli at one temperature level causing the correction to approach 50%. In order to verify these values, a specimen was reduced in thickness to 1/4 inch, a factor of about 2.5. This decreased the load-deflection ratio by a factor of about 16 and decreased the correction to about 5%. The agreement of the values was excellent for the two specimen configurations.

Calibration of the deflection measurement system was made by use of a specially designed calibrator employing a precision micrometer dial. Load was measured by a Baldwin SR-4 load cell which was calibrated against dead weights. These calibrations were checked at regular intervals and were found to be highly consistent. Continuous signals from the load cell and differential transformer were received and plotted by a Moseley X-Y recorder yielding a load deflection curve.

As a final check of the system, runs were made on several specimens at room temperature on a Tinius-Olsen testing machine using a dial gage to measure midpoint deflection. Extreme care was taken to ensure no shifting of the specimen or extraneous deflection of the loading parts. The accuracy of these measurements was well within 2%. The same specimens were then run in the MOR apparatus, and the curves were compared to ensure agreement to within less than 5% departure.

Temperature was monitored by thermocouples within their range and by optical pyrometers at elevated temperatures. The deflection rate was controlled by a deflection-time recorder.

Procedure

The specimen was measured with a micrometer and the corners were slightly rounded. The specimen was lowered into position and aligned. The deflection rod was installed and the instrumentation system actuated. A small load was then applied several times to check the proper operation of the apparatus. The furnace was then secured and purged with helium before the heating period began.

After heat soaking for about five minutes at the testing temperature, the specimen was loaded to about 20% of ultimate several times to ensure proper seating of the loading parts. After verifying that the load-deflection curves were straight and consistent, the specimen was loaded to its ultimate strength. The furnace was then allowed to cool before removing and inspecting the broken specimen. The time period between initial heating and fracture was normally 1/2 to 1-1/2 hours.

The X-Y recorder provided a continuous plot of load versus midpoint deflection of the specimen. From this plot, the values of modulus of rupture and initial flexural modulus were determined. The modulus of rupture was calculated by the classic formula:

$$S_u = \frac{Mc}{I}$$

which simplified to

$$S_u = \frac{P_u L}{bh^2} \quad (7)$$

for a specimen with a rectangular cross section employing the third span loading method, and where the fracture occurs within the middle one third of the specimen span length. In this equation:

S_u = modulus of rupture
 P_u = maximum applied load indicated by the recorder
 L = span length
 b = width of specimen
 h = depth of specimen

The initial modulus in flexure was calculated from the formula:

$$E_f = \frac{6 P \left[\frac{a^3}{3} + \frac{ac}{2} \left(a + \frac{c}{4} \right) \right]}{bh^3 \delta} \quad (8)$$

where E_f was the elastic modulus in flexure, P/δ was the ratio of load to corrected midpoint deflection at any point along the elastic portion of the curve, a and c were the distances between the supports and loading points, b was the width of the cross section, and h was the height of the cross section. The above equation neglected the deformation due to shear and assumed the neutral axis coincided with the center of the cross section. Substituting for a and c gives:

$$E_f = \frac{23 P}{4 bh^3 \delta} \quad (9)$$

The corrected midpoint deflection, δ , was determined for any level of load from the equation:

$$\delta_{\text{midpoint}} = \delta_{\text{recorded}} - C_t P \quad (10)$$

where δ_{recorded} is the deflection as recorded by the X-Y recorder, C_t is the correction factor which varies with the temperature, and P is the particular value of load. The values used for the correction factor are shown in Table XXXII.

As some of the materials of the program approached their upper temperature limit, the values of strength became extremely small. This was indicated by the negligible readout of load on some materials and by the penetration of the deflection measurement rod into the specimen. The spring force of the rod was less than one pound and produced a bearing stress of less than 70 psi. The values of strength of these specimens were considered of no engineering significance and were reported as 0 psi.

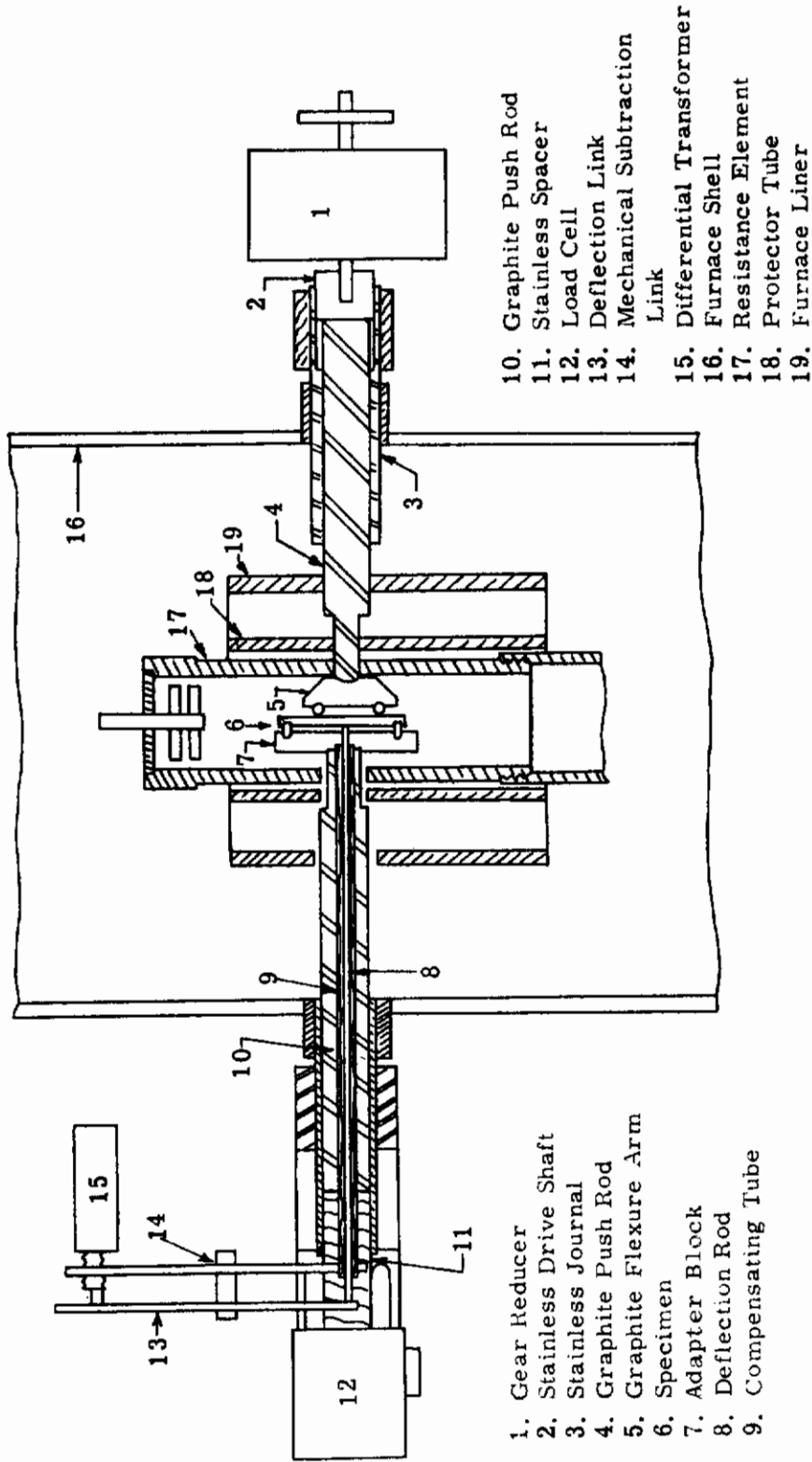


FIGURE 273 - CROSS SECTIONAL SCHEMATIC OF THE HIGH TEMPERATURE FLEXURAL APPARATUS

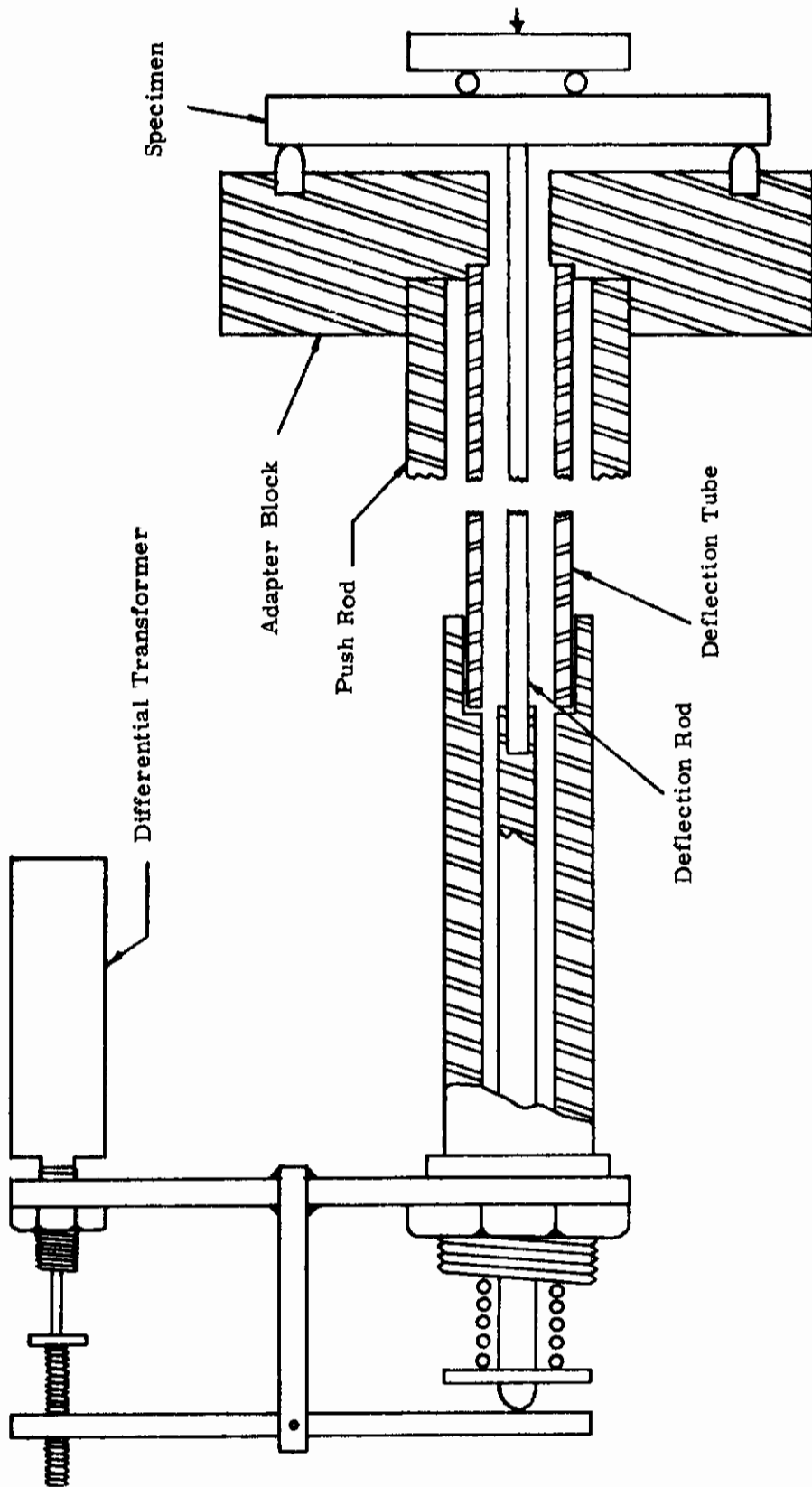


FIGURE 274--SCHEMATIC CROSS SECTION OF THE DEFLECTION MEASUREMENT SYSTEM.

TABLE XXXII
VALUES OF CORRECTION FACTOR, C_f

Test Temperature °F	Correction Factor, C_f , 10 ⁻⁶ in./lb.
500	4.85
1200	4.70
2000	4.40
2700	3.62
3400	2.85
4000	3.19
4500	4.57
5000	2.10

APPENDIX III

ANALYTICAL THERMAL MODEL

The use of porous ceramic materials in high temperature applications requires accurate knowledge of material properties such as thermal conductivity and surface emittance. Under the present program, a typical heat shield design consists of a thin outer skin of relatively dense ceramic material, a layer of low density ceramic, and a refractory metal substructure. In order to predict temperature distributions accurately through the composite structure and to determine the required thickness of the ceramic material necessary to insulate the substructure, the modes of heat transfer through the porous ceramic must be fully understood. An analytical expression which relates such parameters as pore size, pore shape, cell wall thickness, transmissivity, and emissivity to the effective thermal conductivity would be valuable both in regard to material development and to the reduction of experimental data as well as to the theoretical prediction of component temperatures.

The transfer of heat through a porous ceramic material at high temperatures is a complex process in which all three modes of heat transmission (i.e., conduction, convection, and radiation) may be present to some degree. In conduction, heat may be transferred by molecular interaction within the solid material and also within the gas present in the pores. In convection, heat is transferred by the actual movement of particles with a high energy level to another part of the system where the energy level is lower, such as the gas within the pores. In radiation, heat is transferred by the emission and absorption of radiant energy between two surfaces at different temperatures, such as the opposite sides of a pore. If a material is transparent to any degree, some radiant energy may even travel through a portion of the solid material and be absorbed elsewhere within the material. Thus, for a porous material, the term "effective thermal conductivity" should probably be replaced by the term "overall heat transfer coefficient," since the transfer of heat is not merely by conduction.

Past efforts to relate the heat transfer characteristics of a porous medium to such parameters as cell size, shape, etc., have resulted in a number of theoretical expressions. (Reference 15 contains a summary of many of these investigations.) Most of the formulas for the "conductivity" due to solid conduction and radiation are quite cumbersome to use and require knowledge of some parameters which are very difficult to evaluate. For the solid conduction contribution, the following simple formula employing the porosity and the conductivity of the solid material has been used:

$$K = K_s (1 - \delta) \quad (11)$$

where

K = conductivity of porous sample
K_s = conductivity of solid sample
δ = porosity

Several investigations of radiation heat transfer in opaque, porous materials have resulted in equations similar to the following:

$$K_R = 4 \delta \epsilon \sigma D T_m^3 \quad (12)$$

where

- K_R = conductivity due to radiation
- δ = porosity
- ϵ = emissivity
- σ = Stefan-Boltzmann's constant
- D = pore diameter
- T_m = mean temperature ($^{\circ}R$)

Only fair agreement with experimental data has been obtained with any theoretical treatment, partly due to the accuracy of the measurements and partly to the assumptions made in the analytical work.

Generally speaking, since the conductivity of many non-metals decreases with increasing temperature, the conductivity of the porous material due to solid conduction would be expected to decrease with increasing temperature. Also, since the emissive power of a material is proportional to the fourth power of the absolute temperature, the overall heat transfer due to radiation is predominant at temperatures above $3000^{\circ}F$. The effects of air conduction and air convection are insignificant, especially at high temperatures and at reduced pressures. For the current investigation, the mechanism of radiation heat transfer has been examined in detail, using Matra's approach to the problem as a guide (Reference 16).

A geometrical model consisting of closely packed uniform pores of maximum dimension $2r$ was chosen to represent the porous medium. Matra, using a spherical pore, and assuming that the temperature difference between two differential black surfaces is directly proportional to the vertical projection of the distance between them, arrives at the following expression for the net radiant interchange across a single pore:

$$q_{net} = 4F\sigma\pi r^2 T_m^3 \Delta T \quad (13)$$

where T_m is the mean temperature, r is the pore radius, and the factor F equals $1/2$ to account for that portion of the energy leaving one hemisphere which arrives at the opposite hemisphere. (The other $1/2$ of the energy is returned to the original hemisphere because the surface can "see" itself.)

Matra also develops the following general expressions for the effective radiation shape factor for curved surfaces and for plane surfaces when the transmissivity equals zero:

for curved surfaces,

$$F' = \frac{1}{\frac{2}{\epsilon} - 2 + \frac{1}{F}} \quad (14)$$

for plane surfaces,

$$F'' = \frac{1}{\frac{1}{\epsilon} \frac{1}{2F} - \frac{F}{\epsilon} + \frac{2F}{\epsilon} - F} \quad (15)$$

where

ϵ = surface emittance ($\epsilon_1 = \epsilon_2 = \epsilon = a$)
 a = absorptance
 F = geometrical view factor

For the same view factor (other than unity), the above expressions show that curved surfaces have a greater interchange of radiant energy than plane surfaces. Since $F = 1/2$ for a sphere, F' equals $\epsilon/2$ and the expression for the net interchange across a single pore becomes:

$$q_{net} = 2\sigma \epsilon \pi r^2 T_m^3 \Delta T \quad (16)$$

(Note that this equation differs by a factor of 1/2 from Matra's equation since he has included the geometric view factor twice.)

To determine the total effect of internal radiation through a porous medium, the net interchange for one pore was multiplied by the number of pores in the total porous volume ($A_t \cdot 2r$). An effective thermal conductivity due to radiation can then be obtained by equating the resulting expression to the Fourier heat equation, as follows:

$$4 \sigma F' \pi r^2 T_m^3 \Delta T \cdot \frac{A_t \cdot 2r}{\frac{4}{3} \pi r^3} \left(1 - \frac{\rho_f}{\rho_s}\right) = K_{eff} A_t \frac{\Delta T}{2r} \quad (17)$$

$$\therefore K_{eff} = 12 r \sigma F' T_m^3 \left(1 - \frac{\rho_f}{\rho_s}\right) \quad (18)$$

where

ρ_f = porous material density
 ρ_s = solid material density

For a cubical pore with each side equal to $2r$, the net interchange between two opposite sides connected with non-conducting but re-radiating walls may be written as follows:

$$q_{net} = 4 \sigma A F'' T_m^3 \Delta T \quad (19)$$

$$\text{Since } A = 4r^2$$

$$q_{net} = 16 \sigma r^2 F'' T_m^3 \Delta T \quad (20)$$

The effective thermal conductivity for the porous volume can then be obtained as was done for the case of spherical pores:

$$16 \sigma r^2 F'' T_m^3 \Delta T \frac{A_t \cdot 2r}{8r^3} \left(1 - \frac{\rho_f}{\rho_s}\right) = K_{\text{eff}} A_t \frac{\Delta T}{2r} \quad (21)$$

$$\text{or } K_{\text{eff}} = 8 \sigma r F'' T_m^3 \left(1 - \frac{\rho_f}{\rho_s}\right) \quad (22)$$

The ratio of the two expressions derived for the effective conductivity due to radiation for cubical and spherical pore shapes is shown by Figure 275 for a geometric view factor of 1/2. (Reference 17 gives a value of 0.534 for the view factor between two squares connected by non-conducting but re-radiating walls and separated by a distance equal to the length of one side. Thus, the pore considered here is not exactly a cube, however, for comparative purposes, the factor of 1/2 was assumed for both the cube and sphere.) As indicated, this ratio is less than one for all values of emissivity. Thus, it is concluded that a porous material having cubical pores would be a better insulation material than one having spherical pores. Since the geometric view factor for two radiating surfaces decreases as the distance between them increases, the effective conductivity for pores having elliptical or rectangular cross sections would be lower (in the direction parallel to the longer side) than for spherical or cubical pores, respectively. Such a material would have anisotropic conductance like pyrolytic graphite, in that the conductivity would depend upon the direction of the heat flow relative to the orientation of the pores.

To determine the effect of transmissivity on the net exchange of energy between the upper and lower surfaces of a spherical pore, the diagram shown in Figure 276 was employed. This diagram traces the energy that leaves the upper surface and shows that a portion of this energy is returned to the upper surface (because it can "see" itself) where it is partially absorbed, transmitted, and reflected. A portion of the original energy also arrives at the lower surface where it is partially absorbed, transmitted, and reflected. From each reflection on both surfaces, a portion is again returned where it is partially absorbed and transmitted. Tracing the energy through a number of reflections and neglecting the effects of transmitted energy from surrounding pores, the net exchange between the upper and lower surfaces can be expressed as follows:

$$q_{\text{net}} = \sigma A F^* (T_1^4 - T_2^4) \quad (23)$$

where

$$F^* = \frac{1}{\frac{(\epsilon + \tau)^2}{\epsilon^2 F} + \frac{2(\epsilon + \tau)^2}{\epsilon^2} + \frac{2(\epsilon + \tau)}{F}}$$

This expression is obtained by summing up the q_{DN_a} and Δq_{DN_a} terms shown in Figure 276 over a number of reflections.

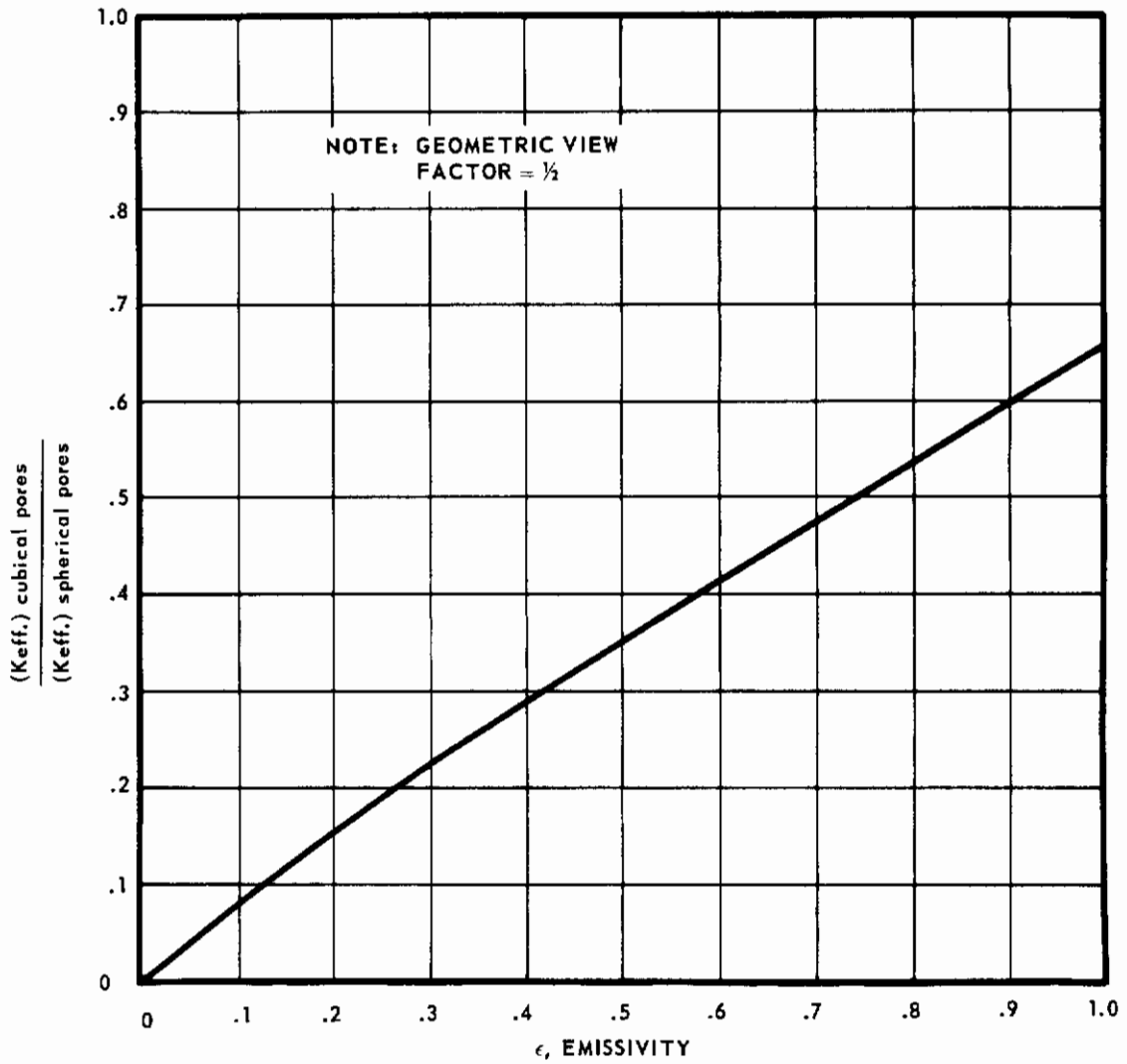


FIGURE 275 - COMPARISON OF CONDUCTIVITY DUE TO RADIATION FOR CUBICAL AND SPHERICAL SHAPED PORES

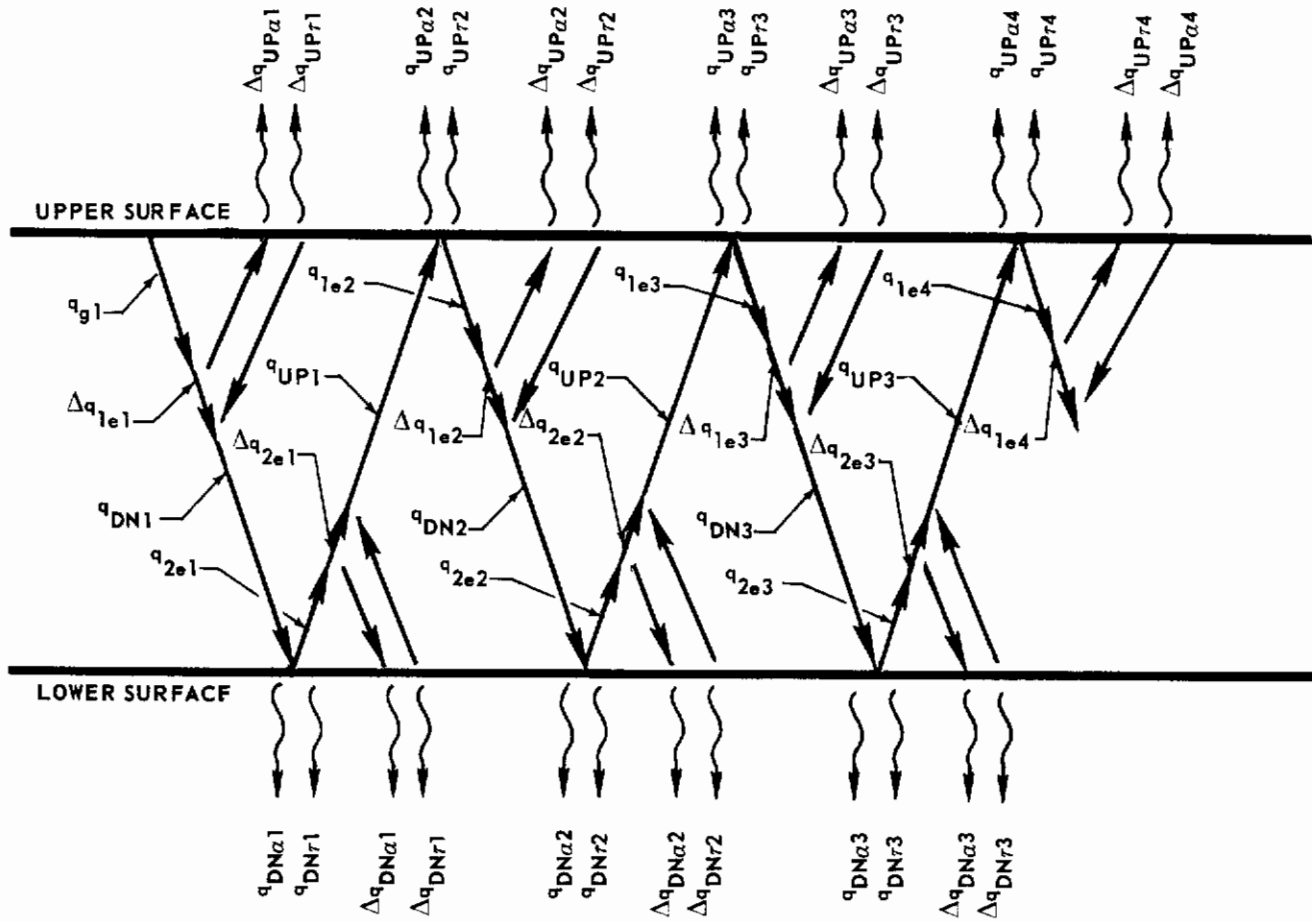


FIGURE 276 - ENERGY PATHS BETWEEN UPPER AND LOWER SURFACES OF A SPHERE

Figure 277 presents F^* vs. ϵ with τ as a parameter for geometric view factors of 1.0, 0.5, and 0.2. For $F = 1/2$, as for a spherical pore,

$$F^* = \frac{\epsilon^2}{2(\epsilon + \tau)} \quad (24)$$

In addition to the net heat leaving the upper surface which was absorbed by the lower surface, the amount of heat transmitted through the lower surface, the amount re-absorbed by the upper surface, and the amount transmitted back through the upper surface must be accounted for. The portion of energy emitted from the upper surface which was transmitted through the lower surface is given by the following expression, for $F = 1/2$:

$$q_{(1-2)\tau} = q_{g1} \left[\frac{\tau}{2(\epsilon + \tau)} \right] \quad (25)$$

where $q_{g1} = \sigma \epsilon T_1^4$

$$F^* = \frac{1}{\frac{2(\epsilon + \tau)}{\epsilon^2} + \frac{(\epsilon + \tau)^2}{\epsilon^2 F} - \frac{2(\epsilon + \tau)^2}{\epsilon^2}}$$

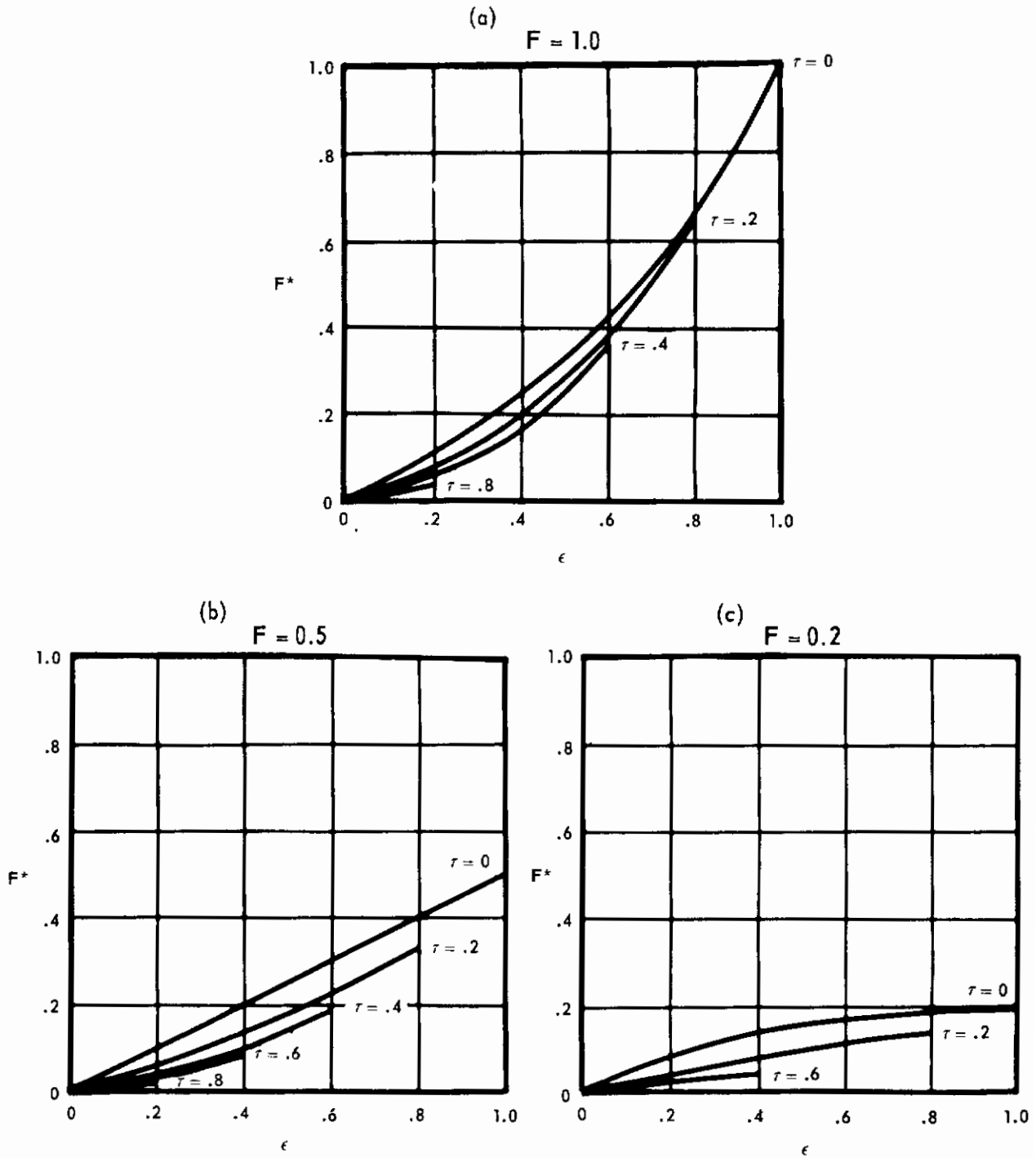


**FIGURE 277 - SHAPE FACTORS (INCLUDING TRANSMISSIVITY)
FOR CURVED SURFACES**

This expression was obtained in the same manner as that used to find the net heat absorbed by the lower surface; i.e., by summing up the $q_{DN\tau}$ and $q_{DN\alpha}$ terms shown in Figure 276 over a number of reflections.

The expression for the portion of the heat which left the upper surface that was re-absorbed by the upper surface is as follows:

$$q(1-l)_a = q_{g1} \epsilon \frac{1}{(\epsilon + \tau) + \frac{F}{1-F}} + \frac{F^2(1 - \epsilon - \tau)}{2F^2(\epsilon + \tau) + (3F - 4F^2)(\epsilon + \tau)^2 + (1 - 3F + 2F^2)(\epsilon + \tau)^3} \quad (26)$$

For a view factor of 1/2, this reduces to:

$$q(1-l)_a = q_{g1} \left[\frac{\tau}{2(\epsilon + \tau)} \right] \quad (27)$$

which is the same relation as was obtained for the portion of heat absorbed by the lower surface.

The portion of the heat leaving the upper surface that was transmitted back through the upper surface is given by a similar expression which, for a view factor of 1/2, is:

$$q(1-l)_a = q_{g1} \left[\frac{\tau}{2(\epsilon + \tau)} \right] \quad (28)$$

Again this is the same relation as obtained previously for the portion of heat transmitted through the lower surface.

Since the effect of transmissivity is to allow a portion of the energy emitted from any surface to escape to surrounding pores, the analysis must now be expanded in order to determine where this transmitted energy is absorbed. For this purpose, the model shown in Figure 278, representing a series of planes between spherical pores, was employed. The arrows represent heat which is transmitted through each plane (with the exception of q_{g1} , the heat emitted from plane 0) and the "X's" represent heat which is absorbed by each plane. Utilizing the results obtained previously,

$$\begin{aligned}
 q_{g1} &= q_{s1} + q_{r1} + q'_{s1} + q'_{r1} & (29) \\
 q_{s1} &= q_{g1} \left[\frac{\epsilon}{2(\epsilon + \tau)} \right] = q'_{s1} \\
 q_{r1} &= q_{g1} \left[\frac{\tau}{2(\epsilon + \tau)} \right] = q'_{r1} \\
 q_{r2} &= q_{r1} \left[\frac{\tau}{2(\epsilon + \tau)} \right] = q_{g1} \left[\frac{\tau}{2(\epsilon + \tau)} \right]^2 \\
 q_{r3} &= q_{r2} \left[\frac{\tau}{2(\epsilon + \tau)} \right] = q_{g1} \left[\frac{\tau}{2(\epsilon + \tau)} \right]^3 \\
 q_{s2} &= q_{r1} \left[\frac{\epsilon}{2(\epsilon + \tau)} \right] = q_{g1} \left[\frac{\epsilon}{2(\epsilon + \tau)} \right] \left[\frac{\tau}{2(\epsilon + \tau)} \right] \\
 q_{s3} &= q_{r2} \left[\frac{\epsilon}{2(\epsilon + \tau)} \right] = q_{g1} \left[\frac{\epsilon}{2(\epsilon + \tau)} \right] \left[\frac{\tau}{2(\epsilon + \tau)} \right]^2 \\
 q_{s4} &= q_{r3} \left[\frac{\epsilon}{2(\epsilon + \tau)} \right] = q_{g1} \left[\frac{\epsilon}{2(\epsilon + \tau)} \right] \left[\frac{\tau}{2(\epsilon + \tau)} \right]^3
 \end{aligned}$$

Tracing the energy leaving plane 0 which is transmitted through the adjacent planes, the total heat absorbed at any plane can be expressed as follows:

$$q_s = q_{g1} \left[\frac{\epsilon}{2(\epsilon + \tau)} \right] \sum_{n=1}^{\infty} K_{(yn)} \left[\frac{\tau}{2(\epsilon + \tau)} \right]^n \quad (30)$$

where "n" is the number of transmissions the energy has gone through before being absorbed and $K_{(yn)}$ is the number of absorbed terms after n transmissions (the subscript y refers to the plane being considered). $K_{(yn)}$ varies for each plane and can only be found by utilizing the model shown in Figure 278. It should be pointed out that the above expression is for a completely "internal" plane which is free from any edge effects.

Since that portion of the original emitted energy which was transmitted equals:

$$2 q_r = 2 q_{g1} \left[\frac{\tau}{2(\epsilon + \tau)} \right] \quad (31)$$

a factor \mathcal{F} , the portion stored in phase 1 plane, is defined as follows:

$$\mathcal{F} = \frac{\epsilon}{2\tau} \sum_{n=1}^{\infty} K(n) \left[\frac{\tau}{2(\epsilon + \tau)} \right]^n \quad (32)$$

By expanding the model shown in Figure 278, \mathcal{F} can be found as a function of $(\epsilon + \tau)$ for any other plane. The results are shown on Figure 279, and indicate that nearly all of the transmitted energy is absorbed within the first five adjacent planes. Since the number of absorbed terms for a particular plane depends on the location of the plane relative to a free surface, models similar to the one shown on Figure 278 must be investigated and \mathcal{F} factors determined for each plane. These models would incorporate a free surface located at various distances away from the plane from which the emitted energy originates. The net heat exchanged between any two planes could then be determined after all \mathcal{F} factors have been calculated.

The expressions developed for the effects of transmissivity within a porous material appear to be readily adaptable for use in a finite difference computer program. Due to the amount of time required to investigate other aspects of the present heat shield development program, further work in the area of the analytical heat transfer model was not possible.

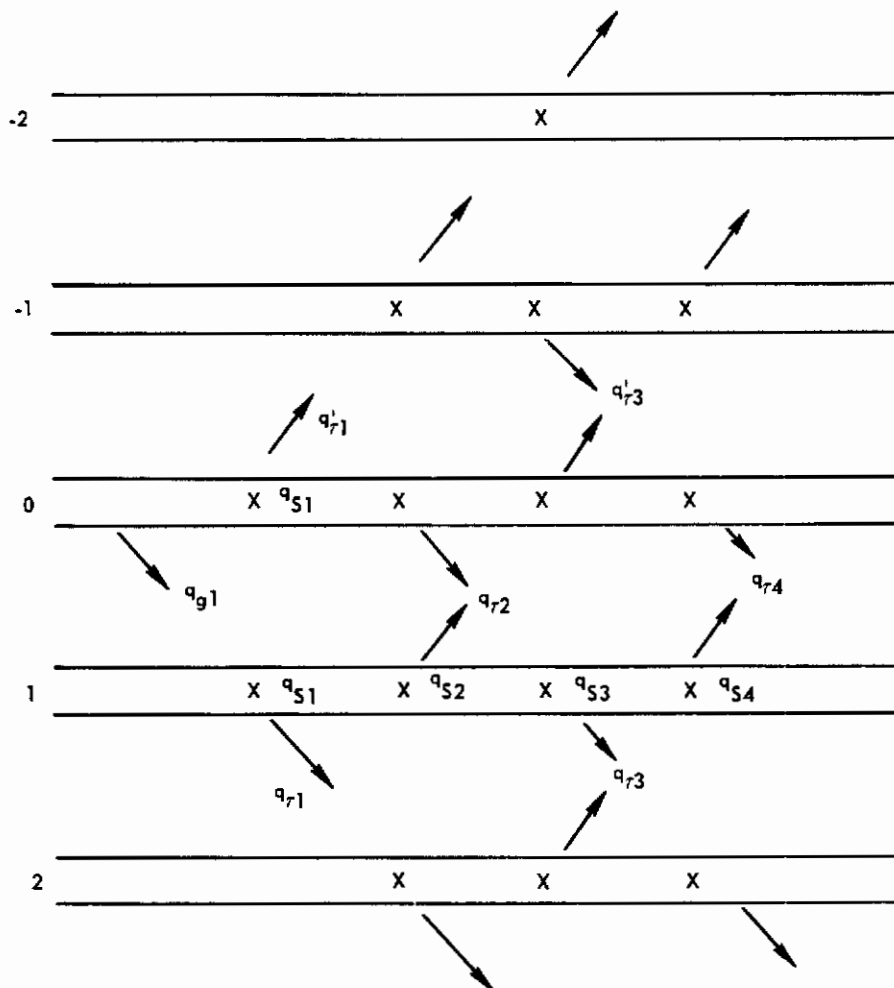


**FIGURE 278 - TRANSMITTED AND ABSORBED ENERGY
WITHIN A SERIES OF PLANES BETWEEN PORES**

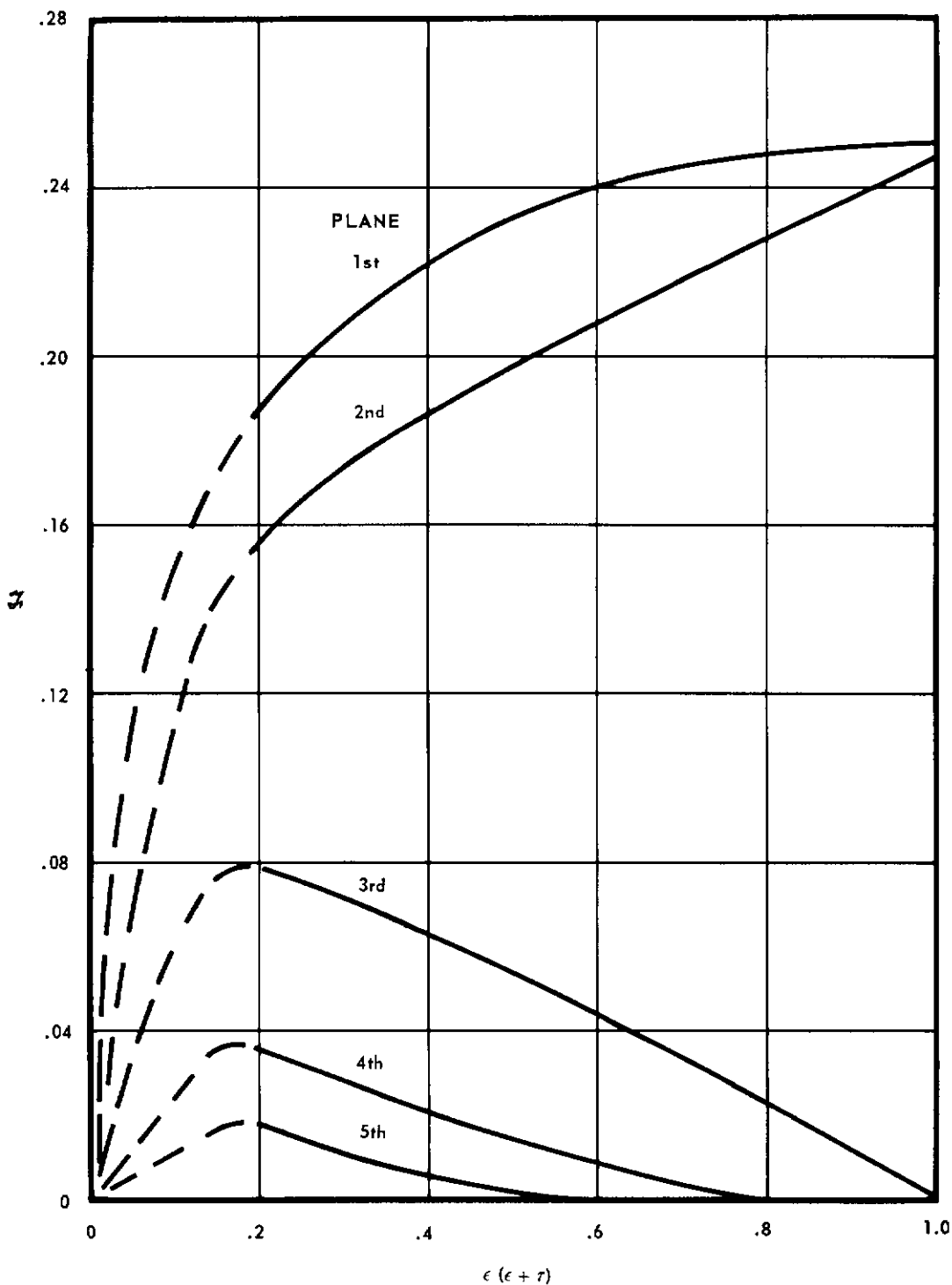


FIGURE 279 - HEAT ABSORBED AT ANY PLANE DUE TO TRANSMISSION

Note: Page 362 is a blank page.

APPENDIX IV

STUDY TO DETERMINE THE STRESSES WITHIN A CERAMIC

BODY DURING RAPID HEATING

1. INTRODUCTION

This study was concerned with defining the stress state within a ceramic body, including edge effects, during exposure to a "thermal shock" environment. The ceramic material was considered to be orderly in its behavior so that a system could be formulated that closely approximated actual usage and was amenable to analytical treatment. The parameters chosen to define this system were carried throughout the study as explicit terms so that their respective effects on the stress state could be evaluated. The range of the defining parameters was taken so as to be representative of the ceramic materials being investigated.

The parameters defining the general thermal stress problem, and therefore the "thermal shock" problem were as follows:

(a) Character of the thermal environment (Surface heating rate; Initial temperature of the body; Heat dissipation rate).

(b) Body geometry (Size; Shape).

(c) Character of the body material (Density; Specific heat; Thermal conductivity; Modulus of elasticity; Poisson's ratio; Coefficient of thermal expansion).

The results of this study provided the information necessary to predict the most critical area, mode and magnitude of "thermal shock" failure for the class of ceramic bodies studied.

It was found, that for purposes of structural analysis, the "thermal shock" phenomena were caused by certain combinations of the defining parameters. Hence, the characteristics of the resulting stress state are contained in the solution of a generalized thermal stress problem with emphasis on analysis of those portions of the body adjacent to its free edges.

Some attempts were made to utilize this study to predict "thermal shock" failures in laboratory specimens. However, testing was not extensive enough to provide complete correlation. Additional programs would be necessary for this purpose.

2. LIST OF SYMBOLS

<u>Symbol</u>	<u>Dimension</u>	<u>Description</u>
a	inches	Surface dimension of the parallelepiped
A, B, C, D	None	Constants or coefficients

<u>Symbol</u>	<u>Dimension</u>	<u>Description</u>
c_p	$\frac{\text{Btu}}{\text{lb} \cdot ^\circ\text{F}}$	Specific heat
d	$\text{in.}^2/\text{sec}$	Thermal diffusivity
E	psi	Modulus of Elasticity
erfc	None	Complimentary error function (Ref. 1)
F	pounds	Force
f	psi	Axial stress associated with a two-dimensional body
\bar{f}	None	Dimensionless axial stress associated with a two-dimensional body
H	$^\circ\text{F}/\text{sec}$	Linear surface heating rate
h	inches	Thickness of the parallelepiped
K	$\frac{\text{Btu-in}}{\text{Hr-in}^2\text{-sec}}$	Thermal conductivity
n	None	Exponent
S	psi	Shear stress associated with a two-dimensional body
\bar{S}	None	Dimensionless shear stress associated with a two-dimensional body
T	$^\circ\text{F}$	Temperature
t	seconds	Time
x	inches	Surface distance along the x, axis
Y_s	inches	"Soak Depth," depth of heat penetration, depth at which the temperature is 5.68% of surface temperature.
y	inches	Distance along the y axis measured from the backside of the parallelepiped.
y_1	inches	Distance along the y axis measured from the heated surface of the parallelepiped.
α	$\text{in.}/\text{in.}\cdot^\circ\text{F}$	Coefficient of thermal expansion
ρ	$\text{lb}/\text{in.}^3$	Material density
f	psi	"Loading" function

ϵ	in./in.	Unit strain
ν	None	Poisson's ratio
$\phi = \epsilon(x)\psi(y)$	pounds	Stress function
$\epsilon(x)$	pounds	Portion of the stress function which is a function of x only
$\psi(y)$	pounds	Portion of stress function which is a function of y only
$\mu + i\beta$	None	A complex number
σ	psi	Axial stress associated with a three-dimensional body
$\bar{\sigma}$	None	Dimensionless axial stress associated with a three-dimensional body
τ	psi	Shear stress associated with a three-dimensional body
$\bar{\tau}$	None	Dimensionless shear stress associated with a three-dimensional body

Subscripts

<u>Symbol</u>	<u>Description</u>
x	along the x axis
y	along the y axis
z	along the z axis
xy	in the xy plane
xz	in the xz plane
yz	in the yz plane
S	heated surface
B	backside surface
P	principal stress

3. ASSUMPTIONS

3.1 THERMAL ENVIRONMENT

(a) One surface only of the body is heated.

(b) The temperature of the exposed surface is a linear function of time.

(c) The backside and edges of the body are insulated with a material which is the same as the body material.

The thermal environment assumed above causes one-dimensional heat flow through the body. The assumed thermal environment restricts this study to the heat-up periods of a thermal history or trajectory (region OA in Figure 280).

An analysis of the restrictions imposed by the assumed thermal environment shows that they cause no large deviations from actual occurrences for trajectories of the type used in this program.

The following considerations apply:

(a) The size of the components precludes a large surface temperature variation; therefore, the heat flow is approximately one-dimensional.

(b) The critical thermal stresses will be shown to occur at time periods when the backside of the body is at a temperature close to ambient. Hence no great amount of heat has flowed into the insulation. The characteristics of the insulation, therefore, have negligible effect on the heat flow within the body.

(c) Analysis of the trajectories of this project indicated that the maximum thermal stresses occurred during the heat-up portion of the trajectory (region OA of Figure 280).

3.2 BODY GEOMETRY

(a) The shape of the body is a parallelepiped.

(b) The parallelepiped has the thickness h and a surface area $4ca^2$.

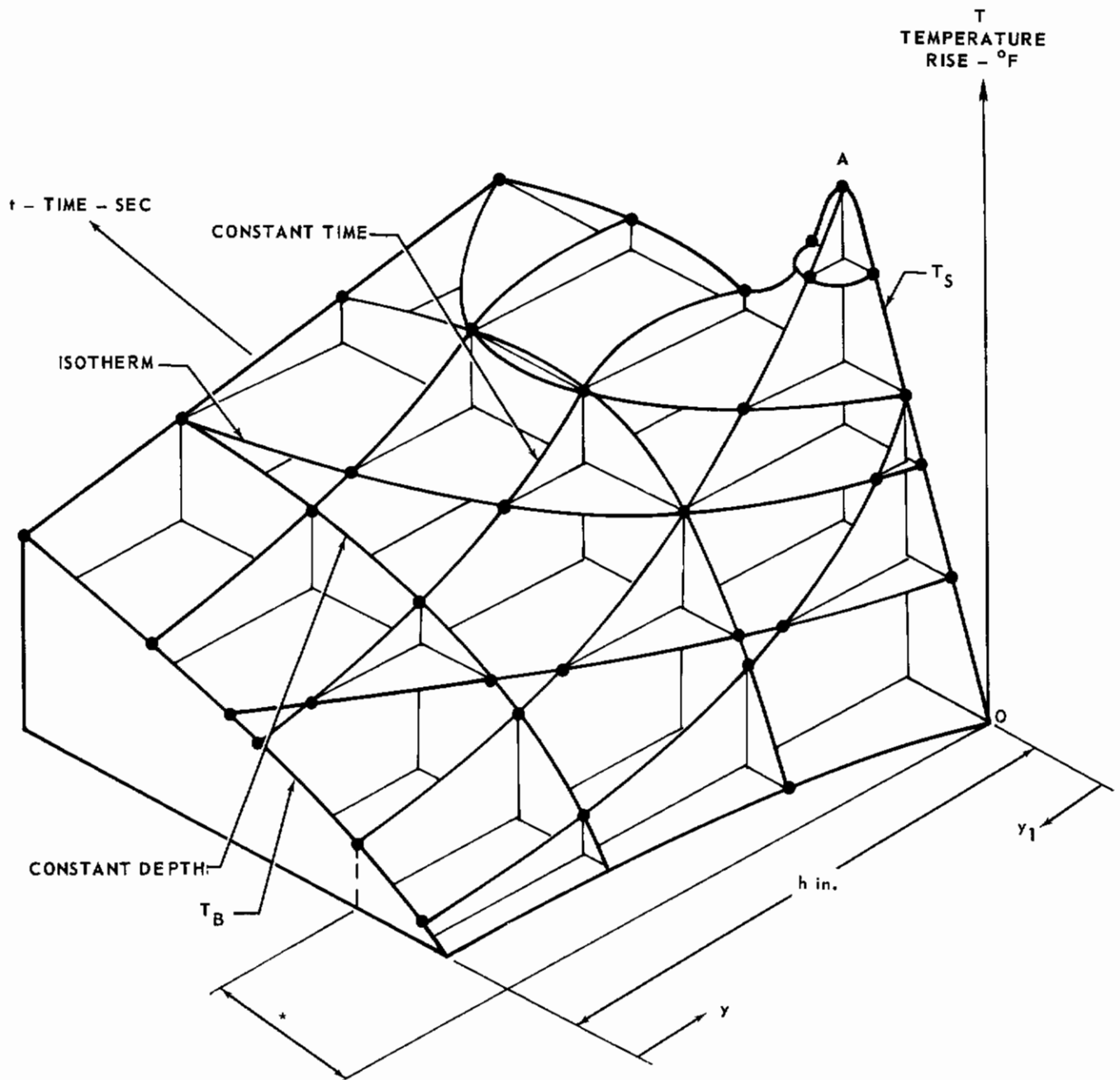
(c) The parallelepiped is unrestrained.

The assumed body geometry was chosen for the following reasons:

(a) This body shape is encountered often in practical structures, and includes shapes where the radius of curvature does not materially influence the stress distribution.

(b) For this body the thermal stress is due only to the existence of a second derivative of the temperature gradient other than zero. Many other body geometries may, in fact, be idealized as a parallelepiped with various mechanical restraints.

(c) Stresses due to mechanical restraints add nothing to the basic understanding of the "thermal shock" phenomena, merely being additive throughout the body.



* PORTION STUDIED

FIGURE 280 - TYPICAL THERMAL HISTORY COMPONENT OF RE-ENTRY VEHICLE

3.3 BODY MATERIAL

(a) The mechanical and thermophysical properties of the material are constant throughout the temperature range experienced.

The conventional assumption that material properties remain constant with temperature requires that the results of this study be used with caution. The variation with temperature of properties such as ν and α may be handled by using average values covering the temperature range in question. To handle the variation of E with temperature, however, the quantity σ/E must be evaluated at several time periods during the trajectory to find the period when the critical stresses occur.

4. IDEALIZED SYSTEM

4.1 GEOMETRY AND CONFIGURATION

The geometry of the body studied is shown in Figure 281, which is consistent with the assumptions stated in Section III of this Appendix.

4.2 THERMAL ENVIRONMENT

Figure 280 shows a representative thermal history which is typical for this project. It was determined that, for the representative thermal history, thermal shock damage to the assumed body, if damage did occur, would be exhibited during the heat-up period shown in Figure 280 at the time interval from $t = 0$ to $t = A$.

Noting that the surface temperature rise during this time period is nearly linear, the surface temperature, T_s , can be defined as:

$$T_s = Ht \tag{33}$$

where

H = surface heating rate - °F/sec
t = time from initiation of history - sec

With an environment as shown in Figure 282, the one-dimensional heat flow is governed by the differential heat conduction equation for a semi-infinite body, because of the assumptions made concerning the backside environment. This equation is:

$$\frac{\partial T}{\partial t} = d \frac{\partial^2 T}{\partial y_1^2} \tag{34}$$

where

T = temperature - °F
t = time from initiation - sec
d = thermal diffusivity - in.²/sec
 y_1 = distance from the heated surface - inches

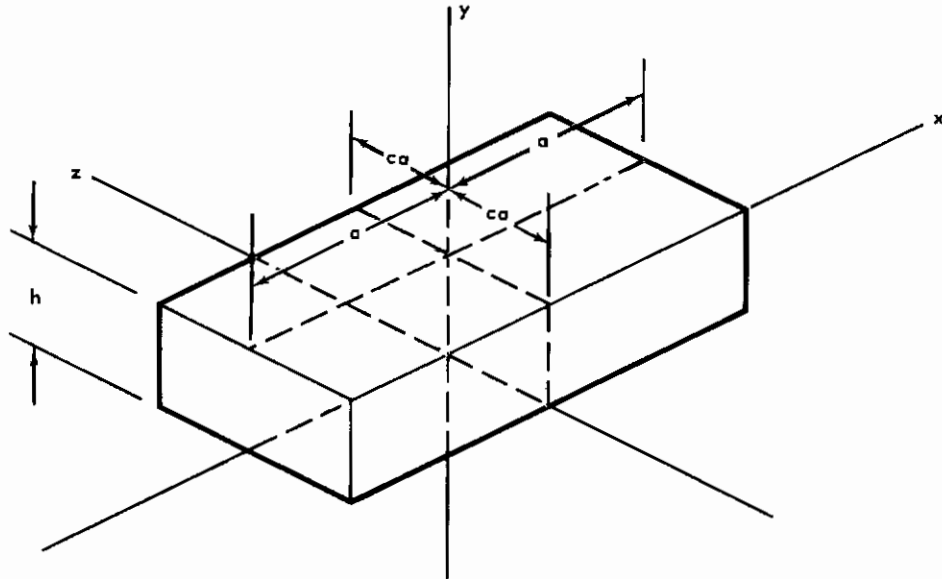


FIGURE 281 - BODY GEOMETRY

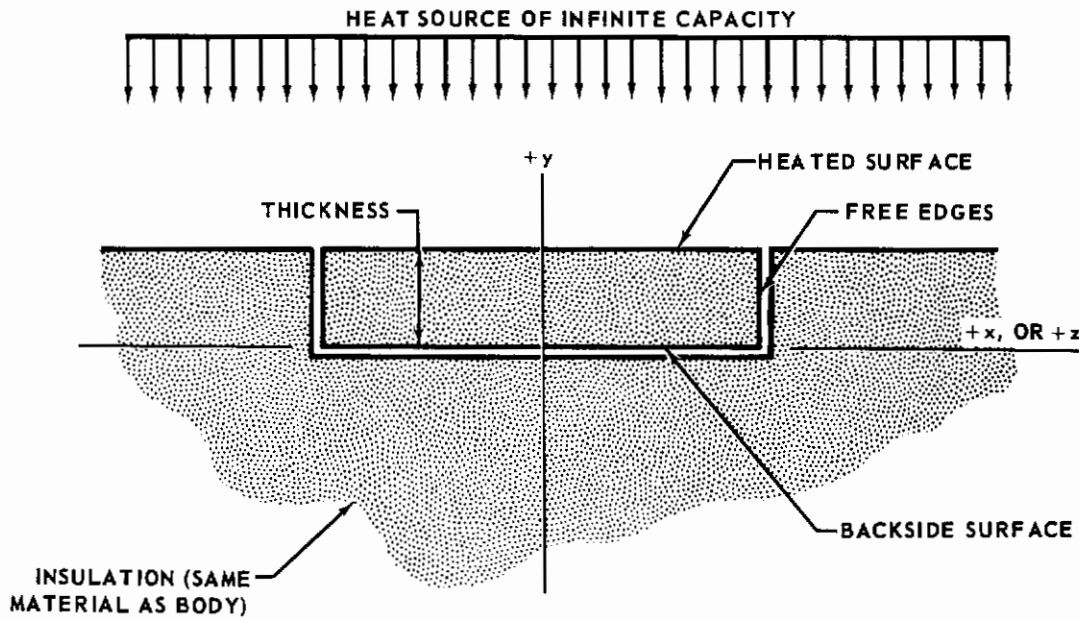


FIGURE 282 - BODY ENVIRONMENT

The solution of the differential equation is:

$$\frac{T}{Ht} = 4i^2 \operatorname{erfc} \frac{y_1}{Y_s} \quad (35)$$

where

erfc = the complementary error function

$$Y_s = 2\sqrt{dt} \quad (36)$$

If the heated surface of the body is specified as $y_1 = 0$, and the backside of the body as $y_1 = h$, then the backside temperature and the temperatures of all points within the body may be determined as a proportion of the surface temperature, T_s . This solution is shown in Figure 283. At any particular value of h/Y_s , the temperature gradient through the thickness of the body can be defined adequately by the polynomial:

$$\frac{T}{Ht} = A \left(\frac{y}{h} \right)^n + B \left(\frac{y}{h} \right) + C \quad (37)$$

where

y = the distance from the backside - inches
 A , B , and C are coefficients for a particular value of h/Y_s .

The thermal characteristics of the environment adjacent to the backside of the body will be shown to be inconsequential at the time when maximum thermal stresses occur; therefore, the thermal environment is adequately defined with the single parameter H , the surface heating rate.

5. STRESS ANALYSIS OF THE IDEALIZED SYSTEM

5.1 STRESS AT POINTS REMOTE FROM THE FREE EDGES

With the temperature gradient through the thickness of the body defined at any time during the thermal history, the thermal stresses through the thickness of the body can be determined by standard methods. The resulting thermal stresses for particular values of h/Y_s are shown in Figures 284 and 285. Figure 285 in particular shows the thermal stress history within the body. This figure does not include the influence of the free edges of a finite body on the stress state within the body. Its use should be confined to estimating the structural effects of various heating rates, the feasibility of proposed structure, and to compare various materials. The stress state and environment of the body is specified at each instant by Figure 285. For instance, investigate the instant in time $h/Y_s = 2.50$, for a body where the tensile stress is critical:

Since the maximum tensile stress in the x direction is:

$$f_{K_{t_{MAX}}} = (1-\nu)(.156 E \alpha H t) \text{ at } h/Y_s = 2.5 \quad (38)$$

$$h/Y_s = 2.5 = \frac{h}{2\sqrt{dt}} \quad (39)$$

$$t_1 = \frac{h^2}{25d} \text{ sec.} \quad (40)$$

$$T_s = H t = \frac{H h^2}{25d}, \quad ^\circ F$$

$$f_{KEMAX} = \frac{6.25(1-\nu)EdHh^2}{d} \times 10^{-3} \quad (41)$$

$$\overline{T}_B = \text{AMBIENT} \quad (42)$$

5.2.1 Two-Dimensional Case - Area Away From Corners

For the determination of the thermal stresses near the edge of a two-dimensional body (i.e. a thin plate), an energy solution is widely used which assumes the stress state to be governed by the Airy stress function $\phi = \gamma\xi$ where γ is a function of y only and ξ is a function of x only. The solution of the thermal stress equation:

$$\nabla^4 \phi + \alpha E \nabla^2 T = 0 \quad (43)$$

where

$$\nabla^2 = \frac{\partial^2}{\partial x^2} + \frac{\partial^2}{\partial y^2} \quad (44)$$

involves the determination of the function ξ and its derivatives since:

$$f_x = \ddot{\gamma} \xi \quad (45)$$

$$f_y = \gamma \ddot{\xi} \quad (46)$$

$$S_{xy} = -\dot{\gamma} \dot{\xi} \quad (47)$$

and since the function γ is known from analysis of a two-dimensional body infinite in the x direction.

Standard methods were utilized for minimizing the strain energy in the two-dimensional body and the resulting stress expressions are presented in Table XXXIII. The values of stress for a number of locations within the body are presented in Tables XXXIV through XLV. As an example, the stress distributions for a particular body and plane within the body are shown in Figure 286, for $y/h = .80$, $h/Y_B = 2.00$, and $a/h = .50$.

5.2.2 Three-Dimensional Case - Area Including Body Corner

In considering the stresses in a three-dimensional body, six stresses exist at a point:

$$\sigma_x, \sigma_y, \sigma_z, \tau_{xy}, \tau_{yz}, \tau_{xz} \quad (48)$$

The distribution of these stresses must obey the equations of compatibility and equilibrium and satisfy the boundary conditions.

The solution for ξ does not depend on the elastic constants of the material E , and ν . This has been widely reported, particularly by Timoshenko and Goodier, Theory of Elasticity; Heldenfels and Roberts, NACA TN2769; and Roberts and Mendelson, NASA TND-1740.

If this is the case, then the function ξ , obtained by analysis of a two-dimensional body, can possibly exist on mutually perpendicular planes (i.e. x-y, y-z) of the three-dimensional body. This hypothesis is based on the fact that the influence between perpendicular planes is through the mechanism of ν , Poisson's ratio, and as stated above the function ξ is independent of ν .

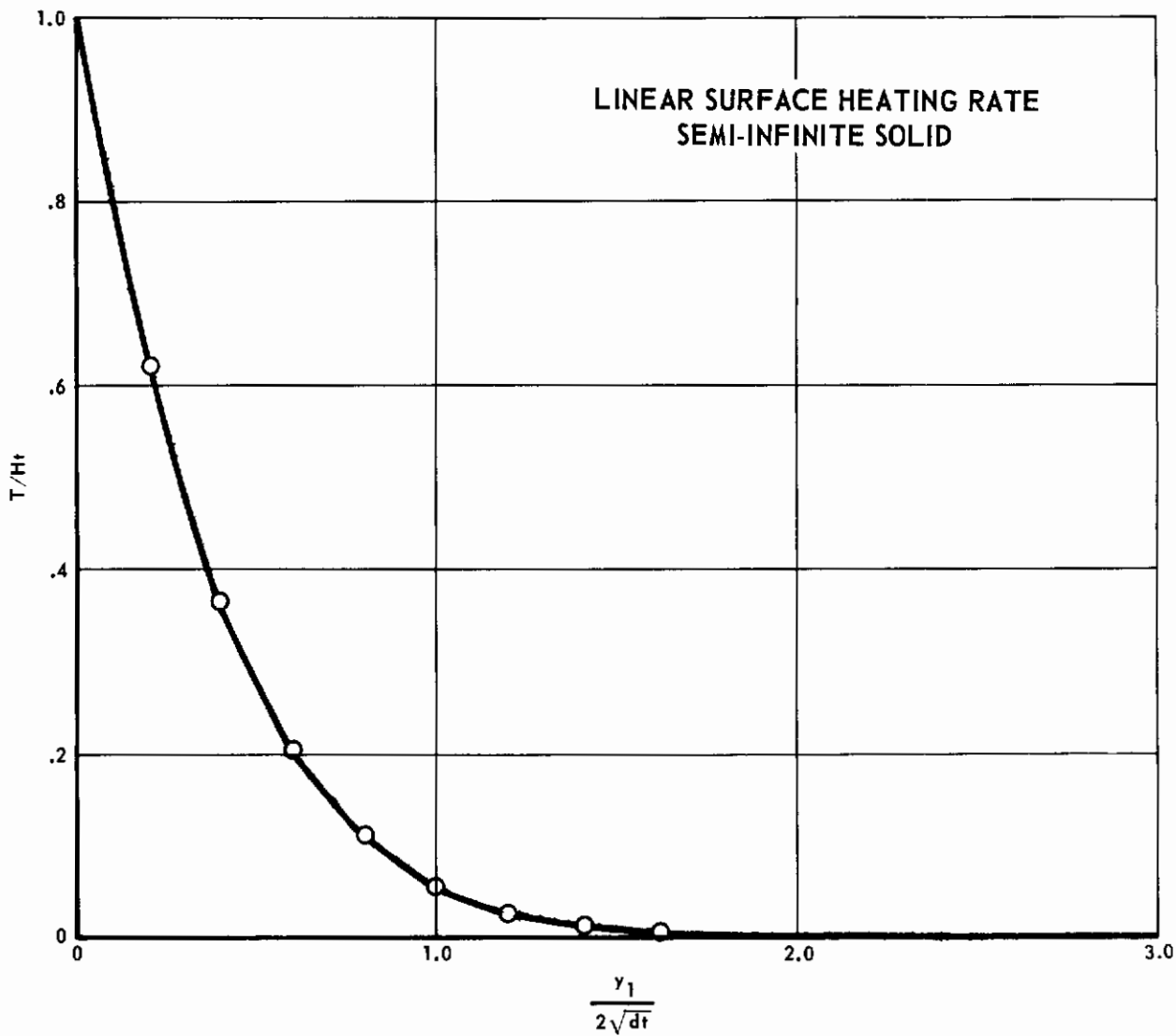


FIGURE 283 - SOLUTION OF THE ONE-DIMENSIONAL HEAT FLOW SYSTEM

Text continued on page 389

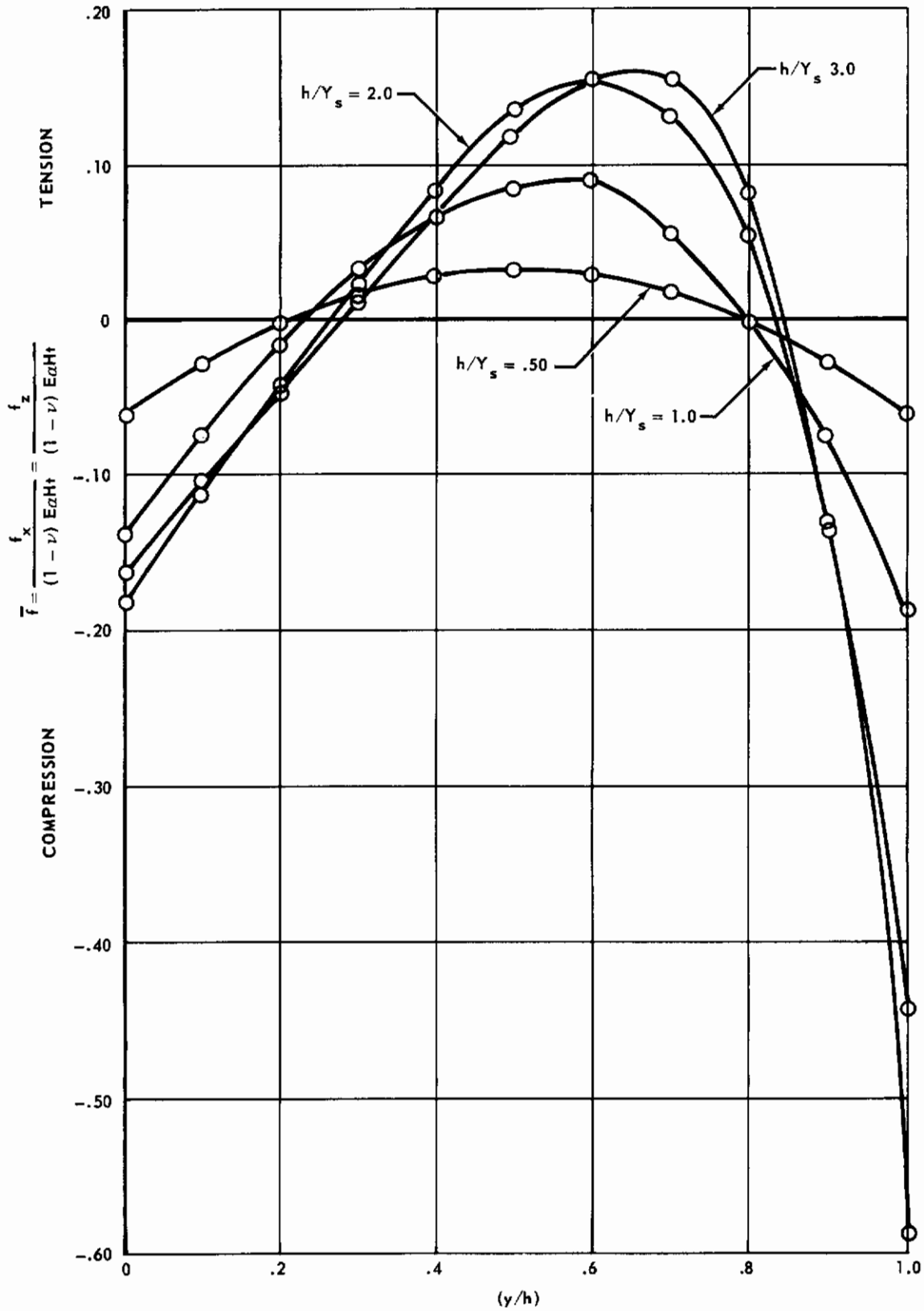


FIGURE 284 - DIMENSIONLESS THERMAL STRESS AT POINTS REMOTE FROM FREE EDGES

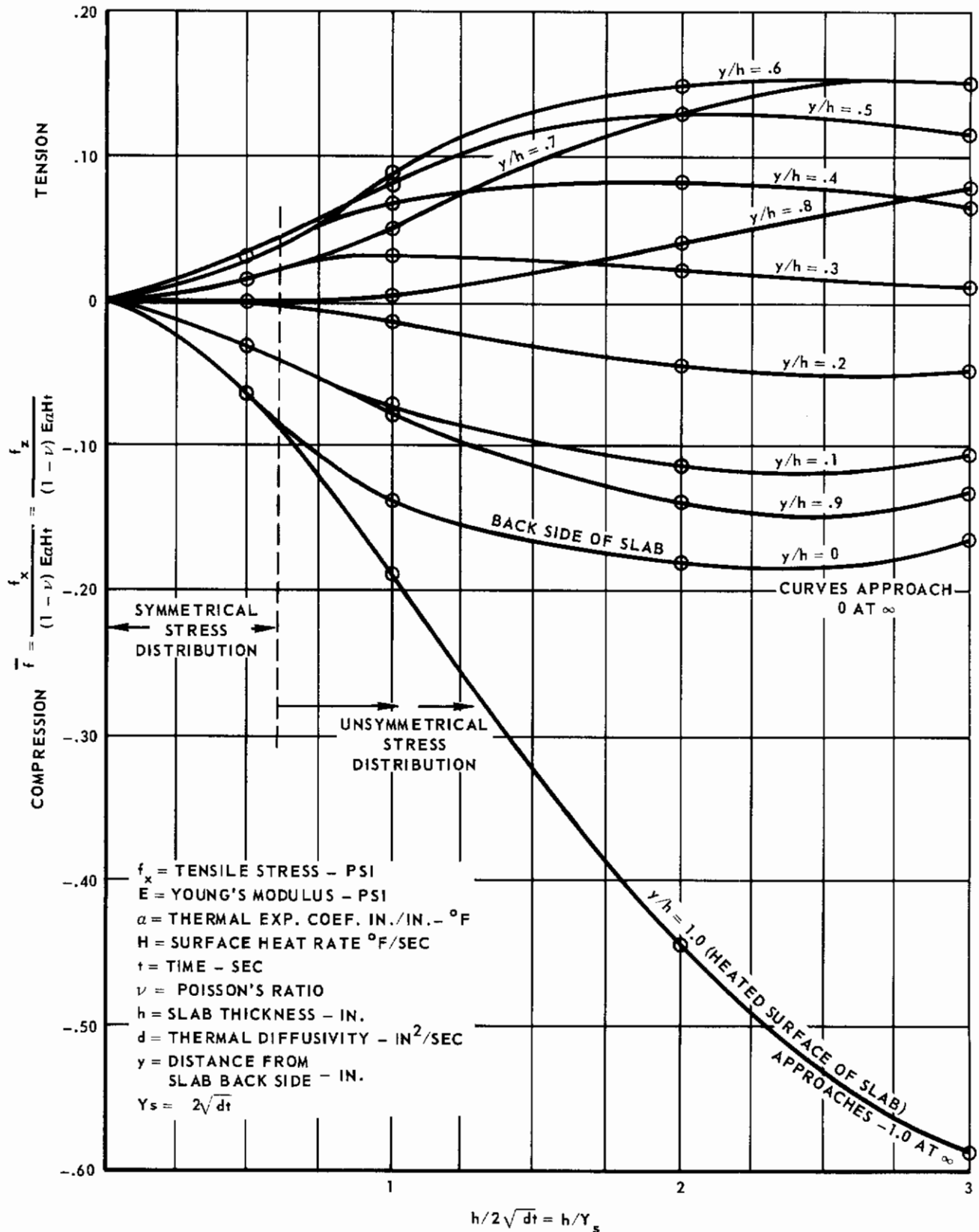


FIGURE 285 - DIMENSIONLESS THERMAL STRESS AT POINTS REMOTE FROM FREE EDGES

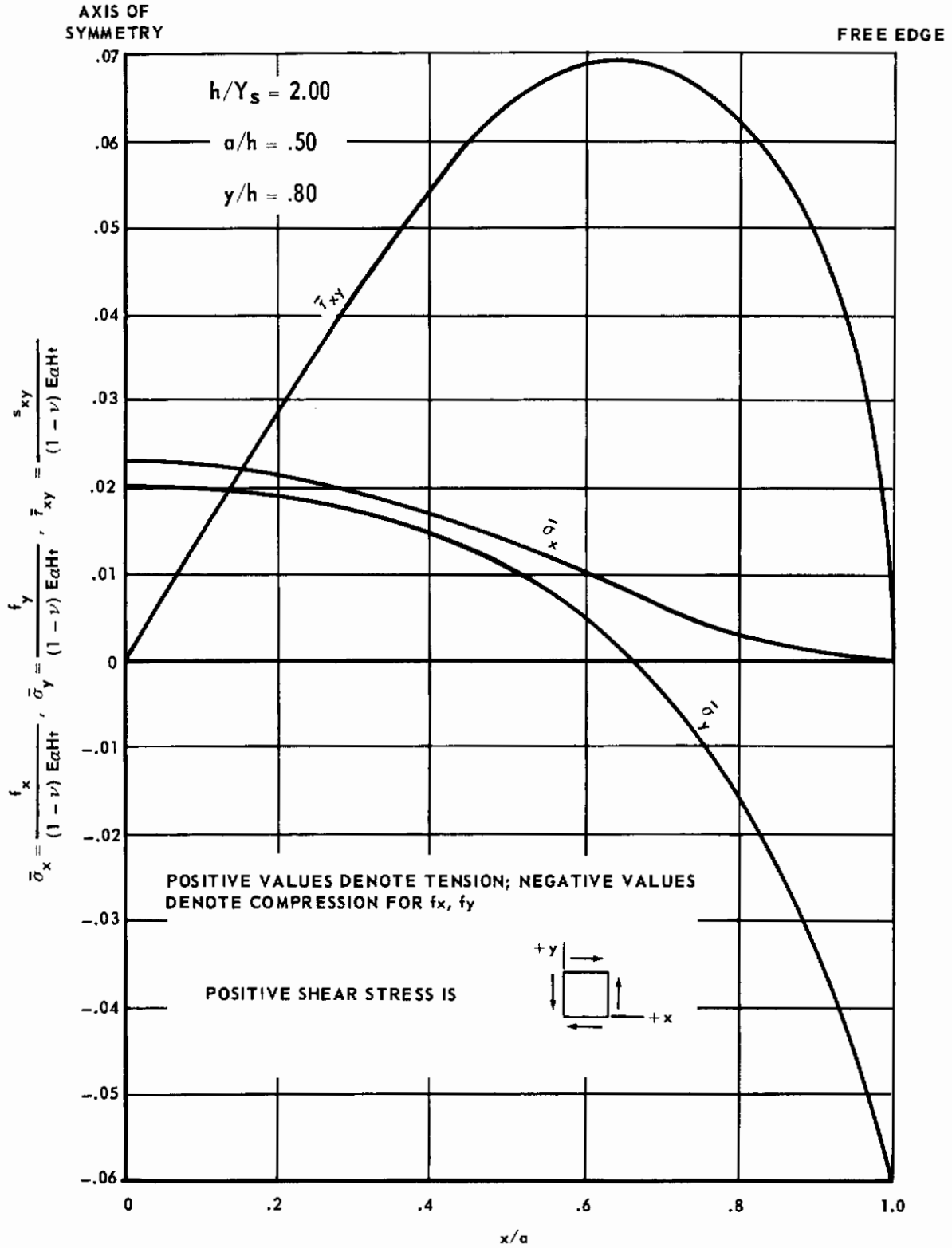


FIGURE 286 - DIMENSIONLESS STRESS DISTRIBUTION TWO-DIMENSIONAL BODY

TABLE XXXIII — STRESS EXPRESSIONS FOR AREAS ADJACENT TO FREE EDGES REMOTE FROM CORNERS

$$\begin{aligned}
 -\sigma_x &= \frac{1}{(1-\nu)} \frac{f_x}{E \alpha \Delta t} = \left[(A - m) \left(\frac{y}{h}\right) - A \left(\frac{y}{h}\right)^n - g \right] \left[1 - \frac{1}{BC - DE} \left(2 C \sin \beta \frac{x}{h} \sinh \mu \frac{x}{h} - 2 E \cos \beta \frac{x}{h} \cosh \mu \frac{x}{h} \right) \right] \\
 -\tau_{xy} &= \frac{1}{(1-\nu)} \frac{S_{xy}}{E \alpha \Delta t} = \left[\frac{(A - m)}{2} \left(\frac{y}{h}\right)^2 - \frac{A}{(n+1)} \left(\frac{y}{h}\right)^{n+1} - g \left(\frac{y}{h}\right) \right] \left\{ \frac{1}{BC - DE} \left[E \left(2 \beta \sin \beta \frac{x}{h} \cosh \mu \frac{x}{h} - 2 \mu \cos \beta \frac{x}{h} \sinh \mu \frac{x}{h} \right) \right] \right. \\
 &\quad \left. + C \left(2 \mu \sin \beta \frac{x}{h} \cosh \mu \frac{x}{h} + 2 \beta \cos \beta \frac{x}{h} \sinh \mu \frac{x}{h} \right) \right\} \\
 -\sigma_y &= \frac{1}{(1-\nu)} \frac{f_y}{E \alpha \Delta t} = \left[\frac{(A - m)}{6} \left(\frac{y}{h}\right)^3 - \frac{A}{(n+1)(n+2)} \left(\frac{y}{h}\right)^{n+2} - \frac{g}{2} \left(\frac{y}{h}\right)^2 \right] \left\{ \frac{1}{BC - DE} \left[E \left(2 \mu \beta \sin \beta \frac{x}{h} \sinh \mu \frac{x}{h} - (\mu^2 - \beta^2) \cos \beta \frac{x}{h} \cosh \mu \frac{x}{h} \right) \right] \right. \\
 &\quad \left. + C \left((\mu^2 - \beta^2) \sin \beta \frac{x}{h} \sinh \mu \frac{x}{h} + 2 \mu \beta \cos \beta \frac{x}{h} \cosh \mu \frac{x}{h} \right) \right\}
 \end{aligned}$$

$B = 2 \sin \beta a/h \sinh \mu a/h$
 $C = (2 \mu \cos \beta a/h \sinh \mu a/h - 2 \beta \sin \beta a/h \cosh \mu a/h)$
 $D = 2 \cos \beta a/h \cosh \mu a/h$
 $E = (2 \beta \cos \beta a/h \sinh \mu a/h + 2 \mu \sin \beta a/h \cosh \mu a/h)$

b/y_0	A	m	g	n	μ	β
.5	.365	0	.0608	2.00	3.40	2.76
1.0	.706	.050	.1390	2.75	3.50	2.32
2.0	.958	.263	.1810	4.75	4.21	2.42
3.0	1.00	.425	.1620	6.96	4.71	2.75

where: A = coefficient of temperature gradient polynomial
 m & g = coefficients necessary for equilibrium of cross section
 n = exponent in temperature gradient polynomial
 $\mu + i\beta$ = a complex number which is part of the solution to $\nabla^4 \phi + E \alpha \nabla^2 T = 0$

**TABLE XXXIV -
STATE OF STRESS ADJACENT TO THE FREE EDGES REMOTE FROM CORNER**

$h/Y_s = .50 \quad a/h = .50$

$\bar{\sigma}_x = f_x/EaHt(1 - \nu)$

$\bar{\sigma}_y = f_y/EaHt(1 - \nu)$

$\bar{\tau}_{xy} = S_{xy}/EaHt(1 - \nu)$

		x/a					
		0	0.2	0.4	0.6	0.8	1.0
y/h	1.0	$\bar{\sigma}_x \times 10^3$ -30.20 0 0	$\bar{\sigma}_x \times 10^3$ -28.10 0 0	$\bar{\sigma}_x \times 10^3$ -22.05 0 0	$\bar{\sigma}_x \times 10^3$ -13.44 0 0	$\bar{\sigma}_x \times 10^3$ -4.860 0 0	0 0 0
	0.8	$\bar{\sigma}_x \times 10^3$ -1.192 5.600 0	$\bar{\sigma}_x \times 10^3$ -1.110 5.090 4.110	$\bar{\sigma}_x \times 10^3$ -.8710 3.400 7.410	$\bar{\sigma}_x \times 10^3$ -.5300 .1560 8.870	$\bar{\sigma}_x \times 10^3$ -.1920 -6.0250 7.070	0 -13.90 0
	0.6	$\bar{\sigma}_x \times 10^3$ 13.32 12.55 0	$\bar{\sigma}_x \times 10^3$ 12.40 11.40 2.020	$\bar{\sigma}_x \times 10^3$ 9.730 7.630 3.640	$\bar{\sigma}_x \times 10^3$ 5.920 .3500 4.360	$\bar{\sigma}_x \times 10^3$ 2.140 -13.52 3.480	0 -31.20 0
	0.5	$\bar{\sigma}_x \times 10^3$ 15.10 13.63 0	$\bar{\sigma}_x \times 10^3$ 14.05 12.40 0	$\bar{\sigma}_x \times 10^3$ 11.030 8.280 0	$\bar{\sigma}_x \times 10^3$ 6.720 .380 0	$\bar{\sigma}_x \times 10^3$ 2.430 -14.70 0	0 -33.80 0
	0.4	$\bar{\sigma}_x \times 10^3$ 13.32 12.55 0	$\bar{\sigma}_x \times 10^3$ 12.40 11.40 -2.020	$\bar{\sigma}_x \times 10^3$ 9.730 7.630 -3.640	$\bar{\sigma}_x \times 10^3$ 5.920 .3500 -4.360	$\bar{\sigma}_x \times 10^3$ 2.140 -13.52 -3.480	0 -31.20 0
	0.2	$\bar{\sigma}_x \times 10^3$ -1.192 5.600 0	$\bar{\sigma}_x \times 10^3$ -1.110 5.090 -4.110	$\bar{\sigma}_x \times 10^3$ -.8710 3.400 -7.410	$\bar{\sigma}_x \times 10^3$ -.5300 .1560 -8.870	$\bar{\sigma}_x \times 10^3$ -.1920 -6.025 -7.070	0 -13.90 0
	0	$\bar{\sigma}_x \times 10^3$ -30.20 0 0	$\bar{\sigma}_x \times 10^3$ -28.10 0 0	$\bar{\sigma}_x \times 10^3$ -22.05 0 0	$\bar{\sigma}_x \times 10^3$ -13.44 0 0	$\bar{\sigma}_x \times 10^3$ -4.860 0 0	0 0 0

**TABLE XXXV -
STATE OF STRESS ADJACENT TO THE EDGES REMOTE FROM CORNER**

$h/Y_s = .50 \quad a/h = 1.0 \quad (\text{TWO DIM.})$

$$\begin{aligned} \bar{\sigma}_x &= f_x/EaHt(1-\nu) \\ \bar{\sigma}_y &= f_y/EaHt(1-\nu) \\ \bar{\tau}_{xy} &= S_{xy}/EaHt(1-\nu) \end{aligned}$$

			x/a					
			0	0.2	0.4	0.6	0.8	1.0
y/h	1.0	$\bar{\sigma}_x \times 10^3$ $\bar{\sigma}_y \times 10^3$ $\bar{\tau}_{xy} \times 10^3$	-60.8 0 0	-60.5 0 0	-52.5 0 0	-34.9 0 0	-14.8 0 0	0 0 0
	0.8	$\bar{\sigma}_x \times 10^3$ $\bar{\sigma}_y \times 10^3$ $\bar{\tau}_{xy} \times 10^3$	-2.40 1.39 0	-2.38 1.76 2.30	-2.07 2.54 5.55	-1.38 2.42 9.55	-.585 -1.64 10.9	0 -15.0 0
	0.6	$\bar{\sigma}_x \times 10^3$ $\bar{\sigma}_y \times 10^3$ $\bar{\tau}_{xy} \times 10^3$	26.8 3.12 0	26.6 3.96 1.13	23.2 5.70 2.73	15.4 5.45 4.70	6.55 -3.68 5.38	0 -33.8 0
	0.5	$\bar{\sigma}_x \times 10^3$ $\bar{\sigma}_y \times 10^3$ $\bar{\tau}_{xy} \times 10^3$	30.4 3.38 0	30.2 4.30 0	26.2 6.20 0	17.5 5.91 0	7.40 -3.99 0	0 -36.7 0
	0.4	$\bar{\sigma}_x \times 10^3$ $\bar{\sigma}_y \times 10^3$ $\bar{\tau}_{xy} \times 10^3$	26.8 3.12 0	26.6 3.96 1.13	23.2 5.70 2.73	15.4 5.45 4.70	6.55 -3.68 5.38	0 -33.8 0
	0.2	$\bar{\sigma}_x \times 10^3$ $\bar{\sigma}_y \times 10^3$ $\bar{\tau}_{xy} \times 10^3$	-2.40 1.39 0	-2.38 1.76 2.30	-2.07 2.54 5.55	-1.38 2.42 9.55	-.585 -1.64 10.9	0 -15.0 0
	0	$\bar{\sigma}_x \times 10^3$ $\bar{\sigma}_y \times 10^3$ $\bar{\tau}_{xy} \times 10^3$	-60.8 0 0	-60.5 0 0	-52.5 0 0	-34.9 0 0	-14.8 0 0	0 0 0

**TABLE XXXVI -
STATE OF STRESS ADJACENT TO THE FREE EDGES REMOTE FROM CORNER**

$h/Y_s = .50 \quad a/h = 1.50$

$\bar{\sigma}_x = f_x/EaHt(1 - \nu)$

$\bar{\sigma}_y = f_y/EaHt(1 - \nu)$

$\bar{\tau}_{xy} = S_{xy}/EaHt(1 - \nu)$

			x/a					
			0	0.2	0.4	0.6	0.8	1.0
y/h	1.0	$\bar{\sigma}_x \times 10^3$ $\bar{\sigma}_y \times 10^3$ $\bar{\tau}_{xy} \times 10^3$	-60.8 0 0	-60.8 0 0	-60.8 0 0	-51.9 0 0	-29.8 0 0	0 0 0
	0.8	$\bar{\sigma}_x \times 10^3$ $\bar{\sigma}_y \times 10^3$ $\bar{\tau}_{xy} \times 10^3$	-2.40 0 0	-2.40 .141 0	-2.40 1.06 1.16	-2.05 2.60 5.29	-1.18 1.45 11.10	0 -15.05 0
	0.6	$\bar{\sigma}_x \times 10^3$ $\bar{\sigma}_y \times 10^3$ $\bar{\tau}_{xy} \times 10^3$	26.8 0 0	26.8 .317 0	26.8 2.38 .568	22.9 5.82 2.60	13.1 3.25 5.45	0 -33.8 0
	0.5	$\bar{\sigma}_x \times 10^3$ $\bar{\sigma}_y \times 10^3$ $\bar{\tau}_{xy} \times 10^3$	30.4 0 0	30.4 .344 0	30.4 2.58 0	25.9 6.32 0	14.9 3.52 0	0 -36.70 0
	0.4	$\bar{\sigma}_x \times 10^3$ $\bar{\sigma}_y \times 10^3$ $\bar{\tau}_{xy} \times 10^3$	26.8 0 0	26.8 .317 0	26.8 2.38 -.568	22.9 5.82 -2.60	13.1 3.25 -5.45	0 -33.8 0
	0.2	$\bar{\sigma}_x \times 10^3$ $\bar{\sigma}_y \times 10^3$ $\bar{\tau}_{xy} \times 10^3$	-2.40 0 0	-2.40 .141 0	-2.40 1.06 -1.16	-2.05 2.60 -5.29	-1.18 1.45 -11.10	0 -15.05 0
	0	$\bar{\sigma}_x \times 10^3$ $\bar{\sigma}_y \times 10^3$ $\bar{\tau}_{xy} \times 10^3$	-60.8 0 0	-60.8 0 0	-60.8 0 0	-51.9 0 0	-29.8 0 0	0 0 0

**TABLE XXXVII-
STATE OF OF STRESS ADJACENT TO THE FREE EDGES REMOTE FROM CORNER**

$h/Y_s = 1.0 \quad a/h = .50$

$$\begin{aligned} \bar{\sigma}_x &= f_x/EaHt(1-\nu) \\ \bar{\sigma}_y &= f_y/EaHt(1-\nu) \\ \bar{\tau}_{xy} &= S_{xy}/EaHt(1-\nu) \end{aligned}$$

			x/a					
			0	0.2	0.4	0.6	0.8	1.0
y/h	1.0	$\bar{\sigma}_x \times 10^3$ $\bar{\sigma}_y \times 10^3$ $\bar{\tau}_{xy} \times 10^3$	-77.2	-70.0	-56.5	-33.4	-11.33	0
			0	0	0	0	0	0
			0	0	0	0	0	0
	0.8	$\bar{\sigma}_x \times 10^3$ $\bar{\sigma}_y \times 10^3$ $\bar{\tau}_{xy} \times 10^3$	1.23	1.11	.897	.531	.180	0
			13.2	12.1	8.21	.595	-12.7	-34.3
			0	10.10	18.10	21.8	17.5	0
	0.6	$\bar{\sigma}_x \times 10^3$ $\bar{\sigma}_y \times 10^3$ $\bar{\tau}_{xy} \times 10^3$	37.2	33.8	27.2	16.1	5.46	0
		29.1	26.6	18.1	1.31	-27.9	-75.5	
		0	4.04	7.25	8.75	7.05	0	
0.5	$\bar{\sigma}_x \times 10^3$ $\bar{\sigma}_y \times 10^3$ $\bar{\tau}_{xy} \times 10^3$	34.6	31.4	25.3	14.95	5.07	0	
		30.8	28.2	19.1	1.39	-29.6	-80.0	
		0	-819	-1.47	-1.77	-1.43	0.40	
0.4	$\bar{\sigma}_x \times 10^3$ $\bar{\sigma}_y \times 10^3$ $\bar{\tau}_{xy} \times 10^3$	27.4	24.8	20.1	11.85	4.02	0	
		27.40	25.0	17.05	1.23	-26.3	-71.2	
		0	-5.32	-9.55	-11.52	-9.29	0	
0.2	$\bar{\sigma}_x \times 10^3$ $\bar{\sigma}_y \times 10^3$ $\bar{\tau}_{xy} \times 10^3$	-6.54	-5.94	-4.79	-2.83	-.960	0	
		11.40	10.42	7.10	.515	-10.96	-29.6	
		0	-8.89	-15.95	-19.25	-15.5	0	
0	$\bar{\sigma}_x \times 10^3$ $\bar{\sigma}_y \times 10^3$ $\bar{\tau}_{xy} \times 10^3$	-56.9	-50.2	-41.5	-24.6	-8.34	0	
		0	0	0	0	0	0	
		0	0	0	0	0	0	

**TABLE XXXVIII -
STATE OF STRESS ADJACENT TO THE FREE EDGES REMOTE FROM CORNER**

$h/Y_s = 1.0 \quad a/h = 1.0$

$\bar{\sigma}_x = f_x/EaHt(1 - \nu)$

$\bar{\sigma}_y = f_y/EaHt(1 - \nu)$

$\bar{\tau}_{xy} = S_{xy}/EaHt(1 - \nu)$

		x/a						
		0	0.2	0.4	0.6	0.8	1.0	
y/h	1.0	$\bar{\sigma}_x \times 10^3$	-184	-177	-152	-106	-42.7	0
	$\bar{\sigma}_y \times 10^3$	0	0	0	0	0	0	0
	$\bar{\tau}_{xy} \times 10^3$	0	0	0	0	0	0	0
	0.8	$\bar{\sigma}_x \times 10^3$	2.92	2.81	2.42	1.68	.677	0
	$\bar{\sigma}_y \times 10^3$	3.00	4.30	5.62	5.09	-3.76	-34.0	
	$\bar{\tau}_{xy} \times 10^3$	0	6.96	15.9	26.2	28.9	0	
	0.6	$\bar{\sigma}_x \times 10^3$	88.6	85.2	73.3	51.0	20.6	0
$\bar{\sigma}_y \times 10^3$	7.19	10.3	13.5	12.2	-9.04	-81.5		
$\bar{\tau}_{xy} \times 10^3$	0	2.80	6.37	10.5	11.6	0		
0.5	$\bar{\sigma}_x \times 10^3$	82.6	79.1	68.0	47.3	19.1	0	
$\bar{\sigma}_y \times 10^3$	8.07	11.6	15.2	13.7	-10.1	-91.5		
$\bar{\tau}_{xy} \times 10^3$	0	-566	-1.29	-2.13	-2.35	0		
0.4	$\bar{\sigma}_x \times 10^3$	65.2	62.7	53.9	37.5	15.1	0	
$\bar{\sigma}_y \times 10^3$	7.63	10.95	14.35	13.0	-9.59	-86.5		
$\bar{\tau}_{xy} \times 10^3$	0	-3.69	-8.40	-13.82	-15.3	0		
0.2	$\bar{\sigma}_x \times 10^3$	-15.6	-15.0	-12.9	-8.96	-3.62	0	
$\bar{\sigma}_y \times 10^3$	3.46	4.97	6.50	5.87	-4.35	-39.3		
$\bar{\tau}_{xy} \times 10^3$	0	-6.15	-14.02	-23.1	-25.6	0		
0	$\bar{\sigma}_x \times 10^3$	-135.4	-130	-112	-77.9	-31.4	0	
$\bar{\sigma}_y \times 10^3$	0	0	0	0	0	0		
$\bar{\tau}_{xy} \times 10^3$	0	0	0	0	0	0		

**TABLE XXXIX -
STATE OF STRESS ADJACENT TO THE FREE EDGES REMOTE FROM CORNER**

$h/Y_s = 1.0 \quad a/h = 1.5$

$$\begin{aligned} \bar{\sigma}_x &= f_x/EaHt(1-\nu) \\ \bar{\sigma}_y &= f_y/EaHt(1-\nu) \\ \bar{\tau}_{xy} &= S_{xy}/EaHt(1-\nu) \end{aligned}$$

		x/a					
		0	0.2	0.4	0.6	0.8	1.0
y/h	1.0	$\bar{\sigma}_x \times 10^3$ -189	$\bar{\sigma}_x \times 10^3$ -189	$\bar{\sigma}_x \times 10^3$ -183	$\bar{\sigma}_x \times 10^3$ -150	$\bar{\sigma}_x \times 10^3$ -74.0	$\bar{\sigma}_x \times 10^3$ 0
		$\bar{\sigma}_y \times 10^3$ 0	$\bar{\sigma}_y \times 10^3$ 0	$\bar{\sigma}_y \times 10^3$ 0	$\bar{\sigma}_y \times 10^3$ 0	$\bar{\sigma}_y \times 10^3$ 0	$\bar{\sigma}_y \times 10^3$ 0
		$\bar{\tau}_{xy} \times 10^3$ 0	$\bar{\tau}_{xy} \times 10^3$ 0	$\bar{\tau}_{xy} \times 10^3$ 0	$\bar{\tau}_{xy} \times 10^3$ 0	$\bar{\tau}_{xy} \times 10^3$ 0	$\bar{\tau}_{xy} \times 10^3$ 0
	0.8	$\bar{\sigma}_x \times 10^3$ 3.00	$\bar{\sigma}_x \times 10^3$ 3.00	$\bar{\sigma}_x \times 10^3$ 2.90	$\bar{\sigma}_x \times 10^3$ 2.39	$\bar{\sigma}_x \times 10^3$ 1.18	$\bar{\sigma}_x \times 10^3$ 0
		$\bar{\sigma}_y \times 10^3$.157	$\bar{\sigma}_y \times 10^3$.696	$\bar{\sigma}_y \times 10^3$ 2.59	$\bar{\sigma}_y \times 10^3$ 5.15	$\bar{\sigma}_y \times 10^3$ 2.38	$\bar{\sigma}_y \times 10^3$ -35.9
		$\bar{\tau}_{xy} \times 10^3$ 0	$\bar{\tau}_{xy} \times 10^3$.910	$\bar{\tau}_{xy} \times 10^3$ 4.93	$\bar{\tau}_{xy} \times 10^3$ 15.75	$\bar{\tau}_{xy} \times 10^3$ 29.4	$\bar{\tau}_{xy} \times 10^3$ 0
	0.6	$\bar{\sigma}_x \times 10^3$ 91.0	$\bar{\sigma}_x \times 10^3$ 91.0	$\bar{\sigma}_x \times 10^3$ 88.0	$\bar{\sigma}_x \times 10^3$ 72.5	$\bar{\sigma}_x \times 10^3$ 35.7	$\bar{\sigma}_x \times 10^3$ 0
	$\bar{\sigma}_y \times 10^3$.378	$\bar{\sigma}_y \times 10^3$ 1.67	$\bar{\sigma}_y \times 10^3$ 6.22	$\bar{\sigma}_y \times 10^3$ 12.35	$\bar{\sigma}_y \times 10^3$ 5.74	$\bar{\sigma}_y \times 10^3$ -86.1	
	$\bar{\tau}_{xy} \times 10^3$ 0	$\bar{\tau}_{xy} \times 10^3$.365	$\bar{\tau}_{xy} \times 10^3$ 1.98	$\bar{\tau}_{xy} \times 10^3$ 6.32	$\bar{\tau}_{xy} \times 10^3$ 11.80	$\bar{\tau}_{xy} \times 10^3$ 0	
0.5	$\bar{\sigma}_x \times 10^3$ 84.5	$\bar{\sigma}_x \times 10^3$ 84.5	$\bar{\sigma}_x \times 10^3$ 81.6	$\bar{\sigma}_x \times 10^3$ 67.3	$\bar{\sigma}_x \times 10^3$ 33.2	$\bar{\sigma}_x \times 10^3$ 0	
	$\bar{\sigma}_y \times 10^3$.424	$\bar{\sigma}_y \times 10^3$ 1.88	$\bar{\sigma}_y \times 10^3$ 6.99	$\bar{\sigma}_y \times 10^3$ 13.85	$\bar{\sigma}_y \times 10^3$ 6.44	$\bar{\sigma}_y \times 10^3$ -96.9	
	$\bar{\tau}_{xy} \times 10^3$ 0	$\bar{\tau}_{xy} \times 10^3$ -.074	$\bar{\tau}_{xy} \times 10^3$ -.410	$\bar{\tau}_{xy} \times 10^3$ -1.28	$\bar{\tau}_{xy} \times 10^3$ -2.39	$\bar{\tau}_{xy} \times 10^3$ 0	
0.4	$\bar{\sigma}_x \times 10^3$ 67.0	$\bar{\sigma}_x \times 10^3$ 67.0	$\bar{\sigma}_x \times 10^3$ 64.6	$\bar{\sigma}_x \times 10^3$ 53.3	$\bar{\sigma}_x \times 10^3$ 26.2	$\bar{\sigma}_x \times 10^3$ 0	
	$\bar{\sigma}_y \times 10^3$.401	$\bar{\sigma}_y \times 10^3$ 1.78	$\bar{\sigma}_y \times 10^3$ 6.60	$\bar{\sigma}_y \times 10^3$ 13.1	$\bar{\sigma}_y \times 10^3$ 6.09	$\bar{\sigma}_y \times 10^3$ -91.5	
	$\bar{\tau}_{xy} \times 10^3$ 0	$\bar{\tau}_{xy} \times 10^3$ -.481	$\bar{\tau}_{xy} \times 10^3$ -2.61	$\bar{\tau}_{xy} \times 10^3$ -8.35	$\bar{\tau}_{xy} \times 10^3$ -15.6	$\bar{\tau}_{xy} \times 10^3$ 0	
0.2	$\bar{\sigma}_x \times 10^3$ -16.0	$\bar{\sigma}_x \times 10^3$ -16.0	$\bar{\sigma}_x \times 10^3$ -15.5	$\bar{\sigma}_x \times 10^3$ -12.7	$\bar{\sigma}_x \times 10^3$ -6.26	$\bar{\sigma}_x \times 10^3$ 0	
	$\bar{\sigma}_y \times 10^3$.182	$\bar{\sigma}_y \times 10^3$.805	$\bar{\sigma}_y \times 10^3$ 3.00	$\bar{\sigma}_y \times 10^3$ 5.95	$\bar{\sigma}_y \times 10^3$ 2.76	$\bar{\sigma}_y \times 10^3$ -41.5	
	$\bar{\tau}_{xy} \times 10^3$ 0	$\bar{\tau}_{xy} \times 10^3$ -.804	$\bar{\tau}_{xy} \times 10^3$ -4.36	$\bar{\tau}_{xy} \times 10^3$ -13.92	$\bar{\tau}_{xy} \times 10^3$ -26.0	$\bar{\tau}_{xy} \times 10^3$ 0	
0	$\bar{\sigma}_x \times 10^3$ -139	$\bar{\sigma}_x \times 10^3$ -139	$\bar{\sigma}_x \times 10^3$ -134	$\bar{\sigma}_x \times 10^3$ -111	$\bar{\sigma}_x \times 10^3$ -54.5	$\bar{\sigma}_x \times 10^3$ 0	
	$\bar{\sigma}_y \times 10^3$ 0	$\bar{\sigma}_y \times 10^3$ 0	$\bar{\sigma}_y \times 10^3$ 0	$\bar{\sigma}_y \times 10^3$ 0	$\bar{\sigma}_y \times 10^3$ 0	$\bar{\sigma}_y \times 10^3$ 0	
	$\bar{\tau}_{xy} \times 10^3$ 0	$\bar{\tau}_{xy} \times 10^3$ 0	$\bar{\tau}_{xy} \times 10^3$ 0	$\bar{\tau}_{xy} \times 10^3$ 0	$\bar{\tau}_{xy} \times 10^3$ 0	$\bar{\tau}_{xy} \times 10^3$ 0	

**TABLE XL -
STATE OF STRESS ADJACENT TO THE FREE EDGES REMOTE FROM CORNER**

$h/Y_s = 2.0 \quad a/h = .50$

$\bar{\sigma}_x = f_x/EaHt(1 - \nu)$

$\bar{\sigma}_y = f_y/EaHt(1 - \nu)$

$\bar{\tau}_{xy} = S_{xy}/EaHt(1 - \nu)$

			x/a					
			0	0.2	0.4	0.6	0.8	1.0
y/h	1.0	$\bar{\sigma}_x \times 10^3$ $\bar{\sigma}_y \times 10^3$ $\bar{\tau}_{xy} \times 10^3$	-236	-220	-172	-100	-26.6	0
	0.8	$\bar{\sigma}_x \times 10^3$ $\bar{\sigma}_y \times 10^3$ $\bar{\tau}_{xy} \times 10^3$	23.2	21.6	16.9	9.85	2.62	0
	0.6	$\bar{\sigma}_x \times 10^3$ $\bar{\sigma}_y \times 10^3$ $\bar{\tau}_{xy} \times 10^3$	81.1	75.2	58.8	34.4	9.12	0
	0.5	$\bar{\sigma}_x \times 10^3$ $\bar{\sigma}_y \times 10^3$ $\bar{\tau}_{xy} \times 10^3$	70.4	65.3	51.0	29.8	7.92	0
	0.4	$\bar{\sigma}_x \times 10^3$ $\bar{\sigma}_y \times 10^3$ $\bar{\tau}_{xy} \times 10^3$	45.2	42.0	32.8	19.2	5.09	0
	0.2	$\bar{\sigma}_x \times 10^3$ $\bar{\sigma}_y \times 10^3$ $\bar{\tau}_{xy} \times 10^3$	-22.7	-21.1	-16.5	-9.63	-2.56	0
	0	$\bar{\sigma}_x \times 10^3$ $\bar{\sigma}_y \times 10^3$ $\bar{\tau}_{xy} \times 10^3$	-96.5	-89.5	-70.0	-40.9	-10.9	0

**TABLE XLI -
STATE OF STRESS ADJACENT TO THE FREE EDGES REMOTE FROM CORNER**

$h/Y_s = 2.0 \quad a/h = 1.0$

$\bar{\sigma}_x = f_x/EaHt(1 - \nu)$

$\bar{\sigma}_y = f_y/EaHt(1 - \nu)$

$\bar{\tau}_{xy} = S_{xy}/EaHt(1 - \nu)$

			x/a					
			0	0.2	0.4	0.6	0.8	1.0
y/h	1.0	$\bar{\sigma}_x \times 10^3$ $\bar{\sigma}_y \times 10^3$ $\bar{\tau}_{xy} \times 10^3$	-439	-427	-381	-281	-121	0
			0	0	0	0	0	0
			0	0	0	0	0	0
	0.8	$\bar{\sigma}_x \times 10^3$ $\bar{\sigma}_y \times 10^3$ $\bar{\tau}_{xy} \times 10^3$	43.1	42.0	37.4	27.6	11.9	0
			3.93	5.35	9.09	11.27	-1.99	-68.7
			0	11.45	30.0	57.6	76.0	0
			0	0	0	0	0	0
0.6	$\bar{\sigma}_x \times 10^3$ $\bar{\sigma}_y \times 10^3$ $\bar{\tau}_{xy} \times 10^3$	150	146	130	96.2	41.5	0	
		11.03	15.02	25.55	31.65	-5.58	-193.0	
		0	3.76	9.85	18.90	25.0	0	
0.5	$\bar{\sigma}_x \times 10^3$ $\bar{\sigma}_y \times 10^3$ $\bar{\tau}_{xy} \times 10^3$	131	127	113	83.6	36.0	0	
		12.18	16.60	28.2	34.9	-6.15	-213	
		0	-1.01	-2.64	-5.06	-6.69	0	
0.4	$\bar{\sigma}_x \times 10^3$ $\bar{\sigma}_y \times 10^3$ $\bar{\tau}_{xy} \times 10^3$	83.9	81.5	72.8	53.7	23.2	0	
		12.20	16.60	28.2	35.0	-6.15	-213	
		0	-4.59	-12.0	-23.1	-30.5	0	
0.2	$\bar{\sigma}_x \times 10^3$ $\bar{\sigma}_y \times 10^3$ $\bar{\tau}_{xy} \times 10^3$	-42.1	-41.0	-36.5	-27.0	-11.6	0	
		5.81	7.91	13.45	16.67	-2.94	-102	
		0	-6.45	-16.9	-32.4	-42.9	0	
0	$\bar{\sigma}_x \times 10^3$ $\bar{\sigma}_y \times 10^3$ $\bar{\tau}_{xy} \times 10^3$	-179	-174	-155	-115	-49.4	0	
		0	0	0	0	0	0	
		0	0	0	0	0	0	

**TABLE XLII -
STATE OF STRESS ADJACENT TO THE FREE EDGES REMOTE FROM CORNER**

$h/Y_s = 2.0 \quad a/h = 1.50$

$$\begin{aligned} \bar{\sigma}_x &= f_x/EaHt(1-\nu) \\ \bar{\sigma}_y &= f_y/EaHt(1-\nu) \\ \bar{\tau}_{xy} &= S_{xy}/EaHt(1-\nu) \end{aligned}$$

			x/a					
			0	0.2	0.4	0.6	0.8	1.0
y/h	1.0	$\bar{\sigma}_x \times 10^3$ $\bar{\sigma}_y \times 10^3$ $\bar{\tau}_{xy} \times 10^3$	-444 0 0	-444 0 0	-444 0 0	-378 0 0	-218 0 0	0 0 0
	0.8	$\bar{\sigma}_x \times 10^3$ $\bar{\sigma}_y \times 10^3$ $\bar{\tau}_{xy} \times 10^3$	43.6 0 0	43.6 -519 .774	43.6 2.86 7.11	37.2 8.20 30.2	21.4 7.34 71.1	0 -70.0 0
	0.6	$\bar{\sigma}_x \times 10^3$ $\bar{\sigma}_y \times 10^3$ $\bar{\tau}_{xy} \times 10^3$	152 0 0	152 1.46 .254	152 8.05 2.34	128 23.05 9.90	74.5 20.65 23.4	0 -196 0
	0.5	$\bar{\sigma}_x \times 10^3$ $\bar{\sigma}_y \times 10^3$ $\bar{\tau}_{xy} \times 10^3$	132 0 0	132 1.61 -.0690	132 8.87 -.625	113 25.4 -2.65	64.6 22.75 -6.25	0 -206 0
	0.4	$\bar{\sigma}_x \times 10^3$ $\bar{\sigma}_y \times 10^3$ $\bar{\tau}_{xy} \times 10^3$	84.8 0 0	84.8 1.61 -.310	84.8 8.87 -2.85	72.4 25.4 -12.10	41.5 22.75 -28.5	0 -207 0
	0.2	$\bar{\sigma}_x \times 10^3$ $\bar{\sigma}_y \times 10^3$ $\bar{\tau}_{xy} \times 10^3$	-42.6 0 0	-42.6 .768 -.436	-42.6 4.26 -4.01	-36.4 12.15 -17.0	-20.9 10.9 -40.1	0 -103 0
	0	$\bar{\sigma}_x \times 10^3$ $\bar{\sigma}_y \times 10^3$ $\bar{\tau}_{xy} \times 10^3$	-181 0 0	-181 0 0	-181 0 0	-155 0 0	-88.7 0 0	0 0 0

TABLE XLIII-
STATE OF STRESS ADJACENT TO THE FREE EDGES REMOTE FROM CORNER

$h/Y_s = 3.0 \quad a/h = .50$

$$\bar{\sigma}_x = f_x/EaHt(1 - \nu)$$

$$\bar{\sigma}_y = f_y/EaHt(1 - \nu)$$

$$\bar{\tau}_{xy} = S_{xy}/EaHt(1 - \nu)$$

		x/a														
		0	0.2	0.4	0.6	0.8	1.0									
y/h	1.0	$\bar{\sigma}_x \times 10^3$ -393	$\bar{\sigma}_y \times 10^3$ 0	$\bar{\tau}_{xy} \times 10^3$ 0	-368	0	0	-295	0	0	-185	0	0	-65.8	0	0
	0.8	$\bar{\sigma}_x \times 10^3$ 54.1	$\bar{\sigma}_y \times 10^3$ 21.2	$\bar{\tau}_{xy} \times 10^3$ 0	50.7	20.3	28.1	40.7	16.3	53.3	25.5	5.16	68.8	9.07	-20.9	-74.4
	0.6	$\bar{\sigma}_x \times 10^3$ 102	$\bar{\sigma}_y \times 10^3$ 59.0	$\bar{\tau}_{xy} \times 10^3$ 0	95.7	56.3	4.84	76.9	45.4	9.18	48.1	14.4	11.9	17.1	-58.1	-207
	0.5	$\bar{\sigma}_x \times 10^3$ 78.2	$\bar{\sigma}_y \times 10^3$ 71.6	$\bar{\tau}_{xy} \times 10^3$ 0	73.3	68.5	-8.06	58.7	55.2	-15.3	36.7	17.45	-19.8	13.1	-70.7	-252
	0.4	$\bar{\sigma}_x \times 10^3$ 44.2	$\bar{\sigma}_y \times 10^3$ 75.2	$\bar{\tau}_{xy} \times 10^3$ 0	41.4	71.9	-16.0	33.2	58.0	-30.2	20.8	18.3	-39.1	7.40	-74.2	-264
	0.2	$\bar{\sigma}_x \times 10^3$ -31.4	$\bar{\sigma}_y \times 10^3$ 44.4	$\bar{\tau}_{xy} \times 10^3$ 0	-29.4	42.4	-17.7	-23.6	34.2	-33.6	-22.1	10.8	-43.5	-5.26	-43.8	-156
	0	$\bar{\sigma}_x \times 10^3$ -108	$\bar{\sigma}_y \times 10^3$ 0	$\bar{\tau}_{xy} \times 10^3$ 0	-102	0	0	-81.4	0	0	-50.9	0	0	-18.2	0	0

TABLE XLIV-
STATE OF STRESS ADJACENT TO THE FREE EDGES REMOTE FROM CORNER

$h/Y_s = 3.0 \quad a/h = 1.0$

$$\bar{\sigma}_x = f_x/EaHt(1 - \nu)$$

$$\bar{\sigma}_y = f_y/EaHt(1 - \nu)$$

$$\bar{\tau}_{xy} = S_{xy}/EaHt(1 - \nu)$$

		x/a															
		0	0.2	0.4	0.6	0.8	1.0										
y/h	1.0	$\bar{\sigma}_x \times 10^3$ -587	$\bar{\sigma}_y \times 10^3$ 0	$\bar{\tau}_{xy} \times 10^3$ 0	-582	0	0	-530	0	0	-419	0	0	-191	0	0	
	0.8	$\bar{\sigma}_x \times 10^3$ 81.0	$\bar{\sigma}_y \times 10^3$ 1.81	$\bar{\tau}_{xy} \times 10^3$ 0	80.4	3.27	6.26	73.2	7.64	20.6	57.9	12.2	48.7	26.4	-1.85	75.1	-74.1
	0.6	$\bar{\sigma}_x \times 10^3$ 153	$\bar{\sigma}_y \times 10^3$ 5.04	$\bar{\tau}_{xy} \times 10^3$ 0	152	9.09	1.08	138	21.2	3.55	109	33.8	8.37	49.8	-5.13	12.9	-206
	0.5	$\bar{\sigma}_x \times 10^3$ 117	$\bar{\sigma}_y \times 10^3$ 6.12	$\bar{\tau}_{xy} \times 10^3$ 0	116	11.1	-1.80	106	25.8	-5.92	83.5	41.1	-14.0	38.1	-6.24	-21.6	-251
	0.4	$\bar{\sigma}_x \times 10^3$ 66.1	$\bar{\sigma}_y \times 10^3$ 6.44	$\bar{\tau}_{xy} \times 10^3$ 0	65.5	11.6	-35.6	59.7	27.1	-11.7	47.1	43.2	-27.6	21.6	-6.55	-42.6	-263
	0.2	$\bar{\sigma}_x \times 10^3$ -47.0	$\bar{\sigma}_y \times 10^3$ 3.80	$\bar{\tau}_{xy} \times 10^3$ 0	-46.6	6.85	-3.95	-42.4	16.0	-13.0	-33.6	25.5	-30.7	-15.3	-3.87	-47.5	-155
	0	$\bar{\sigma}_x \times 10^3$ -162	$\bar{\sigma}_y \times 10^3$ 0	$\bar{\tau}_{xy} \times 10^3$ 0	-161	0	0	-146	0	0	-116	0	0	-52.9	0	0	0

**TABLE XLV -
STATE OF STRESS ADJACENT TO THE FREE EDGES REMOTE FROM CORNER**

$h/Y_s = 3.0 \quad a/h = 1.5$

$\bar{\sigma}_x = f_x/EaHt(1 - \nu)$

$\bar{\sigma}_y = f_y/EaHt(1 - \nu)$

$\bar{\tau}_{xy} = S_{xy}/EaHt(1 - \nu)$

		x/a						
		0	0.2	0.4	0.6	0.8	1.0	
y/h	1.0	$\bar{\sigma}_x \times 10^3$ $\bar{\sigma}_y \times 10^3$ $\bar{\tau}_{xy} \times 10^3$	-587 0 0	-587 0 0	-587 0 0	-587 0 0	-319 0 0	0 0 0
	0.8	$\bar{\sigma}_x \times 10^3$ $\bar{\sigma}_y \times 10^3$ $\bar{\tau}_{xy} \times 10^3$	81.0 0 0	81.0 .144 0	81.0 1.83 2.55	81.0 7.89 20.2	44.0 11.15 64.5	0 -75.4 0
	0.6	$\bar{\sigma}_x \times 10^3$ $\bar{\sigma}_y \times 10^3$ $\bar{\tau}_{xy} \times 10^3$	153 0 0	153 .400 0	153 5.08 .439	153 21.9 3.48	83.3 31.0 11.1	0 -210 0
	0.5	$\bar{\sigma}_x \times 10^3$ $\bar{\sigma}_y \times 10^3$ $\bar{\tau}_{xy} \times 10^3$	117 0 0	117 .486 0	117 6.18 -.731	117 26.6 -5.80	63.6 37.7 -18.5	0 -255 0
	0.4	$\bar{\sigma}_x \times 10^3$ $\bar{\sigma}_y \times 10^3$ $\bar{\tau}_{xy} \times 10^3$	66.1 0 0	66.1 .510 0	66.1 6.49 -1.45	66.1 28.0 -11.5	36.0 39.6 -36.6	0 -268 0
	0.2	$\bar{\sigma}_x \times 10^3$ $\bar{\sigma}_y \times 10^3$ $\bar{\tau}_{xy} \times 10^3$	-47.0 0 0	-47.0 .301 0	-47.0 3.82 -1.61	-47.0 16.5 -12.8	-25.6 23.1 -40.8	0 -158 0
	0	$\bar{\sigma}_x \times 10^3$ $\bar{\sigma}_y \times 10^3$ $\bar{\tau}_{xy} \times 10^3$	-162 0 0	-162 0 0	-162 0 0	-162 0 0	-88.1 0 0	0 0 0

The following considerations were used in determining the thermal stresses near the edges of a three-dimensional body. If stresses at points symmetrical in x and z are computed, then from consideration of the two-dimensional stress distribution:

$$\sigma_x = \sigma_z = C_1 f_x = C_1 \frac{\partial^2 \phi}{\partial y^2} \quad (49)$$

$$\sigma_y = C_2 f_y = C_2 \frac{\partial^2 \phi}{\partial x^2} \quad (50)$$

$$\tau_{xy} = \tau_{yz} = C_3 S_{xy} = -C_3 \frac{\partial^2 \phi}{\partial x \partial y} \quad (51)$$

$$\tau_{xz} : \text{ to be determined} \quad (52)$$

If these equations are substituted in the general differential equations of compatibility and equilibrium the constants C_1 , C_2 , C_3 , and the stress τ_{xz} can be determined. The expression for the stress τ_{xz} found in this analysis must be confined along 0-0 of Figure 287 since part of the expression for τ_{xz} is eliminated because of the symmetry of this analysis.

Because of the symmetry of the problem, the nine equations of equilibrium and compatibility reduce to the following:

$$(1-\nu) \frac{\partial^2 \sigma_x}{\partial y^2} - \nu \frac{\partial^2 \sigma_y}{\partial y^2} + \frac{\partial^2 \sigma_y}{\partial x^2} - 2\nu \frac{\partial^2 \sigma_x}{\partial x^2} - 2(1+\nu) \frac{\partial^2 \tau_{xy}}{\partial x \partial y} = -E\alpha \frac{\partial^2 T}{\partial y^2} \quad (53)$$

$$(1-\nu) \frac{\partial^2 \sigma_x}{\partial x^2} - \nu \frac{\partial^2 \sigma_y}{\partial x^2} = (1+\nu) \frac{\partial^2 \tau_{xy}}{\partial x^2} \quad (54)$$

$$(1-\nu) \frac{\partial^2 \sigma_x}{\partial x \partial y} - \nu \frac{\partial^2 \sigma_y}{\partial x \partial y} = (1+\nu) \frac{\partial^2 \tau_{xy}}{\partial x \partial y} \quad (55)$$

$$\frac{\partial^2 \sigma_y}{\partial x^2} - 2\nu \frac{\partial^2 \sigma_x}{\partial x^2} = (1+\nu) \left(-2 \frac{\partial^2 \tau_{xy}}{\partial x \partial y} - \frac{\partial^2 \tau_{xy}}{\partial y^2} \right) \quad (56)$$

$$\frac{\partial \sigma_x}{\partial x} + \frac{\partial \tau_{xy}}{\partial y} + \frac{\partial \tau_{xy}}{\partial x} = 0 \quad (57)$$

$$\frac{\partial \sigma_y}{\partial y} + 2 \frac{\partial \tau_{xy}}{\partial x} = 0 \quad (58)$$

Combining the above equations further reduces the number of equations to be satisfied to five, which are presented below.

$$[(1-\nu)\ddot{Y}\ddot{E} - 2\nu\ddot{Y}\ddot{E}']C_1 + [Y\ddot{E}'' - \nu\ddot{Y}\ddot{E}''']C_2 + [2(1+\nu)\ddot{Y}\ddot{E}''']C_3 = -E\alpha\ddot{T} \quad (59)$$

$$[(1-\nu)\ddot{Y}\ddot{E}''']C_1 - [\nu Y\ddot{E}''''']C_2 = (1+\nu) \frac{\partial^2 \tilde{\tau}_{xz}}{\partial x^2} \quad (60)$$

(61)

$$-[2\nu\ddot{Y}\ddot{E}''']C_1 + [Y\ddot{E}''''']C_2 + [2(1+\nu)\ddot{Y}\ddot{E}''''']C_3 = -(1+\nu) \frac{\partial^2 \tilde{\tau}_{xz}}{\partial y^2}$$

$$[\ddot{Y}\ddot{E}''']C_1 - [\ddot{Y}\ddot{E}''']C_3 = - \frac{\partial \tilde{\tau}_{xz}}{\partial x} \quad (62)$$

$$[\ddot{Y}\ddot{E}''']C_2 - [2\nu\ddot{Y}\ddot{E}''']C_3 = 0 \quad (63)$$

It can then be shown that the solution of these equations may be expressed in the following form:

$$\sigma_x = \sigma_z = \frac{1}{(1-\nu)} \frac{\partial^2 \phi}{\partial y^2} = \frac{1}{(1-\nu)} f_x \quad (64)$$

$$\sigma_y = \frac{4}{(1-\nu^2)} \frac{\partial^2 \phi}{\partial x^2} = \frac{4}{(1+\nu^2)} \frac{\partial^2 \phi}{\partial y^2} = \frac{4}{(1-\nu^2)} f_y \quad (65)$$

$$\tau_{xy} = \tau_{yz} = - \frac{2}{(1-\nu^2)} \frac{\partial^2 \phi}{\partial x \partial y} = - \frac{2}{(1-\nu^2)} \frac{\partial^2 \phi}{\partial y \partial z} = \frac{2}{(1-\nu^2)} S_{xy} \quad (66)$$

$$\tau_{xz} = \frac{1}{(1+\nu)} \frac{\partial^2 \phi}{\partial y^2} = \frac{1}{(1+\nu)} f_x \quad (67)$$

where f_x , f_y , and S_{xy} are the stresses obtained for the two-dimensional case summarized in Tables XXXIV through XXXV.

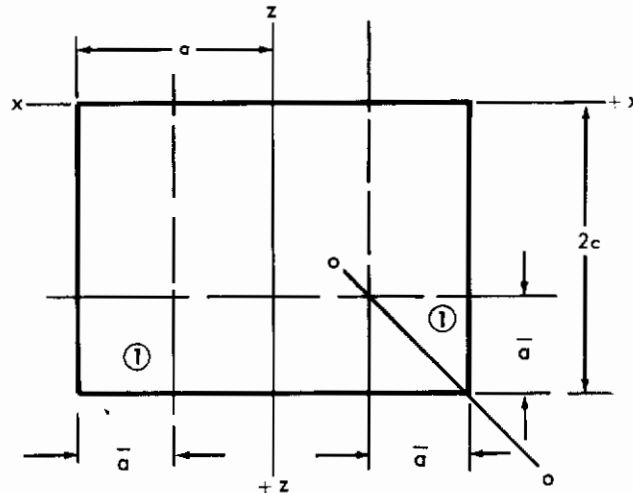


FIGURE 287- GENERAL BODY GEOMETRY (TOP VIEW)

The stresses shown above for the three-dimensional case indicate the probable mode of failure in the parallelepiped. If the stresses in Tables XXIX through XL for the stresses remote from the corner are multiplied by the factors shown above, these resulting stresses at the corner are higher than at any other point in the solid. It will be seen that a very high compression stress (σ_y) exists at $x = a$, $z = ca$, $y/\eta \approx 0.5$ (points located at the corners approximately midway through the thickness). Likewise, very high shearing stresses exist through this point at a 45° plane as a result of the high compressive stress σ_y . The probable mode of failure is, therefore, a shear failure at 45° through a point midway through the thickness at the corners of the parallelepiped.

In summation, the analysis of stresses at points adjacent to the free edges shows that the corners are the areas of highest stress and; therefore, critical in thermal shock failures. The stress expressions derived in the three-dimensional case are a function of surface heating rate and material properties and can be utilized to determine the mode of failure and magnitude of the stresses produced by thermal shock environments.

6. COMPARISON OF TEST RESULTS WITH THEORETICAL PREDICTIONS

6.1 TEST SETUP

Eight small blocks of zirconia were tested in such a manner as to produce the desired thermal environment. The surface heating rate was chosen to insure thermal stress failure of the blocks. Figure 288 shows the test setup used. The torch head was moved toward the zirconia specimen in such a way to give a linear surface temperature rise on the specimen.

6.2 ANALYSIS OF TEST RESULTS

It was noticed that cracks formed in the corners of the specimens at about 45° to the heated surface. This fact substantiates the theoretical results derived in stress analysis of areas adjacent to the free edges, particularly the corners. The occurrence of these failures can be rationalized in also another way.

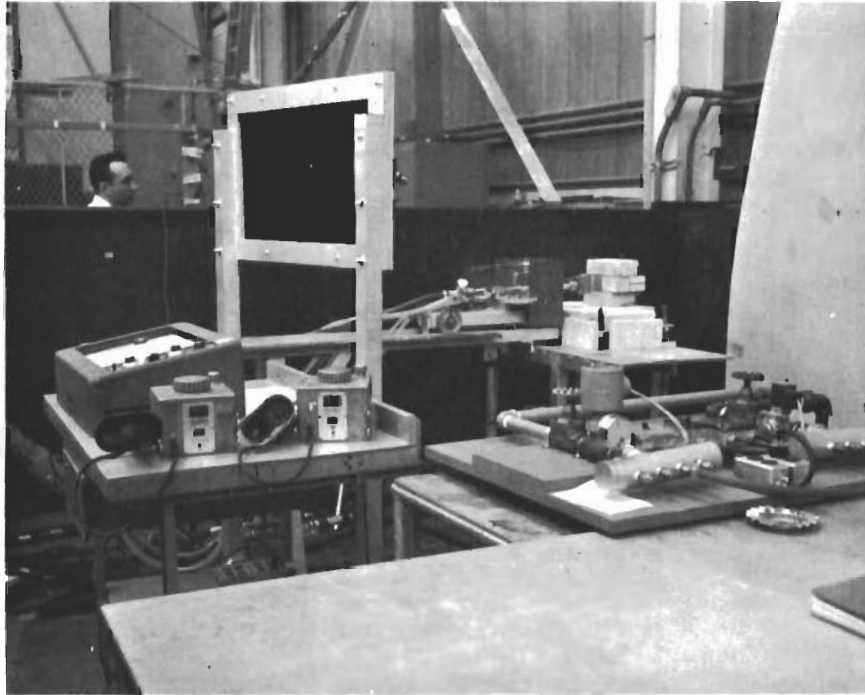


FIGURE 288 -SUBSCALE THERMAL TEST FACILITY

Suppose the test specimen blocks consisted of numerous thin layers parallel to the heated surface. Because of the non-linear temperature gradient through the thickness of the block, the radii of curvature of adjacent layers, each with a different ΔT across their individual thicknesses, would not be the same. The radii of curvature would be greatest near the heated surface of the block due to the larger change in temperature per unit thickness in this area, causing the layers to try to separate some finite distance at the center.

To force these different curvatures to be compatible at their interfaces requires that compressive stresses exist at the corners reacting the tensile stresses in the center of the block. The plane of maximum shear stress would be located at 45° to the horizontal axis at these corners.

Because of the foregoing considerations, it is concluded that the mode of failure predicted in the areas that included the corners is substantially correct.

6.3 PREDICTION OF THERMAL FAILURES

If the thermophysical properties of a ceramic material are known, then the preceding work can be used to predict failure or non-failure for a specified set of conditions, i.e. heating rate, surface temperature, and body geometry. Some preliminary attempts were made to verify these predictions using the test setup shown in Figure 288. The results of these attempts cannot be considered conclusive, as more work would be necessary for complete correlation of actual behavior to theoretical results.

6.4 USE OF THEORETICAL MATERIAL

It is recommended that the expressions derived in Section V be used to estimate the feasibility of designs, the structural potential of various ceramics, and to guide material development.

Note: Page 394 is a blank page.

REFERENCES

1. "High Temperature Composite Structure," The Martin Company, Final Report, ASD-TDR-62-418, September 1962.
2. Lees, L., Recovery Dynamics "Heat Transfer at Hypersonic Speed in a Planetary Atmosphere", Space Technology, Ed H. Siefert, John Wiley and Sons, Inc., New York
3. "Development of Frontal Section for Super-Orbital, Lifting, Re-Entry Vehicle," Solar Aircraft Company, RTD-TDR-64-59, v. I-III
4. Eckert, E.R.G., "Survey on Heat Transfer at High Speeds," WADC Technical Report 54-70
5. Hansen, C. F., "Approximations for the Thermodynamic and Transport Properties of High Temperature Air," NASA TRR-50, 1959
6. Furukawa, G. T., Douglas, T. B., McCoskey, R. E., and Ginnings, D. C., "Thermal Properties of Aluminum Oxide from 0° to 1200°K," NBS Journal of Research, v. 57, n. 2, August 1956, pages 67-82
7. Snyder, N. W., Gier, J. T., and Dunkle, R. V., "Total Normal Emissivity Measurements on Aircraft Materials between 100° and 1000°F," A.S.M.E. Transactions, v. 771
8. Gier, J. T. and Boelter, L. M. K., "The Silver-Constantan Plated Thermopile Temperature - Its Measurement and Control in Science and Industry," American Institute of Physics, pages 1284, 1941
9. Man, W. H., Jr. and Pears, C. D., "A Radial Heat Flow Method for the Measurement of Thermal Conductivity Methods at Batelle Memorial Institute, October 26-28, 1961
10. Goldsmith, Alexander, Hirschorn, Harry J., and Waterman, Thomas C., "Thermophysical Properties of Solid Materials," Armour Research Foundation, Chicago, Illinois, USAF WADC TR58-476 v. 1-5, November 1960
11. R. W. Powell, "N.P.L. Work on Thermal Conductivity Standards," The Third Thermal Conductivity Conference, Metals and Ceramics Division, Oak Ridge National Laboratory, Oak Ridge, Tennessee, v. I, page 326, 1963
12. Pears, C. D., "The Thermal Properties of Twenty-Six Solid Materials to 5000°F or Their Destruction Temperature," Southern Research Institute, Birmingham, Alabama, USAF ASD TDR 62-765, January 1963
13. Pears, C. D., The Third Thermal Conductivity Conference, hosted by Metals and Ceramics Division, Oak Ridge National Laboratory, Oak Ridge, Tennessee, 1963, pages 453-479

14. Fieldhouse, I. B., Hedges, J. C., and Waterman, T. E., "Measurements of Thermal Properties", USAF-WADC-TR55-495, part 3, November 1956
15. Weschler, Alfred E., and Glaser, Peter C., "Investigation of the Thermal Properties of High Temperature Insulation Materials," Arthur D. Little, Inc., USAF-ASD-TDR-63-574, July 1963
16. Matra, J. P., Jr., "On the Development of Theoretical Methods of Predicting Thermal Properties of a Hetrogeneous Material," The Martin Company, RM-94, March 1961
17. Jakob, Max, and Hawkins, George A., "Elements of Heat Transfer", Wiley and Sons, New York, 1957

DISTRIBUTION LIST - GOVERNMENT*

DEPARTMENT OF AIR FORCE

AFML (MAA - Mr. J. Teres)
WPAFB, Ohio 45433

AFML (MAAE*)
WPAFB, Ohio 45433

AFML (MAAM - Librarian)
WPAFB, Ohio 45433

AFML (MATF) (6)
WPAFB, Ohio 45433

AFML (MAX - Dr. A. M. Lovelace)
WPAFB, Ohio 45433

(AFFDL) (FDDS)
Attn: Aerospace Dynamics Branch
WPAFB, Ohio 45433

AFFDL (FDTS)
Attn: Applied Mechanics Branch
WPAFB, Ohio 45433

MOAMA (MCAE)
Technical Library

AFFTC (FTBAT-2)
Edwards AFB
California 93523

SSD (SERTH)
AF Unit Post Office
Los Angeles 45, Calif. 90045

Hq. USAF (AFRSTC)
Wash. DC 20013 (Pentagon)

SEG (RTD)
SEPIE
Technical Reports Div.
WPAFB, Ohio 45433

SEG (RTD)
SEPIR
Technical Information Ref. Dr.
WPAFB, Ohio 45433

FTD (TD-E2B)
WPAFB, Ohio 45433

AIR MATERIAL AREAS (AMA'S)

MAAMA (MAE)
Technical Library
Olmsted AFB, Pa. 17057

MOAMA (MCAE)
Technical Library
Brookley AFB, Ala. 36615

OOAMA (OCAE)
Technical Library
Hill AFB, Utah 84401

OCAMA (OCAE)
Technical Library
Tinker AFB, Okla. 73145

ROAMA (ROAEPP-1)
Technical Library
Griffin AFB, N. Y. 13442

SMAMA (SMAE)
Technical Library
McClellan AFB, Calif. 95652

SAAMA (SANE0)
Technical Library
Kelly AFB, Texas 78241

SRAMA (SBAE)
Technical Library
Norton AFB, Calif. 92409

WRAMA (WRAE)
Technical Library
Robins AFB, Ga. 31094

DEPARTMENT OF THE ARMY

Commander
Army Research Office
Arlington Mail Station
Arlington, Virginia 22210

*One copy each except as noted in
parenthesis after first title

Commanding General
U.S. Army Ballistic Missile Agency
Documentation and Technical Info. Dr.
ORDAR-IKE
Redstone Arsenal, Ala.

Commanding General
U. S. Army Rocket and Guided Missile
Agency, ORDAR-RMS
Redstone Arsenal, Ala.

Commanding General
Ordnance Materials Research Office
Watertown Arsenal RFD
Watertown 72, Mass.

Frankford Arsenal
Research Institute
Attn: Mr. E. R. Rachel
Deputy Director
Philadelphia, Pa. 19104

Chief, Research & Development
U. S. Army Research & Development
Liason Group
Attn: Dr. B. Stein
APO 747, New York
New York 10001

Office, Chief of Ordnance
Attn: ORDTs Materials
Department of the Army
Wash. D.C. 20013

DEPARTMENT OF THE NAVY

Chief, Bureau of Naval Weapons
Department of the Navy
Industrial Division
Attn: (PID-2) Industrial Readiness Branch
Wash, D.C. 20013

Department of Navy
Office of Naval Research
Attn: Code 422
Wash, DC 20013

Commander
U.S. Naval Research Laboratory
Attn: J. B. Strandley
Anacostia Station
Wash, D.C. 20813

Department of the Navy
Special Projects Office
Attn: SP 271
Wash, D.C. 20013

DEPARTMENT OF DEFENSE

Office of the Dir. of Defense, R&E
Attn: Mr. J. C. Barrett
Room 3D-1077, Pentagon
Wash, D.C. 20013

Advanced Research Project Agency
Asst. Dir., Materials Sciences
Attn: Chas. F. Yost, 3D-155, Pentagon
Wash, D.C. 20013

Defense Materials Information Center
Battelle Memorial Institute
505 King Avenue
Columbus, Ohio 43216

Defense Documentation Center (20)
Cameron Station
Alexandria, Virginia 22314

GOVERNMENT AGENCIES

National Aeronautics & Space Div.
George C. Marshall Space Flight Center
Attn: MS and M-M/ Dr. W. R. Lucas
Huntsville, Ala. 35801

Jet Propulsion Laboratory
California Institute of Technology
Attn: Dr. L. Jaffe
4800 Oak Grove Drive
Pasadena, Calif. 91102

National Aeronautics and Space Admin.
Attn: Mr. C. C. Deutch
Wash, D.C. 20013

NASA, Lewis Research Center
Attn: G. Mandal, Chief Librarian
Cleveland 25, Ohio

Scientific & Technical Information Facility
Attn: NARA Representative
RQT-16448
P.O. Box 5700
Bethesda, Maryland 20014

DISTRIBUTION LIST - DEFENSE CONTRACTORS

Aerodynamics Corp.
Chief Librarian
San Diego 12, Calif. 92101

Aerojet General Corp.
Chief Librarian
6362 North Irwindale Ave.
Azusa, Calif.

Aeronca Manufacturing Corp.
Attn: Technical Library
1712 Germantown Road
Middletown, Ohio

Aeronutronic Division
Ford Motor Company
Technical Library
Ford Road
Newport Beach, Calif.

Aerospace Corporation
Attn: Technical Library
2400 E. El Segundo Blvd.
El Segundo, Calif.

AiResearch Manufacturing Company
Attn: Technical Library
9851 Sepulveda Blvd.
Los Angeles, Calif. 90045

Allison Division
General Motors Corp.
Attn: Technical Library
P.O. Box 894
Indianapolis, Indiana 46206

American Machine and Foundry
Attn: Engineering Library
1025 Royal Street
Alexandria, Virginia

Avco Corp.
Research and Advanced Development
Attn: Technical Library
201 Lowell Street
Wilmington, Mass

Avco Corp.
Attn: Technical Library
Nashville, Tennessee

Battelle Memorial Institute
Attn: Material Joining Div.
505 King Avenue
Columbus, Ohio 43216

Bell Aerosystems Company
Attn: Technical Library
P.O. Box 1
Buffalo, New York 14205

Bell Aerosystems Company
Attn: Librarian
P.O. Box 482
Ft. Worth, Texas

Beryllium Corp.
Attn: Librarian
P.O. Box 1462
Reading, Pennsylvania

Boeing Company
Attn: Technical Library
P.O. Box 3707
Seattle, Wash. 98101

Brush Beryllium Corp.
Attn: Librarian
17876 St. Clair Ave.
Cleveland, Ohio

Chance-Vought Corp.
Aeronautic Division
Attn: Technical Library
P.O. Box 5907
Dallas, Texas 75201

Chrysler Corporation, Missile Div.
Attn: Technical Library
P.O. Box 2628
Detroit, Mich. 48233

Convair Division of
General Dynamics Corp.
Attn: Technical Library
P.O. Box 1011
Pomona, Calif. 91408

Ceramic Industry
Attn: Alfred C. Allen
5 South Wabash Ave.
Chicago, Ill. 60603

Curtiss-Wright Corp.
Attn: Librarian
760 Northland Avenue
Buffalo, New York

Douglas Aircraft Co., Inc.
Missile and Space System Division
Technical Library
3000 Ocean Park Blvd.
Santa Monica, Calif. 90406

Douglas Aircraft Co., Inc.
Attn: Technical Library
El Segundo Division
827 Laphen Street
El Segundo, Calif.

E. I. Du Pont Company
Attn: Technical Library
Wilmington, Delaware

Fairchild Engine and Airplane Corp.
Fairchild Aircraft Div.
Attn: Technical Library
Hagerstown, Maryland

Forest Products Laboratory
Attn: Librarian
Madison, Wisconsin

Garrett Corp.
AiResearch Manufacturing Division
402 South 36th Street
Phoenix, Arizona 85026

General Dynamics Corp.
Attn: Technical Library
P.O. Box 166
San Diego, Calif. 92101

General Dynamics
Attn: Technical Library
Mail Zone C-68, P.O. Box 74-B
Fort Worth, Tex. 76101

General Dynamics
Astronautics
Attn: Librarian
San Diego, Calif. 92101

General Electric Co.
Flight Propulsion Laboratory Department
Attn: Technical Library
Cincinnati, Ohio 43202

Goodyear Aerospace Corp.
Attn: Technical Library
1210 Macmillon Road
Akron, Ohio 44135

Grumman Aircraft Corp.
Attn: Technical Library
New South Road
Bethpage, L.I., New York

Hughes Aircraft Company
Technical Library
Florence and Teale Street
Culver City, Calif.

IIT Research Institute
Attn: Librarian
10 West 35th Street
Chicago, Illinois

Lear Siegler Inc.
Attn: Librarian
110 Iona Northwest
Grand Rapids, Mich.

Lockheed Aircraft Corp.
Missiles and Space Div.
Attn: Librarian
Palo Alto, Calif. 94302

Lockheed Aircraft Corp.
Attn: Technical Library
Marietta, Georgia 30061

Ling-Temco-Vought, Inc.
Attn: Technical Library
P.O. Box 5907
Dallas, Texas 75222

Marquardt Aircraft Corp.
Attn: Technical Library
16555 Saticoy Street
Van Nuys, Calif. 91408

Marquardt Aircraft Corp.
Attn: Technical Library
1000 West 33rd Street
Ogden, Utah 84401

The Martin Company
Denver Division
Attn: Technical Library
P.O. Box 179
Denver, Colorado 80201

Narmco Research & Development
Attn: Librarian
8125 Aero Drive
San Diego, Calif. 92101

North American Aviation, Inc.
Technical Information Center
12214 Lakewood Blvd.
Downey, Calif.

North American Aviation, Inc.
Attn: Technical Library
4300 East Fifth Avenue
Columbus, Ohio 43216

North American Aviation, Inc.
Attn: Technical Library
International Airport
Los Angeles, Calif. 90052

Northrop Corporation
Norair Division
Attn: Technical Library
1001 E. Broadway
Hawthorne, Calif.

Pratt & Whitney Aircraft
United Aircraft Corp.
Attn: Librarian
362 South Main St.
East Hartford, Connecticut

Republic Aviation Corp.
Structural Development Section
Attn: Technical Library
Farmingdale, Long Island
New York 11735

Rocketdyne Division
North American Aviation, Inc.
Attn: Technical Library
6633 Canoga Ave.
Canoga Park, Calif.

Rohr Aircraft Corp.
Attn: Librarian
Post Office Box 643
Riverside, Calif. 95801

Rohr Aircraft Corp.
Attn: Librarian
Post Office Box 878
Chula Vista, Calif.

Ryan Aircraft Corp.
Material and Process
Attn: Technical Library
2701 Harbor Drive
San Diego, Calif. 92101

Ryan Aeronautical Co.
Attn: Technical Library
Lindberg Field
San Diego, Calif.

Space General Corporation
Attn: Technical Library
9200 East Flair Drive
El Monte, Calif.

Solar Aircraft Corp.
Division of International Harvester Co.
Attn: Technical Library
2200 Pacific Highway
San Diego, Calif. 92101

Southwest Research Institute
Attn: Technical Library
8500 Calabra Road
San Antonio, Texas 78205

Sperry Rand Corporation
Attn: Technical Library
Administration and Engineering Center
Detroit, Michigan

Stanford Research Institute
Documents Center
Attn: Acquisitions
Menla Park, California

Thompson-Ramo-Wooldridge, Inc.
Attn: Technical Library
23555 Euclid Avenue
Cleveland, Ohio 44177

Vitro Corp. of America
Vitro Laboratories
Attn: Librarian
200 Pleasant Valley Way
West Orange, New Jersey

Westinghouse Electric Corp.
Astro Nuclear Laboratories
P.O. Box 10864
Pittsburgh, Pennsylvania 15219

Note: Page 402 is a blank page.

Unclassified
Security Classification

DOCUMENT CONTROL DATA - R&D		
(Security classification of title, body of abstract and indexing annotation must be entered when the overall report is classified)		
1. ORIGINATING ACTIVITY (Corporate author) McDonnell Aircraft Corporation St. Louis, Missouri	2a. REPORT SECURITY CLASSIFICATION Unclassified 2b. GROUP	
3. REPORT TITLE Final report on Shielded Ceramic Composite Structure		
4. DESCRIPTIVE NOTES (Type of report and inclusive dates) Final report - 1 June 1963 through 18 June 1965		
5. AUTHOR(S) (Last name, first name, initial) Kummer, Donald L. Rosenthal, Jerome J. Lum, David W. et al		
6. REPORT DATE October 1965	7a. TOTAL NO. OF PAGES 405	7b. NO. OF REFS 17
8a. CONTRACT OR GRANT NO. AF33(657)-10996 b. PROJECT NO. NR7-997 c. d.	9a. ORIGINATOR'S REPORT NUMBER(S) AFML-TR-65-331 9b. OTHER REPORT NO(S) (Any other numbers that may be assigned this report) MAC Report A131	
10. AVAILABILITY/LIMITATION NOTICES DDC Release to CFSTI not authorized because this report contains technology identifiable with items on the strategic embargo lists.		
11. SUPPLEMENTARY NOTES <small>This document is subject to special export controls and each transmittal to foreign governments or foreign nationals may be made only with prior approval of the Manufacturing Technology Division.</small>	12. SPONSORING MILITARY ACTIVITY <small>Advanced Publication Techniques Branch (MAPT-2) Air Force Materials Laboratory Research and Technology Division Air Force Systems Command United States Air Force Wright-Patterson Air Force Base, Ohio</small>	
13. ABSTRACT Alumina, zirconia, and thoria were selected for use in composite ceramic heat shields for the leading surfaces of lifting orbital re-entry vehicles. Coated columbium and molybdenum were selected for substructure materials. Commercially available low density ($\leq 40\%$ of theoretical) and high density ($> 60\%$ of theoretical) alumina, zirconia, and thoria ceramics were evaluated for thermal shock resistance; and many high density, but no low density ceramics were found to be satisfactory. A sintered low density (95 lb/ft^3) thermal shock resistance zirconia was developed, but it was difficult to reproducibly manufacture. A sintered low density (125 lb/ft^3) thoria was developed that had low thermal shock resistance but could be reproducibly manufactured. Chemically bonded low and high density thermal shock resistant varieties of alumina, zirconia, and thoria were developed. Thermophysical properties were determined to temperatures as high as 4500°F for the ceramics utilized in this project. Analytical techniques were derived for predicting the thermal stress behavior of ceramics. Twenty-two sub-scale heat shield modules and three full size components were designed, fabricated, and environmentally tested. The full size components were a 3.0 inch radius, 3400°F leading edge; a 1.5 inch radius, 4000°F leading edge; and a 6.0 inch radius, 5000°F nose cap. The ceramic phase densities for these components were 57 lb/ft^3 , 97 lb/ft^3 , and 166 lb/ft^3 respectively. Satisfactory techniques were developed for processing, fabricating, and assembling ceramic heat shields. Typical launch vibration and acoustical environmental conditions were not found to be critical, but re-entry thermal environment was found to be very critical. A MAPP-OX thermal test facility was developed for full scale testing. The 1.5 inch radius leading edge survived thermal testing although testing was prematurely terminated due to a test fixture failure. During thermal testing, the 3.0 inch radius leading edge cracked but remained intact and did not spall; and the 6.0 inch radius nose cap underwent severe surface erosion. These two failures were attributed to a combination of design and material shortcomings and the severity of the MAPP-OX thermal test environment.		

Unclassified
Security Classification

14. KEY WORDS Alumina Ceramics Chemically Bonded Ceramics Component Fabrication Glide Re-Entry Trajectory Analyses Heat Transfer Analyses Low-Density Ceramics Non-Metallic Materials Refractory Composite Structures Refractory Materials Structural Analyses Thermal Insulation Thermal Protection Thermal Shock Tests Thoria Zirconia	LINK A		LINK B		LINK C	
	ROLE	WT	ROLE	WT	ROLE	WT

INSTRUCTIONS

1. **ORIGINATING ACTIVITY:** Enter the name and address of the contractor, subcontractor, grantee, Department of Defense activity or other organization (*corporate author*) issuing the report.

2a. **REPORT SECURITY CLASSIFICATION:** Enter the overall security classification of the report. Indicate whether "Restricted Data" is included. Marking is to be in accordance with appropriate security regulations.

2b. **GROUP:** Automatic downgrading is specified in DoD Directive 5200.10 and Armed Forces Industrial Manual. Enter the group number. Also, when applicable, show that optional markings have been used for Group 3 and Group 4 as authorized.

3. **REPORT TITLE:** Enter the complete report title in all capital letters. Titles in all cases should be unclassified. If a meaningful title cannot be selected without classification, show title classification in all capitals in parenthesis immediately following the title.

4. **DESCRIPTIVE NOTES:** If appropriate, enter the type of report, e.g., interim, progress, summary, annual, or final. Give the inclusive dates when a specific reporting period is covered.

5. **AUTHOR(S):** Enter the name(s) of author(s) as shown on or in the report. Enter last name, first name, middle initial. If military, show rank and branch of service. The name of the principal author is an absolute minimum requirement.

6. **REPORT DATE:** Enter the date of the report as day, month, year, or month, year. If more than one date appears on the report, use date of publication.

7a. **TOTAL NUMBER OF PAGES:** The total page count should follow normal pagination procedures, i.e., enter the number of pages containing information.

7b. **NUMBER OF REFERENCES:** Enter the total number of references cited in the report.

8a. **CONTRACT OR GRANT NUMBER:** If appropriate, enter the applicable number of the contract or grant under which the report was written.

8b, 8c, & 8d. **PROJECT NUMBER:** Enter the appropriate military department identification, such as project number, subproject number, system numbers, task number, etc.

9a. **ORIGINATOR'S REPORT NUMBER(S):** Enter the official report number by which the document will be identified and controlled by the originating activity. This number must be unique to this report.

9b. **OTHER REPORT NUMBER(S):** If the report has been assigned any other report numbers (*either by the originator or by the sponsor*), also enter this number(s).

10. **AVAILABILITY/LIMITATION NOTICES:** Enter any limitations on further dissemination of the report, other than those

imposed by security classification, using standard statements such as:

- (1) "Qualified requesters may obtain copies of this report from DDC."
- (2) "Foreign announcement and dissemination of this report by DDC is not authorized."
- (3) "U. S. Government agencies may obtain copies of this report directly from DDC. Other qualified DDC users shall request through _____."
- (4) "U. S. military agencies may obtain copies of this report directly from DDC. Other qualified users shall request through _____."
- (5) "All distribution of this report is controlled. Qualified DDC users shall request through _____."

If the report has been furnished to the Office of Technical Services, Department of Commerce, for sale to the public, indicate this fact and enter the price, if known.

11. **SUPPLEMENTARY NOTES:** Use for additional explanatory notes.

12. **SPONSORING MILITARY ACTIVITY:** Enter the name of the departmental project office or laboratory sponsoring (*paying for*) the research and development. Include address.

13. **ABSTRACT:** Enter an abstract giving a brief and factual summary of the document indicative of the report, even though it may also appear elsewhere in the body of the technical report. If additional space is required, a continuation sheet shall be attached.

It is highly desirable that the abstract of classified reports be unclassified. Each paragraph of the abstract shall end with an indication of the military security classification of the information in the paragraph, represented as (TS), (S), (C), or (U).

There is no limitation on the length of the abstract. However, the suggested length is from 150 to 225 words.

14. **KEY WORDS:** Key words are technically meaningful terms or short phrases that characterize a report and may be used as index entries for cataloging the report. Key words must be selected so that no security classification is required. Identifiers, such as equipment model designation, trade name, military project code name, geographic location, may be used as key words but will be followed by an indication of technical context. The assignment of links, rules, and weights is optional.